Lecture Notes in Electrical Engineering 546

Vijay Janyani
Ghanshyam Singh
Manish Tiwari
Antonio d'Alessandro *Editors*

Optical and Wireless Technologies

Proceedings of OWT 2018

Springer

Lecture Notes in Electrical Engineering

Volume 546

Series Editors

Leopoldo Angrisani, Department of Electrical and Information Technologies Engineering, University of Napoli Federico II, Napoli, Italy
Marco Arteaga, Departament de Control y Robótica, Universidad Nacional Autónoma de México, Coyoacán, Mexico
Bijaya Ketan Panigrahi, Electrical Engineering, Indian Institute of Technology Delhi, New Delhi, Delhi, India
Samarjit Chakraborty, Fakultät für Elektrotechnik und Informationstechnik, TU München, München, Germany
Jiming Chen, Zhejiang University, Hangzhou, Zhejiang, China
Shanben Chen, Materials Science & Engineering, Shanghai Jiao Tong University, Shanghai, China
Tan Kay Chen, Department of Electrical and Computer Engineering, National University of Singapore, Singapore, Singapore
Rüdiger Dillmann, Humanoids and Intelligent Systems Lab, Karlsruhe Institute for Technology, Karlsruhe, Baden-Württemberg, Germany
Haibin Duan, Beijing University of Aeronautics and Astronautics, Beijing, China
Gianluigi Ferrari, Università di Parma, Parma, Italy
Manuel Ferre, Centre for Automation and Robotics CAR (UPM-CSIC), Universidad Politécnica de Madrid, Madrid, Madrid, Spain
Sandra Hirche, Department of Electrical Engineering and Information Science, Technische Universität München, München, Germany
Faryar Jabbari, Department of Mechanical and Aerospace Engineering, University of California, Irvine, CA, USA
Limin Jia, State Key Laboratory of Rail Traffic Control and Safety, Beijing Jiaotong University, Beijing, China
Janusz Kacprzyk, Systems Research Institute, Polish Academy of Sciences, Warsaw, Poland
Alaa Khamis, German University in Egypt El Tagamoa El Khames, New Cairo City, Egypt
Torsten Kroeger, Stanford University, Stanford, CA, USA
Qilian Liang, Department of Electrical Engineering, University of Texas at Arlington, Arlington, TX, USA
Ferran Martin, Departament d'Enginyeria Electrònica, Universitat Autònoma de Barcelona, Bellaterra, Barcelona, Spain
Tan Cher Ming, College of Engineering, Nanyang Technological University, Singapore, Singapore
Wolfgang Minker, Institute of Information Technology, University of Ulm, Ulm, Germany
Pradeep Misra, Department of Electrical Engineering, Wright State University, Dayton, OH, USA
Sebastian Möller, Quality and Usability Lab, TU Berlin, Berlin, Germany
Subhas Mukhopadhyay, School of Engineering & Advanced Technology, Massey University, Palmerston North, Manawatu-Wanganui, New Zealand
Cun-Zheng Ning, Electrical Engineering, Arizona State University, Tempe, AZ, USA
Toyoaki Nishida, Graduate School of Informatics, Kyoto University, Kyoto, Kyoto, Japan
Federica Pascucci, Dipartimento di Ingegneria, Università degli Studi "Roma Tre", Rome, Italy
Yong Qin, State Key Laboratory of Rail Traffic Control and Safety, Beijing Jiaotong University, Beijing, China
Gan Woon Seng, School of Electrical & Electronic Engineering, Nanyang Technological University, Singapore, Singapore
Joachim Speidel, Institute of Telecommunications, Universität Stuttgart, Stuttgart, Baden-Württemberg, Germany
Germano Veiga, Campus da FEUP, INESC Porto, Porto, Portugal
Haitao Wu, Academy of Opto-electronics, Chinese Academy of Sciences, Beijing, China
Junjie James Zhang, Charlotte, NC, USA

The book series *Lecture Notes in Electrical Engineering* (LNEE) publishes the latest developments in Electrical Engineering - quickly, informally and in high quality. While original research reported in proceedings and monographs has traditionally formed the core of LNEE, we also encourage authors to submit books devoted to supporting student education and professional training in the various fields and applications areas of electrical engineering. The series cover classical and emerging topics concerning:

- Communication Engineering, Information Theory and Networks
- Electronics Engineering and Microelectronics
- Signal, Image and Speech Processing
- Wireless and Mobile Communication
- Circuits and Systems
- Energy Systems, Power Electronics and Electrical Machines
- Electro-optical Engineering
- Instrumentation Engineering
- Avionics Engineering
- Control Systems
- Internet-of-Things and Cybersecurity
- Biomedical Devices, MEMS and NEMS

For general information about this book series, comments or suggestions, please contact leontina.dicecco@springer.com.

To submit a proposal or request further information, please contact the Publishing Editor in your country:

China
Jasmine Dou, Associate Editor (jasmine.dou@springer.com)

India
Swati Meherishi, Executive Editor (swati.meherishi@springer.com)
Aninda Bose, Senior Editor (aninda.bose@springer.com)

Japan
Takeyuki Yonezawa, Editorial Director (takeyuki.yonezawa@springer.com)

South Korea
Smith (Ahram) Chae, Editor (smith.chae@springer.com)

Southeast Asia
Ramesh Nath Premnath, Editor (ramesh.premnath@springer.com)

USA, Canada:
Michael Luby, Senior Editor (michael.luby@springer.com)

All other Countries:
Leontina Di Cecco, Senior Editor (leontina.dicecco@springer.com)
Christoph Baumann, Executive Editor (christoph.baumann@springer.com)

**** Indexing: The books of this series are submitted to ISI Proceedings, EI-Compendex, SCOPUS, MetaPress, Web of Science and Springerlink ****

More information about this series at http://www.springer.com/series/7818

Vijay Janyani · Ghanshyam Singh ·
Manish Tiwari · Antonio d'Alessandro
Editors

Optical and Wireless Technologies

Proceedings of OWT 2018

Springer

Editors
Vijay Janyani
Department of Electronics and Communication Engineering
Malaviya National Institute of Technology
Jaipur, Rajasthan, India

Ghanshyam Singh
Department of Electronics and Communication Engineering
Malaviya National Institute of Technology
Jaipur, Rajasthan, India

Manish Tiwari
Department of Electronics and Communication Engineering
Manipal University Jaipur
Jaipur, Rajasthan, India

Antonio d'Alessandro
Department of Information Engineering, Electronics and Telecommunications
Sapienza University of Rome
Rome, Italy

ISSN 1876-1100 ISSN 1876-1119 (electronic)
Lecture Notes in Electrical Engineering
ISBN 978-981-13-6158-6 ISBN 978-981-13-6159-3 (eBook)
https://doi.org/10.1007/978-981-13-6159-3

Library of Congress Control Number: 2018968086

© Springer Nature Singapore Pte Ltd. 2020
This work is subject to copyright. All rights are reserved by the Publisher, whether the whole or part of the material is concerned, specifically the rights of translation, reprinting, reuse of illustrations, recitation, broadcasting, reproduction on microfilms or in any other physical way, and transmission or information storage and retrieval, electronic adaptation, computer software, or by similar or dissimilar methodology now known or hereafter developed.
The use of general descriptive names, registered names, trademarks, service marks, etc. in this publication does not imply, even in the absence of a specific statement, that such names are exempt from the relevant protective laws and regulations and therefore free for general use.
The publisher, the authors and the editors are safe to assume that the advice and information in this book are believed to be true and accurate at the date of publication. Neither the publisher nor the authors or the editors give a warranty, expressed or implied, with respect to the material contained herein or for any errors or omissions that may have been made. The publisher remains neutral with regard to jurisdictional claims in published maps and institutional affiliations.

This Springer imprint is published by the registered company Springer Nature Singapore Pte Ltd.
The registered company address is: 152 Beach Road, #21-01/04 Gateway East, Singapore 189721, Singapore

Conference Committee Members

Organizing Committee

Patron

Prof. Udaykumar R. Yaragatti, Director, MNIT Jaipur

General Chairs

Prof. Vijay Janyani, MNIT Jaipur
Prof. Ghanshyam Singh, MNIT Jaipur
Prof. Manish Tiwari, Manipal University Jaipur

Conveners

Dr. Sandeep Vyas, JECRC University, Jaipur
Dr. Amit Kumar Garg, Manipal University Jaipur
Dr. Ravi Maddila, MNIT Jaipur

Organizing Secretaries

Dr. Ritu Sharma, MNIT Jaipur
Mr. Dinesh Kumar Yadav, Manipal University Jaipur
Mr. Ashok Kumar, GWEC Ajmer
Mr. Nidhish Tiwari, Jagannath University, Jaipur
Dr. Ashish Kr. Ghunawat, MNIT Jaipur

IETE Oversight Committee

Prof. Deepak Bhatnagar, FIETE
Prof. S. K. Bhatnagar, FIETE
Mr. K. M. Bajaj, FIETE

Sponsorship Committee

Mr. Lokesh Sharma, Manipal University Jaipur
Mr. Sanjeev Yadav, GWEC Ajmer

Mr. Ashok Kumar, GWEC Ajmer
Mr. Narendra Kr. Godara, MNIT Jaipur

Registration Committee

Dr. Ravi Maddila, MNIT Jaipur
Dr. Mukesh Gupta, MNIT Jaipur
Dr. Amit Garg, Manipal University Jaipur
Dr. Monika Mathur, SKIT Jaipur
Mr. Bipin Kumar Saw, MNIT Jaipur

Publication Committee

Dr. Ritu Sharma, MNIT Jaipur
Dr. Seema Varma, Banasthali University, Tonk
Dr. Rekha Mehra, GEC Ajmer
Dr. Mukesh Gupta, MNIT Jaipur
Mr. Ashish Kumar, MNIT Jaipur

Hospitality Committee

Dr. C. Periasamy, MNIT Jaipur
Dr. Ashok Sirohi, RCEW Jaipur
Mr. K. R. Yadav, Government Ram Chandra Khaitan Polytechnic College, Jaipur
Mr. Abhinav Bhatnagar, MNIT Jaipur
Dr. Sourabh Sahu, MNIT Jaipur

International Advisory Committee

Prof. Hiroyuki Tsuda, Keio University, Japan
Prof. Ali Gharsallah, University of Tunis E. M., Tunisia
Prof. Buryy Oleh Anatolievyach, LPNU, Ukraine
Prof. Ajoy Kar, Heriot-Watt University, Edinburgh, UK
Dr. Suchandan Pal, CEERI Pilani, India
Dr. Akshay Kr Rathore, Concordia University, Canada
Prof. Takasumi Tanabe, Keio University, Japan
Prof. Kolin Poul, IIT Delhi, India
Prof. Konstantin Kozadaev, Belarusian State University, Minsk, Belarus
Dr. Lotfi Osman, University of Carthage, Tunisia
Prof. Mário F. S. Ferreira, University of Aveiro, Portugal
Dr. Miklos Veres, HAS, Budapest, Hungary
Prof. Sergii Ubizskii, LPNU, Ukraine
Prof. Yuri Shpolyanskiy, University of Saint Petersburg, Russia
Prof. Toshiharu Saiki, Keio University, Japan
Dr. Bishnu Prasad Gautam, WAKHOK, Japan
Dr. Reza Abdi-Ghaleh, University of Bonab, Iran

Technical Program Committee

Prof. Sandeep Sancheti, President, Manipal University Jaipur
Prof. Vishwanath Sinha, MNIT Jaipur
Prof. K. K. Sharma, MNIT Jaipur
Prof. Vijay Janyani, MNIT Jaipur
Prof. Manish Tiwari, Manipal University Jaipur
Prof. Ghanshyam Singh, MNIT Jaipur
Dr. Kalpana Dhaka, IIT Guwahati, India
Dr. Manish Mathew, CEERI Pilani, India
Dr. Preetam Kumar, IIT Patna
Dr. C. Periasamy, MNIT Jaipur
Dr. Sanjeev Kumar Metya, National Institute of Technology, Arunachal Pradesh
Dr. Narendra Kumar Yadav, JECRC University, Jaipur
Dr. Bramha P. Pandey, GLA University, Mathura
Dr. Sanyog Rawat, Manipal University, Jaipur
Dr. Anil Yadav, Amity University, Gurgaon
Dr. Dinesh Goyal, Suresh Gyan Vihar University, Jaipur
Dr. Ashok Sirohi, RCEW Jaipur
Dr. Jitendra Kumar Deegwal, EC Ajmer
Dr. Nagesh Janrao, Government Polytechnic, Pune

Preface

Optical and wireless technologies are advancing at an accelerating rate recently. The traditional approaches to providing high data rates to the masses are transforming and expanding in a way that is beyond our imagination. The challenges in providing uninterrupted data and broadband communications have not changed. Our mission as a technical community is to understand these challenges and find ways to mitigate them. This includes the development and management of appropriate channels, novel devices, new protocols, efficient networks, and their integration. Keeping in view the amalgamation of these issues, the proceedings of the Second International Conference on Optical and Wireless Technologies (OWT 2018) is being presented herewith.

The conference (OWT 2018) was held in the campus of Malaviya National Institute of Technology, Jaipur, during February 10–11, 2018. A total of 120 participant, including the invited speakers, contributing authors, and attendees participated in the conference. The participants were explored to a broad range of topics critical to our society and industry in the related areas. The conference provided an opportunity to exchange ideas among global leaders and experts from academia and industry in topics like optical materials, optical signal processing and networking, photonic communication systems and networks, all-optical systems, microwave photonics, optical devices for optical communications, nonlinear optics, nanophotonics, software-defined and cognitive radio, signal processing for wireless communications, antenna systems, spectrum management and regulatory issues, vehicular communications, wireless sensor networks, machine-to-machine communications, and cellular–WiFi integration.

Apart from a high-quality contributed paper presented by delegates from all over the country and abroad, the conference participants also witnessed a informative demonstrations and technical sessions from the industry as well as invited talks from renowned experts aimed at advances in these areas. Overall response to the conference was quite encouraging. A large number of papers were received. After a rigorous editorial and review process, 66 papers were invited for the presentation during the conference. Among the presented papers, 59 papers were selected for inclusion in the conference proceedings. We are confident that the papers presented

in this proceeding shall provide a platform for young as well as experienced professionals to generate new ideas and networking opportunities.

The editorial team members would like to extend gratitude and sincere thanks to all contributed authors, reviewers, panelist, local organizing committee members, and the session chairs for paying attention to the quality of the publication. We are thankful to our sponsors for generously supporting this event and Institutional Partner (MNIT Jaipur) for providing all the necessary support, encouragement, and infrastructure in this beautiful campus. At last, we pay the highest regard to the Irisworld Science & Technology Education and Research (IRISWORLD), a "not-for-profit" society from Jaipur for extending support for financial management of OWT 2018.

Best Wishes from:

Jaipur, India	Prof. Vijay Janyani
Jaipur, India	Prof. Ghanshyam Singh
Jaipur, India	Prof. Manish Tiwari
Rome, Italy	Prof. Antonio d'Alessandro

Acknowledgements

The editors wish to extend heartfelt acknowledgement to all contributing authors, esteemed reviewers for their timely response, members of the various organizing committee, and production staff whose diligent work put shape to the OWT 2018 proceedings. We especially thank our dedicated reviewers for their volunteering efforts to check the manuscript thoroughly to maintain the technical quality and for useful suggestions.

We also pay our best regards to the faculty members from Institutional Partners (MNIT Jaipur and Manipal University Jaipur) for extending their enormous assistance during the conference-related assignments, especially to Mr. Dinesh Kumar Yadav, Mr. Lokesh Kumar from Manipal University Jaipur; Sanjeev Yadav, Ashok Kumar, Jitendra Deegwal from Government Engineering College, Ajmer; Mr. Nidhish Tiwari from JNIT Jaipur; Mr. Ramesh Dewanda, Executive Member, Irisworld Society Jaipur; and Sh. Narendra Godara from MNIT Jaipur.

We also acknowledge the financial supports received from our esteemed sponsors such as JV Micronics, IETE Rajasthan Centre Jaipur, and OSA student chapter of MNIT Jaipur. At last, we extend our sincere thanks to Springer for agreeing to be our publishing partner. Especially, the efforts made by Swati Meherishi, Executive Editor, are highly appreciable.

Prof. Vijay Janyani
Prof. Ghanshyam Singh
Prof. Manish Tiwari
Prof. Antonio d'Alessandro

Our Reviewers

Dr. Surendra Agarwal, NIT Kurukshetra, skagarwal5@rediffmail.com
Dr. Mushtaq Ahmed, MNIT Jaipur, India, mahmed.cse@mnit.ac.in
Dr. Parvez Alvi, Banasthali University, drpaalvi@gmail.com
Dr. Mohd. Samar Ansari, Malaviya National Institute of Technology, Jaipur, msansari.ece@mnit.ac.in
Dr. Ashwini Arya, KAIST, Republic of Korea, ashwiniarya.iitr@gmail.com
Dr. Ramesh Battula, Malaviya National Institute of Technology, Jaipur, ramsbattula@gmail.com
Dr. Sanjay Dabhole, Sant Gajanan Maharaj Rural Polytechnic, sankop1217@gmail.com
Dr. Upena Dalal, Sardar Vallabhbhai National Institute of Technology, Surat, upena_dalal@yahoo.com
Dr. Jitendra Deegwal, Government Engineering College, Ajmer, Rajasthan, jitendradeegwal@gmail.com
Dr. Kalpana Dhaka, Indian Institute of Technology Guwahati, dhaka.kalpana@gmail.com
Dr. Tarun Dubey, Manipal University Jaipur, tarunkumar.dubey@jaipur.manipal.edu
Dr. Umesh Dwivedi, Amity University, Jaipur, Rajasthan, umeshkudwivedi@gmail.com
Mr. Kuldeep Goswami, Government Women Engineering College Ajmer, kuldeep4career@gmail.com
Dr. Dinesh Goyal, Suresh Gyan Vihar University, dinesh8dg@gmail.com
Dr. Mukesh Gupta, Malaviya National Institute of Technology, Jaipur, mkgupta06@gmail.com
Dr. Nikhil Deep Gupta, Malaviya National Institute of Technology, Jaipur, 2012rec9530@mnit.ac.in
Dr. Tawfik Ismail, NILES, Cairo University, tawfik@niles.edu.eg
Dr. Shruti Jain, JUIT, Waknaghat, shruti.jain@juit.ac.in
Dr. Nagesh Janrao, Technical Education, janrao.nl@gmail.com
Dr. Alok Joshi, JIIT, Noida, 20.alok@gmail.com

Dr. Amit Joshi, Malaviya National Institute of Technology, Jaipur, amjoshi.ece@mnit.ac.in
Dr. Rajesh Khanna, Thapar University, rkhanna@thapar.edu
Dr. Vijaya kumar Krishnasamy, MNIT Jaipur, vijayk.ee@mnit.ac.in
Dr. Arjun Kumar, Intel, akdec.iitr@gmail.com
Mr. Ashok Kumar, GWEC Ajmer, India, kumarashoksaini@gmail.com
Dr. Preetam Kumar, Indian Institute of Technology Patna, pkumar@iitp.ac.in
Dr. Ravi Maddila, Malaviya National Institute of Technology, Jaipur, rkmaddila.ece@mnit.ac.in
Mr. Saurabh Maheshwari, Government Women Engineering College Ajmer, dr.msaurabh@gmail.com
Dr. Manish Mathew, CEERI Pilani, manish.mathew@gmail.com
Dr. Monika Mathur, Rajasthan Technical University, monikamathur16@gmail.com
Mr. Sudarshan Maurya, Government Mahila Engineering College, maurya.sudarshan@gmail.com
Dr. Arka Prokash Mazumdar, MNIT Jaipur, apmazumdar.cse@mnit.ac.in
Dr. Rekha Mehra, Government Engineering College, Ajmer, mehrarekha710@gmail.com
Dr. Sanjeev Metya, National Institute of Technology, Arunachal Pradesh, smetya@ieee.org
Dr. Satyasai Nanda, Malaviya National Institute of Technology, Jaipur, nanda.satyasai@gmail.com
Prof. Lotfi Osman, Higher School of Communication of Tunis, University of Carthage, lotfi.osman@supcom.tn
Dr. Vipin Pal, NIT Shillong, vipinrwr@yahoo.com
Dr. Trilochan Panigrahi, National Institute of Technology Goa, tpanigrahi80@gmail.com
Dr. Girish Parmar, Rajasthan Technical University, girish_parmar2002@yahoo.com
Dr. C Periasamy, Malaviya National Institute of Technology, Jaipur, cpsamy.ece@mnit.ac.in
Dr. Emmanuel Pilli, Malaviya National Institute of Technology, Jaipur, espilli.cse@mnit.ac.in
Mr. Pravin Prajapati, Gujarat Technological University, ec.pravin.prajapati@adit.ac.in
Dr. Sanyog Rawat, Manipal University Jaipur, sanyog.rawat@jaipur.manipal.edu
Prof. Kanad Ray, Amity University, Jaipur, Rajasthan, kanadray00@gmail.com
Dr. Chitrakant Sahu, MNIT Jaipur, chitrakant.ece@mnit.ac.in
Dr. Preeta Sharan, The Oxford College of Engineering, Bangalore, sharanpreeta@gmail.com
Dr. Jankiballabh Sharma, Rajasthan Technical University, jbsharma@rtu.ac.in
Ms. Neeru Sharma, Jaypee University of Information Technology, neeru.sharma@juit.ac.in
Dr. Ritu Sharma, MNIT Jaipur, rsharma.ece@mnit.ac.in
Dr. Sumit Srivastava, Manipal University Jaipur, sumit.310879@gmail.com

Dr. Fazal Talukdar, National Institute of Technology, Silchar, fatalukdar@gmail.com
Dr. Meenakshi Tripathi, MNIT Jaipur, mtripathi.cse@mnit.ac.in
Dr. Yogesh Trivedi, Nirma University, yogesh.trivedi@nirmauni.ac.in
Prof. Hiroyuki Tsuda, Keio University, tsuda@elec.keio.ac.jp
Prof. Manisha Upadhyay, Nirma University, manisha.upadhyay@nirmauni.ac.in
Dr. Karan Verma, Universiti Teknologi Petronas, vermakara@gmail.com
Dr. Pankaj Verma, National Institute of Technology, Kurukshetra, pankaj@nitkkr.ac.in
Mr. Santosh Vipparthi, MNIT Jaipur, skvipparthi@mnit.ac.in
Dr. Rajesh Vishwakarma, JUET Noida, rajesh.vishwakarma@juet.ac.in
Dr. Sandeep Vyas, Malaviya National Institute of Technology, Jaipur, vyas.sandeep@vitej.ac.in
Mr. Dinesh Yadav, Manipal University Jaipur, dinesh.yadav@jaipur.manipal.edu
Dr. Narendra Yadav, JECRC University, narensinghyadav@yahoo.com
Mr. Sanjeev Yadav, Government Women Engineering College Ajmer, sanjeev.yadav.in@ieee.org
Dr. Rajveer Yaduvanshi, AIACTR, yaduvanshirs007@gmail.com
Prof. Vijay Janyani, Malaviya National Institute of Technology, Jaipur, vjanyani.ece@mnit.ac.in
Prof. Ghanshyam Singh, Malaviya National Institute of Technology, Jaipur, gsingh.ece@mnit.ac.in
Prof. Manish Tiwari, Manipal University Jaipur, mt.jaipur@gmail.com

Invited Speakers

Prof. Antonio d'Alessandro, Department of Information Engineering, Electronics and Telecommunications, Sapienza University of Rome, Italy

Profile Summary: Professor Antonio d'Alessandro is working with Department of Information Engineering, Electronics and Telecommunications of Sapienza University of Rome. He had been the post-doctoral member of Technical Staff with Bell Communication Research, New Jersey USA and associated with various scientific societies such as President of the Italian Liquid Crystal Society (since 2010), Vice President of IEEE Photonics Society—Italy Chapter (2016), Member of the Optical Society of America. He currently serves as Associate Editor of IEEE Photonics Journal and as referee for the following scientific journals: *IEEE Photonics Technology Letters, Molecular Crystals and Liquid Crystals, Optics Express, OSA Journal of Applied Optics, Journal of Applied Physics, IOP Journal of Physics D: Applied Physics, Journal of Optics A: Pure and Applied Optics*. He has been referee for the Evaluation of research projects on behalf of the Italian Ministry of Education, University and Research and the Evaluation of research products on behalf of ANVUR.

Dr. Rajesh Kumar, Malaviya National Institute of Technology Jaipur

Profile Summary: Dr. Rajesh Kumar received the B.Tech. degree from National Institute of Technology (NIT), Kurukshetra, India in 1994, the M.E. from Malaviya National Institute of Technology (MNIT), Jaipur, India in 1997 and the Ph.D. degree from MNIT, University of Rajasthan, India in 2005. Since 1995, he has been a Faculty Member in the Department of Electrical Engineering, MNIT, Jaipur, where he is serving as an Associate Professor. He was Post Doctorate Research Fellow in the Department of Electrical and Computer Engineering at the National University of Singapore (NUS), Singapore, from 2009 to 2011. His field of interest includes theory and practice of intelligent systems, machine learning, bio and nature inspired algorithms, power conversion, smart grids, robotics and bioinformatics. Dr. Kumar is a Senior Member IEEE, Fellow Member IE (INDIA), Fellow Member IETE, Senior Member IEANG and Life Member ISTE.

Dr. Tawfik Ismail, Cairo University, Egypt

Profile Summary: Dr. Tawfik Ismail received the B.Sc. (with honors) from the department of Electronics and Communication, Faculty of Engineering, Cairo University, Giza, Egypt, in 2001. He joined the National Institute of Laser Enhanced Science (NILES) in the department of Engineering Application of Laser (EAL), Cairo University in 2003 as research Assistant. He received the M.Sc. and Ph.D. degrees in the department of EAL in 2009 and 2013, respectively. He is currently an Assistant Professor in the Department of Engineering Applications of Laser (NILES), Cairo University, Egypt. Dr. Tawfik's research interests include optical and wireless networks, IoT, Biomedical telemetry and Optoelectronics. Dr. Tawfik is currently the CoPI of two successful research projects funded by the National Telecom Regularity Authority (NTRA) and Information Technology Industry Development Agency (ITIDA). These projects with collaboration between University of Cairo, Egypt and University of Toronto, Canada.

Dr. Kalpana Dhaka, Indian Institute of Technology Guwahati

Profile Summary: Kalpana Dhaka received the B.E. degree in electronics and communication engineering from the Mody College of Engineering, Rajasthan, in 2005, the M.Tech. degree in information and communication technology from the Dhirubhai Ambani Institute of Information and Communication Technology, Gujarat, in 2008 and the Ph.D. degree in electrical engineering from the Indian Institute of Technology Delhi, New Delhi, in January 2013. Since May 2013, she is Assistant Professor with the Department of EEE, Indian Institute of Technology Guwahati. Her research interests include cooperative communications, multi-hop relaying systems, device-to-device communications, and MIMO wireless communication.

Prof. Seema Verma, Banasthali Vidyapith

Profile Summary: Professor Seema Verma, Scholar of Electronics & Communication stream, is working as Dean, School of Aviation, Banasthali Vidyapith, India. She is associated with various scientific/professional societies such as Fellow of IETE, life Member of Indian Science Congress, Life Member, *Indian Society for Technical Education* (*ISTE*), & member of International Association of Engineers, (IAENG). She has produced 15 Ph.Ds. Currently, 5 students are working for their doctoral work under her supervision in the areas of wireless sensor & Ad-hoc networks (Aircraft Ad-hoc Network). She has authored close to 100 papers in various peer-reviewed Journals & Conferences. She has authored 6 books with renowned publishers. She has been granted 3 fully funded projects from UGC & AICTE. She currently serves as member of Editorial board of various scientific journals, member of organizing committee of various national/international conferences. She is a member of expert committee of National Board of Accreditation (NBA). She has been an expert for the Evaluation of research (Ph.D.) thesis of various Indian Universities. She is a recipient of IBM Mentor Award, Certificate of Appreciation from Texas Instruments, Certificate of Excellence in Education, Digital Seal from Institute of women of Aviation Worldwide[iWOAW], Global Education Excellence

Awards, 2017, "Most Innovative Female Teacher of Electronics and Telecommunications in Rajasthan" by Prime time news channel.

Dr. Preetam Kumar, India Institute Technology Patna

Profile Summary: Preetam Kumar is currently working as an Associate Professor in the Department of Electrical Engineering, India Institute Technology Patna. He did his Ph.D. from IIT Kharagpur in the area of Wireless Cellular Communications. He was associated with Birla Institute of Technology Mesra, Ranchi from 2003 to 2008 before joining IIT Patna. He has in total 17 years of teaching, research and industry experience. Physical Layer Issues in Wireless Communications, Error Control Coding and Digital Communication Systems are his areas of research interest. He has extensively published several research papers in various refereed Journals and National/International Conferences of repute. He is also serving as an Editorial Board Member of Springer's Wireless Personal Communications. He was the Organizing Chair of 1st IEEE 5G Symposium in Asia held at IIT Patna in 2016. He is a regular reviewer of premier journals published by IEEE, Elsevier and Springer and served as Technical Program Committee member of several IEEE conferences.

Contents

About the Editors

Dr. Vijay Janyani obtained Bachelors and Masters degrees in Electronics and Communication Engineering from Malaviya Regional Engineering College Jaipur (now MNIT Jaipur) and Ph.D. from the George Green Institute (GGIEMR) of Nottingham, UK under Commonwealth Scholarship Plan in 2005. He is a recipient of various awards & honours such as the Derrick Kirk Prize of University of Nottingham, Commonwealth Scholarship UK, AICTE Career Award etc. He has completed various national and international Government funded major research projects funded by UKIERI, DRDO, DST etc., in collaboration with UK, Japan, Egypt, Ukraine etc. He has been a visiting faculty to AIT Bangkok and UoTEM Tunisia. His current research interests include Optical Communication, Optoelectronics and Photonics, Numerical Modelling, Nonlinear Optics, RF and Microwaves, Optical Networks, Solar Energy.

Dr. Ghanshyam Singh received Bachelors in ECE from National Institute of Technology Silchar, Masters and Ph.D. degrees in ECE from Malaviya National Institute of Technology Jaipur. He has been Visiting Scholar/Visiting Professor at the Department of Physics, Herriot Watt University, Edinburgh, UK, the Institute of Photonics, University of Eastern Finland, Joensuu campus, Finland (CIMO Fellowship, Government of Finland) and Department of EEE, Keio University, Hiyoshi Campus, Japan. Dr. Singh is engaged with joint research projects with partner researchers from Keio University (Japan), University of Vienna (Austria) University of Cairo (Egypt) and LNPU, Lviv (Ukraine). His current research interest includes Antenna engineering, Micro and Nano-structured photonic devices, and networks and non-linear characteristics of photonic crystal fibers.

Dr. Manish Tiwari received Ph.D. in ECE in the field of Photonics from MNIT Jaipur. Presently, he is Professor in Department of ECE at Manipal University Jaipur. He has been visiting researcher to City University, London under UKIERI project in Microstructured Optical Fibers during 2010 and 2011 and Tsinghua University, Beijing during 2016 Dr. Tiwari has presented talk in PolyU-Hong Kong, KMUT-Bangkok, Kasetsart University-Bangkok, City University-London and several UKIERI workshops. He has also served on panel of experts in various workshops by CSTT, MHRD, Government of India. His current research interest includes Micro/Nano-structure photonic devices, nonlinear optics and photonic crystal fibers.

Prof. Antonio d'Alessandro is working with Department of Information Engineering, Electronics and Telecommunications of Sapienza University of Rome. He had been the post-doctoral member of Technical Staff with Bell Communication Research, New Jersey, USA and associated with various scientific societies such as President of the Italian Liquid Crystal Society (since 2010), Vice President of IEEE Photonics Society—Italy Chapter (2016), Member of the Optical Society of America. He currently serves as Associate Editor of *IEEE Photonics Journal* and as referee for the following scientific journals: *IEEE Photonics Technology Letters*, *Molecular Crystals and Liquid Crystals*, *Optics Express*, OSA *Journal of Applied Optics*, *Journal of Applied Physics*, IOP *Journal of Physics D: Applied Physics*, *Journal of Optics A: Pure and Applied Optics*. He has been referee for the Evaluation of research projects on behalf of the Italian Ministry of Education, University and Research and the Evaluation of research products on behalf of ANVUR.

Performance Evaluation of Transparent and Non-transparent Flexible Antennas

Maitri Kantharia, Arpan Desai, Parthesh Mankodi, Trushit Upadhyaya and Riki Patel

Abstract Performance evaluation of transparent and non-transparent flexible wearable antennas using different substrates is analysed and presented over here. Substrate in the form of PET and jeans is used, whereas conductive materials like AgHT-4 and Copper sheet are used as patch and ground, respectively. Performance evaluation in terms of S11, gain and radiation pattern is presented. PET which is transparent in nature is embedded with AgHT-4 to make a flexible transparent antenna. Jeans is used with copper sheet to design a non-transparent antenna. The electrical conductivity of copper is higher compared to AgHT-4, which leads to higher gain and return loss but it has a disadvantage of being non-transparent. The transparent flexible antenna resonates at 2.42 and 3.88 GHz making it suitable for its use in WLAN and WiMAX applications.

Keywords Flexible · Transparent · Non-transparent · Wearable · Antenna · Wireless applications

1 Introduction

In any communication systems, antennas are useful where electromagnetic wave is to be radiated or absorbed [1]. Wireless communication has seen new trends in antenna design such as metamaterial antennas [2, 3], fractal antennas [4], ultra-wideband (UWB) and flexible antennas [5, 6]. The addition of flexibility to such antennas makes sure that it can be used on the surfaces, which are not having planar geometry. In defence, the antennas can mainly be used in the form of wearable ones [7]. Body-centric communications play important role and presents wide variety of applications. Development of wearable low power device has increased the requirement of solution

M. Kantharia · P. Mankodi
G. H. Patel College of Engineering and Technology, V.V.Nagar, Anand, Gujarat, India

A. Desai (✉) · T. Upadhyaya · R. Patel
Charotar University of Science and Technology, Changa, Gujarat, India
e-mail: arpandesai.ec@charusat.ac.in

© Springer Nature Singapore Pte Ltd. 2020

V. Janyani et al. (eds.), *Optical and Wireless Technologies*,
Lecture Notes in Electrical Engineering 546,
https://doi.org/10.1007/978-981-13-6159-3_1

for WBANs (wireless body area networks) and WSNs (wireless sensor networks) which is lightweight, low cost, flexible, bendable and easy to maintenance on-body antennas to provide a reliable WBANs for personal devices [8]. It is also widely used in applications like in fire-fighters, police, military operations [9], body motion, heart rate, blood pressure monitoring and other healthcare services [10, 11], along with industrial monitoring [12]. Flexible antennas are also used for monitoring the patient through computer or mobile phone technology [13]. Wearable flexible antennas are used as R.F. sensor because they are easily integrated into garments [14]. Several techniques to increase the radiation efficiency is used in which the quarter wavelength height is required, but the overall size may increase and it is challenging to make the antenna flexible and re-configurable [15]. In [16], authors have designed the wearable antenna using substrate as foam material for fire-fighters which resonates at 2.4 GHz. In paper [17], microstrip line on plastic perforated substrate fitted over the 50 mm $\times$ 350 mm ground plane after sticking copper tape on the substrate is used, which is mainly used for Wi-Fi and HiperLAN frequency bands. In paper [18], UWB antenna based on slotted design is used where the performance parameter of the antenna is changed due to its interfacing with the human body. There are two different types of antennas for transmission and reception where one antenna is placed far from the body and the other is placed on the body. The antenna works in the range of 5.25 GHz for WLAN applications. Another ultra-wideband-slotted flexible antenna using Mylar Polyester film substrate having 0.3 mm thickness is designed which is used for WLAN, WiMAX, and UWB band applications [19]. The electro textile or E-Textile which are known as conductive fabric with common examples like silver-plated knitted fabric and nickel-plated woven fabric are used mostly for Bluetooth Technology operating in the ISM band of frequencies. The ordinary textile such as cotton is used as a substrate material to make the antenna operable [20]. In paper [21]; flexible wearable antenna using the folded slot and a stub which is re-configurable where the re-configurability is achieved by turning ON and OFF a PIN diode is proposed. This antenna is used for monitoring the patient where the data transmission is done by WBAN and WiMAX bands, respectively. The authors have also proposed a flexible wearable antenna using cotton, jeans and silk fabrics as a substrate which operates for ISM frequency band applications at 2.4–2.4875 GHz frequency [22]. Another antenna based on copper film and an AgHT-8 film is presented where the use of copper makes the antenna semi-transparent [23]. In [24], the flexible and wearable antenna is designed for Frequency Modulation radio applications at 100 MHz using jeans as a substrate. The antenna gain of the transparent antenna can be increased by using slotted monopole structure [25] and the size of the antenna can be lowered by using the concept of the electrically small antenna [26, 27].

In this paper; we have done the performance evaluation of flexible wearable antennas using transparent and non-transparent materials. Due to the transparency of the antennas, they are undetectable which makes it a better option over non-transparent antennas. The transparent antenna presented here resonates at 2.42 and 3.88 GHz which makes it suitable for WLAN and WiMAX applications. The antenna design geometry and simulation results are presented in Sects. 2 and 3. Section 4 presents the conclusion.

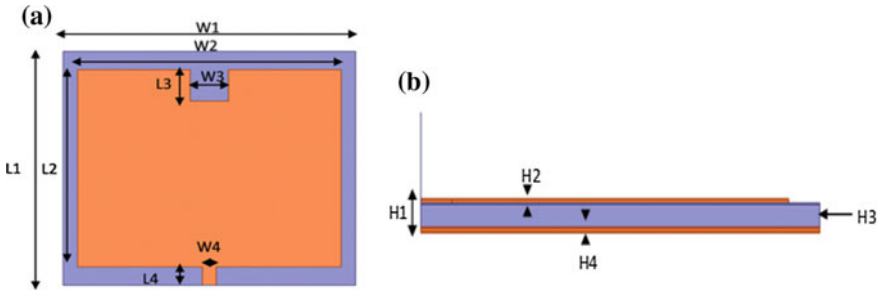

Fig. 1 The patch antenna geometry design **a** top view **b** side view

Table 1 Substrate materials for flexible antenna

Material	Dielectric constant	Loss tangent	Height (mm)
PET	2.5	0.0001	1
Jeans	1.7	0.05	1

Table 2 Materials for substrate, patch and ground

Antenna layer	Substrate	Patch	Ground
Material (transparent antenna)	PET	AgHT-4	AgHT-4
Material (non-transparent antenna)	Jeans	Copper	Copper

2 Antenna Design

The geometry of the flexible antenna using different flexible materials like PET and Jeans is shown in Fig. 1. The flexible antenna is employed by the use of transparent and non-transparent material as a substrate. Dielectric values vary depending on the texture of the material. The PET material which is transparent has a dielectric constant of 2.5 with a loss tangent of 0.0001 and thickness 1 mm. The jean which is non-transparent has a dielectric constant of 1.7 with tangent loss of 0.05 and thickness 1 mm which is listed in Table 1.

The AgHT-4 and thin copper foil are used as conducting material to build the patch and ground for two different antennae with a combination of PET and jeans as a substrate is shown in Table 2.

The flexible antenna proposed here has an overall dimension of $45.13 \times 53.21 \times 1\ \text{mm}^3$. The antenna geometry dimensions are as listed in Table 3.

Table 3 Antenna dimensions (in mm)

Parameter	Transparent antenna	Non-transparent antenna
Substrate height (H3), width (W1) and length (L1)	1, 53.21, 45.13	1, 53.21, 45.13
Dielectric constant of substrate	2.5	1.7
Patch height (H2), length (L2) and width (W2)	0.177, 38, 48	0.2, 38, 48
Ground plane height (H4), length (L1) and width (W1)	0.177, 45.13, 53.21	0.2, 45.13, 53.21
Feed-line width (W4) and length (L4)	2.55, 22.565	2.55, 22.565
Total height (H1)	1.354	1.4
W3, L3	7, 6	7, 6

3 Results and Discussion

The simulations carried out using HFSS software are presented for the transparent and non-transparent flexible antenna designed using conducting materials in the form of AgHT-4, PET, Jeans and Copper over here. The simulations were carried out in HFSS software.

Figure 2 shows the return loss for both the antennas made up of transparent and non-transparent conducting/substrate materials. The antenna made up of PET substrate and AgHT-4 shows a return loss of −18.92 dB and −16.14 dB for 2.42 GHz and 3.88 GHz frequency respectively. The antenna designed using Jeans and Copper sheet has a return loss of −15.05 and −17.38 dB for 2.93 and 5.71 GHz frequency. Copper having conductivity value which is very much higher than AgHT-4 and the substrates having varied dielectric constant leads to shift in the resonant frequency and more bandwidth.

The radiation patterns for E-H plane of designed antennas are presented in Fig. 3. An Omni-directional pattern is obtained for both antennas at lower frequencies while the radiation pattern for higher frequency resembles dipole pattern making the proposed transparent flexible antenna useful in wireless applications.

Figure 4 indicates the current distribution for both the antennas. Current is distributed near sides and feed line in transparent antenna while it is distributed on the outer line of conducting material in case of non-transparent antenna.

The Gain of transparent and non-transparent are shown in Fig. 5 which shows that the gain values for both the antennas are at an acceptable level. Transparent antenna

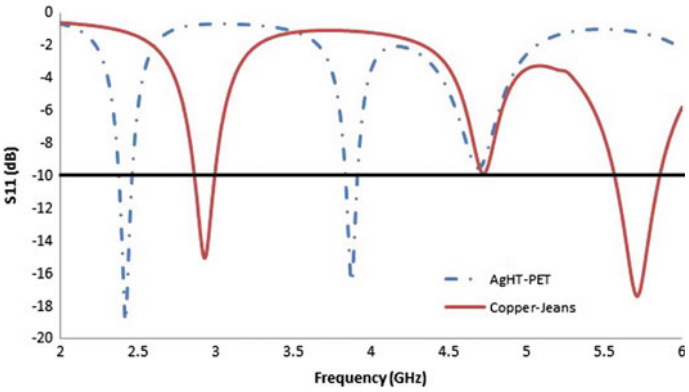

Fig. 2 Comparision of S11 for transparent (dashed) and non-transparent (solid) flexible antenna

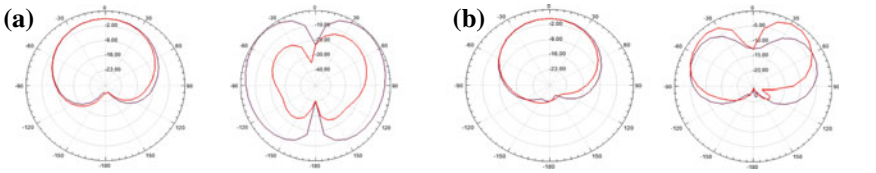

Fig. 3 Radiation pattern E (red) and H (purple) plane in **a** transparent flexible antenna and **b** non-transparent flexible antenna

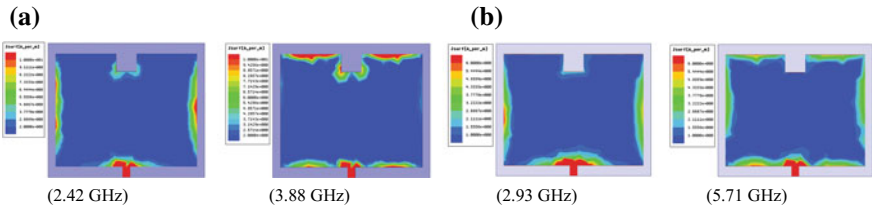

Fig. 4 Current distribution pattern **a** transparent flexible antenna and **b** non-transparent flexible antenna

shows a comparatively higher gain value which makes it a better option for its use in electronics wearable applications as it is invisible to bare eyes.

Table 4 shows the antenna characteristics in terms of return loss, gain and impedance bandwidth. Transparent flexible antenna resonates at 2.42 and 3.88 GHz having return loss of −18.92 and −16.14 dB. Impedance bandwidth is 3.72 and 2.06% with gain of 1.40 and 0.93 dBi for lower and higher frequency bands. In comparison to the transparent antenna; the non-transparent antenna resonates at 2.93 and 5.71 GHz having a return loss of −15.02 and −16.14 dB. Impedance bandwidth is 4.44 and 4.90% with gain of 1.21 and 0.91 dBi for lower and higher frequency bands.

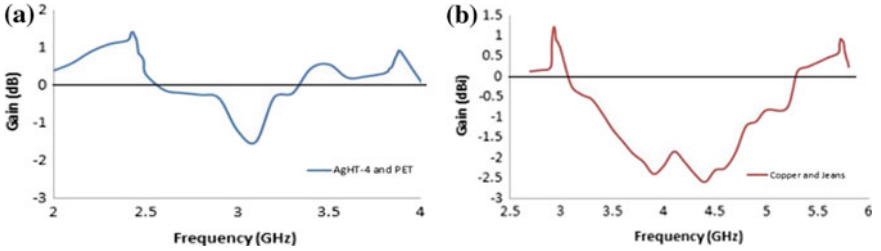

Fig. 5 Gain versus frequency **a** transparent flexible antenna and **b** non-transparent flexible antenna

Table 4 Antenna characteristics

Antenna characteristics	Transparent antenna		Non-transparent antenna	
Resonance frequency (GHz)	2.42	3.88	2.93	5.71
Return loss (dB)	−18.92	−16.14	−15.05	−17.38
Gain (dBi)	1.40	0.93	1.21	0.911
Impedance bandwidth (%)	3.72	2.06	4.44	4.90
Efficiency (%)	85	80	75	72

Impedance bandwidth of copper-based antenna is higher due to higher conductivity value and lower dielectric constant of jeans substrate. The radiation pattern of the proposed transparent flexible antenna is at a satisfactory level which makes it useful for wireless wearable applications.

4 Conclusion

Two different types of transparent and non-transparent flexible antennas are evaluated based on different parameters like gain, return loss and radiation pattern. Transparent antenna which is invisible can be used for many applications in comparison to non-transparent antenna. AgHT-4 and PET which are flexible in nature show very good performance in terms of return loss and impedance bandwidth. Gain and radiation pattern is steady in desired frequency which makes the proposed antenna suitable for wireless wearable applications.

Acknowledgements The authors would like to thank the management of Charotar University of Science and Technology, Changa, Gujarat for their continuous support and encouragement.

References

1. Constantine. A. Balanis. Antenna theory: analysis and design, 4th edn. Wiley, New York

2. Upadhyaya TK, Dwivedi VV, Kosta SP, Kosta YP (2012) Miniaturization of tri band patch antenna using metamaterials. In: IEEE fourth international conference on computational intelligence and communication networks (CICN), pp 45–48
3. Gnanagurunathan G, Selvan KT (2017) Metamaterial-based planar antennas. In: Prabaharan S, Thalmann N, Kanchana Bhaaskaran V (eds) Frontiers in electronic technologies. Lecture notes in electrical engineering, vol 433. Springer, Singapore
4. Bhatt S, Mankodi P, Desai A, Patel R (2017) Analysis of ultra wideband fractal antenna designs and their applications for wireless communication: a survey. In: International conference on inventive systems and control (ICISC), Coimbatore, pp 1–6
5. Zhong S, Yan X, Liang X (2008) UWB planar antenna technology. In: Front Electr Electron Eng China 3:136
6. Archevapanich T, Lertwatechakul M, Rakluea P, Anantrasirichai N, Chutchavong V (2014) Ultra-wideband slot antenna on flexible substrate for WLAN/WiMAX/UWB applications. In: Tanaka S, Hasegawa K, Xu R, Sakamoto N, Turner SJ (eds) AsiaSim. Communications in computer and information science. Springer, Berlin, Heidelberg
7. Cotton S, Scanlon W, Madahar B (2009) Millimeter-wave soldier-to-soldier communications for covert battlefield operations. Commun Mag 47(10):72–81
8. Rao S et al (2014) Miniature implantable and wearable on-body antennas: towards the new era of wireless body-centric systems antenna applications corner. IEEE Antennas Propag Mag 56(1):271–291
9. Forsythe EW et al (2015) Flexible electronics for commercial and defense applications. In: International electron devices meeting (IEDM), Washington, DC. IEEE, pp 19.1.1–19.1.4
10. Haj-Omar A, Thompson WL, Kim YS, Coleman TP (2016) Adaptive flexible antennas for wireless biomedical applications. In: 17th annual wireless and microwave technology conference (WAMICON), Clearwater, FL. IEEE, pp 1–3
11. Porter E, Bahrami H, Santorelli A, Gosselin B, Rusch LA, Popovic M (2016) A wearable microwave antenna array for time-domain breast tumour screening. IEEE Trans Med Imaging. https://doi.org/10.1109/tmi.2016.2518489. IEEE
12. Herbert S, Loh T, Wassell I (2014) Assessment of a low-profile planar antenna for a wireless sensor network monitoring the local water distribution network. In: IET wireless sensor systems. IEEE
13. Kiourti A, Volakis JL (2016) Wearable antennas using electronic textiles for RF communications and medical monitoring. In: 10th European conference on antennas and propagation (EuCAP), Davos. IEEE, pp 1–2
14. Klemm M, Troster G (2006) Textile UWB antenna for on body communications. In: First European conference on antennas and propagation (Eucap). IEEE, pp 1–4
15. Saeed SM, Balanis CA, Birtcher CR, Durgun AC, Shaman HN (2017) Wearable flexible reconfigurable antenna integrated with artificial magnetic conductor. In: Antennas and wireless propagation letters, vol 1. IEEE
16. Hertleer C, Rogier H, Vallozzi L, Van Langenhove L (2009) A textile antenna for off-body communication integrated into protective clothing for firefighters. IEEE Trans Antennas Propag 57:919–925
17. Kumar R, Kumar P, Gupta N, Dubey R (2017) Experimental investigations of wearable antenna on flexible perforated plastic substrate. In: IEEE microwave and optical technology letters
18. Abbasi QH, Rehman MU, Yang X, Alomainy A, Qaraqe K, Serpedin E (2013) Ultrawideband band-notched flexible antenna for wearable applications. IEEE Antennas Wirel Propag Lett 12
19. Archevapanich T, Lertwatechakul M, Rakluea P, Anantrasirichai N, Chutchavong V, Tanaka S et al (eds.) (2014) Ultra-wideband slot antenna on flexible substrate for WLAN/WiMAX/UWB applications. In: Asian Simulation Conference. AsiaSim 2014, CCIS 474. Springer, Berlin, pp 116–126
20. Abdullah M, Khan A (2015) Multiband wearable textile antenna for I.S.M body center communication systems. In: XXth international seminar/workshop on direct and inverse problems of electromagnetic and acoustic wave theory (DIPED). IEEE

21. Saeed SM, Balanis CA, Birtcher CR, Durgun AC, Shaman HN (2016) Wearable flexible reconfigurable antenna integrated with artificial magnetic conductor. In: Antennas and wireless propagation letters, vol 2. IEEE
22. Christina G, Rajeswari A, Lavanya M, Keerthana J, Ilamathi K, Manoranjitha V (2016) Design and development of wearable antennas for tele-medicine applications. In: International conference on communication and signal processing. IEEE
23. Yoon HK, Yoon YJ, Kim H, Lee C-H (2011) Flexible ultra-wideband polarization diversity antenna with band-notch function. Int J Antennas Propag 5(12):1463–1470
24. Ali M, Khan I (2014) Wearable antenna design for FM radio. In: Springer Arab J Sci Eng 39(8):6189–619
25. Desai A, Upadhyaya T, Palandoken M, Patel R, Patel U (2017) Dual band optically transparent antenna for wireless applications. In: IEEE Asia pacific microwave conference, Kualalumpur, Malaysia, 13–16 Nov 2017
26. Patel RH, Desai A, Upadhyaya T (2015) A discussion on electrically small antenna property. Microw Opt Technol Lett 57:2386–2388
27. Patel R, Upadhyaya T (2017) Compact planar dual band antenna for WLAN application. Prog Electromagn Res Lett 70

Analyzing Frequency Spectra of Signals Generated by Chaotic DC–DC Converter and Its Application in Secure Communication

Manish Kumar Thukral, Karma Sonam Sherpa and Kumkum Garg

Abstract In this paper, a hybrid Adaline-Prony-based frequency estimation technique has been developed. Using this technique, the spectral estimation of the signals generated by current mode controlled buck–boost converter operating in chaotic condition is done. From the results obtained, it is shown that the signals generated by buck–boost converter in chaotic condition possess spread spectrum characteristic. Based on the results, a new vista of research can be opened in designing spread spectrum secure communication model using chaotic DC–DC buck–boost converter. To the best of our knowledge, very few researchers have given a thought in direction of using chaotic DC–DC power electronics converters in secure communication.

Keywords Nonlinear dynamics · Adaline · Prony's method · Bifurcation parameter · Buck–boost converter

1 Introduction

A dynamical system is the one which evolves with time. The behavior exhibited by a dynamical system can be linear or nonlinear. A linear dynamical system exhibits periodic behavior. On the other side, nonlinear dynamical systems exhibits a variety of behaviors like periodic, quasi-periodic leading to chaotic condition when some of its parameter is varied [1]. Such parameter of dynamical system which changes the qualitative behavior of the dynamical system when varied is called bifurcation parameter [1].

M. K. Thukral (✉)
Department of Electrical Engineering, Manipal University Jaipur, Jaipur 303007, India
e-mail: Manish.thukral@jaipur.manipal.edu

K. S. Sherpa
Department of Electrical & Electronics Engineering, SMIT, Sikkim 737132, India

K. Garg
Manipal University Jaipur, Jaipur 303007, India

© Springer Nature Singapore Pte Ltd. 2020

V. Janyani et al. (eds.), *Optical and Wireless Technologies*,
Lecture Notes in Electrical Engineering 546,
https://doi.org/10.1007/978-981-13-6159-3_2

In recent times, nonlinear dynamics analysis of power electronics based converters has become an active area of research [2–4]. Also, practicing engineers have started finding important applications of this emerging area in controlling chaos operating region of interleaved boost converters [5]. Power electronics based DC–DC converters operating in the closed configuration are known to exhibit nonlinear dynamics phenomenon [6–13]. In [6] and [8], nonlinear behavior exhibited by current mode controlled boost converter is verified. Similarly, nonlinear dynamics exhibited by current mode controlled buck converter is reported in [7]. In [12], another type of DC–DC converter known as buck–boost converter is shown to exhibit nonlinear behavior. These converters have a tendency to exhibit a variety of dynamical behaviors when some parameters like input voltage or reference current is varied. In order to analyze nonlinear dynamics, such converters are mathematically modeled in the form of iterative maps which is in one way discrete time modeling [6–13].

Although substantial work has been done in the direction of analyzing nonlinear dynamics in power electronics based DC–DC converters not much useful application of it has been found. So far engineers have been using nonlinear dynamics theory just to identify the region of chaotic operation of these converters and avoid it [13].

But the signals generated by DC–DC converters in chaotic condition can be potential candidates for application in secure communication. In the secure communication, the message to be transmitted is masked or hidden by adding it with a noise signal and hence a noise signal generator is required. The chaotic DC–DC converters can be a cheap alternative as noise signal generators. A typical noise signal has spread spectrum characteristic. It is required to analyze the frequency spectra of DC–DC converters in the chaotic condition in order to confirm that the signals generated by them are truly noise like.

In this paper, a suitable frequency estimation technique known as hybrid Adaline-Prony's technique is developed in order to analyze the frequency spectrum of signals generated by chaotic DC–DC converter. The proposed frequency estimation technique is the modification of two-stage Adaline model developed in [14]. The modification is done by reducing the computational burden by using model order estimation technique developed in [15].

For sake of simplicity only current mode controlled buck–boost converter is considered. The nonlinear dynamics in current mode controlled buck–boost converter has been analyzed. The frequency spectrum estimation of the signals generated by this converter in chaotic condition has been done using the proposed technique. Through results, it has been shown that the signals generated by these converters in chaotic condition are spread spectrum in nature. Hence, chaotic DC–DC converter in designing spread spectrum communication model.

2 Nonlinear Dynamics in Buck–Boost Converter

Figure 1 shows the circuit diagram of current mode controlled buck–boost converter. The circuit contains parameters like load resistance (R), inductor L, capacitor C, voltage source V_{in}. The circuit operation is such that when the switch turns ON, the inductor current i rises. Because of current mode controlled operation, the switch turns OFF when the inductor current reaches a value equal to the reference current I_{ref}. If the switching period is considered as T, then the two-dimensional discrete-time model of the circuit can be derived as shown by Eqs. (1), (2), (3), and (4).

As compared to [12], parasitic elements like inductor resistance r_l, capacitor resistance r_c, are considered in discrete time modeling. This would help in correct nonlinear dynamics analysis.

A. ***Discrete Time Model for Condition $t_n \geq T$***

$$v_{n+1} = v_n * e^{-\frac{T}{c(R+r_c)}} \tag{1}$$

$$i_{n+1} = \frac{V_{in}}{r_l} - \left(\frac{V_{in}}{r_l} - i_n\right) * e^{-\frac{r_l}{L}T} \tag{2}$$

B. ***Discrete Time Model for Condition $t_n < T$***

$$v_{n+1} = e^{-\alpha_1 t_{off}/2} * \left(A_1 \cos\left(\omega t_{off}\right) + A_2 \sin\left(\omega t_{off}\right)\right) \tag{3}$$

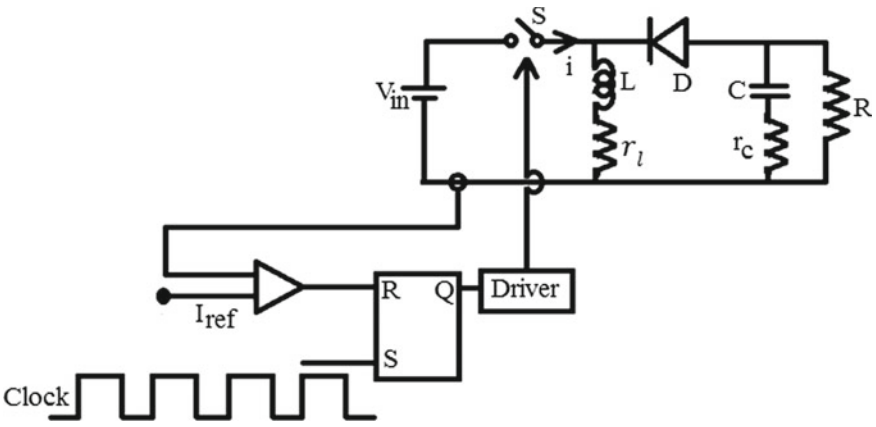

Fig. 1 Current mode controlled buck–boost converter

$$i_{n+1} = c\left(\frac{R + r_c}{R}\right)\left(e^{-\frac{\alpha_1 t_{off}}{2}} \sin(\omega t_{off}) * \left(-A_1\omega - \frac{A_2\alpha_1}{2}\right)\right.$$
$$\left. + e^{-\frac{\alpha_1 t_{off}}{2}} \cos(\omega t_{off}) * \left(A_2\omega - \frac{A_1\alpha_1}{2}\right)\right)$$
$$+ \frac{1}{R} * \left(e^{-\frac{\alpha_1 t_{off}}{2}} * \left(A_1 \cos(\omega t_{off}) + A_2 \sin(\omega t_{off})\right)\right) \quad (4)$$

where in Eqs. (1), (2), (3) and (4)

v_{n+1} = Discrete time value of capacitor voltage after switching period T
i_{n+1} = Discrete time value of inductor current after switching period T
t_n = Switch turn ON time
t_{off} = Switch turn OFF time
v_n = Discrete time value of capacitor voltage just at the instant when switch turns ON
i_n = Discrete time value of inductor current just at the instant when switch turns ON

$$\alpha_1 = \left(\frac{1}{c * (R + r_c)} + \frac{r_l}{L} + \frac{Rr_c}{L * (R + r_c)}\right)$$
$$\alpha_2 = \left(\frac{r_l}{Lc(R + r_c)} + \frac{Rr_c}{Lc(R + r_c)^2} + \left(\frac{R}{R + r_c}\right)^2 * Lc\right)$$
$$\omega = \sqrt{\alpha_2 - \frac{\alpha_1^2}{4}}$$
$$A_1 = v_n * e^{-t_{on}/c(R+r_c)}$$
$$A_2 = \frac{R * I_{ref} - A_1 * \left(1 - \frac{\alpha_1(R+r_c)c}{2}\right)}{c(R + r_c)\omega}$$

Considering the circuit parameter values as follows:

Load Resistance (R) = 20 Ω, Capacitor (C) = 4 μF, Inductor (L) = 0.5 mH, Switching frequency (f_s) = 20 KHz, Reference Current (I_{ref}) = 4 A, Inductor parasitic resistance (r_l) = 1.2 Ω, Capacitor parasitic resistance (r_c) = 0.12 Ω.

Using the above values in Eqs. (1), (2), (3) and (4) the nonlinear dynamics analysis can be done by obtaining the bifurcation diagram. Bifurcation diagram is also termed as fork diagram which is the plot between discrete values of capacitor voltage with respect to the bifurcation parameter. The bifurcation diagram obtained is shown in Fig. 2. It can be seen from Fig. 2 that the circuit shows period-I behavior from 50 to 45.4 V. Period-I behavior bifurcates to period-II at 45.5 V. As bifurcation parameter input voltage is varied the circuit enters into the chaotic region.

Figure 3a, b shows the inductor current and capacitor voltage generated by buck–boost converter in chaotic condition when the input voltage V_{in} is considered 19 V.

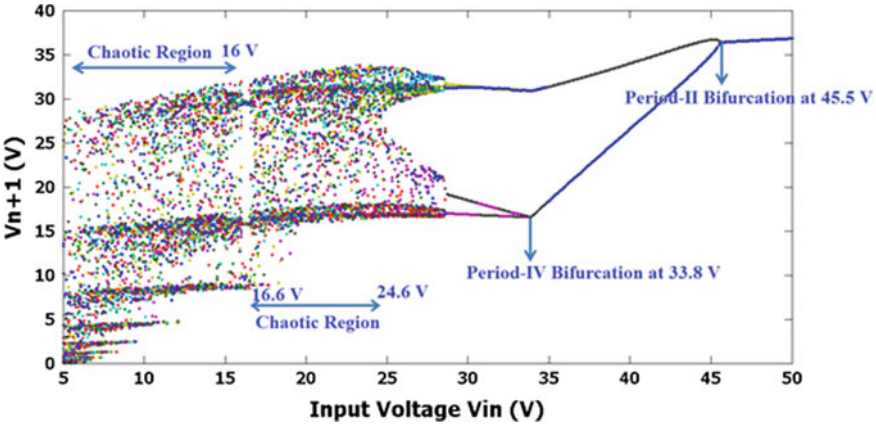

Fig. 2 Bifurcation diagram

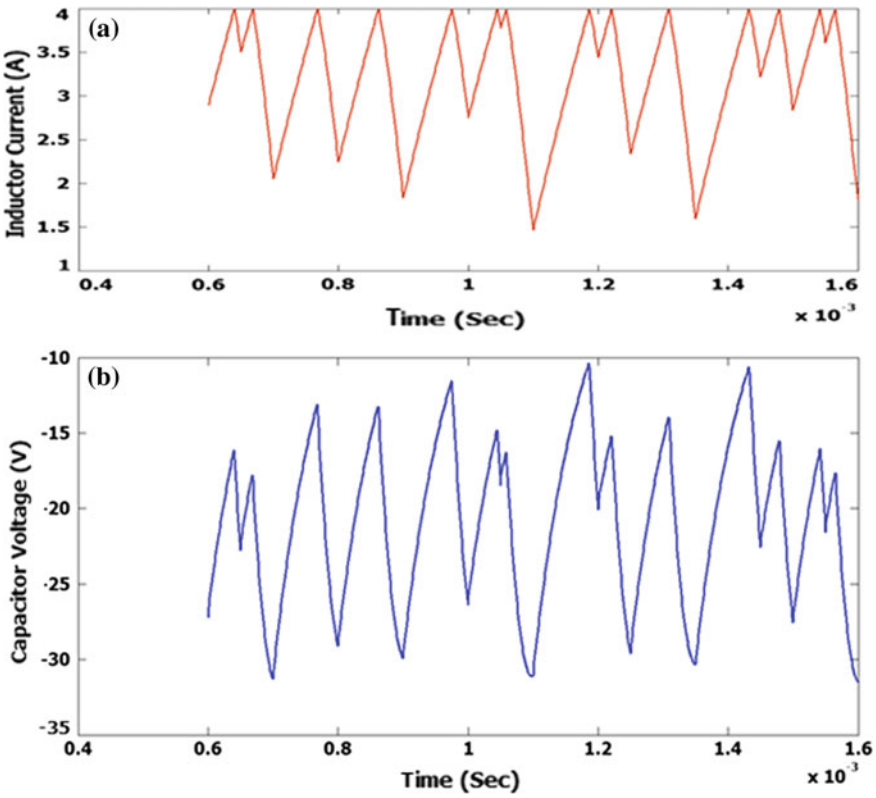

Fig. 3 **a** Inductor current signal at $V_{in} = 19$ V. **b** Capacitor voltage at $V_{in} = 19$ V

3 Hybrid Adaline-Prony's Method for Frequency Spectrum Analysis

As per Prony's method, P number of complex exponential functions are fitted over $2P$-sampled data points and represented as

$$x[n] = \sum_{k=1}^{P} b_k z_k^n \tag{5}$$

where

$$b_k = A_k e^{j\theta_k} \tag{6}$$

$$z_k = e^{(\alpha_k + j2\pi f_k)\Delta t} \tag{7}$$

In Eqs. (6) and (7) θ_k is the phase, α_k is the damping factor, and f_k is the frequency.

Multiplying Eq. (5) with parameter $a[m]$ and shifting index n to $n - m$ one can obtain

$$a[m]x[n-m] = a[m] \sum_{k=1}^{P} b_k z_k^{n-m} \tag{8}$$

Summing both sides of Eq. (8) over $m = 0, 1, \ldots, P$

$$\sum_{m=0}^{P} a[m]x[n-m] = \sum_{k=1}^{P} b_k z_k^{n-P} \sum_{m=0}^{P} a[m] z_k^{P-m} \tag{9}$$

One can observe from Eq. (9) that underlined part is polynomial and when it is solved over it's roots Z_k yields zero result. In order to find the roots, Z_k the polynomial coefficients can be obtained from the following equation:

$$\sum_{m=0}^{P} a[m]x[n-m] = 0 \tag{10}$$

In [14], Adaline-based frequency estimation technique is proposed. It consists of the first stage shown in the figure which evaluates polynomial coefficients shown in Eq. (10) recursively using Adaline model. Once these coefficients $a[m]$ are evaluated, the polynomial roots Z_k can be obtained. From polynomial roots, Z_k the frequency f_k can be evaluated as

$$f_k = \tan^{-1}\left[\frac{Im(z_k)}{Re(z_k)}\right] / (2\pi\,\Delta t) \tag{11}$$

where Δt is the sampling period of the signal whose frequency spectrum is to be estimated.

The second stage Adaline considers the mathematical model of the sampled data signal as given by

$$\widehat{x[n]} = \sum_{k=1}^{M} (A_k \sin(2\pi f_k n) + B_k \cos(2\pi f_k n)) \tag{12}$$

where

$\widehat{x[n]}$ = Estimated output at instant n
$A_k = C_k \cos(\emptyset_k)$
$B_k = C_k \sin(\emptyset_k)$
C_k = Amplitude of kth frequency component
$\emptyset_k$ = Phase of kth frequency component
$C_k = \sqrt{\left(A_k^2 + B_k^2\right)}$
$\emptyset_k = \tan^{-1}(B_k / A_k)$

Equation (12) is modeled using Adaline second stage as shown in Fig. 4b where the frequencies f_k evaluated in first stage are fed into it. The amplitude and phase of the corresponding frequency component are evaluated using the second stage.

It is reported by the author in [14] that the major disadvantage of this technique is computation burden which is directly linked to the number of Adaline considered.

This method can be improved in terms of computation burden if the actual number of frequency components present in the signal can be estimated. For this, the model order estimation technique proposed in [11] is used in the presented paper.

4 Frequency Estimation of Signals Generated by Chaotic Buck–Boost Converter

The frequency spectrum estimation of the inductor current and capacitor voltage signal generated by a chaotic buck–boost converter shown in Fig. 3a, b is done using the proposed technique.

The estimated frequency spectrum of inductor current and capacitor voltage is shown in Fig. 5a, b, respectively.

It can be seen from Fig. 5a, b that there are 190 frequency components present in the signals generated by the converter in chaotic condition. Hence it can be inferred that the signals generated by the converter in chaotic condition are spread spectrum in nature. This leads to a very important application of chaotic buck–boost converter in secure communication.

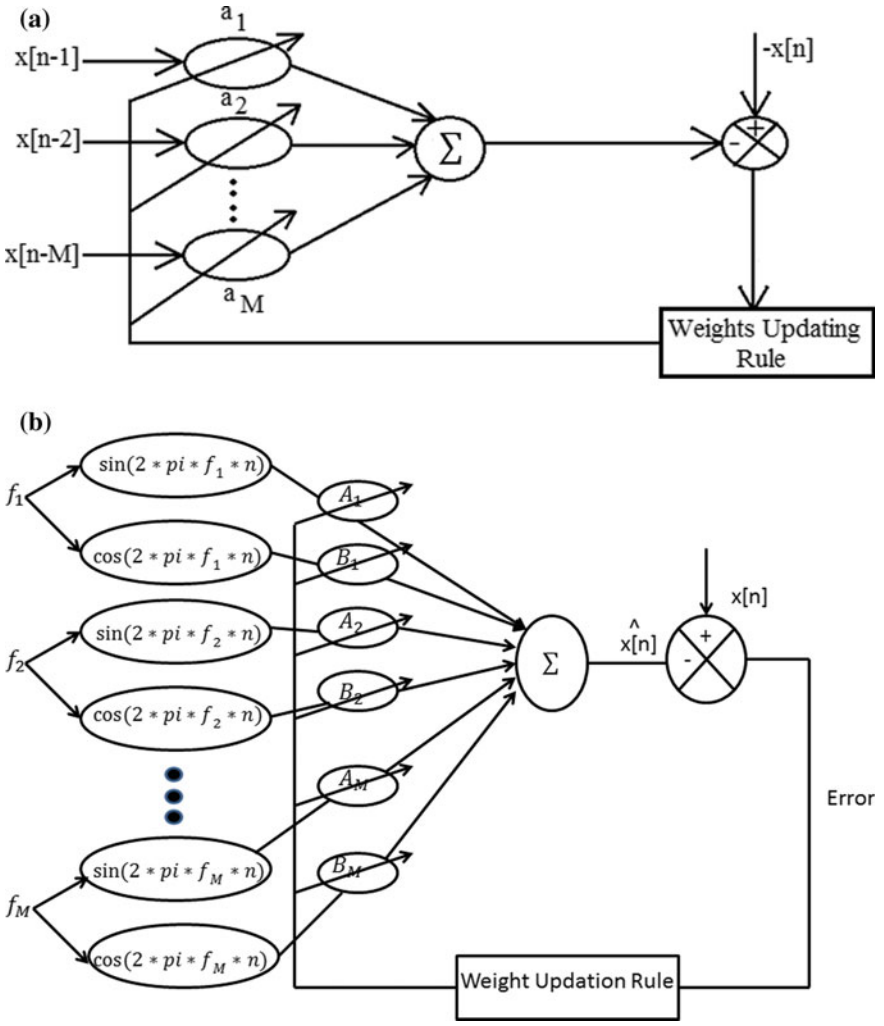

Fig. 4 **a** First stage **b** second stage

5 Conclusion

In this paper nonlinear dynamics in buck–boost converter is analyzed using the bifurcation diagram. From the bifurcation diagram, the chaotic regime is identified.

A frequency spectrum estimation technique named as hybrid Adaline-Prony's method is proposed which uses model order estimation technique. Using this technique, frequency estimation of the signals generated by buck–boost converter in chaotic condition (identified from bifurcation diagram) is done. It evident from the

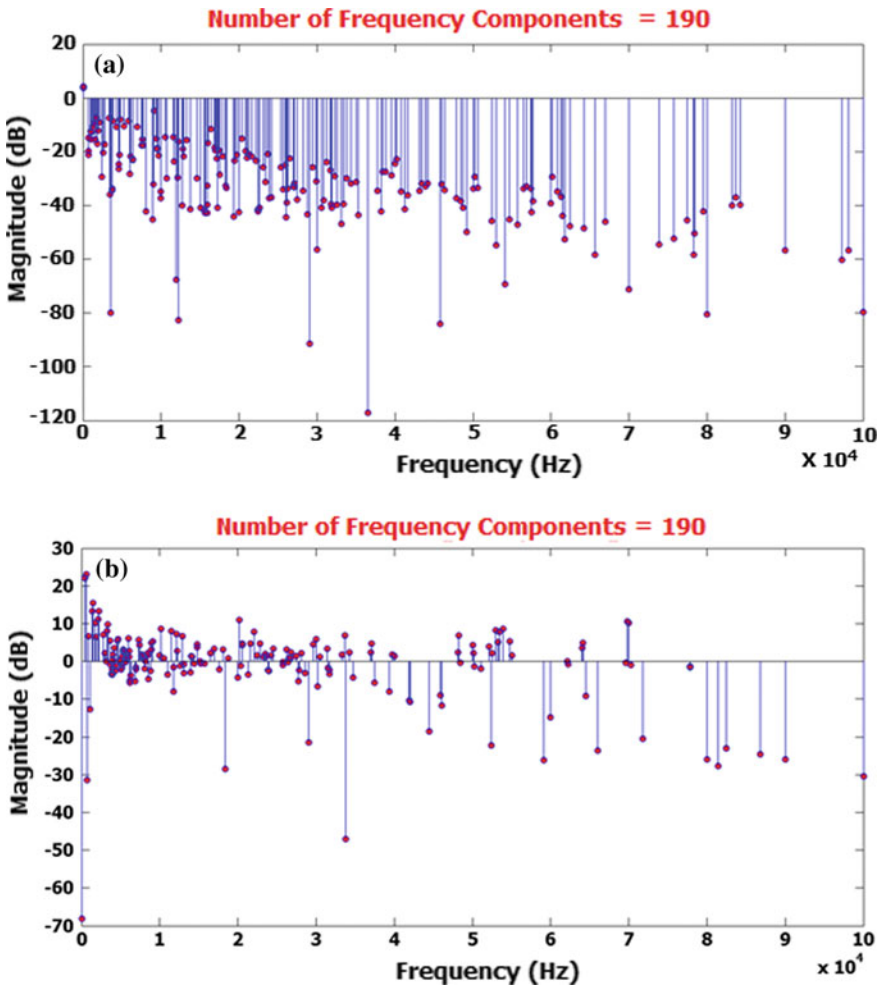

Fig. 5 **a** Estimated frequency spectrum of inductor current **b** estimated frequency spectrum of the capacitor voltage

result that the frequency spectra obtained is spread spectrum in nature which is a typical characteristic of a noise signal.

From the results obtained, an important application of chaotic buck–boost converter can be identified in the area of secure communication. For this message signal to be transmitted, it can be masked or encrypted with the noise-like signal generated by the converter in a chaotic condition. By doing this, the message can be disguised as a noise signal. Designing a decryption circuit can be an area of further research.

The main outcome of this paper is that to best of our knowledge, no one has given a thought on using chaotic DC–DC power electronics converters. Through this research, new secure communication models can be developed which may be better than existing ones.

References

1. Strogatz SH (2014) Nonlinear dynamics and chaos: with applications to physics, biology, chemistry, and engineering. Westview Press, Boulder
2. Aroudi A (2017) A new approach for accurate prediction of subharmonic oscillation in switching regulators—part i: mathematical derivations. IEEE Trans Power Electron 32(7):5651–5665
3. El Aroudi A (2017) A new approach for accurate prediction of subharmonic oscillation in switching regulators—part II: case studies. IEEE Trans Power Electron 32(7):5835–5849
4. Wang Y, Yang R, Zhang B, Hu W (2018) Smale horseshoes and symbolic dynamics in the buck-boost DC–DC converter. IEEE Trans Ind Electron 65(1):800–809
5. Wu H, Pickert V, Giaouris D, Ji B (2017) Nonlinear analysis and control of interleaved boost converter using real-time cycle to cycle variable slope compensation. IEEE Trans Power Electron 32(9):7256–7270
6. Deane JHB, Hamill DC (1990) Instability, subharmonics, and chaos in power electronics circuits. IEEE Trans Power Electron 5(3):260–268
7. Banerjee S, Poddar G, Chakrabarty K (1996) Bifurcation behavior of buck converter. IEEE Trans Power Electron 11(3):439–447
8. Banerjee S, Chakrabarty K (1998) Nonlinear modeling and bifurcation in boost converter. IEEE Trans Power Electron 13(2):252–260
9. Nagy I (2001) Nonlinear phenomena in power electronics. AUTOMATIKA-ZAGREB-42(3/4):117–132
10. Hamill DC, Deane JH, Jefferies DJ (1992) Modeling of chaotic DC-DC converters by iterated nonlinear mappings. IEEE Trans Power Electron 7(1):25–36
11. Banerjee S, Parui S, Gupta A (2004) Dynamical effects of missed switching in current-mode controlled dc-dc converters. IEEE Trans Circuits Syst II Express Briefs 51(12):649–654
12. Cheng KE, Liu M, Wu J, Cheung NC (2001) Study of bifurcation and chaos in the current-mode controlled buck-boost DC-DC converter. In: The 27th annual conference of the IEEE industrial electronics society, 2001. IECON'01, vol 2. IEEE, pp 838–843
13. Kavitha A, Uma G (2010) Resonant parametric perturbation method to control chaos in current mode controlled dc-dc buck-boost converter. J Electr Eng Technol 5(1):171–178
14. Chang GW, Chen CI, Liang QW (2009) A two-stage ADALINE for harmonics and interharmonics measurement. IEEE Trans Ind Electron 56(6):2220–2228
15. Jain SK, Singh SN (2012) Exact model order ESPRIT technique for harmonics and interharmonics estimation. IEEE Trans Instrum Meas 61(7):1915–1923

Survivability Standard Techniques Implementation in Fiber Optic Networks (SSTIFON)—An Overview

K. V. S. S. S. S. Sairam and Chandra Singh

Abstract In communication networks, survivability is a vital factor in Analyzing and Designing Techniques in Fiber Optic Networks (ADTFON). These aspects determine the Restoration Throughput (RT) and Redundant Protection Strategy (RPS). These techniques include Ring-Based Architecture (RBA) toward Path Segment (PS) and Path Restoration (PR). This paper focuses on different architectures that facilitate the High Impact Economical Factor (HIEF) of High Capacity Fiber System Equipment (HCFSE) needed for Signal Transport (ST) Mechanism.

Keywords FONI · DS-N · OC-N · FUSR · DCC · FNA · ONA · PRM

1 Introduction

Survivability resists any disturbance of physical or natural disaster preferably by EMI [1]. Fiber optic communication deals with the high bandwidth. In this fiber network architecture the uses feasible high-capacity fiber system with an High Impact Economical Factor (HIEF) via routing strategy that is from central office or hub [2]. The constructivity of Fiber Network Survivability Planning and Designing (FNSPD) deals with impedent, instant establishment, invigorating through a potential design and restoration aspects [3].

FNSPD can be divided into two categories, namely

(A) Transport Restoration
(B) Competence Transport

Transport restoration is applied to Switched Network, whereas competence transport is applied to Competence Transport Network. It involves routing in the form

K. V. S. S. S. S. Sairam (✉) · C. Singh
Department of E&CE, NMAM Institute of Technology, Nitte, Karkala Taluk, Karnataka, India
e-mail: drsairam@nitte.edu.in

C. Singh
e-mail: chandrasingh146@gmail.com

© Springer Nature Singapore Pte Ltd. 2020

V. Janyani et al. (eds.), *Optical and Wireless Technologies*,
Lecture Notes in Electrical Engineering 546,
https://doi.org/10.1007/978-981-13-6159-3_3

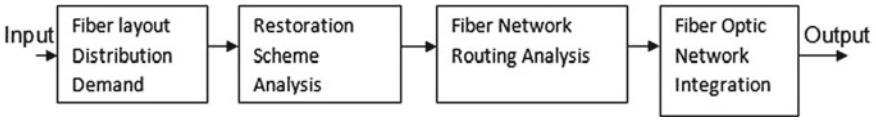

Fig. 1 FNSPD block diagram

Fig. 2 FNSPD types and phases

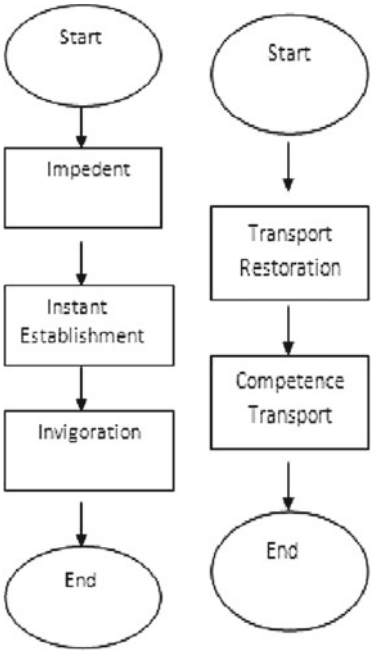

of direct path, indirect path, and a combination of both. It states utilization of Network Bandwidth (NB) including DG (Dynamic Hierarchical Group) and NDG (Non-hierarchical Dynamic Group) mechanisms [4]. It has restoration capabilities than transport restoration scientific knowledge which plays a vital role in FNSPD Block diagram as shown in Fig. 1 [5] and also FNSPD Types And Phases as shown in Fig. 2.

2 Problem Statement

The fiber network is designed as a global network to estimate the Digital Cross-Connectivity System (DCS) with respect to different demand distributions in a given network. To prevent more than one link failure in fiber network, network size, the spare capacity, protection schemes, and survivability ratio are estimated for different network configurations. Survivability at the physical layer is addressed. In this protection mechanism, 1:2 Diverse Protection scheme is used [6].

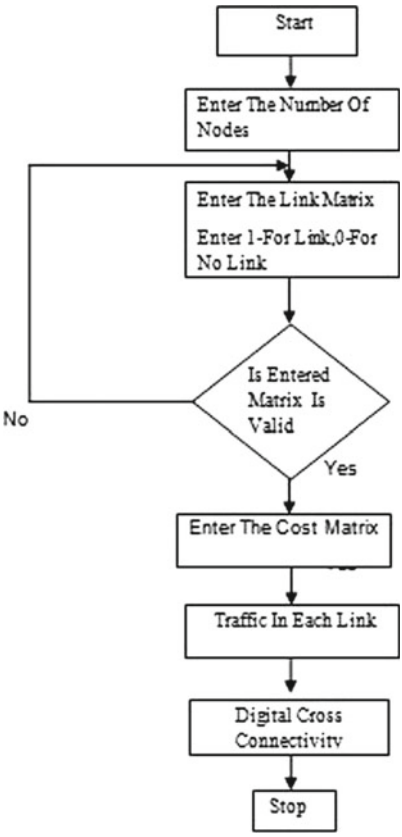

Fig. 3 Flowchart of digital cross-connectivity

2.1 Fiber Layout Distribution Analysis

As shown in Fig. 3 the flowchart of Digital Cross-Connectivity represents the Network Topology in terms of Link Joint (LJ), Link Joint Distance (LJD), Link Product (LP), Demand Signal Connectivity (DSC). Path arrangement and path rearrangement is carried out by means of Hub to Hub, Point to Point is shown in 12 × 12 Network Topology and Results in terms of Link Matrix in Table 1 and Cost Matrix Table 2 and Traffic in each link in Table 3 and also the code. It can be enhanced by means of OCD (Optical Carrier Demand) in terms of DS-3/DS-1 [7].

Table 1 Link matrix

0	1	0	0	0	0	1	0	0	0	0	0
1	0	1	0	0	1	0	0	0	0	0	0
0	1	0	1	0	0	0	0	0	0	0	0
0	0	1	0	1	0	0	0	1	0	0	0
0	0	0	1	0	1	0	1	0	1	0	0
0	1	0	0	1	0	1	1	0	0	0	0
1	0	0	0	0	1	0	0	0	0	1	0
0	0	0	0	1	1	0	0	0	0	1	1
0	0	0	1	0	0	0	0	0	1	0	0
0	0	0	0	1	0	0	0	1	0	0	1
0	0	0	0	0	0	1	1	0	0	0	1
0	0	0	0	0	0	0	1	0	1	1	0

Table 2 Cost matrix

0	4	0	0	0	0	6	0	0	0	0	0
4	0	5	0	0	9	0	0	0	0	0	0
0	5	0	6	0	0	0	0	0	0	0	0
0	0	6	0	13	0	0	0	3	0	0	0
0	0	0	13	0	8	0	15	0	12	0	0
0	9	0	0	8	0	5	14	0	0	0	0
0	0	0	0	0	5	0	0	0	0	8	0
0	0	0	0	15	14	0	0	0	0	4	9
0	0	0	3	0	0	0	0	0	2	0	0
0	0	0	0	12	0	0	0	2	0	0	11
0	0	0	0	0	0	8	4	0	0	0	9
0	0	0	0	0	0	0	6	0	11	9	0

Table 3 Traffic in each link

0	71	0	0	0	0	39	0	0	0	0	0
71	0	57	0	0	61	0	0	0	0	0	0
0	57	0	55	0	0	0	0	0	0	0	0
0	0	55	0	93	0	0	0	55	0	0	0
0	0	0	93	0	55	0	64	0	53	0	0
0	61	0	0	72	0	49	49	0	0	0	0
39	0	0	0	0	49	0	0	0	0	40	0
0	0	0	0	64	49	0	0	0	0	18	37
0	0	0	55	0	0	0	0	0	21	0	0
0	0	0	0	53	0	0	0	21	0	0	41
0	0	0	0	0	0	40	18	0	0	0	37
0	0	0	0	0	0	0	37	0	41	37	0

Program Code

```
for(j=1;j<=number;j++)

cost[i][j]=cost[i][j]/2;

printf("\n\n TRAFFIC IN EACH LINK \n\n");

for(i=1;i<=number;i++)

printf("\n")

printf("\n\n\n\n\press any key to continue ");

getch();

clrscr();
```

Link Joint (LJ): It is given as the no. of paths (P) to the total no. of nodes (N).

$$LJ = P/N \tag{1}$$

Link Joint Distance (LJD): It determines the network traffic (routing flow to the paths' joint)

$$LJD = R/J \tag{2}$$

Link Product (LP): It is the combination of

$$LJ * LJD. \tag{3}$$

Demand Signal Connectivity (DSC): It is given by total no. of node—each nodes to the total no. of nodes. Hence

$$DSC = (TN - EC)/(TN) \tag{4}$$

2.2 Restoration Scheme Analysis

In Network Survivable Connectivity (NSC), the cost is depicted with the flow in terms of associated path, non-associated path and a combination of both. In this, failure is more concerned and hence the protection mechanism takes place and hence path protection, shared path protection techniques in order to improve Network Survivable

Economical Factor (NSEF) as shown in Fig. 4. Table 4 depicts Demand before Failure and Table 5 represents Demand after Failure. Table 6 shows User Survivability Factor (USF).

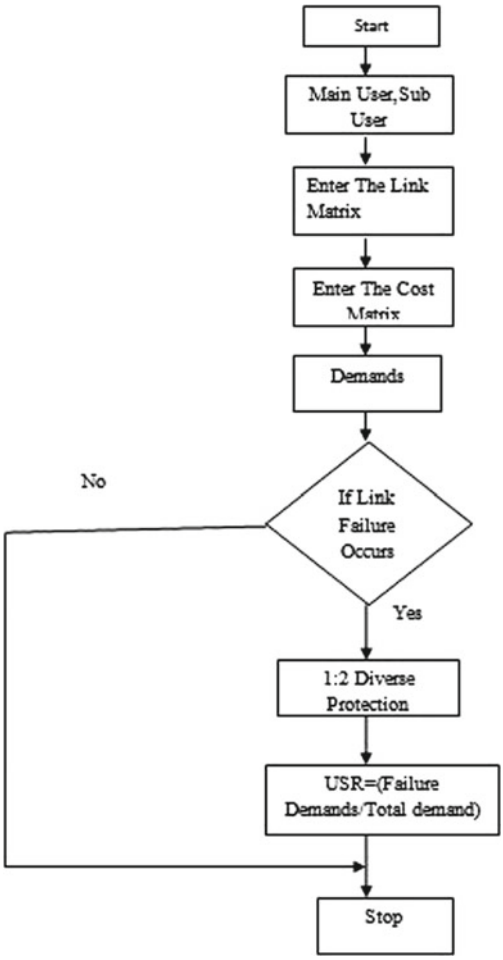

Fig. 4 Flowchart of PRM using 1:2 DP

Table 4 Demand before link failure

Source destination	Demand
(1, 2)	4
(2, 3)	5
(3, 4)	6
(1, 5)	9
(2, 6)	11
(5, 6)	12
(4, 7)	10
(6, 7)	5
(4, 8)	13
(7, 9)	30
(8, 9)	18
(5, 10)	12
(9, 10)	15
(6, 3)	16
(10, 12)	11
(12, 11)	9
Total	186

Table 5 Demand after link failure

Source destination	Demand
(1, 2)	4
(2, 3)	5
(3, 4)	6
(1, 5)	9
(2, 6)	11
(5, 6)	6
(4, 7)	10
(6, 7)	5
(4, 8)	13
(7, 9)	15
(8, 9)	18
(5, 10)	12
(9, 10)	15
(6, 3)	16
(10, 12)	11
(11, 12)	9
Total	165

Table 6 USF

Protection ratio	%Failure demands/total demands
User survivability factor	(165/186) = 88.70%

Program Codes

```
for(i=1;i<=number;i++)

for (j=1;j<=number;j++)

link fail[i][j]=link[i][j];

printf("\n Enter how many links fail: ");
scanf("%d",&tolifl);

printf("\n");
for(i=1;i<=tolifl;i++)
for(j=1;j<=number;j++)
for(l=1;l<=number;l++)
if(linkfail[j][l]==2)
for(k=1;k<found;k++)
{
if((path[k]==j)&&(path[k+1]==l))
{
trdem[i]=trdem[i]/2.0;
restor=restor+trdem[i];
count=1;
}
```

User Survivability Factor (USF): Failure Demands to Total Demands [8].

3 Conclusion

In this paper, the concept of survivability planning and designing issues include the integration approach of fiber layout distribution analysis, restoration scheme analysis, fiber network routing analysis, and protection schemes were discussed. In future direction, it can be enhanced by employing the higher order multiplexing techniques to ensure the sustainable service survivability of fiber optic network.

References

1. Skoog R, Von Lehmen A (2015) Metro network design methodologies and demands. IEEE J Light Wave Technol 22(11):2680–2692
2. Kavian YS, Rashvand HF, Leeson MS, Ren W, Hines EL, Naderi M (2016) Network topology effect on QoS delivering in survivable DWDM optical networks. J Telecommun Inf Technol, pp 68–71
3. Shao X, Zhou L, Cheng X, Zheng W, Wang Y (2015) Best effort shared risk link group (SRLG) failure protection in WDM networks. In: Proceedings of IEEE international conference on communication, pp 5150–5154
4. Singh C, Sairam KVSSSS (2017) Survivable fiber optic networks design by using digital signal levels approach. In: 2017 international conference on intelligent sustainable systems (ICISS), pp 84–86
5. Sairam KVSSSS, Singh C (2019) Link layer traffic connectivity protocol application and mechanism in optical layer survivability approach. In: Smys S, Bestak R, Chen JZ, Kotuliak I (eds) International conference on computer networks and communication technologies. Lecture notes on data engineering and communications technologies, vol 15. Springer, Singapore
6. Sairam KVSSSS, Singh C (2017) Optical network survivability–An overview. Indian J Sci Res 14(2):383–386
7. Sairam KVSSSS, Singh C (2019) FONI by using survivability approach: An Overview. In: Kamal R, Henshaw M, Nair P (eds) International conference on advanced computing networking and informatics. Advances in intelligent systems and computing, vol 870. Springer, Singapore
8. Singh C., Sairam KVSSSS, MBH (2019) Global fairness model estimation implementation in logical layer by using optical network survivability techniques. In: Hemanth J, Fernando X, Lafata P, Baig Z (eds) International conference on intelligent data communication technologies and internet of things ICICI 2018, Lecture notes on data engineering and communications technologies, vol 26. Springer, Cham

Design and Analysis of Novel Dispersion Compensating Model with Chirp Fiber Bragg Grating for Long-Haul Transmission System

Deepika Meena and M. L. Meena

Abstract In this work, a novel dispersion compensation model has been presented with chirped fiber Bragg grating (CFBG) for long-haul transmission system. The proposed model has been designed for 20 Gbps non-return to zero (NRZ) transmission system over 210 km long single-mode fiber (SMF). The proposed model is applied to Dense Wavelength Division Multiplexing (DWDM) also. Performance of the model is optimized through linear-chirped CFBG having 90 mm short grating length and it plays a significant role as a module of dispersion compensation. The proposed model enhance/improves the performance in terms of bit error rate (BER) and quality factor is $\geq$18 at the receiver end of systems. Further, it has also been compared with existing reported work on the basis of quality factor, BER, and eye-diagrams. The simulations of the proposed model have been carried out through OptiSystem 7.

Keywords Bit error rate · Chirp fiber Bragg grating · Dispersion compensation · Quality factor · Eye diagram

1 Introduction

Recently, the demand for optical fiber technology is increased day by day in telecommunication industry due to high bandwidth, data rates/capacity, and low-cost reliable optical communication links. When the different wavelength signals are transmitted over an optical fiber, these optical signals travel with different speeds due to the variations in core and cladding refractive index. Therefore, the optical signals are overlap/broaden/spread out after travelling a long distance through the fiber. Hence, the broadening of the pulse causes dispersion and losses in transmitted signals which lead to the error signal at receiver end [1, 2].

D. Meena (✉) · M. L. Meena
Department of Electronics Engineering, Rajasthan Technical University, Kota 324010, India
e-mail: meenadeepika666@gmail.com

M. L. Meena
e-mail: madan.meena.ece@gmail.com

© Springer Nature Singapore Pte Ltd. 2020

V. Janyani et al. (eds.), *Optical and Wireless Technologies*,
Lecture Notes in Electrical Engineering 546,
https://doi.org/10.1007/978-981-13-6159-3_4

The erbium-doped fiber amplifier (EDFA) scheme has been proposed by several authors to overcome or compensate the signal loss [3–5] because EDFA works on 1550 nm wavelength band and an average positive dispersion of single-mode fiber (SMF) is 15–20 ps/nm/km, which is much large in mentioned wavelength band. Hence, dispersion is the key issue to restrict the long-distance optical fiber communication [6, 7]. To overcome dispersion issue, Dispersion Compensation Fiber (DCF) has been introduced having negative dispersion coefficient to compensate the effect of positive dispersion in an optical fiber communication link [8]. However, the Dispersion Compensation Fiber technique increases nonlinear effects as well as the cost of fiber communication systems [9]. To overcome the challenges of dispersion compensation fiber technique, Fiber Bragg Grating (FBG) technique has been suggested to compensate the dispersion in fibers. Therefore, FBG is characterized by insignificant nonlinear effect, low loss, cost competence, and high competence for working in wavelength division multiplexing (WDM) optical transmission systems [10].

The WDM optical transmission systems have been designed by Kaur et al. [11] using pre/post/symmetrical DCF schemes for 250 km long optical fiber byintroducing the 50 km dispersion compensation fiber for a bit rate of 10 Gbps. The performance of different DCF scheme has been investigated and compared in terms of quality factor (Q-factor), bit error rate (BER) and eye-diagram. They establish a symmetrical dispersion compensation scheme which has been superior to pre/post-compensation schemes. The best value for BER and Q-factor are 5.86×10^{-26} and 10.45 dB, respectively. It has been observed that the designed system needs proper matching with EDFA and fiber length to achieve the best performance. Therefore, dispersion compensation techniques increase the nonlinear effect, losses of WDM system and high cost because the span of DCF is 50 km beside the 250 km long fiber optic. Further, Bhardwaj and Soni [12] have proposed an optical communication model using FBG to compensate the dispersion for different lengths of fiber at a bit rate of 20 Gbps. They also give the relation between the length of optical fiber and Q-factor, which is inversely proportional to quality factor. Therefore, Q-factor measures the performance of communication systems and they find out the best value of Q-factor is 23.82 dB at fiber length of 10 km. It has been observed that the Q-factor is very good, but distance is very short and insufficient to transmit data for long distance optical network.

Furthermore, Kaur and Sarangal [13] have proposed an optical WDM system using chirped FBG as dispersion compensator for different lengths of grating and apodization functions at a bit rate of 10 Gbps and 210 km length of fiber. The optimized grating length of the proposed model is 80 mm and Gaussian apodization function has been chosen. The best performance parameters of the proposed model have been given in terms of Q-factor and BER are 10.59 dB and 1.55×10^{-26}, respectively. Therefore, the choice of chirped FBG as dispersion compensation is very good technique and its parameters can be modified to obatin optimized and better results in terms of BER and Q-factor in the designed optical link.

In the present work, a novel dispersion compensation model has been proposed with Chirped Fiber Bragg Grating (CFBG) for wavelength division multiplexing or long-haul optical transmission systems. The optimized parameters of the chirped

FBG have been identified which are chirp parameter, apodization function, and chirped grating length, after simulation performance parameters of the proposed model has been analyzed in terms of Q-factor, BER, and eye-diagram. The main aim of the presented work is to improve the performance of proposed communication systems. Further, the proposed model has also been compared with an existing similar literature work using DCF as dispersion compensator [11–17]. The proposed chirped FBG configurations have been modeled and simulated using the advanced tools of OptiSystem 7.0 simulator.

2 Dispersion Compensation with CFBG

In this section, the schematic and basic principle of Chirped Fiber Bragg Grating (CFBG) has been presented as dispersion compensator for wavelength division multiplexing. Further, the design and simulation set up of the proposed chirped FBG model have been studied and demonstrated in order to improve the performance of communication systems without changing the parameters of any other block discussed earlier reported work [15]. Only the length of fiber or communication distance has been increased and the performance of the proposed model is compared with the previous model.

2.1 Principle of Chirped Fiber Bragg Grating

Fiber Bragg grating is a little portion, scattered reflectors of an optical fiber having a periodic disparity in refractive index beside an axis of the fiber. It means that the FBG is a small segment of fiber, which is separated with equal/different spaces inside an optical fiber.

By creating the periodic disparity in refractive index, each segment reflects or reproduces the exact wavelength of the light signal and transmits all others signals. When all reflected wavelength signals through each piece of reflectors are combining logically into one huge reflection at a particular wavelength. This is referred to as Bragg condition and wavelength at which reflection occurs is called the Bragg wavelength in reverse direction as given by [3, 18]:

$$\lambda_{Bragg} = 2 \cdot n_{eff} \cdot \wedge \tag{1}$$

where n_{eff} and $\wedge$ are the effective refractive index in core and grating period of the fiber, respectively. The basic principle of chirped FBG is presented in Fig. 1. It consists a single-mode fiber (SMF) having modulated core of refractive index, which has been divided by grating the plane with chirped spaces that create chirped fiber Bragg grating as shown in Fig. 1.

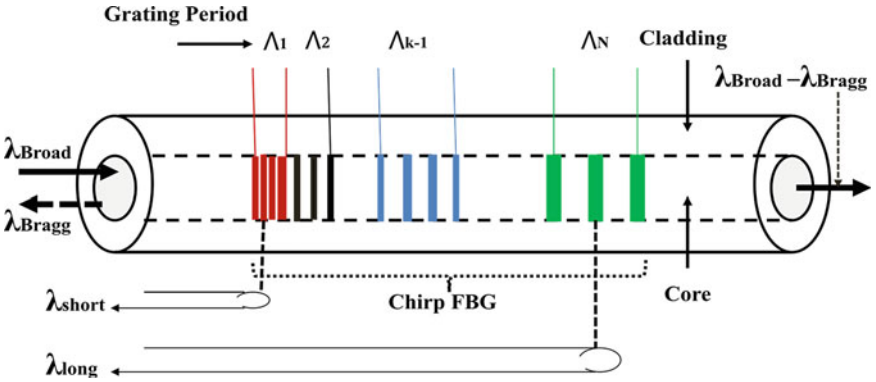

Fig. 1 Configuration of a chirped fiber Bragg grating used as a dispersion compensator

Further, the wavelength difference $\Delta\lambda$ between the two split ends of the grating planes are given by [19]:

$$\Delta\lambda = 2 \cdot n_{eff} \cdot (\wedge_{long} - \wedge_{short}) \tag{2}$$

The time delay (τ) of different reflected wavelengths can be calculated as given by

$$(\tau_\lambda) = (\lambda_{Bragg} - \lambda) \cdot \frac{2 \cdot n_{eff}}{\Delta\lambda \cdot c} \cdot l \tag{3}$$

where c and l are speed of light signal in vacuum and length of grating, respectively.

Dispersion of chirped fiber Bragg grating (D_g) can be calculated as given by [19].

$$D_g = \frac{2 \cdot n_{eff}}{\Delta\lambda \cdot c} \cdot l \tag{4}$$

2.2 *Design and Simulation of Proposed CFBG Model*

The proposed chirped FBG model has been presented to compensate dispersion in wavelength division multiplex (WDM) optical communication as shown in Fig. 2. The proposed CFBG-WDM simulation set up consists of a source (transmitter), medium of communication, and receiver. First, a source signal contains binary sequences (0 and 1), which are generated by pseudorandom generator having a bit rate of 20 Gbps and using binary sequence non-return to zero pulse has been generated. Then Mach–Zender modulator having 20 dB extinction ratios has been connected to the pulse generator and 193.1 THz frequency continuous wave (CW) semiconductor laser with the output power of 17 dBm. Second, the information/optical signal have

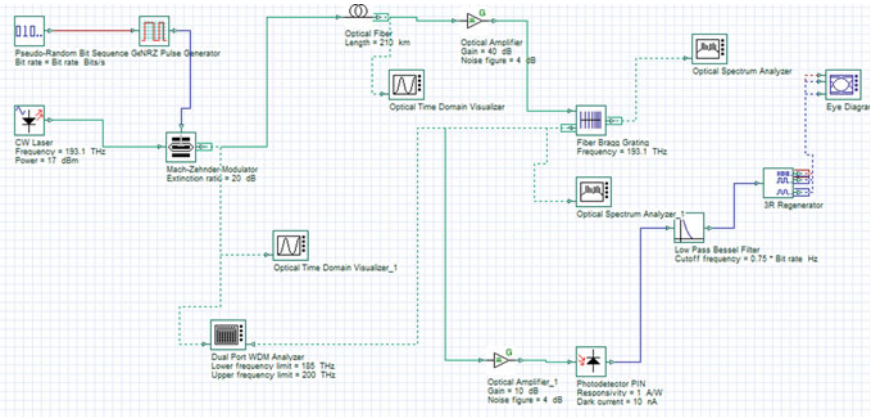

Fig. 2 Proposed chirped fiber Bragg grating simulation model by OptiSystem 7 software

Table 1 Simulation parameters of the single-mode fiber

Parameters	Value
Dispersion (ps/nm/km)	17.25
Dispersion slop (ps/nm^2/km)	0.085
Input power (dBm)	17
Attenuation (dB/km)	0.2
Optical fiber cable (OFC) length (km)	210
Gain (db) of EDFA amplifier with 4 dB NF	40
Gain (dB) of EDFA amplifier with 4 dB NF	10

been transmitting through fiber cable to the receiver. The parameters of optical cable have been given in Table 1.

Lastly, receiver contains a two (02) erbium-doped fiber amplifiers (EDFA) having different gains of 40, 10 dB and both amplifiers have a same noise figure (NF) of 4 dB. The gain of 40 dB EDFA has been used to triumph over the fiber loss and amplify the signal. After that, it passes through chirped Fiber Bragg Grating to compensate the dispersion and EDFA having 10 dB gain has been connected between the output of CFBG and input in PIN photo detector, which has been converted to the optical signal into electrical signal. Then output signals have been filtered via Bessel filter (LPBF) and optical regeneration, Eye-diagram analyzer has been used to show the simulated result in the form of the eye pattern, for calculating the bit error rate (BER), Q-factor, respectively, for the proposed model.

3 Results and Discussions

The proposed chirped fiber Bragg grating model has been simulated by OptiSystem 7 simulator. The effect of chirped dispersion compensator on eye-diagram of received signals at 210 km optical transmission system has been shown in Fig. 3. It can be observed that the eye-opening or eye gap is much clear and higher due to the high quality of received signals. Therefore, Chirped FBG offers better dispersion compensator for WDM long-haul optical communication systems, when compared to the existing reported work in the literature [8, 10, 14, 15]. Further, to improve the Q-factor optimized parameters of chirped FBG as dispersion compensator have also been specified in Table 2.

Furthermore, the performance characteristics of the proposed model have also been compared with [8, 10, 14, 15] in terms of Q-factor and bit error rate as given in Table 3. As can be seen in Table 3, Q-factor and BER of the proposed model are 18.46 dB and 1.59×10^{-57}, respectively, whereas Q-factor and BER are 14.91 and 3.41×10^{-51}, respectively on the same model used by Sayed et al. [15]. Hence, the proposed chirped FBG model improves Q-factor with 50% when compared to existing work in the literature [8–15].

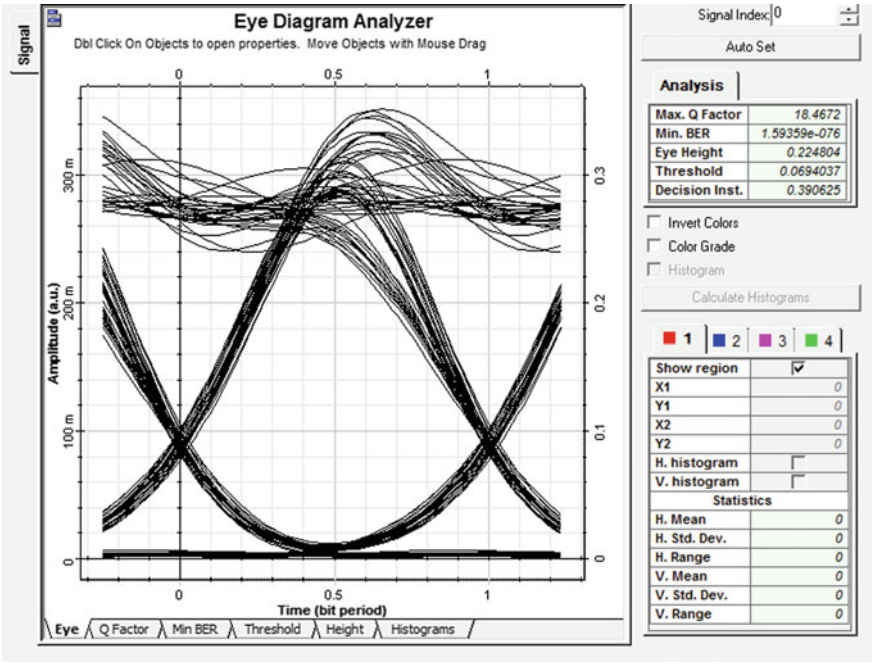

Fig. 3 Simulated result of eye-diagram after CFBG dispersion compensation

Table 2 Optimized parameters of the Chirped Fiber Bragg Grating

Parameters	Value
Effective refractive index n_{eff}	1.47
Frequency (THz)	193.1
Grating length l (mm)	90
Chirp function	Linear
Apodization function	Gaussian
Gaussian parameter	0.5
Delta lambda $\Delta\lambda$ (nm)	1
Chirp linear parameter (μm)	0.0001

Table 3 Comparative analysis of the proposed model with existing references

References	SMF length (km)	CFBG length (mm)/DCF length (km)	Q-Factor (dB)	BER
[8]	50	10 km	7.28	7.28×10^{-12}
[10]	100	8 mm	9.85	6.45×10^{-21}
[11]	200	50 km	10.45	5.86×10^{-26}
[12]	10	15 mm	23.82	3.45×10^{-25}
[13]	210	80 mm	10.59	2.55×10^{-26}
[14]	180	20 mm	66.17	2.50×10^{-11}
[15]	210	80 mm	14.91	3.41×10^{-51}
Proposed model	210	90 mm	18.46	1.59×10^{-57}

4 Conclusion

In the present paper, a novel chirped FBG model has been designed as dispersion compensator for 210 km long-distance optical communication network. The proposed model has been simulated with software OptiSystem 7 simulator. The Q-factor and BER have been found from eye-diagram analyzer after simulation. The performance of the simulated model in terms of Q-factor and BER are 18.46 dB, 1.59×10^{-57}, respectively. Further, the evaluated performances of the proposed model have also been compared with existing work in literature. Hence, it can be accomplished that Q-factor was improved by 50% when compared to the results of Sayed et al. [15] Therefore, CFBG uses a competent dispersion compensator to improve Q-factor, minimum bit error rate, and transmit huge data capacity that increases the overall performance of optical fiber network.

References

1. Chakkour M, Hajaji A, Aghzout O (2015) Design and study of EDFA-WDM optical transmission system using FBG at 10 Gbits/s chromatic despersion compensation effects. In: Mediterranean conference on information & communication technologies
2. Hu B-N, Jing W, Wei W, Zhao R-M (2010) Analysis on dispersion compensation with DCF based on optisystem. In: 2nd international conference on industrial and information systems, pp 40–43
3. Ismail M, Othman M (2013) EDFA-WDM optical network design system. Proc Eng 53:294–302 (Elsevier)
4. Gujral J, Singh M (2013) Performance analysis of 4-channel WDM system with and without EDFA. IJECT 4
5. Choi BH, Park HH, Chu MJ (2003) New pump wavelength of 1540-nm band for long-wavelength-band erbium-doped fiber amplifier (L-Band EDFA). IEEE J Quantum Electron 39
6. Kaler RS, Sharma AK, Kamal TS (2002) Comparison of pre-, post- and symmetrical-dispersion compensation schemes for 10 Gb/s NRZ links using standard and dispersion compensated fibers. Opt Commun 209:107–123 (Elsevier)
7. Singh P, Chahar R (2014) Performance analysis of dispersion compensation in long haul optical fiber using DCF. Int J Eng Sci 3:18–22
8. Shukla R, Kumar M (2012) Performance analysis of dispersion in optical communication link using different dispersion compensation fiber (DCF) models. In: IJRTE, vol 1
9. Agrawal G (2002) Fiber-optic communication systems, 3rd edn. Wiley-India Edition
10. Mohammadi SO, Mozzaffari S, Shahidi M (2011) Simulation of a transmission system to compensate dispersion in an optical fiber by chirp gratings. Int J Phys Sci 63:7354–7360
11. Kaur M, Sarangal H, Bagga P (2015) Dispersion compensation with dispersion compensating fibers (DCF). Int J Adv Res Comput Commun Eng 4:2319–5940
12. Bhardwaj A, Soni G (2015) Performance analysis of 20Gbps optical transmission system using fiber Bragg grating. Int J Sci Res Publ 5:2250–3153
13. Kaur M, Sarangal H (2015) Simulation of optical transmission system to compensate dispersion using chirped fiber Bragg grating (FBG). Int J Adv Res Comput Commun Eng 4:2319–5940
14. Fahd C, Anas H, Mounia C, Mounir Y (2015) Chirped Bragg grating dispersion compensation in dense wavelength division multiplexing optical long-haul network. Int J Microw Opt Technol 10:5
15. Sayed AF, Barakat TM, Ali IA (2017) A novel dispersion compensation model using an efficient CFBG reflectors for WDM optical networks. Int J Microw Opt Technol 12:3
16. Dar AB, Kumar Jha R (2017) Chromatic dispersion compensation techniques and characterization of fiber Bragg grating for dispersion compensation. Springer Science Business Media, New York, pp 49–108
17. Rath PS, Satyam A, Mani Jha D, Khalid I (2017) Performance analysis of long fiber optic link using fiber Bragg grating for dispersion compensation. Int J Eng Sci Comput 10279–10284
18. Venghaus H (2006) Wavelength filters in fiber optics. Springer, Berlin, pp 234–236
19. Kashyap R (1999) Fiber Bragg grating. Academic Press, San Diego, pp 310–316

External Modulation Using MZM for Visible Wavelengths

Poonam Devi and Ravi Kumar Maddila

Abstract External modulation is preferred over direct modulation. Some important reasons are reviewed in this paper. The performance of electro-optic modulator (external modulator) is reviewed for visible-light communication over direct modulation. Here, operating wavelength range is 400–700 nm and voltage-length product ($V_\pi L$) is 0.8 V cm. Calculated insertion loss is very low compared to other available devices and the extinction ratio is very high.

Keywords External modulation · Mach–Zehnder interferometer (MZI) · Visible-light communication (VLC)

1 Introduction

Visible-Light Wireless Communication is a technology which uses visible light as a carrier signal in communication and it is present everywhere around us. White LEDs have been invented for various uses. White LEDs are famous for low-power consumption, longer lifetime, small size, and faster response. But recently researchers have realized that these LEDs can not only be used for illuminating rooms, but also for a communicating system. This function of LED has produced a new branch of communication, i.e., Visible-Light Communication [1, 2].

To exploit the benefits of the optical domain as a transport medium, we require to convert data from the electrical domain to the optical domain. This is done through the modulation process. There are two methods through which a signal can be modulated in the optical domain—Direct modulation and External modulation. External modulation dominates over direct modulation to achieve chirp free, high data rate and

P. Devi (✉) · R. K. Maddila
Department of Electronics and Communication, Malaviya National Institute of Technology Jaipur, Jaipur 302017, Rajasthan, India
e-mail: 2016pwc5271@mnit.ac.in

R. K. Maddila
e-mail: rkmaddila.ece@mnit.ac.in

© Springer Nature Singapore Pte Ltd. 2020

V. Janyani et al. (eds.), *Optical and Wireless Technologies*,
Lecture Notes in Electrical Engineering 546,
https://doi.org/10.1007/978-981-13-6159-3_5

long link length modulation [3]. In external modulation, electro-optic effect is used, i.e., refractive index changes proportionally to the applied electric field. It results in a change of phase of the wave passing through the crystal. If two waves are combined with different phase changes, an interferometrically amplitude-modulated wave is obtained.

As external modulator, we use Lithium Niobate Mach–Zehnder Modulator (LN-MZM). In the past few years, Lithium Niobate has been proved to be the best material in the fabrication of photonics devices. It comprises of an excellent electro-optic coefficient, low loss, and linear response to the applied electric field.

Till now in VLC, Direct modulation is used. But if data rate or range of communication is increased, frequency chirping occurs [3]. Due to frequency chirping, information could be destroyed. In external modulation, frequency chirping can be reduced [4]. In this paper, a design of external modulator, i.e., MZM is proposed which works in the range of visible light. The results are based on the simulations performed on OPTI-BPM simulator.

2 Theory and Design Analysis

The MZM structure is shown in Fig. 1. It has one input waveguide and one output waveguide with two 3 dB couplers, which are working as power splitter and combiner. It has three electrodes along with the interferometer arm (length L).

When an input optical signal is applied at input waveguide, it gets split into two equal power optical signals by the 3 dB coupler which is working as an optical

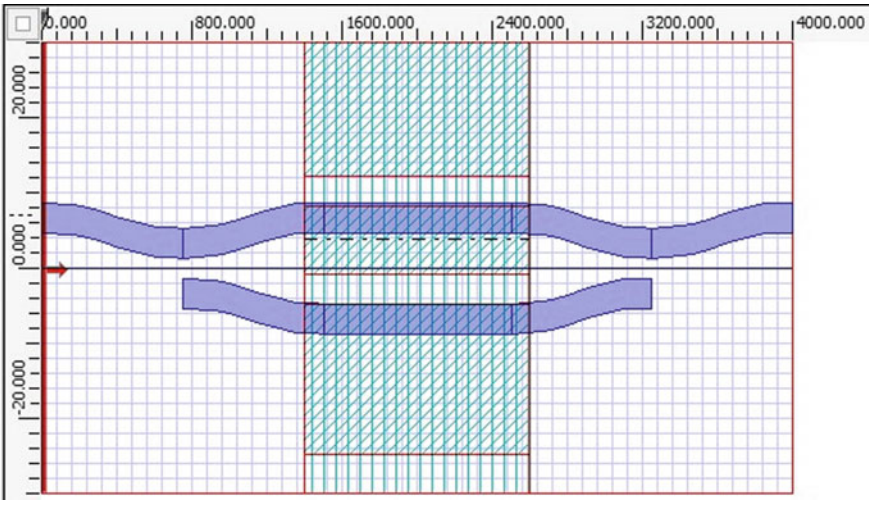

Fig. 1 LN MZM

power splitter. When a voltage is applied in electrodes, it will generate an electric field around interferometric arms. This generated electric field will produce a phase shift in the optical signal passing by because of Pockels effect. This phase change is converted to amplitude modulation by MZI structure [5, 6]. To use this switch as a modulator, only one output port power is to be considered, and the other one is to be discarded. For that port, the insertion loss *I.L.* can be calculated by the following equation:

$$I.L. = 10 \log \frac{P_{out}}{P_{in}}. \tag{1}$$

A normal MZI switch is available in optiwave systems tutorial [7]. Further working on wavelength and size, the following design is proposed.

- Wafer range is 4 mm and width is 60 μm.
- Waveguide width is 4 m, electrode length is 1 mm.
- Electrode material has refractive index 1.47, electrode thickness is 20 m, the gap between two electrodes is 4 m and the center position is 3.7 m. Half Switching voltage can be calculated using the following formula:

$$V_{\pi} = \frac{d\lambda}{r\, n^3 L} \tag{2}$$

where d is the separation between electrodes, λ is operating wavelength, n is the extraordinary refractive index, r is electro-optic coefficient and L is the length of the electrode. In this design, V_{π} is 8 V.

3 Results and Discussion

In Fig. 2, optical field propagation through the waveguide is shown. Here a 1 mW signal is applied at the input waveguide. That signal is equally distributed into two waveguides because of 3 dB coupler. There is electrode along the interferometric arms, so there will be some phase change in signal. Again when this signal will pass through the second 3db coupler, coupler will act as a combiner. It will give intensity modulation. Here input is 1 mW and output power at port 1 is 0.94 mW. So we can say 90% signal will be switching in output 1.

One input and one output arm are removed here from one 22 MZI switch, because these are not required. The signal is applied at only one input waveguide and the modulated signal is obtained from only one waveguide.

In Fig. 3, the optical power in waveguide versus voltage applied in electrode graph is plotted. In basic tutorial of MZI switch, it is shown when applied voltage is zero the signal passes through output 2, which is removed here [2]. But to get the modulated signal, a voltage is applied across the electrode so that the output passes

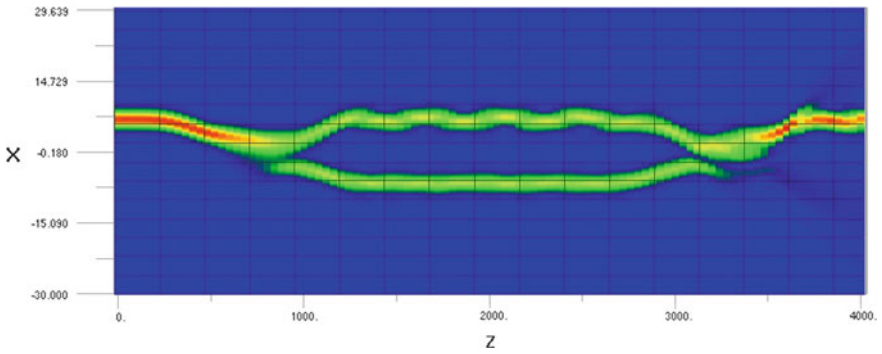

Fig. 2 Optical field propagation for the above design

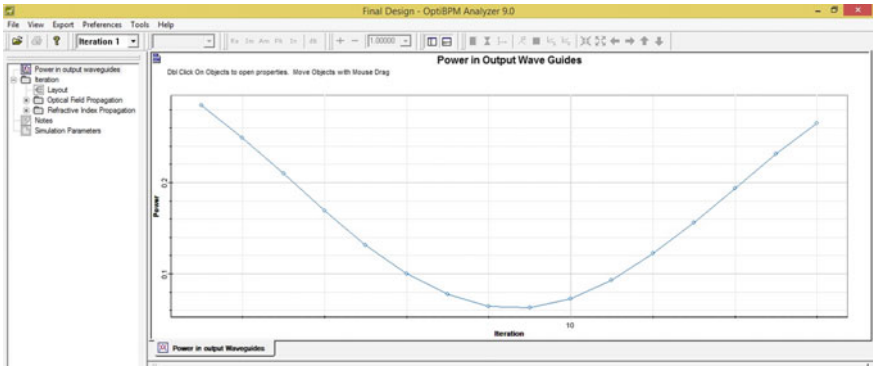

Fig. 3 Optical power through waveguide w.r.t to electrode voltage

through output waveguide. From Fig. 3, it is clear how optical power is switching from output 2 to output 1.

In Fig. 3, it can be found that the switching voltage V_π is at 8 V and the power at output end (Pout 1) is 0.94 mW. The calculated value of insertion loss is 0.2632 dB which is very low.

4 Conclusion

Given results are taken when the modulator is working in visible-light range. Hence, this modulator can be used for modulation purpose in visible-light communication system. This device is giving high extinction ratio approximately 44 dB and low insertion loss approximately 0.2632 dB. The switching voltage-length product is also very small (0.8 V cm) when compared to previous modulator designs. The low value of switching voltage-length product refers to a compact and energy-efficient

device. This device gives a new idea to modulate a signal in visible-light communication which can reduce frequency chirping, while increasing the data rate and communication range.

Acknowledgements This work was supported by Visvesvaraya Young Faculty Research Fellowship, MeitY, Govt. of India.

References

1. Shinwasusin E, Charoenlarpnopparut C, Suksompong P, Taparugssanagorn A (2015) Modulation performance for visible light communications. In: 2015 6th international conference of information and communication technology for embedded systems (IC-ICTES), pp 1–4
2. Jha PK, Mishra N, Sriram Kumar D (2017) Challenges and potentials for visible light communications: state of the art. In: AIP conference proceedings, vol 1849, no 1
3. Koyama F, Iga K (1986) Frequency chirping of external modulation and its reduction. In: Optical fiber communication. Optical Society of America, pp WBB5
4. MS Windows NT chirp in mach-zehnder lithium niobate modulators. https://optiwave.com/resources/applications-resources/chirp-in-mach-zehnder-lithium-niobatemodulators/. Accessed 22 Nov 2017
5. Mohammed NA, Elnasr HSA, Aly MH (2014) Analysis and design of an electro optic 2 × 2 switch using Ti:$KNbO_3$ as a waveguide based on mzi at 1.3 μm. Opt Quantum Electron 46(2):295–304
6. Zetie KP, Adams SF, Tocknell RM (2000) How does a mach-zehnder interferometer work? Phys Educ 35(1):46
7. MS Windows NT mach-zehnder interferometer switch. https://optiwave.com/optibpmmanuals/bpm-lesson-14-mach-zehnder-interferometer-switch-2/. Accessed 22 Nov 2017

A Detailed Survey of Rectenna for Energy Harvesting: Over a Wide Range of Frequency

Rachit Dana, Parthit Sardhara, Akshay Sanghani and Prarthan Mehta

Abstract This Survey Paper aims at providing a comprehensive analysis of various Energy Harvesting techniques based on Rectennas. Several Research Papers published over the years have been studied in detail. The Rectennas mentioned in these papers are classified according to the frequency/frequency range and are thereupon compared with reference to conversion efficiency, output voltage, impedance matching techniques, and antenna type. Based on the survey performed, a conclusion has been drawn.

Keywords Wireless power transfer · Rectenna · Impedance matching · Conversion efficiency

1 Background

The method of Wireless Power Transfer has been around for more than a century. It is basically a method of transferring energy (electrical) through the medium which does not involve wires (i.e., variables). Although there were many notable scientists who put forward their ideas in the field of Electromagnetics, such as M. Faraday, who proposed the law of Electromagnetic Induction, J. C. Maxwell, who put forward Maxwell's equations, J. H. Ponyting, who gave us Poynting's theorem and several others, it was not until 1890 that someone worked on an experiment which focused on Wireless Power Transfer.

R. Dana (✉) · P. Sardhara · A. Sanghani · P. Mehta
Dharmsinh Desai University, Nadiad, India
e-mail: rachitdana.ec@ddu.ac.in

P. Sardhara
e-mail: parthitsardhara3630@hotmail.com

A. Sanghani
e-mail: akshaysanghani73@gmail.com

P. Mehta
e-mail: mehtaprarthan.ec@ddu.ac.in

© Springer Nature Singapore Pte Ltd. 2020

V. Janyani et al. (eds.), *Optical and Wireless Technologies*,
Lecture Notes in Electrical Engineering 546,
https://doi.org/10.1007/978-981-13-6159-3_6

N. Tesla was the first one to successfully demonstrate Wireless Power Transfer. In the 1890s, he conducted a series of experiments in which he demonstrated how Geissler tubes and Incandescent light bulbs could be lit from across the stage. He used resonant transformers which worked on inductive and capacitive coupling, which later came to be known as Tesla Coils. Although this was a short-range power transfer system, it still proved vital for future progress in the field of Wireless Power Transfer.

After World War II, the idea of transmitting power through microwaves was thoroughly researched. It was W. C. Brown, who revolutionized the field of Wireless Power Transmission by inventing Rectenna. Rectenna, i.e., Rectifying Antenna is a special class of antenna which converts Electromagnetic energy into DC electricity. Brown demonstrated his idea by flying a model helicopter, which was being powered by the microwaves that were sent from the ground and were received by the Rectenna which was mounted on top of the helicopter.

Over the coming decades, Rectenna found extensive applications in RFID tags, smart cards, etc. As the field of Wireless Communication flourished, the field of Wireless Energy Harvesting was born. There are several other Energy Harvesting Techniques known for harvesting energy from sources such as solar, thermal, wind, etc., but Wireless Energy Harvesting seems to be the most promising. Wireless Energy Harvesting is based on the idea that the residual energy that is present in the environment in the form of Electromagnetic Waves can be used to drive electronic circuits. As monolithic integrated circuit industry grows at a fast pace, there is a demand for finding an efficient way of harvesting the wireless power that is present around us.

Over the past several decades, significant research has been done on Wireless Energy Harvesting which uses Rectennas to scavenge energy. The number of Research Papers in the past several decades published by the esteemed journals clearly demonstrates the interest in the field of Wireless Power Transfer has only increased. This Survey Paper is based on several Research Papers collected from these journals which focus on Rectennas and efficient methods to implement Wireless Power Harvesting.

The upcoming section titled Introduction aims to offer the reader with the basic idea of what a Rectenna is, and what are its basic components. After providing a brief knowledge, the next section—Rectenna Classified covers all the Research Papers surveyed and provides in-depth knowledge of the experiments and research that has been conducted over the past decades. Finally, the information is tabulated consisting of necessary fields which can be used for a quick reference.

2 Introduction

The basic block diagram of Rectenna is as shown in Fig. 1.

As it can be seen, the Rectenna element consists of a receiving antenna, an impedance matching network, a Rectifying Circuit, and an Output Load.

The design and type of receiving antenna involved do affect the efficiency of the Rectenna. The impedance of the receiving antenna is always taken as 50 Ω for

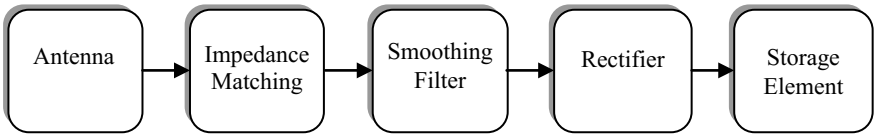

Fig. 1 Block diagram of rectenna

the impedance matching purpose. The second stage in the circuit is the Impedance Matching Circuit. In order to facilitate maximum power transfer from the receiving antenna side to the rectifying circuit side, Impedance Matching Circuits are extremely useful. There are a variety of devices and electrical components known, which can be used for "Impedance Matching". Usually, Transformers, Transmission lines, Resistors, Capacitors, Inductors, and any of their combinations are used for matching networks. Quarter-wave Transformer, Lumped LC Network, PI Matching Network, L-Matching Network, Stubs are used extensively.

A Rectifying Circuit performs the RF-to-DC conversion. In many cases, a special type of Diode Rectifier Circuit is used for this purpose, the Voltage Doubler. The Greinacher Voltage Doubler circuit consists of two capacitors and two diodes. It is very effective in reducing the ripple in the input signal. Schottky diodes are used because they provide faster switching at high frequencies (i.e., low switching time). If the output voltage is still not favorable, a Voltage Quadrupler can be used. Voltage Quadrupler consists of two Greinacher voltage doubler cells of opposite polarities which quadruples the input voltage. The final stage consists of Load across which the output DC voltage has to be measured.

3 Rectenna Classified

Out of the all Research Papers that have been referred, 17 are based on the Wi-Fi frequency, i.e., the 2.4 GHz band. In most papers, the HSMS family of Schottky diodes is used for the purpose of rectification, manufactured by different vendors. The simulation software used are Agilent's Advanced Design System (ADS), ANSYS High-Frequency Electromagnetic Simulation (HFSS), and CST Microwave Studio. The substrates used are FR-4 Substrate and RT/duroid Substrate.

In the research paper [1], HFSS Simulator is used to simulate a Rectenna design. With the input power of 12.9 dBm, an output voltage of 4.5 V is observed. In [3], two different Rectenna Architectures employing RF-combiner and DC-combiner topology have been analyzed and compared. In addition, a 2×2 array antenna is utilized for the purpose of RF power harvesting. It was concluded that the performance of the topologies depends on the number of antennas used in the array. In order to improve the isolation and gain of the antenna, [4] employs a dual-polarized antenna with an annular rectangular ring slot. Furthermore, the paper correlates many different families of Schottky diodes. The maximum efficiency of 25.98% and 1.57 V output

voltage is observed when SMS7630 is used. An improved efficiency is noticed in [5], i.e., 30% with 1 $\mu W/cm^2$ incident power density, owing to an additional reflector element in the receiving antenna. In [6], a cost-effective Rectenna design is used with a unique optically transparent Plexiglas substrate. Employing a 6-element Rectenna array and SMS 7630, an output of 70 and 190 mV is observed at 1 and 5 $\mu W/cm^2$ of input power, respectively. In [7], the conversion efficiency found under simulation environment is 86% at 27 dBm of input power and 220 Ω load. The efficiency is seen to drop down as the input power increases above 27 dBm. The result after fabrication differs a lot; the maximum efficiency drops down to 40.1% at 24 dBm and 220 Ω load. This difference is believed to be due to the diode parameters and the welding positions of the diode and capacitor. A thorough comparison between the Voltage Doubler (VD)-type Rectenna and the Half-Wave Rectifier (HWR)-type Rectenna is compiled in [9]. For an input power of 1 mW/cm^2, the conversion efficiency of 56.9 and 21.8% is noted for VD and HWR-type, respectively. In order to tackle the problem of higher order harmonic intervention, symmetric stubs were introduced in the Rectenna design as seen in [12]. Furthermore, an increase in the conversion efficiency to 63% was observed. CPW stub was utilized for the purpose of Impedance Matching. In [13], though no such stub was utilized as both the antenna feeding and rectifier input port had 50 Ω impedances for good impedance matching. A slight increase in the efficiency was observed in this case; 66% at 270 Ω with 2.6 V output voltage. The proposed Rectenna was also able to maintain an efficiency of more than 50% for a frequency range of 2–3 GHz, thus acting as a broadband Rectenna. Instead of using a single antenna design, [15] uses two different types, one singly fed and one differentially fed. The overall efficiency observed is 73.9% for the input power density of 207 $\mu W/cm^2$. In another paper, the antenna with harmonic suppression capability was proposed, which would eliminate the need of LPF [16]. The conversion efficiency measured was 74% for 10 dBm input power and 0.3 mW/cm^2 power density. In addition, SMA connectors are also eliminated to improve the efficiency. In [17], the conversion efficiency observed is 75%. Two different types of Rectenna are proposed, Single-Branch Matching type (SRC) and Double-Branch Matching Type (DRC). With SRC, the Rectenna achieves 75.5% conversion efficiency with 19 dBm input signal power, and higher than 63% between 10 and 19 dBm [17]. DRC outperforms SRC in terms of reducing ripples, but a reduction in the efficiency is observed. In order to suppress unwanted harmonics, an open stub is used on the transmission line which has the added advantage of making the circuit compact. Also, the antenna used is circularly polarized, which improves the ambient power collecting capacity. A large conversion efficiency of 77.8% is obtained in case of [18]. The antenna used is harmonic-rejecting circular sector antenna, which eliminates the need of LPF in the antenna's side. The quarter wave transformer is used for impedance matching. The maximum conversion efficiency is observed in [19], with 82% efficiency and a gain of 3.5 dB with 600 Ω load. A third-order stepped-impedance Low-Pass Filter is used for higher order harmonic suppression. It is observed that as the junction capacitance of the rectifying diode decreases, better efficiency is obtained.

The data corresponding to 2.45 GHz frequency-based Rectenna is tabulated in Table 1.

Table 1 Rectenna designs based on 2.45 GHz frequency

No	Reference	Type of antenna	Comments
1	[1]	Dipole antenna with a rectangular section	Output voltage of 4.5 V is obtained under the input power 12.9 dBm
2	[2]	Half-wave dipole antenna	GaAsPt Schottky barrier diodes and SMS family of diodes are used
3	[3]	2 * 2 planar antenna array	Quadrupler circuit used with matching network
4	[4]	Dual-polarized suspended square plate antenna	The dual-polarized antenna was etched the annular rectangular ring slot
5	[5]	Folded dipole with an inductive feed and a corner reflector	Additional reflector element used improves efficiency
6	[6]	6 patch antenna array (2 * 3)	Measured output dc voltages of 70 and 190 mV at 1 and 5 $\mu W/cm^2$, respectively
7	[7]	Microstrip Patch Antenna	Output voltage is 9.7 V for 220 Ω
8	[8]	Square aperture coupled patch antenna with a cross-shaped slot	The antenna has orthogonal polarization which helps in increasing efficiency
9	[9]	Not specified	DCP (Dickson charge pump) and HWR (half-wave rectifier) antenna and distance between source and rectenna is 4.5 m in the far field
10	[10]	Dual circularly polarized antenna	Rectenna proposed provides efficiency higher than 61% irrespective of incident wave's polarization
11	[11]	Stacked patch antenna	4 input power levels are considered: −30, −20, −10 and 0 dBm
12	[12]	Linearly polarized PBG antenna	The rectenna design uses a miniature microstrip LPF with DGS (defected ground structure) in order to suppress the higher order harmonics of the unwanted signals. To achieve enhanced performance from the LPF, symmetric stubs were introduced to increase the filter's band stop suppression in the high-frequency band

(continued)

Table 1 (continued)

No	Reference	Type of antenna	Comments
13	[13]	Printed monopole broadband antenna	The conversion efficiency is maintained from 2 to 3 GHz above 50%. A tapped line geometry is used to design the broadband stub band-pass filter
14	[14]	GCPW-fed slot antenna	It uses grounded coplanar waveguide as a feeding structure to the antenna. This helps in high gain, a broader bandwidth, and a simple structure
15	[15]	A differentially fed-patch antenna	A differentially driven rectifier is used in order to eliminate the use of a Balun
16	[16]	Rectangular radiating patch antenna	In order to reduce insertion loss, no LPF is used. Efficiency is high without SMA connectors
17	[17]	Rectangular radiation patch	SRC and DRC are used
18	[18]	Harmonic-rejecting circular sector antenna	No LPF block in the Rectenna circuit
19	[19]	Microstrip dipole antenna	The capacitive reactance of the diode is set by varying the distance between the diode and the output capacitor. With a decrease in the junction capacitance of the diode, efficiency is improved

There are many Rectennas which works on more than one frequency. Some of these are band specific while others are termed broadband in general. Some Rectennas works on dual frequency.

The Research Paper [20] works with multiple bands of frequencies; DTV (417–610 MHz), GSM900, GSM1800, and 3G. The conversion efficiency of 40% is obtained in case of GSM900 and in the case of DTV and 3G, more than 20% efficiency is observed. In addition to RF harvesting, the paper also focuses on Inductive Power Transfer (IPT) and puts forward an IPT system; Class E-coil driver. It is able to achieve a conversion efficiency of 66% for coil separations limited to 30 cm and an efficiency of more than 50% for distances more than 30 cm. For a frequency band of 1.75–2.5 GHz, a dual-polarized Rectenna designed is explored [22]. Moreover, two different rectifier circuits with single-branch and two-branch structure have been designed and their performances are compared. For a single-branch rectifier, more than 40% conversion efficiency is seen, while for two-branch structure 45% efficiency is obtained for 0.85–0.95 and 1.7–2.45 GHz band both.

The Research Paper discussed in [23] and [24] provides different Rectenna Designs focusing on the GSM 900 band. In [23], about 2.3 DC Voltage is obtained

when the harvester circuit is placed at 110 m from the GSM base station whose input power level is known to vary from −27 to −50 dBm. Its operation in the ISM band is also demonstrated and an output voltage of 1 V is observed across a 0.5 MΩ load at a range of 19 m when the signal is transmitted indoor. The Rectenna proposed in [24] uses a microstrip-fed printed shorted ring slot antenna with circular polarization. For an incident power density of 162 $\mu W/cm^2$, the efficiency of 45.47% is obtained with an output voltage of 3.8 V. In [26], A Broadband Rectenna focusing on the 3G band is described. For an optimum load of 1700 Ω, 48% efficiency is noticed with 400 mW output voltage. All the measurements are done in a free environment which allows the Rectenna to capture RF signals from other bands. For a frequency band of 700–900 MHz, [27] presents a Rectenna design which is able to achieve 65% at 800 MHz with input power ranging within −10 to 0 dBm. A low cost and simpler design is presented in [28], which uses a pair of super-strip lines in the wideband folded antenna to reject the unwanted harmonic signals. Conversion Efficiency of 72.9% is obtained when power at 30 dBm is transmitted by a signal generator.

In [29], a Rectenna design has been discussed with works on the X band frequencies (8–12 GHz). At 9.98 GHz, they were able to measure the output voltage of 3.86 V across a load of 200 Ω and conversion efficiency of 75%. The concept of aperture coupling is also used to match the antenna with the Rectenna circuit. The maximum conversion efficiency is observed when a 4-element receiving array antenna is used. Out of this group of Research Papers, [31] had the maximum efficiency of 84.4 and 82.7% at 2.45 and 5.8 GHz respectively. The paper proposes a Dual-Frequency Rectenna T-strip CPS (coplanar strip line) band-stop filters which effectively blocks higher order harmonics. The GaAs Schottky barrier diode is used for the purpose of rectification and diode analysis has been performed for impedance matching purpose.

Several Rectenna designs have used unconventional frequencies and unconventional methods for the purpose of RF-to-DC conversion. Another frequency which has been heavily used for Energy Scavenging is 5.8 GHz. The Research paper [34] is based on a Rectenna working at 868 MHz. Two different Rectenna setups have been put forward, one with impedance matching and one in which direct matching with the antenna has been done. This not only miniaturizes the antenna, it also improves the conversion efficiency (55% at −10dBm input power). Another such Rectenna design discussed in [35] gives a conversion efficiency of 49.7% across a 10 kΩ load. The impedance of the Voltage Doubler is computed and using that the LC Matching Network has been designed. The output voltage observed is 0.705 V. The Rectenna put forward in [37] is tuned to mid-infrared wavelengths. Two different types of diodes are used in this design; MIM (Metal–Insulator–Metal) and MIIM (Metal–Insulator–Insulator–Metal) because of their fast electron switching speeds. While most designs employ a single stage of Voltage Doubler circuit, the Rectenna design in [38] uses multiple stages of Voltage Doubler circuits in order to optimize the RF-DC conversion. For an input power level of −40 dBm, the 7-stage Voltage Doubler based Rectenna is able to produce 3 mW across a 100 kΩ load, while at 0 dBm, the DC output voltage of 5 V is produced. In [39], a similar 7-stage Voltage Doubler based Rectenna is discussed, but the design is able to achieve 4.5 V at 10 dBm.

Table 2 shows all the information into different fields. Several unique Rectennas have also been documented, such as FM Rectenna [41], which uses the Fractal Antennas for acquiring the RF signals. In [42], a quartz resonator is used for impedance transformation. Although the conversion efficiency is less (22%), the output voltage measured is 1 V. The paper thus provides a unique way to capture the RF signals. Finally, the Optical Antennas and Nanoantennas have also been studied, albeit in brief, but nonetheless, the result has been tabulated.

Table 2 Rectenna designs based on other frequencies

No	Reference	Type of Antenna	Comments
1	[20]	Folded dipole omnidirectional	Works on GSM 900, TV & 3G
2	[21]	Copper tape antenna on Perspex	It utilizes a multiband array architecture corresponding to every band and the output voltage is obtained by using a switching and summing mechanism
3	[22]	Dual-polarization antenna	Two broadband rectifier circuits with single-branch structure
4	[23]	Dual-band antenna	The antenna is placed within 110 m of a GSM base station. The power received is used to operate the thermo-hygrometer sensor
5	[24]	Shorted square ring slot antenna	Dipole antenna transmitting in the GSM band with 20 dBm power is used as RF source rectenna output voltage and efficiency at various distances from a cell tower at 950 MHz is tabulated
6	[25]	Circularly polarized microstrip patch antenna (1×2 and 2×2 arrays)	Coplanar Waveguide is used to feed the array and array is modified to improve AR bandwidth and impedance bandwidth
7	[26]	Modified double slot coplanar waveguide (CPW)	Measurements were realized in the free environment; without an anechoic chamber allowing the antenna to recover others RF signal
8	[27]	SLOT antenna	The rectenna is able to provide a voltage higher than 0.5 V with relatively low input power, –6 dBm. Diode package model in the simulation for a correct evaluation of the diode parasitic

(continued)

Table 2 (continued)

No	Reference	Type of Antenna	Comments
9	[28]	Wideband folded dipole antenna	A pair of super-strip lines is introduced in the wideband folded dipole to reject the second harmonic signal
10	[29]	Circularly polarized antennas (microstrip)	The maximum efficiency is obtained with 4 element array antenna
11	[30]	A broadband triangular monopole antenna array (Zin = 200 Ω)	A voltage of 6.95 V for a load of 4.3 kΩ is obtained close to a cell phone making a call
12	[31]	Long and short dipole	The paper proposes dual frequency Rectenna with T-strip CPS (coplanar strip line) band stop filters, which effectively blocks higher order harmonics
13	[32]	Stepped-impedance dipole antenna	The antenna used is 23% shorter in length when compared to conventional uniform strip dipole
14	[33]	Patch (1 × 4) antenna	Provides conversion efficiency of 70%
15	[34]	Broadband printed Yagi-Uda antenna (50 Ω) Rectangular loop-like antenna with arm-like structures	Direct impedance matching of the antenna with the rectifier is implemented
16	[35]	Yagi-Uda patch antenna	The input impedance of the Voltage Doubler circuit is 27-j*222Ω at the frequency of 868 MHz
17	[36]	Planar dipole antenna	Schottky diode and antenna are integrated via coplanar waveguide. The variation of output power versus frequency, input power, and series resistance are individually plotted
18	[37]	Log periodic antenna, spiral nanoantenna and Bowtie nanoantenna are analyzed	Many rectenna designs operating in THz range are reviewed
19	[40]	Microstrip patch antenna	All the matching networks mentioned and the analytical models constructed are covered in detail along with the mathematical computation

(continued)

Table 2 (continued)

No	Reference	Type of Antenna	Comments
20	[41]	Fractal antennas (Sierpinski triangle and Kuch curve antenna)	The developed Rectenna is cheap, efficient, simple to implement and environmental friendly
21	[43]	Differential microstrip antenna	Circuit and electromagnetic simulations are performed in order to design the rectenna
22	[44]	Nanoantennas are used (which capture infrared light)	The paper discusses the matching technique and NOT the optical rectenna. A DC–DC Converter LTC3108 is used. The internal impedance of nanoantennas was simulated in the range of 250–1000 THz frequency

4 Conclusion

With regards to the Rectenna design, if voltage doubler stages are increased, it was observed that output voltage and RF-DC conversion efficiency was also increased. Based on the Rectenna Papers referred, it is observed that Wi-Fi (2.4–2.45 GHz) frequency is the frequency which is worked upon the most and significant result has been obtained in terms of conversion efficiency and output voltage. Broadband Rectennas working on GSM, 3G, and ISM bands have also achieved noteworthy results, indicating that there is a growing interest in the field of Wireless Energy Harvesting. Also, it is noted that as the input power level is increased, output power and efficiency are also increased. Experiments performed in the anechoic chamber completely absorb electromagnetic waves and avoids unwanted electromagnetic interferences, which improve the conversion efficiency.

References

1. Athira AT, Shoukath S, Mohammad SK (2017) Design of a compact voltage-doubler-type rectenna. In: IOSR journal of electronics and communication engineering (IOSR-JECE), the national symposium on antenna signal processing & interdisciplinary research in electronics 2017 (ASPIRE-2017)
2. Zhang J, Huang Y (1980) Rectennas for wireless energy harvesting. Department of Electrical Engineering and Electronics, University of Liverpool, Liverpool, L69 3GJ
3. Olgun U, Chen CC, Volakis J (2011) Investigation of rectenna array configurations for enhanced RF power harvesting. IEEE Antennas Wirel Propag Lett 10. https://doi.org/10.1109/lawp.2011.2136371
4. Phongcharoenpanich C, Boonying K (2015) A 2.4-GHz dual polarized suspended square plate rectenna with inserted annular rectangular ring slot. Int J RF Microw Comput Aided Eng, Received 28 June 2015. https://doi.org/10.1102/mmce.20949

5. Ramos I, Popović Z (2015) A compact 2.45 GHz, low power wireless energy harvester with a reflector-backed folded dipole rectenna. In: IEEE wireless power transfer conference (WPTC). https://doi.org/10.1109/wpt.2015.7140159
6. Takhedmit H, Cirio L, Costa F, Picon O (2014) Transparent rectenna and rectenna array for RF energy harvesting at 2.45 GHz. In: The 8th European conference on antennas and propagation (EuCAP), IEEE. https://doi.org/10.1109/eucap.2014.6902451
7. Chuc DH, Duong BG (2014) Design, simulation and fabrication of rectenna circuit at S-band for microwave power transmission. VNU J Sci Math Phys 30(3):24–30
8. Vera GA, Georgiadis A, Collado A, Via S (2010) Design of a 2.45 GHz rectenna for electromagnetic (EM) energy scavenging. In: Radio and wireless symposium (RWS), IEEE. https://doi.org/10.1109/rws.2010.5434266
9. Mitani T, Kawashima S, Nishimura T (2017) Analysis of voltage doubler behavior of 2.45-GHz voltage doubler-type rectenna. IEEE Trans Microw Theory Tech 65(4). https://doi.org/10.1109/tmtt.2017.2668413
10. Sun H, Geyi W (2015) A new rectenna with all polarization receiving capability for wireless power transmission. IEEE Antennas Wirel Propag Lett. https://doi.org/10.1109/lawp.2015.2476345
11. Huang Y, Shinohara N, Toromura H (2016) A wideband rectenna for 2.4 GHz-band RF energy harvesting. In: IEEE wireless power transfer conference (WPTC). https://doi.org/10.1109/wpt.2016.7498816
12. Ji S, Qi H, Zhang H (2014) Rectenna serves 2.45-GHz wireless power transmission. In: SCRIBD microwave and RF
13. Hong TU, Oh KM, Lee HW, Nam H, Yun TS, Lee DS, Hwang HI, Lee JC (2010) Novel broadband rectenna using printed monopole antenna and harmonic-suppressed stub filter. Microw Opt Technol Lett 52(5). Wiley Periodicals, Inc. https://doi.org/10.1102/mop.25130
14. Nie MJ, Yang XX, Tan GN, Han B (2013) A compact 2.45-GHz broadband rectenna using grounded coplanar waveguide. IEEE Antennas Wirel Propag Lett. https://doi.org/10.1109/lawp.2015.2388789
15. Sun H (2015) An enhanced rectenna using differentially-fed rectifier for wireless power transmission. IEEE Antennas Wirel Propag Lett. https://doi.org/10.1109/lawp.2015.2427197
16. Harouni Z, Osman L, Gharsallah A (2010) Efficient 2.45 GHz rectenna design with high harmonic rejection for wireless power transmission. IJCSI Int J Comput Sci Issues 7(5). ISSN (Online): 1694–0814
17. Cao Y, Hong W, Deng L, Li S, Yin L (2016) A 2.4 GHz circular polarization rectenna with harmonic suppression for microwave power transmission. In: Internet of things (iThings) and IEEE green computing and communications (GreenCom) and IEEE cyber, physical and social computing (CPSCom) and IEEE smart data (SmartData), IEEE international conference (2016). https://doi.org/10.1109/ithings-greencom-cpscom-smartdata.2016.85
18. Park JY, Han SM, Itoh T (2004) A rectenna design with harmonic-rejecting circular-sector antenna. IEEE Antennas Wirel Propag Lett 3. https://doi.org/10.1109/lawp.2004.827889
19. Ojha SS, Singhal PK, Agarwal A, Gupta AK (2013) 2-GHz dual diode dipole rectenna for wireless power transmission. Int J Microw Opt Technol 8(2)
20. Pinuela M, Yates DC, Lucyszyn S, Mitcheson PD (2012) Current state of research at Imperial College London in RF harvesting and inductive power transfer. In: 2nd international workshop on wireless energy transport and harvesting
21. Piñuela M, Mitcheson P, Lucyszyn S (2013) Ambient RF energy harvesting in urban and semi-urban environments. IEEE Trans Microw Theory Tech 61(7). https://doi.org/10.1109/tmtt.2013.2262687
22. Song S, Su M, Liu Y, Li S, Tang B (2016) A novel broadband rectenna for energy harvesting. In: International symposium on antennas and propagation (ISAP), IEEE. ISBN: 978-88552-131-7
23. Nimo A, Beckedahl T, Ostertag T, Reindl L (2015) Analysis of passive RF-DC power rectification and harvesting wireless RF energy for micro-watt sensors. AIMS Energy 3(2). https://doi.org/10.3934/energy.2015.2.184

24. Ghosh S (2017) Design and testing of rectifying antenna for RF energy scavenging in GSM 900 band. Int J Comput Appl
25. Liu Y, Huang K, Luo X (2017) Circularly polarized antenna array fed by air-bridge free CPW-slotline network. Int J Antennas Propag 2017, Article ID 5230142, Hindawi. https://doi.org/10.1155/2017/5230142
26. Khemar A, Kacha A, Takhedmit H, Abib G (2017) Design and experiments of a 3G-band rectenna for radio frequency energy harvesting, vol 62, no 1, pp 82–86. Bucarest. researchgate.net/publication/315757027 (2017)
27. Palazzi V, Prete MD, Fantuzzi M (2017) Scavenging for energy. IEEE microwave magazine. https://doi.org/10.1109/mmm.2016.2616189
28. Zhang F, Liu X, Meng FY, Wu Q, Lee JC, Xu JF, Wang C, Kim NY (2014) Design of a compact planar rectenna for wireless power transfer in the ISM band. Hindawi Publishing Corporation International Journal of Antennas and Propagation, Article ID 298727. https://doi.org/10.1155/2014/298127
29. Xuexia Y, Junshu X, Deming X, Changlong X (2008) X-band circularly polarized rectennas for microwave power transmission applications. China J Electron 25(3). https://doi.org/10.1107/s11767-006-0273-4
30. Arrawatia M, Baghini MS, Kumar G (2016) Broadband rectenna array for RF energy harvesting. In: International symposium on antennas and propagation (APSURSI) conference publications, IEEE conference. https://doi.org/10.1109/asp.2016.7696641
31. Suh YH, Chang K (2002) A high-efficiency dual-frequency rectenna for 2.45- and 5.8-GHz wireless power transmission. IEEE Trans Microw Theory Tech 50(7). https://doi.org/10.1109/tmtt.2002.800430
32. Tu WH, Hsu SH, Chang K (2007) Compact 5.8-GHz rectenna using stepped-impedance dipole antenna. IEEE Antennas Wirel Propag Lett 6. https://doi.org/10.1109/lawp.2007.898555
33. Sun H, Geyi W (2016) A new rectenna using beamwidth-enhanced antenna array for RF power harvesting applications. IEEE Antennas Wirel Propag Lett. https://doi.org/10.1109/lawp.2016.2642124
34. Visser HJ, Keyrouz S, Smolders AB (2015) Optimized rectenna design. In: Wireless power transmission for sustainable electronics (WiPE), vol 2, no 1. Cambridge University Press. https://doi.org/10.1017/wpt.2014.14
35. Keyrouz S, Visser H (2013) Efficient direct-matching rectenna design for RF power transfer applications. In: PowerMEMS 2013 journal of physics: conference series 476. https://doi.org/10.1088/1742-6596/476/1/012093
36. Mustafa F, Parimon N, Hashim AM, Rahman SFA, Rahman ARA, Osman MN (2010) RF–DC power conversion of Schottky diode fabricated on AlGaAs/GaAs heterostructure for on-chip rectenna device application in nanosystems. Microsyst Technol. Springer. https://doi.org/10.1007/s00542-010-1099-4
37. Citroni R, Leggieri A, Passi D, Paolo FD, Carlo AD (2017) Nano energy harvesting with plasmonic nano-antennas: a review of MID-IR rectenna and application. Adv Electromagn 6(2). https://doi.org/10.7716/aem.v6i2.462
38. Devi KKA, Din NM, Chakrabarty CK (2012) Optimization of the voltage doubler stages in an RF-DC convertor module for energy harvesting. Sci Res Circuits Syst. https://doi.org/10.4236/cs.2012.33030
39. Yuvaraju P, Premkumar S (2016) Enhancement of the voltage doubler stages in a RF-DC: converter module for energy harvesting. J Chem Pharm Sci. ISSN:0974-2115, JCHPS Special Issue 6 (2016)
40. Nimo A, Grgić D, Reindl L (212) Optimization of passive low power wireless electromagnetic energy harvesters. Sensors, 12. ISSN 1424-8220. https://doi.org/10.3390/s121013636
41. Ahmad ME. Energy harvesting using a cheap easy-to-fabricate FM rectenna. Online J Electronics and Electrical Eng (OJEEE) 1(1), Reference Number: W09-0005
42. Ungan T, Polozec XL, Walker W, Reindl L (2009) RF energy harvesting design using high Q resonators. In: Croatia, IEEE MTT-S international microwave workshop on wireless sensing, local positioning, and RFIO (IMWS 2009). https://doi.org/10.1109/imws2.2009.5307869

43. Toyoda I, Nishiyama E (2017) Rectenna design using electromagnetic field simulation including nonlinear devices. In: IEEE international conference on computational electromagnetics (ICCEM). https://doi.org/10.1109/compem.2017.7912771
44. Garbo CD, Livreri P, Vitale G (2017) Optimal matching between optical rectennas and harvester circuits. In: Environment and electrical engineering and 2017 IEEE industrial and commercial power system Europe (EEEIC/I&CPS Europe) IEEE international conference. https://doi.org/10.1109/eeeic.2017.7977686

Trap-Assisted Enlarged Photoresponsivity of Er-Doped In_2O_3 Thin Films

Anupam Ghosh, Shyam Murli Manohar Dhar Dwivedi and Aniruddha Mondal

Abstract Undoped and Erbium (Er) doped In_2O_3 (In_2O_3:Er) thin films (TFs) were deposited on p-Si (100) substrates by sol-gel spin coating technique followed by open-air annealing. Gold (Au) Schottky contact based devices showed lower ideality factor and higher barrier height for the In_2O_3:Er in comparison with the undoped one. The enhanced photocurrent for the In_2O_3:Er TFs makes it more photosensitive than undoped In_2O_3 TFs. The responsivity curve shows a blue shift in near band edge absorption for the In_2O_3:Er TFs. As a whole, there was a reduction in trap density with the incorporation of Er into In_2O_3 lattice and room temperature photo responsivity curves can be directly used to track the trap-related optoelectronic properties of a light-sensitive material.

Keywords Indium oxide · Defect states · Electrical properties · Traps · Optical properties

1 Introduction

Transparent oxide semiconductors (TOSs) are of paramount interest in the field of optoelectronics. A unique combination of two mutually exclusive properties, i.e., high electrical conductivity along with optical transparency are essential for the applications in optoelectronic devices such as solar cells and organic light emitting diodes (OLEDs) [1]. In solar cells, these TOSs help to photo-generate charge carriers and subsequently extract them from the absorbing region [2]. In OLEDs, they inject charge carriers to efficiently out-couple the light [2]. Doped TOSs films are also attracting interest due to their various advantages over undoped TOSs. The deposition of doped TOS with controlled doping concentration also has widespread applications. Erbium-doped Indium Oxide (In_2O_3:Er) is a good TOS in this context, which is under research for last few decades [3–6]. Among various metal oxide

A. Ghosh · S. M. M. Dhar Dwivedi · A. Mondal (✉)
Department of Physics, National Institute of Technology Durgapur, Durgapur 713209, India
e-mail: aniruddhamo@gmail.com

© Springer Nature Singapore Pte Ltd. 2020

V. Janyani et al. (eds.), *Optical and Wireless Technologies*,
Lecture Notes in Electrical Engineering 546,
https://doi.org/10.1007/978-981-13-6159-3_7

semiconductors, amorphous oxide semiconductors show clear advantages for optoelectronic applications due to the combination of good optical transparency, reduced defects, easy and cost-effective synthesis method, mechanical flexibility and large-area electrical uniformity [1]. In the following sections, we shall focus on the role of trap states in light responsivity of one of such amorphous TOS, i.e., In_2O_3:Er thin film (TF) [6] based Schottky photodetectors. Ultraviolet (UV) photodetectors have several applications in the field of optical communication [7], missile plume detection [7], astronomical studies [8], etc. UV sensors also find military and industrial safety applications such as ZigBee-based wireless flame sensor [9]. Silicon-based photodetectors were used for UV photodetection but it suffers from lack of sensitivity [10]. The present work is technologically important as it leads to carry further research on the material and to improve the reliability of diode under irradiation of UV light.

2 Experimental Details

Undoped In_2O_3 and In_2O_3:Er TFs were deposited on p-type Silicon (100) substrates (MTI, USA, pre-cleaned with hydrofluoric acid and deionized water) by spin coating technique using the chemical route. The solution for preparing In_2O_3 TF was prepared by dissolving 0.50 g Indium Chloride ($InCl_3$) anhydrous powder (purity $\geq$ 99.999%, Sigma Aldrich) into 30 ml of acetylacetone (purity > 99%, Merck) under ultrasonication (~50 °C, 15 min) and left for aging for 24 h. It was then spin-coated (spin NXG-P1, apexicindia) on a p-Si substrate (rotation speed ~1000 r.p.m. for 1 min, acceleration time 20 s). The as-deposited film was then open-air annealed at ~400 °C for 10 min in a muffle furnace. The entire process was repeated for four times and finally annealed at 400 °C for 30 min to get a uniform film over the p-Si substrate. To prepare In_2O_3:Er solution, 0.04 g weight of Er_2O_3 nanopowder (99.9% purity, Sigma Aldrich) was dissolved in 10 ml sulfuric acid (H_2SO_4) by ultra-sonication and added to the previously prepared 30 ml of $InCl_3$ solution. This doped solution was ultra-sonicated (50 °C, 15 min). After the completion of ultra-sonication, the solution was left for 48 h aging. The Er:In_2O_3 sol-gel was then spin-coated with substrates rotation speed ~6000 r.p.m. for 2 min (acceleration time 1 min) followed by 10 min open-air annealing (~400 °C) for four times (final annealing 400 °C, 30 min) as has already been discussed. The details of the structural characteristics of those TFs were described elsewhere [6]. Indium was used as an ohmic contact on the backside of p-Si, whereas the Gold (Au) Schottky contacts of diameter 1 mm were prepared on the TFs by thermal evaporation using a thermal evaporator (Pro-Vak, Pune). In this way, undoped In_2O_3 and In_2O_3:Er TF based Schottky devices (Au/In_2O_3 TF/p-Si and Au/In_2O_3:Er TF/p-Si) were prepared. The schematic diagram of the devices is presented in Fig. 1.

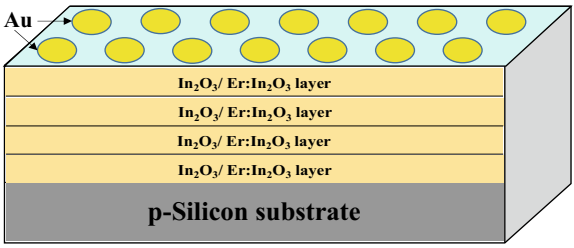

Fig. 1 Schematic diagram of the prepared Schottky devices

The corresponding current-voltage (I–V), current-time (I–t) performance of the devices were measured by using Keithley 2401 sourcemeter (interfaced with computer) and light was applied to the devices from an Ozone free Xenon arc lamp source through a monochromator (Sciencetech 9055, Canada) in an open beam configuration at room temperature (300 K).

3 Results and Discussions

3.1 I–V Responses of the Schottky Devices

Figure 2 shows ln I–V characteristics using different wavelengths of light for Au/In_2O_3 TF/p-Si and Au/In_2O_3:Er TF/p-Si device [Fig. 2 (inset)]. The ideality factor (η) was calculated from forward dark ln I–V characteristics considering thermionic field emission theory and the Schottky nature of the diodes using Eq. (1):

$$\eta = \frac{q}{kT}\left[\frac{\partial V}{\partial (lnI)}\right], \tag{1}$$

where, q is the electronic charge, kT is the thermal voltage and $\frac{\partial (lnI)}{\partial V}$ is the slope of the linear fit of the dark ln I–V curve taken between 0.4 and 1.2 V). For the doped device the η value is lower (~6) as compared to the Au/In_2O_3 TF/p-Si device (~12). The saturation current value (I_0) was also lower (calculated from the intercept of the linear fits) for Au/In_2O_3:Er TF/p-Si device (~1.8×10^{-7} A) as compared to Au/In_2O_3 TF/p-Si device (~7.1×10^{-6} A). The barrier height (ϕ_B) for both devices were calculated using Eq. (2)

$$\phi_B = \frac{kT}{q} ln\left(\frac{AA^*T^2}{I_0}\right), \tag{2}$$

where, A is the device area and A^* is Richardson constant. The values of ϕ_B were ~0.64 eV for undoped and ~0.72 eV for the doped device at T = 300 K. The ratio of forward and reverse currents at ±3 V are ~80 and ~16,381 for Au/In_2O_3 TF/p-Si

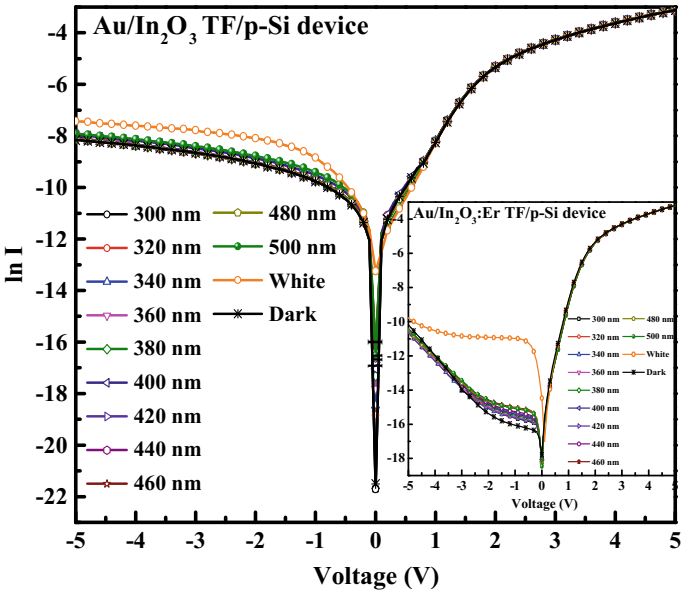

Fig. 2 ln I–V characteristics using different wavelengths of light for both devices

and Au/In_2O_3:Er TF/p-Si diodes respectively. These high values suggest that a good Schottky contact was formed between Au and the TFs. The lower η, I_0 values and higher ϕ_B values for the Au/In_2O_3:Er TF/p-Si device elucidate its better Schottky diode performance over the Au/In_2O_3 TF/p-Si device. The presence of large number of oxygen-related defect states at the interface of metal-semiconductor increased the probability of multistep tunneling process due to trapping of holes, which in turn enhanced the ideality factor [6]. Both the samples were light sensitive in the wavelength range 300–500 nm, as it is clear from Fig. 2. But, the light currents are far higher than the dark current for the In_2O_3:Er TFs in reverse bias condition, which makes it more light sensitive than the undoped In_2O_3 TF-based devices. The ratios of photocurrent (under white light illumination) and dark current are ~2.6 and ~86.5 for Au/In_2O_3 TF/p-Si and Au/In_2O_3:Er TF/p-Si devices at an applied bias of -2 V. Therefore, there was a nearly 33-fold enhancement in white light sensitivity for the doped TF as compared to the undoped one at -2 V (light sensitivity is defined as the ratio of the light current to the dark current at a particular wavelength of light). The fact suggests that the Au/In_2O_3:Er/p-Si device can serve as a good UV-Visible light sensing device at room temperature.

3.2 *Responsivity and Function of Defect States*

The wavelength-dependent (300–600 nm) responsivity of the devices was obtained at room temperature (by dividing the photocurrents by optical power) to find out the role of trap states in photocurrent conduction mechanism. Figure 3 shows the light responsivity (in A/W) curves for both devices under the applied reverse bias of −5 V, respectively. There are two responsivity peaks for Au/In_2O_3 TF/p-Si device at 400 nm (~3.1 eV) and 360 nm (~3.4 eV), which corresponds to the near band edge (NBE) photon absorption and subsequent photocurrent conduction, as the bandgap of the In_2O_3 material was calculated to be ~3.54 eV [6]. The NBE responsivity peak was blue shifted to 380 nm (~3.26 eV) for the Au/In_2O_3:Er TF/p-Si device, which may be due to the enhancement in the optical band gap of the In_2O_3 material with Er doping, which was previously reported [6].

It is observed from Fig. 3 that there is a broad peak in responsivity curve between 500 and 580 nm for undoped In_2O_3 material, which corresponds to the oxygen-related defect states and singly ionized oxygen vacancies of the undoped In_2O_3 material [6, 11]. However, those oxygen-related traps were eliminated and only shallow level traps (SLTs) for the material remained with Er doping [12]. The peak was also reduced for the Au/In_2O_3:Er TF/p-Si device, which suggests the decrease in trap density for In_2O_3:Er TF. The ratio of SLT related peak at 580 nm to NBE related peak at 400 nm for undoped In_2O_3 is ~0.58 which reduces to ~0.37 for the In_2O_3:Er TF considering the ratio of SLT related peak at 580 nm to NBE related peak at 380 nm. This ~1.6-fold decrease in the ratio at −5 V suggests that there is also a

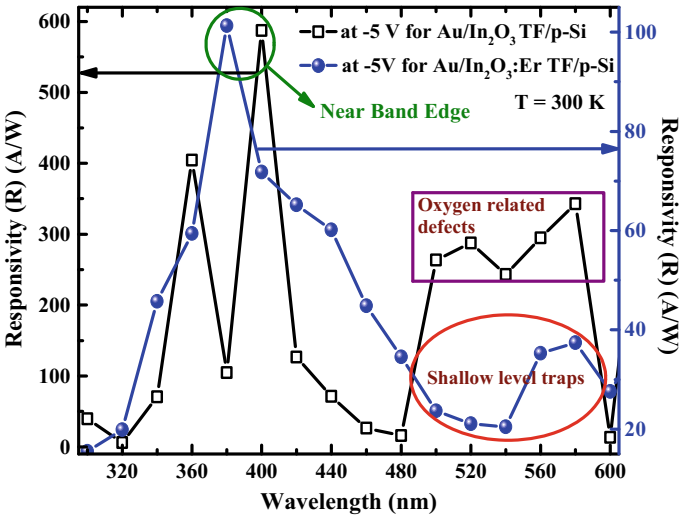

Fig. 3 Responsivity at different wavelengths for both the devices

reduction in the shallow level trap density with the incorporation of Er in the In_2O_3 lattice.

3.3 *Photosensitivity and Temporal Responses of the Schottky Devices*

The room temperature photosensitivity of the devices was tested by taking the ratios of light current to dark current under irradiation of different wavelengths of light at an applied bias of −2 V and is shown in Fig. 4a. The photosensitivity is more for the Au/In_2O_3:Er TF/Si device, which gives another evidence to the fact that the defect states are removed in doped material. In the case of undoped In_2O_3 TFs, there are more number of shallow level trap states in addition to oxygen-related defects, in which the photo-excited carries are trapped and as a result, the sensitivity of the device decreases. However, in the Au/In_2O_3:Er TF/Si device, the oxygen-related defects were almost completely removed, which was discussed before [6]. There exist only a few shallow level traps near conduction band, from which the carriers can be easily excited by photons to the conduction band, resulting in an increased light current, which in turn enhances the light sensitivity for the doped device.

The suitability of the devices as optical sensors was studied using the time-dependent photocurrent measurement (temporal response) under light off–on switching irradiation and plotted in Fig. 4b. Under the illumination of white light from Xenon arc lamp, at −5 V bias the undoped and doped TF device responds with almost same rise time (T_r) ~0.13 s and fall time (T_f) ~0.14 s respectively. The T_r is the time required by the pulse to increase from 10% to 90% of its peak value and the T_f is defined as the time required by the pulse to decrease from 90% of the peak

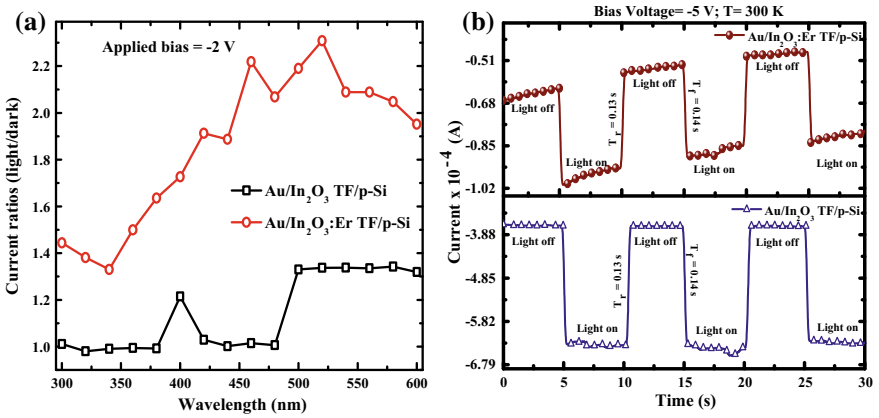

Fig. 4 **a** Light sensitivity (ratio of light current to dark current) versus wavelength for both devices, **b** temporal response with white light for both devices

value to 10%. The incident photons mostly got absorbed in the depletion region, which results in a high drift of carriers and reduces the effect of carrier diffusion on the temporal response of the device. Both the T_r and T_f values were very small and hence it can be manifested that the devices can be readily applied to the optoelectronic sensing applications. But, with lesser number of defects and traps the In_2O_3:Er TFs can be more suitably applied as a UV-Visible detector.

4 Conclusion

In this report, an efficient technique has been introduced to study of the role of traps in terms of room temperature photoresponse of the devices. The In_2O_3:Er TF-based diode performed better than the undoped one in both under the dark condition and with light illumination. The NBE peak in responsivity curves implies an enhancement in optical bandgap for the doped TF. Also, there is a reduction in oxygen-related defects and SLT-related trap states with the incorporation of Er in the In_2O_3 lattice. Finally, it is concluded that the room temperature responsivity curves can be directly used to determine the role of traps in the current conduction mechanism for the light-sensitive materials. Also, the enhanced light sensitivity and fast photoswitching performance of the In_2O_3:Er TF based device proves its superiority as an UV-Visible light sensor over undoped In_2O_3 TF-based device.

Acknowledgements The authors gratefully acknowledge C.S.I.R. (03(1355)/16/EMR-II), N.I.T. Durgapur and Govt. of India for financial support.

References

1. Yu X, Marks TJ, Facchetti A (2016) Metal oxides for optoelectronic applications. Nat Mat 15:383–396. https://doi.org/10.1038/NMAT4599
2. Kumar A, Zhou C (2010) The race to replace tin-doped indium oxide: which material will win? ACS Nano 4:11–14. https://doi.org/10.1021/nn901903b
3. Kim HK, Li CC, Nykolak G, Becker PC (1994) Photoluminescence and electrical properties of erbium doped indium oxide films prepared by rf sputtering. J Appl Phys 76:8209–8211. https://doi.org/10.1063/1.357882
4. Kim HK, Li CC, Barrios PJ (1994) Erbium-doped indium oxide films prepared by radio frequency sputtering. J Vac Sci Technol A 12(6):3152–3456. https://doi.org/10.1116/1.579230
5. Podhorodecki A, Kudrawiec R, Misiewicz J et al (2006) 1.54 μm photoluminescence from Er-doped sol–gel derived In_2O_3 films embedded in porous anodic alumina. Opt Mater 28:685–687. https://doi.org/10.1016/j.optmat.2005.09.044
6. Ghosh A, Mondal A, Das A, Chattopadhyay S, Chattopadhyay KK (2017) Removal of oxygen related defects from chemically synthesized In_2O_3 thin film doped with Er by spin-on technique. J Alloys Compd 695:1260–1265. https://doi.org/10.1016/j.jallcom.2016.10.254
7. Inamdar SI, Rajpure KY (2014) High-performance metal-semiconductor-metal UV photodetector based on spray deposited ZnO thin films. J Alloys Compd 595:55–59. https://doi.org/10.1016/j.jallcom.2014.01.147

8. Clarke JT, Skinner WR, Vincent MB et al (1999) Laboratory studies of alkali metal filter deposition, ultraviolet transmission, and visible blocking. Appl Opt 38:1803–1813. https://doi.org/10.1364/AO.38.001803
9. Cheong P, Chang K-F, Lai Y-H et al (2011) A ZigBee-based wireless sensor network node for ultraviolet detection of flame. IEEE Trans Ind Electron 58:5271–5277. https://doi.org/10.1109/TIE.2011.2119455
10. Shi L, Nihtianov S (2016) Comparative study of silicon-based ultraviolet photodetectors. IEEE Sens J 12:2453–2459. https://doi.org/10.1109/JSEN.2012.2192103
11. Guha P, Kar S, Chaudhuri S (2004) Direct synthesis of single crystalline In_2O_3 nanopyramids and nanocolumns and their photoluminescence properties. Appl Phys Lett 85:3851–3853. https://doi.org/10.1063/1.1808886
12. Ghosh A, Dwivedi SMMD, Chakrabartty S, Henini M, Mondal A (2018) Detailed investigation of defect states in Erbium doped In_2O_3 thin films. Mater Res Bull 99:211–218. https://doi.org/10.1016/j.materresbull.2017.11.020

Optical Wireless Hybrid Networks for 5G

Laxmi Sharma, Abhishek Javali, Sutapa Sarkar, Richa Tengshe, Mahesh K. Jha and Sudhir K. Routray

Abstract The suggested 5th generation (5G) mobile communication features are very much attractive due to their advanced specifications. Starting from the data rates, to the latency, to the overall coverage, in every aspect it is far beyond its predecessor, 4G. In addition to provide all these advanced features, the 5G network will not be completely wireless. Rather it will be a hybrid of both optical and wireless networks. In this paper, we present the main reasons why such a hybrid system is required and also provide its architectures.

Keywords 5G · Optical wireless hybrid · Optical wireless hybrid for 5G · Hybrid systems for 5G · 5G optical wireless

1 Introduction

Broadly, optical and wireless systems are complementary to each other though either of them have the complete features. In the modern communication networks, we normally see the optical networks in the core, regional and metro areas; while wireless

L. Sharma (✉) · A. Javali · S. Sarkar · R. Tengshe · M. K. Jha · S. K. Routray
CMR Institute of Technology, Bangalore, India
e-mail: laxmi.sh@cmrit.ac.in

A. Javali
e-mail: abhishek.j@cmrit.ac.in

S. Sarkar
e-mail: sutapa.s@cmrit.ac.in

R. Tengshe
e-mail: richa.t@cmrit.ac.in

M. K. Jha
e-mail: mahesh.j@cmrit.ac.in

S. K. Routray
e-mail: skr@ieee.org

© Springer Nature Singapore Pte Ltd. 2020

V. Janyani et al. (eds.), *Optical and Wireless Technologies*,
Lecture Notes in Electrical Engineering 546,
https://doi.org/10.1007/978-981-13-6159-3_8

networks are normally popular in the access parts of the networks. Therefore, it seems like they are very much each others' compliments. The recent developments of 5G indicate a big paradigm shift in communication and networking. The end-to-end data rates and overall throughputs of the networks are gigantic. Wireless networks alone are not in a position to handle such gigantic demands. In the last mile, it is fine for the access areas to provide tens of gigabits/s data rate. However in the reminder of the network, high capacity trunks are required which can only be fulfilled by optical networks. Therefore, optical wireless integration is going to be an essential aspect of 5G networks.

Optical wireless communication was proposed since the beginning of the commercial optical communications in the early 1970s. However, it did not get a good response in the industry due to the absence of appropriate hybrid technologies. In the cellular communication era, radio over fiber technology was started as a hybrid of the two. Since then, several research initiatives have been taken to bring different types of optical wireless hybrid communication systems. In [1], optical wireless communications for high speed has been proposed at multi-Gbps data rates. In [2], common features of 5G have been presented which shows the overall nature of 5G. The spectrum proposed for 5G is very much different from the existing legacy generations. Normally higher frequency bands in the mm-wave ranges will be utilized in 5G [3–5]. The justification of mm-waves for 5G is provided in [4]. Optical networks provide high throughputs and data rates. For 5G several modifications in optical networks have been proposed which are very much achievable in the current technology frameworks [5]. In [6], several advanced changing trends of optical communication have been presented. It shows how the optical and wireless communication techniques are following each others' advanced features [6]. In fact, it is very much helpful in the joint integration for 5G. Emerging optical network technologies for 5G have been presented in [7]. The post 3G wireless networks needed several structural and characteristic changes [8]. These changes are very much necessary to adapt with the emerging technologies and the handle the increasing demands. Software defined networking (SDN) is essential for the all round success of 5G. The SDN frameworks for optical networks and 5G are presented in [9] and [10].

In this paper, we provide the essence of optical wireless hybrid network architectures for 5G. We show the complimentary properties of the wireless and optical networks are very much required for successful deployment of 5G networks. We also show a few hybrid architectures of 5G at the end.

The remaining parts of the paper are arranged as follows. Section 2, contains the basics of 5G and its requirements. In Sect. 3, we present the justification of optical network integration in 5G. Section 4, presents the matching characteristics of 5G with optical communication networks. In Sect. 5, we show a few optical wireless hybrid architectures for 5G.

2 Basics of 5G

5G will have several advanced features. It will operate at extremely high carrier frequencies such as the mm-waves to provide greater coverage [1]. It will involve very high densities of base stations and devices. It will have extraordinarily large number of antennas. It is a well-defined combination of all small units to provide high data rates or around 3 Gb/s to tens to thousands of users in a locality [11]. It will 5G LTE and enhanced Wi-Fi to achieve unified experience. One needs to account the design issues involved with 5G networks such as reduction in latencies, power saving, cost saving and supporting slow connections. Currently, the innovations address the above aspects with respect to the waveform signaling, multiple access, the development of cloud-based architectures with virtualization, latency and control signaling, and energy efficiency [1].

With the increase in the number of mobile users, the wireless data traffic has to grow tremendously. In addition to that it will have support for Internet of things (IoT). One way to put up such huge amount of wireless data traffic is by restructuring the existing spectrum and by adding new spectrum. It is proposed that 5G technology may be 1000 times better in terms of throughput, 10 times better in spectrum efficiency, and 100 times better in utilizing the energy resources. To meet these stringent requirements, 5G researchers are looking forward to the use of mm-waves. In order to enhance the spatial reuse gains 5G networks must be denser and more heterogeneous than the present networks. For example, it is expected that 5G networks will use number of picocells, femtocells, and microcells. At the same time, 5G networks will reduce the cell sizes for providing access to more users. Enhancement in the spectral efficiency can be achieved by advanced modulation schemes. Even the of techniques such as device-to-device communication, non-orthogonal multiple access, cognitive radio, full-duplex communication in a single band would help in the effective spectrum utilization. Even the unlicensed spectrum in the LTE framework has also been proposed for 5G.

2.1 Technological Specifications of 5G

Several ambitious applications such as two-way gaming, on the go video streaming and content sharing, vehicle-to-vehicle and vehicle-to-infrastructure transfer of information, virtual reality services, IoT will be part of 5G. In order to cater such applications it has several advanced specifications. Here, we present some main requirements of 5G network in Table 1.

High data rates: The average data rate for 5G is set at 3 Gb/s by the ITU experts committee under the static conditions [11]. However for mobile conditions the lower threshold is 100 Mb/s. The peak data rate is set at 20 Gb/s in the direct line of sight conditions.

Table 1 Specifications of 5G [11]

#	Performance indicators	Range	Proposed technologies
1	Speed	100 Mb/s–20 Gb/s	Massive MIMO (MMIMO), MM-waves
2	Devices/km^2	1 million/km^2	Small cells, device to device
3	Information processing	10 Mb/s/m^2	RAN vitalization, small cells
4	High energy efficiency	1 μJ per 100 bits	MMIMO
5	Mobility	Up to 500 km/h	HetNet fabric
6	No. of bits/Hz	4.5	Device to device, MMIMO, full duplex
7	Latency	1 ms	Content caching among nearing users

Latency: To support anticipated 5G applications like virtual reality, touch screen activated technologies, two-way gaming, mission critical applications a round trip latency of less than 1 ms [11] is required.
Number of interconnected devices: It has to increase by a huge number which will be more than 10 folds of the current device density.
Longer battery life: About 10 times reduction in the power consumption for low-power massive machine communications (MMC) and IoT applications is required in 5G networks.

3 Why Optical Systems Required for 5G

As presented in the previous section 5G needs gigantic throughput and data rates. This gives rise to the need of high –speed- and high-capacity broadband communications with perfect end-to-end switching facilities. The bandwidth requirements for these communications will be also huge. Currently, only optical communications can provide that bandwidth. The power efficiency requirements of 5G networks too can be justified through the optical networks where the energy efficiency is very much comparable with the 5G specifications.

3.1 Features of 5G and Its Matching Aspects with Optical Communication

Optical networking is an already existing reliable framework of communication which when integrated with wireless communication system can provide a wonderful solution for high capacity mobile fronthaul and backhaul networks. As the cell

size gets reduced in 5G to cope with the requirement of high capacity data communication, the already existing passive optical network (PON) can be used to set up the fronthaul network of mobile communication. The existing PON comes at a low cost as those are already deployed and are having a wide number of access points. 10–100 Gb capable PONs already exist in many countries. The mobile fronthaul networks consist of centralized baseband unit (BBU) [1] in an effort to reduce the complexity of terminal equipments and thereby to reduce the cost of deployment and ease of maintenance. Single mode fiber optic cable is used to connect the BBU with the remote radio units. This approach is useful in cloud-based mobile applications and provides a low latency and high-speed connectivity for mobile fronthaul network. This approach also supports software defined network (SDN) for a dynamic architecture where the data plane and the control plane are separated from each other, thereby providing more flexibility in control, deployment and maintenance [9]. This architecture has the potential to support mobile backhaul networks also as that needs very little deployment effort [10].

Wavelength Division Multiplexing (WDM) in the optical networks is one more motivating factor to use optical networks along with 5G which implements massive MIMO systems in dense cellular structures. Optical networks can have the low latency for end-to-end communication which is a very crucial requirement for 5G fronthaul network [8]. The number of optical transceivers required is very high to support the massive MIMO systems deployed in 5G communications. Hence it is required to develop low cost, low power-consuming optical transceivers which can be implemented using DSP techniques along with optical fibers. Optical networks for 5G have the ability to contribute to an improved end-user experience by improving the speed and capacity of communication along with a possible reduction of cost.

Cloud-based services and high definition streaming of videos are the main activities which consume large amount of data now. These huge data consumption takes place indoors, in vehicles and also in the aircrafts. The high request for video and cloud-based data is expected to increase. This is a prime reason for the shortage of the currently available spectrum. Optical wireless communications (OWCs) are popular in different situations. Similarly, free space optical (FSO) communications are also recommended for short-range high-speed data transfer. In the next few years we will witness deployment of OWC systems in many new and existing applications. FSOs can be used for short-range 5G backhauling. All these are possible through the advances in the optical wireless hybrid communication systems which will also need the support of signal processing.

4 Hybrid Optical Wireless Architecture for 5G

Hybrid optical wireless integration can solve the problems of high-speed trunks required for 5G. End-to-end multi Gb/s data rates need high-speed core ad regional networks. It is possible to handle the large data rates, if the optical networks are used for the core and regional parts of the networks. In fact, for the fulfillment of 5G

Fig. 1 Differences between the core and the access parts of 5G network

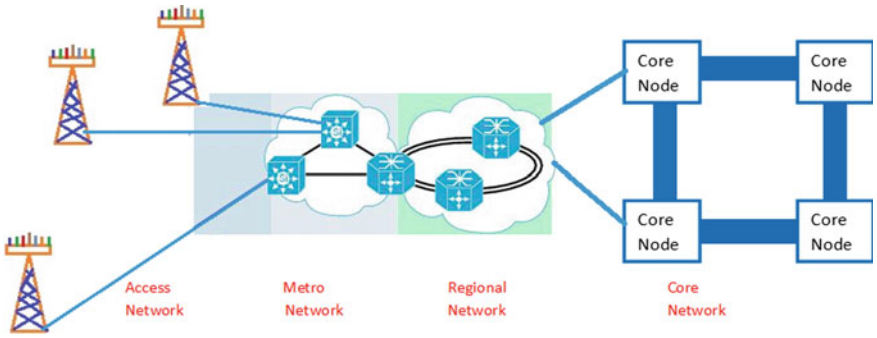

Fig. 2 Hybrid optical wireless architecture of 5G (in this architecture, only the access part is wireless and the rest are optical)

features, optical fiber is needed till the end of each base station. That means both the backhaul as well as the fronthaul of 5G has to be optical fiber. Only the last hop of the communication between the base station and the user equipment is wireless. In Fig. 1 we show the block diagram of the optical wireless hybrid network.

In fact, in this case, the core part consists of the core, regional and metro networks of the whole 5G system. At each core node, the core traffic enters/leaves the respective regions. Similarly at each regional node further traffic diversification and aggregation takes place. Then the fibers can provide the connections to the base stations from their respective metro nodes. Finally we reach the access network in which the base stations use wireless communication. The optical to wireless conversion and vice versa has to take place at the base stations. In Fig. 2, we illustrate the hybrid optical wireless architecture which can fulfill the 5G specifications without any major difficulties at the network level. However, depending on the traffic statistics some changes can be incorporated for the urban and rural architectures.

5 Conclusions

We presented the essence of having a hybrid optical wireless communication system for 5G. High throughput and data rates required in 5G suggest for a high-speed core, regional and metro networks. It can be justified by optical networks with good switching facilities. In addition to that other 5G requirements too can be fulfilled by

the optical networks. We provided the optical wireless hybrid architecture required for 5G which can handle the current 5G specifications of ITU. The proposed architecture is based on the known features of 5G and the future changes may need some changes at the architecture level.

References

1. Rakotondrainibe L, Kokar Y, Zaharia G, El Zein G, Tanguy E, Li H, Charbonnier B (2009) Hybrid, optical and wireless near-gigabit communications system. In: Proceedings of 6th IEEE international symposium on wireless communication system (ISWCS), pp 249–253
2. Andrews JG et al (2014) What will 5G be? IEEE J Sel Areas Commun 32(6):1065–1082
3. Zhang L, Xiao M, Wu G, Alam M, Liang YC, Li S (2017) A survey of advanced techniques for spectrum sharing in 5G networks. IEEE Wirel Commun, 44–51
4. Rappaport T et al (2013) Millimeter wave mobile communications for 5G cellular: it will work! IEEE Access 1:335–349
5. Cvijetic N (2014) Optical network evolution for 5G mobile applications and SDN-based control. In: 2014 16th international telecommunications network strategy and planning symposium (networks), INSPEC Accession Number: 14771595
6. Routray SK (2014) Changing trends in optical communication. IEEE Potentials 33(1):28–33
7. Liu X, Effenberger F (2016) Emerging optical access network technologies for 5G wireless. IEEE/OSA J Opt Commun Netw 8(12)
8. Ghosh S, Basu K, Das SK (2005) What a mesh! An architecture for next-generation radio access networks. IEEE Netw 19(5)
9. Routray SK, Jha MK, Javali A, Sharma L, Sarkar S, Ninikrishna T (2016) Software defined networking for optical networks. In: Proceedings of IEEE international conference on distributed computing, VLSI, electrical circuits and robotics (DISCOVER 2016), Surathkal, Mangalore, 13–14 Aug 2016
10. Routray SK, Sharmila KP (2017) Software defined networking in 5G. In: Proceedings of 4th IEEE international conference on advanced computing and communication systems (ICACCS), Coimbatore, 6–7 Jan 2017
11. Routray SK, Sharmila KP (2017) Green initiatives in 5G. In: Proceedings of 2nd IEEE international conference on advanced computing and communication systems (ICACCS), Coimbatore, 6–7 Jan 2017

A Dual-Band Minkowski-Shaped MIMO Antenna to Reduce the Mutual Coupling

K. Vasu Babu and B. Anuradha

Abstract This paper describes the performance of minkowski patch antenna wherein the size of antenna is maintained at 60 mm × 40 mm with an overall area occupied by the antenna including substrate, ground and patch at 2400 mm^2. A neutralization line is inserted between the two small microstrip patches by maintaining a separation value of 0.12 λ_0 at the two edges of antenna. By using this type of technique, the electromagnetic interference between the antennas (mutual coupling) is strongly reduced at the resonant frequency of the proposed antenna with a value of 63.08 dB at 3.376 GHz and 49.23 dB at 7.216 GHz. The resonating frequency of the proposed design greatly improves the impedance bandwidth from 2.77 to 4.0 GHz is around 1.23 GHz and the resonate frequency from 6.94 to 7.55 GHz is around 610 MHz.

Keywords Minkowski patch antenna · Neutralization line · Mutual coupling · Impedance bandwidth

1 Introduction

In the present communication technology antenna plays an important role in application areas like WiMAX, WLAN, satellite, and radar applications. By using the technique of electric and magnetic fields to reduce the isolation with an overall size of 70 mm × 60 mm and separation between the two edges 0.45 λ_0 as proposed in [1]. A loop antenna is used in order to reduce the isolation with an overall size is 2500 mm^2 operating at 2.4, 5.2, and 5.8 GHz which reduces the mutual coupling around 35.7 dB [2]. A coradiator dual-polarization MIMO system in [3] produced S_{12} of 28 dB. The frequency operated from 3.1 to 10.6 GHz is used in the applications area of handheld devices, robots and PDA's with spacing between the elements is 0.35 λ_0 with overall

K. Vasu Babu (✉) · B. Anuradha
Department of ECE, Sri Venkateswara University, Tirupati, Andhra Pradesh, India
e-mail: vasubabuece@gmail.com

B. Anuradha
e-mail: anubhuma@yahoo.com

© Springer Nature Singapore Pte Ltd. 2020

V. Janyani et al. (eds.), *Optical and Wireless Technologies*,
Lecture Notes in Electrical Engineering 546,
https://doi.org/10.1007/978-981-13-6159-3_9

Table 1 comparison with other existing methods

Published literature	Total occupied size (mm^2)	Operating frequency (GHz)	Edge-to-edge distance (λ_0)	S_{11} (dB)	S_{12} (dB)
[1]	4200	3.5	0.45	32.5	37
[2]	2500	2.4	0.62	28	35.7
[4]	1501.5	3.5	0.35	35	32.8
[5]	1800	2.45	0.23	32	41.2
[6]	1269	2.45	0.27	41.2	36
Minkowski MIMO antenna	2400	3.376 7.216	0.12 0.12	49.93 15.98	63.08 49.23

Table 2 Rectangular MIMO design parameters

Design parameters	Ls	Ws	L	W	a	b	c	d	e
Value (mm)	50	40	20	30	5	8	4	40	3

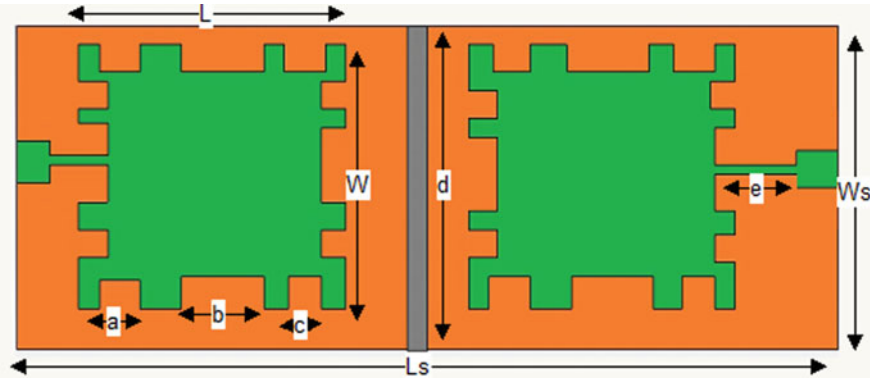

Fig. 1 Minkowski MIMO patch antenna

dimension maintained 33 mm × 45.5 mm in [4]. In [5], the parameter of mutual coupling is reduced to 32 dB and it in turns improves the return loss at around 38 dB with area occupied by 30 mm × 60 mm. The technique mentioned is the decoupling structure operated with a UWB range with a size of MIMO antenna is 27 mm × 47 mm with separation of edge to edge is 0.27 λ_0 in [6]. Different approaches were observed [7, 8] to reduce the isolation and to maintain the value less than or equal to 15 dB. In the proposed structure of antenna a separation between the edges is very compact with a value of 0.12 λ_0. By considering this type of arrangement to reduce the isolation greatly 68 dB and improve the return loss 48 dB. Table 1 represents the comparison with other existing methods. Table 2 demonstrates the parameters of the proposed minkowski patch MIMO antenna (Fig. 1).

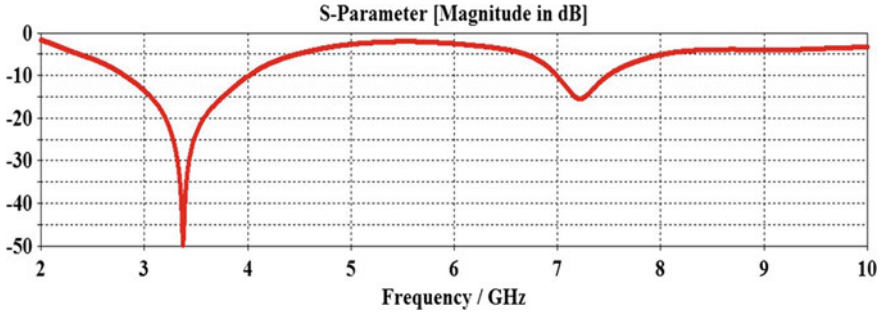

Fig. 2 Return loss, S_{11} graph

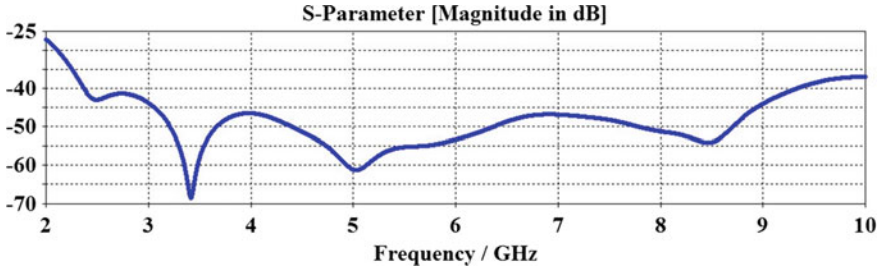

Fig. 3 Mutual coupling, S_{12} graph

2 Antenna Geometry and Analysis

The minkowski MIMO patch antenna is made using a substrate of RT/Duriod 5880 ($\varepsilon_r = 2.2$) with a thickness of 0.685 mm and surface area occupied by the substrate is 2000 mm^2.

3 Results and Discussion

The proposed technique yields better results in comparison to the previous works, especially the parameter mutual coupling (resonant frequencies are 63 and 47.32 dB). The return loss value (S_{11}) of the design is depicted in Fig. 2. Reduction of mutual coupling parameter as shown in Fig. 3. Comparison of S-parameters of the proposed design is depicted in Fig. 4. Surface current distribution of the dual-band minkowski-shaped MIMO antenna design is shown in Fig. 5. From the simulation, the envelope correlation coefficient parameter at the resonant frequency of 3.3 GHz is 0.00337 and at the second resonant frequency is 0.00364 is depicted in Fig. 6.

Figures 7 and 8 demonstrate the co-polarization and cross-polarization of the proposed minkowski patch antenna producing the radiation patterns when one of the

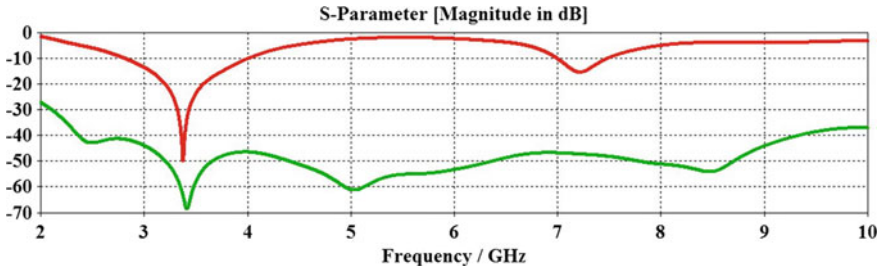

Fig. 4 S-parameters comparison

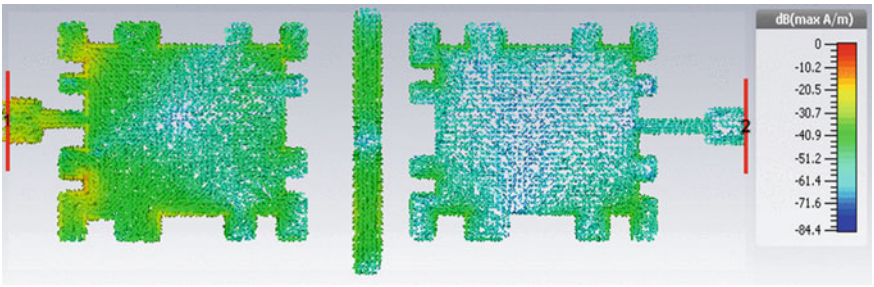

Fig. 5 Surface current distribution

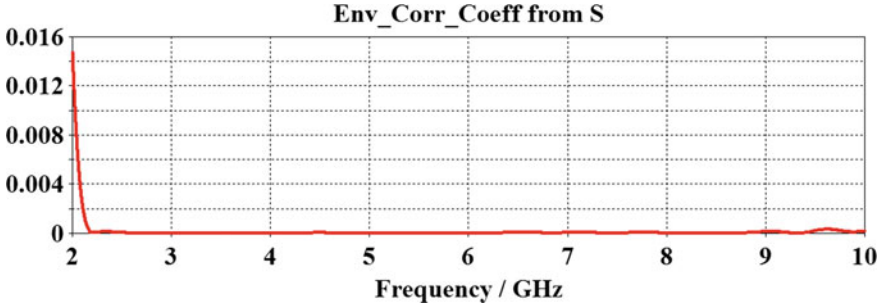

Fig. 6 Envelope correlation coefficient

antenna is excited and the other antenna is terminated with a characteristic impedance of 50 Ω. Here the radiation pattern of magnetic field (x-z plane) is omnidirectional and electric field (yz-plane) of nearly bidirectional shape is observed at the dual resonant frequencies of 3.376 and 7.2166 GHz. At highest frequency of 7.216 GHz, it is observed that the radiation patterns showed a moderate decline because of the unequal phase distribution in the cutting slots that produced higher order modes in electric fields.

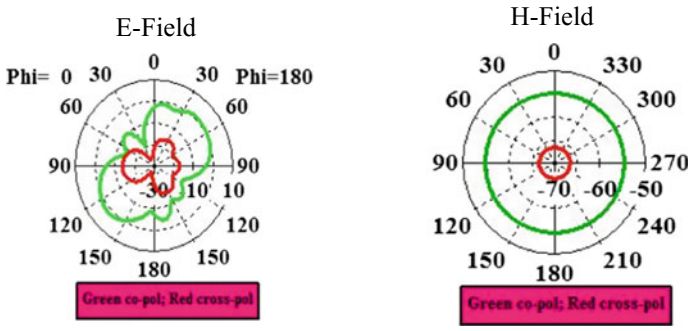

Fig. 7 Co- & cross-polarization at 3.376 GHz

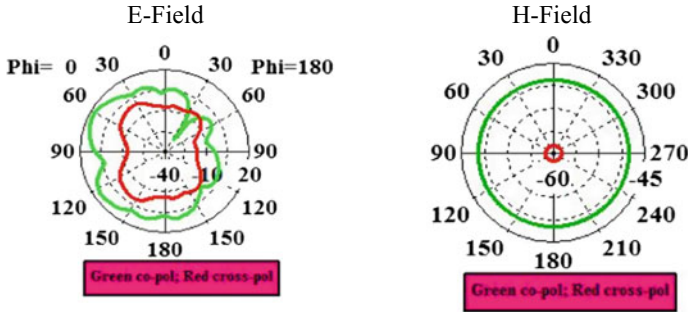

Fig. 8 Co & cross polarization at 7.2166 GHz

4 Conclusions

In this paper, a minkowski-shaped patch antenna is implemented for Wi-Fi and C-band applications. The antenna is resonating at frequencies of 3.376 and 7.216 GHz with a return loss of 49.93 and 15.47 dB and mutual coupling (isolation) at 63.08 and 49.23 dB. Here the spacing between the two antenna elements is maintained at 0.15 λ_0 to reduce the isolation greatly improved. The envelope correlation coefficient is 0.0364 at the resonant frequency and VSWR is maintained less than or equal to at these resonant frequencies.

References

Xue C-D, Zhang XY (2017) MIMO antenna using hybrid electric and magnetic coupling for isolation enhancement. IEEE Trans Antennas Propag 65:5162–5169

Su SW, Su SW (2010) High-gain dual-loop antennas for MIMO access points in the 2.4/5.2/5.8 GHz bands. IEEE Trans Antennas Propag 58:2414–2419

Mao CX, Xhu QX (2014) Compact coradiator UWB-MIMO antenna with dual-polarization. IEEE Trans Antennas Propag 62:4474–4480

Khan MS, Capobianco AD, Najam AI, Shoaib I, Autizi E, Shafique MF (2014) Compact ultrawideband diversity antenna with a floating parasitic digitated decoupling structure. IET Microw Antennas Propag 8:747–753

Su SW, Lee CT, Chang FS (2012) Printed MIMO-antenna system using neutralization-line technique for wireless USB-dongle applications. IEEE Trans Antennas Propag 60:456–463

Khan MS, Shafique MF, Capobianco AD, Autizi E, Shoaib I (2013) Compact UWB-MIMO antenna array with a novel decoupling structure. In: Proceeding of 10th international Bhurban conference on applied sciences and technology, vol 25, pp 347–350

Shafique MF, Qamar Z, Riaz L, Saleem R, Khan SA (2015) Coupling suppression in densely packed microstrip arrays using metamaterial structure. Microw Opt Technol Lett 57:759–763

Khandelwal MK, Kanaujia BK, Dwari S, Kumar S, Gautam AK (2014) Analysis and design of wide band microstripline fed antenna with defected ground structure for Ku band applications. AEU Int J Electron Commun 68:951–957

A Novel EBG-Loaded Dual Band-Notched UWB Antenna

Jaiverdhan, Ajay Yadav, Nikhil Temani, M. M. Sharma and R. P. Yadav

Abstract In this research paper, a coplanar waveguide (CPW) fed dual band-notched antenna is presented. Electromagnetic Band Gap (EBG) and Defected Ground Structure (DGS) are used to create dual band notched at two frequencies WLAN (5.2–5.6 GHz) and X-band (7.25–8.4 GHz). The structure uses for Novel EBG designs are like polarization-dependent EBG (PDEBG) or stacked EBG. The planar EBG structure used here is mushroom-shaped EBG for comparing potential applications. The use of electromagnetic band gap in the antenna is used to investigate for improving various RF and microwave component.

Keywords Ultra wideband (UBW) antenna · Coplanar waveguide (CPW) · Electromagnetic bandgap (EBG) structure · Band notched

1 Introduction

According to the US Federal Communication Commission (FCC) in the year 2002, the UBW define as antenna transmission over the frequency range of 3.0–10.6 GHz, that can be used over a short range application for low energy path and for the large level it can be used as a high bandwidth transmission [1]. Ultra wideband

Jaiverdhan (✉) · A. Yadav · M. M. Sharma · R. P. Yadav
Department of ECE, Malaviya National Institute of Technology, Jaipur, India
e-mail: 2016rec9051@mnit.ac.in

A. Yadav
e-mail: ajay.yadav.1981@ieee.org

M. M. Sharma
e-mail: mmsharma.ece@mnit.ac.in

R. P. Yadav
e-mail: rpyadav.ece@mnit.ac.in

A. Yadav · N. Temani
Department of ECE, Global Institute of Technology, Jaipur, India
e-mail: nikhiltemani6@gmail.com

© Springer Nature Singapore Pte Ltd. 2020

V. Janyani et al. (eds.), *Optical and Wireless Technologies*,
Lecture Notes in Electrical Engineering 546,
https://doi.org/10.1007/978-981-13-6159-3_10

(UWB) contain many narrow band systems like WiMAX [3.3–3.6 GHz], WLAN [5.15–5.35 GHz], C-band for downlink uses [3.7–4.2 GHz] and for uplink uses [5.925–6.425 GHz] and X-band [7.0–11.2 GHz] and work as a band-stop characteristic. The advantages of UWB include low-power transmission, robustness for multi-path fading, and low-power dissipation. UBW has been approved for indoor and short range outdoor communication. Planar antenna is most attractive part of UBW because of low cost and easy fabrication [2]. Electromagnetic band gap (EBG) widely used in the microwave, as it improves the gain, bandwidth, tunability, and compactness. EBG structure with patch antenna is used for an increment of bandwidth and decrement of losses in the transmission line. As one notch can be arrived by EBG structure placed near to microstrip feedline and it works as a band-stop and also unit-cell EBG reduced the surface waves but it increases the antenna gain. From most methods, one of the surface waves reduction method is Electromagnetic band gap. EBG also known as photonic band gap (PBG) because of the photonic crystals of forbidden band gaps in light emissions. EBG has a shielding property which uses as Specific Absorption Rate (SAR) for mobile operator [3]. In this study, the mushroom-type EBG not only considered the shape but also the radius and position of via. The reduction of size changed the permittivity of the substrate [4]. Among these techniques used in this paper, the Defected Ground Structure (DGS) is employed for stop-band to suppress higher mode harmonics and mutual coupling, which is used for improving the microwave devices, i.e., cross-polarization, narrow bandwidth, and low gain, etc. The DGS used for many parameters like microstrip, stripline, or coplanar waveguide for the ground plane which is used for modified or we can say to enhance the performance of the device [5]. In this paper mushroom-like EBG structure with a single via is investigated to enhance the bandwidth. By using single via and optimize their position for bandwidth to be wide. UBW works on very large-scale bandwidth due to this it allows the power spectral density to be low [6]. For reducing interference the band-notched is considered. In this paper, the dual notched-band is stimulated and considered as pulse receiving signal. It consists of EBG band notching which rejects certain frequency for improved bandwidth [7, 8]. At band-reject condition all the electromagnetic waves will reflect back and the structure behaves like a mirror. In these designs, by inserting the EBG structure in the interior of radiating patch and proper slits in ground plane, two rejected band-notched is obtained.

In this paper, a novel EBG-loaded UWB band with dual notched is considered. In this proposed antenna, it uses a rectangular microstrip feed line with quarter wave feeding. A rectangular stub on the back side of the radiating patch and two parallel rectangular slots in the ground plane are used to realize dual band-notch characteristics. The EBG structure is placed at the back side of the substrate. From increasing the length or changing the position of EBG, the sustained band-notched occur. The EBG structures consist of cylindrical holes which are etched in the substrate. The CPW feed on UWB antenna, as partial ground structure contain two parallel cutted slots which provides wider frequency and create the band-notch feature for WLAN. The stimulations indicate the dual band rejection with center frequencies of 5.3 GHz and 7.8 GHz respectively.

In earlier research the unit-cell EBG have proposed with small slots for rejection of band notch, but this study reveals that without cutting slot we can improve the stop-band bandwidth.

2 Design and Analysis

The design and structure of suggested UWB antenna have been simulated using ANSOFT HFSS v.16 software. The primary antenna is a microstrip patch antenna designed with the FR4 dielectric material. The thickness of the substrate is 1.6 mm and permittivity of dielectric is $\varepsilon_r = 4.4$ and dielectric loss tangent 0.02. The radiating patch is a circular shape patch printed on top of the substrate.

Figure 1 shows the design and specification of primary UWB antenna. The proposed antenna has dimension of 36 mm × 46 mm with thickness 1.6 mm using CPW feed. The antenna fed with quarter wave transformer line with width of 1.8 mm and length 19 mm to deliver maximum power to the antenna and to attain the port impedance of 50 Ω, a metal strip with width of 3.0 mm used. The effective parameter for the impedance matching is the gap distance between the radiating patch and the ground plane. Figure 2a shows the dimension and geometry of single band-notched UBW antenna. The antenna is constructed using FR4 (lossy) substrate because it has low cost and its availability. The metal strip of the EBG is laid on the back of substrate against CPW feed line and presented in Fig. 2c. Figure 2b shows the side view of proposed antenna with ground and positive feed line between them. The thickness of the substrate is 1.6 mm. The EBG structure is constructed at the back side of the radiating patch and two parallel slots feed on CPW at ground plane Fig. 2c.

The two small parallel slots of width ws = 0.3 mm and length ls = 7.9 mm of rectangular shape are etched on the ground plane to produce band-notching characteristics and shown in Fig. 3. Because of these two parallel slots on the ground, which is used to reject the WLAN application frequencies. The patch having a via of radius r = 0.4 mm which couple the radiating field with backside EBG patch.

In Fig. 2c the EBG has a rectangular shape as width W = 5 mm and length L = 8.5 mm and placed on the back side of the substrate. It has been observed that the EBG-based antenna depends only on length of EBG patch not on width [3]. So by choosing the EBG patch length 8.55 mm, it gives band-reject frequency from 7.2 to 8.48 GHz, which is used for X-band satellite communication.

3 Results and Discussion

Figure 4 shows, the VSWR is less than 2 throughout the radiating frequency band, except WLAN and X-Band which is necessary condition to produce band-notch characteristics. The proposed antenna satisfies the requirement of VSWR < 2 for pass band whereas VSWR > 2 for band-notched frequencies (WLAN and X-Band).

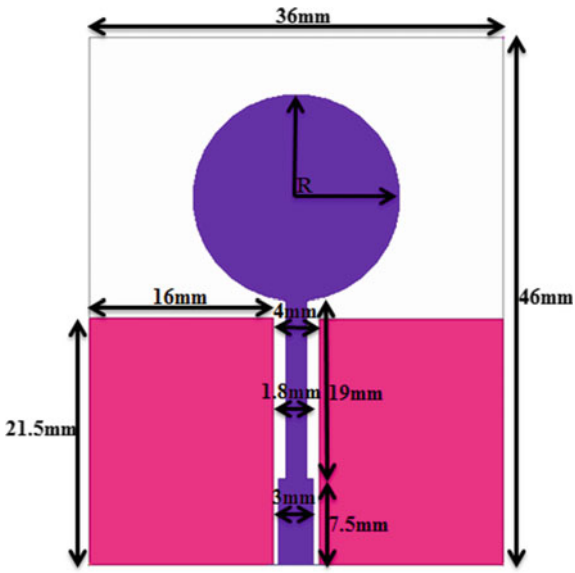

Fig. 1 Primary UWB antenna

Table 1 Comparison of proposed antenna with used references

Ref.	Size (mm^2)	ε_r	No. of notch	Frequency band (GHz)
[2]	13 × 14	3.55	2 (WiMAX, WLAN)	3.3–3.6 5.15–5.35
[3]	38 × 40	4.5	1 (WLAN)	5.15–5.35
[6]	34.36 × 48	3.28	2 (WiMAX, WLAN)	3.3–3.6 5.15–5.35
[7]	35 × 35	3	1 (WLAN)	5.15–5.35
Present work	36 × 46	4.4	2 (WLAN, X-Band)	5.2–5.6 7.25–8.4

Figure 5 shows the current distribution of the proposed antenna at 5.3, 6.5 and 7.8 GHz. Figure 5a shows the maximum current accumulation at the parallel etched slots on ground plane. Figure 5b shows the uniform current distribution and it is an evident that antenna radiates or receives the power whereas Fig. 5c shows the maximum current accumulation at the radiating patch near the EBG structure which is placed back side of the patch. The requirement of bandwidth at the notches has been satisfied and the interference signal can be eliminated by the proposed antenna. As it is clearly shown that the stronger current accumulation near ground slot and the EBG structure which are the positive sign to create band-notch characteristics. Some useful information has been listed in Table 1 in comparison to used references.

The radiation pattern of the proposed antenna at 6.5 GHz (pass band) has been presented in Fig. 6. The antenna displays the omnidirectional radiation pattern for the $\phi = 90°$ and dipole like

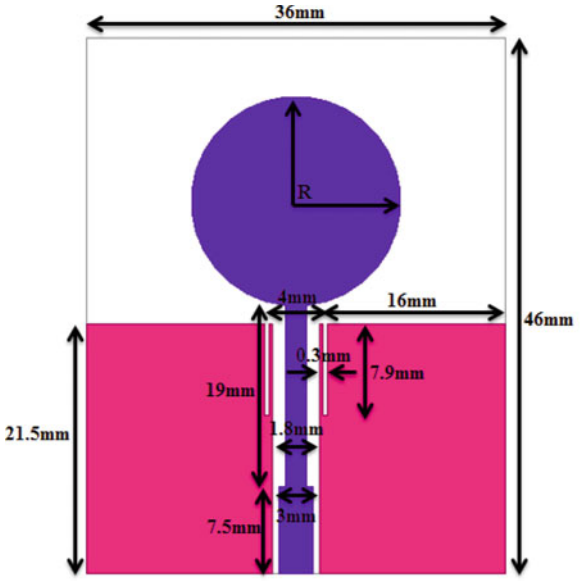

(a) Front view

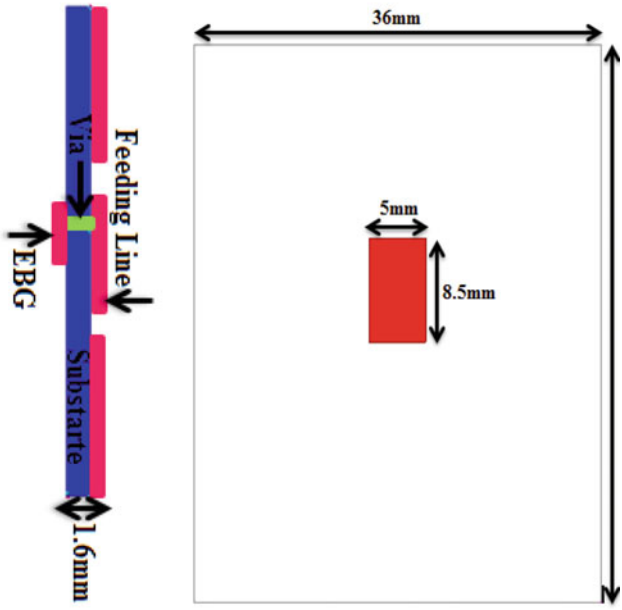

(b) Side View (c) Back View

Fig. 2 Proposed design of dual band-notched UWB antenna

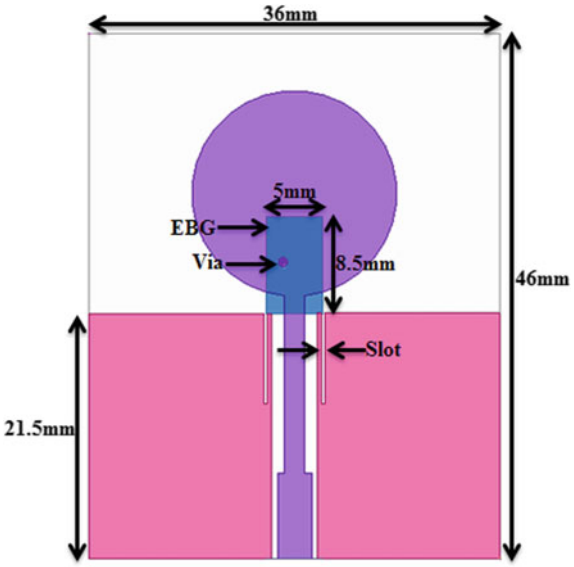

Fig. 3 Schematic view of proposed antenna

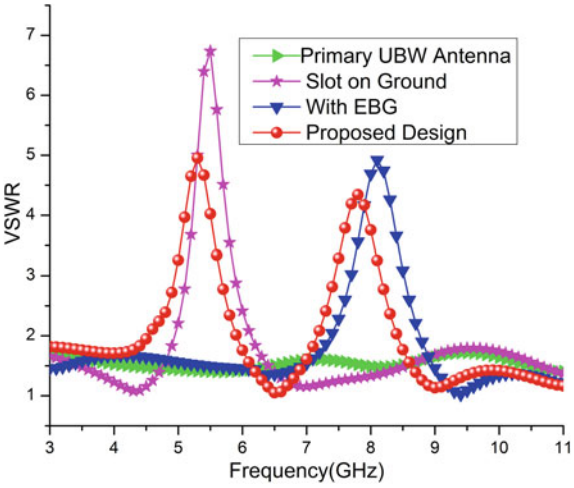

Fig. 4 Simulated VSWR versus frequency

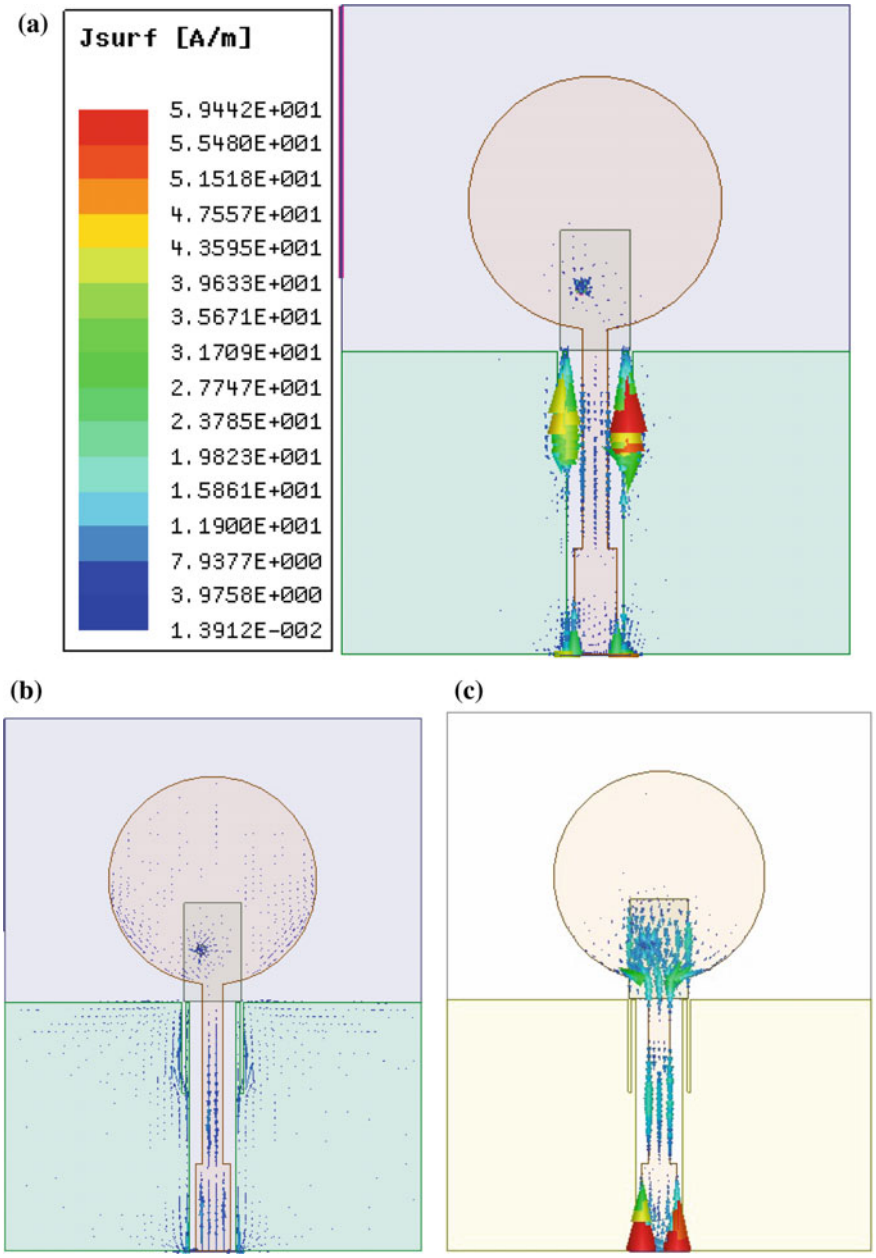

Fig. 5 Current distribution **a** at 5.3 GHz, **b** at 6.5 GHz and **c** at 7.8 GHz

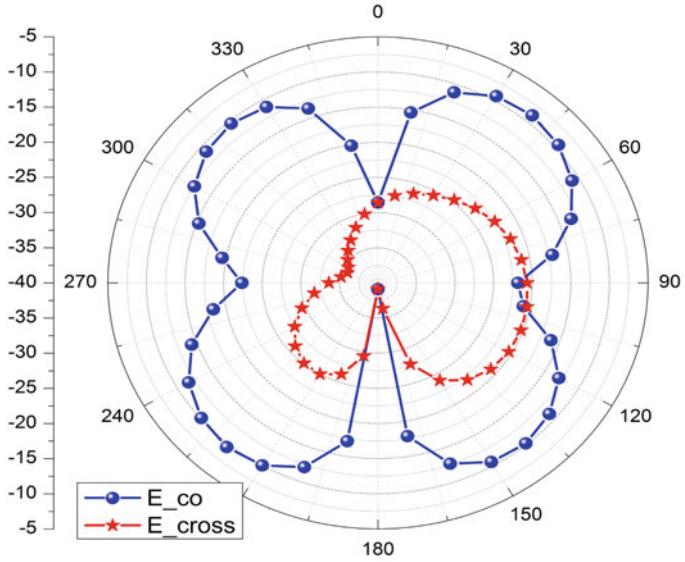

(a) E-Field Co & Cross Polarization at 6.5 GHz

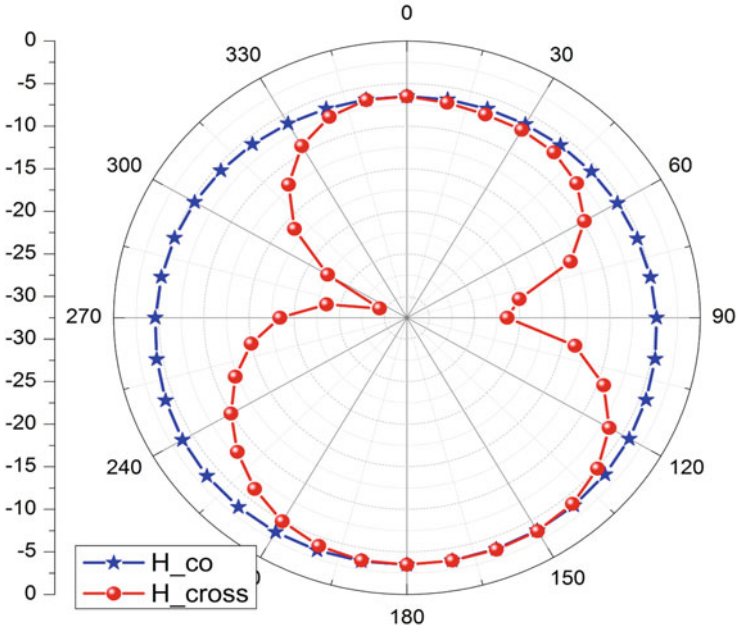

(b) H-Field Co & Cross Polarization at 6.5 GHz

Fig. 6 Simulated radiation pattern of proposed antenna

Shape for the $\phi = 0°$.

4 Conclusion

In this paper, a novel EBG-loaded UWB antenna with desired band-rejection characteristic has been proposed. The proposed antenna radiated over 3.0–11.0 GHz with VSWR < 2 and it rejects two bands WLAN (5.15–5.35 GHz) and X-Band (7.25–8.35 GHz). The antenna is useful to suppress the electromagnetic interferences due to WLAN and X-Band applications. The proposed antenna successfully created band-notching characteristics using EBG and symmetrical slot in ground plane. The antenna has good omnidirectional characteristic over pass band which is necessary condition for any UWB antenna.

References

1. Norzaniza AT, Matin MA (2013) Design of microstrip UWB antenna with band notch characteristics. In: IEEE 2013 Tencospring
2. Jiang W, Che W (2012) A novel UWB antenna with dual notched bands for WiMAX and WLAN applications. IEEE Antennas Wirel Propag Lett 11
3. Peng L, Ruan C-L (2011) UWB band-notched monopole antenna design using electromagnetic-bandgap structures. IEEE Trans Microw Theory Tech 59(4)
4. Rajo-Iglesias E, Inclán-Sánchez L, Vázquez-Roy J-L, García-Muñoz E (2007) Size reduction of mushroom-type EBG surfaces by using edge-located vias. IEEE Microw Wirel Compon Lett 17(9)
5. Kim M, Kam DG (2014) A wideband and compact EBG structure with a circular defected ground structure. IEEE Trans Compon Packag Manuf Technol 4(3)
6. de Cos ME, Las-Heras F (2012) Dual-band uniplanar CPW-fed monopole/EBG combination with bandwidth enhancement. IEEE Antennas Wirel Propag Lett 11
7. Mehdipour A et al (2009) Miniaturised coplanar waveguide-fed antenna and band-notched design for ultra-wideband applications. IET Microw Antennas Propag 3(6):974–986
8. Folayan O, Langley R (2009) Dual frequency band antenna combined with a high impedance band gap surface. IET Microw Antennas Propag 3(7):1118–1126

Time-Correlated MIMO Channels Using Decision Feedback Receiver

A. Muthumanicckam and N. Janakiraman

Abstract We design bit loading, precoding also receives filters to a Multiple-Input Multiple-Output (MIMO) computerized correspondence framework. Both these transmitter and the recipient are relied upon the channel grid superbly. It may be greatly distinguished that, for straight MIMO transceivers, orthogonal transmission (i.e., diagonalization of the channel matrix) will be perfect to a portion of benchmarks for example, most extremely imparted majority of the data. It needs to be uncovered that assuming that these recipient hones those linear Minimum Mean Squared Error (MMSE) detector. Those ideal transmission approaches may be settled on touch-stacking with respect to orthogonal sub-channels. That transmission rate of the channel is improved toward passing on the odds rapidly on the sub-channels of the MIMO framework. A variable-rate MIMO framework with a choice sentiment recipient may be deliberated. Those nested sub-matrices need aid induced that might make modernized concerning illustration the long run progresses. The transmission rate to the channel is adapted by assigning bits dynamically to the sub-channels of the MIMO system. To derive the optimal predictor of the next bit loading for predictive quantization and obtain the statistics of the prediction error using this method, that quantizer may be pointed on the scope of a littler quantization slip. That transform for linking those deciphering strategy is arranged to improve those outline what's more its procedure. This offers better result associated with the MMSE and spot rate, same time relating with those traditional techniques.

Keywords MIMO · Convolutional coding · Trellis diagram · MMSE · Variable rate · Correlation · Predictive quantization

A. Muthumanicckam (✉)
Department of Electronics and Communication Engineering, Shanmuganathan Engineering College, Pudukkottai, Tamilnadu, India
e-mail: muthumanickama@yahoo.com

N. Janakiraman
Department of Electronics and Communication Engineering, K.L.N. College of Engineering, Madurai, Tamilnadu, India
e-mail: janakiramanforu@yahoo.com

© Springer Nature Singapore Pte Ltd. 2020

V. Janyani et al. (eds.), *Optical and Wireless Technologies*,
Lecture Notes in Electrical Engineering 546,
https://doi.org/10.1007/978-981-13-6159-3_11

1 Introduction

1.1 Wireless Communication: An Overview

Remote correspondence frameworks as shown in Fig. 1 indicate a standout among the practically alluring features from claiming today's existent correspondence frameworks. The central occurrences that make our destination challenging will finish the time-varying multipath blurring. In the time-varying multipath channel fading, those numerous proliferation ways concerning those transmitters besides collector yield an accepted indicator anguish starting with unsystematic wrap and period oscillations. Those multipath blurring kits (the irregular envelope besides stage fluctuations) might prompt an extreme framework execution hardship for remote correspondence frameworks.

1.2 Multiple-Input Multiple-Output (MIMO)

The subject remote communications done, a single radio wire may be picked during the source, also extra absolute radio wire will be picked toward the end. To sure cases, this offers ascent on challenges with multipath impacts. The utilization about two or that is only the tip of the iceberg antennas, alongside the transmission of numerous signs (one to each antenna). In those wellsprings and the destination, dispenses with those a bad position brought on by multipath wave propagation, besides could indeed take profit for MIMO impact. MIMO employments various transmitters besides receivers will exchange greater amount of information at the same chance concerning illustration indicated for Fig. 2. Those antennas toward every wind of the interchanges circlet need aid joined that should decrease errors besides enhance information speed. It additionally offers to get in channel heartiness and secondary throughput remote items for 802.11n help MIMO.

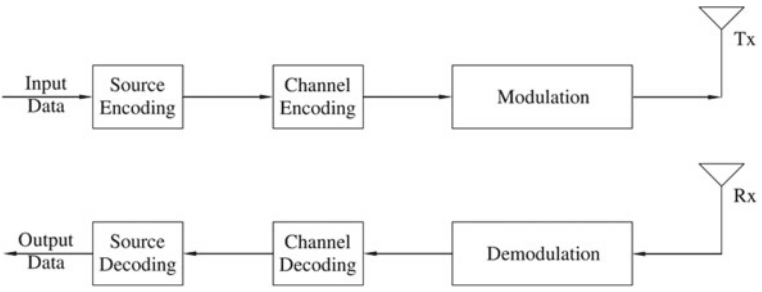

Fig. 1 Basic block diagram of wireless communication system

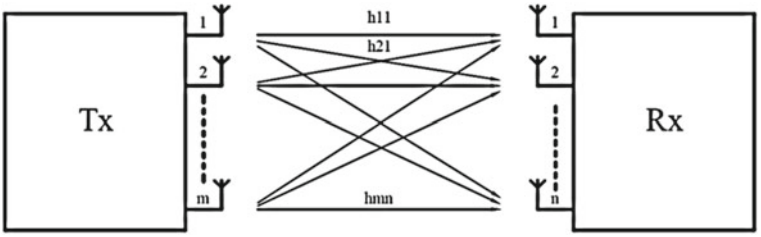

Fig. 2 Model of MIMO transmission

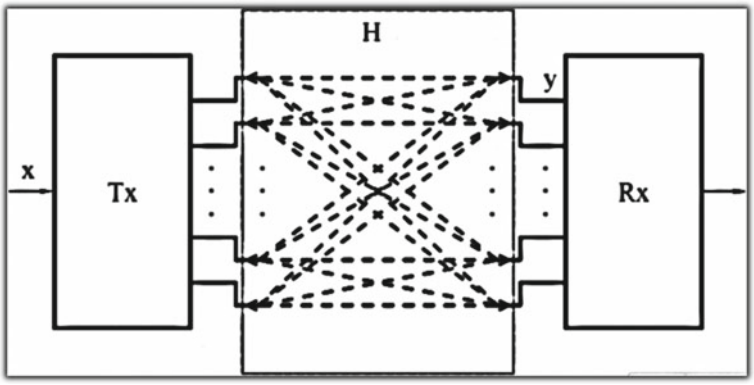

Fig. 3 MIMO communication systems

MIMO innovation organization leverages multipath conduct by utilizing various "smart" transmitters besides receivers with an included "spatial" extent that will dramatically increase execution and reach. Advanced mobile transmitters and receivers need aid utilized for constantly on 802.11n gadgets. Utilizing numerous antennas of those information camwood a chance to be sent and accepted through different signs. Those switches likewise should have numerous antennas and fully backing all of the offers for 802.11n should increase the most noteworthy velocity workable as shown in Fig. 3.

We think as of variable-rate transmission for a gradually time-varying MIMO channel. The point when choice sentiment may be utilized at the collector. The data that is accessible of the transmitter may be the input from the collector. Provided for lapse rate constraint, odds are rapidly allocated to each sub-channel as stated by the channel data as on Per-Antenna Rate Control (PARC) with the goal that those transmission rates could get a chance to be adjusted of the present channel. Because of those fleeting connection of the channel, the bit stacking will be additionally run through associated. When decision feedback is employed at the receiver with reverse detection order, it is known that the Cholesky decomposition of the channel Gram matrix can be used to determine the sub-channel signal-to-noise ratios and hence also the bit loading.

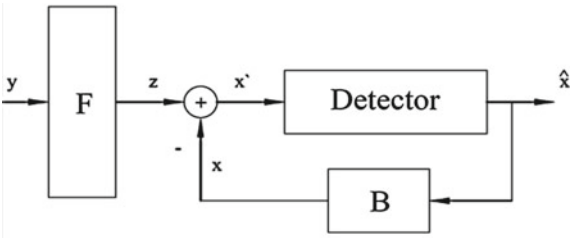

Fig. 4 Decision feedback receiver

Those ML (Maximum Likelyhood) identifiers might endure from helter-skelter computational complexity, which motivates the utilization of the suboptimal to be that as less perplexing MMSE identifier. An intermediate identifier as far as unpredictability furthermore execution is concerned is Decision Feedback (DF) identifier as shown in Fig. 4. The primary effect reveals to that to a DF-MIMO transceiver the place the spot stacking will be mutually optimized for those transceiver filters, the orthogonal transmission will be ideal.

2 Space–Time Coding Strategies for MIMO-OFDM

OFDM will be an animated besides low-complexity approach to distributing for frequency-selective channels. An OFDM transmitter parts the recurrence band under decreased sub-channels furthermore propels modified succession about images through each sub-channel. The point when those sub-channels' transfer speed is enough narrow, the recurrence response crosswise over every sub-channel is practically flat, avoiding the confounded time-domain adjustment. In this way, OFDM transforms a frequency-selective channel under an accumulation of differentiating flat-fading channels. In the same way, as a OFDM transmitter may be utilized toward every claiming transmit antennas, furthermore a OFDM front-end is utilized eventually perusing from claiming to get antennas, a MIMO frequency-selective channel may be changed under an accumulation from claiming flat-fading MIMO channels, to quit offering on that one for each tone, with each hosting extent.

2.1 Linear Predictive Coding (LPC)

LPC will be an instrument utilized most accioli done sound indicator preparing and discourse preparing to speak to the ghastly envelope of an advanced indicator of discourse for compacted form, utilizing the majority of the data of a straight predictive model. It may be a standout among the practically capable discourse dissection techniques, besides a standout among those a large portion functional routines for encoding beneficial nature discourse at alow touch rate and gives greatly

exact estimates from claiming discourse parameters. LPC is every now and again utilized to transmitting ghastly envelope information, also in that capacity it needs a chance to be tolerant of transmission errors.

3 Proposed Method

There would a large number of time permits slip control methodologies for MIMO-OFDM frameworks. As done by any framework there need aid essential performance-complexity tradeoffs. Furthermore, contingent upon the application, the fancied BER might bring about the compelling reason to best negligible alternately no-slip correction; namely, the regulation code might be an addition on gatherings give those required BER. Likewise, turbo codes are exceptional situations about LDPCs, we concentrate on the individuals. Also, we begin our depiction for single-input-single-output (SISO) channels as huge numbers useful for lapse control methodologies for MIMO frameworks will get a chance to be outlined to SISO channels et cetera mapped to MIMO channels. Flow chart is shown in Fig. 5.

3.1 Convolutional Encoding

To encode information convolutionally, begin for k memory registers, each holding 1 enter spot. Unless generally specified, all memory registers begin for an esteem for 0. The encoder need n modulo-2 adders (a modulo 2 adder might a chance to be executed for a solitary boolean XOR gate, the place the rationale is: $0 + 0 = 0$, $0 + 1 = 1$, $1 + 0 = 1$, $1 + 1 = 0$), furthermore n generator polynomials person to each adder (see figure below). An enter touch m_1 will be nourished under that leftmost register. Utilizing the generator polynomials and the existing values in the remaining registers, the encoder outputs n images. These images might be transmitted alternately punctured contingent upon those wanted code rate. Now bit shift all register values to the right (m_1 moves to m_0, m_0 moves to m_{-1}) and wait for the next input bit. If there are no remaining input bits, the encoder continues shifting until all registers have returned to the zero state. Assuming that there are no remaining enter bits, the encoder proceeds moving until the registers need come back of the zero state (flush spot termination).

3.2 Trellis Diagram

Envision that the encoder (shown looking into Fig. 6) need "1" in the left memory cell (m_0) Furthermore "0" in the straight you quit offering on that one (m_{-1}). (m_1 is not truly An memory cell as a result it speaks to a present esteem).

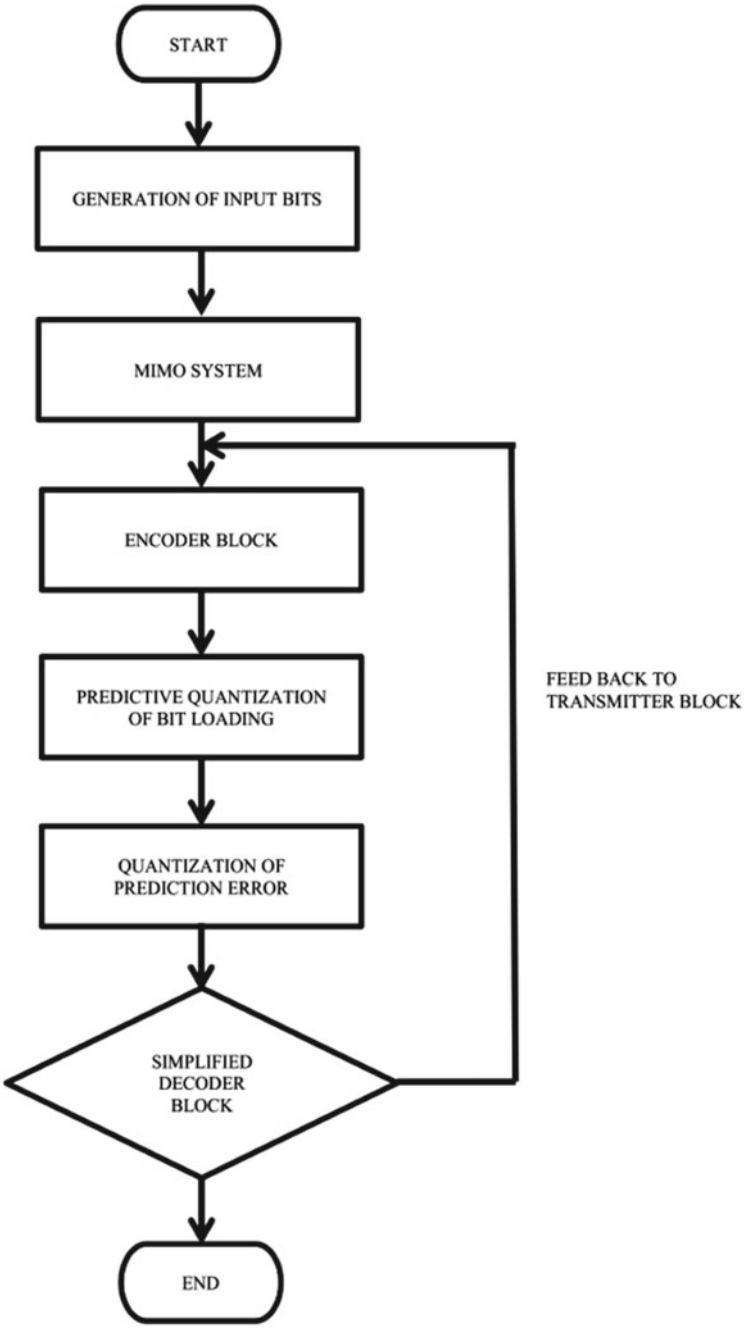

Fig. 5 Flow chart

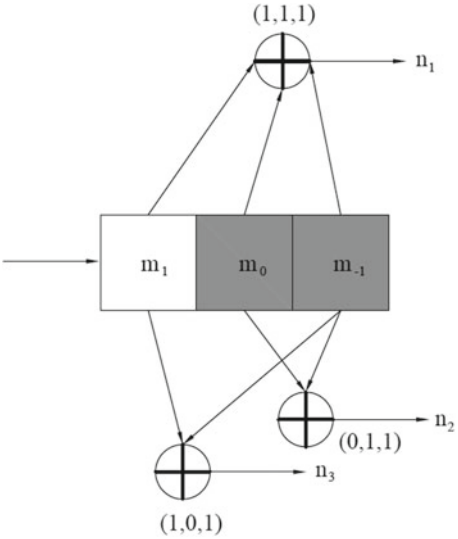

Fig. 6 Encoder

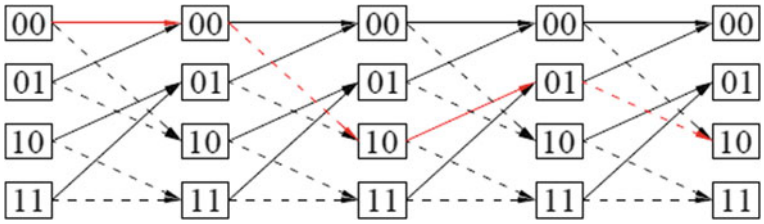

Fig. 7 Trellis diagram

We will designate such a state similarly as "10". As stated by an enter bit the encoder in those next turn might change over whichever of the "01" state or the "11" state. Particular case camwood view that not all moves need aid workable for (e.g., a decoder cannot change over from "10" state to "00" or actually remain to "10" state). Know that conceivable moves could make indicated concerning illustration (Fig. 7).

An trellis outline to those encoders ahead Fig. 7 will be demonstrated over. A way through the trellis is demonstrated likewise a red line. Those robust lines will be demonstrated by entering a "0" and for dashed lines the a "1" is entered. Block diagram is shown in Fig. 8.

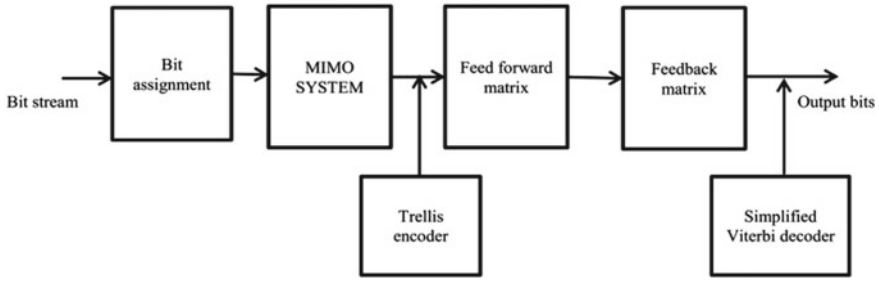

Fig. 8 Block diagram

3.3 Decoding the Convolutional Codes

A few calculations exist to deciphering convolutional codes. To generally little values about k, the Viterbi calculation will be universally utilized. Similarly, as it gives most extreme probability execution besides is exceptionally parallelizable. Viterbi decoders need aid subsequently not difficult to execute Previously, VLSI fittings and for programming on CPUs with SIMD direction book sets.

4 Simulation Result

In this paper, the idea about blurring will be showed eventually perusing those approach exhibited to MATLAB. In this section, discourse on the comes about obtained utilizing MATLAB simulations is carried out. It is necessary to investigate what happens if the indicator similarly as it sets out starting with the transmitter of the collector. Clinched alongside remote correspondences it is exceptionally casual with understanding the ideas. As demonstrated earlier, a standout among those critical viewpoints of the way the middle of the transmitter and collector may be the presence from claiming blurring. MATLAB conveys a straightforward and simple approach to figure out blurring occurring previously, remote frameworks. We recreated the RF (Radio Frequency) signs for fitting measurable properties. Measurable testing might thus a chance to be used to propel those power of the blurring models utilized within remote frameworks recurrently. We depicted the diverse blurring models also MATLAB-based reproduction methodologies. To the demonstrating and reproduction from claiming frameworks Simulink, a graphical development like MATLAB is utilized. Frameworks would be drawn ahead screen similarly as square diagrams. previously, Simulink. For piece diagrams, numerous components would receptive (such similarly as exchange functions, summing junctions, and so on.), and in addition, virtual enter units besides yield gadgets. Simulink is joined together with MATLAB and information camwood a chance to be effectively transmitted the middle of those projects.

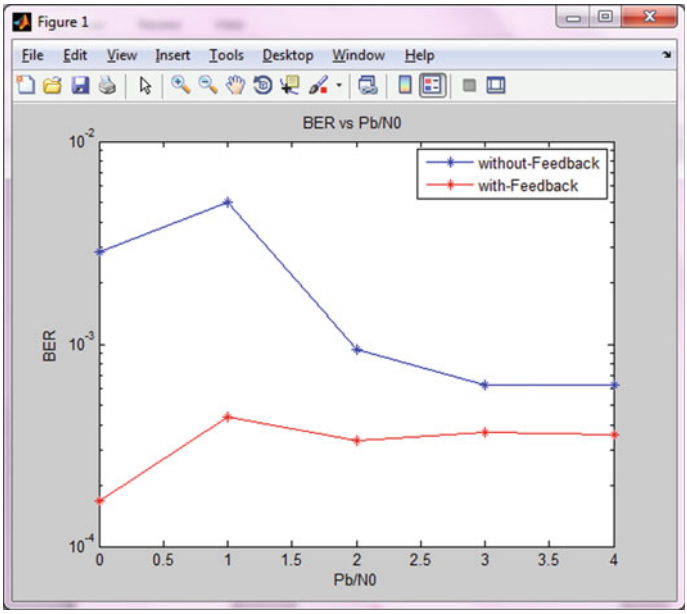

Fig. 9 SNR versus BER

Registering those lapse checks through the aggregate number for odds will be finished. Estimation of BER will be finished toward thinking about those transmitted sign with those accepted indicators. BER will be typically communicated as far as indicator signal to noise ratio (SNR) to any provided for regulation as shown in Fig. 9. With this graph we can understand that the comparison between conventional work with proposed work its giving better performance than conventional work. It may be giving unrivaled execution over the customary worth of effort. Bit Error Rate (BER) of a correspondence framework may be different concerning illustration those proportion from claiming number about lapse odds furthermore aggregate amount of odds exchanged throughout a positive period. It will be the probability that an absolute lapse bit will emerge inside accepted bits, autonomous of rate about transmission. To decrease BER there need aid numerous routes. Here, we accentuation for spreading code also modulation systems. On our case, we need to acknowledge those majority regularly utilized channel: those added substance Additive White Gaussian Noise (AWGN) channel the place that the commotion gets degree over those entirety ranges from claiming frequencies. BER needs to be be measured toward analyzing those transmitted sign with those accepted sign, furthermore ascertaining those lapse number again and those aggregate number for odds. BER is regularly communicated as far as an indicator will clamor proportion (SNR) to whatever provided for regulation.

In the over simulation, the BERs would get eventually changing the values from claiming P_b/N_0 from 1 to 10. In spite of the fact that to this body of evidence P_b/N_0 is

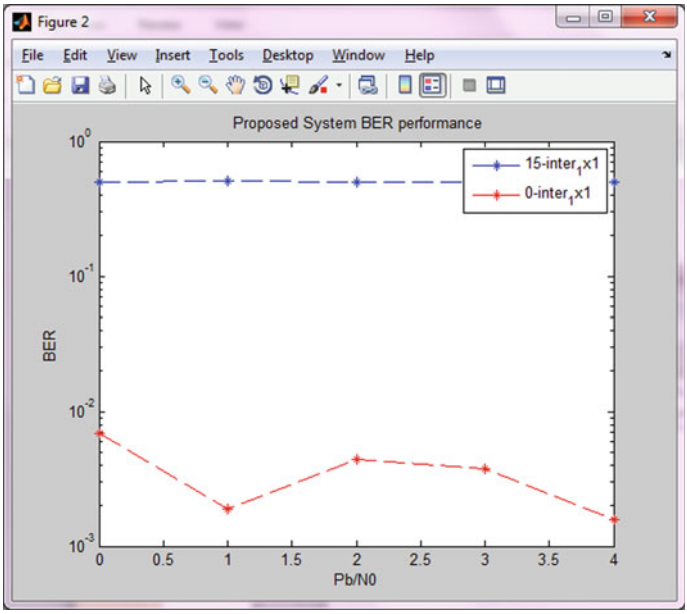

Fig. 10 SNR versus BER with various noise interference

developing linearly as shown in Fig. 10. Any way to separate qualities for P_b/N_0, spot lapse rate will be about consistent. Reproduction consequence for assessment around BER versus SNR for AWGN channel is two clients. Those number of information odds would 300 for QPSK modulation. It shows that amount from claiming client may be greater normal spot slip rate that will be very nearly indistinguishable twin with respect to the solitary client.

Figure 11 indicates the rate of sentiment and the equally achieved throughput with a normal SNR from claiming 20 db. Likewise the throughputs with this suggested framework display a fortifying propensity alongside those developments for input rate. When those feedback rates will be close to 0.33 bits/subcarrier, those throughputs with CS approach the impeccable throughputs. Moderately, the throughputs with suggested framework would be perfect throughputs to the point when the reaction rate may be close to 0.56 bits/subcarrier. Subsequently, the recommended framework needs enhanced throughput execution over the customary worth of effort with the same sentiment rate.

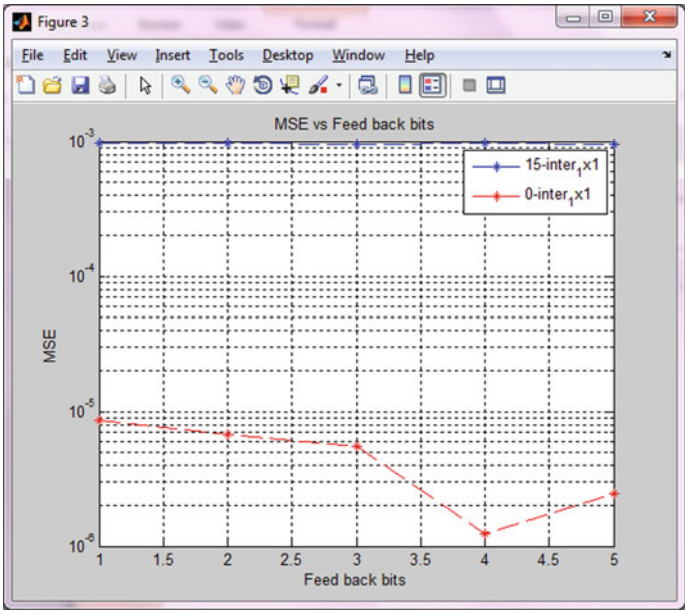

Fig. 11 Feedback bits versus MSE

5 Conclusion

In this work, we investigate a variable-rate MIMO framework with a decision feedback receiver. Similarly, as for every radio wire rate control, the bit loading will be rapidly allocated of the sub-channels. In this way, that those transmission rates will be changed permitting of the present channel condition. Predictive quantization, which may be recognized to make verwoerd suitableness for coding interconnectedness signals, is used to quantize those bit stacking to the reaction. Utilizing the update, we create those ideal predictors of the following bit stacking to a closed form. The statistics of the prediction error have also been derived and exploited in the design of the quantizer to achieve a smaller quantization error. The adjustments finished in the deciphering methodology will abbreviate besides improving those low reaction rate over the sooner fill in. Simulations are given to demonstrate that the proposed predictive quantization gives a good approximation of the desired transmission rate to be faster with a low feedback rate.

Link Budget Profile for Infrared FSO Link with Aerial Platform

Rahul Bosu and Shanthi Prince

Abstract This paper investigates the implementation of infrared (IR) free-space optical (FSO) communication to enhance the data transmission capacity to aerial platforms. As such, the study introduces a geometrical model of establishing an FSO link between a base station (BS) and an unmanned surveillance aerial vehicle (USAV) drifting along an inclined straight track using the Gaussian beam theory. The analytical analysis along with the MATLAB simulation envisages that the optimum received power required to ensure FSO link availability along the track depends on the track inclination angle, separation distance between BS-USAV and the source beam divergence angle for covering the track. Based on the received power, the error rate performance of the OOK-FSO system is illustrated for data rates ranging from 100 to 300 Mbps and is observed to improve with a reduction in the beam coverage length. Finally, the link budget analysis is incorporated for gauging the theoretical power limited link range of BS-USAV FSO system in different weather conditions. Based on the analytical study, the proposed system model can enact continual FSO communication between BS and USAV moving over an inclined straight track.

Keywords Free-space optical communication · Laser beams · Optical propagation · Infra-red surveillance · Unmanned aerial vehicle · Link budget

1 Introduction

Free-space optical (FSO) communication is essentially a line-of-sight (LOS) technology that employs infrared (IR) beam [1, 2] as a carrier and is the preferred option for wireless accessing technique in areas where the applications of RF systems are limited or restricted, like: hospitals, aerial vehicles, and military applications [3]. As

R. Bosu (✉) · S. Prince
SRM Institute of Science & Technology, Kattankulathur, Tamil Nadu, India
e-mail: rohulbosu.g@ktr.srmuniv.ac.in

S. Prince
e-mail: shanthi.p@ktr.srmuniv.ac.in

© Springer Nature Singapore Pte Ltd. 2020

V. Janyani et al. (eds.), *Optical and Wireless Technologies*,
Lecture Notes in Electrical Engineering 546,
https://doi.org/10.1007/978-981-13-6159-3_12

such, unmanned aerial vehicle (UAV) can be equipped with FSO transceivers for surveillance of civil works [4], e.g., bulk data collection from disaster-prone areas, building cracks, to name a few; and maintaining high data throughput link with base-stations (BSs). In contrast to the radio frequency (RF) systems, FSO offers advantages like: unlicensed spectrum, quick link deployment, immunity to electromagnetic interferences, and low power spillage with enhanced security [5, 6].

The major challenge for the implementation of FSO communication between two mobile nodes is the vulnerability of maintaining the LOS condition [7] against mobility. As such, Khan and Yuksel [8] presented a novel scheme of establishing FSO communication between two mobile nodes with auto steerable optomechanical system and estimated the coverage area and link duration. Furthermore, a geometrical model has been reported in [9, 10] for establishing FSO link between a static transmitter (Tx) and receiver (Rx) node moving over non-inclined straight and curved tracks. Moreover, the authors in [11] have experimentally demonstrated the implementation of orbital angular momentum (OAM) based multiplexing [12] in FSO communication between the ground station and a flying USAV with a data rate of 40 Gbps. However, the length of the track covered by the Tx beam spot is restricted as the widening of the beam spot and track inclination angle can increase the divergence losses resulting in partial collection of the relayed beam by the Rx aperture.

In view of the aforementioned limitations, multiple BSs can be established at optimum separation distance so that the optical beam, relayed from each BS, can cover fraction of the entire track. Thus, all the beams altogether can cover the entire track with limited divergence loss. Furthermore, this paper presents a geometrical model for establishing FSO link between BS and USAV drifting over an inclined straight path. In addition to the study of the various system specific and nonspecific loss mechanisms experienced in such links, an optical link budget is also presented to estimate the optimal link margin for achieving the desired performance level.

The rest of the paper is addressed as follows: Sect. 2 introduces the proposed system with a geometrical model. The system performance analysis is then presented in Sect. 3. Section 4 highlights the link budget analysis for examining the link margin and beam propagation distance in different weathers, followed by, conclusions in Sect. 5.

2 System Model

Figure 1 illustrates a typical base station (BS) to unmanned surveillance aerial vehicle (USAV) FSO communication link. The illustrated link comprises of multiple BSs and optical transceivers (Tx/Rx) placed on the USAV. The transmission of the data from the BS to the USAV involves modulation of the IR beam intensity using internal modulator and driver circuitry. Thereafter, the BS relays the laser beam of optimum divergence angle through the transmitter aperture so as to cover a partial portion of the straight path covered by the USAV. Multiple BSs with optimal separation distance can be deployed to maintain FSO communication with the USAV moving

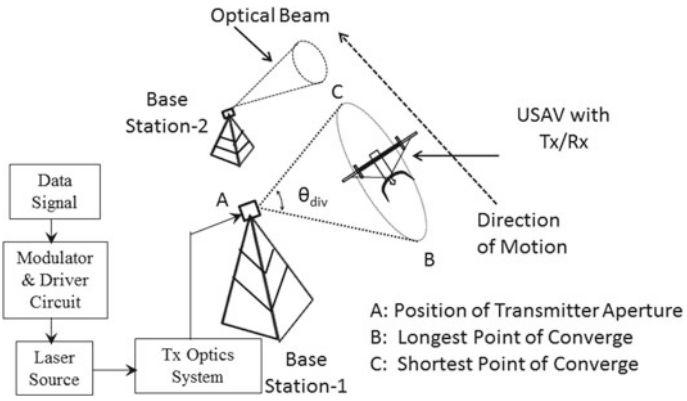

Fig. 1 System block diagram of BSs to USAV FSO communication link

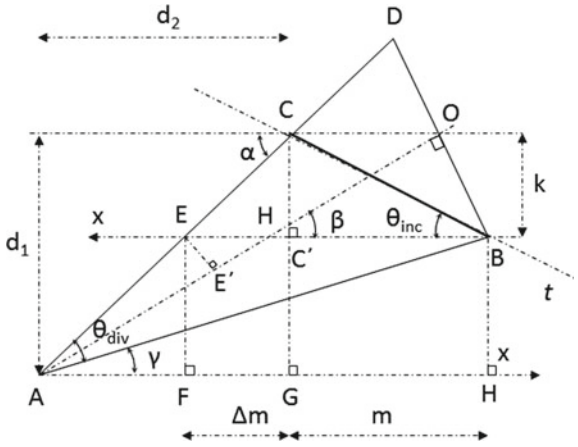

Fig. 2 Schematic geometrical model for FSO communication between one BS and USAV

over a longer path. The receiver Rx optics system positioned in the USAV comprises of beam collimator, photodetector (PD) and post-detection circuit.

Figure 2 depicts a two-dimensional geometrical model proposed for downlink FSO communication with the USAV moving along a straight track of length l, and is inclined to the horizontal axis x by an angle θ_{inc}. The Tx aperture, positioned on the BS is denoted by **A**, emits a beam of divergence angle θ_{div}. However, the narrow beam-width of the transmitted laser signal restricts the length of the track over which the FSO communication with the traversing USAV is feasible. As such, in order to establish the FSO communication with the USAV traversing a portion of the track of length $L(<l)$, denoted by **BC**, the beam divergence angle should be expanded and the Tx aperture is required to be tilted away from x by an angle γ. Based on the proposed geometry, the beam divergence angle, estimated as

$$\theta_{\text{div}} = \tan^{-1}\left[\frac{d_1 \cdot m + d_2 \cdot k}{d_1^2 + d_2^2 + d_2 \cdot m - d_1 \cdot k}\right], \tag{1}$$

relies on the horizontal and vertical separation distance, denoted by d_2 and d_1 respectively, of the active BS from the longest beam coverage point **F**. From the basic trigonometric identities, $m = L \cdot \cos\theta_{\text{inc}}$, $k = L \cdot \cos(90° - \theta_{\text{inc}})$. The resultant optical power with a Gaussian beam profile, given as [13]

$$P_{\text{Rx}} = \frac{2 \cdot P_{\text{Tx}} A_{\text{collimator}}}{\pi w^2} \exp\left(-\frac{2r^2}{w^2}\right)$$
$$\text{where, } w = w_0 \sqrt{\left[1 + \left(\frac{\lambda z}{\pi w_o^2}\right)^2\right]} \text{ and } w_0 = \frac{4\lambda f_{\text{lens}}}{\pi D_{\text{beam}}}, \tag{2}$$

impinges at the Rx while traversing the track **BC**. Here, P_{tx} is the transmitted power, $A_{\text{collimator}}$ is the FOV area of the collimator lens with focal length f_{lens}, w is the optical beam radius covering the track **BC**, w_0 is the beam waist of the laser source, and λ is the wavelength of the Tx laser of beam diameter D_{beam}. Subsequently, the radial offset of the laser beam, denoted as **OB** and obtained as,

$$r = L\left[\cos\theta_{\text{inc}} + \left(\frac{\sin\theta_{\text{inc}}}{\tan\alpha}\right)\right]\sin\beta - \left[\sqrt{(d_1 - k)^2 + (d_2 + \Delta m)^2}\right]\sin\left(\frac{\theta_{\text{div}}}{2}\right), \tag{3}$$

along the axis of propagation **AO**, obtained as

$$z = \left[\sqrt{(d_1 - k)^2 + (d_2 - \Delta m)^2}\right]\cos\left(\frac{\theta_{\text{div}}}{2}\right) + L\left[\cos\theta_{\text{inc}} + \left(\frac{\sin\theta_{\text{inc}}}{\tan\alpha}\right)\right]\cos\beta, \tag{4}$$

alters with the change in beam divergence angle θ_{div}, coverage length L of the track and the track inclination θ_{inc}. Here, $\Delta m = k/\tan\alpha$, $\alpha = \theta_{\text{div}} + \gamma$ and $\beta = \gamma + \theta_{\text{div}}/2$. As evident from the above equations, wide beam divergence and the position of the USAV from the BS results in a situation in which the field-of-view (FOV) of the Rx aperture is capable of collecting and collimating only a fraction of the impinging beam. The FSO channel for the BS-USAV link is considered as an AWGN channel for numerical simulation in MATLAB. Figure 3 demonstrates that both track inclination angle and the separation distance of the USAV from BS (d_1, d_2) govern the changes in the beam divergence angle. Here, we observe that, in contrast to $\theta_{\text{inc}} = 0°$, the source beam divergence angle initially increases for $2\text{m} \leq d_1 \leq 4\text{m}$ and then decreases as $d_1 \geq 4\text{m}$ for $\theta_{\text{inc}} = 30°$. Eventually, the results from the plot suggest that higher track inclination angle minimizes the need of wide divergence angle, which in turn, reduces the geometric loss for large separation distance between the BS and USAV.

Additionally, Fig. 4 illustrates that initially, the received power at the Rx swiftly fades away for $2\text{m} \leq d_1 \leq 4\text{m}$. However, after reaching a threshold vertical separation distance and beyond ($d_1 \geq 4\text{m}$), the received power profile appears to be escalating.

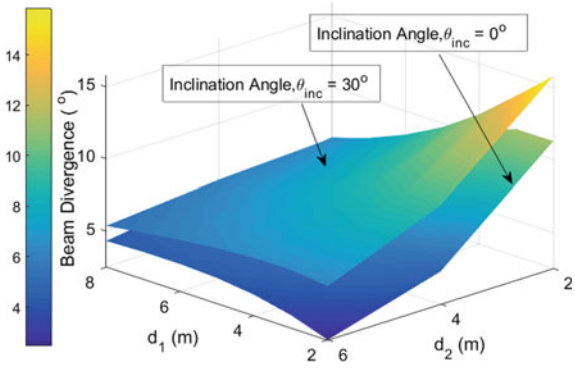

Fig. 3 3-D schematic illustrating optimum source beam divergence angle for varying horizontal and vertical separation distances, $L = 1$ m

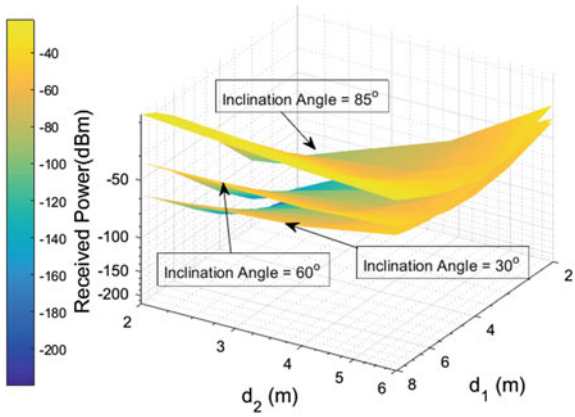

Fig. 4 3-D schematic illustrating the received power profile for varying horizontal and vertical separation distance, $L = 1$ m

This result is the outcome of the fact that the as the USAV is beyond a threshold separation distance due to which the source beam divergence angle required to cover the entire track gets narrower. This situation results in a reduced geometric loss; thus, concentrating more beam intensity the Rx. Furthermore, as the track inclination angle gets higher, the graphical plot clearly indicates that the power received by the moving USAV will be increasing due to a further reduction in beam divergence angle.

3 Performance Analysis

The primary requirement for maintaining uninterrupted FSO communication with the USAV traversing along the path BC that the Rx aperture positioned on the USAV remains tilted towards the impinging beam at an angle $\gamma + \theta_{\text{inc}}$. This tilting angle ensures that the field-of-view of the Rx aperture is still within the relayed source beam divergence angle while the USAV is moving within the shortest and longest coverage points **C** and **B**, respectively. Subsequently, the Rx aperture focusses the collected

Table 1 Summary of angular parameters with $(d_1, d_2) = (6\text{ m}, 4.13\text{ m})$

Parameters	Value	Parameters	Value
Wavelength, λ	780 nm	Track inclination angle, θ_{inc}	30.0°
Collimator Area, $A_{collimator}$	78 cm^2	Beam divergence angle, θ_{div}	7.7°
Responsivity at 800 nm, R	0.4 uA/uW	Beam tilting angle at B, γ	47.8°
Focal length of the collimator lens, f	50 mm	Beam tilting angle at F, α	55.5°
Length of track BC, L	1 m	Rx tilting angle, β	51.6°
Beam Diameter, D_{beam}	5 mm	Noise power, P_{noise}	1.6e−12 W

fraction of the impinging beam on the photodetector where the signal conditioning and post-detection circuit recover the transmitted data.

Here, we consider on-off keying (OOK) modulation scheme for BS-USAV FSO communication because of the design simplicity and its implementation. The Rx performance is then analysed by incorporating (2) in the analytical result for the bit error rate (BER) for OOK nonreturn to-zero signaling scheme [14], and is given by

$$P_{\text{error}} = \frac{erfc(\gamma_g)}{2} = \frac{1}{2} erfc\left[\frac{R P_{\text{Rx}}}{\sigma^2_{\text{Total Noise}}}\right], \tag{5}$$

where, the responsivity R is considered unity for p-i-n photodetector and the total noise variance $\sigma^2_{\text{Total Noise}}$ at the detector comprises of background, thermal and shot noise [15]. For numerical simulation of the BER performance of the USAV Rx moving along a given track length, the separation distance between the BS and USAV is initially varied. Typical photodetectors with femtowatt receiver sensitivity and modulation bandwidth in the order of MHz are available in the market [16]. Based on the aforementioned parameters, the optimum angular and system parameters are estimated through (1)–(4) for P_{Tx}= 1 W and are summarized in Table 1. Figure 5 illustrates the BER performance of the OOK-based BS-USAV FSO communication for different bit rates. The graphical plot reveals that the power required for achieving the data rate of 200 Mbps for BER = 10^{-9} over the coverage track of 1 m with θ_{inc} = 30° is approximately −62.1 dBm. By reducing the data rate to 150 Mbps, the power required to achieve similar BER performance at the Rx is further reduced by 0.8 dB. Nonetheless, when the track inclination angle is increased from 30° to 60°, the system error performance is significantly improved. Here, a BER of 10^{-9} is considered as the communication benchmark [3] for maintaining reliability of the proposed BS-USAV FSO system with wide beam divergence angle.

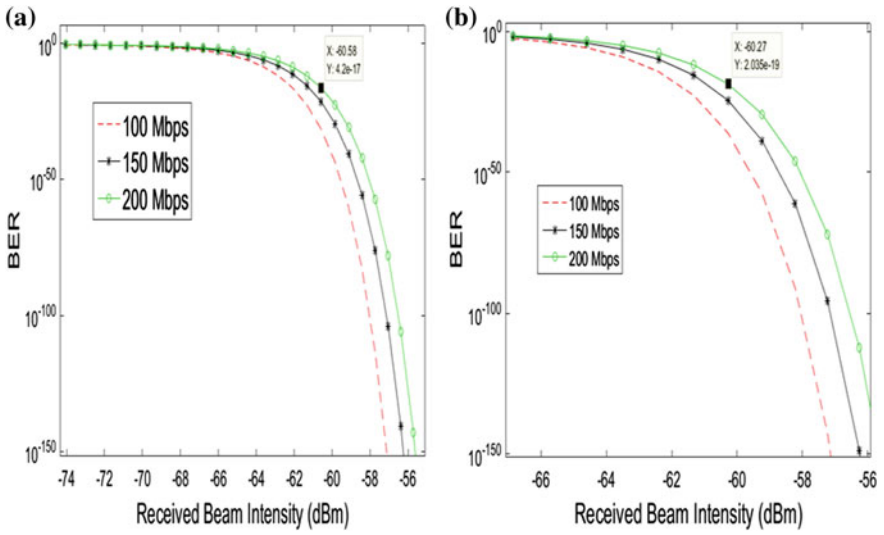

Fig. 5 Plot for BER versus received optical power for different bit rates when the track ($L = 1$ m) inclination is **a** 30° and **b** 60°

Consider a scenario where the USAV is traversing a 2 m track inclined by θ_{inc}= 60°. Tracking the USAV by a single BS with $(d_1, d_2) = (6\text{ m}, 4.13\text{ m})$ will require a wide source beam divergence θ_{div}= 14.7° and an Rx sensitivity of $P_{\text{Rx}} < -200$ dBm.

Alternatively, two optical beams with narrow divergence angle can be relayed from two different BSs, optimally separated by 1 m, in order to cover half portion of the entire track. Tracking the USAV by the two BSs with $(d_1, d_2) = (6.8\text{ m}, 2.5\text{ m})$ will now require a narrow source beam divergence θ_{div}= 6.7° and Rx sensitivity P_{Rx}= −59.2 dBm [as obtained from (1) to (4)]. Note that θ_{div}= 6.7° is the optimum beam divergence angle that can be attained to maintain reliable FSO communication between the USAV and two BSs. The next section highlights power loss mechanisms and an evaluation of the underlying link margin.

4 Link Budget Analysis

The link budget analysis assists in analyzing the proposed FSO system link margin by taking into account of the system specific and nonspecific losses and is given as [17],

$$P_{\text{Rx}}(\lambda, z) = P_{\text{Tx}}(\lambda, 0) - 4.343 z \beta_a(\lambda) - L_{\text{Geom}} - L_{\text{op}} - L_{\text{P}} - L_{\text{M}}. \quad (6)$$

Here, $\beta_{\text{a}}(\lambda)$ is the channel attenuation coefficient at a particular wavelength, L_{op} is the loss induced by the optical windows, and L_{P} is the loss associated with the

Table 2 Summary of angular parameters with $(d_1, d_2) =$ (6 m, 4.13 m)

Parameters	Value	Parameters	Value
Receiver aperture diameter, d_R	10 cm	Receiver sensitivity, P_{Rx}	−30 dBm
Tx aperture diameter, d_{Tx}	5 cm	Optical loss, L_{op}	1 dB
Transmitted power, P_T	1 W	Pointing loss, L_P	1 dB
Track length, L	1 m	Wavelength, λ	780 nm

pointing errors. Any additional power losses, namely changes in the component specification and aging of the laser source, etc., are considered as link margin L_M. The inclusion of L_M helps to tackle undesired power penalties and improve system performance [18].

The system nonspecific losses are associated with the beam scintillation, channel attenuation, and link visibility, to name a few. Furthermore, the system-specific losses comprises of power losses associated with the Rx aperture and the relayed beam. As an illustration, the geometric loss [19], along the propagation axis **AO**, given as

$$L_{\text{Geom}}(\text{dB}) = -20\left[\log\left(\frac{d_{\text{Rx}}}{d_{\text{Tx}} + \theta_{\text{div}} \cdot z}\right)\right], \tag{7}$$

becomes prominent with the wide beam divergence angle, as given by (1). For a typical BS-USAV FSO system, whose specifications are summarized in Table 2, the achievable of beam propagation distance as a function of the link margin is illustrated in Fig. 6. The graphical results are based on the visible waveband visibility range [20] in different weather conditions for a fixed Rx sensitivity. By operating the link at 2 dB link margin in clear air conditions with $\theta_{\text{inc}} = 20°$, a link length of ~9.6 m is attainable; operating the link at the same link margin in moderate foggy weather truncates the achievable link length to 9.4 m. As the track gets more inclined, the propagation length is further reduced to 8.25 m. However, after attaining the valley point in the curve, the beam propagation distance increases with an increase in link margin. These graphical trends are due to the reduction in θ_{div}, leading to reduced beam divergence loss beyond threshold separation distance between BS and USAV, as discussed in Sect. 2.

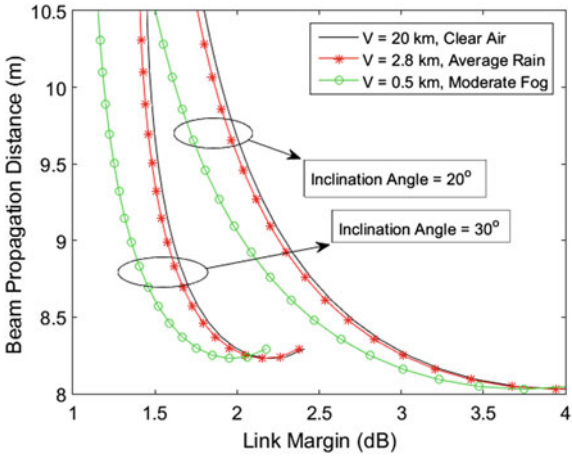

Fig. 6 Beam propagation distance against the available FSO link margin in different weather

5 Conclusion

The intent of the paper is to develop and characterize an IR-FSO communication model between BSs and USAV moving over an inclined straight track. As such, an analytical expression for the received power is derived based on the geometrical position of the USAV from the BS. It is observed that the BER performance of the proposed system progressively worsens as the track length, covered by a single IR beam, is increased. As such, IR beams from multiple BSs can be spatially deployed to cover up the entire track altogether. Additionally, a study has been carried out to and achieve the desired system performance level. Finally, the link budget equation is incorporated so as to explore the impact of the different losses induced by the system-specific and nonspecific parameters and analyze the optimal beam propagation distance for keeping the incoming signal power just above the minimum sensitivity level so as to maintain the desired BER level. Nonetheless, it is advisable to append extra link margin in the link budget for additional system reliability.

Acknowledgements This research work is supported and sponsored by the RESPOND ISRO program.

References

1. Shah S, Latiff M, Riaz T (2015) Performance measurement of free-space optical 980 nm channel using multiple sets of environmental conditions. Wirel Pers Commun 85:345–357. https://doi.org/10.1007/s11277-015-2742-2
2. Bosu R, Prince S (2016) Perturbation methods to track wireless optical wave propagation in a random medium. JOSA-A 244–250. https://doi.org/10.1364/josaa.33.000244

3. Ghassemlooy Z, Popoola W, Rajbhandari S (2013) Optical wireless communications: system and channel modelling with MATLAB. CRC Press, Florida (USA)
4. Leitgeb E, Zettl K, Muhammad S, Schmitt N, Rehm W (2007) Investigation in free space optical communication links between unmanned aerial vehicles (UAVs). In: 9th IEEE conference transparent optical networks, pp 152–155. https://doi.org/10.1109/icton.2007.4296268
5. Kedar D, Arnon S (2004) Urban optical wireless communication networks: the main challengers and possible solutions. IEEE Commun Mag 42:s2–s7. https://doi.org/10.1109/MCOM.2004.1299334
6. Yang L, Gao X, Alouini MS (2014) Performance analysis of free-space optical communication systems with multiuser diversity over atmospheric turbulence channels. IEEE Photon J 6. https://doi.org/10.1109/jphot.2014.2311446
7. Arain S, Shaikh MN, Waqas A, Ali Q, Chowdhry BS, Themistos C (2017) Comparative study and packet error rate analysis of advance modulation schemes for optical wireless communication networks. Wirel Pers Commun 95:593–606. https://doi.org/10.1007/s11277-016-3912-6
8. Khan M, Yuksel M (2014) Maintaining a free-space-optical communication link between two autonomous mobiles. In: IEEE wireless communications and networking conference, pp 3154–3159. https://doi.org/10.1109/wcnc.2014.6953020
9. Paudel R, Ghassemlooy Z, Minh HL, Rajbhandari S (2013) Modelling of free space optical link for ground-to-train communications using a Gaussian source. IET Optoelectron 7:1–8. https://doi.org/10.1049/iet-opt.2012.0047
10. Paudel R, Poliak J, Ghassemlooy Z, Wilfert O, Leitgeb E (2014) Curved track analysis of FSO link for ground-to-train communications. Radio Eng 23:452–459
11. Li L, Zhang R, Zhao Z, Xie G, Liao P, Pang K, Song H, Liu C, Ren Y, Labroille G, Jian P, Starodubov D, Bock R, Tur M, Willner AE (2017) 80-Gbit/s 100-m free-space optical data transmission link via a flying UAV using multiplexing of orbital-angular-momentum beams. arXiv:1708.02923
12. Huang H, Xie G, Yan Y, Ahmed N, Ren Y, Yue Y, Rogawski D, Willner MJ, Erkmen BI, Birnbaum K, Dolinar S, Lavery MPJ, Padgett MJ, Tur M, Willner AE (2014) 100 Tbit/s free-space data link enabled by three-dimensional multiplexing of orbital angular momentum, polarization, and wavelength. Optics Lett 39:197–200. https://doi.org/10.1364/OL.39.000197
13. Song T, Wang Q, Wu MW, Kam PY (2016) Performance of laser inter-satellite links with dynamic beam waist adjustment. Optics Exp 24:11950–11960. https://doi.org/10.1364/OE.24.011950
14. Agrawal G (2002) Fiber-optic communication systems. Wiley, New York (USA)
15. Yang Y, Gao J, Zhang Y (2017) Effects of fog-haze random media on the short-range optical wireless communications link. Optik 138:8–14. https://doi.org/10.1016/j.ijleo.2017.03.027
16. Si transimpedance amplified photodetectors. https://www.thorlabs.com/newgrouppage9.cfm?objectgroup_id=3257
17. Popoola (2009) Subcarrier intensity modulated free-space optical communication systems. PhD dissertation, School of Computing, Engineering and Information Sciences
18. Anthonisamy A, James A (2016) Formulation of atmospheric optical attenuation model in terms of weather data. J Optics 45:120–135. https://doi.org/10.1007/s12596-016-0325-6
19. Tang X, Wang Z, Xu Z, Ghassemlooy Z (2014) Multihop free-space optical communications over turbulence channels with pointing errors using heterodyne detection. J Lightwave Technol 32:2597–2604. https://doi.org/10.1109/JLT.2014.2330594
20. Bouchet O, Sizun H, Boisrobert C, Fornel FD, Favennec P (2006) Free-space optics: propagation and communication. ISTE Ltd., London

Design of Optical Quaternary Multiplier Circuit Using Polarization Switch

Sumana Mandal, Dhoumendra Mandal, Mrinal Kanti Mandal and Sisir Kumar Garai

Abstract In all-optical network, optical multiplier circuit is an essential component for data processing. In the present scenario, the conventional binary logic-based data processing system has been suffering from the speed limitation and has also less information handling capacity. Use of multiple-valued logic (MVL) instead of the conventional binary logic system can overcome these limitations. Quaternary logic is one of the promising multi-valued logics. In this article, the authors have developed quaternary multiplier circuit using SOA-based polarization switch. The frequency-encoded data have been used here because of its inherent property of constancy during reflection, refraction, and transmission. Therefore, in spite of any intensity fluctuation, different bits can be processed or communicated without any error and thus, the bit error rate can be minimized which makes the scheme novel one.

Keywords Quaternary logic · Quaternary multiplier · Semiconductor optical amplifier · Polarization switch

S. Mandal · M. K. Mandal
Department of Physics, National Institute of Technology Durgapur, Durgapur 713209, West Bengal, India
e-mail: sumanamandal1@gmail.com

M. K. Mandal
e-mail: nitmkm@yahoo.co.in

D. Mandal
Department of Physics, Saldiha College, Saldiha, Bankura 722173, West Bengal, India
e-mail: dhoumendra@gmail.com

S. K. Garai (✉)
Department of Physics, M.U.C. Women's College, Burdwan 713104, West Bengal, India
e-mail: skgarai@gmail.com

© Springer Nature Singapore Pte Ltd. 2020

V. Janyani et al. (eds.), *Optical and Wireless Technologies*,
Lecture Notes in Electrical Engineering 546,
https://doi.org/10.1007/978-981-13-6159-3_13

1 Introduction

The conventional binary logic-based data processing system has been suffering from the speed limitation. It has also less information handling capacity because binary logic has only two states to represent a data. Use of multiple-valued logic (MVL) in optical domain has successfully overcome this situation as more than two states are involved here. In the optical domain, speed and bandwidth are consistent with the future generation's demand. In this domain, the advantages of optical fiber and other optoelectronic devices can be exploited also. On the other hand, with the use of MVL, more information can be transmitted, processed, or stored with a single bit. Quaternary logic is one of the most promising MVLs. In all-optical network, optical multiplier circuit is a basic component for designing arithmetic and logical processor (ALU). Various techniques have been reported so far in this regard. Ishizuka et al. explained "VLSI design of a quantum multiplier with direct generation of partial products" [1]. Chattopadhyay developed all-optical quaternary circuits using T gates [2]. Patel et al. explained arithmetic operation such as addition, subtraction, and multiplication in Modulo-4 arithmetic and also addition and multiplication in Galois field using multi-valued logic [3].

In this article, the authors propose a new method of developing optical multiplier based on quaternary logic. The frequency encoding technique is used here for data representation because if a light beam having a particular frequency encounters reflection, refraction, or attenuation, then the frequency of it remains unaltered which is helpful to get reliable data communication. The problem which may arise in case of intensity-encoded data due to the lower noise margin between two qudits can be eliminated using frequency-encoded data. The four qudits '0', '1', '2', and '3' are encoded with four different optical beams of frequencies ν_0, ν_1, ν_2, and ν_3, respectively.

Switching characteristics of semiconductor optical amplifier (SOA) is adopted here to develop these basic units. On the other hand, wavelength division-based DMUXs and MUXs are used here for the purpose of frequency routing.

2 Working Principles of the Proposed Scheme

The working principle of the proposed scheme is based on polarization switching action of SOA. Here, two optical beams having specific frequencies are applied as the input beams of the SOA as shown in Fig. 1. One beam is of higher intensity, called pump beam and other having lower intensity, called the probe beam. Polarization switching signifies that in the absence of pump beam (having higher intensity), the amplified probe beam appears at the output port 1 of the SOA, and in the presence of pump beam there is no beam at output port-1, and the amplified probe beam appears at the output port-2 of the SOA.

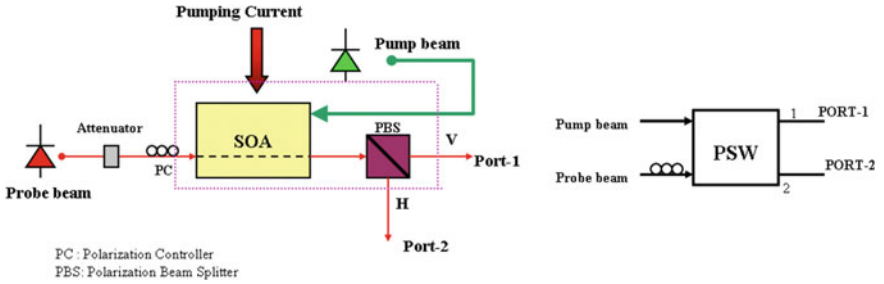

Fig. 1 SOA as a polarization switch (PSW)

Dorren et al. explained [4] the polarization switching property of a strained bulk SOA in the light of simple rate equation model. According to this theory in the absence of pump beam, the probe beam in SOA is divided into TE and TM mode of vibration and these two modes propagate with equal velocities, and they interfere constructively at the output end. But when the highly intense pump beam is present, due to the asymmetry of some parameters of TE and TM modes, birefringence effect comes into play. As a result of this, TE and TM modes of the probe beam travel with unequal velocities, and they interfere at the output with different phases. The phase difference between TE and TM mode is given by [4–7]

$$\Delta\Phi = \frac{1}{2}\left(\frac{\alpha^{TE}\Gamma^{TE}g^{TE}}{v_g^{TE}} - \frac{\alpha^{TM}\Gamma^{TM}g^{TM}}{v_g^{TM}}\right)L \tag{1}$$

where Γ is the confinement factor; α is the phase modulation parameter; α_i is the model loss; 'g' represents the anisotropic gain of the semi-conducting medium; v_g is the group velocity; 'L' is the length of the SOA.

And the resultant power of the output probe beam is

$$P_o = P_o^{TE} + P_o^{TM} + 2\sqrt{P_o^{TE} \cdot P_o^{TM}}\cos(\Delta\Phi) \tag{2}$$

In the absence of pump beam $\Phi = 0$, the PBS at the output is oriented in such a way that maximum power (0.5 mW with 12 dB gain) is obtained at output port-2 of the SOA. On the other hand, in the presence of pump beam of power 0.4 mW, the phase difference would be $\Phi = 180$, and then the power appearing at port-1 is 0.9 W which is almost negligible. So, the total power appears at output port-2 of the SOA [4].

3 Scheme of Optical Quaternary Multiplier

The proposed scheme of the optical quaternary multiplier circuit consists of three DMUXs (D1, D2, D3), ten PSWs (P1, P2, …, P10), and five MUXs (M1, M2, …, M5) as shown in Fig. 2. Input signal 'A' is applied to D1. D1 has four channels.

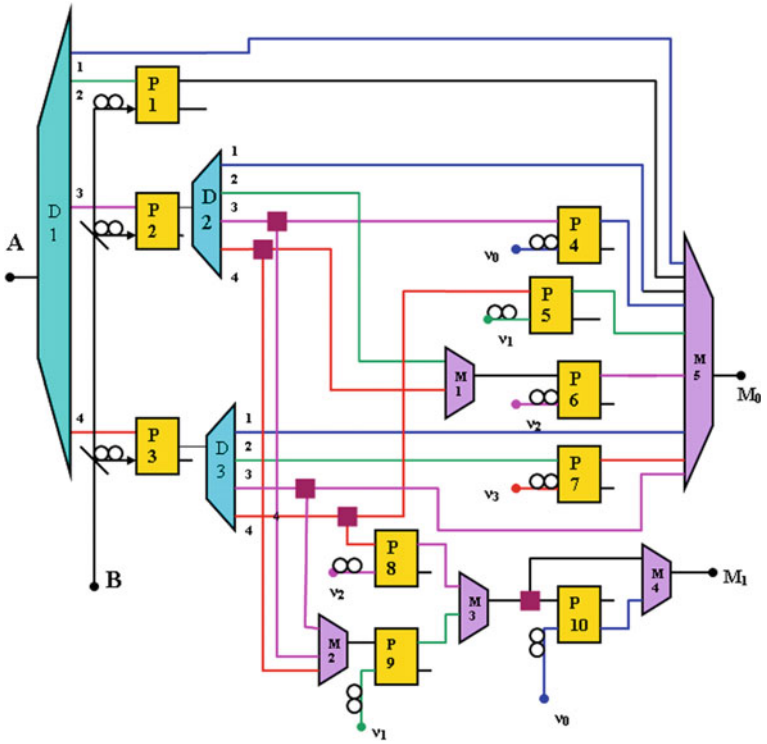

Fig. 2 Scheme of optical quaternary multiplier

These four channels pass the input signal depending upon its frequency. Channels 1, 2, 3, and 4 pass the beams of frequencies ν_0, ν_1, ν_2, and ν_3, respectively. The channel 1 is connected to the output 'M_0' through M5. The beam of frequency ν_1 passes through the channel 2 and serves as the pump beam of P1. Similarly, the beams of frequencies ν_2 and ν_3 after passing through the channels 3 and 4 serve as the pump beams of P2 and P3, respectively. On the other hand, the input signal 'B' is divided into three equal parts, and each part serves as the probe beams of P1, P2, and P3, respectively. The output port-1 of P1 is connected to the final output (M_0) via M5. On the other hand, the output port-1 of P2 and P3 are connected to the inputs of D2 and D3, respectively. The channels 1, 2, 3, and 4 of D2 and D3 pass the frequencies ν_0, ν_1, ν_2, and ν_3, respectively. Both the channel 1 outputs of D2 and D3 are connected to the output (M_0) via M5. The beam of frequency ν_2 emerging from the channel 3 of D2 is divided into two parts and are amplified. One part serves as the pump beam of P4 and other part serves as the pump beam of P9 through M2.

Now, the beam of frequency ν_0 is applied to P4 as the probe beam. The output beam of port-1 of P4 supplies the output 'M_0' via M5. Now the beam of frequency ν_3 of channel 4 of D2 is also split up into two parts. One part of this beam is used as the pump beam of P6 through M1. Another part of this beam supplies the pump

beam of P9 through M2. The beam of frequency ν_2 is applied to P6 as the probe beam. The output beam of port-1 of P6 is connected to final output 'M_0' via M5. On the other hand, the beam of frequency ν_1 of the channel 2 of D3 serves as the pump beam of P7. The frequency of the probe beam applied to P7 is ν_3. The output port-1 of P7 is connected to output 'M_0' via M5. Now the beam of frequency ν_2 of the channel 3 of D3 is divided into two equal parts and amplified. One part serves as the output 'M_0' via M5. The other part of the beam supplies the pump beam of P9 through M2. A beam of frequency applied to P9 as the probe beam. On the other hand, beam of frequency ν_3 of the channel 4 of D3 is divided into two parts. One part is applied as pump beam of P5, and the other is also applied as pump beam of P8. Probe beams of frequencies ν_1 and ν_2 are applied to P5 and P8, respectively. The output beam of port-1 of P5 serves as the output 'M_0' via M5. On the other hand, both the port-1 outputs of P8 and P9 are connected to the input of M3. The beam emerging from the output of M3 is divided into two equal parts and amplified. One part of the beam appears at the output 'M_1' via MUX (M4), and the other part is applied as the pump beam of P10. The frequency of the probe beam applied to P10 is ν_0. The output port-1 of P10 remains open, and the port-2 of P10 is connected to output 'M_1' via MUX (M4). So, in the presence of any input in M3, the pump beam is supplied to P10, and consequently, the port-2 of P10 remains off. But in the absence of pump beam, the probe beam of frequency ν_0 switches to port-2 of P10, and it gives the final output 'M_1'.

Now we explain the operation of the multiplier circuit for the different combinations of input signals.

Case 1: Input beam 'A' is of frequency ν_0, 'B' is of frequency $\nu_0/\nu_1/\nu_2/\nu_3$

If the input signal 'A' is of frequency ν_0, and the input signal 'B' is of frequency $\nu_0/\nu_1/\nu_2/\nu_3$, then the signal 'A' passes through the channel 1 of D1 and serves as the output 'M_0' through M5 without depending on the frequency of the input 'B'. So, whatever be the frequency of input 'B', the beam of frequency ν_0 appears as the output 'M_0'. It should be mentioned that in this case P1, P2, and P3 do not get any pump beam. So, port-1 outputs of these PSWs remain off. On the other hand, P10 also does not get any pump beam. So, at output port-2 of it, the beam of frequency ν_0 appears and serves the output 'M1' via MUX (M4).

Case 2: Input beam 'A' is of frequency ν_1, 'B' is of frequency $\nu_0/\nu_1/\nu_2/\nu_3$

In this case, the input beam 'A' is of frequency ν_1. So, it passes through the channel 2 of D1 and serves as the pump beam of P1. Now the input beam 'B' serves as the probe beams of P1, P2, and P3. P2 and P3 do not get any pump beam, and so port-1 outputs of these PSWs remain off. But P1 gets the probe beam as well as the pump beam. So, at output port-1 of P1, the beam of frequency $\nu_0/\nu_1/\nu_2/\nu_3$ (same as the frequency of the input 'B') arises. This beam serves as the output 'M_0' via M5. As similar to the previous case, P10 does not get any pump beam. So, the beam of frequency ν_0 appears as the output 'M_1'.

Case 3: Input beam 'A' is of frequency ν_2

Input beam 'A' of frequency ν_2 enters D1 and passes through the channel 3 of D1. Then the beam serves as the pump beam of P2. Now, the input beam 'B' is applied to P2 as the probe beam. So depending upon the frequency of beam 'B', port-2 of P2 gives the corresponding beam. So, different cases arise for different frequencies of the input 'B'. Some cases are discussed below.

(a) Input beam 'B' is of frequency ν_0

Now, when input beam 'B' is of frequency ν_0, it serves as the probe beam of P2. So, at output port-1 of it, the beam of frequency ν_0 appears. After that, it passes through the channel 1 of D2 and serves as the output 'M_0' via M5. So, the beam of frequency ν_0 appears as M_0 output. In this situation, P10 does not get any pump beam. So, the beam of frequency ν_0 appears at port-2 of P10, and it serves as the M_1 output via MUX (M4). It should be mentioned that in this condition, there is no beam to pass through the channels 1 and 3 of D1. So, the corresponding PSWs contribute nothing to the final output.

(b) Input beam 'B' is of frequency ν_1

In this situation, P2 gets the pump beam of frequency ν_2 and probe beam is of frequency ν_1. So, at output port-1 of P2, the beam of frequency ν_1 appears and passes through the channel 2 of D2. Then, this beam serves as the pump beam of P6 after passing via M1. So, the probe beam of frequency ν_2 switches to port-1 and after passing through M5, the beam serves as the output 'M_0'. In this case, also P10 does not get any pump beam. So, the probe beam of frequency ν_0 applied to P10 appears as output 'M_1' after passing via MUX (M4).

Similarly, when the input beam 'B' is of frequency ν_2, the outputs 'M_0' and 'M_1' are of frequencies ν_0 and ν_1, respectively, and when the input beam 'B' is of frequency ν_3, the outputs 'M_0' and 'M_1' are of frequencies ν_2 and ν_1, respectively, which are in accordance with the truth table (Table 1).

Case 4: Input beam 'A' is of frequency ν_3

Input beam 'A' of frequency ν_3 passes through the channel 4 of D1 and serves as the pump beam of P3. Now, a portion of beam 'B' is applied to P3. So, different cases arise for different frequencies of the input 'B'. Some cases are discussed below. Here, the port-1 outputs of P1 and P2 remain off as these PSWs do not get any pump beam and contribute nothing to the final outputs.

(a) Input beam 'B' is of frequency ν_0

Input beam 'B' of frequency ν_0 serves as the probe beam of P3. So, at output port-1 of P3, the beam of frequency ν_0 appears. This beam passes through the channel 1 of D3. After passing via M5, the beam of frequency ν_0 serves as the output 'M_0'. On the other hand, P10 does not get any pump beam. So, at the output port-2, the beam of frequency ν_0 appears, and after passing via MUX (M4), this beam serves as the output 'M_1'. Here, as P8 and P9 do not get any pump beam, these PSWs contribute nothing to the final outputs.

Table 1 Truth table of frequency-encoded quaternary multiplier

Frequency of the input signals		Frequency of the output signal	
A	B	M0	Ml
v_0	v_0	v_0	v_0
v_0	v_1	v_0	v_0
v_0	v_2	v_0	v_0
v_0	v_3	v_0	v_0
v_1	v_0	v_0	v_0
v_1	v_1	v_1	v_0
v_1	v_2	v_2	v_0
v_1	v_3	v_3	v_0
v_2	v_0	v_0	v_0
v_2	v_1	v_2	v_0
v_2	v_2	v_0	v_1
v_2	v_3	v_2	v_1
v_3	v_0	v_0	v_0
v_3	v_1	v_3	v_0
v_3	v_2	v_2	v_1
v_3	v_3	v_1	v_2

(b) Input beam 'B' is of frequency v_1

Here, P3 gets the pump beam of frequency v_3 and probe beam of frequency v_1. So at output port-1 of P3, the beam of frequency v_1 appears and after passing via the channel 2 of D3, it serves as the pump beam of P7. The probe beam of P7 is of frequency v_3. So, at the output port-1 of P7, the beam of frequency v_3 appears and after passing via M5, this beam serves as the output of M_0. Also, in this case, P10 does not get pump beam. So the beam of frequency v_0 appears at port-2 of P10 and serves the output 'M_1' through M4.

Similarly, when the input beam 'B' is of frequency v_2, the outputs 'M_0' and 'M_1' are of frequencies v_2 and v_1, respectively, and when the input beam 'B' is of frequency v_3, the outputs 'M_0' and 'M_1' are of frequencies v_1 and v_2, respectively, which are in accordance with the truth table (Table 1).

Thus, all the cases as explained above follow the truth table as mentioned in Table 1.

The authors have simulated the optical circuit using MATLAB software. In Fig. 3, the power spectrums of input beams and the simulated output beams are shown. The authors have considered the Gaussian power distribution of the optical beams with full width at half maxima (i.e., FWHM) of 0.4 nm. The authors have encoded the four qudits '0', '1', '2', and '3' with four optical beams of different frequencies. The qudit '0' is encoded with the optical beam of frequency $1.9367 * 10^{14}$ Hz (i.e., v_0) and the corresponding wavelength is 1548 nm. The qudit '1' is encoded with the optical

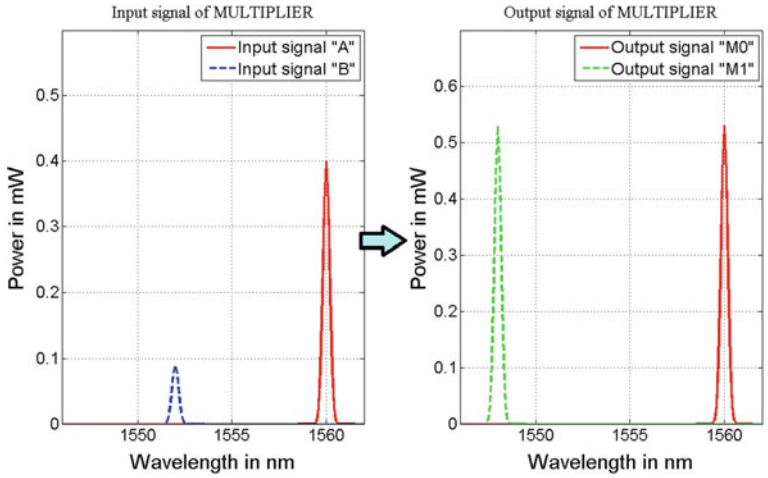

Fig. 3 Simulation result of optical quaternary multiplier

beam of frequency 1.9317 * 10^{14} Hz (i.e., ν_1) and the corresponding wavelength is 1552 nm. Similarly, other two qudits '2' and '3' are encoded with the optical beam of frequency 1.9267 * 10^{14} Hz (i.e., ν_2) and 1.9219 * 10^{14} Hz (i.e., ν_3), respectively, and corresponding wavelengths are 1556 nm and 1560 nm, respectively.

4 Discussion

In the proposed scheme, qudits are processed directly without converting them to binary bits, and thereby the speed of processing is enhanced. For realizing the switching action of SOA, tensile strained bulk JDS uniphase SOA is used here. Here, the power of pump beam should be at least 0.4 mW and the power of probe beam should not be greater than 0.03 mW.

For multiplier circuit, input beam 'B' is divided into three parts. So, the power of beam 'B' should be 0.09 mW. The power of input beam 'A' should be 0.4 mW as it serves as the pump beam of respective PSWs (P1, P2, and P3) through D1. The outputs of DMUXs (D2 and D3) are of power 0.4 mW. So, the output beams which are divided after emerging from the DMUXs and serves as the pump beam of respective PSWs should be amplified followed by the diagram.

The switching speed of the SOA-based PSW is very high, but at higher speed, SOA shows some undesired pattern at the output due to slow gain recovery. Using various techniques, this undesirable pattern effect in SOA can be mitigated. Another phenomenon, observed in SOA, is the noise due to spontaneous recombination of electron–hole in the active region. This noise can be reduced using proper bandpass filter at the output.

5 Conclusion

WDM communication network provides us with enormous data handling capacity. Frequency-encoded quaternary units like adder, subtractor, and multiplier are indispensable in this respect. The wavelength spacing is nearly 0.4 nm for the channel spacing of frequency 200 GHz, so that the ever-increasing bandwidth hunger of the consumer can be accommodated. Shortcomings like data traffic security, etc. which arises in the electronic-based data communication network can also be overcome using such types of an all-optical quaternary data processing unit.

References

1. Ishizuka O, Ohta A, Tanno K, Tang K, Handoko D (1997) VLSI design of a quaternary multiplier with direct generation of partial products. In: Proceedings of the 27th international symposium on multiple-valued logic, pp 169–174
2. Chattopadhyay T (2010) All-optical quaternary circuits using quaternary T-gate. In: Optik Int J Light Electron Opt 121(19):1784–1788
3. Patel V, Gurumurthy KS (2010) Arithmetic operation in multi-valued logic. Int J VLSICS 1(1):21–32
4. Dorren HJS, Lenstra D, Liu Y, Hill MT, Khoe G-D (2003) Nonlinear polarization rotation in semiconductor optical amplifiers: theory and application to all-optical flip-flop memories. IEEE J Quantum Electron 39(1):141–148
5. Garai SK (2015) All-optical quaternary logic gates – An extension of binary logic gates. Opt LASER Technol 67:125–136
6. Mandal S, Mandal D, Mandal MK, Garai SK (2017) Design of frequencyencoded data-based optical master-slave-JK flip-flop using polarization switch. Opt Eng 56(6)
7. Mandal S, Mandal D, Garai SK (2014) An all-optical method of developing data communication system with error detection circuit. Opt Fibre Technol 20(2):120–129

Coverage Optimization of a VLC-Based Smart Room with Genetic Algorithm

Koyyada Dinesh Kumar, Ravi Kumar Maddila and Satyasai Jagannath Nanda

Abstract In smart rooms, light-emitting diodes (LEDs) are used for visible light communications. In this communication process, it is observed that there is uneven distribution of received optical power and signal-to-noise ratio (SNR) on the same receiving plane. This affects the performance of the LED panel as some of the LEDs have to transmit more power to the get connected to the far away receivers. Here, this is developed as an optimization problem, i.e., optimization of received optical power and SNR together by controlling the distance between LED panel and receiver. The optimization is performed by genetic algorithm. A case study is presented for a 5 m × 5 m × 3 m size room with a single 4 × 4 LED panel placed at the center. Simulation study reveals that after optimization there is almost uniform optical power distribution and SNR in the same receiving plane.

Keywords Visible light communication · Genetic algorithm · LED panel · Received optical power · Signal-to-noise ratio · Coverage optimization

1 Introduction

The visible light communication (VLC) system is popular and going to get standardized in 5G indoor communication due to high bandwidth, rapid communication, strong security, high system capacity, and its robustness toward security [1, 2]. As it is an upcoming technology, a lot of research is going on several aspects of communication before making its benchmark. In this paper, the problem taken is to obtain

K. D. Kumar · R. K. Maddila · S. J. Nanda (✉)
Department of Electronics and Communication, Malaviya National Institute of Technology Jaipur, Jaipur 302017, Rajasthan, India
e-mail: nanda.satyasai@gmail.com

K. D. Kumar
e-mail: 2016pwc5343@mnit.ac.in

R. K. Maddila
e-mail: rkmaddila.ece@mnit.ac.in

© Springer Nature Singapore Pte Ltd. 2020

V. Janyani et al. (eds.), *Optical and Wireless Technologies*,
Lecture Notes in Electrical Engineering 546,
https://doi.org/10.1007/978-981-13-6159-3_14

uniform optical received power and SNR in a given receiving plane of a smart room. It finds potential application in providing Internet connectivity in common public halls, switching on and off the smart appliances in a room.

Recently, Kumawat et al. [3] proposed a technique to position several LED panels in a room to obtain uniform illuminance (lx) and received optical power (dBm). The authors have used whale optimization for determining the optimal locations of 4–6 LED panels in a room. Similar problem of layout optimization of LED panel was addressed with gene density improved genetic algorithm by Liu et al. [4]. The application taken here concentrates on effective communication using a single LED panel and not considering illuminance.

Sun et al. in [5] reported coverage optimization of VLC using a power regulator factor for each LED in a panel. The authors used improved cuckoo search algorithm to compute the power regulator factors associated with every LED such that the received optical power and SNR are optimized on a plane. Wang et al. in [6] optimized the SNR for indoor VLC by selecting the specific communicating LEDs.

In this manuscript, the received optical power and SNR are optimized on a given plane for a smart room with a single LED panel at its roof. This optimization is done based on distance between LED panel and receiver on a plane using genetic algorithm. The binary genetic algorithm is considered over here as it is most popular [7], and after nearly 40 years of the initial algorithm it still provides convincing accurate results in many platforms [8].

The rest part of the paper is organized as follows. In Sect. 2, the model of a VLC system for an indoor environment is described. The proposed concept of coverage optimization using binary genetic algorithm is discussed in Sect. 3. The simulation studies for the proposed model using MATLAB are described, and obtained results are highlighted in Sect. 4. The concluding remarks are given in Sect. 5.

2 Model of Visible Light Communication System for Indoor Environment

The VLC system for a room with length, width, and height of 5 m $\times$ 5 m $\times$ 3 m, respectively, is shown in Fig. 1. Here, the LED panel is used as a light source, and each element in the panel is uniformly distributed on top of ceiling line of sight (LOS) that is considered here for analysis. The LED array is installed at the ceiling, at height of 3 m from positioning LED array for uniform power distribution.

2.1 VLC Channel Model for Indoor Environment

Received signal from the LED transmitter is described in [5]

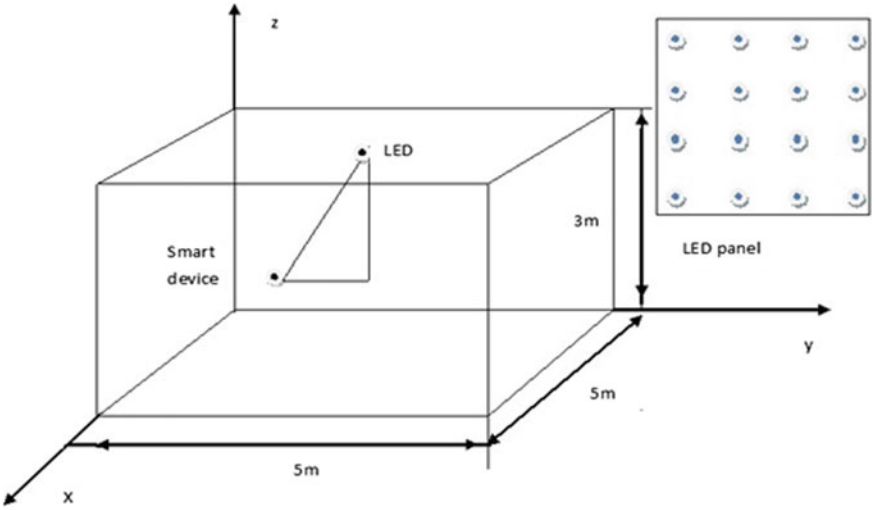

Fig. 1 Indoor visible light communication system model environment

$$y_i = rxh_i + n \tag{1}$$

where y_i is the received signal from ith LED transmitter, r is the detecting sensor, x represents the transmission optical pulse, and n is the white Gaussian noise with mean 0. h_i is the channel impulse response between the ith transmitter and receiver that is discussed in [5] given by

$$h_i = \frac{(m+1)A}{2\pi D_d^2} \cos^m(\emptyset) T_s(\Psi) g(\Psi) \cos(\Psi), \quad 0 \le \Psi \le \Psi_c \tag{2}$$

h_i is equal to 0 when $\Psi > \Psi_c$ and A is the area of photodetector D_d is the distance between receiver and LED light source and $\emptyset$ emission angle, $T_s(\Psi)$ is the gain of optical filter, $g(\Psi)$ is the gain of optical concentrator, Ψ_c is the half-power angle of receiver, and m is the Lambert index, which is described in [5].

2.2 Lambert Index

$$m = \frac{-\ln 2}{\ln\left(\cos \emptyset_{1/2}\right)} \tag{3}$$

where $\emptyset_{1/2}$ is the half-power angle of LED.

2.3 VLC Received Optical Power

$$P_r\left(L_j\right) = \sum_{i=1}^{N} P_t H(0) + \int_{Assur} P_t H_{ref}(0) \tag{4}$$

The received optical power P_r is obtained from the direct channel gain $H(0)$, reflection channel gain $H_{ref}(0)$, and optic power of LED source, which is discussed in [5]. The L_j represents the location of j receiver and P_t represents the transmission power of a single LED.

2.4 VLC SNR

$$SNR\left(L_j\right) = \frac{R^2 P_r\left(L_j\right)^2}{\sigma_{noise}^2} \tag{5}$$

where R is the response of PD, $P_r\left(L_j\right)$ represents the average optical power in L_j, σ_{noise} represents the noise power.

3 Coverage Optimization of VLC

The objective here in a smart room is to achieve uniform optical power throughout a receiving plane. Here, a power regulator factor [5] is introduced for each LED and it is adjusted to normalize the transmission power of each LED.

3.1 Power Regulator Factor of LED

The power regulator factor value varies from 0 to 1 given by

$$P_r\left(L_j\right) = \sum_{i=1}^{N} n_i P_t H(0) + \int_{Assur} n_i P_t H_{ref}(0) \tag{6}$$

By introducing the power-regulating factor, each VLC device receiving power can be described as follows:

$$P_r(L_1) \approx P_r(L_2) \approx P_r(L_3) \cdots \approx P_r(L_i) \tag{7}$$

Similarly, by introducing power-regulating factor in receiving SNR,

$$SNR\left(L_j\right) = \frac{n_i R^2 P_r\left(L_j\right)^2}{\sigma_{noise}^2} \tag{8}$$

$$SNR(L_1) \approx SNR(L_2) \approx SNR(L_3) \cdots \approx SNR(L_i) \tag{9}$$

3.2 Genetic Algorithm for Coverage Optimization

The binary genetic algorithm is used here to optimize the received optical power and SNR. The pseudocode of the algorithm is described below:

Pseudo code of genetic algorithm for coverage optimization

```
1 Initialize the population
        current_generation := 1
        for i := 1 to N
        for j := 1 to L
        p[i][j] := random_number(0,1) end; end;
2 Evaluate the fitness of population
        for i := 1 to N
        evaluate fitness ( p[i] )
        end
3 selection
        for i := 1 to N
        parents[i] := tournament ( p, tournament_size )
        end
4 Crossover
        for i := 1 to N
         for j := 1 to L
         if ( j <= crossover point )
         offspring[i][j] := parents[i][j]
         offspring[i+1][j] := parents[i+1][j]
         else
        offspring[i][j] := parents[i+1][j]
        offspring[i+1][j] := parents[i][j]
       end;  end;  end
5  Mutation
        for i := 1 to N
        if ( random_number < mutation_rate )
        mutation(offspring[i])
       end ; end
6  Evaluate the fitness of off springs
        for i := 1 to N
        evaluate(offspring[i])
        end
7  Population for next generation
        p := offspring
       current_generation += 1
8  Termination condition
       if ( current_generation < max_generation )
       return to step 3
      end
9  The solution is the individual with the best evaluation
```

Then after the optimized value is achieved for 100 generations, the result is divided by each individual power from all the different locations and then we get a value within a range of 0–1; this value is power regulated factor and it is multiplied with transmitted power of each LED; and thus by this, uniform power is maintained throughout the same receiving plane and this is the process that happens the post-genetic algorithm.

4 Simulation and Results

In this section, simulation is carried out using MATLAB 2014. The parameters used here are as follows: size of the room is 5 m × 5 m × 3 m, area of the photodetector is 10^{-4} m^2, gain of the optical filter is 1, gain of optical concentrator is 0.8, half-power angle is 55, field of view is 80, and height of receiver location is 0.85 m. White communication LED can be used for the implementation. The optimization task is carried out using binary genetic algorithm described in [8]. In genetic algorithm, the number of chromosomes taken here is 10, number of genes taken is 10, probability of crossover is 0.8, and probability of mutation 0.1; there are the different constraints considered in binary genetic algorithm. The plot of optimized power and SNR value with respect to generation is shown in Fig. 2a, b, respectively. Here, the minimization is carried out for 100 generations. The optimized value of received optical power is −51.6 dB, and optimized value of SNR is −20.6 dB.

In Fig. 3a, in non-optimized case, it is observed that the received optical power distribution varies from −41.9 to −46.9 dB and the difference is 5 dB. In case of optimized power shown in Fig. 3b, it is reported that the power varies from −48.4 to −50.5 dB and the difference is 2.1 dB. Hence, in the optimized case, the difference in received optical signal is decreased by 58%. With this, there is uniform power distribution in the room at different positions. In Fig. 3c, in non-optimized SNR case, it is evident that the SNR distribution varies from −2 to −12 dB. The peak

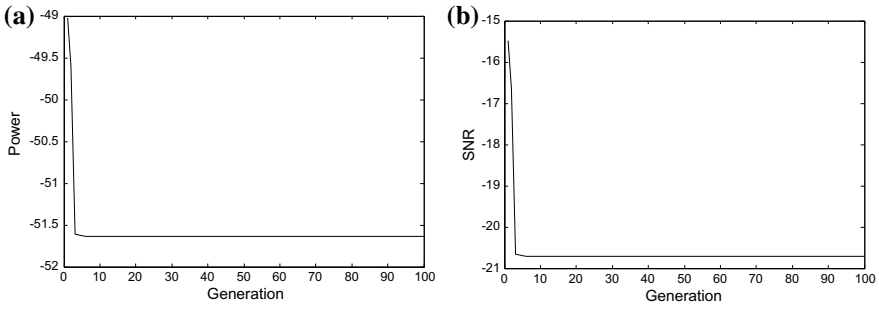

Fig. 2 Optimized value of power and SNR over generation **a** optimized power is −51.6 dB, **b** optimized SNR is −20.6 dB

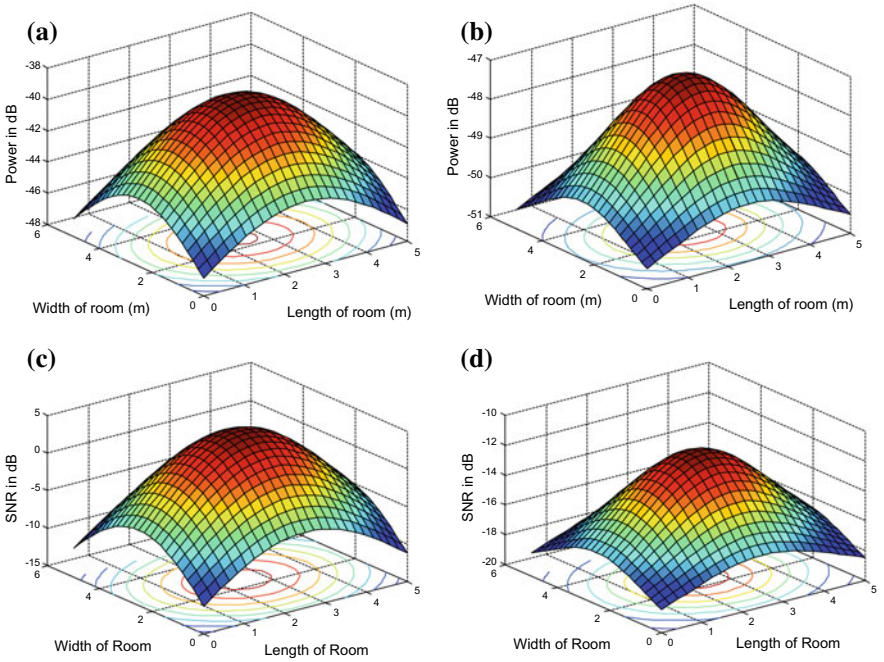

Fig. 3 Optimized value of power and SNR before and after optimization in the room **a** non-optimized power, **b** optimized power, **c** non-optimized SNR, **d** optimized SNR

Table 1 Non-optimized and optimized case power and SNR optimal values in the 3D plot of Fig. 3

Parameters	Non-optimized		Optimized		Percentage decrease after optimization (%)
	Peak value (dB)	Valley value (dB)	Peak value (dB)	Valley value (dB)	
Power	−41.9	−46.9	−48.4	−50.5	58
SNR	−2	−12	−14.5	−18.5	60

value of SNR is −2 dB, and valley value is −12 dB, and their difference is 10 dB. In optimized SNR case as shown in Fig. 3d, the SNR varies from −14.5 to −18.5 dB and the difference is 4 dB. Hence, the optimized SNR is decreased by 60%. With this, it is clear that a uniform SNR distribution is achieved in a room at different positions. This total observation is reported in a concise manner in Table 1.

5 Conclusion

In this manuscript, genetic algorithm is used to maximize received optical power and SNR in a smart room with a single LED panel connected on the roof. Then, a power regulator factor is used for normalization of transmission power. From the simulations, it is observed that after optimization with genetic algorithm the uniformity achieved is 58% in case of power and 60% in case of SNR compared to the non-optimized case. Thus, with this formulation, uniform distribution of optical power and SNR is achieved on a given receiving plane of a smart room.

References

1. Grobe L, Paraskevopoulos A, Hilt J, Schulz D, Lassak F, Hartlieb F, Kottke C, Jungnickel V, Langer KD (2013) High-speed visible light communication systems. IEEE Commun Mag 51(12):60–66
2. Pathak PH, Feng X, Hu P, Mohapatra P (2015) Visible light communication, networking, and sensing: a survey, potential and challenges. IEEE Commun Surv Tutor 17(4):2047–2077
3. Kumawat IR, Nanda SJ, Maddila RK (2017) Positioning LED panel for uniform illuminance in indoor VLC system using whale optimization. In: Proceedings of international conference on optical and wireless technologies. Lecture notes in electrical engineering, vol 472. Springer, pp 131–139
4. Liu H, Wang X, Chen Y, Kong D, Xia P (2017) Optimization lighting layout based on gene density improved genetic algorithm for indoor visible light communications. Opt Commun 390:76–81
5. Sun G, Liu Y, Yang M, Wang A, Liang S, Zhang Y (2017) Coverage optimization of VLC in smart homes based on improved cuckoo search algorithm. Comput Netw 116:63–78
6. Wang L, Wang C, Chi X, Zhao L, Dong X (2017) Optimizing SNR for indoor visible light communication via selecting communicating LEDs. Opt Commun 387:174–181
7. Goldberg DE (2006) Genetic algorithms. Pearson Education India
8. Goldberg DE (2013) The design of innovation: lessons from and for competent genetic algorithms, vol 7. Springer Science & Business Media

A Compact Wideband Polygon Patch Antenna for Ku-Band Applications

G. Anjaneyulu, T. A. N. S. N. Varma and J. Siddartha Varma

Abstract This research paper presents a design of polygon-shaped microstrip patch antenna for wideband Satellite Application. The aim of this work is to design a compact-sized patch antenna, which operates at Ku-band. Two circular slots are incorporated on the polygon patch to obtain the required resonant frequency. The proposed antenna achieves an impedance bandwidth of 1.3 GHz and maximum reflection coefficient is achieved at 14.10 GHz. The antenna is a planar geometry with coaxial probe feed. The bandwidth varies with varying width of slit rings in the microstrip patch antenna. The several parameters of microstrip patch antenna are discussed in this paper such as return loss, bandwidth, gain.

Keywords Polygon microstrip patch antenna · Satellite application · Ku-band

1 Introduction

The need for compact size antennas is increasing rapidly with the growth of wireless communication technologies. Due to this development, several modern communication systems are employing microstrip antennas. There are numerous benefits with microstrip antennas such as low cost, lesser weight, small size and compatible to install on any complex surface [1, 2]. Additionally, this type of antennas can be effortlessly fabricated with the support of printed technologies on a large scale thus manufacturing cost is significantly reduced.

These microstrip antennas have disadvantages such as narrow bandwidth and low gain [1]. So, enhancing the bandwidth of antenna with keeping the size in mind is very crucial for any antenna designers. In order to obtain wideband, several types of antennas are studied [3] and many different shapes of patch antennas are reported

G. Anjaneyulu (✉) · T. A. N. S. N. Varma
ECE Department, MVGR College of Engineering, Vizianagaram, Andhra Pradesh, India
e-mail: anjaneyulu.mvgr@gmail.com

J. Siddartha Varma (✉)
MVGR College of Engineering, Vizianagaram, Andhra Pradesh, India

© Springer Nature Singapore Pte Ltd. 2020

V. Janyani et al. (eds.), *Optical and Wireless Technologies*,
Lecture Notes in Electrical Engineering 546,
https://doi.org/10.1007/978-981-13-6159-3_15

in the open literature, which are used in the satellite application in Ku-band [4–8]. But, still there is a lot of scope for antenna miniaturization with enhanced gain and bandwidth for satellite applications.

The effectiveness of various parameters of the antenna depend on the size, shape, type of substrate used and location of the feed point. Therefore, for diverse applications various shapes of antennas are proposed by many researchers. In this research paper a polygon shaped patch antenna is designed and simulated using commercially available HFSS software. The propounded antenna is aimed to operate in Ku-band for the satellite applications.

2 Antenna Configuration

The prime focus of this work is to design a patch antenna having a resonance frequency in Ku-band. In order to obtain higher frequencies, we have chosen a polygon shape for the patch to design the proposed antenna in this study. To avoid radiation loss and to provide larger quality factors than the other configurations such as rectangular patches, polygon-shaped patch has been selected for this work. Primarily, this kind of patch has only one aspect of freedom to control, i.e., the radius of the patch. So, we have tried to add another control parameter, two slit rings inside the patch.

Design Parameters of the antenna are considered from the conventional circular patch antenna and converted into polygon shape. The transmission line model equations are used to obtain the fundamental geometry of the propounded circular patch antenna. The following equations [1] are used to obtain the radius of the patch for the required resonant frequency:

Radius

$$a = \frac{F}{\left\{1 + \frac{2h}{\pi \varepsilon_r F}\left[\ln\left(\frac{\pi F}{2h}\right) + 1.7726\right]\right\}^{\frac{1}{2}}}, \tag{1}$$

where

$$F = \frac{8.791 \times 10^9}{f_r \sqrt{\varepsilon_r}}$$

Based on the above equations, radius of the circular patch is calculated as 3.381 mm. The dimensions of the ground plane and substrate are considered as $17.38 \times 15.10\ \text{mm}^2$. The substrate taken for printing the proposed antenna is Rogers RT Duroid 5880 (tm), having a relative permittivity of 2.2 with a loss tangent of 0.0009 and thickness of 1.588 mm. Coaxial feeding technique is used to provide feed to the antenna. The diameter of the outer conductor of coaxial feed is 1.6 mm

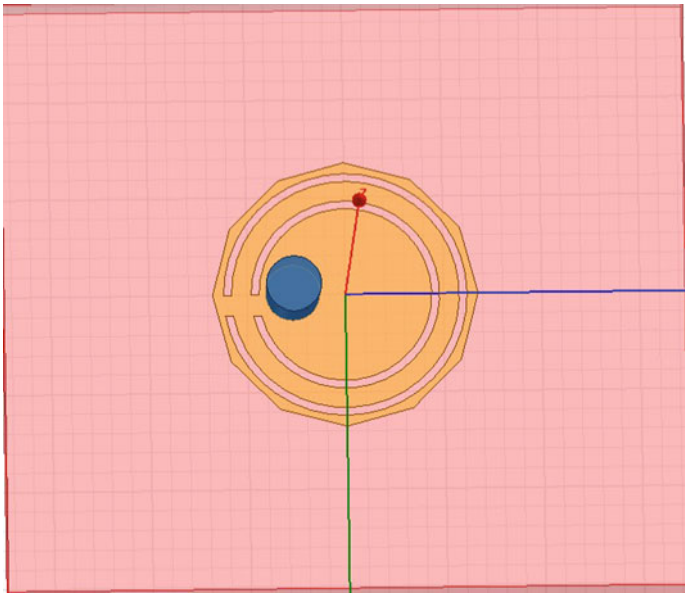

Fig. 1 Top view of the propounded polygon patch antenna

and inner conductor is 0.7 mm. The location of the feed is optimized for the best impedance matching. The proposed antenna is shown in Fig. 1.

Employing two slots on the polygon patch play a significant role in defining the resonant frequency of the antenna. The two ring slots on the patch have a width of 0.2 mm and these dimensions are optimized to have a better result. As the feed point position in the antenna varies the parameters like impedance and gain are also changed. Impedance will be zero if the feed point is placed in the center of the patch. Hence, by optimizing the design, a perfect feed location for the proposed patch is obtained at (0, −0.5, 0).

3 Results and Discussion

The simulated results of the various parameters are presented in this section. The frequency range is from 10 to 18 GHz.

The proposed antenna is simulated using HFSS, and from the S parameter result as shown in Fig. 2, it is observed that return loss of −10 dB is obtained at a frequency close to the 14 GHz, which lies in the Ku-band. The antenna gain at the resonant frequency of 14 GHz is at 6.86 dB and it can be observed from the Fig. 3, which is very good in that frequency. The VSWR of the proposed antenna is 1.0295, which is close to 1, it means the antenna is matched perfectly as shown in the Fig. 4.

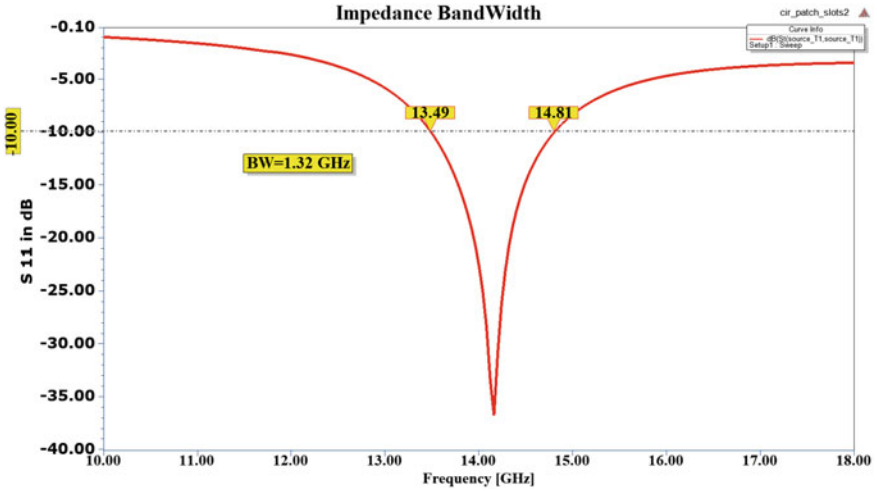

Fig. 2 S parameter versus frequency plot of propounded patch in dB

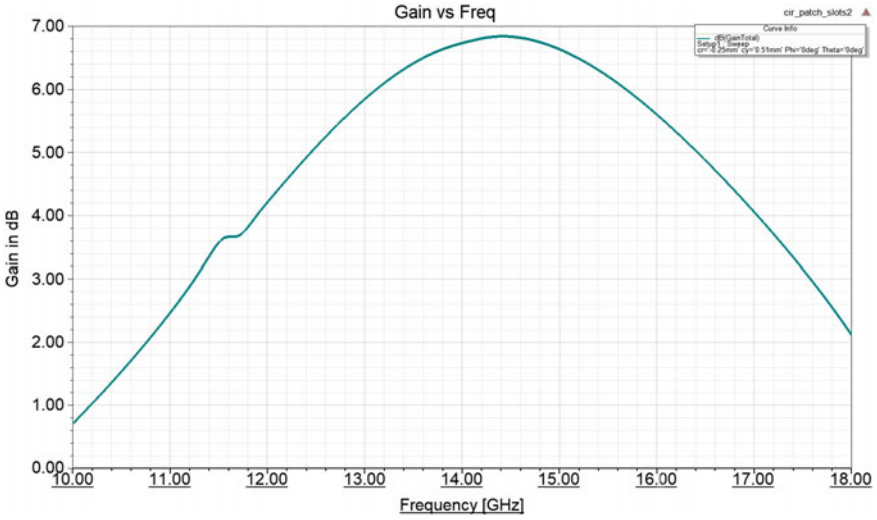

Fig. 3 Gain at a resonance frequency of 14 GHz

The bandwidth of the proposed antenna at the resonant frequency of 14 GHz is about 1.3 GHz as shown in Fig. 2, where it can be used as the Ku-band antenna. The high intensity of simulated current distribution on the antenna surface is shown in Fig. 5. The E Plane and H Plane Radiation pattern of the antenna at 14 GHz are depicted in Fig. 6, confirms the stable radiation in the operating region. The proposed antenna is very compact in size and can be used at Ku-band frequencies

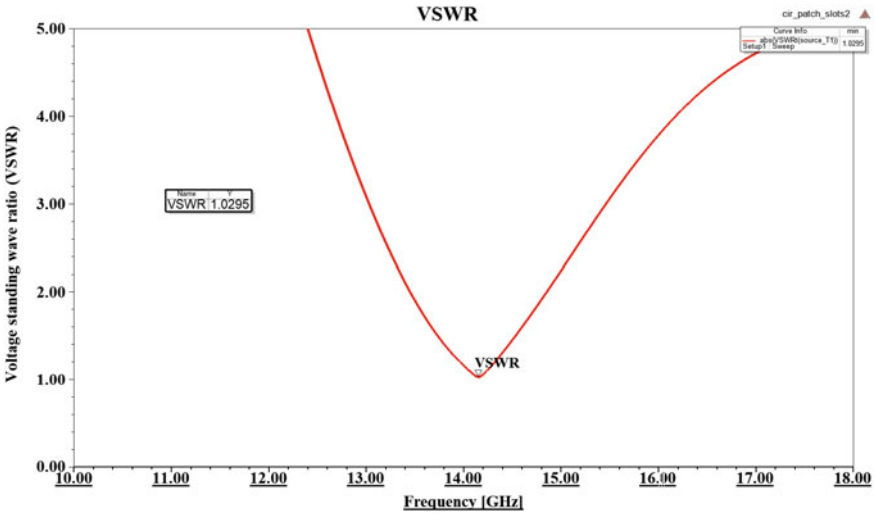

Fig. 4 VSWR at a resonance frequency of 14 GHz

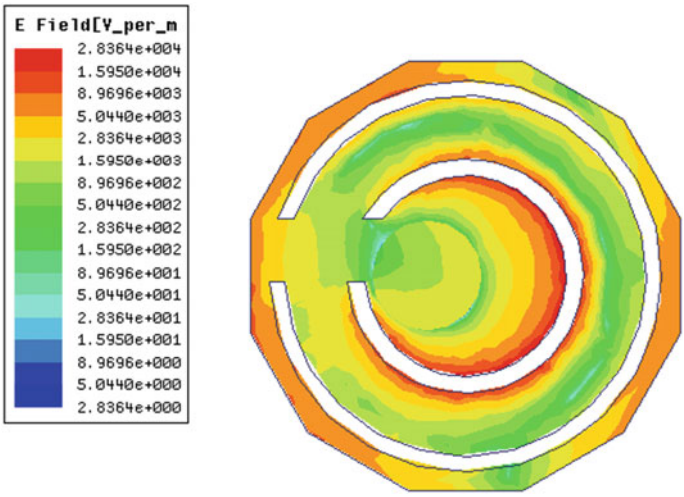

Fig. 5 Current distribution at frequency of 14 GHz

very effectively because of wide bandwidth available. The fabricated antenna is shown in Fig. 7.

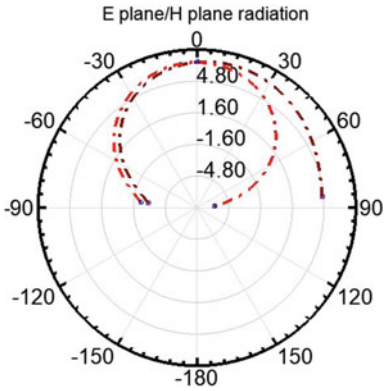

Fig. 6 Radiation pattern of the antenna at Phi=0° and Phi=90°

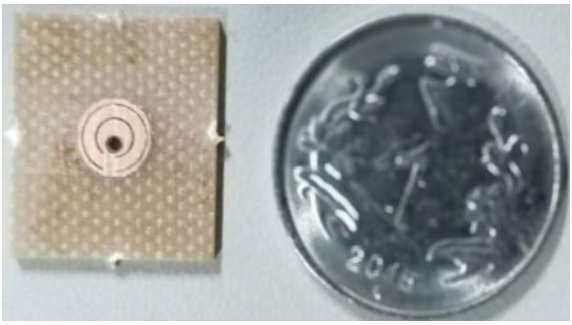

Fig. 7 Top view of the fabricated antenna

4 Conclusion

The proposed antenna has achieved an impedance bandwidth of 1.3 GHz between 13.49 and 14.81 GHz frequency it means that the antenna is wide band antenna in Ku-band. Maximum reflection coefficient is achieved at 14.10 GHz, i.e., −36.744 dB and gain is 6.86 dBi. The antenna is a planar geometry with coaxial probe feed. The antenna is designed and simulated using HFSS (High-Frequency Structural Simulator). The bandwidth changes with the change in width of the slit ring slots in the microstrip patch antenna. Ku-band is mostly used for wireless and military applications. Further, an array can be implemented to obtain high gain.

Acknowledgements This work (Major project) was funded by Science and Engineering Research Broad, the Department of Science and Technology (DST), Government of India, Sanction No. EEQ/2016/000396 and Order No. SERB/F/8020/2017-18.

References

1. Balanis C (1997) Antenna theory, analysis, and design, 2nd edn. Wiley, New York
2. Raju GSN, Microwave engineering. IK International Publishers, New Delhi
3. James JR, Hall PS (1989) Handbook of microstrip antennas. IET
4. Kouhalvandi L, Paker S, Yagci HB (2015) Ku-band slotted rectangular patch array antenna design. In: 23th IEEE signal processing and communications applications conference (SIU), pp 447–450
5. Parikh H, Pandey S, Sahoo M (2012) Design of a modified e-shaped dual band patch antenna for ku band application. In: 2012 IEEE international conference on communication systems and network technologies (CSNT), pp 49–52
6. Dubey SK, Pathak SK, Modh KK (2011) High gain multiple resonance Ku-band microstrip patch antenna. In: 2011 IEEE applied electromagnetics conference (AEMC), pp 1–3
7. Prasad PC, Chattoraj N (2013) Design of compact ku band microstrip antenna for satellite communication. In: 2013 international conferences on communications and signal processing (ICCSP), pp 196–200
8. Kumari R, Kumar M (2013) Design of multiband antennas for wireless communication. In: 2013 IEEE international conference on communication systems and network technologies (CSNT), pp 1–6

Design of Uniform Linear Practical Antenna Arrays for Ultralow

T. A. N. S. N. Varma and G. Anjaneyulu

Abstract Modern radars and communication systems demand the use of array antennas to generate patterns of high directivity with extremely low sidelobes for effective search and track applications. In this paper, the design of uniform linear arrays with ultralow sidelobe sum patterns is presented. Novel techniques like Genetic Algorithm (GA), Particle Swarm Optimization (PSO), and Simulated Annealing (SA) algorithms, are used to optimize Electromagnetic problems for design. In the process of optimal design, intensive investigations are carried out to generate the sum patterns of ultralow sidelobes from the array of dipoles and waveguides with a constraint fixed on major lobe beam width. The results show that radiation patterns from arrays of waveguides and dipoles have ultralow sidelobe levels and they are very close to the patterns from an array of isotropic elements. In addition, the sidelobe levels for an array of waveguides are better when compared to the array of dipoles.

Keywords Antenna arrays · Optimization algorithms · Genetic algorithms (GA) · Particle swarm optimizations (PSO) · Simulated annealing (SA) · Dipole array · Waveguide array · Ultralow sidelobe patterns

1 Introduction

In many long-distance applications, an antenna with high directivity is an important requirement. This can be achieved by arrays, which are nothing but placing all radiating elements in electrical and geometrical configuration [1]. Antenna arrays are widely used in communications applications, SONAR and radar applications.

T. A. N. S. N. Varma (✉) · G. Anjaneyulu
MVGR College of Engineering, Vizianagaram, Andhra Pradesh, India
e-mail: tansnvarma@gmail.com

G. Anjaneyulu
e-mail: anjaneyulu.mvgr@gmail.com

© Springer Nature Singapore Pte Ltd. 2020

V. Janyani et al. (eds.), *Optical and Wireless Technologies*,
Lecture Notes in Electrical Engineering 546,
https://doi.org/10.1007/978-981-13-6159-3_16

They are useful in high-power transmission applications with reduced power consumption and improved spectral efficiency [2]. Directive pattern is obtained from fields of the array elements that add constructively in some desired directions and add destructively in other directions to cancel each other in the remaining space. This is important to reduce the interference from the sidelobes of the antenna.

Sum Patterns are useful in radar applications for range detection of moving targets. Sum pattern consists of a narrow beam in the boresight direction with different minor lobes adjacent to the main beam. In order to have high resolution, the main beam of sum patterns should have a negligibly small width and sidelobe levels should be as small as possible [3–6].

Among the different types of antenna arrays, linear arrays are very popular in radar applications. In this paper, we propose, the use of GA, PSO, and SA methods to determine the optimum set of amplitude weights for linear practical arrays of dipoles and waveguides to generate ultralow sidelobe sum patterns.

2 Formulations

To achieve the desired characteristics nonisotropic radiating elements like dipoles, monopoles, waveguides, horns, slots, and microstrips are used [7–9]. The resultant radiation pattern depends on the array factor and element pattern. They are used depending on the application. In this paper, we considered dipoles and waveguides in antenna arrays.

2.1 Element Pattern of Dipole

Finite-length dipoles are used as simple antennas in the arrays. Dipole radiators are preferred in the low range of frequencies. The dipole is an antenna composed of simple radiating element split into two sections and fed into the split. For a half-wave dipole, the length is λ/2 and has a self-impedance of 40–70 Ω with no reactive component. A dipole of length '2L' extending from –L to L along the Z-axis as shown in Fig. 1 is considered.

The electric field strength for the radiation field is

$$E_\theta = \eta H_\phi$$
$$\text{Here } \eta = 120\pi \tag{1}$$

$$\mathrm{E}_\theta = \frac{jI}{m}\frac{60e^{-jkR}}{r}\left|\frac{\cos(kL\cos\theta) - \cos kL}{\sin\theta}\right| \tag{2}$$

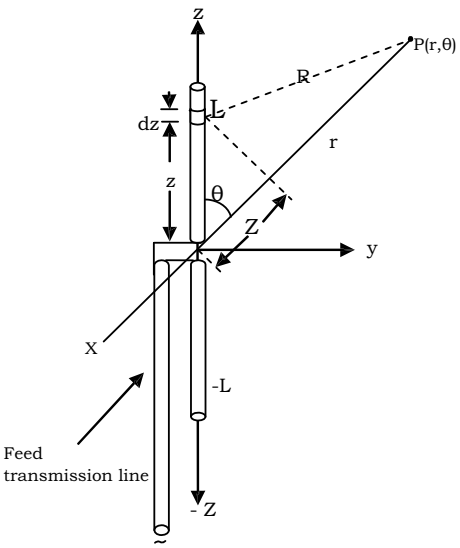

Fig. 1 Typical geometry of dipole antenna

Dipoles are basic omnidirectional antennas and are preferred in the lower range of frequencies. On the other hand, waveguide radiators are useful at microwave and millimeter wave range of frequencies [8, 10].

2.2 Element Pattern of a Rectangular Waveguide

An open-ended rectangular waveguide shown in Fig. 2. is considered. Let 'a' be the broad wall dimension and 'b' be the narrow wall dimension. The radiation can be considered due to the current distribution on the inside walls of the guide, which are associated with the fields propagated in the interior of the waveguide, along with the currents flowing from the open end upon the exterior guide surface. In all important practical cases, the guide allows propagation of only one mode (TE_{10}), called the dominant mode.

$$E_\theta = \left[\frac{\sin\left(\frac{a\pi}{\lambda}\sin\theta\right)}{\left(\frac{a\pi}{\lambda}\sin\theta\right)^2}\right] \tag{3}$$

$$E_\phi = \left[\frac{\cos\left(\frac{b\pi}{\lambda}\sin\theta\right)}{\left(\frac{b\pi}{\lambda}\sin\theta\right)^2 - \left(\frac{\pi}{2}\right)^2}\right] \tag{4}$$

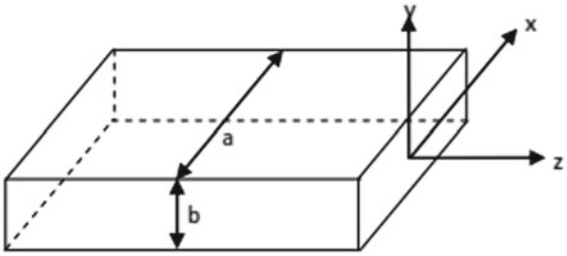

Fig. 2 Geometry of open-ended rectangular waveguide

The E-plane pattern is the pattern due to the uniformly illuminated slit of width 'a'. The pattern in the H-plane is due to slit of width 'b' across the guide in the X-direction over which the illumination is distributed sinusoidally.

2.3 Sum Patterns from an Arrays of Waveguides and Dipoles

If N radiating elements are placed along Z-axis, shown in Fig. 3.

The resultant field of a linear array of N elements shown in the above figure is given by

$$E(\theta, \phi) = \sum_{n=1}^{N} E_n(\theta, \phi) = F(\theta, \phi) \sum_{n=1}^{N} A(x_n) e^{j\left(\frac{2\pi}{\lambda} x_n \cos\theta + \phi(x_n)\right)} \tag{5}$$

where the amplitude distribution $A(x_n)$ is obtained by optimizing excitation coefficients using GA, PSO, and SA methods.

The summation term in the above expression is nothing but the array factor. The term $F(\theta, \phi)$ varies from element to element. For the array of present interest, we have

Fig. 3 Linear array

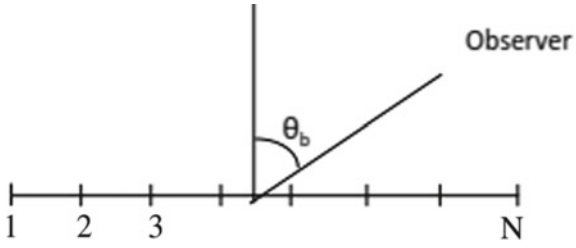

$$E_s(\theta_b) = F(\theta_b) \sum_{n=1}^{N} A(x_n) e^{j\left(\frac{2\pi}{\lambda} x_n \sin\theta_b + \phi(x_n)\right)} \tag{6}$$

where θ_b is the angle of the line of observer with boresight.

3 Results

The expressions (2) and (4) are considered for computation of element patterns of dipoles and waveguides.

Using the optimized amplitude excitation coefficients proposed in expressions (5) and (6), the radiation patterns are numerically computed for the arrays of dipoles and waveguides.

The resultant radiation patterns of arrays of dipoles of half wavelength and also arrays of open ended rectangular waveguide radiators for b = 1.016 cm, a = 2.286 cm and λ = 3.2 cm are numerically computed.

The computed sum and difference patterns for linear array of dipoles and linear array of waveguides for the number of elements N = 30, 60 and 90, are presented in Figs. 4, 5, 6, 7, 8, 9, 10, 11, and 12 and the amplitude excitations used for computation obtained by optimization process are presented in Figs. 13, 14, and 15 for N = 30 elements.

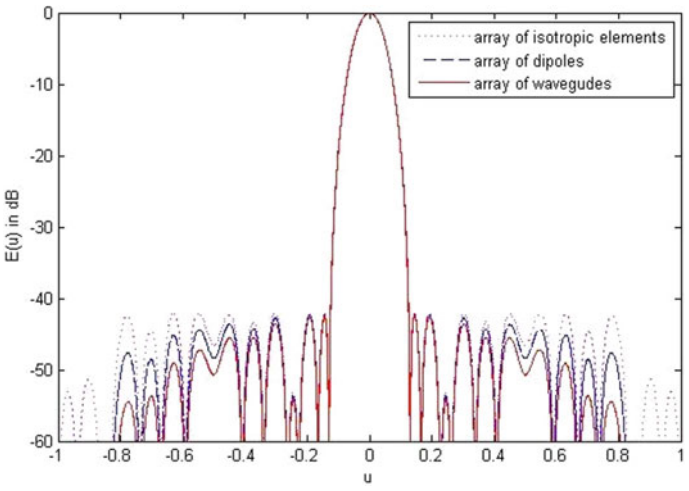

Fig. 4 GA-optimized sum pattern for the linear array of elements N = 30

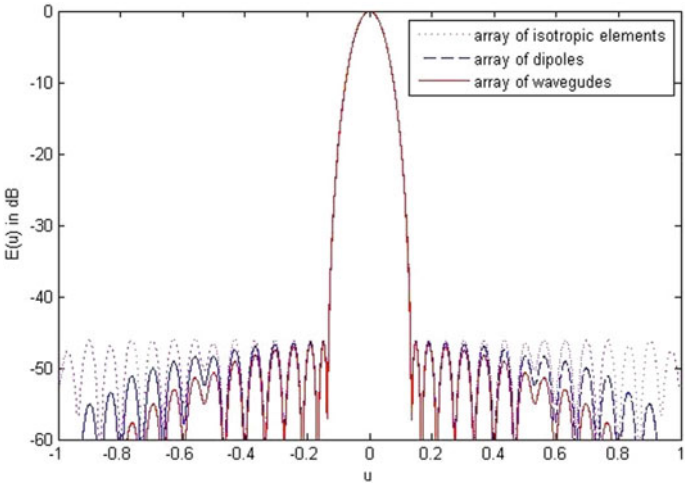

Fig. 5 PSO-optimized sum pattern for the linear array of elements N = 30

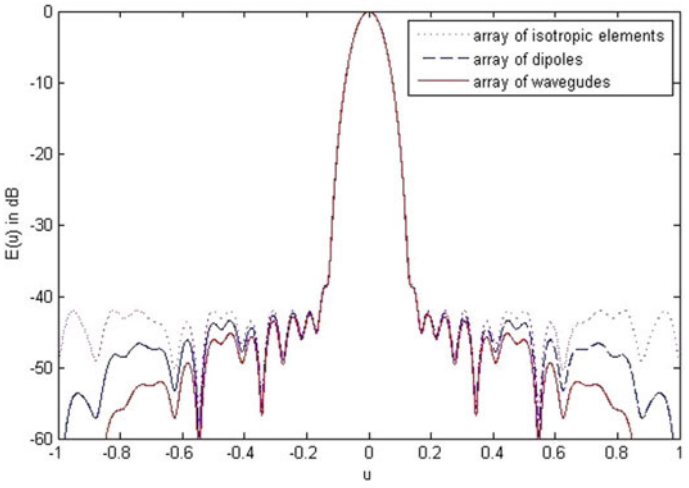

Fig. 6 SA-optimized sum pattern for the linear array of elements N = 30

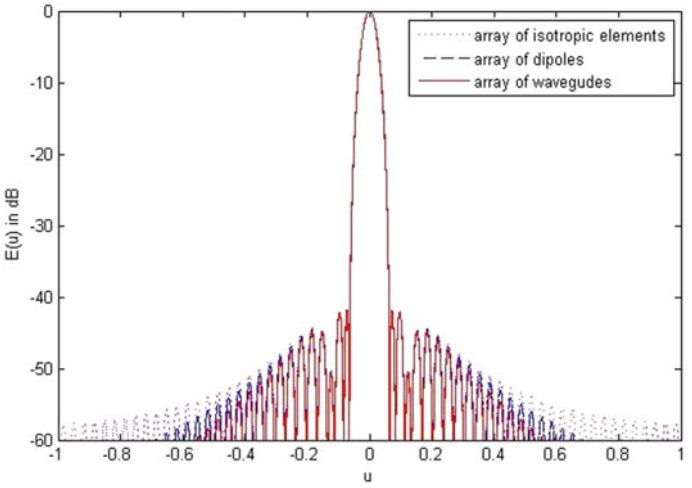

Fig. 7 GA-optimized sum pattern for the linear array of elements N = 60

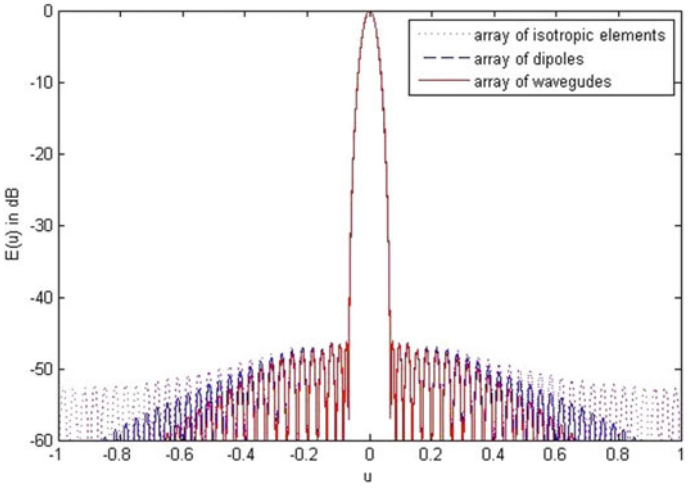

Fig. 8 PSO-optimized sum pattern for the linear array of elements N = 60

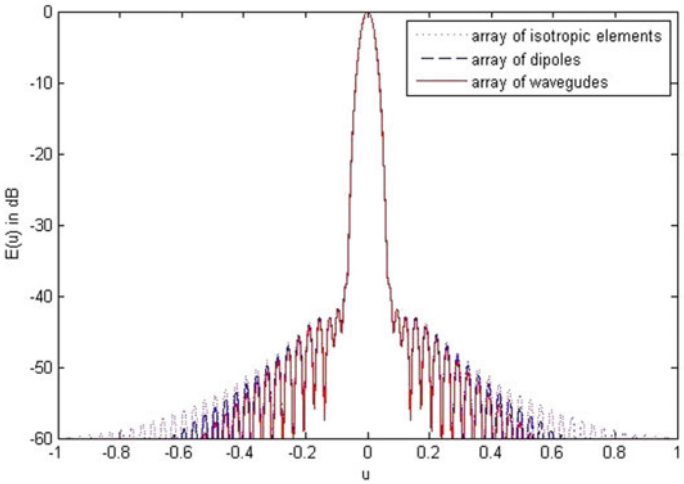

Fig. 9 SA-optimized sum pattern for the linear array of elements N = 60

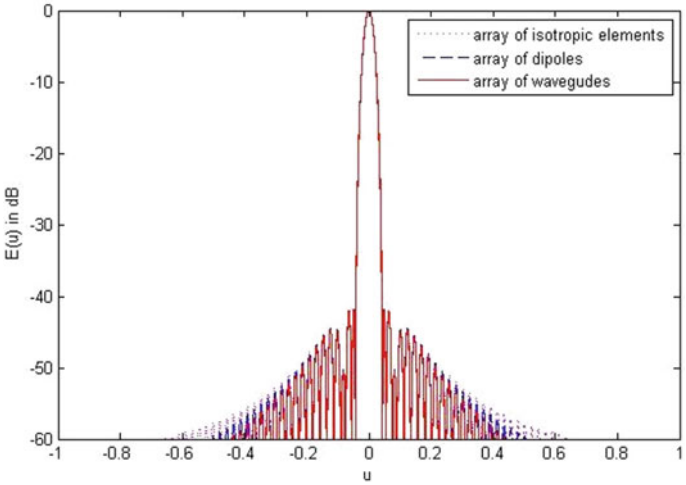

Fig. 10 GA-optimized sum pattern for the linear array of elements N = 90

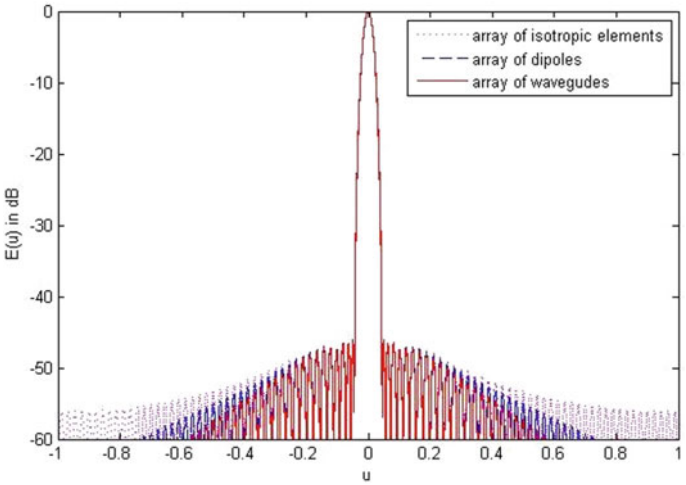

Fig. 11 PSO-optimized sum pattern for the linear array of elements N = 90

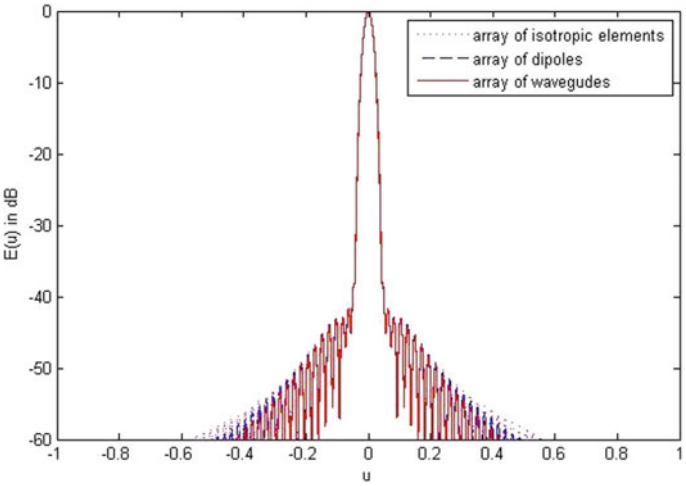

Fig. 12 SA-optimized sum pattern for the linear array of elements N = 90

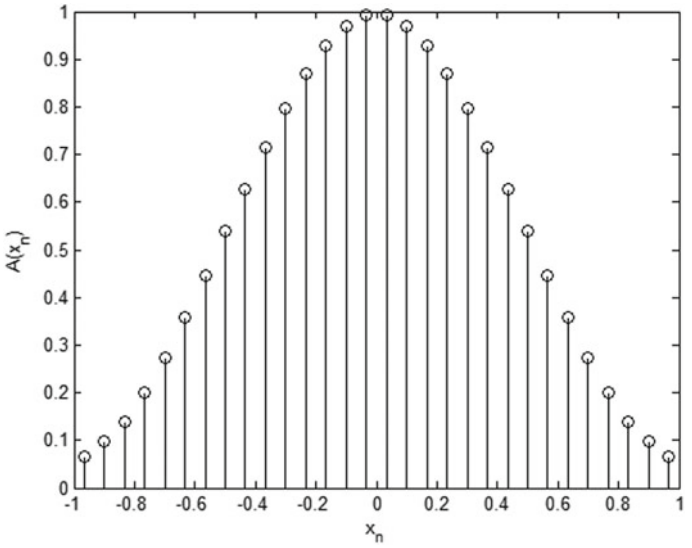

Fig. 13 Amplitude excitation coefficients obtained by GA method for N = 30 element array

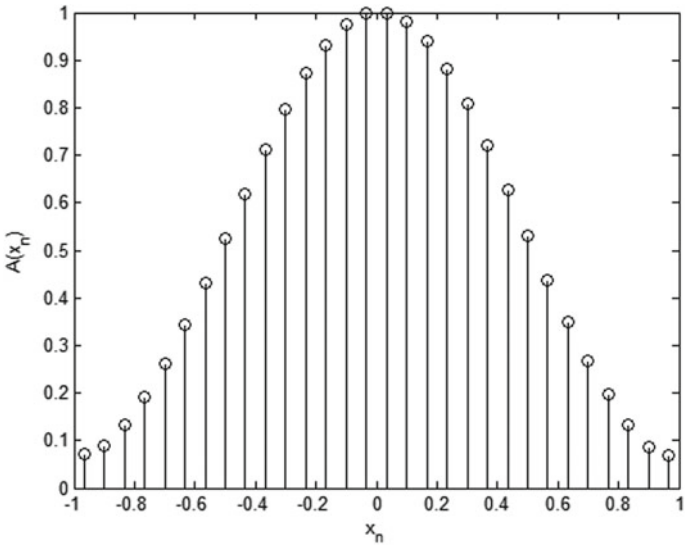

Fig. 14 Amplitude excitation coefficients obtained by PSO method for N = 30 element array

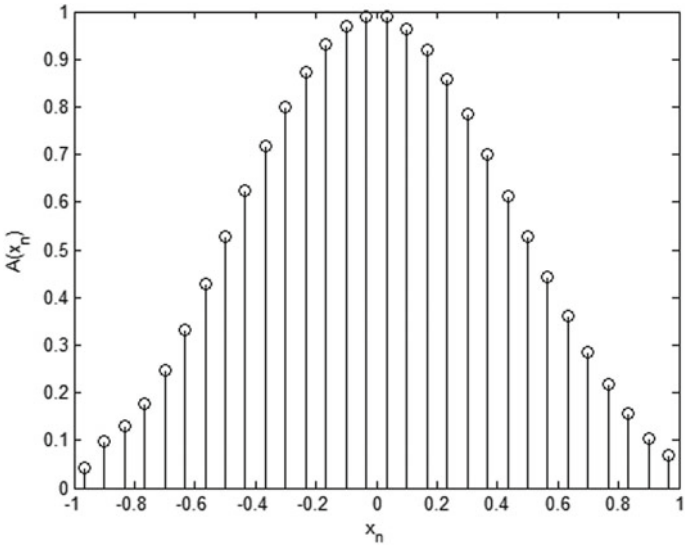

Fig. 15 Amplitude excitation coefficients obtained by SA method for N = 30 element array

4 Conclusions

The radiation patterns from arrays of dipoles and waveguides using proposed new amplitude excitation coefficients optimized by GA, PSO, and SA methods are found to yield useful results. It is evident from the results, radiation patterns from arrays of dipoles and waveguides have ultralow sidelobe levels and they are very close to the patterns from arrays of isotropic elements. Interestingly, the null–to-null beam width is well in control and sidelobes are monotonically decreasing towards the end in the visible region. Also realized difference patterns have a deep null in the direction of boresight. It is evident from the resultant patterns, the sidelobe levels of waveguide arrays are less compared to sidelobe levels of dipole arrays and isotropic arrays. The deviation in the sidelobe levels is found to be minimum in isotropic radiators and the array of practical elements. These types of patterns are extremely useful for a wide range of scanning, direction finding, and IFF radar applications.

References

1. Raju GSN (2005) Antennas and wave propagation. Pearson Education
2. Haupt RL (2010) Antenna arrays: a computational approach. Wiley-Blackwell
3. Murthy PK, Kumar A (1976) Synthesis of linear arrays. IEEE Trans Antennas Propag 24:865–870
4. Rao KS, Karlsson I (1987) Low sidelobe design considerations of large linear array antennas with contiguous sub arrays. IEEE Trans Antennas Propag 35(4):361–366

5. Lundy M, Mees A (1986) Convergence of an annealing algorithm. Math Prog 34:111–124
6. Mandal D, Ghosal SK, Das S, Bhattacharjee S, Bhattacharjee AK (2010) Improvement of radiation pattern for linear antenna arrays using genetic algorithm. In: International conference on recent trends in information, telecommunications and computing, 12–13 March 2010, pp 126–129
7. Varma TANSN, Raju GSN (2014) Investigations on generation of ultra low sidelobe patterns. Int J Eng Sci Technol 6(6)
8. Varma TANSN, Raju GSN (2012) Radiation patterns for tracking applications. In: National conference on advances in communication, navigation and computer networks (ACNCN'12), Visakhapatnam, March 2012
9. Varma TANSN, Raju GSN (2014) Investigations on generation of very low sidelobe difference patterns for EMC applications: IOSR J Electron Commun Eng 6(3)
10. Khodier MM, Christodoulon GG (2005) Linear array geometry synthesis with minimum sidelobe level and null control using particle swarm optimization. IEEE Trans Antennas Propag 53(8):2674–2679

On Maximizing Blind Rendezvous Probability in Cognitive Radio Ad Hoc Networks

Aishwarya Sagar Anand Ukey and Meenu Chawla

Abstract Establishment of wireless communication links among the cognitive radio (CR) users via rendezvous on commonly available channels is the crucial process in cognitive radio ad hoc networks. Extant rendezvous methods utilize the channel hopping (CH) technique (also referred as blind rendezvous) and generate the CH sequence on the top of potential licensed channels and employ random replace operation to contrive the CH sequence for individual CR user. However, incorporation of random replace operation may exhibit poorer performance with the increase in the number of available channels owing to the severe decrease in the probability of replacing an unavailable channel with the same available channel by two or more CR users. In this paper, we present a channel-ranking rendezvous procedure that ranks available channels based on the received SINR and constructs the CH sequence by replacing the unavailable channels with higher ranked available channels. We verify the superiority of channel-ranking procedure through extensive simulation, and the simulation results confirm that utilization of channel-ranking mechanism severely maximizes the rendezvous occurrence probability as compared with the random replace operation.

Keywords Cognitive radio ad hoc network · Blind rendezvous · Rendezvous probability · Channel ranking

1 Introduction

Cognitive radio network (CRN) is an emerging wireless paradigm that alleviates the scarcity and underutilization of spectrum through efficient sharing of licensed spectrum among the primary users (PUs) and cognitive radio (CR) users. CRN utilizes

A. S. A. Ukey (✉) · M. Chawla
Department of Computer Science and Engineering, Maulana Azad National Institute of Technology, Bhopal 462003, India
e-mail: aishwaryaukey@gmail.com

M. Chawla
e-mail: chawlam@manit.ac.in

© Springer Nature Singapore Pte Ltd. 2020

V. Janyani et al. (eds.), *Optical and Wireless Technologies*,
Lecture Notes in Electrical Engineering 546,
https://doi.org/10.1007/978-981-13-6159-3_17

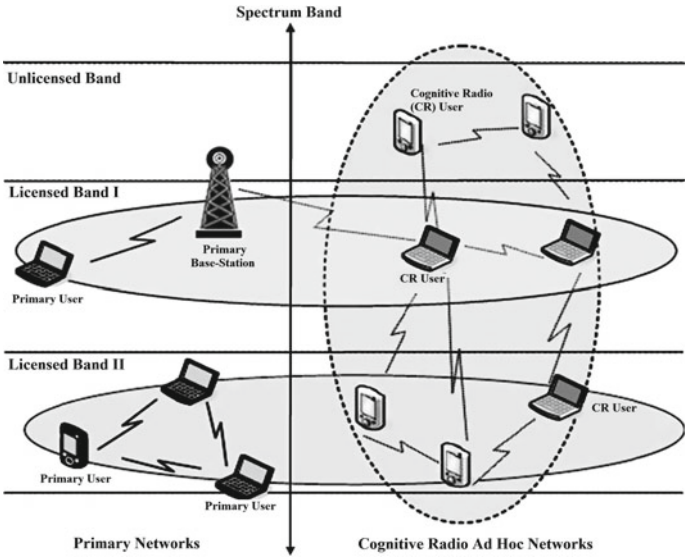

Fig. 1 Cognitive radio ad hoc networks

dynamic spectrum access technology and allows CR users to opportunistically access the free portions of the licensed spectrum (also referred as spectral holes or white spaces) allotted to the PUs. In CRNs, PUs are given higher precedence of using the allotted licensed bands. CR users can opportunistically access to the free portion of licensed bands (or free available channels) that are currently not in use by the PUs, and vacate or switch to some other free available channels on PUs reappearance [1]. Cognitive radio ad hoc networks (CRAHNs) are a specialized type of CRNs (shown in Fig. 1) consisting of mobile CR users that are self-capable to take spectral decisions on the basis of locally sensed surrounding information [2]. In CRAHNs, CR users are required to establish the communication links with potential neighbors prior to data communication. Traditionally, periodic beaconing of control packets over the same predefined channel is employed for the establishment of communication links. However, the periodic beaconing mechanism may not be feasible for establishing the communication links due to the nonavailability of any channel globally available to CR users at all time. This necessitates CR users to figure out commonly available channels in order to establish the wireless communication links [3]. The process of CR users to meet on commonly available channels and to establish communication links is referred to as rendezvous process [4–6]. Rendezvous is the fundamental and crucial operation in the formation of CRAHN and no communication is possible without rendezvous of CR users. However, non-awareness of adjacent CR users and prior network-related information before rendezvous make the rendezvous process extremely challenging. Nonavailability of CR base station, the mobility of CR users, and dynamic environment of CRAHNs further convolute the rendezvous process [7].

A number of algorithms have been devised in the literature to achieve rendezvous among CR users in CRAHNs. Extant rendezvous algorithms usually employ the channel hopping (CH) (also referred as blind rendezvous) technique and construct a global CH sequence on the top of total number of potential licensed channels for all CR users. However, following the same global CH sequence by all CR users may not be an efficient way to accomplish the rendezvous process since each CR user may have diverse availability of potential licensed channels. Also, hopping on any of the unavailable channels not only increases the rendezvous time but also wastes CR nodes energy. To cope with such problems, blind rendezvous algorithms generally employ the random replace operation that replaces the unavailable channels with some random available channels. Random replace operation may achieve the rendezvous if CR users have lesser number of available channels. However, the probability of rendezvous decreases with the increase in the number of available channels. For example, if two CR users have two channels available out of 10 licensed channels than the rendezvous probability via random replace operation which is 1/4 and if CR users have more than two available channels (i.e., 5), then the probability decreases to 1/25. Moreover, if CR users have a large number of potential licensed channels (i.e., 100), then there is a significant decrease in the rendezvous probability via random replace operation. In other words, utilization of random replace operation does not have a significant impact to accomplish the rendezvous process particularly when CR users have a larger number of available as well as potential licensed channels.

In this paper, we attempt to maximize the rendezvous probability by the aid of channel-ranking rendezvous procedure that constructs the CH sequence on top of total number of potential licensed channels and replaces the unavailable channels with higher ranked available channels. Naturally, the likelihood of replacement of an unavailable channel with the same higher ranked channel by two or more CR users is very high as compared to random replacement of an unavailable channel with an available channel. Hence, incorporation of channel-ranking mechanism can significantly improve the performance of blind rendezvous phenomena. Contributions of the work are summarized as follows:

- We focus on the blind rendezvous process and analyze that employment of random replace operation to contrive the CH sequence for individual CR user may not work effectively, particularly, if CR users have a larger number of available channels.
- We present a channel-ranking rendezvous procedure and show that utilization of channel-ranking mechanism can efficiently maximize the rendezvous probability as compared to random replace operation.
- To verify the effectiveness of channel-ranking mechanism, we conduct a number of simulation experiments, and the simulation results confirmed the superiority of channel-ranking mechanism over random replace operation in terms of the rendezvous probability.

Rest of the paper consists of five sections. Section 2 briefly reviews prominent blind rendezvous algorithms. Section 3 describes the system model and details of

channel-ranking rendezvous procedure. Section 4 includes experimental simulations and performance comparison of channel-ranking rendezvous procedure, and at the last, we conclude the paper.

2 Related Work

In this section, we briefly review some state-of-the-art blind rendezvous algorithms presented to achieve the rendezvous among the CR users in short bounded time.

JS algorithm [8] is one of the most prominent blind rendezvous methods that construct a global CH sequence on the top of potential licensed channels. JS executes in rounds, each consisting of a jump pattern of $2P$ time slots and a stay pattern of P time slots, where P is the smallest prime number greater than the number of potential channels M. CR users hop on potential channels in the jump pattern and wait on a specific channel in stay pattern. To optimize the rendezvous performance, JS employs random replace operation that randomly replaces the unavailable channels with available channels. EJS algorithm [9] is an improved version of JS where jump pattern lasts for $3P$ time slots during each round. Similar to JS, HS algorithm [10] also generates the CH sequence in rounds, however, the jump pattern and subsequent stay pattern in HS last for $2P^2$ and $2P$ time slots, respectively. DRDS algorithm [11] exploits difference set theory and constructs a common CH sequence (CCHS) based on the construction of disjoint relaxed difference set. CR users follow the CCHS and utilize random replace operation to contrive the CH sequences. AHW algorithm [12] generates the CH sequence by the aid of two different sequences, namely, hop sequence and wait sequence, where CR users hop on potential channels and wait on a particular channel. CR users exploit their unique identity to construct the bit string and generate the alternate hop and wait sequences according to the respective bits of the bit string. AHW algorithm also employs the random replace operation to replace unavailable channels with available channels. EAHW algorithm [13] is an enhanced version of AHW, where CR users generate alternate CH sequences by exploiting the respective bits of the MAC address.

DSCR algorithm [14] exploits disjoint set cover property and generates the CH sequence with variant permutations of fixed and rotating elements referred to as static and dynamic columns. CR users hop as per the fixed and rotated elements and replace the unavailable channels with randomly selected available channels. Similar to DSCR, ADFC-CH algorithm [15] constructs disjoint finite cover in terms of network locks and generates the CH sequence where CR users have options to control the rendezvous performance via adjusting the value of the lock. SASJ algorithm [16] generates CH sequence in rounds, each consisting of one stay pattern and two jump patterns, where CR users jump on potential channels in the jump pattern and stay on the highest ranked channel in the stay pattern. However, simply staying on the same channel during the entire stay patterns may severely increase the load on the rendezvous channel due to simultaneous transmissions of control packets by multi-

ple CR users at the same time. This over-congestions the rendezvous channel and degrades the network performance.

From the above discussion, it is clear that blind rendezvous algorithms either utilize random replace operation or channel-ranking mechanism to attain the rendezvous among the CR users. However, random replace operation exhibits poorer rendezvous performance, particularly, if CR users have a large number of available channels, whereas channel-ranking mechanism makes the rendezvous channel over congested and degrades the network performance. Thus, a trade-off should be maintained between the rendezvous performance and the load on rendezvous channel to ensure an optimized rendezvous and network performance.

3 Proposed Work

3.1 System Model

In the work, we consider a CRAHN consisting of $N(N \geq 2)$ CR users that coexist with several PUs in the same geographical area. Potential licensed spectrum is partitioned into $M(M \geq 1)$ nonoverlapping licensed channels that are uniquely indexed as $C = \{c_1, c_2, \ldots, c_M\}$, where each c_i has the same bandwidth $B_i = C/M$. CR users are equipped with a half-duplex cognitive radio and acquire idle or free available channels through periodic spectrum sensing. Network time is split into smaller slots of equal size and the length of each time slot is set to $2t$ (as in IEEE 802.22 [17]), where t refers to the time that a CR user takes to establish the communication link. During each time slot, CR users access an available channel and attempt to rendezvous with potential CR users. Rendezvous is said to be achieved if CR users hop on the commonly available channel at the same time irrespective of time lag differences among the CR users. Considering the aforementioned scenario, the objective of the proposed work is to maximize the rendezvous occurrence probability in order to improve the performance of blind rendezvous phenomena.

3.2 Channel-Ranking Rendezvous Procedure

In this subsection, we present a channel-ranking rendezvous procedure that efficiently maximizes the rendezvous probability of blind rendezvous phenomena. The fundamental concept of channel-ranking procedure lies on the construction of a global CH sequence and replacement of unavailable channels with higher ranked channels to contrive individual CH sequence for each CR user. A number of channel-ranking mechanisms have been devised to rank the channels in static or quasi-static multichannel wireless networks. Conventional channel-ranking mechanisms utilize signal-to-noise ratio (SNR), bandwidth, delay, channel quality estimation index, bit

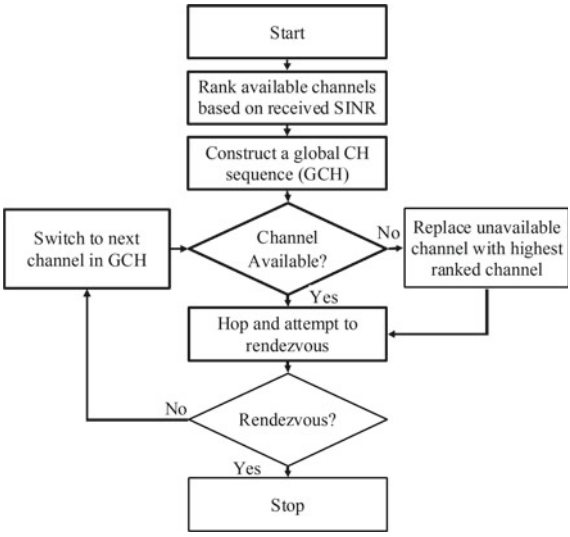

Fig. 2 Flowchart of channel-ranking rendezvous procedure

error ratio, or outage probability as the major channel-ranking parameters [18, 19]. In CRAHNs, CR users have opportunistic access to licensed channels on a noninterference basis. Also, the availability of free available channels varies over time. In such time-varying environment of CRAHNs, incorporation of conventional channel-ranking parameters may not be feasible to efficiently rank available channels. In this work, we exploit the channel-ranking mechanism presented by Ohize and Dlodlo [20] to rank available channels of CR users due to its applicability, suitability, and wide adaptability in the dynamic environment of CRAHNs.

The description of the channel-ranking rendezvous procedure is as follows. The procedure generates a global CH sequence on the top of total number of potential channels, and incorporates a channel-ranking mechanism that ranks available channels and assigns more priority to higher ranked available channels. The flowchart of the channel-ranking rendezvous procedure is shown in Fig. 2. At first, CR users acquire the list of free available channels through periodic spectrum sensing. Next, CR users calculate the SINR as per sensed surrounding radio environment and rank their available channels accordingly. CR users calculate the received SINR on each available channel as follows [20]:

$$SINR_{m,n} = \frac{P^{s}_{m,n} \times g^{s}_{m,n}}{\sum_{n'=1}^{n} \left(P^{s'}_{m,n'} \times g^{s'}_{m,n'}\right) + P_{m,p} \times g^{p}_{m,n} + N_0 \times B_i}$$

where $P_{m,p}$, $P^{s}_{m,n}$, $P^{s'}_{m,n'}$ are the transmitting powers of primary base station, serving CR user and the interfering node n' on channel m. $g^{s}_{m,n}$, $g^{s'}_{m,n'}$, and $g^{p}_{m,n}$ are the channel gains for the serving CR user, the interference CR user and the primary base station on the channel m. After ranking of available channels, CR users utilize an existing

blind rendezvous algorithm (such as JS [8]) and generate a global CH sequence on the top of total potential licensed channels. However, instead of employing the random replace operation, each CR user utilizes the channel-ranking procedure and replaces all unavailable channels with the higher ranked available channel to contrive their CH sequence. Since temporal and geometrically closed CR users share the similar surrounding radio environment, the likelihood of the CR users to have the same channel-ranking table is very high. Thus, if CR users hop to the higher ranked channel, it is highly probable that CR users select the same available channel as the higher ranked channel and hop accordingly. This, thereby, severely increases the rendezvous occurrence probability as compared to the random replace operation.

4 Simulation and Result Analysis

In this section, we investigate the performance of channel-ranking mechanism through extensive simulations. We built the CRAHN environment by defining a number of PUs, PUs' base station and CR users along with their network attributes such as transmission power, transmission range, channel bandwidth, etc. We implement channel-ranking mechanism on the top of JS [8], DRDS [11], and DSCR [14] algorithms in such a manner that instead of performing the random replacement operation, CR users rank their available channels and replace the unavailable channels with the higher ranked available channel. We refer the modified JS, DRDS, and DSCR algorithms as JS-CR, DRDS-CR, and DSCR-CR, respectively. Next, we perform a number of simulations and compare the performance of the JS-CR, DRDS-CR, and DSCR-CR with originally presented JS, DRDS, and DSCR algorithm under the similar CRAHNs environment. We evaluate the performance of each algorithm in terms of MTTR and ATTR which refers to maximum TTR and average TTR, respectively. All simulations are separately executed and averaged over 10,000 iterations to derive the most optimal value of MTTR and ATTR. We define the simulation parameters as follows, M refers to the number of potential licensed channels, m and n refer to the number of available channels of two CR users (i.e., A and B), and G refers to the number of commonly available channels between the CR users. Simulation experiments are primarily conducted with increasing the number of potential channels, available channels, and commonly available channels.

A. Increase in Potential Channels

In the following simulation, we set $m = n = G = M/2$, and calculate the MTTR and ATTR with varying M. Figure 3a, b shows that MTTR and ATTR increase with varying M. It is due to the dependency of each algorithm on M. Thus, when the number of potential licensed channels is comparatively large then a longer CH sequence is generated by the CR users. This, thereby, increases the MTTR and ATTR. However, the variations of JS-CR, DRDS-CR, and DSCR-CR are much lesser than the JS, DRDS, and DSCR since incorporation of channel-ranking mechanism in JS-CR,

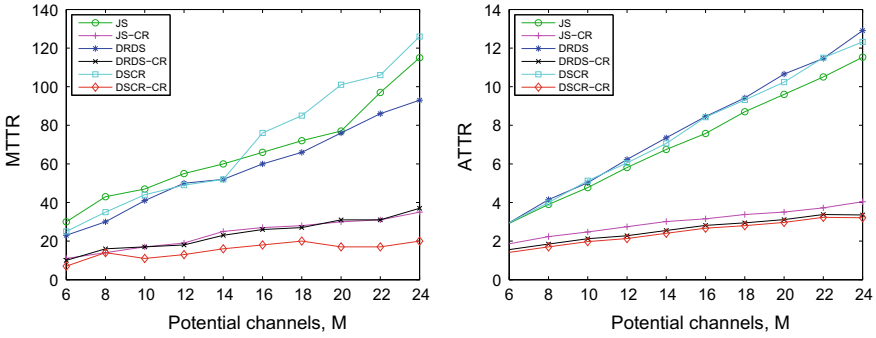

(a) $MTTR$ variation (b) $ATTR$ variation

Fig. 3 Performance comparison with varying the potential channels

DRDS-CR, and DSCR-CR severely maximizes the rendezvous probability.

B. Increase in Available Channels

In the following simulation, we set $M = 25$, $G = 5$, and calculate the MTTR and ATTR with varying m and n, where $m = n$. Figure 4a, b reveals that MTTR and ATTR of JS, DRDS, and DSCR increase with varying the number of available channels since each algorithm constructs the CH sequence on the top of M and randomly replaces unavailable channels with some available channels. Thus, when m and n are lesser, then the probability of random replacement of an unavailable channel with the same available channel is comparatively high. However, the probability of random replacement decreases with increasing m and n, which thereby increases the MTTR and ATTR. On the contrary, JS-CR, DRDS-CR, and DSCR-CR have a lesser impact on MTTR and ATTR with varying m and n. It is due to the increase in the

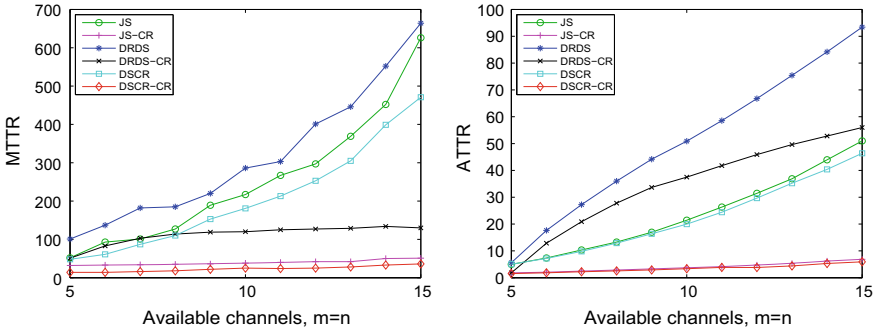

(a) $MTTR$ variation (b) $ATTR$ variation

Fig. 4 Performance comparison with varying the available channels

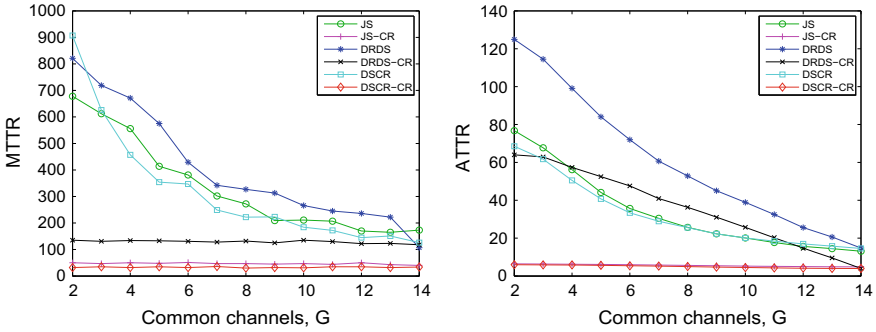

(a) $MTTR$ variation **(b)** $ATTR$ variation

Fig. 5 Performance comparison with varying the common channels

rendezvous probability via the channel-ranking procedure as compared to random replace operation.

C. Increase in Common Channels

In the following simulation, we set $M = 25$, $m = n = 14$, and calculate the MTTR and ATTR with varying G. Figure 5a, b reveals that MTTR and ATTR decrease with increase in the number of common channels since the chance of CR users to rendezvous increases with increasing G. However, JS-CR, DRDS-CR, and DSCR-CR show performance improvement over JS, DRDS, and DSCR owing to the better probability of CR users to replace unavailable channels with the same available channels via the channel-ranking procedure.

From the aforementioned simulations, it is clear that incorporation of channel-ranking mechanism can efficiently maximize the rendezvous probability which, in turn, increases the network stability and improves the network performance.

5 Conclusion

In this paper, we focused on the rendezvous process through which CR users establish necessary wireless links prior to data communication. We explored blind rendezvous solutions and found that random replacement of unavailable channels with available channels show dropped performance when CR users have a larger number of available channels. To maximize the rendezvous probability, we presented a channel-ranking mechanism where CR users rank their available channels as per surrounding radio environment and hop to higher ranked channel whenever an unavailable channel is

encountered while following the CH sequence. We verified the superiority of channel-ranking mechanism over random replace operation through extensive simulations. Future works include design of a novel channel-ranking-based blind rendezvous procedure that can achieve the rendezvous among the CR users in short bound time.

References

1. Akyildiz IF, Lee WY, Vuran MC, Mohanty S (2006) Next generation/dynamic spectrum access/cognitive radio wireless networks: a survey. Comput. Netw. 50(13):2127–2159
2. Akyildiz IF, Lee WY, Chowdhury KR (2009) CRAHNs: cognitive radio ad hoc networks. Ad Hoc Netw. 7(5):810–836
3. Chawla M, Ukey ASA, Reshma P (2017) Comprehensive asynchronous symmetric rendezvous algorithm in cognitive radio networks. Sadhana 42(11):1825–1834
4. Liu H, Lin Z, Chu X, Leung YW (2012) Taxonomy and challenges of rendezvous algorithms in cognitive radio networks. In: 2012 international conference on computing, networking and communications (ICNC). IEEE Press, Maui, USA, pp 645–649
5. Joshi GP, Nam SY, Kim SW (2014) Rendezvous issues in ad hoc cognitive radio networks. KSII Trans. Internet Inform. Syst. 8(11):3655–3673
6. Htike Z, Hong CS, Lee S (2013) The life cycle of the rendezvous problem of cognitive radio ad hoc networks: a survey. J. Comput. Sci. Eng. 7(2):81–88
7. Ukey ASA, Chawla M (2018) Rendezvous in cognitive radio ad hoc networks: a survey. Int. J. Ad Hoc Ubiquitous Comput. 29(4):233–254
8. Liu H, Lin Z, Chu X, Leung YW (2012) Jump-stay rendezvous algorithm for cognitive radio networks. IEEE Trans. Parallel Distrib. Syst. 23(10):1867–1881
9. Lin Z, Liu H, Chu X, Leung YW (2013) Enhanced jump-stay rendezvous algorithm for cognitive radio networks. IEEE Commun. Lett. 17(9):1742–1745
10. Gandhi R, Wang CC, Hu YC (2012) Fast rendezvous for multiple clients for cognitive radios using coordinated channel hopping. In: 9th annual IEEE communications society conference on sensor, mesh and ad hoc communications and networks. IEEE Press, Seoul, South Korea, pp 434–442
11. Gu Z, Hua QS, Wang Y, Lau FC (2013) Nearly optimal asynchronous blind rendezvous algorithm for cognitive radio networks. IN: 2013 international conference on sensing, communications and networking (SECON). IEEE Press, New Orleans, LA, pp 371–379
12. Chuang I, Wu HY, Lee KR, Kuo YH (2013) Alternate hop-and-wait channel rendezvous method for cognitive radio networks. In: Proceedings IEEE INFOCOM'13. IEEE Press, Seoul, South Korea, pp 746–754
13. Chuang IH, Wu HY, Kuo YH (2014) A fast blind rendezvous method by alternate hop-and-wait channel hopping in cognitive radio networks. IEEE Trans. Mobile Comput. 13(10):2171–2184
14. Yang B, Zheng M, Liang W (2016) A time-efficient rendezvous algorithm with a full rendezvous degree for heterogeneous cognitive radio networks. In: 35th annual IEEE international conference on computer communications. IEEE Press, San Francisco, CA, pp. 1–9
15. Qi X, Gao R, Liu L, Yang W (2017) ADFC-CH: adjusted disjoint finite cover rendezvous algorithms for cognitive radio networks. Wirel. Netw. 24(7):2621–2630
16. Ohize H, Dlodlo M (2016) Ant colony system based control channel selection scheme for guaranteed rendezvous in cognitive radio ad-hoc network. In: 27th annual international symposium on personal, indoor, and mobile radio communications (PIMRC). IEEE Press, Valencia, Spain, pp 1–7
17. Stevenson CR, Chouinard G, Lei Z, Hu W, Shellhammer SJ, Caldwell W (2009) IEEE 802.22: the first cognitive radio wireless regional area network standard. IEEE Commun. Mag. 47(1):130–138

18. Huang XL, Zhai YB, Wu J, Xu Y, Wu X, Wu X (2014) Channel quality ranking in cognitive radio networks. In: 10th international conference on wireless communications, networking and mobile computing. IEEE Press, Beijing, China, pp 191–194
19. Elderini T, Kaabouch N, Reyes H (2017) Channel quality estimation metrics in cognitive radio networks: a survey. IET Commun. 11(8):1173–1179
20. Ohize H, Dlodlo M (2017) A channel hopping algorithm for guaranteed rendezvous in cognitive radio ad hoc networks using swarm intelligence. Wirel. Pers. Commun. 96(1):879–893

Effects of Core Count and Layout on the Bending-Radius-Dependent Crosstalk Variations in Heterogeneous and Trench-Assisted Heterogeneous Multicore Fiber

Umar Farooque and Rakesh Ranjan

Abstract Effects of increasing core count in limited cladding diameter and cladding thickness constraints and their arrangements, i.e., core layouts on the crosstalk variation in heterogeneous and trench-assisted (TA) heterogeneous MCFs are investigated using the expression of crosstalk derived from the coupled mode equations and the finite element method (FEM) based FemSIM software. Only two kinds of heterogeneous cores having different core radius and refractive index are used in the present analysis. For 12-Core TA MCF, approx. 35 dB of crosstalk level can be optimized by proper selection of core layout, and whereas for high core count such as 24-Core and 30-Core TA MCFs, this value reduces to 30 dB and 20 dB, respectively, due to the decrease in the core pitch and the increase in the number of surrounding cores. This result shows that core count and layout have a significant impact on the crosstalk variations in MCFs.

Keywords Heterogeneous · Trench-assisted · Multicore fiber · Crosstalk · Core pitch · Core layout · Core count · Bending radius

1 Introduction

Space-division multiplexing (SDM) based multicore fiber (MCF) technology has been proposed as the potential candidate to meet the demand of high transmission capacity of the optical transmission link [1]. Multicore fiber consists of multiple cores within the fixed cladding region of the fiber to increase the transmission capacity. In uncoupled MCF large core-to-core distance, i.e., core pitch, is required such that each core of the MCF behaves as the separate spatial channel [2]. Uncoupled

U. Farooque (✉) · R. Ranjan
Department of Electronics and Communication Engineering, National Institute of Technology Patna, Patna, India
e-mail: ufarooque.mit@gmail.com

R. Ranjan
e-mail: rr@nitp.ac.in

© Springer Nature Singapore Pte Ltd. 2020

V. Janyani et al. (eds.), *Optical and Wireless Technologies*,
Lecture Notes in Electrical Engineering 546,
https://doi.org/10.1007/978-981-13-6159-3_18

MCF has been extensively used in the recent transmission experiments for achieving high transmission capacity of the order of 1 Pbit/s. The main issue in achieving high transmission capacity, while maintaining low crosstalk is the arrangement of cores within fixed cladding region [3]. With sufficiently large core pitch in uncoupled MCF, the crosstalk reduces to a significant level, but as the number of core increases within fixed cladding region to increase the core density, core pitch decreases and correspondingly crosstalk increases. For a fixed core count, different core layouts, namely, circular one-ring structure (ORS), hexagonal ORS, circular dual-ring structure (DRS), hexagonal DRS, and square lattice structure (SLS) affect the crosstalk differently. Therefore, for the high-count MCF, the core layout-dependent crosstalk behavior is important to study. Several attempts have been made to analyze the crosstalk variations in different core count and core layouts in homogeneous and trench-assisted (TA) homogeneous MCFs [3–5]. In the trench-assisted MCF, an inner cladding, having the same value of refractive index (R.I.) as the outer cladding and a trench layer, having low R.I. compared to cladding layer are introduced around each core. A trench layer helps in the confinement of the mode within the core region and avoid coupling of modes between adjacent cores, thus suppressing crosstalk. The worst crosstalk level experienced in high-count, 24-Core and 32-Core homogeneous TA MCFs using SLS core configuration have respective values of −18.4 dB and −4.4 dB at 1550 nm. The achieved crosstalk level is still high for the advanced modulation formats such as, 16-QAM, 32-QAM, and 64-QAM to be used and it is reported that the heterogeneous configuration of the core should be adopted for further reduction in crosstalk [3]. In order to increase the transmission capacity of the MCF, one of the approaches is to increase the core density within a fixed cladding region while minimizing crosstalk between the adjacent cores [6]. For further accommodating more number of cores with low crosstalk between adjacent cores, cladding diameter is to be increased. But, increase in cladding diameter is limited to satisfy the limit of failure probability and also there is a restriction on the cladding thickness, i.e., the distance between the centers of the outer layer core to the cladding boundary due to micro-bending loss constraints [3]. Crosstalk can be minimized by suppressing the phase matching and the mode coupling of the signals propagating in the adjacent cores. Phase mismatch can be achieved by the heterogeneous cores-having different core radius and R.I., while the coupling of modes can be avoided by incorporating trench layers around the core regions. There are some other schemes to improve the confinement of the mode in the core regions such as, air-hole-assisted, rod-assisted, and rectangular-trench-assisted cores [7].

Based on the above schemes of heterogeneous and trench, and rod assisted heterogeneous MCF, several attempts have been made to analyze the crosstalk behaviors for different core counts [8–12]. However, to the best of our knowledge based on the available literature, for a fixed core count and different core layout dependent crosstalk variations in heterogeneous and trench-assisted heterogeneous MCFs have not been studied in detail. In this work, we have analyzed the effects of different core layouts on the crosstalk variation in heterogeneous and trench-assisted heterogeneous MCFs for a fixed value of core count and under limited cladding diameter (CD) and cladding thickness (CT) constraints. Further, the core count increases to

observe their performance for the high density of cores. The different core layouts under this study are namely- circular one ring structure (ORS), hexagonal ORS, circular dual ring structure (DRS), hexagonal DRS, square lattice structure (SLS) and the different counts are 12-Core, 24-Core, and 30-Core. The rest of the paper is organized as follows: Sect. 2 describes the design parameters for the heterogeneous and the trench-assisted heterogeneous MCFs. Section 3 provides the crosstalk behavior in 12-Core, 24-Core, and 30-Core heterogeneous and trench-assisted heterogeneous MCFs. Section 4 presents results and discussion. Lastly, Sect. 5 contains the conclusion of the present work.

2 Design Parameters

In this analysis, we have chosen two different kinds of heterogeneous cores. The design parameters associated with the heterogeneous and trench-assisted heterogeneous MCFs have been mentioned in Table 1.

Where a_1, and a_2 are the radius of the two cores, a_3 is the distance of the inner edge of the trench from the center of the core, and a_4 represents the distance of the outer edge of the trench from the center of the core. Whereas, Δ_1, Δ_2, and Δ_3 represent the relative R.I. difference of core 1, core 2, and trench layer with respect to cladding and n_0 is the refractive index of the cladding region, while, w_{tr} is trench width. R_b, d, and L are the bending radius, correlation length, and the length of the fiber, respectively.

The different core layouts have cores with the same parameters mentioned in Table 1, only their arrangements are different which are shown in the Figs. 1, 2, and

Table 1 Design parameters

Parameters	Heterogeneous MCF	Trench-assisted heterogeneous MCF	Units
a_1, a_2	4.5, 4	4.5, 4	μm
$a_3/a_1, a_3/a_2$	–	2, 2	–
$a_4/a_1, a_4/a_2$	–	3, 3	–
$w_{tr}/a_1, w_{tr}/a_2$	–	1, 1	–
n_0	1.45	1.45	–
Δ_1	0.35	0.35	%
Δ_2	0.45	0.45	%
Δ_3	–	−0.35	%
R_b	0–500	0–500	mm
L	100	100	Km
d	50	50	mm

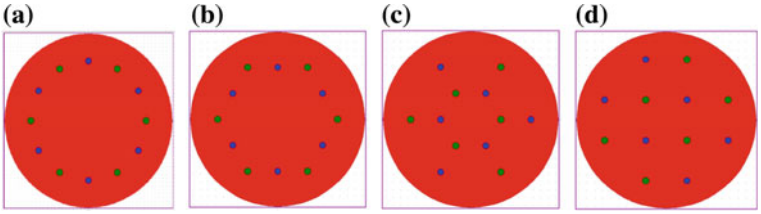

Fig. 1 12-Core **a** circular ORS, **b** hexagonal ORS, **c** circular DRS, **d** SLS

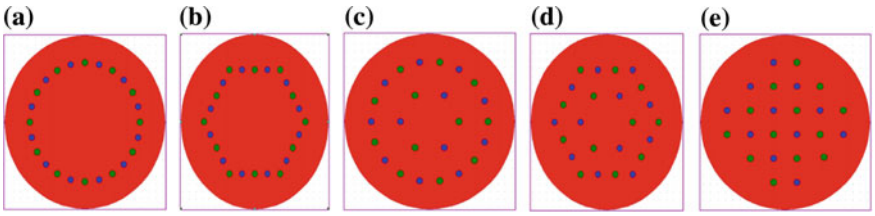

Fig. 2 24-Core **a** circular ORS, **b** hexagonal ORS, **c** circular DRS, **d** hexagonal DRS, **e** SLS

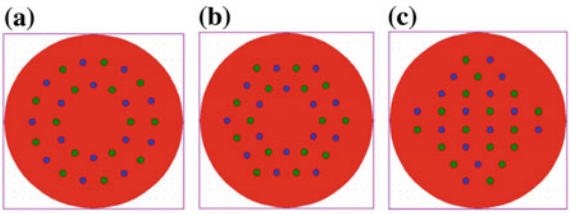

Fig. 3 30-Core **a** circular DRS, **b** hexagonal DRS, **c** SLS

3. Calculation of crosstalk in the different layouts requires the number of adjacent cores contributing in crosstalk level significantly and their respective core pitches, which are mentioned in Table 2.

3 Crosstalk Variations in Different Layouts of Heterogeneous and Trench-Assisted Heterogeneous MCFs

The expression of the crosstalk, XT, between adjacent cores of heterogeneous MCF and the expression of the average power coupling coefficient, $\bar{h}_{12}$, are expressed in

Table 2 Core layout parameters

Number of cores in MCF	Parameters	Circular ORS	Hexagonal ORS	Circular DRS	Hexagonal DRS	SLS
12-Cores	Number of adjacent cores-Heterogeneous (Hetero)/Homogeneous (Homo) and associated core pitch (D) (μm)	2 Hetero cores at D = 40.12	2 Hetero cores at D = 38.75	3 Hetero cores at D = 38.75	3 Hetero cores at D = 38.75	4 Hetero cores at D = 51.6
24-Cores		2 Hetero cores at D = 20	2 Hetero cores at D = 19.38	2 Hetero, 2 Hetero and 1 Homo cores at D_1, D_2, and D_3 = 38.75, 43.17 and 38.75, respectively	2 Hetero, 2 Hetero, and 1 Homo cores at D_1, D_2, and D_3 = 38.75, 34.17 and 38.75, respectively	4 Hetero cores at D = 31
30-Cores		–	–	2 Hetero, 1 Hetero and 2 Homo cores at D_1, D_2 and D_3 = 24.32, 30.5, and 37, respectively	2 Hetero, 1 Hetero and 2 Homo cores at D_1, D_2 and D_3 = 23.5, 30.5, and 28.39, respectively	2 Hetero, 2 Hetero and 4 Homo cores at D_1, D_2 and D_3 = 22.14, 31 and 38.09, respectively

Eq. 1 and Eq. 2 respectively, and the detail explanation is provided in [13, 14]. Further, based on the analysis presented in [15, 16] for the derivation of the expression of mode coupling coefficient for homogeneous and trench-assisted homogeneous MCF, the expressions of mode coupling coefficient between adjacent cores of heterogeneous and trench-assisted heterogeneous MCFs have been derived in current work and expressed in Eq. 3 and Eq. 4, respectively.

$$XT \cong \bar{h}_{12} L \tag{1}$$

$$\bar{h}_{12} = \sqrt{2} K_{12}^2 d \left[\frac{1}{\sqrt{a(b + \sqrt{ac})}} + \frac{1}{\sqrt{c(b + \sqrt{ac})}} \right] \tag{2}$$

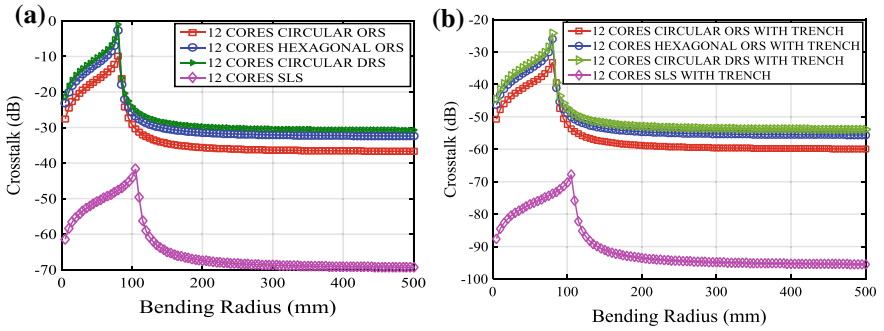

Fig. 4 Bending radius dependent worst crosstalk in 12-Core **a** heterogeneous and **b** trench-assisted heterogeneous MCFs

$$\kappa_{12} = \left(\frac{\sqrt{\Delta_1}}{a_2}\right)\left(\sqrt{\frac{n_1}{n_2}}\right)\left(\sqrt{\frac{\pi a_2}{w_2 D}}\right)\left(\exp\left(-\frac{w_2 D}{a_2}\right)\right)\left(\frac{w_1 w_2}{v_2 J_1(u_1) J_1(u_2)}\right)$$
$$\left(\frac{J_0(u_2)}{K_0(w_2)}\right)\left[\frac{(\frac{w_2 a_1}{a_2}) J_0(u_1) I_1(\frac{w_2 a_1}{a_2}) + u_1 J_1(u_1) I_0(\frac{w_2 a_1}{a_2})}{u_1^2 + \left(\frac{w_2 a_1}{a_2}\right)^2}\right] \tag{3}$$

$$\kappa'_{12} = \sqrt{\frac{w_2}{\left[\frac{w_2 + (w_{22} - w_2) w_{tr}}{D}\right]}} \exp\left[-\left(\frac{2 \times (w_{22} - w_2)(a_3 - a_2)}{a_2}\right)\right] \kappa_{12} \tag{4}$$

where κ_{12} and κ'_{12} are the coupling coefficients of the heterogeneous and TA heterogeneous MCFs, respectively, while, u_1, u_2, w_1, w_2, and w_{22} are the normalized transverse wave numbers of the modes in the two cores, cladding, and the trench regions, respectively. J_0, J_1, I_0, I_1, and K_0, represent the Bessel functions of the first kind in the core region, and the modified Bessel function of the first and second kind in the cladding region. The values of CD and CT have been taken as 225 and 35 μm and are within the limit of failure probability and micro-bending loss constraints [3]. The calculated values of the crosstalk in Figs. 4, 5 and 6 are worst crosstalk. The values of the worst crosstalk at 1550 nm wavelength in different core layouts for different core counts have been tabulated in Table 3 for comparison purpose. From Table 3, it is observed that for 12-Core, 24-Core, and 30-Core TA MCFs, approximately 35, 30, and 20 dB of crosstalk level can be optimized by proper selection of core layout. The values of the crosstalk for the circular ORS and hexagonal ORS 30-Core heterogeneous and TA heterogeneous MCFs have not been calculated due to very small core pitch and correspondingly, very high value of crosstalk.

The values of the worst crosstalk mentioned in Table 3 have been used to investigate the core count dependent crosstalk variations in circular DRS, hexagonal DRS, and SLS layouts for both heterogeneous and trench-assisted heterogeneous MCFs and shown in Fig. 7. For a fixed core count, the worst crosstalk in different core layouts

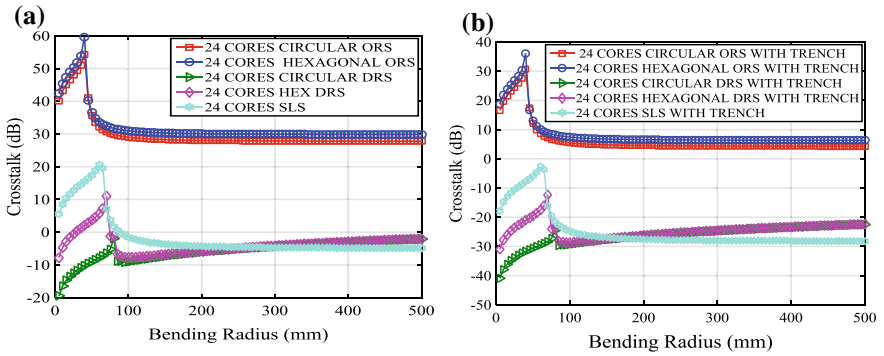

Fig. 5 Bending radius dependent worst crosstalk in 24-Core **a** heterogeneous and **b** trench-assisted heterogeneous MCFs

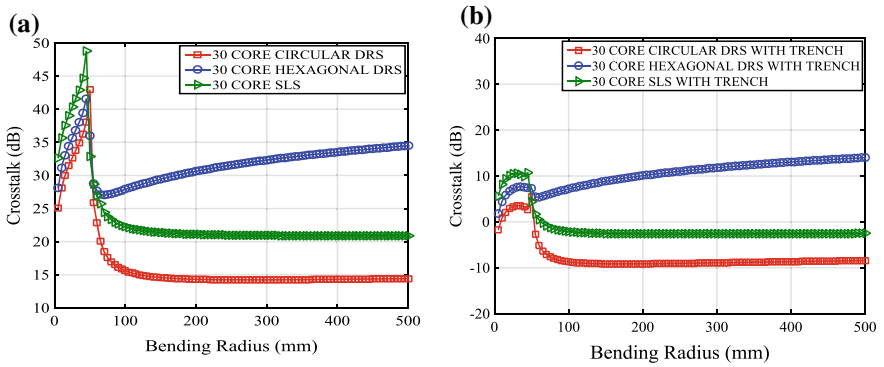

Fig. 6 Bending radius dependent worst crosstalk in 30-Core **a** heterogeneous and **b** trench-assisted heterogeneous MCFs

Table 3 Worst crosstalk value (dB) at 1550 nm wavelength in different core layouts for different core count

MCF layouts	Crosstalk (dB)					
	12-Core without trench	12-Core with trench	24-Core without trench	24-Core with trench	30-Core without trench	30-Core with trench
Circular ORS	−34.65	−57.84	28.25	4.73	–	–
Hexagonal ORS	−30.52	−53.72	30.28	6.74	–	–
Circular DRS	−28.76	−51.96	−7.18	−27.51	14.53	−9.15
Hexagonal DRS	−28.76	−51.96	−6.71	−27.27	29.58	9.00
SLS	−64.35	−91.48	−3.74	−27.04	21.34	−2.54

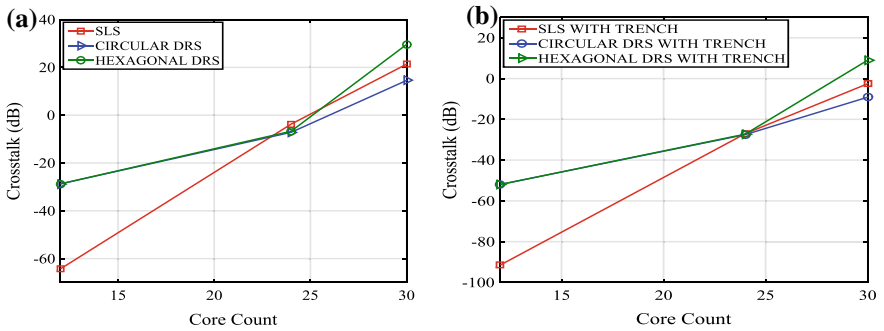

Fig. 7 Core count dependent worst crosstalk in circular DRS, hexagonal DRS and SLS layouts of **a** heterogeneous and **b** trench-assisted heterogeneous MCFs

depends upon the number of surrounding cores and the pitch. For the 12-Core SLS layout, although the number of surrounding cores are large and simultaneously the core pitch is sufficiently large which results in a significantly low value of crosstalk compared to the circular and hexagonal DRS. For high core count 24-Core and 30-Core, the values of the crosstalk in SLS layout are in between that of the other two layouts. Although the slope of the crosstalk in the SLS layout is steeper for low core count and it reduces for the high count, unlike the circular and hexagonal DRS, where the slope increases for high count.

4 Results and Discussion

In order to increase the transmission capacity of the heterogeneous and trench-assisted heterogeneous MCFs by increasing core count while maintaining a low value of crosstalk and under limited cladding diameter (CD) and cladding thickness (CT) constraints, crosstalk variations in different core layouts have been investigated. The bending radius dependent crosstalk variations for different core counts and layouts in heterogeneous and TA heterogeneous MCFs have been investigated using Eqs. 1–4 and are shown in Figs. 4, 5 and 6.

From Fig. 4 it is observed that the crosstalk level is lowest in the SLS layout. Instead of a large number of surrounding cores, the large core pitch in this arrangement reduces the crosstalk significantly. From Table 2, it is observed that the number of adjacent cores and the core pitch in the circular and the hexagonal DRS have same values, therefore, their crosstalk will also be same and it is shown in Fig. 1 for only circular DRS. In Fig. 5, the circular and hexagonal ORS layouts have higher values of crosstalk due to the reduced core pitch. Unlike the bend-insensitive nature of crosstalk in SLS beyond the peak bending radius, the crosstalk in the circular and the hexagonal DRS have bending sensitive nature. This is mainly due to the effect of the presence of similar (homogeneous) cores at low pitch, which increases the crosstalk

due to phase matching. From Table 3, it is analyzed that although all the three core layouts have surrounding homogeneous cores the distance between them in different layouts have different magnitude and affect the crosstalk differently which can be observed in Fig. 6. The crosstalk value in hexagonal DRS layout becomes worst as the bending radius increases. The number of surrounding cores in the SLS layout is maximum, instead of this the crosstalk level is in between that of the other two layouts and also it is bent insensitive. The values of crosstalk by utilizing heterogeneous cores are compared with that of the reported values for homogeneous cores for different core count and layout. Compared to the average measured values of crosstalk, −46.92 dB, and −54.69 dB in 12-Core ORS and DRS layout TA homogeneous MCFs, respectively for the values of the *CD*, *CT*, *D* and *L* of about 225 μm, 38.9 μm, 36.8 μm, 52 km and 230 μm, 37.7 μm, 44.6 μm, and 50 km [3], the values of the worst crosstalk for the same core count and layouts in TA heterogeneous MCF are −60.68 dB, and −54.97 dB for the values of *CD*, *CT*, *D* and *L* of about 225 μm, 35 μm, 40.12 μm, 52 km and 225 μm, 35 μm, 38.75 μm, 50 km. Further, for 24-Core the value of crosstalk in SLS layout TA heterogeneous MCF is −27.04 dB compared to that of −18.4 dB in SLS layout TA homogeneous MCF at 1550 nm [3].

Core count dependent crosstalk variations in the different core layouts of the heterogeneous and the trench-assisted heterogeneous MCFs have been shown in Fig. 7. Among the 12-Core layouts, the value of the crosstalk in SLS layout is significantly low, while for high core count 24-Core and 30-Core, this value in SLS layout is in between that of the other two layouts which is due to the impact of the number of surrounding cores and the core pitch. The value of the crosstalk can be further reduced by utilizing the propagation direction interleaving (PDI) scheme [3]. By utilizing three and more number of heterogeneous cores, the bend-sensitive nature and the value of the crosstalk can be suppressed.

5 Conclusion

For a fixed value of core count within fixed cladding diameter and cladding thickness, the arrangement of cores, i.e., the core layouts have a significant effect in achieving the low value of crosstalk. Further, for high core count, the nature of surrounding cores and the distance between them also affect the crosstalk values. For 12-Core TA MCF, approx. 35 dB of crosstalk level can be reduced by proper selection of core layout, and for high counts such as, 24-Core and 30-Core TA MCFs, this value reduces to 30 dB and 20 dB, respectively.

Acknowledgements The authors are thankful to the National Institute of Technology, Patna for immense support to carry out this work.

References

1. Tu J, Saitoh K, Koshiba M, Takenaga K, Matsuo S (2012) Design and analysis of large-effective-area heterogeneous trench-assisted multi-core fiber. Optic Expr 20:15157–15170
2. Hayashi T et al (2016) Effects of core count/layout and twisting condition on spatial mode dispersion in coupled multi-core fibers. In: 42nd European conference on optical communication, Dusseldorf, Germany, pp 1–3
3. Ye F, Tu J, Saitoh K, Takenaga K, Matsuo S, Takara H, Morioka T (2016) Design of homogeneous trench-assisted multi-core fibers based on analytical model. J Lightwave Technol 34:4406–4416
4. Puttnam BJ et al (2016) High capacity multi-core fiber system. In: 21st European conference on networks and optical communication, Lisbon, pp 29–34
5. Hayashi T, Taru T, Shimakawa O, Sasaki T, Sasaoka E (2011) Design and fabrication of ultra-low crosstalk and low-loss multi-core fiber. Optic Expr 19:16576–16592
6. Chan FYM, Lau APT, Tam HY (2012) Mode coupling dynamics and communication strategies for multi-core fiber systems. Optic Expr 20:4548–4563
7. Tu J, Xie X, Long K (2016) Theoretical analysis on inter-core crosstalk suppression model for multi-core fiber. China Commun 13:192–197
8. Koshiba M, Saitoh K, Kokubun Y (2009) Heterogeneous multicore fibers: proposal and design principle. IEICE Electr Expr 6:98–103
9. Sasaki Y, Amma Y, Takenaga K, Matsuo S, Saitoh K, Koshiba M (2013) Investigation of crosstalk dependencies on bending radius of heterogeneous multicore fiber. In: Optical fiber communication conference and exposition and the national fiber optic engineers conference, Anaheim, CA, pp 1–3
10. Amma Y et al (2015) High-density multicore fiber with heterogeneous core arrangement. In: Optical fiber communications conference and exhibition, Los Angeles, CA, pp 1–3
11. Xie X, Tu J, Zhou X, Long K, Saitoh K (2017) Design and optimization of 32-core rod/trench assisted square-lattice structured single-mode multi-core fiber. Optic Expr 25:5119–5132
12. Fujisawa T et al (2017) Crosstalk analysis of heterogeneous multicore fibers using coupled-mode theory. IEEE Photonics J 9:1–8
13. Koshiba M, Siatoh K, Takenaga K, Matsuo S (2012) Analytical expression of average power-coupling coefficients for estimating intercore crosstalk in multicore fibers. IEEE Photonics J 4:1987–1995
14. Koshiba M, Saitoh K, Takenaga K, Matsuo S (2011) Multi-core fiber design and analysis: coupled-mode theory and coupled-power theory. Optic Expr 19:B102–B111
15. Okamoto K (2006) Fundamentals of optical waveguides, academic. Academic Press, San Diago, USA, pp 159–187
16. Ye F, Tu J, Saitoh K et al (2014) Simple analytical expression for crosstalk estimation in homogeneous trench assisted multicore fibers. Opt Expr 22:23007–23018

Impact of Air–Sea Interface Effects and Bubble and Particulate Scattering on Underwater Light Field Distribution: An Implication to Underwater Wireless Optical Communication System

Rashmita Sahoo, Palanisamy Shanmugam and Sanjay Kumar Sahu

Abstract A study of the effects of air–sea interface, bubble and particulate scattering, and medium inhomogeneity on the underwater light field distribution, downwelling irradiance (E_d) was carried out theoretically using Monte Carlo numerical simulation technique. The downwelling irradiance was computed for different scenarios (with and without waves and bubble effects) and compared with the in situ measured values. The wave effect was included according to a model given by Cox and Munk and the effect of bubble was included by estimating the Bidirectional Transmittance Distribution Function (BTDF) of a bubble layer. Furthermore, the effect of the variation of particulate concentration along the vertically downward direction on downwelling irradiance was studied by stratifying the underwater medium, instead of considering homogeneous water column, for the calculation of E_d. The findings showed the importance of considering the air–sea interface (wave and bubble) effects and stratification in estimating the underwater light field distribution and thereby the channel characteristics of an Underwater Wireless Optical Communication (UWOC) system. In particular, the present study can be helpful to researchers and engineers in modelling the effects of air–sea interface, bubble scattering and particulate scattering on the power budget, channel impulse response and signal-to-noise ratio (SNR) of a vertical communication link between aerial and underwater platforms.

Keywords Monte Carlo method (MC) · Downwelling irradiance (E_d) · Underwater wireless optical communication (UWOC) system · Channel characteristics

1 Introduction

Propagation of light from atmosphere to underwater is greatly affected by the air–sea interface, waves, bubbles and suspended particulates. These effects significantly

R. Sahoo · P. Shanmugam (✉) · S. K. Sahu
Department of Ocean Engineering, Indian Institute of Technology Madras, Chennai 600036, India
e-mail: pshanmugam@iitm.ac.in

© Springer Nature Singapore Pte Ltd. 2020

V. Janyani et al. (eds.), *Optical and Wireless Technologies*,
Lecture Notes in Electrical Engineering 546,
https://doi.org/10.1007/978-981-13-6159-3_19

influence the underwater applications including Wireless Optical Communication between surface and underwater platforms, underwater target detection, underwater imaging, and search and recover operations. Till date, considerable amount of research has been devoted in this direction where the air–sea interface and water column effects are substantiated. Chengan has studied the influence of wind-generated bubble population on the light transmission, from atmosphere to underwater, in the blue-green window [1]. Effect of wavy atmosphere–ocean interface on the underwater light field distribution was studied by Hieronymi [2]. In other studies [3, 4], Sahu and Shanmugam have modelled the scattering properties of particulates and shown the effect of particulate scattering on the channel characteristics of an UOWC system. However, there is no substantial work done in a direction where all these effects are considered together.

In the present work, the simultaneous impact of surface waves, bubble layer, particle scattering and medium inhomogeneity on the underwater light field distribution is studied. Monte Carlo simulations are performed, under various scenarios, to estimate the downwelling irradiance along the depth of the water column. Slope of surface wave and the resulting bubble layer thickness were calculated from wind velocity using the Cox and Munk model [5]. The surface reflectance from the windy and bubble populated sea surface was estimated by using a BTDF model [1, 6]. Values of attenuation coefficient, absorption coefficient, and phase function for MC simulation were acquired at different depths during a cruise conducted in September 2017. The simulated E_d values were finally compared with the in situ measured values.

2 In Situ Data and Methodology

2.1 In Situ Data

Inherent optical properties which depend only on the medium, mainly absorption coefficient, attenuation coefficient, single scattering albedo, volume scattering phase function are deciding factors for the distribution of light propagating in the water column. A hyperspectral absorption-attenuation metre (AC-S) was used to measure continuous profiles of beam attenuation ($c_t(\lambda)$) and absorption coefficient ($a_t(\lambda)$) with respect to depth in the wavelength range of 300–700 nm. The single-scattering albedo (ω) was determined from measured $c_t(\lambda)$ and $a_t(\lambda)$ values at 460 nm (Fig. 1a). Fluorometer-Turbidity sensor (FLNTU) was used to measure chlorophyll concentration with respect to depth, as shown in Fig. 1b. A multi angle polarised light scattering metre (LISST-VSF) was used to measure volume scattering phase function values at discrete depths (maximum up to 50 m) with angular resolution 0.1°–155°. The measured phase functions (at 515 nm) at 1 and 41 m depth are shown in Fig. 1c.

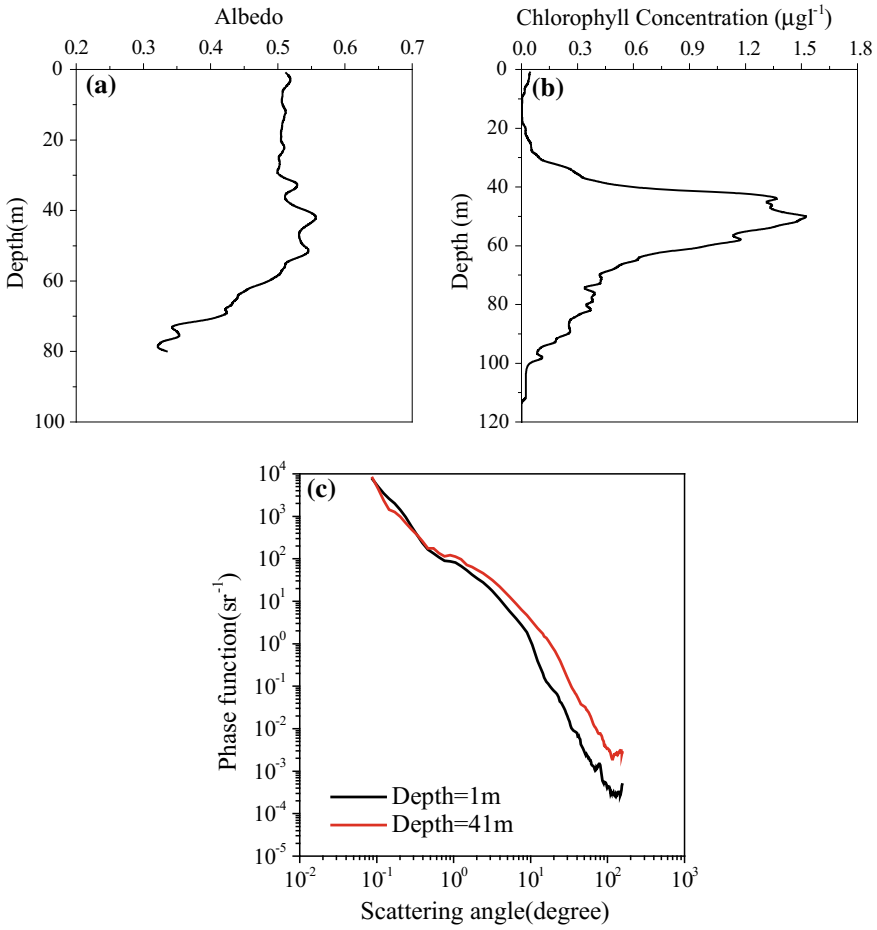

Fig. 1 Vertical profiles of the in situ data **a** single scattering albedo, **b** Chlorophyll concentration, **c** scattering phase function measured in Bay of Bengal waters

2.2 Monte Carlo Simulation

Conducting experiment in open oceanic waters is quite difficult and expensive. Therefore, MC numerical technique is used to obtain an approximate solution to the exact problem [7, 8]. The MC simulation consists of three major parts such as initial condition, photon propagation, and photon reception.

Initial condition

The initial condition includes source and receiver information, simulation geometry (on/off axis) and type of environment (homogenous/stratified). In the present study, collimated source, receiver of unit area, and on axis propagation geometry are taken into consideration for the MC simulation.

Photon propagation
Initially, each photon is associated with three attributes such as initial position (x, y, z), directions (μ_x, μ_y, μ_z) and weight (W). Geometric path length (r) travelled by the photon before scattering by the particle is given by Eq. (1). The photon undergoes multiple scattering during propagation in the medium and the attributes of each photon are updated by using Eqs. (1)–(3).

$$r = \frac{1}{c} \log RND \tag{1}$$

$$\mu_x = \sin\theta \cos\phi, \quad \mu_y = \sin\theta \sin\phi, \quad \mu_z = \cos\theta \tag{2}$$

$$W_{n+1} = W_n\left(1 - \frac{a_t(\lambda)}{c_t(\lambda)}\right) \tag{3}$$

3 Effects Influencing Underwater Light Field Distribution

3.1 Sea Surface Roughness

The open ocean is always wavy due to the wind action. As the wave generation is a random phenomenon, the slope of wave (θ_n) is assumed to follow a normal distribution having variance (σ^2), which is a function of wind speed (U_{10}). The tilt angle of wave and wave slope are calculated from the Cox and Munk probability distribution function (PDF) and normalised by cumulative distribution function (CDF) of $p(\theta_n)$ as expressed in Eqs. (4)–(6).

$$p(\theta_n) = \frac{1}{\pi\sigma^2} \exp\left(-\frac{\tan^2\theta_n}{\sigma^2}\right) \tag{4}$$

$$\sigma^2 = 0.003 + 0.00512U_{10} \tag{5}$$

$$\theta_n = \tan^{-1}\left[\sqrt{-\sigma^2}\ln\left(1 - RND_{\theta_n}\right)\right] \tag{6}$$

The normal vector of a sea surface, i.e., $\hat{n} = (n_x, n_y, n_z)$ has three components n_x, n_y, n_z, which are functions of the wave slope as shown in Eq. (7).

$$n_x = \cos\phi_n \sin\theta_n \quad n_y = \sin\phi_n \sin\theta_n \quad n_z = \cos\theta_n \tag{7}$$

The azimuth angle ϕ_n is expressed as

$$\phi_n = 2\pi RND_{\phi_n} \tag{8}$$

The incidence angle of light (θ_i) with respect to the rough/irregular wavy sea surface is calculated by taking the dot product of surface normal vector, i.e., $\hat{n} = (n_x, n_y, n_z)$ and direction vector of incidence light, i.e., $\hat{u} = (u_x, u_y, u_z)$. The reflection coefficient ($\rho(\theta_t, \theta_i)$) at wavy sea surface is calculated using Fresnel Reflection formula and Snell's law [Eqs. (9) and (10)]

$$\rho(\theta_t, \theta_i) = \frac{1}{2}\left\{\left[\frac{\sin(\theta_i - \theta_t)}{\sin(\theta_i + \theta_t)}\right]^2 + \left[\frac{\tan(\theta_i - \theta_t)}{\tan(\theta_i + \theta_t)}\right]^2\right\} \tag{9}$$

$$\theta_t = \sin^{-1}\left(\frac{n_i}{n_t}\sin\theta_i\right) \tag{10}$$

where n_i and n_t are the refractive indices of air and water. The increase in surface reflectance with the wind speed indicates a higher loss of light signal at the air–sea interface for an increased rough sea condition.

3.2 Bubble Scattering

The presence of bubbles at near-surface waters, generated due to breaking of wind-induced waves, have a significant effect on the light transmission from air to underwater. In this study, the number density, layer thickness, and reflectance of bubble layer are estimated based the models reported in [1, 6]. The effect of bubble layer was included using bidirectional transmittance distribution function (BTDF). Bidirectional transmittance distribution function is a bivariate PDF, which determines the direction and intensity of transmitted photons. BTDF is simulated using the Mont Carlo technique for 6 m/s wind speed, 0.54 m thickness bubble layer, and 515 nm wavelength [1].

3.3 Medium Inhomogeneity

In open oceanic waters, the concentration of chlorophyll varies with respect to depth. This variation often follows a Gaussian trend, which was measured by the FLNTU

sensor during the cruise in September 2017 (Fig. 1b). The depth profile of absorption coefficient was also seen to covary with the chlorophyll concentration. Therefore, stratification of water column was essential for calculation of the underwater light field for different depths. The stratification was carried out at 5 m depth resolution in MC simulation. Each stratified layer was assigned different values of the attenuation coefficient, absorption coefficient, single scattering albedo and phase function. As the phase function variation with respect to depth was negligible and considered as same for all depths, it is considered same for all depths.

4 Results and Discussion

In the present study, three sets of downwelling irradiance (E_d) were computed using the MC technique for homogeneous and stratified medium by considering the effect of waves and bubbles from sea surface to 80 m depth in water column. The results were validated with the in situ radiometric measurement data collected in the Bay of Bengal as shown in Fig. 2. It was observed the estimated irradiances for a vertically homogeneous medium with the presence of waves and bubbles (represented by 'Modelled E_d H-W & B' plot) agree better with the in situ measured downwelling irradiances when compared to a case without the presence of waves and bubble effects (represented by 'Modelled E_d H-No W & B' plot) for all depths. This is due to an increased value of surface reflectance in the presence of waves and bubbles as a result of which the irradiance crossing the air–sea interface decreases and approaches more towards the measured values. Further, the downwelling irradiances were estimated by treating the medium as inhomogeneous (which is evident from the depth variation of single scattering albedo in Fig. 1a) and considering the presence of waves and bubbles. The inhomogeneity was treated by stratifying the water column into a number of layers and assigning the different values of IOPs for each layer, unlike the homogeneous case where the entire water column was assigned the constant optical properties by taking an average over the depth profiles. As evident from Fig. 2, the irradiance values estimated in this case (represented by 'Modelled E_d S-W & B') is in good agreement with the in situ measured values. Therefore, the stratification of the medium along with considering the effects of waves and bubbles has a significant role on underwater light propagation study and thereby the channel characteristics of an air-to-underwater optical wireless communication link.

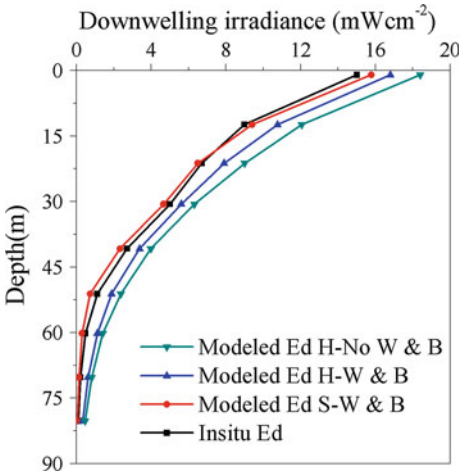

Fig. 2 In situ and modelled downwelling irradiance for homogenous (H) and stratified (S) water columns with and without the effects of waves and bubbles (W & B). The predicted E_d was at 460 nm

5 Conclusion

In the present work, we have described the significant role of medium inhomogeneity, waves, and bubble layer on the behaviour of light propagation in the water column of up to 80 m depth in open oceanic waters. The inhomogeneity of the medium was encountered by stratifying the water column into different layers and assigning different values of IOPs to each layer in the Monte Carlo calculations for downwelling irradiance fields. The effects of waves and bubbles present in the interface were included in the MC simulation according to the existing models. It is found that the downwelling irradiance computed by treating the medium as inhomogeneous and considering the effects of waves and bubbles best agreed with the in situ measured values. This study can help researchers and engineers to characterise the underwater channel properties specific to various underwater applications including underwater wireless optical communication, underwater imaging, underwater target detection, and satellite remote sensing.

References

1. Wang C, Tan J, Lai Q (2016) The influence of bubble populations generated under windy conditions on the blue–green light transmission in the upper ocean: an exploratory approach. Mod Phys Lett B 30(36):1650420
2. Hieronymi M (2013) Monte Carlo code for the study of the dynamic light field at the wavy atmosphere-ocean interface. J Eur Opt Soc Rap Public 8:13039

3. Sahu SK, Shanmugam P (2018) A theoretical study on the impact of particle scattering on the channel characteristics of underwater optical communication system. Opt Commun 408:3–14
4. Sahu SK, Shanmugam P (2017) A study on the effect of scattering properties of marine particles on underwater optical wireless communication channel characteristics. In: OCEANS 2017, Aberdeen, 19 Jun 2017. IEEE, pp 1–7
5. Cox C, Munk W (1956) Slopes of the sea surface deduced from photographs of sun glitter. Scripps Inst Oceanogr
6. Ma L, Wang F, Wang C, Wang C, Tan J (2015) Monte Carlo simulation of spectral reflectance and BRDF of the bubble layer in the upper ocean. Opt Expr 23(19):24274
7. Tang S, Zhang X, Dong Y (2013) On impulse response for underwater wireless optical links. In: OCEANS-Bergen, 2013 MTS/IEEE, pp 1–4
8. Cox Jr WC (2012) Simulation, modeling, and design of underwater optical communication systems. North Carolina State University

Strain Resolution and Spatial Resolution Improvement of BOCDR-Based DSS System Using Particle Swarm Optimization Algorithm

Ramji Tangudu and Prasant Kumar Sahu

Abstract This paper presents, a detailed analysis on the performance of a Brillouin optical correlation domain reflectometry (BOCDR) based distributed strain sensing (BOCDR-DSS) system. Strain resolution and spatial resolution decide the performance of BOCDR-DSS system. Particle swarm optimization (PSO) algorithm is used in this paper to enhance the above-mentioned performance of the available BOCDR-DSS system. With the help of PSO evolutionary algorithm, Brillouin frequency shift (BFS) error of the considered sensing system has been minimized. Finally, 4 m-long strained silica optical fiber (SOF) section over a 700 m fiber under test is successfully detected with ~0.0011% strain resolution and ~43 cm spatial resolution. Simulation was carried out using MATLAB version 15.0.

Keywords Spontaneous Brillouin scattering (SpBS) · Brillouin optical correlation domain reflectometry (BOCDR) · Particle swarm optimization (PSO) · Brillouin frequency shift (BFS)

1 Introduction

Nowadays, distributed fiber optic sensors (DFOS) based on Brillouin scattering are having major role in modern engineering sciences. One of the extensively used versions of DFOS, is Brillouin distributed strain sensing (B-DSS) system, useful for distributed strain measurement. This system has more immunity to electromagnetic interference, small in size, less complexity, resistance to corrosion and more survivability under harsh environmental conditions. Due to these advantages, and high-resolution Brillouin-DSS system is able to detect the minor cracks in bridges/structure

R. Tangudu (✉) · P. K. Sahu
Indian Institute of Technology Bhubaneswar,
Arugul, Odisha, India
e-mail: rt10@iitbbs.ac.in

P. K. Sahu
e-mail: pks@iitbbs.ac.in

© Springer Nature Singapore Pte Ltd. 2020

V. Janyani et al. (eds.), *Optical and Wireless Technologies*,
Lecture Notes in Electrical Engineering 546,
https://doi.org/10.1007/978-981-13-6159-3_20

of national and international importance at an early stage. Brillouin-DSS systems are having more significance in structural health monitoring [1]. This sensing system is highly applicable in civil structural health monitoring applications. Changes of strain on the optical fiber generate changes in acoustic properties of medium and generate changes in its characteristic, i.e., the Brillouin frequency shift (BFS) parameter. These changes are helpful to find real time strain values on the optical fiber. Generally, BFS is ~11 GHz for 1550 nm pumping wavelength under strain free section of an optical fiber [2–4].

As reported in the literature, the Brillouin-DSS system are designed mainly based on two effects, i.e., spontaneous and stimulated Brillouin scattering. Brillouin optical time domain analysis (BOTDA) [5–9], Brillouin optical frequency domain analysis (BOFDA) [10, 11] and Brillouin optical correlation domain analysis (BOCDA) [12, 13] are a case of stimulated Brillouin scattering (SBS). Similarly the spontaneous Brillouin scattering (SpBS) based systems are Brillouin optical time domain reflectometry (BOTDR) [14–20], and Brillouin optical correlation domain reflectometry (BOCDR) [21–26] techniques based systems. Analysis based techniques (SBS) requires the double ended accesses (pump and probe lights), whereas reflectometry based systems requires only single ended accesses and hence design complexity is less in SpBS system. Other major drawbacks of BOTDA, BOFDA and BOCDA techniques are high nonlinearity effects and cost (usage of electro optic modulators and vector network analyzers) [5–13].

In reflectometry-based techniques, BOTDR is used for strain sensing up to tens of kilometers. However, it has limitation in spatial resolution and strain resolution. The typical spatial resolution as reported in literature for a BOTDR-based DSS system is in terms of meters. Because of the theoretical limit, it is not possible to select the pulse width of input optical source lesser than 10 ns, as nonlinearity effects will be generated in an optical fiber [14–20]. For avoiding this problem, BOCDR is used in DSS system [21–26]. Spatial resolution using BOCDR technique can be achieved up to few tens of centimeters. Nevertheless, the major drawback frequently occurs in BOCDR-based DSS system is BFS error. This error occurs for both strained and strain free sections along the fiber. This BFS error value is in terms of MHz for strain [22–26].

In this paper, we have proposed and analyzed the performance of a BOCDR-DSS system. The proposed system is having potential application in the defense areas, security fences, and in aviation sectors besides structural health monitoring. This paper reports the analysis on BFS error in BOCDR-based DSS system. Besides the BFS error, we also focused on spatial resolution improvement. For reduction in BFS error and amelioration in spatial resolution, soft and evolutionary computing algorithm, such as particle swarm optimization (PSO) [27] is used. The reason behind the usage of PSO algorithm are numerous like ease of implementation, computational efficiency as compared to mathematical algorithm as well as robustness to control parameters and fast convergence in both linear and nonlinear problems scenarios [28, 29]. Though the performance of PSO and GA based systems are comparable. However, PSO outperforms GA in terms of the average and the worst fitness values. Compared to PSO algorithm, genetic algorithms (GA) are more complex and take

more time to make convergence [30]. Similarly, ant colony optimization (ACO) has uncertainty in time to make convergence and differential evolution (DE) algorithm gives more complexity and requires more time to make convergence [31, 32]. By minimization of this BFS error, précise values of strains over the fiber was observed.

2 Principle and Theory

2.1 BOCDR Technique

When an input light signal is propagated through an optical fiber, it interacts with acoustic phonons, creating backscattered Stokes and anti-Stokes optical signals. This condition is called as spontaneous Brillouin scattering (SpBS). Corresponding spectrum is known as Brillouin gain spectrum (BGS). The frequency difference between the pump or input light frequency and central frequency of BGS spectrum is called as the Brillouin frequency shift (BFS). When the pump wavelength is ~1550 nm, the BFS in silica single-mode fiber (SMF) is ~11 GHz, it slightly fluctuates depending on the fiber fabrication process. If different strains are applied on silica SMF, the BFS moves toward to higher frequency with 493 MHz/% at ~1550 nm. So, if we measures BFS distribution along a fiber, the applied strain distribution can be evaluated.

BOCDR is one of the Brillouin-based distributed sensing techniques. Conceptual BOCDR system is shown in Fig. 1. Where the source is a narrow band distributed feedback (DFB) laser. This laser source produces a light signal with a frequency f_0. After launching of the light, this light signal's intensity is divided into two intensities with an equal percentage. One part of which traverses in the forward direction and other part traverses in the downward direction as shown in Fig. 1. These two intensities have the same frequency (f_0). In the forward direction, erbium-doped fiber amplifier (EDFA) and a 3-port circulator are fitted. EDFA is used to amplify its input signal. After this amplification process, the light signal passes through the first port of the circulator, circulator sends this signal into its second port. Light from the second port is coupled into the fiber under test (FUT). FUT is subjected to strain change. When an input light signal with frequency (f_0) enters the FUT, the light signal's frequency will changed to ($f_0 \pm f_B$). This frequency change (f_B) is known as BFS. Then the light signal will be backscattered with this modified frequency. This backscattered light pass through the third port of circulator and will be collected by a balanced photo detector (PD) component. Simultaneously the base or fundamental light with frequency (f_0) comes from coupler to this balanced PD component. The backscattered (Stokes or anti-Stokes) optical signal and the reference path signal are proceeded over the balanced PD component. The processed signal over the balanced PD is converted into an electrical signal, which is detected as a BGS with an electrical spectrum analyzer (ESA). By modulating the laser frequency with a sinusoidal signal, correlation peaks are periodically synthesized along the FUT. Typically, FUT length is double the measurement range (distance between two

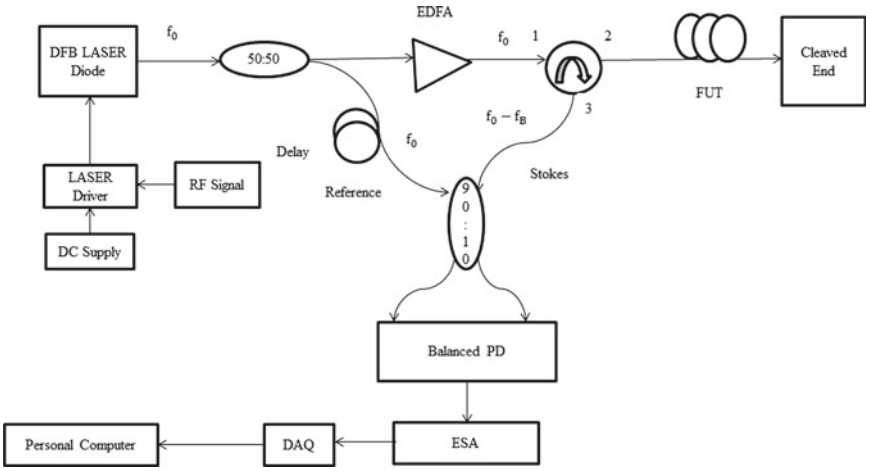

Fig. 1 Illustration of BOCDR-DSS setup. (EDFA: Erbium-doped fiber amplifier; FUT: fiber under test; PD: photo detector; ESA: electrical spectrum analyzer; RF: radio frequency; DC: direct current; DAQ: data acquisition.)

consecutive correlation peaks). FUT needs to be decided in such a way that only one correlation peak is in the FUT. By controlling the light path difference (e.g., by changing the base or reference path length), a correlation peak of any order can be identified in the FUT.

The measurement range d_m of this setup is written as [23]

$$d_m = c/(2nf_m) \tag{1}$$

Since c specifies velocity of light in vacuum and n specifies refractive index of fiber core. By adjusting the modulating frequency (f_m), sensing point or spot will be scanned along the fiber to capture the BGS and BFS distributions. By theoretical concept, when f_m is lesser than the Brillouin bandwidth $\Delta\vartheta_B$, the spatial resolution Δz is expressed by [23]

$$\Delta z = c\Delta\vartheta_B/(2\pi n f_m \Delta f) \tag{2}$$

Here, Δf is the modulation amplitude of the light frequency. Consider f_m is larger than $\Delta\vartheta_B$ that does not involve to the improvement of Δz, and that Δf is practically limited to a half of BFS (ϑ_B) of the fiber because of the Rayleigh noise, the limitation of the spatial resolution Δz_{min} is written by [23]

$$\Delta z = c/(\pi n \vartheta_B) \tag{3}$$

The number of effective sensing points is N_R, this is an evaluation parameter of this system, and it is estimated by [23]

$$N_R = d_m/\Delta z \tag{4}$$

For achieving a maximum value of N_R, Δf needs to be increased but it must be lesser than $\vartheta_B/2$. That is why [23],

$$N_{Rmax} = \pi\vartheta_B/(2\Delta\vartheta_B) \tag{5}$$

Brillouin frequency shift (ϑ_B) is linearly dependent on the strain ($\varepsilon\%$). It can be expressed as [2, 3]:

$$\vartheta_B = \vartheta_{B0} + C_\varepsilon(\varepsilon_{unknown} - \varepsilon_{ref}). \tag{6}$$

Since ϑ_{B0} indicates reference Brillouin frequency shift (under free strained section). C_ε is strain coefficient of SMF. Typically, C_ε has 493 MHz/% and ϑ_{B0} has ~11 GHz for ~1550 nm for silica SMF [3]. $\varepsilon_{unknown}$ and ε_{ref} are non-free and free strained sections.

Reference Brillouin frequency shift (ϑ_{B0}) is expressed as [2–4]:

$$\vartheta_{B0} = 2n_{eff}V_a/\lambda_0 \tag{7}$$

where n_{eff} is effective refractive index of SMF fiber, V_a is the sound (acoustic) velocity of phonons in SMF fiber and λ_0 is the reference or pumping light signal's wavelength.

2.2 *Particle Swarm Optimization Algorithm*

An optimization algorithm is more essential to achieve the best global solution. These algorithms give either global minima or global maxima for particular function or signal. Depending on our requirements, we can focus on maxima or minima value. This algorithm is called as an evolutionary algorithm. Because its current result completely depends upon its previous result. It helps to produce convergence in an advance manner.

In PSO evolutionary optimization algorithm, a group of candidate solutions, referred to as particles are trying to reach an original solution. According to two basic mathematical equations, the optimum solution will be decided. These equations are called as velocity update and position update. In an every iteration or generation, these two basic expressions must be taken. P_{Best} and G_{Best} are called as individual and global best solutions of swarm. These solutions must be calculated in each generation or iteration.

The update equation for velocity is given by [19, 27]:

$$V_i^{g+1} = WV_i^g + C_1 rand_1(P_{Besti} - X_i^g) + C_2 rand_2(G_{Besti} - X_i^g) \quad (8)$$

Here, V_i^g is the velocity of ith particle at gth generation, W is the inertial constant, C_1 and C_2 are the acceleration constants for controlling the previous velocities increases of the particles, $rand_1$ and $rand_2$ are an uniformly distributed random number between 0 and 1, X_i^g is the current position of ith particle at gth generation, P_{Besti} is an individual best fitness value of the ith particle and G_{Besti} is the global best fitness value among all particles. The values of W, C_1 and C_2 are 0.6, 1.1 and 1.9, respectively.

Here, $W > (\frac{C_1+C_2}{2}) - 1$ and $0 < W < 1$

The location of an every particle is modified by the following formulae [19, 27]:

$$X_i^{g+1} = X_i^g + V_i^{g+1}. \quad (9)$$

The procedure of PSO is explained as follows [19], [27]:

Step 1: First consider the position X_i^1 and the velocity V_i^1 of an each particle in a random manner. Create a loop with $g_{min} = 1$ and the maximum number g_{max} of generations in an entire search. In this paper, we have taken the number of initial particles (population size) as 20 and g_{max} as 100.

Step 2: Find out the fitness value $BFS_{Error}(X_i^g)$ of each particle X_i^g for an estimating the local best position P_{Besti} and the global best position G_{Best} up to the current instant. Since BFS_{Error} defines the difference between the actual reference BFS value and an estimated reference BFS value.

Step 3: Estimate V_i^{g+1} and X_i^{g+1} values using (8) and (9), respectively, for obtaining the new position and velocity of an each particle.

Step 4: If the current fitness value of P_{Besti} is lower than the previous fitness value of P_{Besti}, replace P_{Besti} with the present one. Else previous value of P_{Besti} will be continued again. Similarly, if the current fitness value of G_{Best} is lower than the previous G_{Best}, replace G_{Best} with the present one. Else previous value of G_{Best} will be continued again.

Step 5: If $g < g_{max}$ then $g = g + 1$ and jump to **step 2**, else halt the searching process.

3 Simulation Results and Discussions

In this paper, analysis of BOCDR-based DSS system using MATLAB 15 is reported. These simulation results are procured with PSO algorithm.

The system comprises of an optical source with a power of 10 dBm and wavelength of ~ 1.55 μm, base path for light signal of 2 km, velocity of light of 3×10^8 m/s, and FUT (sensing range) of 700 m. Multiparameter of BOCDR-based DSS system

Table 1 Simulation parameters for proposed (BOCDR-PSO based DSS) system

Simulated parameters	Symbols	Values
Measurement range	d_m	350 m
Effective refractive index of fiber core	n_{eff}	1.46–1.50
Modulating frequency	f_m	293.542 kHz
Reference BFS	ϑ_{B0}	10860 ± 2.3 MHz
Reference strain	ε_{ref}	0%
Strain coefficient of SMF	C_ε	493 MHz/%
Brillouin bandwidth	$\Delta\vartheta_B$	30 MHz
Modulation amplitude of the optical frequency	Δf	5403 ± 1.15 MHz
Acoustic wave velocity	V_a	5300–5900 m/s
Pumping wavelength	λ_0	1.5–1.55 μm

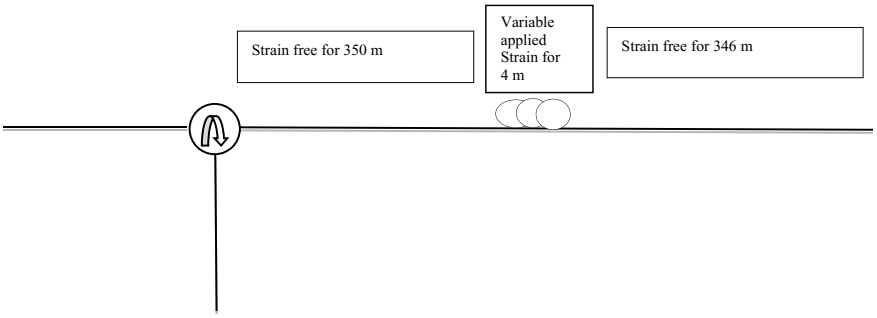

Fig. 2 Structure of SMF under test

are optimized with the help of PSO evolutionary algorithm. The required simulation parameters of our proposed system are given in Table 1.

In this proposed system, FUT is used as standard SMF with a length of 700 m. Out of this FUT length, a 4 m section of FUT was strained from 0 to 0.80%. This 4 m strained section in this FUT starts at 351 m and end at 355 m. System block diagram is shown in Fig. 2. Here, the fiber is having a propagation loss of 0.2 dB/km. Strain resolution and spatial resolution are essential performance metrics in this proposed (BOCDR-PSO-based DSS) system. These metrics amelioration is given in the following segments.

According to Eq. (6), BFS is linearly dependent on the applied strain. If we minimize the BFS error, obviously an error amount in strain parameter will be reduced. In order to minimize this BFS error, we have been used particle swarm optimiza-

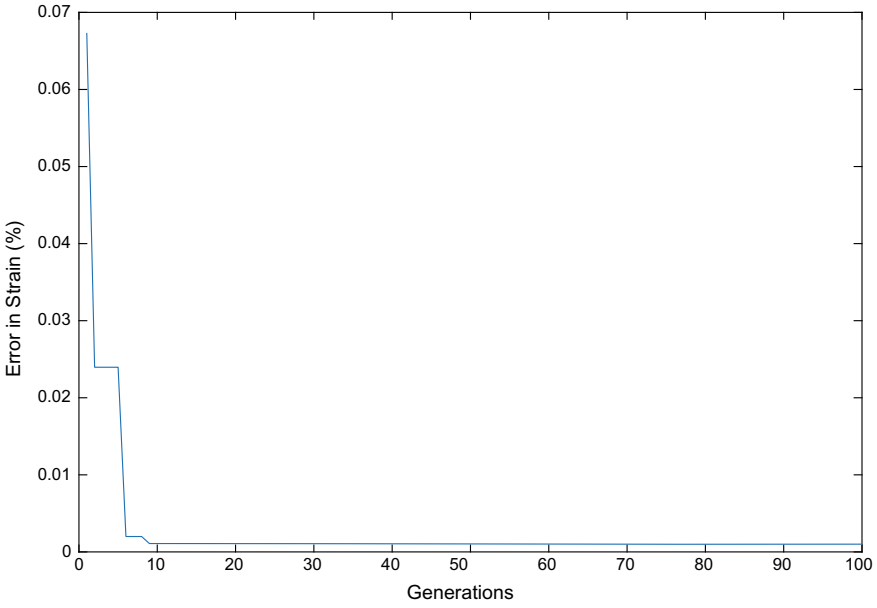

Fig. 3 Error in strain versus generations

tion (PSO) evolutionary algorithm. According to Eqs. (8) and (9), we optimized the effective refractive index of fiber (n_{eff}), acoustic velocity (V_a), and pumping wavelength (λ_0), parameters. The estimated strain error has been reduced from ~0.068 to ~0.0011%, which can be observed from Fig. 3 obtained at 60th stage. In this paper, we have shown PSO evolutionary algorithm with 100 generations. After this 60th generation, the same error is continued up to 100th generation. It means, the used PSO evolutionary algorithm has been convergence at 60th generation with an error of ~0.0011%.

When the specific section or portion of FUT is subjected with different strains, BFS will be varied. If this applied strain raises, the BFS will be shifted to higher frequency level. With the help of this BFS parameter, we can estimate the strain value. Here, the applied strain is varied from 0 to 0.8%, which is observed from a Fig. 4. All these applied strains are evaluated with respective BFS values. In this paper, strained section or segment is from 351 to 355 m of FUT, it has been shown in Fig. 4. From literature review, it is observed that for BOCDR-based DSS system, BFS error has been reported as ± 2.3 MHz [26]. Due to this BFS error, error in estimated strain is ± 0.0046 %. This fluctuation or error can be observed in Fig. 4. This is the major limitation of BOCDR-based DSS system. For an improved accuracy in an estimated strain values, we have used PSO optimization algorithm.

In BOCDR-based DSS system, reference BFS is depending upon the effective refractive index of fiber (n_{eff}), acoustic velocity (V_a), and pumping wavelength (λ_0) parameters. To minimize this BFS error, we have proposed the utilization of

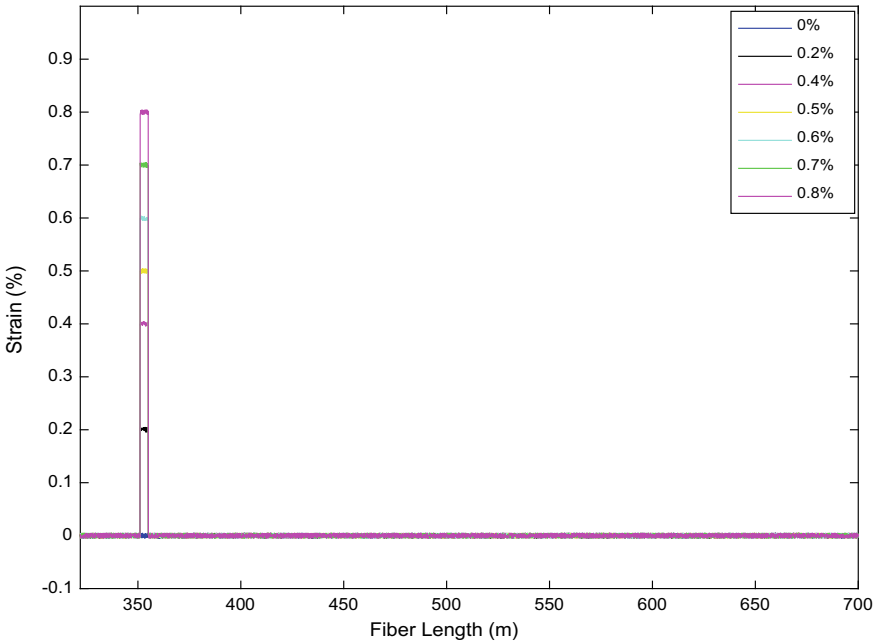

Fig. 4 Estimated strains through BFS in BOCDR-based DSS system

PSO evolutionary algorithm based BOCDR-DSS system. With the help of this PSO algorithm, the above specified parameters have been optimized. In this PSO algorithm, the obtained optimum values of these parameters (n_{eff}, V_a, and λ_0) are 1.483, 5524 m/s and 1.537 μm, respectively. These optimum values obtained at 60th generation stage of PSO method. With the help of these optimum values, BFS error of $\sim \pm 0.5423$ MHz is achieved. Which, in turn, resulted in error minimization of the estimated strain values. It can be observed by Fig. 5. With this BFS error fluctuation minimization, the proposed (BOCDR-PSO based DSS) system has exhibited a strain error of $\sim \pm 0.0011\%$. For this strain extraction process, strain coefficient of SMF is considered to be 0.00202%/MHz, which is fixed for this system.

According to Eq. (6), BFS is linearly dependent on the applied strain. If the applied strain varies, BFS value will vary. Here the applied strain varies from 0 to 0.8%. From Fig. 6, we have two linear lines with blue and red colors. Here blue color specifies conventional BOCDR-based DSS system and red color specifies proposed (BOCDR-PSO based DSS) system. From Fig. 6, it is clearly observed that over the range of applied strain, the proposed sensing system offer less BFS error as compared with a conventional BOCDR-based DSS system.

Figure 7 gives the spatial resolution of a conventional BOCDR based DSS system. This spatial resolution value came with modulation frequency f_m of 293.542 kHz, optical fiber core refractive index of (n) of 1.46. According to Eq. (1), the corresponding measurement range d_m is 350 m. When the modulation amplitude of the

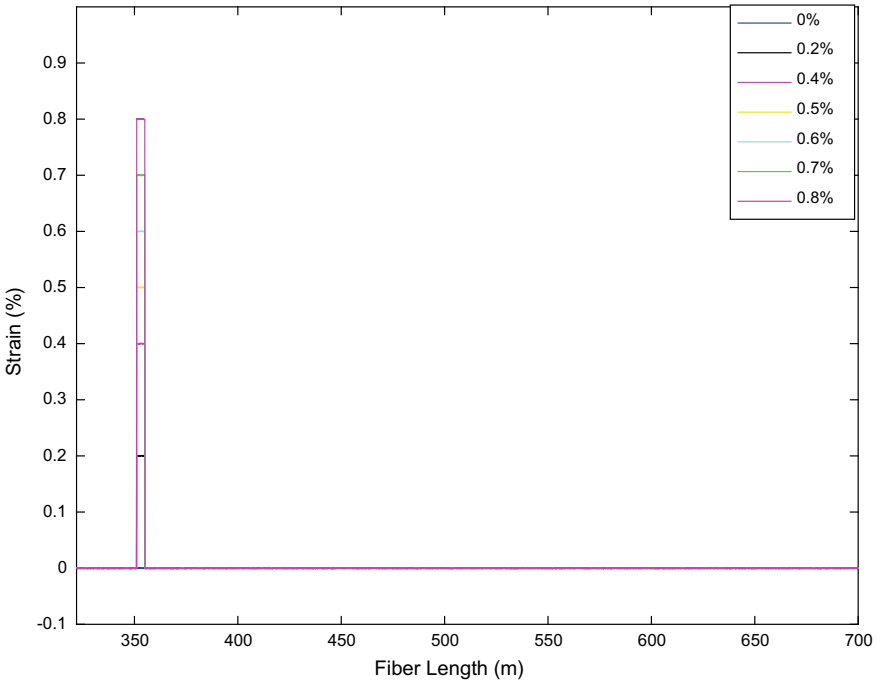

Fig. 5 Estimated strains through BFS in the proposed system

optical frequency Δf is 5403 ± 1.15 MHz and Brillouin bandwidth $\Delta\vartheta_B$ is 30 MHz, according to Eq. (2) resulting spatial resolution is 43.97 cm.

According to theory, spatial resolution is calculated by considering the 10–90% value of estimated strain [17]. Due to the optimization, in effective refractive index of fiber (n_{eff}) and minimization of BFS (ϑ_B) error, the resultant spatial resolution obtained is 43.45 cm. Here, the enhancement in spatial resolution is ~0.5 cm. This improvement can be observed from Fig. 8.

4 Conclusion

In summary, BOCDR-PSO based distributed strain sensing (DSS) system is proposed and analyzed for improving the strain resolution and spatial resolution. By applying multiparameter optimization on effective refractive index of fiber, pumping wavelength and acoustic velocity in fiber, we have achieved better strain resolution and spatial resolution over existing BOCDR-based DSS systems. Here, we have considered a 700 m length of SMF for strain sensing application. With our proposed DSS system, ~0.0011% strain resolution and ~43 cm spatial resolution are achieved and shown through simulation using MATLAB 15.0. The proposed system can be

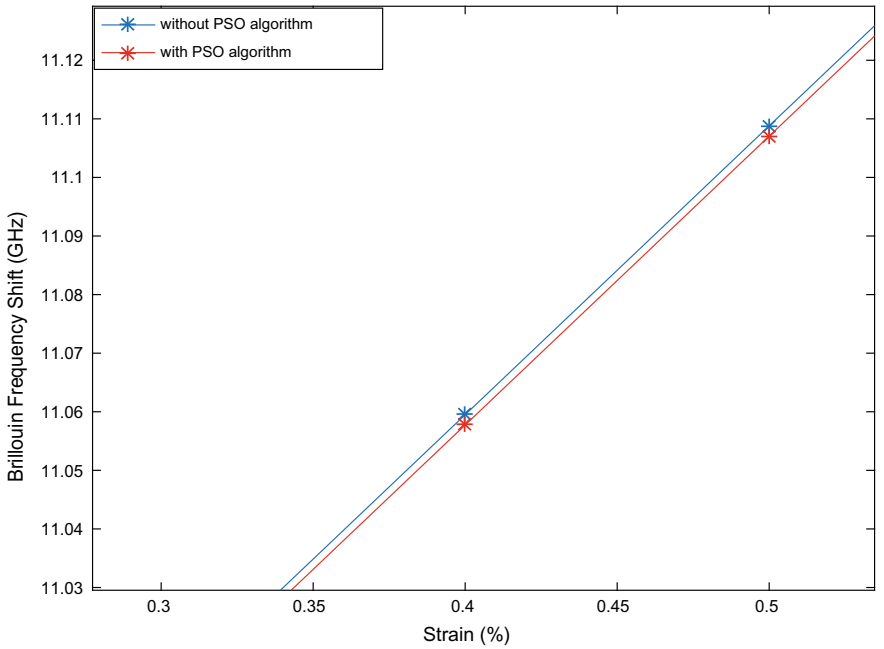

Fig. 6 Estimated BFS for different applied strains in conventional and proposed systems

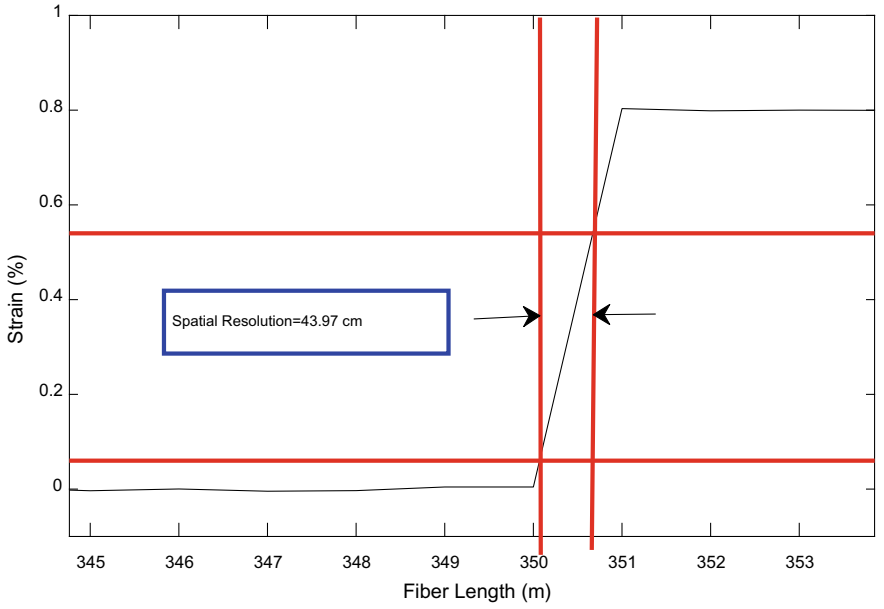

Fig. 7 Spatial resolution in BOCDR-based DSS system

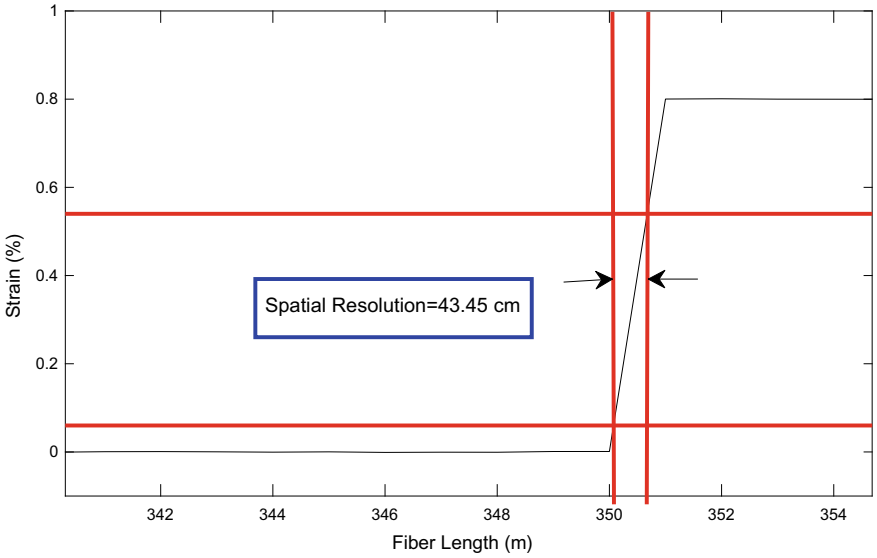

Fig. 8 Spatial resolution of the proposed system

treated as a potential candidate for real-time sensing application such as in structural health monitoring in the field of civil engineering, defense and aviation industries, etc.

References

1. Lee B (2003) Review of the present status of optical fiber sensors. J Opt Fiber Technol 9(2):57–79
2. Abdurrahman G, Gunes Y, Karlik SE (2008) Spontaneous raman power and Brillouin frequency shift method based distributed temperature and strain detection in power cables. J Opt Fiber Technol
3. Horiguchi T, Shimizu K, Kurashima T, Tateda M, Koyamada Y (1995) Development of a distributed sensing technique using Brillouin scattering. J Lightw Technol 13(7):1296–1302. IEEE
4. Yu JW, Park Y, Oh K (2002) Brillouin frequency shifts in silica optical fiber with the double cladding structure. J Optic Exp 10(19):996–1002. OSA
5. Taki M, Soto MA, Pasquale FD, Bolognini G (2011) Long-range BOTDA sensing using optical pulse coding and single source bi-directional distributed raman amplification. J Opt Sens. IEEE
6. Ravet F, Zou L, Bao X, Chen L, Huang RF, Khoo HA (2006) Detection of buckling in steel pipeline and column by the distributed Brillouin sensor. J Opt Fiber Tech, Elsevier, pp 305–311
7. Zhao Z, Soto MA, Tang M, Martin-Lopez S, Thevenaz L (2016) Distributed shape sensing using Brillouin scattering in multi-core fibers. J Opt Exp 24(22):25211–25223. OSA
8. Zhang D, Wang J, Zhang P, Shi B (2017) Internal strain monitoring for coal mining similarity model based on distributed fiber optical sensing. J Opt Meas, Elsevier, pp 234–241

9. Bergman A, Langer T, Tur M (2017) Phase-Based, high spatial resolution and distributed, static and dynamic strain sensing using Brillouin dynamic gratings in optical fibers. J Opt Exp 25(5):5376–5388. OSA
10. Garus D, Krebber K, Schliep F (1996) Distributed sensing technique based on Brillouin optical-fiber frequency domain analysis. Opt Lett 21(17):1402–1404
11. Minardo A, Bernini R, Zeni R (2014) Distributed temperature sensing in polymer optical fiber by BOFDA. IEEE Photon Technol Lett 24(4):387–390. IEEE
12. Hotate K, Hasegawa T (2000) Measurement of Brillouin gain spectrum distribution along an optical fiber using correlation-based technique-proposal experiment and simulation. Trans Electron E83-C(3):405–412. IEICE
13. Song KY, Hotate K (2008) Brillouin optical correlation domain analysis in linear configuration. Lett Photon Technol 20(24):2150–2152. IEEE
14. Gao J, Shi B, Zhang W, Zhu H (2006) Monitoring the stress of the post-tensioning cable using fiber optic distributed strain sensor. J Opt Meas, Elsevier, pp 420–428
15. Li B, Luo L, Yu Y, Soga K, Yan J (2017) Dynamic strain measurement using small gain stimulated Brillouin scattering in STFT-BOTDR. J Opt Sens 17(9):2718–2724. IEEE
16. Soto MA, Sahu PK, Bolognini G, Pasquale FD (2008) Brillouin-Based distributed temperature sensor employing pulse coding. J Opt Sens 8(3):225–226. IEEE
17. Himansu SP, Sahu PK (2016) Brillouin distributed strain sensor performance improvement using FourWaRD algorithm. J Opt, Elsevier, pp 2666–2669
18. Yanjun Z, Yu C, Xinghu F, Wenzhe L, Weihong B (2015) Spectrum parameter estimation in Brillouin scattering distributed temperature sensor based on cuckoo search algorithm combined with the improved differential evolution algorithm. J Opt Comm, Elsevier, pp 15–20
19. Himansu SP, Sahu PK (2015) Brillouin distributed temperature sensor employing phase modulation and optimization techniques. J Opt Comm, Elsevier, pp 788–794
20. Maraval D, Gabet R, Jaouen Y, Lamour V (2017) Dynamic optical fiber sensing with Brillouin optical time domain reflectometry: application to pipeline vibration monitoring. J Lightw Technol 35(16):3296–3302. IEEE
21. Mizuno Y, Zou W, He Z, Hotate K (2010) Operation of Brillouin optical correlation-domain reflectometry: theoretical analysis and experimental validation. J Lightw Technol 28(22):3300–3306. IEEE
22. Mizuno Y, Zou W, He Z, Hotate K (2008) Proposal of Brillouin optical correlation-domain reflectometry (BOCDR). J Opt Exp 16(16):12148–12153. OSA
23. Hayashi N, Mizuno Y, Nakamura K (2014) Distributed Brillouin sensing with centimeter-order spatial resolution in polymer optical fibers. J Lightw Technol 32(21):3999–4003. IEEE
24. Hayashi N, Mizuno Y, Nakamura K (2014) First demonstration of distributed Brillouin measurement with centimeter-order resolution based on plastic optical fibers. In: International Conference. pp 377–379. IEEE
25. Hayashi N, Mizuno Y, Nakamura K (2014) Simplified configuration of Brillouin optical correlation-domain reflectometry. J Photon Technol 6(5). IEEE
26. Hayashi N, Mizuno Y, Nakamura K (2014) Alternative implementation of simplified Brillouin optical correlation-domain reflectometry. J Photon Technol 6(6). IEEE
27. Jiang F, Yu C, Xia H, Tran QA, Ha QM, Tran NQ, Hu J (2017) A new binary hybrid particle swarm optimization with wavelet mutation. J Opt Comm, Elsevier, pp 90–101
28. Ramachandra Murthy KVS, Ramalinga Raju M, Govinda Rao G (2010) Comparison between Conventional, GA and PSO with respect to optimal capacitor placement in agricultural distribution system. In: International Conference of INDICON. IEEE
29. Voratas K (2012) Comparison of three evolutionary algorithms: GA, PSO, and DE. J Ind Eng Manag Sys 11(3):215–223. IEEE
30. McCall J (2005) Genetic algorithms for modelling and optimization. J Comp App Math, Elsevier, pp 205–222

31. Blum C (2005) Ant colony optimization: introduction and recent trends. J Phys, Elsevier, pp 353–373
32. Jiang T, Su X, Han W (2017) Optimization of support scheduling on deck of carrier aircraft based on improved differential evolution algorithm. In: Proceedings of 3rd International Conference on Control Science and Systems Engineering, pp 136–140. IEEE

Interference Minimized Slot Scheduling for Coexisting WBANs: Delay and Priority-Based Approach

Prajna Paramita Pradhan and Sanghita Bhattacharjee

Abstract Nowadays wearable body sensors are widely used for monitoring the physiological signs of the human body. A Wireless Body Area Network (WBAN) usually consists of a single coordinator and multiple computational constraint body sensors. In WBANs, mitigation of interference is an important issue to improve the network throughput. Interference occurs when multiple WBANs come within the proximity of each other, and every one wants to send their data at the same time. In this paper, we mainly focus on interference minimization for coexisting WBANs. The main objective is to schedule all nodes in the network in an interference free manner so that the spatial reuse factor is improved. We use both Protocol and Physical interference model to capture the interference at a WBAN. Moreover, a Delay-Aware Priority-based Scheduling algorithm (abbreviate shortly as DAP) is proposed where the priority of nodes and interfering nodes are taken into account to schedule the body sensors. Simulations are performed in different network scenarios and compared with ID, degree and ITLS based scheduling. The simulation results show that the priority based scheduling has better performance than ID, degree, and ITLS-based scheduling algorithm.

Keywords Wireless body area networks · Protocol interference model · Physical interference model · Interference graph · Priority · Waiting time · Scheduling

P. P. Pradhan (✉) · S. Bhattacharjee
Department of Computer Science and Engineering, National Institute of Technology, Durgapur, Durgapur, India
e-mail: ppp.16cs1103@phd.nitdgp.ac.in

S. Bhattacharjee
e-mail: sanghita.b@gmail.com

© Springer Nature Singapore Pte Ltd. 2020

V. Janyani et al. (eds.), *Optical and Wireless Technologies*,
Lecture Notes in Electrical Engineering 546,
https://doi.org/10.1007/978-981-13-6159-3_21

1 Introduction

Recent advances in real-time technology have made mobile health care [1] as a promising solution to provide services in many domains such as vital physiological sign monitoring, chronological diseases monitoring, risk detection, and telemedicine. Generally, mobile or pervasive healthcare monitoring can be achieved by implanting sensor nodes inside the human body or outside human body. A wireless body area network (WBAN) is a popular example of healthcare monitoring system, which continuously monitors the biological parameters of the body and sends the aggregated information to the remote healthcare server for analysis. A typical WBAN consists of a single coordinator and multiple sensors with limited power, memory, and computational capability. Sensors measure the physiological signals of the body and transmit them to the coordinator. At the same time, the coordinator can act as a sink, which collects the data attained by the sensors, aggregates them, and communicates it to the remote healthcare system.

Interference minimization is one of the challenging issues in WBANs. Due to the broadcasting nature of the wireless medium and the limited available spectrum, a WBAN suffers from unwanted interference [2–4] from the nearby WBANs. The situation becomes worse when multiple WBANs come within the close proximity of each other. High interference may cause low network performance, misinterpretation of the signals, which even lead to the patient's death. Interference minimization in body area networks has been extensively studied in the previous works such as in [5–8]. Scheduling is one of the effective mechanisms to reduce the inter-BAN interference in body area networks. A data priority based slot assignment in WBANs was proposed in [5]. Algorithm in [5] utilizes the slot utilization rate to verify whether the allocation is energy efficient or not. The authors in [6] studied an interference-aware traffic-priority-based link scheduling (ITLS) algorithm to overcome the interference among the coexisting WBANs in dense wireless networks. A game theory based approach to minimize interference by allocating different slots to WBANs was developed in [7]. In [7], the authors have only studied inter-BAN interference, however, intra-BAN interference was not taken into consideration. In [8], the authors proposed a distributed coloring algorithm to achieve conflict-free scheduling of nodes. In [9], the authors offered interleaved schedule-based data transmission method to reduce the interference as well as the waiting time of nodes. Another graph theory based approach, regret matching based transmission was proposed in [10] to allocate different slots to the interfering links. Multichannel MAC can be also used to reduce the interference [11, 12]. In [12], the authors developed three heuristic algorithms to minimize cross-layer interference in WBANs. In [13], the authors adopted link scheduling algorithm with interference prediction (LSIP) to minimize inter-WBAN interference. A node-level self-organizing interference avoidance scheme (SIAC) to minimize node-level interference by incorporating self-organization and smart spectrum allocation to WBANs was developed in [14].

In this paper, we mainly focus our attention on interference mitigation for coexisting WBANs. We propose a Delay-Aware Priority-based scheduling algorithm (abbreviated shortly as DAP), which schedules the nodes in the network in non-interfering slots so that the spatial reuse factor is improved. In our work, we consider both Protocol model [3] as well as Physical model [3] to find the interfering nodes of a WBAN and to capture the level of interference. Since WBANs use wireless communications for data propagation, there exists a certain level of uncertainties in data transmission depending upon the condition of human health. In this paper, we prioritize the body sensors based on the physiological signals. Here, we introduce 2-tuple <*Total collected data*, *Waiting time*> based priority setup for each sensor. We use data generation time and data generation rate to find the total collected data, while maximum delay time, number of interfering nodes and their total collected data are used to find the waiting time of a node. Next, the nodes are scheduled according to their priority so that a high priority node gets service as soon as it requires. Simulations are performed to evaluate the effectiveness of the proposed algorithm with respect to different performance metrics.

The paper is organized as follows. Section 2 describes the system model. In Sect. 3, we present our proposed algorithm briefly. Section 4 describes the simulation environment. Simulation results are also discussed in Sect. 4. Finally, we conclude the paper in Sect. 5.

2 System Model

In this section, we present our system model, including network model and interference model used throughout the paper.

2.1 Network Model and Assumptions

We consider a wireless network composed of M number of WBANs, which are denoted as $\{B_i | i = 1, 2, \ldots, M\}$. Each WBAN ($B_i$) consists of a central coordinator and n_i sensor nodes. The coordinator in B_i is represented as c_i, while the jth sensor in B_i is denoted as n_j^i. We assume that each coordinator is stationary, is equipped with a single half-duplex interface and has a fixed communication range (T_r). The coordinator can be placed anywhere in the body, e.g., abdomen, ankle, arm, wrist, etc. However, in this model, we use the coordinate of sensor nodes in a WBAN to find the position of the coordinator. We take the coordinate (X_j, Y_j) of each sensor j within a WBAN, calculate the mean value and then place the coordinator at that location. The position of c_i in each B_i is given in Eq. (1).

$$c_i(X, Y) = (\frac{1}{|n_i|}\sum_{j \in n_i} X_j, \frac{1}{|n_i|}\sum_{j \in n_i} Y_j) \quad (1)$$

In each WBAN, the nodes send their packet according to their priority. We employ simple Time Division Multiple Access (TDMA) based packet transmission for the nodes, where each superframe (T_f) is divided into an equal number of time slots. Let the length of each time slot is T_s. Sensor nodes belonging to different WBANs can transmit their data to their respective coordinators if and only if they are not interfering with each other.

2.2 Interference Model

Each WBAN can potentially interfere with other WBANs and the interference among coexisting WBANs may degrade the network performance significantly. Therefore, it is essential to find the number of interfering nodes of a WBAN accordingly. Here, we use protocol and physical interference model to capture the interference of a WBAN as well as the interfering nodes.

Case 1: Finding the interfering node set using the Physical Interference model:
In this case, WBANs experience SINR-based interference. Let, δ is the SINR [2] and δ_{th} is the SINR threshold. The high priority sensor n_j^i in B_i is disturbed by the high priority node n_l^k in B_k if δ at n_j^i is less than equal to δ_{th} where δ is

$$\delta = \frac{p_t(j)}{d_{ij}^2(N_0 + p_t(l)d_{il}^{-2})} \leq \delta_{\text{th}} \quad (2)$$

Here, $p_t(j)$ is the transmit power of node j and N_0 is the thermal noise. For sake of simplicity, let, $N_0 \ll 1$ and $p_t(j) = p_t(l) = P$. Then Eq. (2) is rewritten as

$$\delta = \frac{d_{il}^2}{d_{ij}^2} \leq \delta_{\text{th}} \quad (3)$$

Therefore,

$$INS_i = \{n_l^k | n_l^k \in B_k, \delta_{\text{th}}\left(\frac{d_{ij}^2}{d_{il}^2}\right) > 1\} \quad (4)$$

Case 2: Finding the interfering node set using the Protocol Interference model:
In this type of model, WBANs experience distance-based interference. The transmission at coordinator c_k in B_k is interfered by the sensor n_j^i in B_i if $d_{jk} \leq T_r$, where d_{jk} is the distance between the sensor j and c_k. The list of interfering nodes of c_k is denoted by INS_k and it is given as

$$INS_k = \{n_j^i | d_{jk} \leq T_r, n_j^i \in B_i \wedge c_k \neq c_i\}. \quad (5)$$

2.2.1 Interference Graph

Given M number of WBANs, an interference model and set of interfering nodes, we can build the interference graph. The interference graph represented by $G_I = (n(I), E(I))$ is defined as follows:

- $n(I)$: set of nodes in WBANs, where $n = \sum_{i=1}^{M} n_i$
- $E(I)$: set of interfering edges between the nodes in WBANs, i.e.,

$$E(I) = \{(j, l) | j \in B_i, l \in INS_i \vee j, l \in B_i\}$$

2.2.2 An Example

A wireless topology consisting of 3 coexisting WBANs (say B_1, B_2, and B_3) is illustrated in Fig. 1. Sensor distribution in each WBAN is as $B_1 = \{1, 2, 3, 4\}$, $B_2 = \{8, 9, 10\}$, and $B_3 = \{5, 6, 7\}$. The interfering node set of each WBAN is $INS_1 = \{5, 8\}$, $INS_2 = \{4, 7\}$, and $INS_3 = \{3, 8\}$. Figure 2a depicts the interference graph of the 3-WBANs scenario using the physical model, while Fig. 2b shows the interference graph using the protocol model.

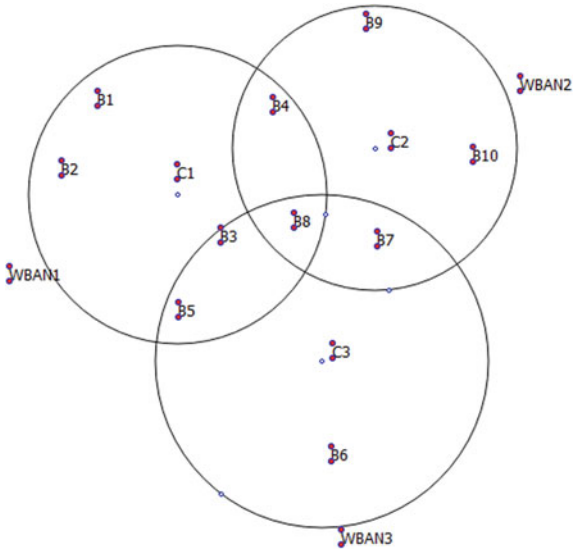

Fig. 1 Coexistence of WBANs

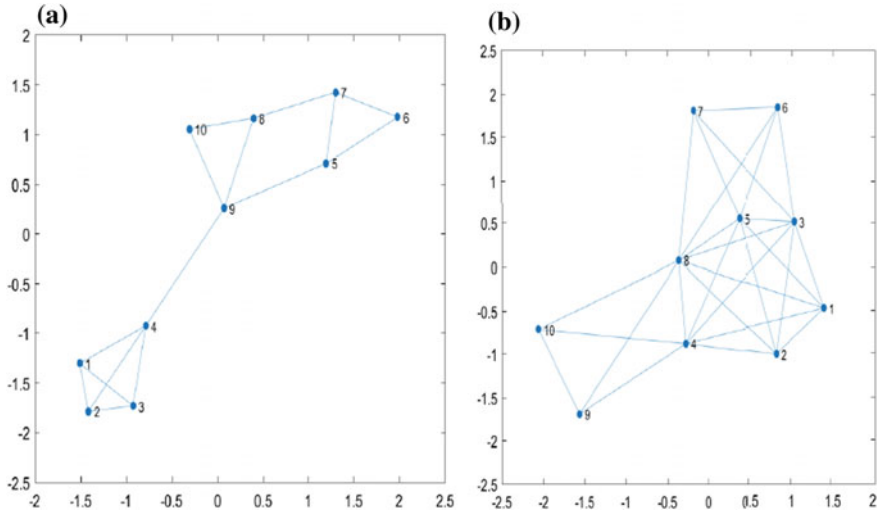

Fig. 2 **a** Interference graph using physical model. **b** Interference graph using protocol model

3 Proposed Approach

In this section, we briefly describe our proposed method. In some medical applications, sensor nodes generate urgent data and that need to be transmitted first. Therefore, nodes in a WBAN can either be urgent type or non-urgent type. For example, sensor data in seriously ill patient should be transmitted as early as possible and also in conflict-free manner. In each WBAN, the coordinator synchronizes the transmission of the nodes according to their priority. The priority of each node is calculated based on the node's level parameters as discussed subsequently.

3.1 Priority Calculation

In our work, we use 2-tuple $< TCD_j, WT_j >$ based priority for each node j in B_i where TCD_j is the total collected data and WT_j is the waiting time of node j. The total collected data of a node is calculated on based on data generation time DGT_j and data generation rate DGR_j. While the waiting time is computed based on the number of interfering nodes and total collected data. The detailed calculation of TCD_j and WT_j of each node j are as follows.

- *Maximum delay time*: It is the maximum time that a node can wait in queue to get its slot in the superframe. An urgent node has minimum delay, while a non-urgent node has higher delay. The maximum delay time of each node j is presented by MDT_j.

- *Data generation time*: It is the time duration which a node collects its data. It is defined as the number of slots given to a node multiplied by the slot duration. Usually, slot duration is fixed for each node. However, data generation time for an urgent node is smaller than that of a non-urgent node.

$$DGT_j = \text{Number of assigned slots for } j \times T_s \tag{6}$$

- *Data generation rate*: Data generation rate is the rate at which a node generates its data. An urgent node has higher rate and a non-urgent node has the lowest rates.
- *Total collected data*: It is the amount of data generated by the node. The total collected data of *j*th node in *i*th WBAN is given by

$$TCD_j = DGT_j \times DGR_j \tag{7}$$

- *Waiting time*: The waiting time is the time that a node has to wait in the queue to get service. It depends on the number of interfering nodes and their total collected data. Higher waiting time implies longer delay in getting service. Urgent nodes should have smaller waiting time than non-urgent nodes in the network. Each WBAN calculates the waiting time for the nodes and the waiting time of *j*th node in *i*th WBAN is calculated using the following formula:

$$WT_j = \sum_{l \in INS_i \wedge j \in B_i} (TCD_l \times \frac{L}{R}) \tag{8}$$

  where L is the packet size and R is transmission rate.
- Let P_Q be a vector in descending order of priority of the nodes, i.e., the vector P_Q contains the urgent nodes followed by non-urgent nodes.

3.2 Delay-Aware Priority Based Scheduling for Coexistence of WBANs

In this section, we present our Delay-Aware Priority (DAP) based Scheduling algorithm for wireless body area networks. The objective of our algorithm is to schedule the body sensors of coexisting WBANs in a conflict-free manner. DAP schedules the nodes through iterations, i.e., at each iteration, we schedule the sensors which are not interfering. The working principle of DAP is as follows. At first, the coordinator calculates the priority of each sensor in each WBAN and puts the sensors in the vector P_Q. Then the vector P_Q is sorted in descending order of the priority. Next, the sorted vector P_Q is divided into two equal sized sets, i.e., P_{Q+1} and P_{Q+2}. The set P_{Q+1} contains the higher priority nodes, while P_{Q+2} contains the lower priority nodes. In our algorithm, we schedule the nodes in P_{Q+1}, followed by nodes in P_{Q+2}. We allocate slot to the highest priority node (say j) in P_{Q+1} only if the waiting time

of j is lower than the maximum delay time of j. Otherwise, the node j is deleted from P_{Q+1} and add it to the head of P_{Q+2}. After scheduling of P_{Q+1}, we start slot allocation for nodes in P_{Q+2}, and repeat the previous steps again and again until all nodes get proper slots. When all nodes in the networks acquire conflict free slots, the algorithm terminates. At every iteration, the waiting time of each non-scheduled node is updated, however, the maximum delay time of each node remains unchanged. The pseudo code of the proposed algorithm is given in Algorithm 1.

Algorithm 1: Delay-Aware Priority based Scheduling for coexisting WBANs

Input: $\mathrm{V}, G_I, P_Q, TCD_j, WT_j, MDT_j, \forall j \in V$

Output: Interference free slots for V

1. **for** each node j = 1 to n **do**
2. Coordinator calculates priority of j
3. Put node j in P_Q
4. **end for**
5. Sort P_Q in descending order of priority
6. Create Current set C_s
7. Initial $C_s = P_Q$, $W = \{n_j^i | j = 1..,2,\ldots.n, i = 1,2,\ldots M\}$
8. **while** $(W \neq \emptyset)$ **do**
9. Divide C_s into two equal sized sets P_{Q+1} and P_{Q+2}
10. **while** $(P_{Q+1} \neq \emptyset)$ **do**
11. Schedule the nodes in P_{Q+1}
12. Take the highest priority node (say j) from P_{Q+1}
13. **if** $WT_j > MDT_j$ **then**
14. Delete j from P_{Q+1}
15. Add j to head of P_{Q+2}
16. Update P_{Q+1} and P_{Q+2}
17. **else**
18. **If** j is not interfering with any node in that slot , schedule j in slot t
19. Update waiting time of each non-scheduled node in P_{Q+1} & P_{Q+2}
20. Delete j from W
21. Otherwise, schedule j in next slot $(t + 1)$
22. **end if**
23. **end while**
24. **If** nodes in P_{Q+1} are scheduled, assign P_{Q+2} to current set C_s and repeat steps (8) to (22).
25. **end while**

3.3 DAP Example

Scheduling of the nodes using the proposed DAP is shown in Fig. 3. In this example, 3 coexisting WBANs illustrated in Fig. 1 is considered. Moreover, the physical interference is used to build the interference graph of the given network topology. The set of urgent nodes in descending order of their priority is denoted as $P_{Q+1} = \{B_4, B_9, B_8, B_7, B_5\}$ and the set of non-urgent nodes is

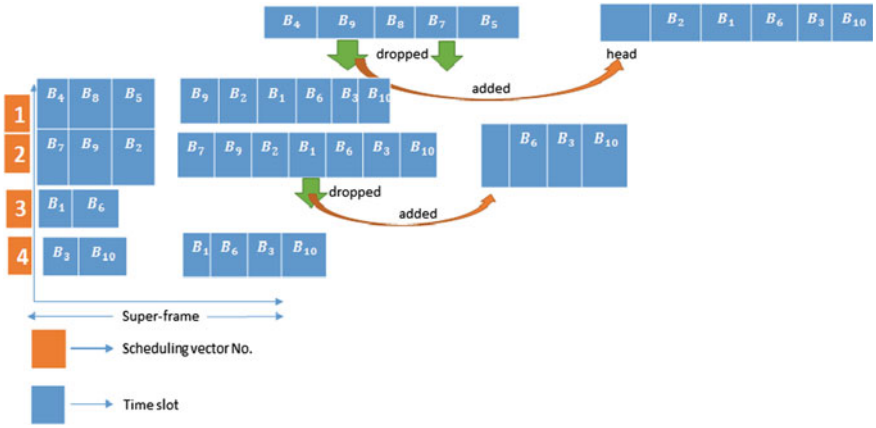

Fig. 3 Scheduling of sensor nodes

as $P_{Q+2} = \{B_2, B_1, B_6, B_3, B_{10}\}$. DAP schedules the urgent nodes in different WBANs first. First, we take the urgent nodes B_4 and B_9. Since they are urgent, they have to be scheduled first. However, B_4 and B_9 are connected by an interfering edge. So, node B_4 is chosen because B_4 has lower waiting time than B_9. Waiting time of B_9 is higher than the maximum delay time, so it is dropped from the priority vector and added to the head of the second vector. B_8 can share the same slot with B_4 as they are not interfering. Let the waiting time of B_7 is higher so, it is dropped and B_5 is scheduled in first scheduling vector of the superframe. Node B_7 gets slot in the second scheduling vector. Similarly, B_1, B_6, and B_3, B_{10} occupied third and fourth scheduling vector of the superframe, respectively. Therefore, four scheduling vector is required to complete scheduling of sensor nodes.

4 Performance Evaluation

In this section, the performance of proposed DAP is evaluated and compared with ID-based scheduling, degree-based scheduling, and ITLS [6]. All algorithms are simulated through MATLAB R2016. In ID-based scheduling, slots are allocated to the nodes according to the node ID (here high to low is used). In degree-based scheduling, the node with the higher degree gets an earlier slot than the node with the smallest degree.

4.1 Simulation Environment

In our simulation, we consider a wireless topology where sensor nodes (nodes in WBANs) are randomly deployed in a square area of size 20 × 20 m^2. To evaluate the performance of the proposed algorithm (DAP), we vary the number of nodes in the range [10, 20] and vary the number of WBANs from 1 to 4. We define the transmission range of a coordinator as the maximum distance from the coordinator to the nodes in the WBAN. The transmission range of the coordinators is [17.5 m, 13.66 m, 10.73 m, 12.42 m]. We set the maximum delay time of each node in the range [0.0318 ms, 0.9 ms]. We also fix the data generation rate of each node in the range [0.0103, 0.9430] kbps. In our study, the length of the superframe is 200 ms and the slot duration is fixed to 8 ms. The transmit power and receiver sensitivity are set as 20 dBm and 90 dBm, respectively, as specified in the IEEE 802.15.4 standard, similar to [6]. We use the free space propagation model with a path loss component of 2. The simulation parameters used in this simulation are listed in Table 1.

4.2 Results and Discussions

To evaluate the performance of the proposed algorithm, we use two metrics: (i) percentage of packet reception, and (ii) spatial reuse factor. The percentage of packet reception at each WBAN is evaluated as Commutative SINR experienced at each node. Higher value implies better packet reception. Figure 4 shows the percentage

Table 1 Simulation parameters

Parameter	Value
Simulation area	20 m × 20 m
WBAN topology	Star topology
Number of WBANs	1, 2, 3, 4
Types of nodes	Urgent node and non-urgent node
Number of nodes	10, 20
Transmission range (m)	17.5, 13.66, 10.73, 12.42
Data generation rate (kbps)	[0.0103, 0.9430]
Length of packet (bytes)	[30.71, 77.92]
Channel capacity (bps)	[0.0057, 0.1872]
Maximum delay time (ms)	[0.0318, 0.9]
Maximum slots	10, 20
Slot duration	8 ms
Path loss component	2
Simulation time	250 s

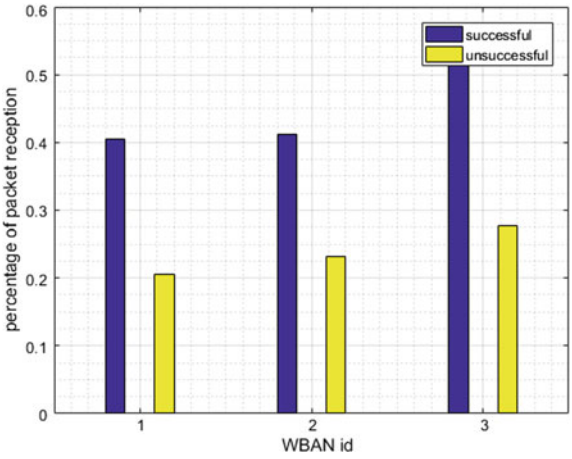

Fig. 4 Percentage of packet reception versus WBAN ID

of packet reception at each WBAN. From Fig. 4, we have seen that WBAN 3 has higher packet reception, whereas WBAN 1 has lower reception. It means WBAN 3 has less number of interfering nodes than that of WBAN 1.

Our next metric is spatial reuse factor and it is defined as the number of slots required for transmitting one packet by all nodes in the network. Higher number of slots implies lower spatial value. Figure 5a, b shows the scheduling vector of nodes. In this experiment, we use 3-WBANs which consist of 10 sensor nodes. We consider also two interference models, i.e., protocol and physical model. Figure 5a shows the slot of the nodes for different algorithms using physical interference, while Fig. 5b displays the slot allocation using protocol interference. From Fig. 5a, we have noticed that a less number of slots (i.e., 4) is required to schedule the nodes when the physical model takes into consideration. In Fig. 5c, d we have compared our proposed DAP algorithm with ITLS [6] algorithm, and observed that urgent nodes in DAP schedule earlier than the urgent nodes in ITLS. In ITLS, nodes in the interference region have higher priority and this restricts the actual urgent nodes to get the slots in earlier. However, this is not true in our case and this is the reason for the lower delay and higher spatial value. The spatial reuse factor versus number of WBANs is shown in Fig. 6b. Reuse factor decreases when more WBANs are added to the network. When number of node increases, high interference may arise among the WBANs, which may result lower reuse factor value. The performance of spatial reuse factor for ID-based, degree-based and priority-based scheduling algorithms are illustrated in Fig. 6a. In both interference models, degree-based scheduling has lowest spatial reuse, i.e., it requires more slots to synchronize the nodes. However, priority-based scheduling achieves higher spatial reuse factor than the other two algorithms. In other words, the maximum number of sensor nodes can get service in the same slot when priority-based scheduling is considered.

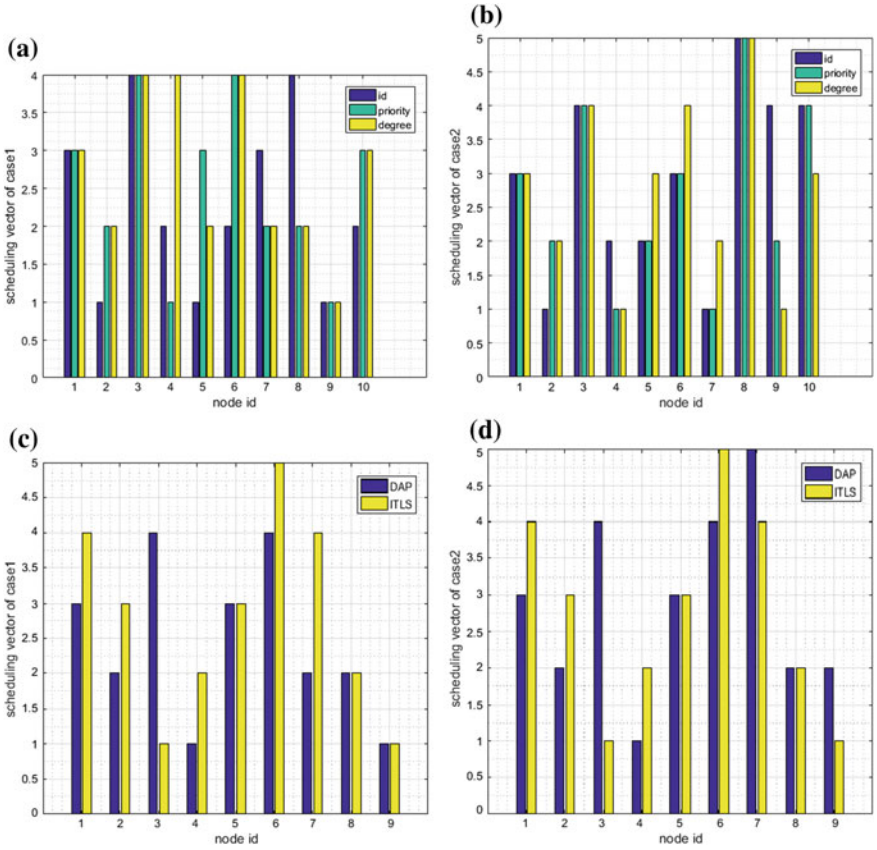

Fig. 5 **a** Scheduling vector of nodes (interference model: the physical model). **b** Scheduling vector of nodes (interference model: the protocol model). **c** Scheduling vector for DAP and ITLS (interference model: the physical model). **d** Scheduling vector for DAP and ITLS (interference model: the protocol model)

5 Conclusion

In this paper, a *Delay-Aware Priority* based scheduling algorithm for coexisting WBANs has been proposed to increase the spatial reuse of the network. Both physical model and protocol model are used to capture the interference at each WBAN. For each node, the proposed algorithm assigns a 2-tuple based priority. Our proposed algorithm schedules the high priority nodes at earlier slots only if the waiting time of the nodes is less than the maximum delay time. The performance of the proposed algorithm is evaluated via simulations and the results show that the proposed method has higher spatial reuse.

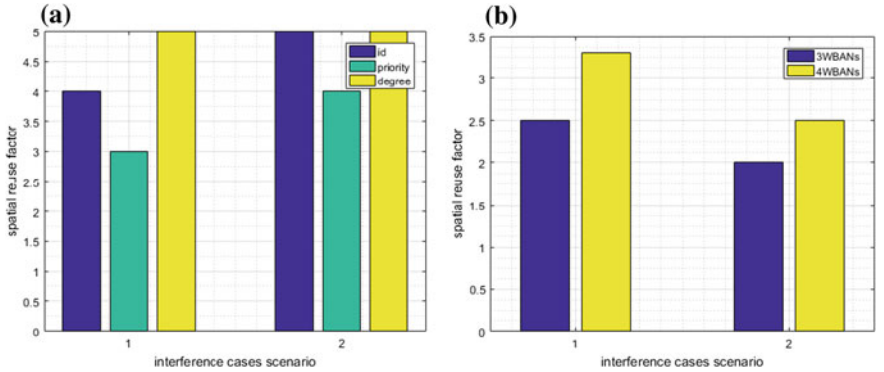

Fig. 6 **a** Spatial reuse factor for different algorithm. **b** Spatial reuse factor for number of WBAN. Case 1: physical interference model. Case 2: protocol interference model

Acknowledgements The first author wishes to thank the Director, National Institute of Technology, Durgapur, India for providing the facilities and support to carry out this work.

References

1. Ko JG, Lu C, Srivastava MB, Stankovic JA, Terzis A, Welsh M (2010) Wireless sensor networks for healthcare. In: Proceedings of IEEE, vol 98, pp 1947–1960
2. Lu J, Wang X (2012) Interference-aware probabilistic routing for wireless sensor networks. J Tsinghua Sci Technol 17:575–585
3. Li X-Y, Moaveni-Nejad K, Song WZ, Wang WZ (2005) Interference-aware topology control for wireless sensor networks. In: Second annual IEEE communications society conference on sensor and ad hoc communications and networks (SECON). IEEE Press, pp 263–274
4. He Y, Yuanyuan Z (2006) Interference-aware topology control problem in wireless sensor networks. In: Proceedings of 6th IEEE international conference on ITS telecommunications. IEEE Press, pp 969–972
5. Kong R, Chen C, Yu W, Yang B, Guan X (2013) Data priority based slot allocation for wireless body area networks. In: IEEE international conference on wireless communications and signal processing (WCSP), pp 1–6
6. Le T, Moh S (2016) An interference-aware traffic-priority-based link scheduling algorithm for interference mitigation in multiple wireless body area networks. J Sens 16:2190
7. Seo S, Bang H, Lee H (2016) Coloring-based scheduling for interactive game application with wireless body area networks. J Supercomput 72:185–195
8. Wen H, Quek TQS (2015) On constructing interference free schedule for coexisting wireless body area networks using distributed coloring algorithm. In: Proceedings of 12th IEEE international conference on wearable and implantable body sensor networks (BSN). IEEE Press, pp 1–6
9. Judhistir M, Misra S, Manjunatha M, Islam N (2012) Interference mitigation between WBAN equipped patients. In: Proceedings of 9th IEEE international conference on wireless and optical communications networks (WOCN). IEEE Press, pp 1–5
10. Vladimir M, Sayrafian K, Barbi M, Alasti M (2015) A regret matching strategy framework for inter-BAN interference mitigation. In: Proceedings of 8th IEEE conference on IFIP wireless and mobile networking. IEEE Press, pp 231–234

11. Haoran L, Chen C, Yu W, Yang B, Guan X (2012) Supersa: superframe design based slot allocation of wireless body area networks for healthcare systems. In: International conference on wireless communications and signal processing (WCSP). IEEE Press, pp 1–6
12. Jocelyne E, Paris S, Krunz M (2015) Cross-technology interference mitigation in body area networks: an optimization approach. IEEE Trans Veh Technol 64:4144–4157
13. Thien TTL, Sangman M (2017) Link scheduling algorithm with interference prediction for multiple mobile WBANs. J Sens 17:2231
14. Samaneh M, Behnam M, David BS, Mehran A (2017) Biologically inspired self-organization and node-level interference mitigation amongst multiple coexisting wireless body area networks. In: Proceedings of 13th international conference on wireless communications and mobile computing conference (IWCMC). IEEE Press, pp 1221–1226

Design and Analysis of Refractive Index Sensor Based on Dual-Core Photonic Crystal Fiber (DC-PCF) with Rectangular Air Hole Lattice Structure

Vishal Chaudhary and Dharmendra Kumar

Abstract We have proposed a refractive index sensor, which is based on dual-core photonic crystal fiber (PCF) with a rectangular air-hole lattice structure. The two fiber cores of the PCF are separated by single air-hole filled with the analyte liquid and the refractive index of the analyte liquid (n_a) varies from 1.33 to 1.41. The highest sensitivity of 9,400 nm/RIU (Refractive index unit) can be acheived when n_a is 1.41 in the simulated results and lowest sensitivity is up to 5,940 nm/RIU when n_a is 1.33.

Keywords Dual-core PCF · Refractive index (RI) sensor · Mode coupling · Sensitivity

1 Introduction

Photonic crystal fiber (PCF) is the new kind of optical fiber having a periodic array of air holes running along the entire fiber length to create the cladding around the core of the cable. Light propagation in PCFs is much superior to conventional fiber. PCFs provide better flexibility in designing of the structure as compared with conventional optical fiber and achieve unique optical properties such as endlessly single-mode operation over a wide range of wavelength, good dispersion characteristics, high birefringence, high nonlinearity, low confinement loss, etc. [1–5].

However, in recent years, a rising number of PCF refractive index sensors for various applications like pressure sensor [6], refractive index sensor [7], bio and temperature sensor [8], etc. In most PCF-based sensors, only single-core photonic crystal fiber was used. Because of their flexible design and easy fabrication, dual-core PCFs have shown many advantages in the applications of optical communication and

V. Chaudhary (✉) · D. Kumar
Department of Electronics and Communication Engineering,
Madan Mohan Malaviya University of Technology, Gorakhpur, Uttar Pradesh, India
e-mail: Vishalchaudhary719@gmail.com

D. Kumar
e-mail: dharmendra0127@gmail.com

© Springer Nature Singapore Pte Ltd. 2020

V. Janyani et al. (eds.), *Optical and Wireless Technologies*,
Lecture Notes in Electrical Engineering 546,
https://doi.org/10.1007/978-981-13-6159-3_22

sensing [9–11]. Dual-core photonic crystal fiber has also shown very good performances in various applications like narrow band-pass filter [12], PCF coupler [11], polarization splitter [13], and wavelength MUX-DEMUX [14].

In this paper, we have proposed a dual-core PCF with a rectangular air-hole lattice structure and the analyte liquid is filled into the central air holes. The configuration of the proposed dual-core PCF is designed by COMSOL Multiphysics software which is based on FEM (Finite Element Method). We have calculated the sensitivity of the proposed dual-core PCF and compared with some other reported PCFs which shows greater sensitivity.

2 PCF Design

The proposed PCF consists of a periodic array of rectangular air holes lattice structure and the analyte liquid is filled into the central air holes, here we take the diameter of circular air holes are $d = 3\,\mu\text{m}$ and hole-to-hole distance pitch $\Lambda = 5\,\mu\text{m}$, respectively, and the background material of PCF is taken as silica. The refractive index of silica and air is 1.45 and 1, respectively, and n_a is varies in the range of 1.33–1.41. The geometry of proposed dual-core PCF is shown in Fig. 1.

Dual-core PCF coupling can be explained by four super modes in the *x*-polarization and y-polarization. These four super modes can be created due to the individual cores. Figure 2 shows the distribution of electric field of the four super modes. Using Eq. (1), we calculate coupling length at different wavelengths. First, we calculate the refractive indices of four super modes and then the difference of effective refractive indices for *x*- and *y*-polarized light has been calculated, after that, their coupling lengths have been calculated from the Eq. (1).

The coupling length of the dual-core PCF is defined as [9, 14]

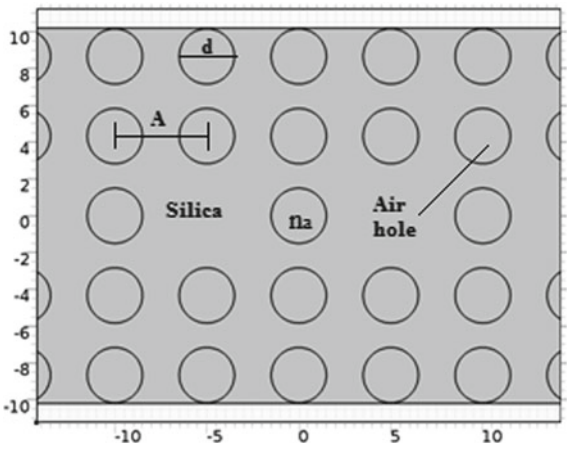

Fig. 1 Geometry of the proposed dual-core photonic crystal fiber

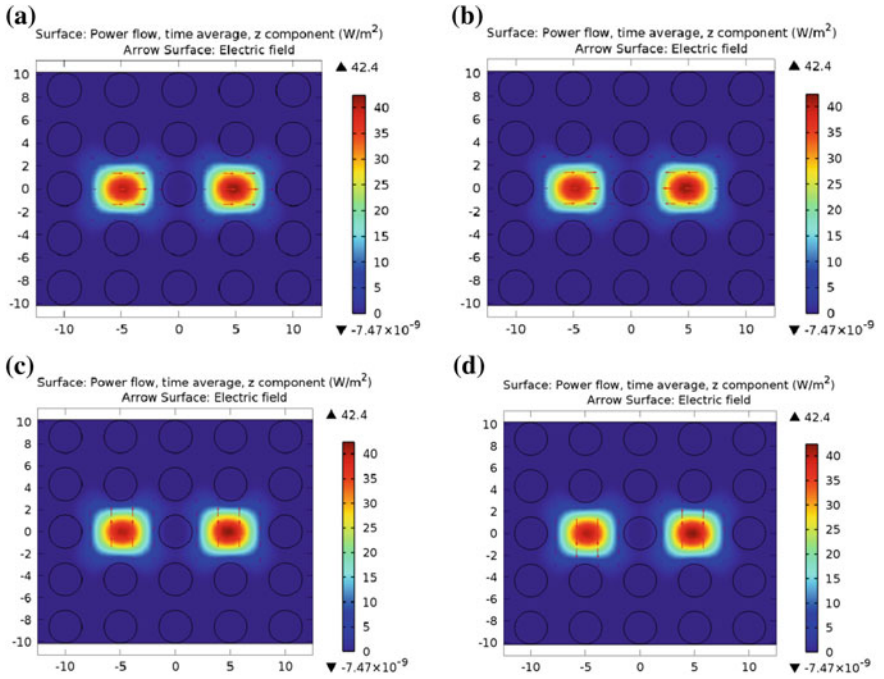

Fig. 2 Distribution of the electric field of the four super modes: **a** *x*-polarized even, **b** *x*-polarized odd, **c** *y*-polarized even, and **d** *y*-polarized odd

$$L_c = \frac{\pi}{\left|\beta_e^i - \beta_o^i\right|} = \frac{\lambda}{2\left|n_e^i - n_o^i\right|}, \quad \mathrm{i} = \mathrm{x}, \mathrm{y} \tag{1}$$

where propagation constants of *i*-polarized even and odd super mode are represented as β_e^i and β_o^i, respectively. The effective refractive indexes of *i*-polarized even and odd super mode are represented as n_e^i and n_o^i, respectively.

Due to the theory of mode coupling, power transfer of the dual-core PCF after a length L is defined as [15]

$$\mathrm{I}(\lambda) = \sin^2\left(\frac{\pi}{\lambda}\Delta n_{eo} L\right) \tag{2}$$

For the sensor purpose, we calculate the sensitivity of the dual-core PCF by shifting of the peaks with the variation of refractive index of analyte liquid. The sensitivity of the dual-core PCF is defined as [16]

$$S_\lambda\left(nmRIU^{-1}\right) = \Delta\lambda_{peak}/\Delta n_a \tag{3}$$

where the shift of the transmission spectra is represented as $\Delta\lambda_{\mathrm{peak}}$ and the change of the analyte refractive index is represented as Δn_a.

3 Simulation Results and Discussion

Figure 3a shows the effective refractive index variation of four super modes of PCF with wavelength when the analyte liquid $n_a = 1.3$ is filled into the central air holes. The effective refractive index decreases with increasing wavelength. Figure 3b shows that the effective refractive index difference (Δn_{eo}), which is $\Delta n_{eo} = |n_e - n_o|$. The effective refractive index difference (Δn_{eo}) increases when the wavelength increases, because as the wavelength increases light spreads into the cladding, confinement is less, so effective refractive index difference increases.

Figure 4a shows the coupling length variation of the x- and y-polarized light with wavelength. According to the mode coupling theory, the optical power transferring from one fiber core to the other core along PCF after a length L. Obviously, coupling lengths of dual-core PCF vary with wavelengths. It can be seen that the coupling length of y-polarized light is larger than x and as wavelength increases the coupling length decreases. Figure 4b shows the power transmission curve of dual-core PCF for the x-polarized light and y-polarized light with a length of 1 cm. The power transmission curve of the proposed PCF is sinusoidal.

The numerical shift in wavelength for different analyte liquid is shown in Fig. 5. This curve gives the maximum sensitivity of the proposed dual-core PCF. According to calculated result, the sensitivity of the proposed dual-core PCF increases when n_a is increases. From the result, the highest sensitivity of 9,400 nm/RIU can be achieved when $n_a = 1.41$ at the wavelength of 1193 nm. The lowest sensitivity of 5,150 nm/RIU can be achieved when $n_a = 1.33$ at the wavelength of 1732 nm. The comparison of the sensitivity of the proposed dual-core PCF and some other PCFs is shown in Table 1.

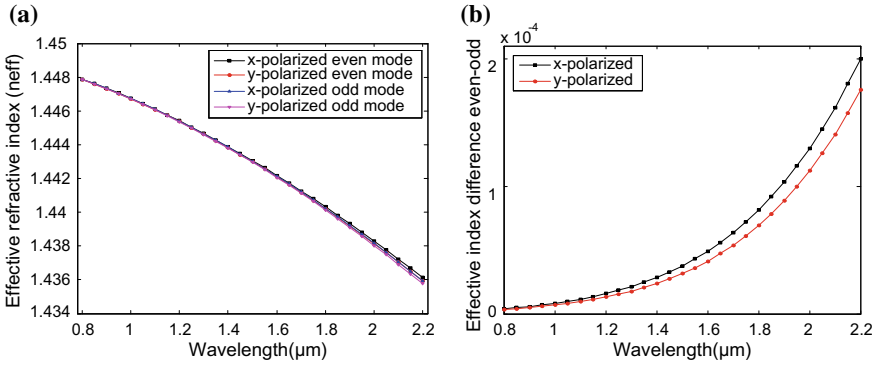

Fig. 3 **a** Effective refractive index variation with wavelength when $n_a = 1.33$ and d = 3.0 μm, **b** effective refractive index difference variation with wavelength when $n_a = 1.33$ and d = 3.0 μm

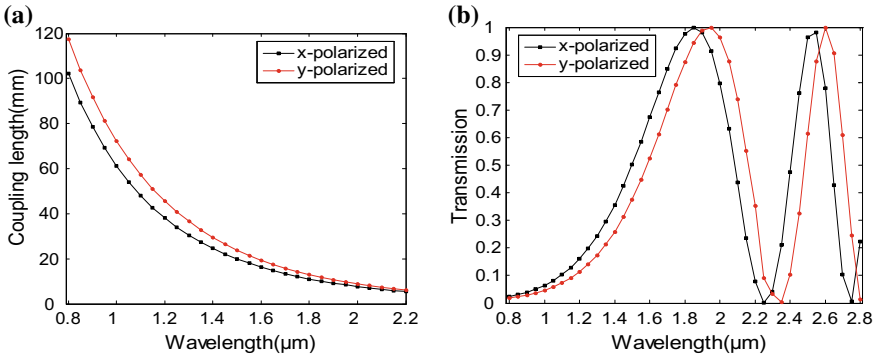

Fig. 4 **a** Coupling length variation of the *x*- and *y*-polarized light with wavelength when analyte refractive index $n_a = 1.33$ and hole diameter d = 3.0 μm, **b** transmission curve of dual-core PCF with a length of 1 cm

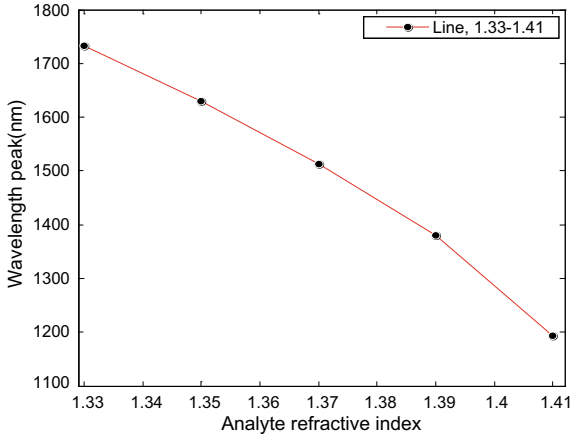

Fig. 5 Numerical result of function between n_a and λ_{peak} (nm)

Table 1 Properties of the proposed dual-core PCF compared with some other PCFs

PCFs design	Sensitivity (S) (nm/RIU)
Ref. [17]	1,500
Ref. [18]	2,929.39
Ref. [19]	7,300
Ref. [20]	8,000
Proposed dual-core PCF	9,400

4 Conclusion

In this paper, we proposed a highest sensitivity dual-core PCF by using Finite Element Method. From the numerical results, it is clear that the proposed PCF sensor can detect the range from 1.33 to 1.41. The maximum sensitivity of 9,400 nm/RIU can be achieved when the refractive index of the analyte $n_a = 1.41$. The lowest sensitivity of 5,150 nm/RIU can be achieved when $n_a = 1.33$. High sensitivity gives fast, real-time, and easy detection.

References

1. Birks TA, Knight JC, Russell PSJ (1997) Endlessly singlemode photonic crystal fiber. Opt Lett 22:961–963
2. Ju J, Jin W et al (2003) Properties of a highly birefringent photonic crystal fiber. IEEE Photon Technol Lett 15:1375–1377
3. Ranka JK, Windeler RS, Stentz AJ (2000) Visible continuum generation in air–silica microstructure optical fibers with anomalous dispersion at 800 nm. Opt Lett 25:25–27
4. Knight JC, Arriaga J, Birks TA et al (2000) Anomalous dispersion in photonic crystal fiber. IEEE Photon Technol Lett 12:807–809
5. Sinha RK, Varshney SK (2003) Dispersion properties of photonic crystal fibers. Microw optical Technol Lett 37:129–132
6. Liu Z, Tse ML, Wu C, Chen D, Lu C, Tam HY (2012) Intermodal coupling of supermodes in a twin core photonic crystal fiber and its application as a pressure sensor. Opt Express 20:21749–21757
7. Dhara P, Singh VK (2015) Effect of MMF stub on the sensitivity of a photonic crystal fiber interferometer sensor at 1550 nm. Opt Fiber Technol 21:154–159
8. Rindorf L, Bang O (2008) Sensitivity of photonic crystal fiber grat-ing sensors: biosensing, refractive index, strain and temperature sensing. J Opt Soc Am B 25:310–324
9. Wang Z, Taru T, Birks TA, Knight JC (2007) Coupling in dual-core photonic bandgap fibers: theory and experiment. Opt Express 15:4795–4803
10. Lagsgaard J (2005) coupling in twin-core photonic bandgap fibers. Opt Lett 30:3281–3283
11. Lagsgaard J, Bang O, Bjarklev A (2004) Photonic crystal fiber design for broadband directional coupling. Opt Lett 29:2473–2475
12. Saitoh K, Florous NJ, Koshiba M, Skorobogatiy M (2005) Design of narrow band-pass filters based on the resonant-tunneling phenomenon in multi-core photonic crystal fibers. Opt Express 13:10327–10335
13. Saitoh K, Sato Y, Koshiba M (2004) Polarization splitter in three-core photonic crystal fibers. Opt Express 12:3940–3946
14. Saitoh K, Sato Y, Koshiba M (2003) Coupling characteristics of dual-core photonic crystal fiber couplers. Opt Express 11:3188–3195
15. Huang WP (1994) Coupled mode theory for optical waveguides: an overview. J Opt Soc Am A 11:963–983
16. Beatrand G, Alireza H, Majid FF, Andrei K, Skorobogatiy MA (2007) Photonic bandgap fiber-based surface plasmon resonance sensors. Opt Express 15:11413–11426
17. Rindorf L, Bang O (2008) Highly sensitive refractometer with a photonic-crystal-fiber long-period grating. Opt Lett 33:563–565

18. Shuai B, Xia L, Zhang Y, Liu D (2012) A multi-core holey fiber based plasmonic sensor with large detection range and high linearity. Opt Express 20:5974–5986
19. Tian M, Lu P, Chen L, Lv C, Liu D (2012) All-solid D-shaped photonic fiber sensor based on surface plasmon resonance. Opt Commun 285:1550–1554
20. Hasan MR, Akter S, Ahmed K, Abbott D (2017) Plasmonic refractive index sensor employing niobium nanofilm on photonic crystal fiber. IEEE Photon Technol Lett 1041–1135

Gain and Bandwidth Enhancement by Optimizing Four Elements Corporate-Fed Microstrip Array for 2.4 GHz Applications

D. Shashi Kumar and S. Suganthi

Abstract This paper presents the performance analysis of an optimized corporate-fed Rectangular Microstrip Antenna Array of four elements and Rectangular Microstrip Antenna array with Semi-Circular Tabs on the nonradiating edges of each element of the array to operate at 2.4 GHz, with detailed steps of the design process. The proposed antenna structures have been designed using FR4 dielectric substrate having a permittivity ε_r of 4.4 with a thickness of 1.6 mm. The simulations have been carried out by using Antenna simulator HFSS version 15.0.0 and performance was analyzed for gain, bandwidth, VSWR, return loss and radiation pattern. The gain of these simulated antenna arrays is 2.4381 dB, 8.2684 dB and 8.5621 dB with a return loss of −22.4123 dB, −14.1095 dB and −15.7621 dB for Single-Element patch, conventional Rectangular Microstrip array and Rectangular Microstrip Antenna array with semicircular tabs respectively at 2.4 GHz. Bandwidths exhibited by Single-Element patch, RMSACT and RMSA are 59.8 MHz, 83.9 MHz, and 212.7 MHz, respectively.

Keywords VSWR · Return loss · Rectangular patch · Microstrip array · Corporate fed

1 Introduction

The microstrip antennas are extensively used in a broad range of application, which comes under communication systems. Due to the ease of fabrication, low profile nature, no hard rules in choosing the shapes and configurations to be used, microstrip antennas are utilized for most demanding applications. Researchers reported varieties of shapes to design microstrip antennas, among them the most

D. Shashi Kumar (✉) · S. Suganthi
Department of ECE, Christ University, Bangalore, India
e-mail: Shashiphd2015@gmail.com

S. Suganthi
e-mail: drssuga@gmail.com

© Springer Nature Singapore Pte Ltd. 2020

V. Janyani et al. (eds.), *Optical and Wireless Technologies*,
Lecture Notes in Electrical Engineering 546,
https://doi.org/10.1007/978-981-13-6159-3_23

commonly used configurations are triangular, rectangular, and circular configurations.

The possibility of microstrip antenna to achieve circular polarization, multiple resonant frequencies, broad bandwidth, dual characteristics, and frequency agility, made them best suited for Direction of Arrival estimation and beamforming applications [1]. For the next-generation communication systems that demand high bitrates and high gain, microstrip antenna arrays are greatly required.

Some major drawbacks connected with a microstrip patch antenna include incapable to operate at higher power levels and narrow bandwidth. The challenge in improving the gain and bandwidth still has its importance among the researchers [2]. One of the methods available to alleviate the mentioned challenges is building an array of antenna elements.

2 Microstrip Patch Antenna Design

The radiating patch, microstrip transmission line on the top and the ground plane created at the bottom seen in any general microstrip antenna fabricated using a substrate material are made of metals which are highly conductive (typically copper). The thickness of the microstrip and the ground is not critically important.

But it is necessary to select the optimized design parameters that include the thickness of the substrate, permittivity of the substrate and resonant frequency, because antenna performance largely depends on these parameters. We can improve bandwidth, gain, and radiation performance by choosing the best configurations and the shape of the patch [3].

While designing the microstrip patch, the physical dimensions used will impact the performance to a greater extent. The dimensions also influence the directivity, radiation efficiency, operating frequency, directivity, return loss, and other related parameters of the fabricated antenna.

To design an effective rectangular patch, the length L_p must be selected as $0.3333\,\lambda_o < L_p < \lambda_o$, where λ_o is the free space wavelength. The acceptable range for the dielectric substrate thickness usually lies between $0.003\,\lambda_o \, and \, 0.05\,\lambda_o$. The thickness of the conducting patch and ground is selected comparatively very less to λ_o [4]. The permittivity ε_r of the substrate exhibits a range from 2.2 to 12. Better radiation characteristic can be achieved by controlling the practical length and width of the patch. Equations (1)–(5) are used to calculate the physical dimensions of single-element patch [1, 5]:

$$W = \frac{c}{2 f_r \sqrt{\frac{2}{\varepsilon_r + 1}}} \tag{1}$$

The actual physical length of the patch is

$$L = L_{eff} - 2\Delta L \tag{2}$$

where

$$\frac{\Delta L}{h} = 0.412\frac{(\varepsilon_{eff} + 0.3)\left(\frac{W}{h} + 0.264\right)}{(\varepsilon_{eff} - 0.258)\left(\frac{W}{h} + 0.8\right)} \tag{3}$$

$$\varepsilon_{eff} = \frac{\varepsilon_r + 1}{2} + \frac{\varepsilon_r - 1}{2\left(1 + 12\frac{h}{W}\right)^{\frac{1}{2}}} \tag{4}$$

To achieve better impedance match the inset position of the patch can be calculated using [6]:

$$y = 10^{-4}[0.001699\varepsilon_r^7 + 0.13761\varepsilon_r^6 - 6.1783\varepsilon_r^5 + 93.187\varepsilon_r^4 - 682.69\varepsilon_r^3 + 2561.9\varepsilon_r^2 - 4043\varepsilon_r + 6697] \tag{5}$$

The above expression holds well for permittivity between 2 and 12, where f_r is the desired frequency of resonance; y is the inset feed length.

3 Microstrip Antenna Array Design

The gain and directivity obtained in conventional patch antenna are very low compared to that obtained from an array. Relatively wide radiation patterns can be seen for a single patch antenna compare to that of an array of patch elements. In most of the applications, it is very much essential for the designed antennas to possess high gain and high directivity to meet the demands of emerging communication systems [7]. It is possible to achieve good gain and directivity if the electrical size of the antenna is increased. Many researchers worked on creating an array of elements to improve the gain and directivity by increasing the dimensions of the antenna, without increasing the size of the individual elements in their geometrical and electrical configuration. To improve the overall performance of the antenna array made of identical elements, we can adjust the relative spacing between the adjacent patches and optimize the geometry of the overall array. The other methods involved are controlling the excitation amplitude and excitation phase of individual elements.

Proposed Antenna Array Design

Microstrip antenna arrays are generally fed either using corporate feed or series feed mechanisms. For passive antenna array design, the most popular feed network is corporate feed network. This method is lossy especially at higher frequencies. In series-fed array, the input fed at one end of the patch is coupled serially to other elements in the array. Series feed mechanism well known for its low insertion loss and high efficiency; however, it suffers from narrow bandwidth and inherent phase variations.

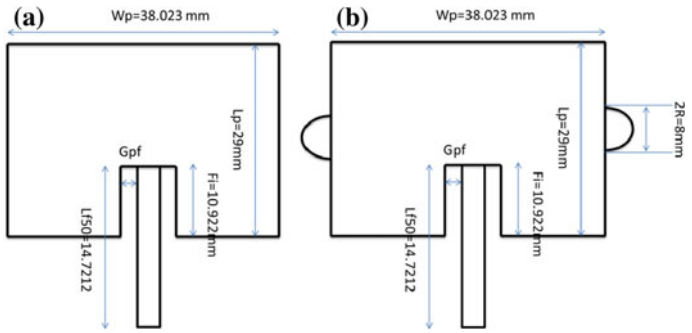

Fig. 1 **a** Single-element patch element patch. **b** Single-element patch with semicircular tabs

Table 1 Specifications of the antenna array designed using FR4 substrate

Parameters	Optimized values (mm)
Length of substrate (Ls)	59.9358
Width of substrate (WS)	116.5926
Radius of edge semi-circles (R)	4
Patch width (Wp)	38.023
Patch length (Lp)	29
Length of inset feed (y)	10.9221
Edge feed length (Lf50)	14.7212
Length of the transition line (Lf100/Lf70)	14.7212
Width of edge feed (Wf50)	3.0612
Width of feed line (Wf100)	0.62764
Spacing between the patches	32.92

Figure 1 shows the dimensions of a single-element patch antenna for a frequency of 2.4 GHz designed on an FR4 substrate of $\boldsymbol{\varepsilon_r} = 4.4$ is 38.023×29 mm^2 with inset feed length of Fi = 10.9221 mm from the center point of the width but along the length direction.

Using the single-element patch, a two-element array is developed and performance is analyzed. Where the gain achieved is close to 6.7 dB with a return loss of −13.29 dB for a resonant frequency of 2.4 GHz. To create a four-element array identical elements are used. The dimension of four-element array has resulted as 254.5×90.7 mm^2.

The specifications of an array designed using FR4 substrate are presented in Table 1.

As seen from Fig. 2a, b a four-element optimized Rectangular Microstrip Antenna (RMSA) array and a Rectangular Microstrip Antenna with Semicircular Tabs (RMSACT), designed with corporate fed mechanism to operate at 2.4 GHz frequency is considered for simulation and analysis. To feed RF power to the proposed antenna array Microstrip transmission line method is followed. For maximum power transfer

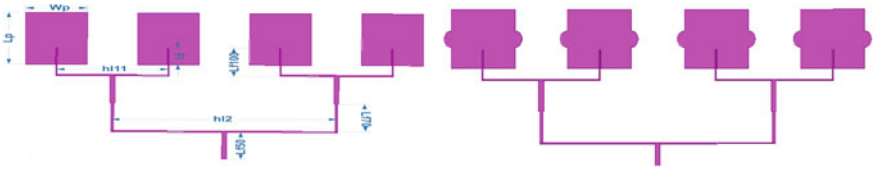

Fig. 2 **a** Four-element optimized RMSA array. **b** Four-element RMSACT array

and to achieve a better impedance match between the patch elements and transmission line Quarter Wavelength transformer (QWT) technique is utilized.

The simulated RMSACT configuration is depicted in Fig. 2. Two semicircular tabs are created on the nonradiating edges of the individual patch with a diameter of 8 mm each. Even though we created tabs, this modification is not giving a significant increase in gain.

4 Simulation Results and Discussions

To analyze the performance of designed antennas, simulations are carried out using HFSS software. From the simulation results, the values of Gain, Return Loss, and VSWR of the conventional patch, RMSA and RMSACT arrays designed with FR4 substrate are compared to draw inferences.

In the initial design of single-element patch, a 50 Ω stripline is used as feed to resonate at 2.4 GHz. The result for the Return Loss, VSWR and a plot of gain versus Frequency is depicted in Fig. 3. From the simulation results, it is observed that the designed Single-Element Patch is resonating at 2.38 GHz with a return loss of − 22.41 dB and VSWR of 1.1639 which is agreeing with the VSWR of 1:2. This indicates that the antenna is very well matched. From the Gain versus frequency plot, we can infer that the gain is maximum at close to 2.4 GHz.

Figure 4 illustrates the performance of proposed four-element array configurations. From the simulated Return loss characteristics, the RMSA and RMSACT are resonating at 2.34 GHz and 2.42 GHz with −17.5409 dB and −18.8493 dB return loss, respectively. The VSWR of RMSA and RMSACT are 1.3 and 1.25, respectively, at the resonant frequency. This confirms that the designed antenna arrays are very well matched. Referring to Gain versus Frequency plot we can find that there is no much difference in terms of gain improvement even after adding semicircular tabs on the nonradiating edges of each element of RMSA.

The 3D radiation patterns of single-element patch, RMSA, and RMSACT are shown in Fig. 5. It is observed that the gain values exhibited by single-element patch, RMSA and RMSACT are 2.4381 dB, 8.2684 dB, and 8.5621 dB, respectively. From these observations, we can confirm that the four-element arrays are giving better gain compared to single-element patch. We can also notice that there is no significant gain

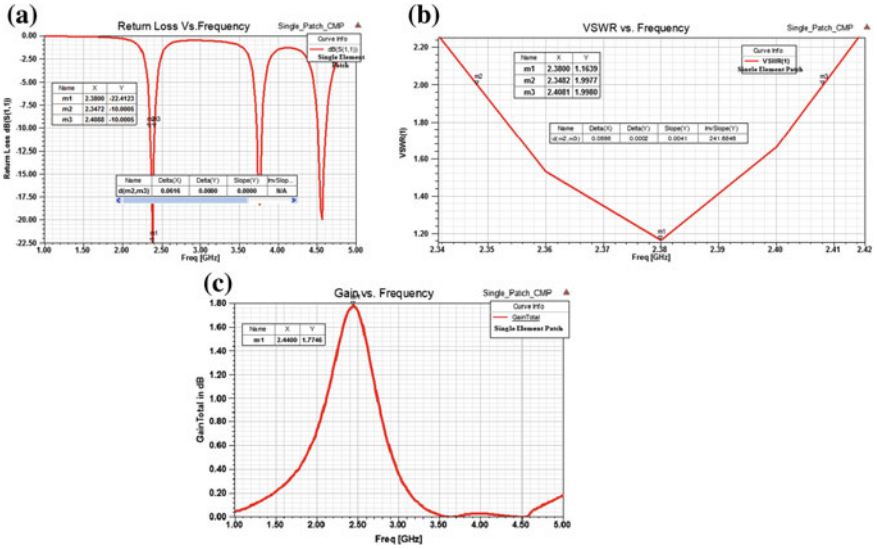

Fig. 3 **a** Single-element patch antenna return loss. **b** Single-element patch VSWR **c** single-element patch gain versus frequency

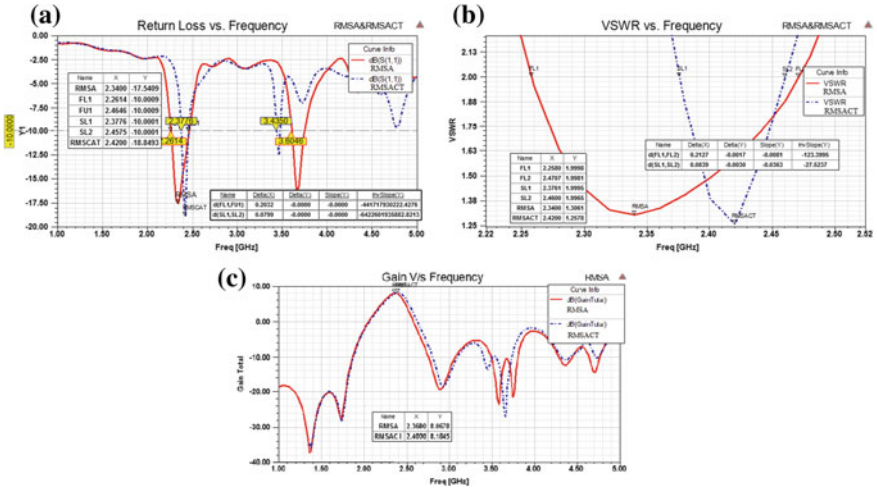

Fig. 4 **a** Simulated return loss. **b** Simulated VSWR. **c** Gain versus frequency

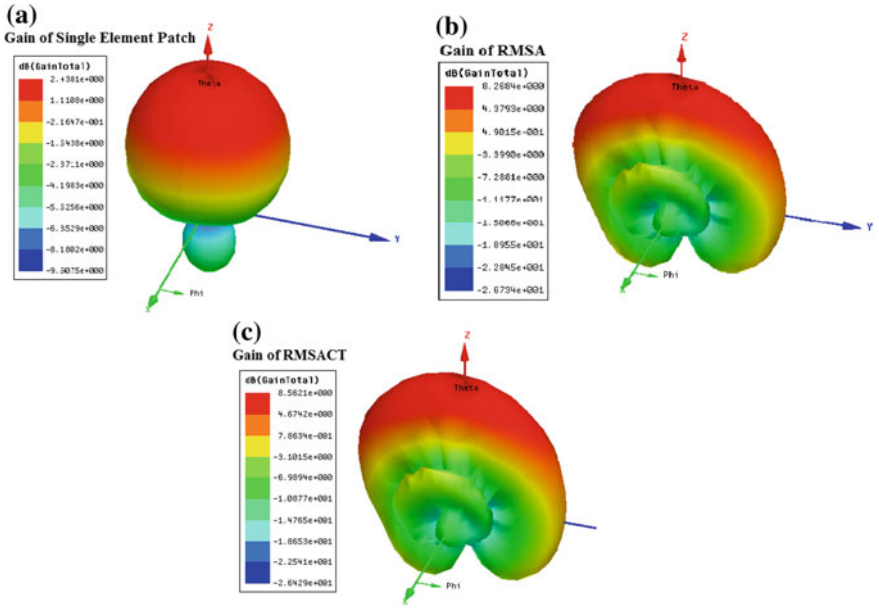

Fig. 5 The 3D radiation patterns **a** single-element patch. **b** RMSA. **c** RMSACT

Table 2 Comparison between simulation results of conventional RMSA and RMSACT array antennas at 2.4 GHz

Sl. no.	Parameter	Single-element patch	RMSA array	RMSACT array
1	Return loss dB (S11)	−22.4123	−14.1097	−15.7621
2	VSWR	1.163	1.4907	1.3892
3	Gain in dB	2.4381	8.2684	8.5621
4	Bandwidth (MHz)	59.8	212.6	83.9
5	Fractional BW (%)	2.49	8.99	3.47

achieved after introducing the semicircular tabs to the RMSA. This tells us further modifications needs to be done to the RMSACT to improve its gain and bandwidth.

The comparison of antenna parameters (return loss, VSWR, gain, and bandwidth and fractional bandwidth) for the simulated antenna configurations is presented in Table 2.

5 Conclusions

In this paper as a first step to design a high-gain and high-bandwidth antenna, a single-element patch is designed and optimized. Then the optimized patch is used in creating a four-element microstrip patch antenna array to improve gain and bandwidth. To further enhance the gain of the microstrip array we used semicircular tabs to rectangular patches but this attempt did not result in significant improvement in the gain. From simulation results obtained and the analysis made, we can infer that the gain of RMSA and RMSACT is close to 8 dB, which is almost three times that of the single-element patch. The fractional bandwidth of the RMSA is almost tripled. Hence, we can suggest that the proposed RMSA can be used in applications that operate at 2.4 GHz. As a future work, to achieve better gain and bandwidth the proposed array may be modified by adding metamaterial loaded structures Electromagnetic Band Gap structures.

Acknowledgements We would like to express our special thanks of gratitude to RF and Microwave Research Lab of Christ University Faculty of Engineering for the constant support provided throughout the preparation of this paper.

References

1. Garg R, Bhartia P, Bahl IJ, Ittipiboon P (2001) Microstrip antenna design hand book. Artech House, Boston, London (2001)
2. Mailloux R, McIlvenna JF, Kernweis NP (1981) Microstrip array technology: antennas and propagation. IEEE Trans 29:25–37
3. Boufrioua A, Benghalia A (2006) Effects of the resistive patch and the uniaxial anisotropic substrate on the resonant frequency and the scattering radar cross section of a rectangular microstrip antenna. Aerosp Sci Technol 10:217–221
4. Huque MTI, Hosain MK, Islam MS, Chowdhury MA (2011) Design and performance analysis of array antennas with optimum parameters for X band applications. Int J Adv Comput Sci Appl 2(4)
5. Balanis CA (2005) Antenna theory: analysis and design, 3rd edn. Wiley-Interscience
6. Ramesh M, Yip KB (2003) Design formula for inset fed microstrip patch antenna. J Microw Optoelectron 3(3):5–10
7. Milligan TA (2005) Modern antenna design, 2nd edn. Wiley-IEEE Press

Speaker Identification Through Natural and Whisper Speech Signal

Amrita Singh and Amit M. Joshi

Abstract The paper presents the identification of a speaker with the help of natural and whisper speech signal. The speaker identification through whisper is also useful in cases where the speaker is unable to speak, or speaker wants to hide his/her identity. However, the changes in whispering speech due to the vocal effort have several challenges in maintaining system accuracy. The accuracy of speaker identification is calculated with Mel Frequency Cepstral Coefficient (MFCC) algorithm and Exponential Frequency Cepstral Coefficient (EFCC) algorithm. MFCC and EFCC are considered for feature extraction. All the samples are clustered using K-means algorithm and Gaussian Mixture Model for feature classification. GMM is containing mean, variance, and weight which are modeling parameters. Here Expectation–Maximization algorithm is used for testing the samples and reestimate the parameters. Finally, GMM algorithm recognizes the speaker that exactly matches for a given database. The algorithms are implemented on MATLAB tool, and the results are also verified.

Keywords EFCC · GMM · MFCC · Feature extraction · K-means

1 Introduction

Speaker Recognition is referred as a speaker biometrics system which helps to identify a speaker based on his/her voice. Speech recognition (speaker identification) has many real-world applications like Financial Applications, Forensic and Legal Applications, Access Control (Security) Application, Teleconferencing Applications [1]. Speech recognition has great potential in the latest Internet of Things (IoT) based applications where the communication may be preferred through voice information

A. Singh · A. M. Joshi (✉)
Malaviya National Institute of Technology Jaipur, Jaipur, India
e-mail: amjoshi.ece@mnit.ac.in

A. Singh
e-mail: 2015peb5115@mnit.ac.in

© Springer Nature Singapore Pte Ltd. 2020

V. Janyani et al. (eds.), *Optical and Wireless Technologies*,
Lecture Notes in Electrical Engineering 546,
https://doi.org/10.1007/978-981-13-6159-3_24

over text information. This would help immensely because illiterate can also be able to communicate through speech signal [2, 3]. Speech can be used in the real-time applications where the customers' sentiments are required to be observed. In many circumstances, customers do not need or want to speak to a live operator. For example, if they have little time or they only require basic information, then speech identification can be used to reduce the waiting times and provide customers with the information they want. Speech can be used for security application also such as a password of personal computers using voice and word recognition, so accuracy in speech recognition is a very important task [4]. To increase in accuracy in recognition rate, novel technique such as dynamic time warping can be used. Due to the recent advancement of the technology, the identification of speaker has become one of the challenging tasks. Although current technology is still far away from the identification of human speech to 100%. Thus, much more research and development is required in this area. Therefore, we explore in this field to give more development in speech application. Today, there are so many algorithms developed for speech recognition for feature extraction like Linear Predictive Coefficient (LPC) and Principle Component Analysis (PCA). The feature matching can be done with Vector quantization, Hidden Markova Model, and Artificial Neural Network but these algorithms are not good for practical speech identification due to some reasons such as high redundancy, complexity, accuracy, and less correlation between original speech of speaker and tested speech sample. The most important task for these algorithms is to be able to identify the originality of a particular speaker. These algorithms are also not suited to recognize a speaker through whisper speech [5]. The whispering based speaker identification is also an emerging research field. It can help to identify the person who hides his/her identity. So, it is important to develop an efficient algorithm for speech identification System. Previous algorithms work on the neutral speech, but there is not enough research is carried out in whisper speech [6]. Therefore, a solution is required to be developed where speaker can be identified through either neutral and/or whisper speech.

The flow of the paper is as follows: Sect. 2 covers the basic theory of feature extraction, and Sect. 3 explains the feature classification while Sect. 4 elaborates speaker identification by steps of training method and testing method. Section 5 analyzes the results, and the conclusion is derived in Sect. 6.

2 Feature Extraction

Feature extraction is a fundamental classification technique of speech signal and it is used to extract the features of speaker. The accuracy is important for further processing to improve the system model. Mel Frequency Cepstral Coefficent (MFCC) and Exponential Frequency Cepstrum Coefficient (EFCC) are useful to extract the feature. Both methods are observed to be efficient than other methods, while whispered is used as input signal for identification. The speech recognition algorithm is classified into two parts. The first part is training phase and the second part

is testing phase. In training phase, the voice samples of each speaker are collected in order to generate the reference database. In the testing phase, the speaker is identified from the reference database. This section introduces the training phase that converts a speech signal into significance feature vector and extracting the parameter of speech such as the pitch of the human voice and cepstral coefficient which is useful in the testing phase. MFCC is based on human hearing perception method. These parameters are important for speech recognition to define the fundamental frequencies and cepstral coefficient which are important for accuracy. MFCC algorithm is explained in details in subsequent section.

2.1 Mel Frequency Cepstral Coefficient (MFCC)

Short time power spectrum of speech signal is defined as a Mel frequency of cepstrum which is calculated as the linear cosine transform of the log power spectrum on a nonlinear Mel scale of frequency. MFCC is used to calculate these two frequencies. First is linear frequency which is below 1000 Hz and second is logarithmic frequency which is above 1000 Hz. Mel frequency scale represents the important feature of the speech. The step for MFCC algorithm process is as follows:

1. Record the speech signal word, utterance, and preemphasis of the same.
2. Divide the signal into a number of frames and applied into hamming window function to make in continuation.
3. Take the FFT of the window function and then square the magnitude of the signal to find the power spectrum.
4. Apply magnitude spectrum into Mel filter bank which is a bank of the triangular filter.
5. Find Discrete Cosine Transform of the signal to convert in the time domain.
6. Unvoiced consonant as well as voiced consonant and other phonemes have different spectral energy in speech analysis. MFCC has the best performance during the extraction process of the feature vector of speech signal by a different scale.

2.2 Exponential Frequency Cepstral Coefficient (EFCC)

MFCC emphasizes the low-frequency component than high-frequency component; So MFFC is not useful in voiced and unvoiced consonant. Thus, EFCC is used for high-frequency component and other phonemes. Extracting the feature vector by exponential frequency scale is the same as proposed in speech under stress [7]. The exponential frequency function is defined as

$$\mathrm{Y} = \mathrm{C} * \left(10^{\left(\frac{f}{k}\right)} - 1\right), \quad 0 \leq \mathrm{f} \leq 8000\,\mathrm{Hz} \tag{1}$$

where C and k are calculated by these two equations:

$$C * \left(10^{\left(\frac{8000}{k}\right)} - 1\right) = 2595 * \log\left(1 + \frac{8000}{700}\right) \tag{2}$$

$$\{c, k\} = \min\{|(10^{4000/k} - 1) - \frac{4000}{k} * \ln 10 * C * 10^{\frac{4000}{k}}|\} \tag{3}$$

EFCC algorithm has same algorithm steps where exponential filter bank is used rather than Mel filter bank of MFCC algorithm. Unvoiced consonants and phonemes are processed by EFCC to enhance the whisper speech signal.

3 Feature Classification

Classification is building a unique model for every speaker in the database. Two methods of classification are discussed. One is the stochastic model and the second is template model. A stochastic model is used where random data, event, and uncertainty are present. It cannot predict the state with full accuracy, and its nondeterministic behavior is anatomization by probability theory. A stochastic model is the opposite of deterministic model whereas the deterministic problem only has one solution while the stochastic model is complicated. In the stochastic based model, there are many algorithms like GMM, HMM, and ANN. In template model, a template is a collection of features vector which can be defined as the repetition of data and continuation of frames. In this model, the prior information is not predicted, and it is not a probabilistic model. In this, each frame is compared with the training frame and the minimum distance is calculated, therefore it is weak in performance as compared to HMM and GMM.

In this paper, one method of the stochastic model known as GMM is used and K-mean based clustering model for template Model is also discussed.

3.1 Gaussian Mixture Model

Gaussian Mixture Model (GMM) is a probabilistic model which is used to define the probability density function of a random variable regarding the weighted sum of its component, in which each component has a Gaussian density function. The Gaussian Mixture Model is used for clustering of the data with hard clustering method. A Gaussian Mixture Model (GMM) is used where normal distribution failed and it is a mixture that varies probability density of normal distribution.

3.2 K-Means Clustering

There are several ways to classify data like semi-parametric, parametric and non-parametric approaches [8, 9]. In parametric approach, data is found by the known distribution and in semi-parametric, the data is calculated by a mixture of Gaussian while in nonparametric, nothing is to be predicted for the data. K-means algorithm works on parametric approaches. Macqueen in 1967 proposed the K-means algorithm. This algorithm is based on the iterative procedure for defining the cluster where K represents the number of clusters. K-means clustering is useful to classify the data based on the minimum distance of the centroid. The whole space is partitioned into k times. The aim is to find K-mean vectors ($\mu 1$, …, μK) the mean will be given the k cluster centroids. It randomly chooses initial cluster centers from the data set. Initially, the input is a set of speech data sample vector and are defined as x1, x2, …, xn for K-clustering method. The number of cluster (K) is also defined.

K-means algorithm is an unsupervised learning algorithm. In this, the speaker feature vectors are considered a set of data points which is divided into k number of cluster. Then, centroids are randomly allocated to the k number of cluster. Once centroid is defined, the nearest data points are calculated from centroid using minimum Euclidean distance is found which would be useful to calculate the mean of data points [10]. This defines a new centroid. This process is repeated until the means are converged. The converge is achieved when the new value of mean and old value of mean are the same.

4 Proposed Speaker Identification Algorithm

In this section, the algorithm of the speaker identification is discussed for both natural and whisper speech using feature extraction method (MFCC and EFCC) and Feature Classification method (GMM or K-means) [11].

4.1 Training Algorithm of Proposed Method

Step 1: First a speech of 10 s is recorded in '.wav' file of each speaker using MATLAB. Speech of speaker is digitized with a sampling frequency of 16 kHz and 16 bits per sample.
Step 2: Then, a database using 'db.mat' file is created in MATLAB which contains cell of the matrix to store all the feature values of speech data.
Step 3: After creating a database, each cell of matrix is denoted the number of speaker which is stored in the database. Each cell contains the MFCC feature vector, length of the signal, mean, variance, weighted average of data, name of the speaker, and the type of their speech.

Step 4: In the next step, the silence part of the speech is removed and the speech signal is applied to MFFC algorithm for training phase.
Step 5: First, preemphasis of the signal is obtained and the signal is divided into number of frame. One frame time is 32 ms and one frameshift is 16 ms which helps to calculate the sample duration in each frame. If speech signal is not divided into even number of frame then we padding it with zero to make even number of frame.
Step 6: After framing, the Hamming window function is applied to make the signal continuous.
Step 7: Then, time domain signal is converted into the frequency domain using FFT, and then the magnitude spectrum of signal is calculated.
Step 8: Magnitude spectrum of FFT signal is applied to 26 triangular bandpass filter which is equally spaced on Mel scale and is useful to calculate the filter bank energy of the unique part of the magnitude spectrum.
Step 9: The log of filter bank energy is considered and multiply with DCT to get cepstral coefficient.

After performing all the operation, feature vector of speaker's speech is obtained, and this feature vector is sent to the testing phase.

4.2 Testing Algorithm of the Proposed Method

In the testing algorithm, the speaker identification process is performed on the extracted feature vector of training phase by GMM and K-means algorithm.

(a) Testing with GMM algorithm

Step 1: First, MFCC feature vector of the testing speech is calculated and these vectors are applied into GMM.
Step 2: For testing of GMM, the mean, variance, and weighted Sum of all the speaker are already calculated and then stored in the database.
Step 3: Now, all parameter of given speech are calculated for the testing phase of GMM Like-mean, variance, and weighted sum.
Step 4: These parameters of testing speech are given into Expectation Maximization Algorithm to calculate the Log-likelihood and probability to find the true speaker.
Step 5: If new value of log-likelihood and old log-likelihood is less than 10^{-5} then the algorithm converges and gives the feature of speech as a probability of the speaker.
Step 6: Then we calculate the mean and absolute values of these features are calculated and find the minimum difference with the mean and absolute value of all the store speaker's feature [12].

(b) Testing with K-means classifier

Step 1: In the first step, the number of clusters is defined. Two clusters of the feature vectors of the speech are used.

Step 2: In the next step, the initial centroid of the clusters is found which is randomly initialized by the K-means function.
Step 3: The minimum distance of vector is found to given clusters centroid which is nearest to the assigned centroid of the vector.
Step 4: Then, the mean and covariance of the clusters around are calculated, and the centroid helps to define that mean and covariance as the new centroid.
Step 5: This process continues until the value is not converged. Therefore, the mean of the centroid is approached the same value again and again.
Step 6: In the last step, find the minimum difference of the store mean value of all the speaker and calculate mean with K-means which defines the value of the speaker and is the minimum of the true speaker [13].

5 Results

Speech samples of 10 s are taken in a room at the noisy condition for both natural and whisper voice with a normal microphone. Speech of 5 persons with 10 different tones including natural and whisper samples are collected. Speeches are preprocessed by sinusoidal lifter filtering to remove noise. Speech database of persons with different tones is separately created. These algorithms are implemented on MATLAB platform. This algorithm is implemented on 10 s of speech data which are phonetically balanced. The feature extraction is done by MFCC and EFCC, and features (vectors or matrix) of each person are stored, respectively. The distance between the extracted train speech sample and extracted test speech sample is calculated. Classification is done based on minimum distance by the mean and absolute value of probability of speaker using GMM classifier and K-means classifier. All speaker data are considered, features are extracted and applied to the classifier. The natural and whisper signal are considered at both training and testing phase, and overall accuracy is reported as shown in Table 1 and Table 2 for MFCC and EFCC feature extraction method, respectively.

From the observation of results in Tables 1 and 2, it is concluded that accuracy of GMM algorithm is best for speech identification. Highest recognition accuracy of 98% for speech recognition in neutral to neutral, while whisper to whisper is 84% for GMM classifier and MFCC as feature extraction. However, EFCC-based

Table 1 Overall accuracy of all speakers in all speech modes using MFCC algorithm

Speech mode		Accuracy (%)	
Training	Testing	GMM	K-means
Natural	Natural	98	74
Natural	Whisper	74	22
Whisper	Whisper	84	60
Whisper	Natural	36	10

Table 2 Overall accuracy of all speakers in all speech modes using EFCC algorithm

Speech mode		Accuracy (%)	
Training	Testing	GMM	K-means
Natural	Natural	80	62
Natural	Whisper	70	20
Whisper	Whisper	76	16
Whisper	Natural	24	8

feature extraction method has relatively lower performance than MFCC method. However, results show that whisper based training data has not performed well. The main reason is that the database is created in a noisy environment, so the feature extraction method of MFCC and EFCC is not able to extract the information in a noisy environment. However, the speaker identification with whisper based training phase is still an open problem and research is going on for the same.

6 Conclusion

The paper presents the speaker identification techniques through natural and whispers speech signals. However, the whispering-based speaker identification is a challenging task. The method has been proposed in the paper to identify the person through whispering. MFCC- and EFCC-based feature extraction algorithms are applied to testing phase as well as training phase with considering natural and whisper signal both. The spectral frequency for both natural and whisper mode is a scale on exponential and mel frequency filter bank. GMM and K-mean clustering methods have been adopted to have feature classification for both speech samples. It has been observed that MFCC-based feature extraction has better results, whereas GMM-based feature classification has good performance with compare to K-mean clustering.

7 Future Scope

In the future, the work can be carried out to improve the accuracy of the whispered speech which is very important. In the proposed algorithm, problem is that the accuracy for whisper to whisper is very less, and if the number of samples is increased then it takes more execution time for the feature extraction time during training phase. So in future, VLSI implementation of proposed scheme can be performed to achieve lesser execution time for the feature extraction. Thus, the overall performance of speaker identification can be increased for real-time applications.

References

1. Fan X, Hansen, JHL (2008) Speaker identification for whispered speech based on frequency warping and score competition. In: Ninth annual conference of the international speech communication association, pp 1313–1316
2. Shukla UP., Patel NB, Joshi AM (2013) A survey on recent advances in speech compressive sensing. In: 2013 international multi-conference on automation, computing, communication, control and compressed sensing (iMac4s), pp 276–280. IEEE
3. Bahdanau D, Chorowski J, Serdyuk D, Brakel P, Bengio Y (2016) End-to-end attention-based large vocabulary speech recognition. In: 2016 IEEE international conference on acoustics, speech and signal processing (ICASSP), pp 4945–4949
4. Xiong W, Droppo J, Huang X, Seide F, Seltzer M, Stolcke A, Yu D, Zweig G (2017) The Microsoft 2016 conversational speech recognition system. In: 2017 IEEE international conference on acoustics, speech and signal processing (ICASSP), pp 5255–5259. IEEE
5. Bhadoria BS, Shukla U, Joshi AM (2014) Comparative analysis of basis & measurement matrices for non-speech audio signal using compressive sensing. In: 2014 IEEE international conference on computational intelligence and computing research (ICCIC), pp 1–5. IEEE
6. Xiong W, Droppo J, Huang X, Seide F, Seltzer M, Stolcke A, Yu D, Zweig G (2016) Achieving human parity in conversational speech recognition. arXiv preprint arXiv:1610.05256
7. Sak H, Senior A, Rao K, Irsoy O, Graves A, Beaufays F, Schalkwyk J (2015) Learning acoustic frame labeling for speech recognition with recurrent neural networks. In: 2015 IEEE international conference on acoustics, speech and signal processing (ICASSP), pp 4280–4284. IEEE
8. Bimbot F, Bonastre JF, Fredouille C, Gravier G, Magrin Chagnolleau I, Meignier S, Merlin T, Ortega-Garcia J, Petrovska Delacreetaz D, Reynolds DA (2004) A tutorial on text-independent speaker verification. EURASIP J Signal Process 4. Hindawi Publishing Cor-poration, pp 430–451
9. ShuklaUP, Patel NB, Joshi AM (2013) Analysis of music signal compression with compressive sensing. Int J Comput Appl 70(26)
10. Bou-Ghazale SE, Hansen JHL (2000) A comparative study of traditional and newly proposed features for recognition of speech under stress. IEEE Trans Speech Audio Process 8(4):429–442. Prentice Hall, Upper Saddle River, NJ, USA
11. Zhou G, Hansen JHL, Kaiser JF (2001) Nonlinear feature based classification of speech under stress. IEEE Trans Speech Audio Process 9(3):201–216
12. Li X (2004) Reconstruction of speech from Chinese Whispers. PhD, Nanjing University, China; Ito T, Takeda K Itakura F (2005) Analysis and recognition of whispered speech. Speech Commun 45:139–152
13. Jin Q, Jou SCS, Schultz T (2007) Whispering speaker identification. In: 2007 IEEE international conference on multimedia and expo, pp 1027–1030. IEEE

Design of Y-Shaped Immensely Wideband Printed Monopole Antenna with Three Notched Bands

H. S. Mewara, J. K. Deegwal and M. M. Sharma

Abstract A Y-shaped design comprising of three band notches and immensely wideband antenna is proposed. The basic antenna having double bevel cut providing Y-shape to patch and bevel cut on upper side of ground plane with step cut at centre upper position of ground plane results in immensely wide operating band 2.8–23.8 GHz for $|S_{11}| < -10$ dB. One stop band results from a pair of C-shaped slot on ground plane for WiMAX (3.3–3.6 GHz) band while the other two stop bands are obtained by inverted U-shaped slot for WLAN (5.15–5.825 GHz) band and C-shaped slot for X-band downlink communication frequency (7.25–7.75 GHz) on patch for $|S11| > -10$ dB. Surface current distributions at centre notch frequencies verify triple band function. The proposed antenna demonstrated dipole-like and nearly omnidirectional radiation pattern in YZ-plane and XZ-plane, respectively.

Keywords Ultra-wideband antenna · Microstrip feed · WiMAX notch · WLAN notch · Downlink of X-band satellite communication system

1 Introduction

For ultra-wideband (UWB) communications, license free band 3.1–10.6 GHz was allocated by Federal Communication Commission (FCC) in the year 2002. Researchers have shown much interest in UWB technology because of various advantages such as high-speed data transmission, low consumption of power level, compact

H. S. Mewara (✉) · J. K. Deegwal
Government Engineering College Ajmer, Near Nareli Jain Temple,
NH-8, Badliya Circle, Ajmer, India
e-mail: hsmewara@gmail.com

J. K. Deegwal
e-mail: jitendradeegwal@gmail.com

M. M. Sharma
Malaviya National Institute of Technology, Jaipur, India
e-mail: mmsjpr@gmail.com; mmsharma.ece@mnit.ac.in

© Springer Nature Singapore Pte Ltd. 2020

V. Janyani et al. (eds.), *Optical and Wireless Technologies*,
Lecture Notes in Electrical Engineering 546,
https://doi.org/10.1007/978-981-13-6159-3_25

size and ease of integration. Many designs were reported for UWB antennas [1–3]. Various wireless narrowband systems such as IEEE 802.16 worldwide interoperability for microwave access (WiMAX) 3.3–3.6 GHz band, IEEE 802.11a Wireless local area network (WLAN) 5.15–5.825 GHz band and X-band downlink communication frequency (X-band) 7.0–7.75 GHz band interferes with the UWB communication. Hence, the requirement of antennas having capabilities to reject some or all of these interfering bands is essential. Simplest approach adopted to design frequency band rejecting antennas includes engraving slots of various shapes on radiating patch, feed line or on ground plane. Based on this technique, single band-notched UWB antenna [4], double band-notched UWB antenna [5, 6] and triple band-notched antenna [7, 8] are reported.

In this paper, a Y-shaped immensely wideband designed antenna with three notched band is proposed. Rectangular radiating patch is modified to form a Y-shape while the partial ground plane with bevel edges on upper side and step cut below feed enhances the impedance bandwidth enormously. Interference suppression from WiMAX band is realized by inscription of a pair of slots on ground plane while interference from WLAN band and X-band is avoided by imprinting two slots on radiator. Computer Simulation Tool (CST) software is used to design and simulate the proposed antenna.

2 Antenna Design and Analysis

Figure 1a, b shows front view and back view of the basic Y-shaped antenna. The basic antenna is a three-layer structure consisting of upper and lower copper layer which acts as patch and ground plane while the middle layer is FR-4 substrate. This FR-4 substrate has thickness 1.6 mm, relative dielectric constant (ε_r) 4.3 and loss tangent (tan δ) 0.025. Microstrip line use to feed the antenna has width 4 mm to match 50 Ω impedance. Radiating patch is converted into Y-shape by cutting bevel edges on upper and lower side of rectangular patch as shown in Fig. 1a. Partial ground plane is also altered by cutting bevel edges on upper side and a step cut is also introduced on ground plane below feed line. These modifications on the radiator and ground plane have increased the current path which ultimately results in extremely wide bandwidth.

Interference from each of the desired bands can be eradicated by introducing resonating elements each having length $\lambda_g/2$. This length can be calculated from Eq. (1)

$$L_{slot} = \frac{\lambda_g}{2} = \frac{\lambda_0}{2\sqrt{\varepsilon_{eff}}} = \left(\frac{c}{2f_n}\right) \times \left(\frac{1}{\sqrt{[(\varepsilon_r + 1)/2]}}\right) \tag{1}$$

where C is the speed of light, ε_{eff} and ε_r is the effective and relative dielectric constants, λ_g and λ_0 are the guided and free space wavelengths, f_n is the centre notch frequency.

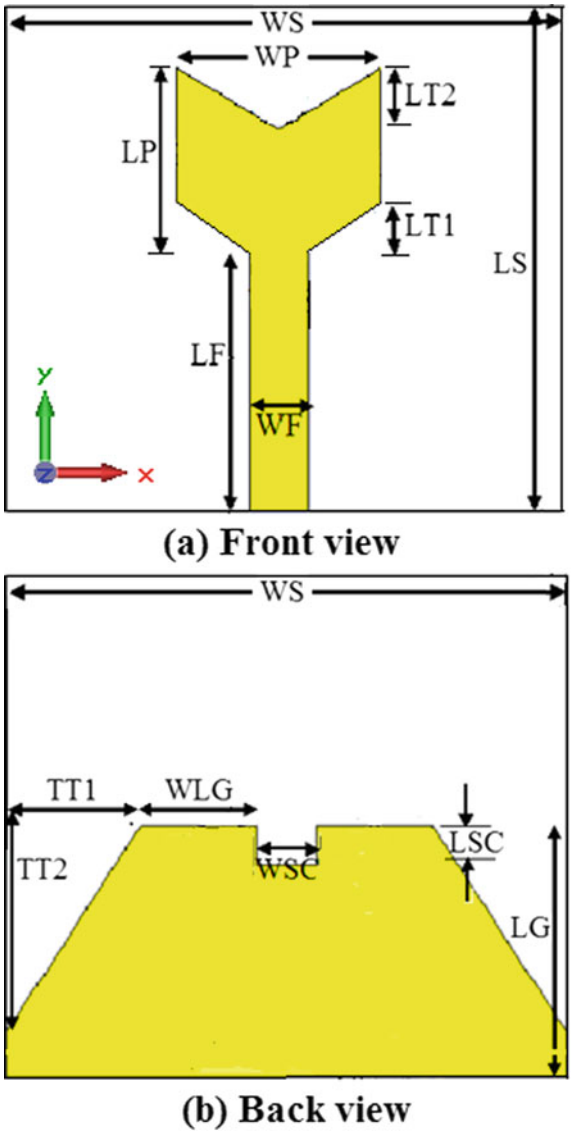

Fig. 1 Basic Y-shaped antenna **a** front view **b** back view

Resonating elements for WiMAX, WLAN and X-band are designed by electing centre notch frequency as 3.45 GHz, 5.5 GHz and 7.5 GHz, respectively. Interference from WiMAX band is eliminated by inserting a pair of C-shaped slots on ground plane.

For removing interference from WLAN and X-band, an inverted U-slot and a C-shaped slot is etched on radiator. The geometry of the proposed Y-shaped antenna with three notched bands is shown in Fig. 2a, b.

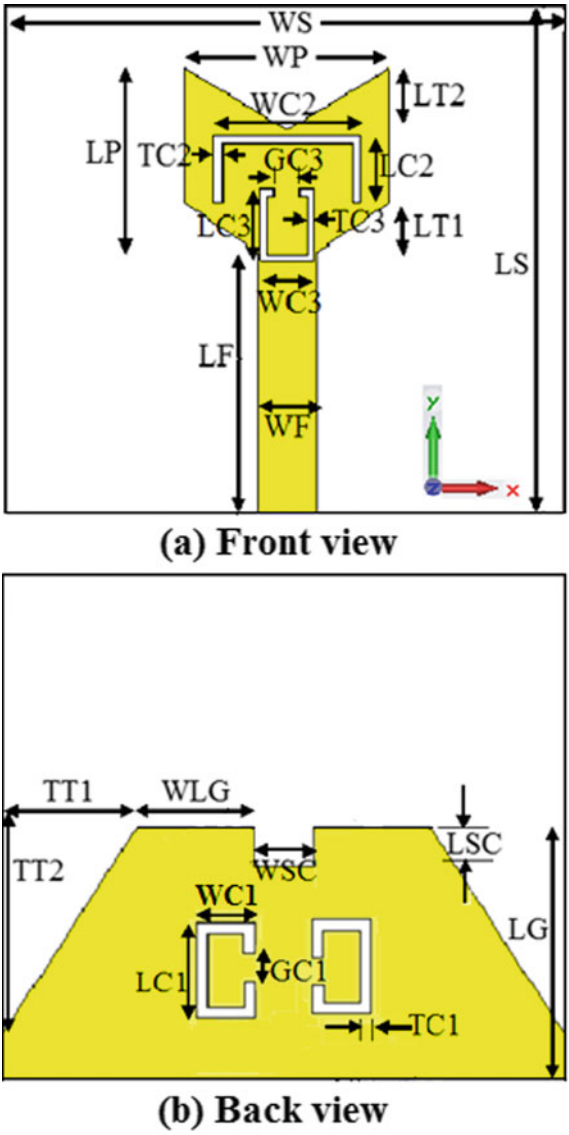

Fig. 2 Geometry of the proposed Y-shaped antenna **a** front view **b** back view

2.1 Parametric Variation Study

The coupling among band notch elements can be known by varying width of each band notch element at a time while the other parameters are kept constant. Figure 3a–c shows $|S_{11}|$ plot for variation in values of each of the width of slots WC1, WC2 and WC3 for WiMAX band, WLAN band and X-band, respectively. It can be derived that the variation in the width of each band notch element results in shifting of centre

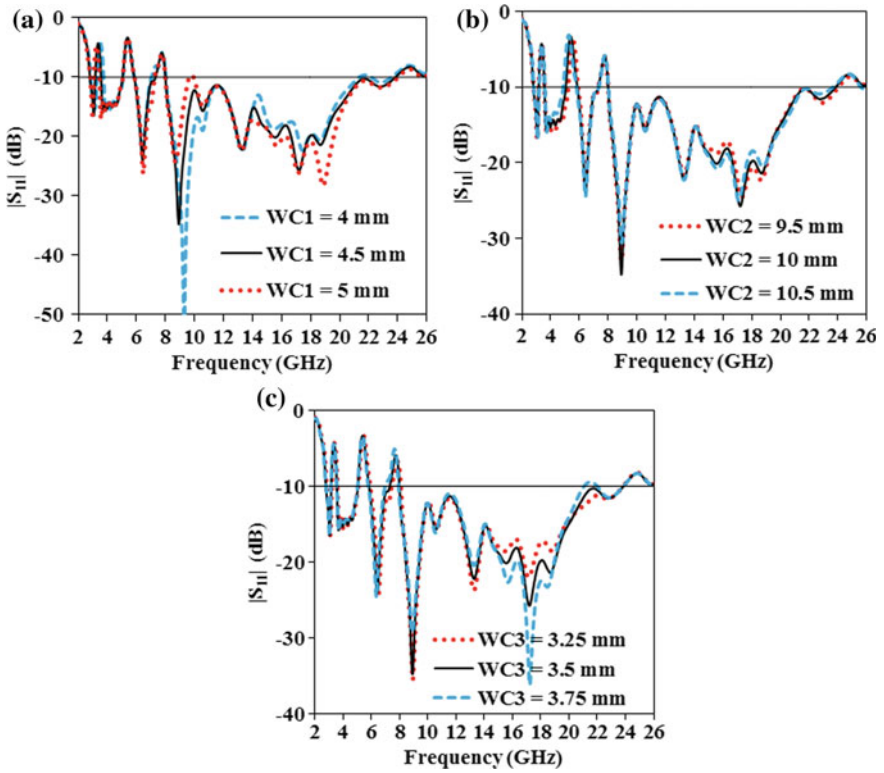

Fig. 3 **a** Magnitude of S_{11} plot for variation in values of width WC1 of WiMAX band notch element, **b** magnitude of S_{11} plot for variation in values of width WC2 of WLAN band notch element, **c** magnitude of S_{11} plot for variation in values of width WC3 of X-band notch element

notch frequency towards lower frequency side while the other band notches have negligible effect. Thus, negligible coupling among the three band-notched elements is verified. Value of parameters optimized to design this proposed antenna is listed in Table 1.

3 Results and Discussion

Figure 4 shows the comparison of the magnitude of S_{11} for basic Y-shaped antenna and proposed Y-shaped antenna with three band notches to diminish interference from WiMAX, WLAN and X-bands. It is perceived from Fig. 2 that basic Y-shaped antenna has extremely large impedance bandwidth 2.95–24.5 GHz for the plot of magnitude of $S_{11} < -10$ dB. Simulated values as displayed in Fig. 3 for centre band notch frequencies for three band notches is 3.36, 5.38 and 7.74 GHz against

Table 1 Final value of optimized parameters for the proposed antenna with three notched bands

Parameter	Value (mm)	Parameter	Value (mm)	Parameter	Value (mm)
GC1	0.2	LS	36	WC1	4.5
GC3	2	LSC	2.5	WC2	10
LC1	10	LT1	3.2	WC3	3.5
LC2	4.5	LT2	4	WF	4
LC3	4.75	TC1	0.3	WLG	8
LF	19.5	TC2 = TC3	0.6	WP	14
LG	18	TT1	9	WS	38
LP	12	TT2	13.5	WSC	4

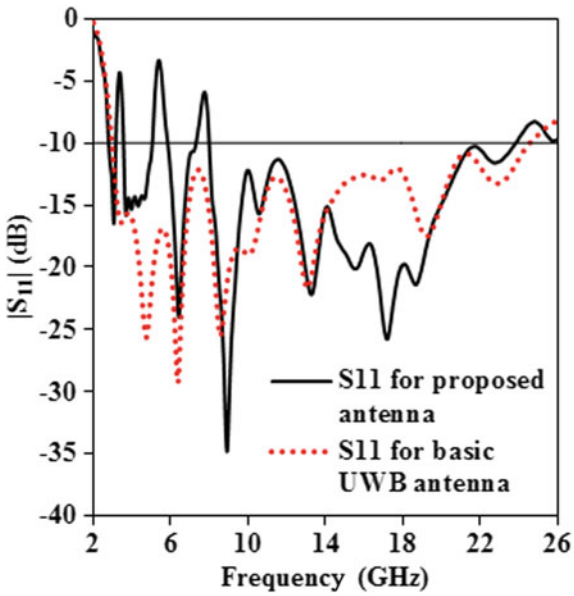

Fig. 4 Comparison of magnitude of S_{11} plot for basic Y-shaped antenna and the proposed Y-shaped antenna with three band notches

the designed centre notch frequencies of 3.45, 5.5 and 7.5 GHz. The first notch at 3.36 GHz for a pair of C-shaped slot has maximum length while the third notch at 7.74 GHz due to C-shaped slot on patch has minimum length. It can be witnessed that simulated value of $|S_{11}| < -10$ dB for proposed Y-shaped antenna with three notches has impedance bandwidth 2.8–23.8 GHz. $|S_{11}| > -10$ dB are obtained for 3.17–3.6 GHz (WiMAX band), 5.05–5.85 GHz (WLAN band) and 7.31–7.99 GHz (X-band).

Operations for each of the band-notched elements can be better explained by watching surface current distributions at each of the centre notch frequency. Figures 5, 6 and 7 display current distributions at 3.45 GHz, 5.5 GHz and 7.5 GHz centre notch frequencies of WiMAX, WLAN and X-band, respectively. Arrows in

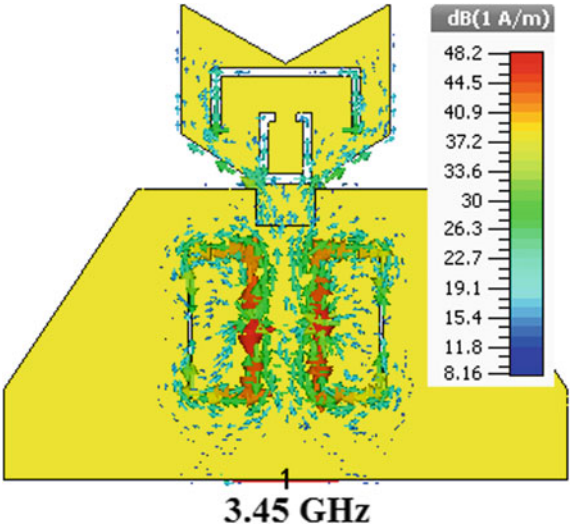

Fig. 5 Surface current distributions for the proposed antenna at 3.45 GHz

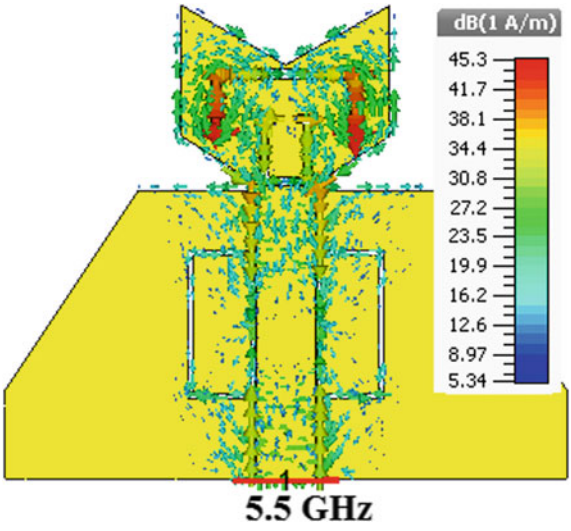

Fig. 6 Surface current distributions for the proposed antenna at 5.5 GHz

red colour indicate maximum value while the blue arrows show minimum values. It can be observed that the red colour arrows (maximum current) are concentrated at external boundaries of each band notching element and are in opposite directions, thus cancelling out each other which indicates very low value of impedance (short circuit) while there are no arrows or blue colour (minimum current) arrows are found at centre of each band notching element indicating maximum impedance (open circuit). This impedance mismatch generates stop bands at 3.45 GHz for WiMAX band, at 5.5 GHz for WLAN band and at 7.5 GHz for X-band.

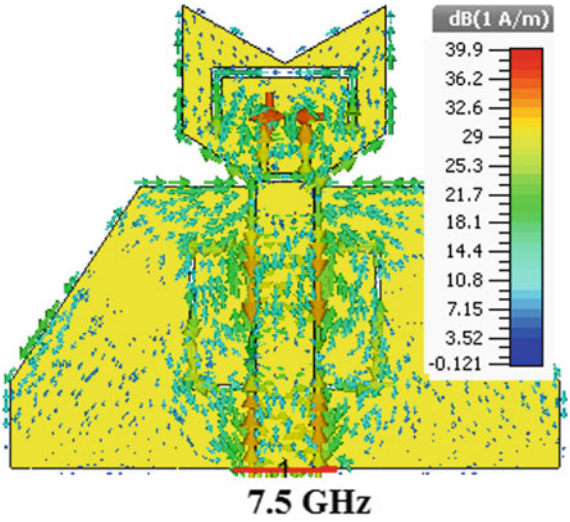

Fig. 7 Surface current distributions for the proposed antenna at 7.5 GHz

Simulated values of realized gain for proposed Y-shaped antenna with three notched bands versus basic Y-shaped antenna are plotted in Fig. 8. There is significant reduction in value of gain for the notched band regions for the proposed antenna. Along the notched bands, peak value of gain reduces to −2.9 dBi at 3.36 GHz, −0.8 dBi at 5.38 GHz and −0.25 dBi at 7.74 GHz for WiMAX, WLAN and X-bands respectively.

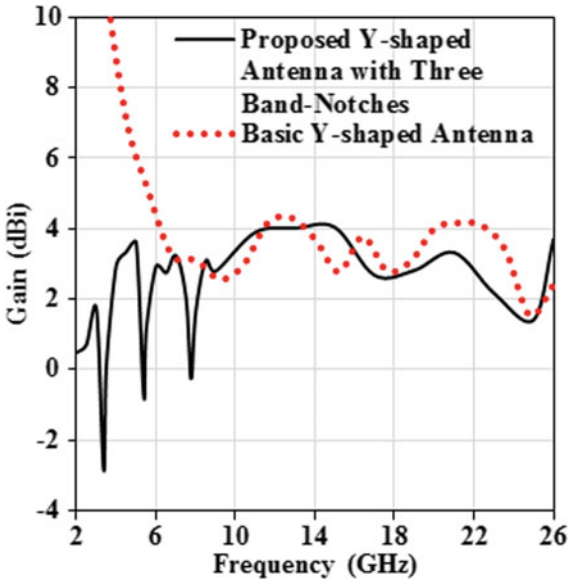

Fig. 8 Gain comparison for proposed Y-shaped antenna with three band notches and basic Y-shaped antenna

Simulated radiation patterns for proposed Y-shaped antenna with three notched bands are plotted in Fig. 9a–d for four resonant frequencies in two principle planes. The four resonant frequencies 3.17, 5.35, 9.52 and 15.87 GHz in operating band show dipole-like pattern for YZ-plane while nearly omnidirectional pattern is obtained for XZ-plane. Cross polarization values increase at higher frequencies for XZ-plane due to increase in horizontal component.

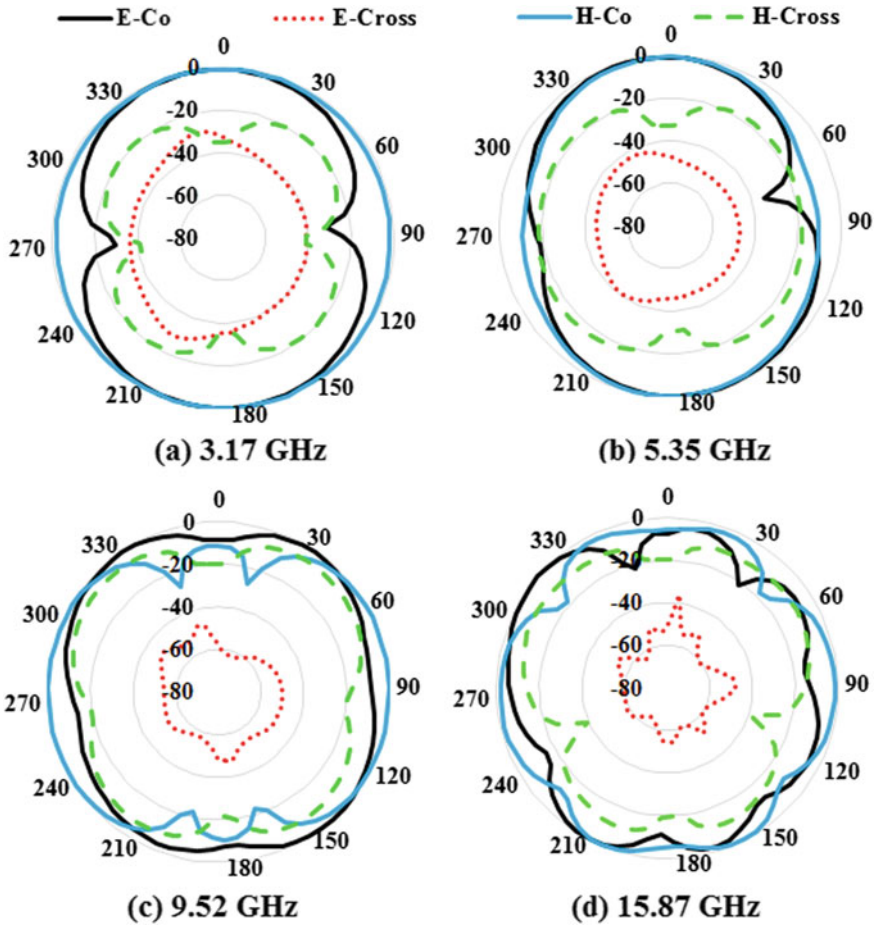

Fig. 9 Radiation pattern for proposed Y-shaped UWB antenna with three notched bands at four resonance frequencies

4 Conclusion

Design of Y-shaped immensely wideband printed monopole antenna with three notched bands is presented. Each stop band is achieved by inserting $\lambda_g/2$ length resonator which acts as energy storage elements. Interference from WiMAX, WLAN band and X-band is removed by etching a pair of C-shaped slots on ground plane, an inverted U-shaped slot and a C-shaped slot on radiator, respectively. Studies based on simulated values of magnitude of S_{11} curve, surface current distributions, realized gain and radiation patterns were presented. Significant decrease in gain values at three regions indicates notched bands behaviour of the proposed antenna. These properties make this antenna suitable for numerous wireless communication services and immensely wideband application including UWB application also with the omission of WiMAX, WLAN and X-bands.

References

1. Mewara HS, Sharma MM, Sharma M, Gupta M, Dadhich A (2016) A planar ultra-wide band antenna design using circularly truncated corners and notches. In: Satapathy S, Raju K, Mandal J, Bhateja (eds) Proceedings of the second international conference on computer and communication technologies. Advances in intelligent systems and computing. Springer, p 379. https://doi.org/10.1007/978-81-322-2517-1_68
2. Huang CY, Chen GH (2012) Compact self-complementary antenna for ultra-wideband application. Microw Opt Technol Lett 47(16):2144–2146
3. Li L, Zhou ZI, Hong JS, Wang BZ (2011) Compact ultra-wideband printed monopole antenna. Electron Lett 47(16):894–896. https://doi.org/10.1049/el.2011.1529
4. Mewara HS, Kumawat R, Sharma MM (2017) Design and analysis of an ultra-wide band antenna consisting of extra radiating patch with bandwidth enhancement and band notch characteristics. In: International conference on recent advances and innovations in engineering (ICRAIE). IEEE, pp 1–5. https://doi.org/10.1109/icraie.2016.7939601
5. Fakharian MM, Rezaei P, Azadi A (2015) A planar UWB bat-shaped monopole antenna with dual band-notched for WiMAX/WLAN/DSRC. Wirel Personal Commun 81:881–891. https://doi.org/10.1007/s11277-014-2162-8
6. Sharma MM, Deegwal JK, Govil MC, Kumar A (2015) Compact printed ultra-wideband with two notched stop bands for WiMAX and WLAN. Int J Appl Electromagn Mech 47(2):523–531. https://doi.org/10.3233/JAE-140007
7. Mewara HS, Jhanwar D, Sharma MM, Deegwal JK (2017) A novel hammer-shaped UWB antenna with triple notched-band for rejecting RLS WLAN and XSCS bands. Adv Electromagn 6(4):36–41. https://doi.org/10.7716/aem.v6i4.527
8. Mewara HS, Jhanwar D, Sharma MM, Kumar A (2017) An extremely wideband/multiresonance monopole antenna with multiple notched stop bands. In: International conference on computer, communication and electronics (comptelix). IEEE, pp 669–671. https://doi.org/10.1109/comptelix.2017.8004053

A Printed Ultra-wideband Monopole Antenna with Triple Band Notch Characteristics

H. S. Mewara, J. K. Deegwal and M. M. Sharma

Abstract Design of a printed ultra-wideband (UWB) monopole antenna with three band notches is presented. The proposed UWB antenna uses circular and bevel shaped radiator while the ground plane has bevel shape with step notch to enhance impedance bandwidth. Microstrip line having 50 Ω impedance is used to feed the proposed antenna which operates in the range 3.24–14.27 GHz having nearly 11.03 GHz impedance bandwidth. The proposed triple band-notched antenna design consists of an inverted U-shaped and two C-shaped slots, all etched on radiating patch for suppressing interference from WiMAX (3.3–3.6 GHz) band, WLAN (5.15–5.85 GHz) band and X-BAND satellite communication system (7.25–8.4 GHz) band. Current distribution at each of the centre band notch frequency, radiation pattern at resonance frequencies and gain of the antenna are also analysed.

Keywords Printed UWB antenna · Microstrip feed · WiMAX · WLAN · X-band satellite communication system · Multiple band notch

1 Introduction

In the year 2002, Federal Communication Commission (FCC) has approved unlicensed band 3.1–10.6 GHz for ultra-wideband (UWB) communications. Recently, UWB technology has grabbed much attention due to advantages such as high data rate transmission, low power level, low cost and ease of fabrication. Various types

H. S. Mewara (✉) · J. K. Deegwal
Government Engineering College Ajmer, Near Nareli Jain Temple,
NH-8, Badliya Circle, Ajmer, India
e-mail: hsmewara@gmail.com

J. K. Deegwal
e-mail: jitendradeegwal@gmail.com

M. M. Sharma
Malviya National Institute of Technology, Jaipur, India
e-mail: mmsjpr@gmail.com; mmsharma.ece@mnit.ac.in

© Springer Nature Singapore Pte Ltd. 2020

V. Janyani et al. (eds.), *Optical and Wireless Technologies*,
Lecture Notes in Electrical Engineering 546,
https://doi.org/10.1007/978-981-13-6159-3_26

of designs have been reported for UWB antennas [1–3]. One major problem faced by UWB antenna designs is the coexistence of several narrowband communication systems such as worldwide interoperability for microwave access (WiMAX) 3.3–3.6 GHz band, wireless local area network (WLAN) 5.15–5.825 GHz band, X-band for satellite communication systems (XSCS) 7.25–8.4 GHz band. Hence, it is essential to design UWB notched band antennas that minimize interferences from these narrowband communication systems. Researchers have published several designs for single [4, 5, 8], double [6, 8] and triple band-notched UWB antennas [7, 8].

In this paper, a design for triple band-notched antenna is proposed. Modified radiating patch with bevelled edges on lower side, quarter cut circle at top corners of the patch along with the partial ground plane with bevel edges and step cut below feed enhances the UWB impedance bandwidth. Interference from WiMAX, WLAN and XSCS band is achieved by etching three slots that are an inverted U1-slot, C1-slot and C2-slot on patch, respectively. The design and simulation of the proposed antenna are carried out on Computer Simulation Tool (CST) version 14.

2 Antenna Design and Analysis

The proposed antenna is designed on FR-4 substrate having relative permittivity (ε_r) 4.3 and loss tangent (tan δ) 0.025. This FR-4 substrate is sandwiched between two electroplated copper depositions each having thickness MT, front layer acting as radiating patch while the back side acts as ground plane. The geometry of the proposed triple band-notched UWB antenna is as shown in Fig. 1a, b showing front and back view, respectively.

The antenna is fed by microstrip line having width 3 mm to match 50 Ω impedance. Overall dimensions of the proposed notched band antenna are $35 \times 37 \times 1.6$ mm^3. The UWB bandwidth of the antenna is extended by modifying patch with bevel edges on lower side, quarter cut circles on the upper left and right corners as shown in Fig. 1. The bevel edges along with the step cut below microstrip feed line on the ground plane also enhance bandwidth. These modifications on the patch and ground plane amends inductance and capacitance which results in better impedance matching and thus bandwidth is improved.

Band notching function for suppressing WiMAX, WLAN and XSCS band is designed by choosing centre notch frequency as 3.45 GHz, 5.5 GHz and 7.8 GHz, respectively. Interference from WiMAX band is minimized by inserting an inverted U-shaped slot named as slot-U1 on upper side of patch as displayed in Fig. 1a. For suppressing interference from WLAN and XSCS bands, two C-shaped slots named as slot-C1 and slot-C2 are inserted on radiating patch as shown in Fig. 1a. Length of each band-notched element slot (L_{slot}) for suppressing individual notched band is half the guided wavelength and is given in (1).

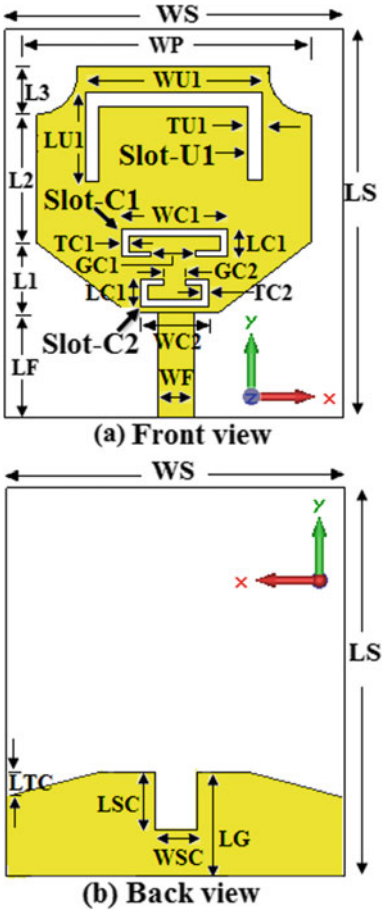

Fig. 1 Proposed triple band-notched UWB antenna design **a** front view **b** back view

$$L_{slot} = \frac{\lambda_g}{2} = \frac{\lambda_0}{2\sqrt{\varepsilon_{eff}}} = \left(\frac{c}{2f_n}\right) \times \left(\frac{1}{\sqrt{[(\varepsilon_r + 1)/2]}}\right) \tag{1}$$

2.1 Parametric Variation Study

For studying the coupling effect among band notches, width of each band notch element is varied one at a time while the other parameters are kept constant. Figure 2a–c shows plot of the magnitude of S_{11} for variation in values of each of the width of slots WU1, WC2 and WC3 for WiMAX, WLAN and XSCS bands, respectively. It

was observed from each of Fig. 2a–c that the variation in width of each band notch element results in shifting of centre notch frequency towards lower frequency side. It is also observed that variation in width of each band notch element affects the bandwidth of individual band notch while the other band notches are affected negligibly. Thus, there is negligible coupling among the three band-notched elements.

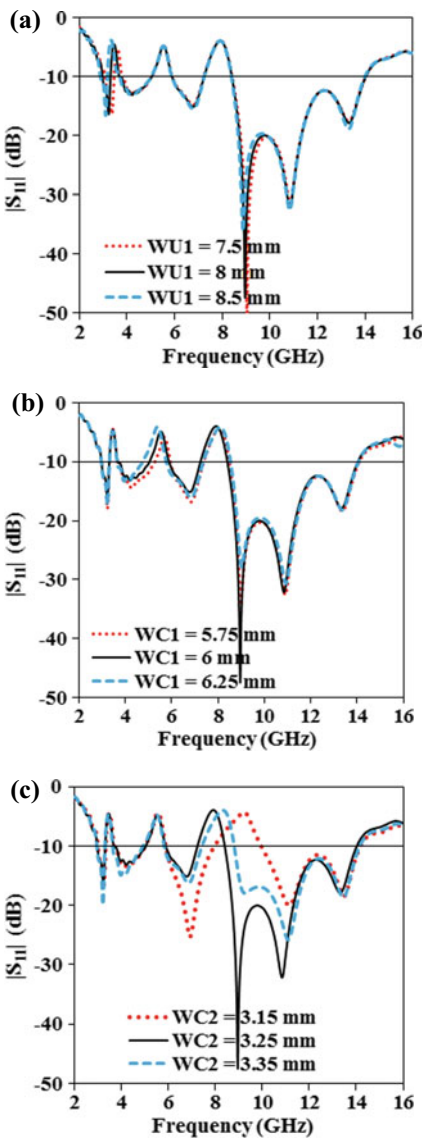

Fig. 2 **a** Magnitude of S_{11} plot for variation in values of width WU1 of WiMAX band notch element. **b** Magnitude of S_{11} plot for variation in values of width WC2 for WLAN band notch element. **c** Magnitude of S_{11} plot for variation in values of width WC3 for XSCS band notch element

Table 1 Final value of optimized parameters for proposed triple band-notched antenna

Parameter	Value (mm)	Parameter	Value (mm)	Parameter	Value (mm)
GC1	4	LF	10.5	WF	3
GC2	4.8	LS	35	WP	23
L1	5	LSC	5	WC1	12
L2	10	LTC	3.5	WC2	6.5
L3	3	LU1	7.8	WS	37
LC1	2	TC1	0.5	WSC	3
LC2	0.75	TC2	0.2	WU1	16
LG	9	TU1	1	MT	0.035

The final values of parameters shown are optimized to get desired triple band-notched antenna and are mentioned in Table 1.

3 Results and Discussion

Figure 3 shows the magnitude of S_{11} curve for the proposed antenna without three slots for basic UWB antenna and with three slots for triple band notching to minimize interference from WiMAX, WLAN and XSCS bands. It is apparent from Fig. 3 that basic UWB antenna fed by microstrip line has impedance bandwidth 3.24–14.27 GHz for the simulated plot of magnitude of $S_{11} < -10$ dB. It is observed from Fig. 3 that the values of simulated centre band notch frequencies is 3.45, 5.52 and 7.92 GHz. The first notch at 3.45 GHz for inverted U1-slot has the maximum dimensions, the second notch at 5.52 GHz is due to C1-slot and the third notch at 7.92 GHz due to C2-slot has minimum dimensions on the radiating patch. It is also detected that the proposed UWB antenna triple band-notched antenna has impedance bandwidth 2.97–14.03 GHz for the simulated plot of magnitude of $S_{11} < -10$ dB except for the band notches. Simulated values of magnitude of $S_{11} > -10$ dB for three band notches realized are 3.30–3.67 GHz, 5.04–5.87 GHz and 7.24–8.40 GHz for rejecting WiMAX, WLAN and XSCS band, respectively. Dimension and position of individual slot decides the operating frequency for notched band.

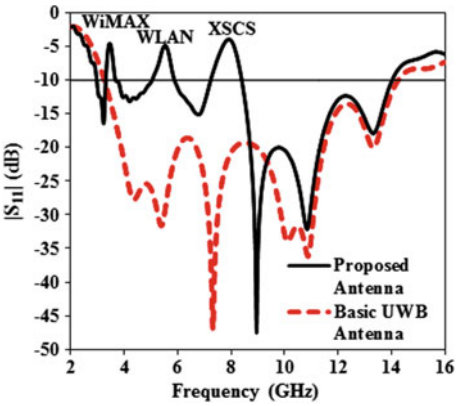

Fig. 3 Comparison of magnitude of S_{11} plot for basic UWB antenna and the proposed triple band-notched UWB antenna

The working mechanism for each of the notched bands can be better understood by considering the surface current distributions. The designed centre notch frequencies for WiMAX, WLAN and XSCS bands are 3.45 GHz, 5.5 GHz and 7.8 GHz, respectively. Surface current distributions at 3.45, 5.5 and 7.8 GHz the centre notch frequency for inverted U1-slot for WiMAX, C1-slot for WLAN and C2-slot for XSCS bands rejection are shown in Fig. 4a–c, respectively. It can be seen that current is maximally concentrated on the outer edges of the slot in the opposite directions cancelling each other, indicating nearly zero impedance (short circuit) while there is minimum current at centre of the slot indicating maximum impedance (open circuit). This mismatch in impedance creates notched band at WiMAX band. Similar trends for current distributions are observed at other two centre notch frequencies at 5.5 GHz for C1-slot and 7.8 GHz for C2-slot creating band notches for rejecting WLAN and XSCS bands, respectively.

The simulated realized gain for the proposed triple band-notched antenna is shown in Fig. 5. Variation in gain is in the range 2.26–3.96 dBi for the operating frequency range while the peak value of gain is 5.9 dBi at 6.8 GHz. The gain plot shows substantial decrease in the value of gain at three notch frequencies confirming notch band regions. The simulated E-plane and H-plane (Co- and Cross pol) patterns at resonant frequencies 3.23 GHz, 6.8 GHz, 8.95 GHz and 10.8 GHz are plotted in Fig. 6a–d, respectively. It is apparent that E-plane (Co-polarization) has bidirectional radiation pattern while H-plane (Co-Polarization) has nearly omnidirectional radiation patterns.

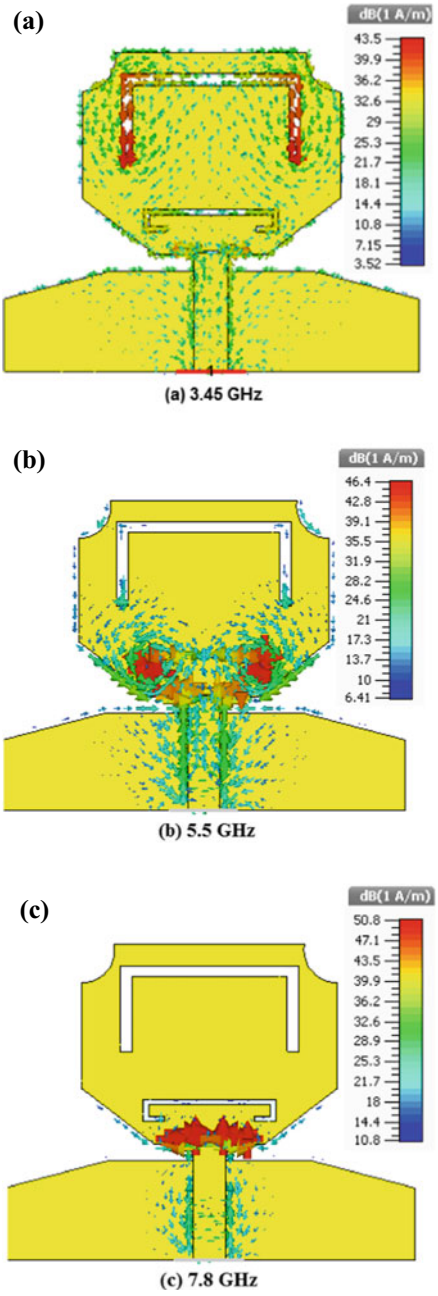

Fig. 4 **a** Surface current distributions at 3.45 GHz **b** surface current distributions at 5.5 GHz **c** surface current distributions at 7.8 GHz

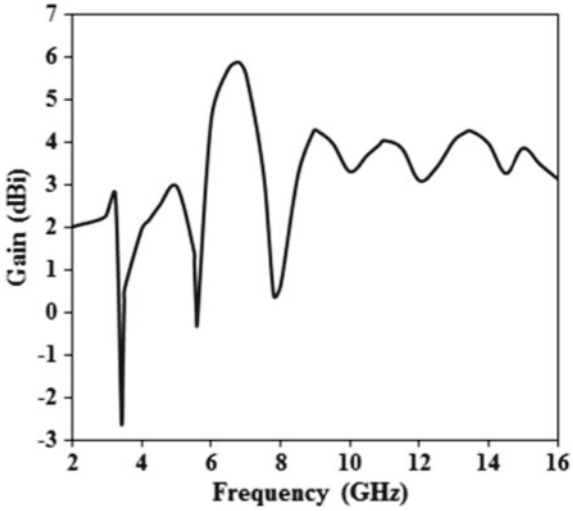

Fig. 5 Gain for proposed triple band-notched antenna

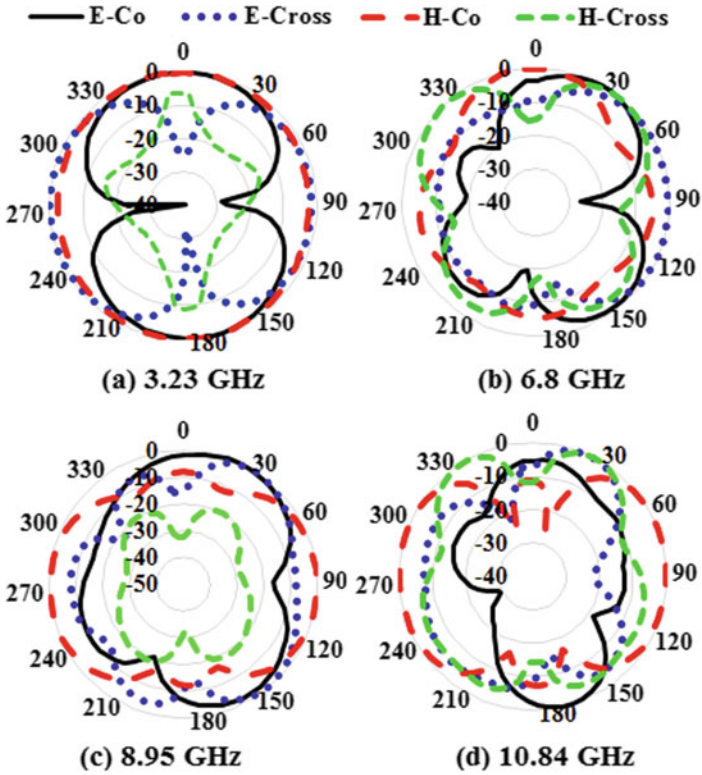

Fig. 6 Radiation pattern for proposed triple band-notched antenna at four resonance frequency

4 Conclusion

A printed UWB monopole antenna with three band notches is demonstrated. The proposed antenna design uses three slots, one inverted U1-slot, one C1-slot and other C2-slot on patch for avoiding WiMAX, WLAN and XSCS bands, respectively. Investigations regarding simulated magnitude of S_{11} plot, surface current distribution, realized gain and radiation pattern were carried out. The substantial decrease in the value of gain at three band notches confirms the triple band notch behaviour of the proposed design. This proposed antenna is appropriate for UWB application with exception of WiMAX, WLAN and XSCS bands.

References

1. Mewara HS, Sharma MM, Sharma M, Dadhich A (2013) A novel ultra-wide band antenna design using notches, stepped microstrip feed and beveled partial ground with beveled parasitic strip. In: IEEE applied electromagnetics conference (AEMC). IEEE, pp 1–2. https://doi.org/10.1109/aemc.2013.7045091
2. Zitouni A, Boukli-Hacene N (2011) A new four truncated corners ultra-wideband antenna with two crossed slits in the path. Int J Microw Opt Technol 6(4):217–220
3. Ojaroudi M, Yazdanifard Sh, Ojaroudi N, Naser-Moghaddasi M (2011) Small square monopole antenna with enhanced bandwidth by using inverted T-shaped slot and conductor-backed plane. IEEE Trans Antennas Propag 59(2):670–674
4. Mewara HS, Kumawat R, Sharma MM (2017) Design and analysis of an ultra-wide band antenna consisting of extra radiating patch with bandwidth enhancement and band notch characteristics. In: International conference on recent advances and innovations in engineering (ICRAIE). IEEE, pp 1–5. https://doi.org/10.1109/icraie.2016.7939601
5. Soltani S, Azamanesh A, Lotfi P, Dadashzadeh G (2011) Two novel very small antenna having frequency band notch function using DGS for UWB application. Int J Electron Commun (AEU) 65:87–94
6. Sharma MM, Deegwal JK, Govil MC, Kumar A (2015) Compact printed ultra-wideband with two notched stop bands for WiMAX and WLAN. Int J Appl Electromagnet Mech 47(2):523–531
7. Mewara HS, Jhanwar D, Sharma MM, Deegwal JK (2017) A novel hammer-shaped UWB antenna with triple notched-band for rejecting RLS WLAN and XSCS bands. Adv Electromagnet 6(4):36–41. https://doi.org/10.7716/aem.v6i4.527
8. Vendik IB, Rusakov A, kanjanasit K (2017) Ultrawideband (UWB) planar antenna with single-, dual-, and triple-band notched characteristic based on electric ring resonator. IEEE Antennas Wirel Propag Lett 16:1597–1600

Parabolic Pulse Generation at 1550 nm Raman Amplifier Utilizing High Power Pump Laser

Dipika D. Pradhan and Abhilash Mandloi

Abstract To increase the range of 1550 nm signal transmission, Raman amplifier can be used. We demonstrate the design and performance of 1550 nm Raman amplifier utilizing single pump laser 1450 nm. The both codirectional and counter-directional pumping Raman amplifier is compared. The maximum gain for counter pumping is 45.87 dB and minimum noise figure is 7 dB. The 1550 nm Raman amplifier gain is function of wavelength corresponds to 8–25 nm amplification bandwidth. The saturation input power of Raman amplifier is from 10 to 15 dBm as the pump wavelength increases from 200 to 800 mW in case of counter propagation pumping configuration. Parabolic pulse generation in standard single mode fiber is investigated for the fiber length 10–100 km.

Keywords Raman scattering · Distributed amplifier · Dispersion compensated fiber · Dense wavelength division multiplexing · Coupler

1 Introduction

To mitigate the demand for high transmission bandwidth, the optical amplifier technology is implemented. Raman amplifier is a broadband amplifier. Nowadays, DCF has quietly used Raman amplifier in DWDM system. The 1310 nm Raman amplifier shows the gain bandwidth of 14–18 nm [1]. Previous work reported the C band ranging from 1530 to 1565.4 nm designed in DWDM system. The performance analysis is investigated with four pumps backward multimap Raman amplifier. Generally, DCFs are characterized very small effective area and offers high Raman gain [2]. The Raman gain spectrum depends on polarization state and orientation of the pump. Raman amplifier is a promising technology to achieve the high bandwidth require-

D. D. Pradhan (✉) · A. Mandloi
Sardar Vallabhbhai National Institute of Technology, Surat, Gujarat, India
e-mail: d14ec004@eced.svnit.ac.in

A. Mandloi
e-mail: asm@eced.svnit.ac.in

© Springer Nature Singapore Pte Ltd. 2020

V. Janyani et al. (eds.), *Optical and Wireless Technologies*,
Lecture Notes in Electrical Engineering 546,
https://doi.org/10.1007/978-981-13-6159-3_27

ment of the user. This presents the scheme for R-EDFA/Raman hybrid amplifier using stimulated Raman scattering [3]. To cover the C and L band in the optical domain, a novel high gain hybrid amplifier is designed with combination of Raman amplifier and EYDFA [4]. Raman amplifier with a combination of gain-clamped semiconductor optical amplifier is used as hybrid amplifier has 20 dB gain and Noise figure below 2.7 dB [5]. A design optimization of data rate 16 × 40 Gbps data rate EDFA in DWDM system from 100 to 500 mW pump power. The BER and noise figure are less than 10^{-9} and 7 dB, respectively, with channel spacing 100 GHz [6]. The L Band R-EDFA and RAMAN hybrid amplifier has been demonstrated. The gain clamping effect is reduced by tuning the pump wavelength to a region away from the amplification bandwidth [7]. A EDFA-Raman hybrid amplifier is demonstrated which is operating in C and L band over 65 nm bandwidth upshots gain of 17 dB. [8]. Raman amplifier is designed with 100 nm bandwidth ranging from 1416 to 1502 nm at eight pump power of 130 mW [9]. The presented research on multichannel 10 × 10 Gbps transmission over 7200 km. The Raman amplifier noise performance 2 dB better than lumped EDFA has been attempted [10].

In this paper, we present the design and performance of 1550 nm Raman amplifier. The performance of Raman amplifier is evaluated by using simulation method. The Raman amplifier bandwidth is 18–20 nm. We present the performance of distributed Raman amplifier for different fiber lengths. The 1450 nm pump is utilized as a single pump to generate parabolic pulse at wavelength ranging from 1500 to 1580 nm. We also investigated the codirectional and counter-directional pumping with different pump power varies from 200 to 1200 mW.

2 Raman Amplifier Modeling

Raman amplification is based on Raman scattering effect in optical fibers. In the broadband communication system, the maximum gain is obtained when the difference between signal frequencies and the pump is nearly 13.2 THz. In the signal wavelength 1550 nm, the bandwidth is 100 nm as the pump wavelength shifted downward is 1450 nm. A high pump power is inserted into the fiber in co-propagating and counter-propagating directions. The counter-propagating scheme is better than co-propagating due to better transmission properties of Raman amplifier.

There are two types of Raman amplifiers: discrete and distributed Raman amplifiers. The discrete type is a lumped element inserted in the transmission line and provides high gain. The gain of the Raman amplifier is defined as the ratio of the signal power Ps with and without pumping [1].

$$\text{Gain (G)} = \frac{Ps(L)}{Ps(0)} = \exp(\text{grPpLeff}) \tag{1}$$

where L is the length of the fiber is the Pp and Ps is the pump power and signal power through the length of the fiber L, respectively, where gr is the Raman gain coefficient of the fiber and the effective length of fiber is Leff.

$$\text{Leff} = \frac{1 - exp(\alpha pL)}{\alpha p} \tag{2}$$

where αp is the attenuation coefficient of the fiber at pump wavelength. The noise is generated in the Raman amplifier due to spontaneous Raman scattering and Rayleigh scattering effects.

The noise figure is the signal degradation in the optical amplifier is defined as [1].

$$\text{NF} = 1 + \frac{G - 1}{G} + 2\alpha s \ln \text{G} \tag{3}$$

3 Simulation Setup

In Figs. 1 and 2, the transmitter consisted of a CW laser with 1550 nm at 0 dBm input power inserted into the fiber. The transmitter is implemented of a CW laser with 1550 nm at 0 dBm input power propagated into the fiber. A single Raman pump 1450 nm wavelength was used as counter-propagating pump and co-propagating pump power ranging from 0 to 1200 Mw, respectively. The parameters of standard single mode fiber (SSMF) were attenuation at 1550 nm is 0.2 dB/km, nonlinear index 2.6×10^{-20} m^2/w, slope 0.075 ps/nm/km. The transmission fiber length was 10–100 km.

The signal wavelength ranges from 1500 to 1580 nm for 1550 nm signal amplification. The Raman gain varies with the application of pump power and length of fiber as shown in Fig. 3.

For the codirectional pumping configuration, the maximum gain for pump powers 1200 mW, 800 mW, and 600 mW are 21.68 dB, 20.7 dB, and 22.47 dB, respectively.

Fig. 1 Counter propagating configuration of Raman amplifier

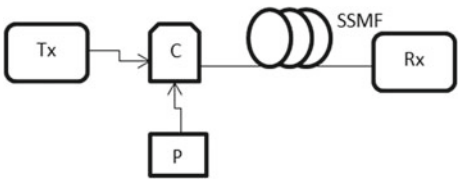

Fig. 2 Co-propagating configuration of Raman amplifier

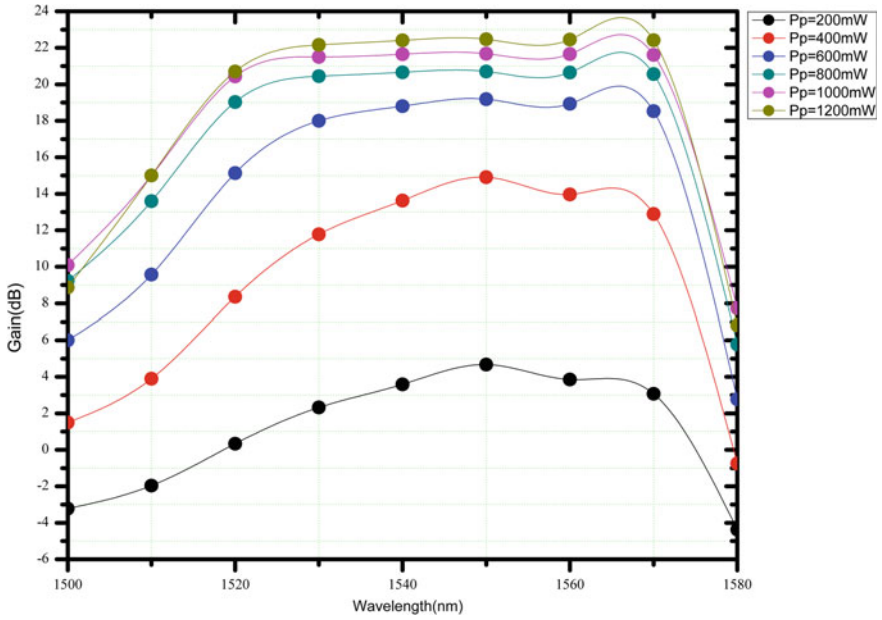

Fig. 3 Raman gain versus signal wavelength for the different value of pump power in codirectional pump configuration

Gain bandwidth for the pump power 1200 mW is 8 nm and it increases from 1200 to 200 mW. The gain bandwidth for 200 mW is 25 nm and for 800 mW is 10 nm. The saturation power for Raman amplifier is around 0–5 dBm.

As the fiber length increases from 10 to 100 km, the gain sharply decreases. The gain peak is obtained at the fiber length of 20 km of fiber length in Fig. 4.

In Fig. 5, the counter-directional pumping configuration for pump powers 1200 mW, 800 mW and 600 mW the maximum gains are 45.87 dB, 39.12 dB, 27.9 dB, respectively. Gain bandwidth for the pump power 1200 mW is 8 nm and it increases from 1200 to 200 mW. The gain bandwidth for 200 mW is 25 nm and for 800 mW is 10 nm. The saturation power for Raman amplifier is around 0–5 dBm.

As the fiber length increases from 10 to 100 km the Gain sharply decreases. The gain peak is obtained at the fiber length of 40 km length of optical fiber Fig. 6.

The gain versus fiber length and pump power as shown in Figs. 6 and 7. The pump power from 1200–200 mW for different fiber length is considered. The saturation power for the 800 mW pump power is 10–15 dBm and for 800 mW is 5 dBm.

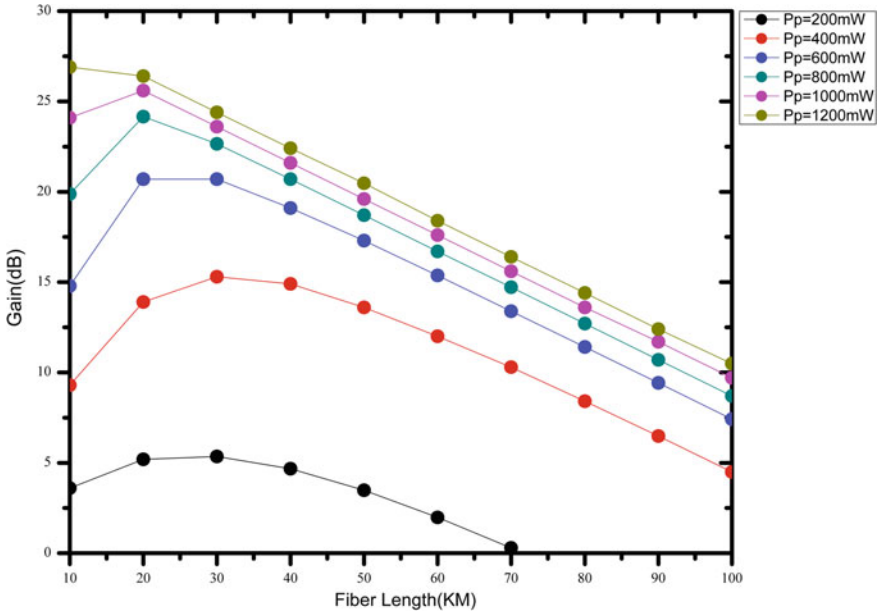

Fig. 4 Raman gain versus fiber length for the different values of pump power in codirectional pump configuration

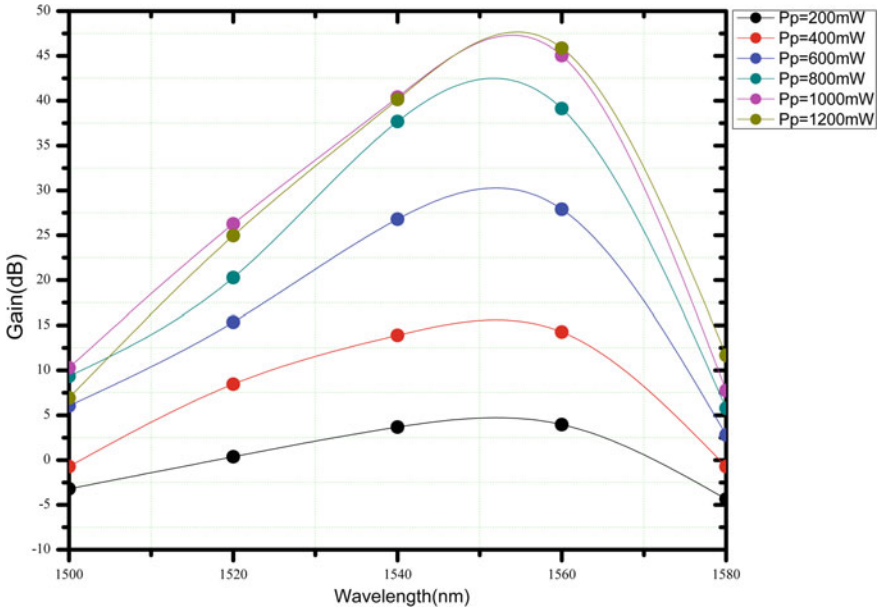

Fig. 5 Raman gain versus signal wavelength for the different values of pump power in counter-directional pump configuration

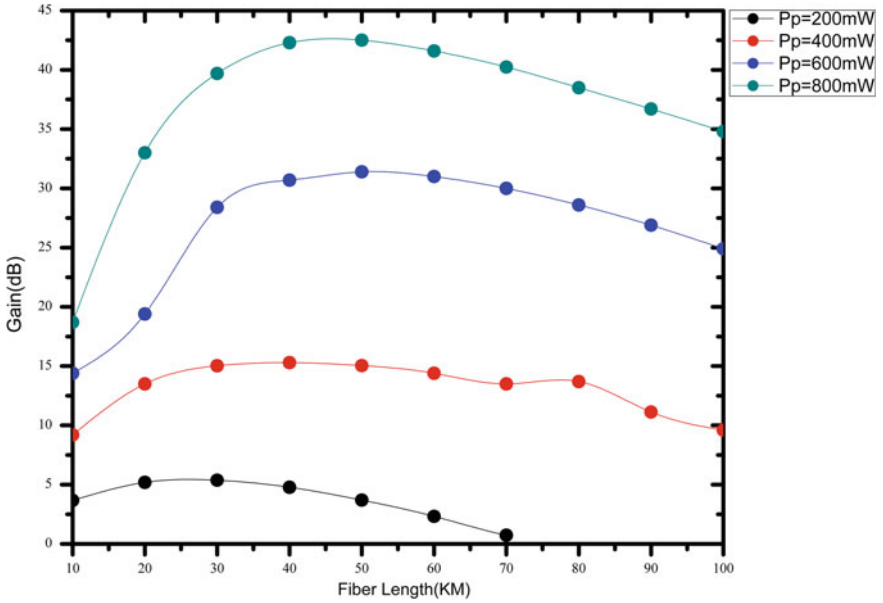

Fig. 6 Raman gain versus fiber length for the different value of pump power in counter-directional pump configuration at 40 km length of optical fiber

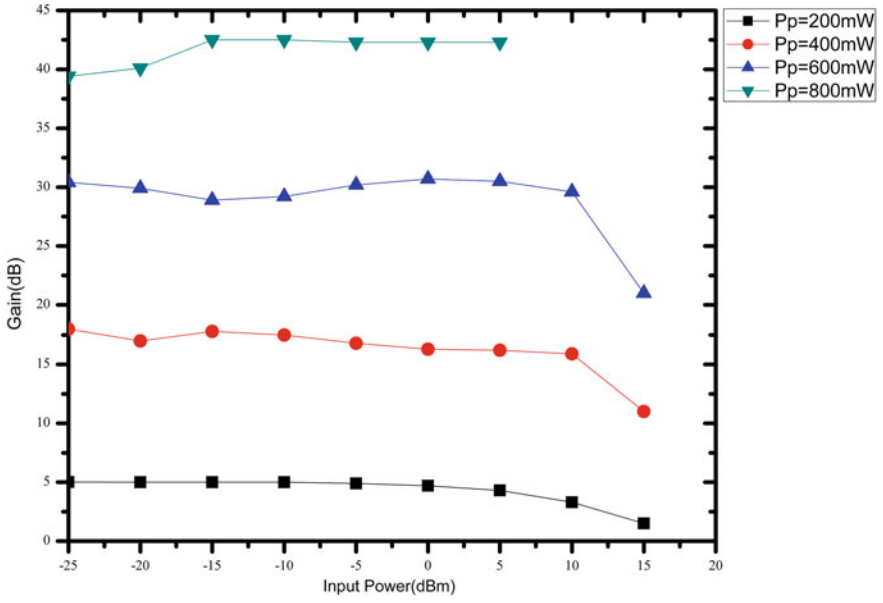

Fig. 7 Raman gain versus input power for the different values of pump power in counter-directional pump configuration at 40 km length of optical fiber

4 Conclusion

The Raman amplifier based on CW laser is utilized to amplify 1550 nm signals. For the codirectional pumping configuration, the maximum gain for pump powers 1200 Mw is 21.68 dB and noise figure is 6–7 dB. Gain bandwidth for the pump power 1200 mW is 8 nm. The gain bandwidth for 200 mW is 25 nm and for 800 mW is 10 nm. The saturation power for Raman amplifier is around 0–5 dBm. The counter-directional pumping configuration the maximum gain for pump powers 1200 Mw is 45.87 dB and noise figure is 7 dB. The high gain peak is obtained at 40 km length of optical fiber. The saturation power for the 800 mW pump power is 10–15 dBm and for 800 mW it is 5 dBm.

References

1. Czyzak P, Mazurek P, Turkiewicz JP (2014) 1310 nm Raman amplifier utilizing high power, quantum dot pumping lasers. Opt Laser Technol 64:195–203
2. Pradhan D, Mandloi A (2017) Performance analysis of backward multipumped Raman amplifier in DWDM system. Procedia Comput Sci 115:182–187
3. Abu Bakar MH, Mahamad Adikan FR, Ibrahim NH (2013) L band R-EDFA/Raman hybrid amplifier with enhanced higher order pumping scheme utilizing stimulated stimulated Raman scattering. Opt Commun 291:155–161(2013)
4. Sivanantha Raja A, Vigneshwari S, Selvendran S (2016) Novel high gain and wide band hybrid amplifier designed with a combination of an EYDFA and a discrete Raman amplifier. J opt Technol 83(4):69–79
5. Lee HH, Lee D, Chung HS (2004) Again clamped semiconductor optical amplifier combined with a distributed Raman fiber amplifier a good candidate as an inline amplifier for WDM networks. Opt Commun 229:249–252
6. Pradhan D, Mandloi A (2016) Design optimization of data rate 16 × 40 Gbps EDFA in DWDM system. In: International conference on fiber optics and photonics, p 64, Tu4A
7. Abu Bakar MH, Mahamd Adikan FR, Ibrahim NH (2013) L band R-EDFA/Raman hybrid amplifier with enhanced higher order pumping scheme utilizing stimulated Raman scattering. Opt Commun 291:155–161
8. Beninca MO, Pontes MJ, Segatto ME (2011) Design of a wideband Hybrid EDFA with a fiber Raman amplifier. IEEE, pp 282–285. 978-1-4577-1664-5
9. Kidorf H, Rottwitt K, Nissov M, Ma M (1999) Pump interactions in a 100 nm bandwidth Raman amplifier. IEEE Photonics Technol Lett 11(5):532–535
10. Morten N, Davidson CR, Rottwitt K, Menges R, Corbett PC (1997) 100 Gb/s (10 × 10 Gb/s) WDM transmission over 7200 km using distributed Raman amplification. ECOC 97:448

Performance Evaluation of Polar Code for Ultrareliable Low Latency Applications of 5G New Radio

Arti Sharma and Mohammad Salim

Abstract Channel coding for 5G New Radio is confronting everyday with novel challenges as to uphold and encourage various emerging use cases and new applications. State-of-the-art channel codes for existing mobile generations are already having questionable performance for many 5G applications. Polar code is prominent advancement in the channel coding area of this decade. The unprecedented performance of polar codes compelled 3GPP to adopt them for 5G eMBB control channels and over the physical broadcast channel. The 5G-URLLC scenario has strict requirement on the ultrahigh reliability and ultralow latency. Also, NR-URLLC scenario has analogous data rate necessity as that of the control channels. The low decoding complexity and latency with high reliability certainly makes polar code a strong contender in this race. This paper focuses on channel coding schemes particularly for NR-URLLC use case and evaluating the performance of polar codes for this scenario. Polar and LDPC code are compared on the basis of various parameters desired for URLLC scenario.

Keywords Polar code · URLLC · Reliability · Turbo code · LDPC code · 5G new radio

1 Introduction

5G and future wireless networks will endorse innumerous emerging use cases and applications with various performance aspects. Concerning this, ITU-R in September 2015 agreed upon its vision for IMT-2020 and beyond networks [1] and outlined three main 5G usage scenarios: (i) enhanced mobile broadband (eMBB); (ii) Ultra-reliable and Low Latency Communication (URLLC); and (iii) Massive Machine Type Communication (mMTC). 5G NR is not just an addendum advance over 4G

A. Sharma (✉) · M. Salim
Department of ECE, Malaviya National Institute of Technology Jaipur, Jaipur 302017, Rajasthan, India
e-mail: 2013rec9048@mnit.ac.in

© Springer Nature Singapore Pte Ltd. 2020

V. Janyani et al. (eds.), *Optical and Wireless Technologies*,
Lecture Notes in Electrical Engineering 546,
https://doi.org/10.1007/978-981-13-6159-3_28

Radio Access Technologies. The 5G-NRAT includes combinational influence of various new technologies like new heterogeneous cellular architecture, GHz Frequency bands with huge available bandwidths, Massive MIMO, mm wave communication, Massive Machine type communication, IoT, etc. Even, there is a paradigm shift in channel coding techniques for 5G scenarios [2]. Turbo codes and LDPC codes which are key enablers in existing mobile generations, i.e., 3G and 4G systems (UMTS and LTE) are already unproven for many new 5G applications [3]. Polar code, invented by Erdal Arikan (in year 2009) [4] is a new contender in race of 5G channel coding techniques. Recently, polar codes take the place of turbo codes in the 5G eMBB control channels and on the physical broadcast channel. 3GPP decided in RAN 86 and 87 meetings to standardize LDPC codes for data channels and polar codes for control channel in 5G eMBB scenario. No decision has been made yet on channel coding for remaining use cases, i.e., URLLC and mMTC. This is an open issue for research and 3GPP has already started its contribution from RAN 85.

Design of Channel coding for URLLC scenario is very complicated to comprehend due to two adverse demands of URLLC: Ultrahigh reliability and low latency [5]. Apart from this, data rate demands for URLLC are comparable to that of the control channels. Polar code can achieve excellent BLER performance, reliability of 99.999% with no error floor and low complexity decoding with very low latency of order of 1 ms. Therefore, polar code is a most powerful contender for URLLC scenario among all FEC candidate codes.

This paper focuses on channel coding schemes particularly for URLLC use case and analyzes all FEC candidates under consideration. Error correcting performance of state-of-the-art polar code is investigated under the consideration of several URLLC parameters. Performance of polar code in terms of BLER versus Es/N_0 is evaluated and compared with that of LDPC code for URLLC use case.

This paper is organized as follows: In Sect. 2, Channel coding requirements for URLLC scenario are highlighted; FEC candidates for URLLC are presented in Sect. 3. In Sect. 4, performance evaluation of polar codes for URLLC scenarios through simulation results is discussed and compared with LDPC codes for various information block lengths and code rates.

2 Channel Coding Requirements for NR-URLLC Scenario

This section briefly explains major requirements of NR-URLLC use case and maps those requirements on channel coding methods. Ultrareliable-low latency communications use case of 5G NR imposes harsh requirements on two conflicting parameters (i) low latency and (ii) ultrahigh reliability [5]. Lowering the latency requires short information that results in coding gain deterioration. On the other hand, increasing the reliability requires more parity/redundancy bits and sometime retransmission which will result in higher latency. After adopting standards for eMBB scenario, 3GPP started working toward 5G URLLC scenario. 3GPP in endorsement with IMT 2020 defines the Key Performance Indicator (KPI) requirements of 5G URLLC [6],

(i) *Latency*: The overall/end-to-end latency is 1 ms (0.5 ms for uplink transmission and 0.5 ms for downlink) for one packet.
(ii) *Reliability*: The transmission reliability is defined in terms of targeted block error rate of 10^{-5} within 1 ms period with or without support of HARQ. For the ultrahigh reliability of order of five nine (99.999%) and beyond, the BLER should be error floor free.

Above URLLC demands for short latency and reliable transmission are calibrated for the channel coding techniques. Although NR-URLLC specifications are still under study, some of its major suggestions for optimum channel coding scheme would be defined by the following FEC coding characteristics [3, 6, 7, 8],

(a) Small information block/packet length of order of tens to hundreds of bytes is required for the low latency.
(b) The codeword with low code rates is desired, typically lower than R = 1/3. Simple rate matching mechanisms are needed.
(c) Error floor free BLER performance is wished below block error rate of 10^{-5}.
(d) The self-contained 1-OFDM duration decoding latency is permissible. CRC bit reduction can be used for overhead reduction.
(e) Simple encoding and low decoding complexity techniques are praised. For this, low power consumption algorithms are proposed in [9].
(f) Code with ultralow latency especially low decoding latency is desirable.
(g) Robust performance of code over various fading channel with strong burst error correction ability is admired.

A paradigm shift in state-of-the-art coding techniques is mandatory to find efficient channel coding methods for such reliability and latency requisites of NR-URLLC. The optimum channel coding scheme verdict is an open issue to be discussed for 5G-URLLC scenario.

3 FEC Code Candidates for NR-URLLC

After Shannon's coding theory, various channel coding schemes are proposed, from capacity approaching to capacity achieving that perform good over larger block lengths. But some powerful code like convolutional code, turbo code, LDPC code, and polar code exhibit promising performance for shorter block lengths and lower code rates, therefore, are examined for URLLC scenarios.

3.1 Turbo Code

Turbo code invented in 1993 employs parallel concatenation of two convolutional codes at the encoder and serial concatenation at the decoder. The concept of inter leaver raises the error performance very near to Shannon's limit. Turbo codes are

used in deep space communication and digital video broadcasting, and also are key enablers in 3G and 4G (both UMTS and LTE services). Unfortunately, turbo codes are already out of 5G race. This is because of (i) Poor BLER performance for shorter block lengths and at low code rates, (ii) High complexity iterative decoding results in low throughput and high latency, (iii) Presence of error floor makes them unfit for high reliability applications [7]. This is why turbo code is considered to be inadequate for 5G-URLLC scenario.

3.2 LDPC Code

LDPC code rediscovered in 1997 is a linear block code that has sparse parity check matrix, H, with low density of 1's. LDPC codes have outstanding capacity approaching performance, even better than turbo codes in terms of error floor, decoding complexity and for higher code rate. LDPC codes find their applications in WiMAX 802.16 and various IEEE standards. LDPC codes are admired for their fabulous performance for large block lengths and high code rate. For this reason, 3GPP standardized LDPC codes for data channels in 5G-eMBB scenario [10].

But, LDPC code is not a good choice for 5G-URLLC use case because, (i) all of the proposed LDPC decoders (Normalized offset min-sum, normalized Layered min-sum, etc.) show inferior performance for short block lengths (<400 bits) and low code rates ($R < 1/3$) [8, 10], (ii) Practical implementation complexity and iterative decoding complexity are high in case of small blocks and low code rate. Otherwise, LDPC codes decoders are the least complex for larger blocks and higher rates. (iii) Error floor occurs with LDPC code when small blocks are considered, (iv) Short decoding latency is not true for very low code rates [7]. Low code rate and short block length need more number of iterations that will lead to higher computational complexity, higher power consumption and hence, longer decoding latency for equivalent performance [11].

3.3 Convolutional Code

LTE-TBCC (Long-Term Evolution-Tail-Biting Convolutional Code) finds its application in LTE systems as a channel coding scheme for control channels. These codes show good performance for short block lengths but the same is not true in case of low code rates [8]. Also, due to tail biting, extra operations are needed before the decoding begins. This will enhance the decoder complexity and hence increase the decoding latency [7].

3.4 Polar Code

In 2009, Arikan introduced [4] the polar codes as a class of linear block codes that are first explicitly proven capacity achieving channel codes. Polar codes break the wheel in channel coding area with its unconventional perspective of code construction than that of the traditional codes and become the youngest contender in the 5G race [8]. Additionally, simple encoder with modest complexity SC decoder renders polar code attractive for a lot of 5G applications.

Polar codes are established by the concept of *channel polarization* where N copies of an ordinary channel W (with capacity I (W)) are transformed into extreme channels whose symmetric capacities reaches to either 1 or 0, as N goes large. These obtained N polarized channels are either (i) perfect/reliable channels which transmit noiselessly (with max. capacity of 1), or, (ii) extremely noisy/unreliable channels which transmit only random noise. Then, the polar encoder transmits K information bits over reliable channels while remaining N-K bits are made frozen bits (0 or 1) and transmitted over unreliable channels.

Fundamental polar decoder is successive cancelation (SC) decoder that can proven achieve Shannon's capacity with modest complexity. Various improved SC decoding algorithms have been proposed for the betterment of the finite length performance of polar code [9, 12]. SC-list (SCL) decoders are currently investigated for 5G studies that employ L simultaneous decoding paths to get improved performance over MAP decoders. CRC aided polar code (CA Polar) with SCL decoding can even surpass state-of-the art codes (LTE-Turbo code and LDPC code). Parity check polar code (PC–CA Polar Code) has been recommended for low latency hence considered for URLLC scenario [13].

4 Polar Code Fitness for NR-URLLC

All channel coding candidates of URLLC scenario are discussed in the last section. This section provides some highly probable aspects for the appropriateness of polar codes for URLLC use case. A Chinese firm Huawei is the main leader that brings Polar codes as a channel coding method in 5G field trials and in October 2016, it achieved the downlink speed of 27 Gbps [14]. Also, in 3GPP meetings, polar code replaced deep-rooted turbo codes in 5G eMBB scenario and over physical broadcast channels.

Lot of research is going on the channel coding methods for URLLC case and winner has not been announced yet. Polar codes are considered as most acceptable contender in this contest. This is because;

(i) Supreme BLER performance for short information block lengths at low code rates with easy code shorting and puncturing mechanisms, respectively. For this, polar codes have lower SNR requirements when compared to other

candidate codes for similar error rate, hence, attain higher coding gain and enhanced spectral efficiency [3, 7, 8].

(ii) An FEC code with higher coding gain and no error floor should be preferred for reliability constraint of URLLC. The transmission reliability is determined by error floor free performance below BLER of 10^{-5} [6]. Turbo code and LDPC code show the occurrence of error floor for short block lengths around BLER of 10^{-5}. Polar code has error floor free performance [8] and, hence, it is more reliable than other FEC candidates for the desired SNR.

(iii) Decoder power consumption is complementary of computational complexity of the decoder. Polar decoders consumed less power due to the use of low complexity SC-based decoding (SC and SCL) decoding algorithms. Terminal power consumption in polar code is even 20 times lesser than turbo codes for equivalent complexity [11].

(iv) Polar code satisfies the latency demands of URLLC use case [7, 11].

5 Performance Evaluation of Polar Code Through Simulation Results for NR-URLLC

This paper evaluates the performance of polar codes in terms of Block error rate (BLER) and SNR (E_S/N_0), based on some parameters. Out of all FEC code candidates, turbo code and LTE-TBCC code are considered to be unworthy for URLLC scenario [3, 7, 8]. Thus, the comparative analysis of the polar codes and LDPC codes for typical range of information block lengths and code rates for NR-URLLC are simulated. Different short block lengths and low code rates have been concerned with QPSK modulation over AWGN and fading channels (with Raleigh distribution, TDL-C 300). Table 1 shows specifications of parameters for URLLC use case.

PC–CA polar code design suggested in [13] is taken with CRC aided (27 bits) CA–SCL (L = 8) decoding. LDPC code design BG-2 (Base Graph-2) with LOMS (Layered Offset Min-Sum) decoder for 20 iterations is taken for analysis [13].

Table 1 Parameter specifications for URLLC scenario

Parameters	Specifications	
Channel coding	LDPC	Polar (PC–CA)
Channel	AWGN and fading channel	
Modulation	QPSK	
Info. block length (bits w/o CRC)	40, 200,1000	
Code rate	1/12, 1/6, 1/3	
Decoding algorithm	LOMS (20 iterations) with CRC 24	SCL (L = 8) with CRC 27

5.1 Performance Parameters Under Consideration

5.1.1 BLER Performance

Error performance of a code is a main asset that can also define many other performance parameters. Polar code takes advantage of short block lengths and low code rates, but it is hard to design LDPC code with good BLER performance for the same conditions. For identical performance, the LDPC code requires more number of iterations that means more power consumption, higher computational complexity, lower energy efficiency and hence, higher decoding latency that are undesirable for URLLC.

BLER performance of Polar and LDPC codes are compared for interested range of block lengths and code rates over AWGN and fading channels. It is clearly observed from Figs. 1 and 2 that the polar code surpasses LDPC code for considered block lengths and code rates over both types of channels.

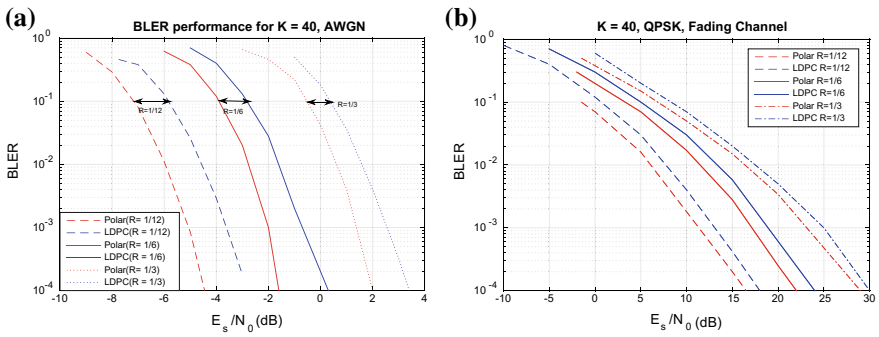

Fig. 1 BLER performance comparison for K = 40 over **a** AWGN and **b** fading channel

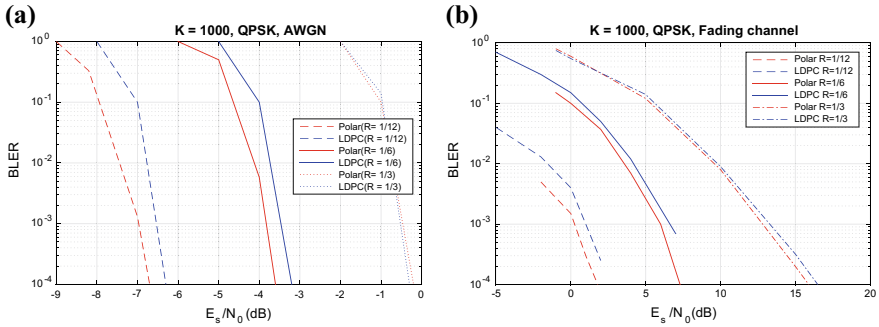

Fig. 2 BLER performance comparison for K = 1000 over **a** AWGN and **b** fading channel

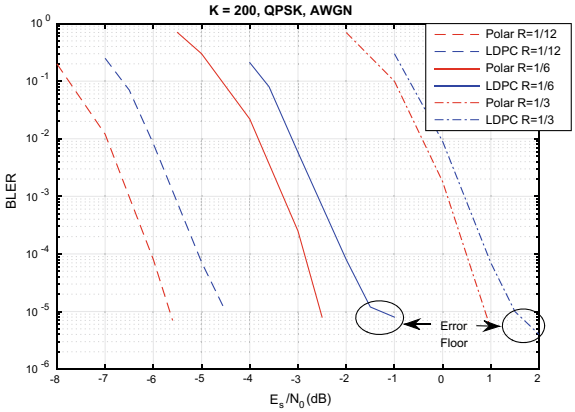

Fig. 3 Results for reliability and error floor at K = 200 over AWGN channel

5.1.2 Reliability and Error Floor

To obtain reliability of transmission in case of URLLC, a channel coding method should support error floor free BLER performance with high coding gain. For this reason, our analysis is mainly focused on error floor performance and coding gain of polar and LDPC codes to check the reliability constraint.

It is obvious from Fig. 3 that LDPC code shows error floor above BLER of 10^{-5} for K = 200, R = 1/6 and 1/3 over AWGN channel. Polar code is error floor free for all considered cases. Additionally, from reliability perspective, it is apparent from Fig. 3 that the reliability of polar code is higher than that of LDPC code at any given SNR value.

5.1.3 Computational Complexity/Decoder Power

Computational complexity of any decoding algorithm is highly associated with the decoder power consumption. Also, lower the decoder complexity/power higher the energy efficiency of a code. Number of operations needed to decode the information, i.e., the decoder computational complexities of all FEC code candidates are evaluated in [11]. It is proved that the computational complexity of the polar code is lower than that of the other codes for short blocks and low code rates.

5.1.4 Decoding Latency

For time constraint applications, the overall latency of 1 ms is demanded for transmission of one packet. The overall latency is mainly comprised of encoding time, channel delay, and decoding latency. Out of these, decoding latency is an eminent

parameter of performance measurement. Although decoding latency of polar successive cancelation (SC) decoder is lower than the SC list (SCL) decoder, SC decoder shows poorer performance as compared to that of SCL decoder.

SCL decoder chooses L best paths from 2L paths branching from L (denotes list size) most likely previous paths. Minimal decoding latency of SCL decoder, counted in clock cycle with P parallel processors, is given in [15]. Also, the decoding latency of SCL decoder can be minimized with low value of L but, at the cost of performance degradation. So, there is a trade-off between latency and performance of SCL decoders.

Polar code reaches to the target latency for short block and low code rate case in URLLC scenario [7, 11].

6 Conclusion

Polar code is very renowned innovation that makes space in channel coding race of 5G and adopted for 5G eMBB and PBCH. In this paper, various channel coding candidates for 5G-URLLC scenario are discussed. For ultrahigh reliability and low latency, error floor free performance with short information block lengths and low coding rates are considered. Polar and LDPC codes are compared on the basis of BLER performance, reliability, error floor, decoding complexity and latency. It is observed through simulations that BLER performance of polar code surpasses that of LDPC code for short block lengths and low code rates. Also, polar code is error floor free and more reliable than LDPC code at any given SNR. Polar-SCL decoder complexity is lower than that of LDPC-LOMS decoder for typical range of block lengths and code rates of 5G-URLLC scenario. Decoding latency demands is fulfilled by polar code. Therefore, polar code is the strongest channel coding contender for 5G-URLLC scenario.

References

1. IMT Vision (2015) Framework and overall objectives of the future development of IMT for 2020 and beyond. Recomm ITU-R, M.2083, Sept 2015
2. Shafi M, Molisch AF, Smith PJ (2017) 5G: a tutorial overview of standards, trials, challenges, deployment and practice. IEEE J Sel Areas in Commun 99, Apr 2017
3. Sybis M, Wesolowski K, Jayasinghe K (2016) Channel coding for ultra-reliable low latency communication in 5G Systems. IEEE Veh Technol Conf, Sept 2016
4. Arıkan (2009) Channel polarization: a method for constructing capacity achieving codes for symmetric binary-input memoryless channels. IEEE Trans Inf Theory 55(7):3051–3073, July 2009
5. Ji H, Park S (2017) Introduction to ultra reliable and low latency communications in 5G. ArXiv: 1704.05565v1, Apr 2017
6. GPP TS 38.913 (2016) Study on scenarios and requirements for next generation access technologies, Mar 2016

7. R1-1611692 Channel coding schemes for URLLC scenario, Huawei, HiSilicon
8. Sharma A, Salim M (2017) Polar code: the channel code contender for 5G scenarios. IEEE Comptelix Conf, July 2017
9. Ercan F, Condo C, Hashemi SA (2017) On error-correction performance and implementation of polar code list decoders for 5G. ArXiv: 1708.04706v2, Oct 2017
10. R1-1610059 Evaluation of LDPC codes for eMBB, NTT DOCOMO, RAN1 #86bis, Lisbon, Portugal
11. R1-164040 (2016) On latency and complexity, Huawei, HiSilicon, May 2016
12. Tal I, Vardy A (2015) List decoding of polar codes. IEEE Trans Inf Theory 61(5):2213–2226, Mar 2015
13. R1-1706965 (2017) Polar coding design, Huawei, HiSilicon, June 2017
14. Huawei achieves 27Gbps 5G speeds with Polar Code. Retrieved 10 Oct 2016
15. R1-1609073 (2016) Discussion on latency of channel codes for NR, Samsung, Oct 2016

Low Confinement Loss Solid Core Rectangular Photonic Crystal Fiber

Shahli Tabassum, Shahiruddin, Dharmendra K. Sing and M. A. Hassan

Abstract The proposed design achieves single polarization in fundamental mode using the rectangular photonic crystal fiber, having inner ring filled with 60% glucose solution in water. The proposed structure is composed of silica material having finite number of air holes in cladding. The proposed structure has very low confinement loss between the wavelength ranging from 1 to 1.8 μm and flat zero dispersion can be achieved within the wavelength ranging from 1.4 to 2 μm. This rectangular photonic crystal fiber operating in single mode can be used where a wide operating bandwidth is required. Chromatic dispersion, confinement loss, and normalize frequency have been calculated for three different air fill fractions.

Keywords Photonic crystal fiber · Dispersion · Confinement loss · Air fill fraction · Normalized frequency

1 Introduction

Photonic Crystal Fiber (PCF) [1] has certain geometrical arrangement of air holes in the cladding area. Cladding around the core region is arranged in a periodic fashion forming a microstructure and thus it is also known as microstructure fiber. The geometrical pattern and the size of air holes in the cladding region affect the various optical parameters such as confinement loss, effective area and nonlinear coefficient of the PCF. Light is confined either through total internal reflection or through band gap in the PCF. The PCF can be designed for various specific applications such as gas sensor, pollution control, temperature sensor, biomedical application, etc. [2]. Lin Zhao et al. in 2013 presented a photonic crystal fiber with octagonal and square lattice having confinement loss in order of 10^{-3} dB/m [3]. In this paper, the

S. Tabassum (✉) · Shahiruddin · M. A. Hassan
Birla Institute of Technology, Patna Campus, Patna, India
e-mail: tabassumshahli5@gmail.com

D. K. Sing
National Institute of Technology, Patna, Patna, India

© Springer Nature Singapore Pte Ltd. 2020

V. Janyani et al. (eds.), *Optical and Wireless Technologies*,
Lecture Notes in Electrical Engineering 546,
https://doi.org/10.1007/978-981-13-6159-3_29

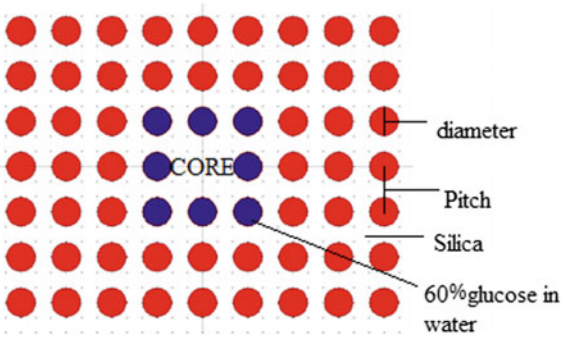

Fig. 1 Cross-sectional view

designed PCF has very low confinement loss in order of 10^{-6}. Designed PCF is two dimensional and can be used in nonlinear devices and to guide exotic wavelength. The designed PCF has silica as background material having finite number of air holes in the rectangular pattern. The proposed structure has three concentric rings surrounding the core region. The inner ring is filled with 60% glucose solution in water having refractive index of 1.4394. The entire outer ring represents the air holes. This R-PCF (rectangular photonic crystal fiber) has solid silica core. The refractive index of cladding is the combination of refractive index of air holes and silica. The effective refractive index (n_{eff}) changes with the change in wavelength. The two dimensional cross-sectional area is shown in Fig. 1. The light is well confined in the center of the core in the fundamental mode as shown in Fig. 2. When the number of air hole increases, the confinement loss decreases. The air fill fraction is defined as the ratio of diameter (d) and pitch (Λ), i.e., center to center distance of adjacent air hole. The pitch remains constant and diameter is varied. Dispersion, confinement loss, and normalized frequency are calculated at three different air fill fractions d_1/Λ, d_2/Λ, and d_3/Λ where $d_1 = 1$ μm, $d_2 = 1.2$ μm, $d_3 = 1.4$ μm. R-PCF shows flat zero dispersion above wavelength of 1.4 μm and remains unchanged with the change in air fill fraction. Dispersion defines the information carrying capacity of the PCF and hence it is an important parameter. The confinement loss is the leakage of light from the core region to the cladding and it is necessary to minimize the confinement loss. The proposed R-PCF has very low confinement loss of 1.53×1^6 dB/m at wavelength 1.55 μm and confinement loss decreases with increase in diameter of air holes. RSOFT simulation tool has been used to implement this structure.

2 Numerical Analysis

The R-PCF goes under fine meshing of rectangular and triangular latex. Boundary condition is used to find the confinement loss of the PCF. Sellemier equation is used to find the effective refractive index of the PCF. A refractive index is a property

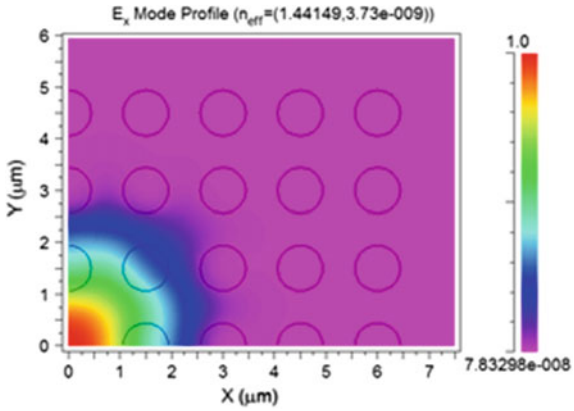

Fig. 2 Field intensity distribution

of the material itself. Now, an effective refractive index can be given for an optical component as a measure of the overall delay of a light beam in that component.

The effective refractive index consists of two parts, first part is real and used to find the dispersion and the second part is imaginary used to find all type of losses in the PCF [4–7]. The effective index n_{eff} of fundamental mode is determined by

$$n_{eff} = \mathrm{Re}(\beta/k_0) \tag{1}$$

where $k_0 = \frac{2\pi}{\lambda}$ is wavenumber and β is the propagation constant. Propagation constant can be obtained by solving the eigenvalue equation. The effective refractive index has two parts one is real and the second is imaginary part. The confinement loss can be obtained from the imaginary part of effective refractive index. The leakage of light from the core to the cladding results in confinement loss [8–10], and the confinement loss for the corresponding mode is derived

$$L_c = 8.686 \times k_0 \mathrm{Im}[n_{eff}] \tag{2}$$

The unit of confinement loss is dB/m. Second derivative of the real part gives the exact value of dispersion.

$$D(\lambda) = -\frac{\lambda}{c}\frac{d^2}{d\lambda^2} Re[n_{eff}] \tag{3}$$

where c is the speed of light, $\mathrm{Re}[n_{eff}]$ is the real part of the effective refractive index and λ is the operating wavelength. The unit of dispersion is ps/km-nm. The chromatic dispersion graph is shown in Fig. 4.

Figure 3 shows the effective refractive index of the proposed PCF. The effective refractive index decreases with increase in wavelength. When the diameter of air holes increases the effective refractive index decreases. Dispersion is the bending of different wavelengths at different angles. Blue and violet light of the visible

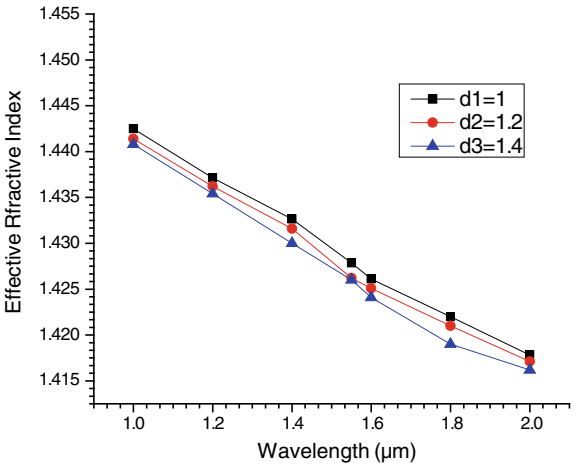

Fig. 3 Effective refractive index

spectrum has maximum deviation then the red because of different wavelengths. The consequence of dispersion is the change in the angle of refraction of different colors of light. When the diameter of air hole in the cladding region increases, the dispersion changes. When diameter of air holes is 1 μm, the zero dispersion will be at and above wavelength of 1.4 μm. The dispersion will remain almost similar for the slight changes in air fill fraction. When the diameter is increased to 1.2 μm, the dispersion will be zero at and above wavelength of 1.4 μm. When the diameter is increased further to 1.4 μm, the zero dispersion shifts toward wavelength 1.6 μm (Fig. 4).

Confinement loss arises due to the leaky nature of mode and structure of the PCF. The confinement loss at wavelength $\lambda = 1.55$ μm when $d_1 = 1$ μm is 1.53×1^6 dB/m. When the diameter is increased, i.e., $d_2 = 1.2$ μm, the confinement loss at wavelength $\lambda = 1.55$ μm is 2.208×1^6 dB/m. When the diameter is increased further $d_3 = 1.4$ μm, the confinement loss is 2.755×1^6 dB/m. The confinement loss remains approximately constant up to wavelength $\lambda = 1.6$ μm and increases rapidly when the wavelength is increased further as shown in Fig. 5. Confinement loss depends on the imaginary part of the effective refractive index and the operating wavelength (Fig. 6).

In PCF, the V-number can be interpreted as normalized optical frequency. V-parameter determines the fraction of the optical power in a certain mode which is confined to the fiber core [11–13]. It has to maintain lower values of normalized frequency because it makes PCF to low absorption loss in cladding region of PCF [14]. V-number can be calculated using formula:

$$V = \frac{2\pi R}{\lambda}\sqrt{n_{co}^2 - n_{cl}^2} \tag{4}$$

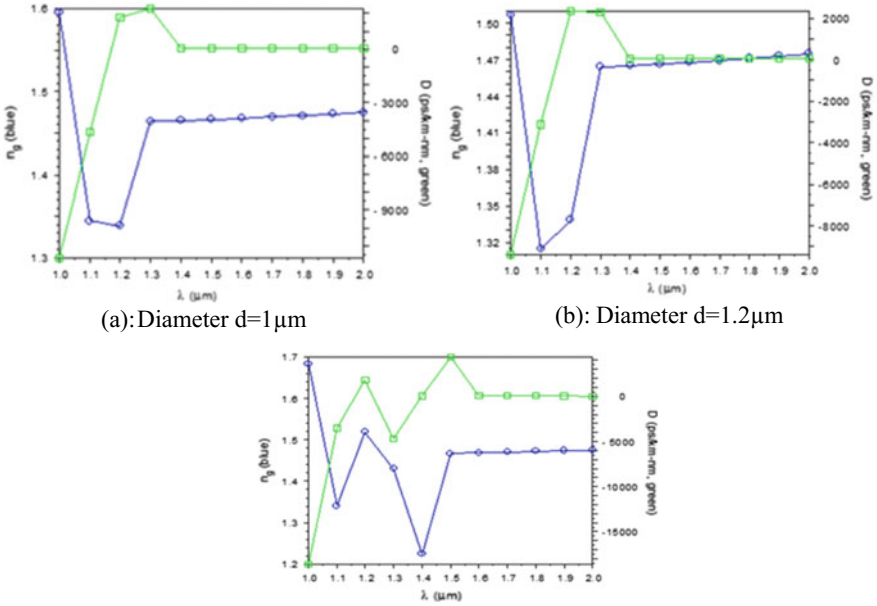

Fig. 4 Dispersion graph for different diameters **a** diameter d = 1 μm **b** diameter d = 1.2 μm **c** diameter d = 1.4 μm

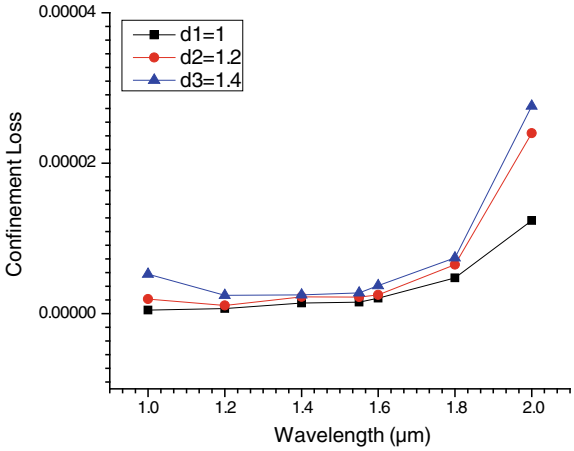

Fig. 5 Confinement loss graph

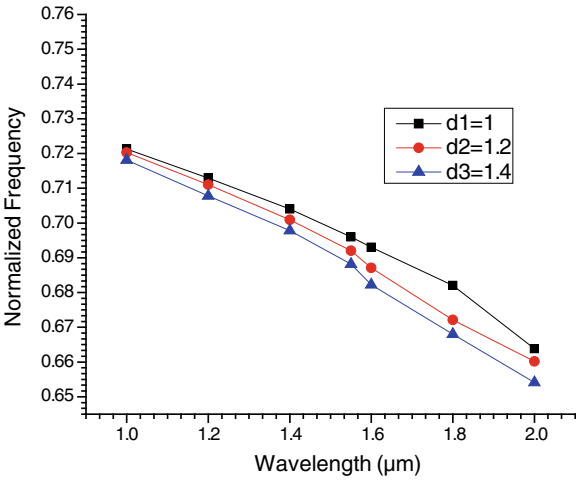

Fig. 6 Normalized frequency graph

where n_{co} is the core refractive index and n_{cl} is the cladding refractive index. In core, we use material silica n_{co} is the refractive index of silica. Index of the cladding region can be defined in terms of propagation constant of the lowest mode that could propagate in the infinite cladding material. The normalized frequency decreases with increase in wavelength. As the diameter of the air hole increased, normalize frequency decreases. At operating wavelength of 1.55 μm, the normalize frequency is 0.696 as the diameter is increased to 1.2 μm the normalize frequency will be 0.689. When the diameter is increased further, the normalize frequency will be 0.680.

3 Conclusion

In this paper, the proposed PCF shows flat zero dispersion over a wide range of wavelength that is ranging from 1.4 to 2 μm and has very low confinement loss for wavelength over the range of 1–1.8 μm. The dispersion and confinement loss can be controlled by changing the air fill fraction or by changing the diameter of air holes in the cladding region of R-PCF. Additional parameter is also calculated such as normalize frequency which is used to find the effective area at different diameters. The designed fiber can be easy to implement [16].

References

1. Poli F, Selleri S (2007) Photonic crystal fibers, properties and applications. Springer Series, The Netherlands
2. Razzak SMA et al (2007) Guiding properties of a decagonal photonic crystal fiber. J Microw Optoelectron 6:44–47
3. Liang et al (2015) Characteristics analysis of hybrid photonic crystal fiber with hexagonal structure. Optik 126(20):2335–2337
4. Olyaee Saeed et al (2011) Design of new square-lattice photonic crystal fibers for optical communication applications. Int J Phys Sci 6(18):4405–4411
5. Agarwal A et al (2008) Golden spiral photonic crystal fiber: polarization and dispersion properties 33(22):2716–2718
6. Islam MA et al (2012) Design optimization of equiangular spiral photonic crystal fiber for large negative flat dispersion and high birefringence 30(22):3545–3551
7. Hossain MN et al (2010) A highly nonlinear spiral photonic crystal fiber for tailoring two zero dispersion wavelengths in the visible region. Photonics Lett Poland 2(3):143–145
8. Kubota Hirokazu et al (2009) Simple analysis of water filled hollow core silica photonic bandgap fiber. IEICE Electron Express 6(12):870–875
9. Shadiul Islam Md et al (2017) Design and numerical analysis: effect of core and cladding area on hybrid hexagonal microstructure optical fiber in environment pollution sensing applications. Karbala Int J Mod Sci 3(1):29–38
10. Birks TA et al (1999) Dispersion compensation using single-material fibers. IEEE Photon Technol Lett 11:674
11. Sharma C et al (2015) V parameter of photonic crystal fiber 3(5)
12. Mortensen NA et al (2003) Model cut off and the V-parameter in photonic crystal fiber. Opt Lett 28:1879
13. Mortensen et al (2003) Low-loss criterion and effective area considerations for photonic crystal fibers. J Opt A Pure Appl Opt 5:163
14. Nielsen MD et al (2003) Reduced micro deformation attenuation in large-mode-area photonic crystal fibers for visible applications. Opt Lett 28:1645
15. Espindola RP et al (1999) External refractive index insensitive air-clad long period fiber grating. Electron Lett 35(4):327–328
16. Rifat AA et al (2017) Photonic crystal fiber-based plasmonic biosensor with external sensing approach. J Nano photonics 12(1)

Integration of Contactless Power Measuring Instruments to PLC and SCADA Through Industrial Wireless Sensor Network for EMS

B. Ajeya and Shweta Vincent

Abstract Optimization of an energy management system measuring and continuous monitoring of the quantities (Power, Voltage, etc.) of an electrical system is of utmost importance for achieving efficient control of power usage in an industry. For an already established industry, the existing measuring instruments are not versatile and location of these instruments cannot be changed with ought changes in the power system and the data interface between the instrument and control system are not efficient. This paper is about a method of integration of contactless power-measuring instruments which are placed in different locations which are easily relocatable and are capable of sending all the measured data over an industrial wireless network to an integrated PLC and SCADA system which is already in use for the process control and in addition will be used to monitor and control the power usage of the system to obtain optimized energy management system.

Keywords EMS · Wireless sensor network · Contactless power measurement · Integrated PLC/SCADA

1 Introduction

An industry always tries to reduce the processing cost or production cost so as to reduce the final cost of the product with ought compromising on the quality of the product to increase profit and to stay competitive. Significant reduction in production cost can be achieved by optimizing energy consumption [1] which can be achieved by adapting energy management systems. For an energy management system basic requirement is energy measurement system which depends on the type of energy consumed in that industry, for example, a rolling mill using electrical motors to drive

B. Ajeya · S. Vincent (✉)
MIT, Manipal Academy of Higher Education, Manipal, India
e-mail: shweta.vincent@manipal.edu

B. Ajeya
e-mail: bajeya.b@gmail.com

© Springer Nature Singapore Pte Ltd. 2020

V. Janyani et al. (eds.), *Optical and Wireless Technologies*,
Lecture Notes in Electrical Engineering 546,
https://doi.org/10.1007/978-981-13-6159-3_30

the rollers, here the energy is in electrical form hence a power metre is required. For further discussion in this paper let us consider an electrical form of energy to be optimized. To measure energy consumption measurements of ampere, voltage, real power, reactive power, power factor and phase angle is essential and for each measuring quantity a particular instrument should be used [2]. The major type of the instruments that are used to measure the said quantities require physical or ohmic contact to the electrical system being measured. The normal way to get the data from the measurement device is to manually note the reading and then record it, other method is to use automatic instruments which collect data for particular time intervals and store. In an industry, it is not practical to note and write down the measured readings manually and hence a control system is used to note and record the readings. The control system for the measurement may also consist of a controller to control the energy consumed, this control system is generally called as Energy Management System (EMS).

This paper is focusing on the scenario of an already established industry in which EMS has to be implemented. The existing or common method of doing so is by creating a network of power metres to collect the readings from the power distribution stations and send all the data to a central control station where the optimization scheme will be applied and intern will control the energy consumption. There are several problems observed from this conventional method of implemented EMS, namely (1) The location of the power metres are predefined and hence efficient optimization of energy may not be possible because of lack of power metres on the required locations for example for a particular process in the industry which needs power metres at its input and output to obtain an efficient energy consumption report. (2) The interconnection of those power metres to the central control station may be wired, i.e., copper cable to directly take the measured value or twisted pair communication cable, when number of power metres are more wired conception will be tedious to maintain and troubleshoot. (3) For an EMS system a controller is required to process all the collected measured values and accordingly calculate the energy consumption over a period, current EMS system controllers are of standalone type, i.e., the dedicated controller is used for the EMS control system and normally used EMS controllers do not have a clear user interface and specific engineers may be required to configure and maintain this controller.

In this paper, a scheme for EMS control system is proposed keeping the above said problems in focus, for the mobility and accessibility problem of the power metre a contactless measuring instruments [3] may be used which can be clamped on the electrical cables based on the required location and the electrical quantities that are required for an EMS will be measured. For data transfer problem and restriction on number of sensors that can be used, these contactless measurement instruments can be designed to transfer the measured data over an wireless communication to the central controller [4] and the wireless communication is chosen such that the required number of sensors can be used without any restriction with least liable to interference and capable to handle industrial environment conditions. The industrial wireless communication network which can handle many (hundred) wirelessly connected

sensor nodes over a long range is defined as wireless sensor network (WSN) [5], some of the commonly used wireless communication standards for WSN [6] are,

1. IEEE 802.11
2. IEEE 802.15.4
3. ZigBee/ZigBee Pro
4. IEEE 802.15.1
5. Bluetooth
6. WirelessHART
7. ISA 100.11a
8. WISA.

Most of the current industries are using PLC or DCS (Distributed control station) systems for plant process control. For the purpose of EMS controller, we propose an integrated PLC system which can control both plant process and EMS. Already existing SCADA (Supervisory Control And Data Acquisition) linked to the PLC [7] can be used for EMS user interface and can be easily monitored by the same process operator. The plant maintenance engineers are sufficient to maintain the EMS system which is integrated to plant process control system but one-time configuration by the EMS engineer may be required.

2 Proposed Scheme for EMS

The proposed scheme for EMS has three parts, i.e., measurement, communication/data transfer and integrated process data processing/storage and EMS control Fig. 1 shows basic representation of the proposed scheme. The measurement of the electrical quantities of the industrial process is done through contactless (non-intrusive) measuring instrument and the measured parametres are sent to an integrated central controller which is used as both process controller and EMS controller through a wireless sensor network to calculate the energy consumption at any time and is monitored using human–machine interface (HMI).

2.1 Measurement Scheme

The energy consumption of a process is not directly measured but calculated by multiplying the measured power consumed and the time for which the process is running. The power consumption of the process can be measured in two ways one by directly measuring power and other by measuring voltage, current and power factor and then using the formula,

$$\mathrm{P} = \sqrt{3}\mathrm{VI}\cos\theta \tag{1}$$

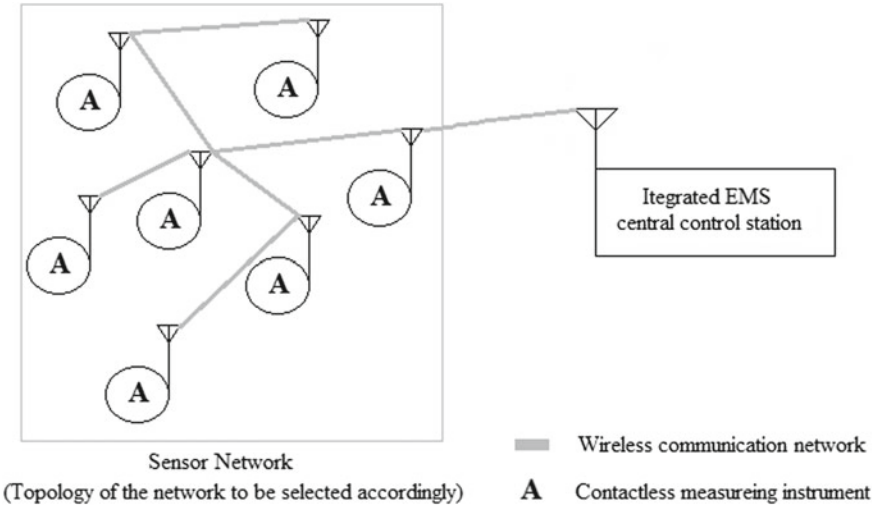

Fig. 1 Basic scheme of the proposed EMS system

While measuring power without any ohmic connection, i.e., non-contact type the second method of measuring power is used and then energy is calculated by the formula,

$$E = P * t, \tag{2}$$

where 't' is the time for which the energy consumed have to be calculated.

For the contactless power measurement, two types of sensors are used, i.e., for voltage capacitive coupling sensor and for current inductive coupling sensor.

Voltage capacitive coupling sensor. The voltage of a current carrying conductor (Power line) in a power system is measured using a capacitor coupling sensor. The working principle of the sensor is two metallic probes are placed on the insulation of the power line which works as capacitor pickup, i.e., a capacitance is created between the metal strips or the pickup and the power line, this capacitive pick up senses voltage given by Q(t) = CV(t) where, 'V(t)' is the voltage across the pickup which is nothing but the voltage of the power line, 'C' is the capacitance between the pickup and the conductor of the power line and 'Q(t)' is the charge generated (electric field) in the capacitor because of the voltage V(t), hence by measuring the charge Q(t) which is proportional to the voltage of the power line we can measure the voltage of the power line [8].

The electric field (charge Q(t)) can be measured by one pick up as an omnidirectional pickup but by using two pickups in differential design which will provide better performance with a slight increase in complexity and with this design, sensor can be directed towards the position of the conductor in the power line [3]. In the differential design there are two ways the pickups can be positioned on the power

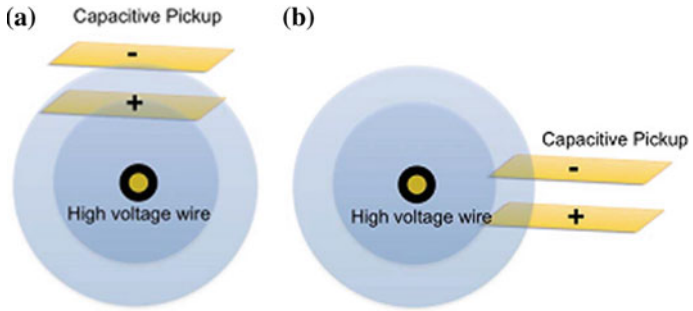

Fig. 2 Differential design of the pickup **a** differential mode. **b** Common mode. As illustrated in [3, Fig. 11]

line as shown in Fig. 2. In the common mode, field generated by the conductor right below the pickup will be greater than that on the top pickup, in differential mode generated field will be equal on both the pickups [3]. The above-said method of sensing voltage in non-intrusive method is applicable to DC also [9].

The calibration of the capacitive coupled voltage sensor is done by measuring the coupling capacitance for a standard signal of frequency of 100–300 kHz injected using an external source into the power line and then using that value to compare the actual measured capacitance for the power line to obtain the calibrated value [8].

Current inductive coupling sensor. Current measurement in non-intrusive/contactless method can be achieved using the principle of Ampere's Law, which states that the magnetic field and current are related linearly, i.e. a current carrying conductor will produce a magnetic field which is directly proportional to the current in that conductor. Using an inductive coupling sensor, the magnetic field can be measured intern current passing through the power line can be measured. Let us consider two methods for sensing current of a power line using inductive coupling principle, (1) using Hall effect sensor (2) using TMR (Tunnelling Magneto Resistive) sensor.

Hall effect sensor is widely used for the current measurement purpose in wide areas and it works on the principle of hall effect. That is, when a particular current carrying material is placed in a magnetic field perpendicular to the direction of the current then charges will be acuminated on the other perpendicular faces of the material, because of this charge there exists a voltage between those faces and that voltage is proportional to the current passing through the material keeping the strength of magnetic field constant. In context of our current sensor the magnetic field produced by the power line is sensed by the hall effect sensor and is calibrated using a constant known current passing through the sensor which will produce a voltage on the faces of the sensor which will be proportional to the magnetic field which intern is proportional to the current in the power line.

TMR sensor works on the principle of tunnelling magneto-resistive effect which is described as the change in resistance of the material due to magnetic fields applied

to it. Using this principle for our current sensor, the magnetic field produced by the current carrying conductor of the power line changes the resistance proportionally of the TMR sensor which intern is proportional to the current on the power line [3]. One major disadvantage of TMR sensor is for large changes in magnetic field the change in the resistance is nonlinear and also proportionality decreases. That is, ratio of the change in the magnetic field and the corresponding change in the sensor output is not a constant and hence additional compensation has to be provided to resolve the nonlinearity [3].

Block diagram and basic representation of the measuring instrument. Typical block diagram and basic schematics of a three-phase power metre are shown in Fig. 3 and Fig. 5, for the power metre to measure and send the measured data it needs power for itself and this power can either be harvested from the power line itself [4] or separate supply may be given to the instrument.

The experiment representation of the contactless power measurement sensor is shown in Fig. 4. The construction of the contactless power metre [10–12] can be done in different types but the working principle remains same.

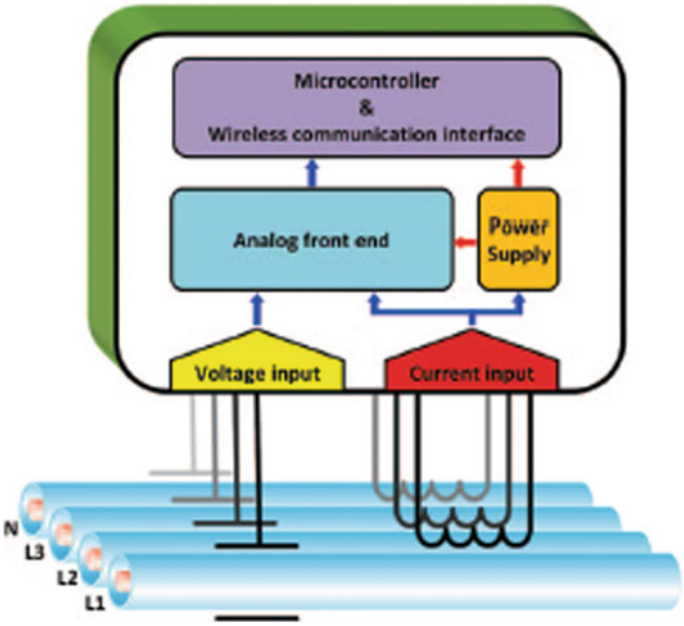

Fig. 3 Block diagram of the power meter. As illustrated in [4, Fig. 1]

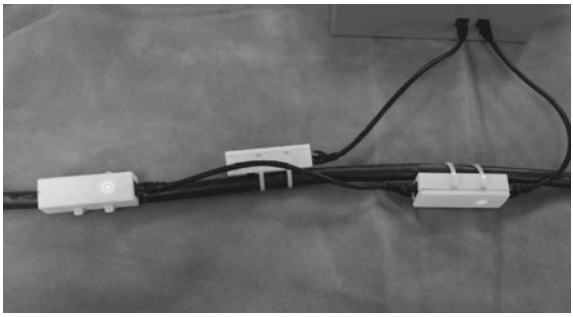

Fig. 4 Experimental model of the contactless power meter. As illustrated in [3, Fig. 16]

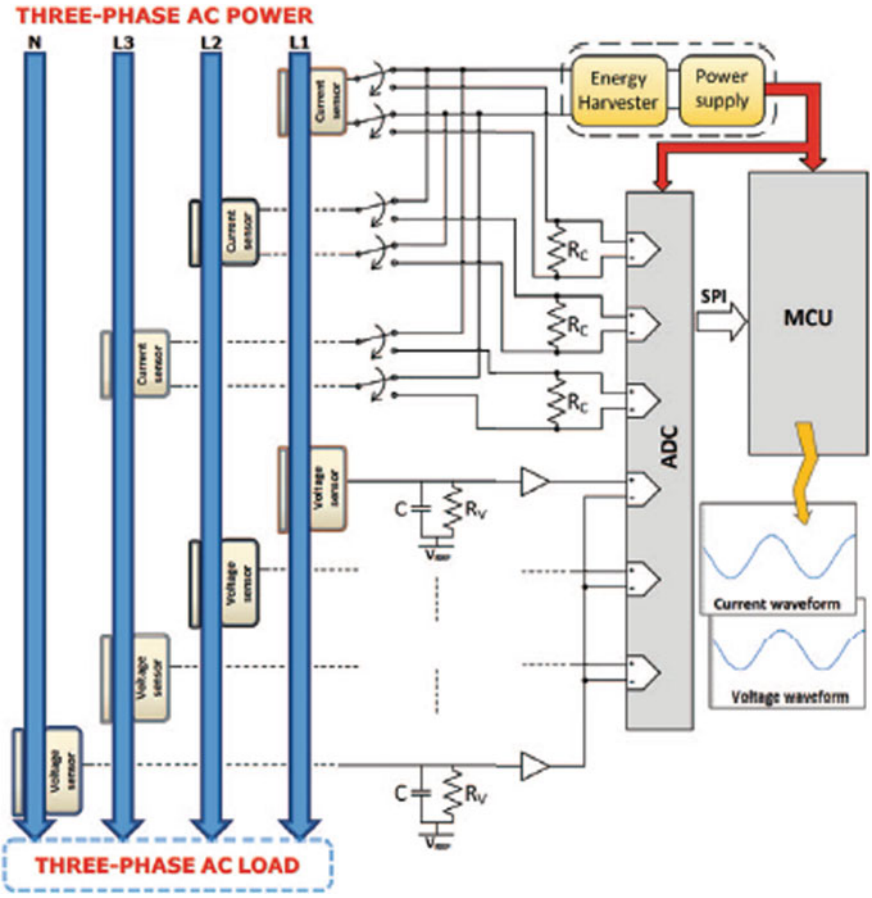

Fig. 5 Basic schematics of the meter with energy harvesting. As illustrated in [4, Fig. 2]

2.2 Communication Scheme

The measured power value from the power metre is transmitted to the central control station via wireless communication. For the harsh condition in the industries, proper communication protocols have to be selected by comparing the parametres such as interference, number of sensor node to be accessed, rate of data transfer, robustness and low power consumption.

Wireless communication is more preferred compared to wired communication network because of following advantages of wireless over wired communication network [13]:

(1) Cable lay, connection, cable tray setup, and all other related activities are labour-intensive for wired but not applicable for wireless network.
(2) A wireless system is easy to commission as for a wired lot of loop checking and troubleshooting has to be done before commissioning.
(3) Eliminate the need of junction box, cable trays which are important component in the loop of the wired network, control room side terminal panels, marshalling cabinets, field interface cards are also eliminated to an extent in wireless network.
(4) A wireless system simply translates to savings on wiring cost.
(5) Wireless has increased availability compared to wired network, because any problem in the hardware of the wired network (cables, routers, etc.) is difficult to diagnose and hence network downtime will be more.
(6) Scalability of wireless network, i.e. once wireless network is established with a process area, new devices can be added effortlessly without worrying about spare capacity in the junction boxes and adding any new hardware on the distributed control system (DCS) side.
(7) Wireless network is more energy efficient as compared to wired network.

Commonly wireless networks which are used industrial application such as to communicate between sensors and controllers are called as wireless sensor network (WSN). The network protocols which can handle the industrial environments are in the category of WSN. Let us consider some of the widely used standards and protocols for WSN.

IEEE 802.11x standards family has high bandwidth that is necessary for continuous data logging but gets affected by interference from other devices which is common in an industry. Because of its long transmission range efficient and less challenging methodologies for deployment, with few nodes in the network large industrial area can be covered. This is also the reason why IEEE 802.11x network has low density [6] hence this network is only applicable for some case of WSN.

IEEE 802.15.1 network standard has small bandwidth, transmission range and low scalability but has good real-time response due to the TDMA algorithm used and because of only seven slave nodes can be active per master node at any given time as per the standard. Thus IEEE 802.15.1 is best suited for alarm condition monitoring in industrial systems wherein a matter of seconds conditions change. It is not suited

for continuous data transfer or logging as the bandwidth is low and a typical data logging application may not be satisfied with the network [6].

The IEEE 802.15.4 network standard has medium transmission range, bandwidth and good scalability but has bad time characteristics due to the use of CSMA-based MAC layer. communication range may be increased up to few hundreds of metres by increasing transmission power resulting in lower power awareness [6].

ZigBee and ZigBee Pro networks are based on IEEE 802.15.4 standards, ZigBee devices have low power consumption (sleep mode enabled when device is not in use), relatively short range, self-healing and redundancy capabilities, small data packet transfer and low cost. ZigBee uses mesh routing scheme this provides more redundancy and if a device fails router will find alternate route to relay the data to keep the network running. ZigBee network is highly scalable and supports high number of devices up to 64,000 [14]. ZigBee Pro differ from ZigBee in the range, i.e. longer range is achieved in ZigBee Pro by using high power transmission systems.

Bluetooth is a network which was designed for short-range applications. This network has low-cost transceiver technology used for transmission, a variety of duty cycles with medium data rate and higher quality of service because of small number of active nodes but has high power consumption, highly susceptible to interference and low scalability [6] hence application is limited in industrial point of view.

WirelessHART network standard uses mesh topology and is mainly used in industrial process automation applications. It is nothing but already existing HART (Highway Addressable Remote Transducer) protocol with wireless capabilities. WirelessHART is built over the IEEE 802.15.4 standards and operates in the 2.4 GHz ISM band and is available with a 10 mW radio transceiver. The greatest advantage of WirelessHART is the Time Synchronized Mesh Protocol (TSMP) which provides redundancy, fail-over switching in time and has very high reliability in the challenging industrial environments [15].

ISA 100.11a is a network protocol developed by ISA (International Society of Automation—a non-profit organization dedicated to solve problems related to automation). ISA 100.11a is based on 802.15.4 WPAN technology and has the same features of self-healing, self-organizing mesh architecture as of ZigBee and WirelessHART. Additionally, it also offers low power consumption and scalability of the network. The difference of ISA 100.11a with ZigBee and WirelessHART is that IAS 100.11a works on different protocols and hence allows to be implemented into an existing network which uses different protocol to communicate. ISA 100.11a was developed to cater both process as well as factory automation network needs, i.e. simple data acquisition such as monitoring, logging and alerting as well as complex factory level process automation applications [14].

WISA (Wireless Interface for Sensors and Actuators) network protocol is also based on IEEE 802.15.4 having deterministic behaviour because of TDMA-based MAC algorithm optimized to provide more number of nodes (sensors/actuators) per base station with short cycle time in the order of milliseconds. Advanced mitigation techniques are used to minimize interference for the harsh industrial environment conditions and the need for frequency planning for multiple cells is eliminated by providing separation between consecutive hops [6].

Table 1 Comparison of the commonly used wireless communication standards based on the requirements of industrial application [6]

Wireless network protocols	Range	Robustness	Real-time performance	Power awareness	Network scalability	Link throughput
IEEE 802.11	High	Low	Low	Low	Medium	High
IEEE 802.15.1	Low	Medium	High	Medium	Low	Medium
IEEE 802.15.4	Medium	Medium	Low	High	Medium	Low
ZigBee	Medium	Medium	Medium	High	High	Low
Bluetooth	Low	Medium	High	Medium	Low	Medium
WirelessHART	Medium	High	High	High	Medium	Low
ISA 100.11a	Medium	High	High	High	Medium	Low
WISA	Low	High	High	High	Medium	Medium

Comparing all the above-said standards and protocols as shown in the Table 1, it can be inferred that IEEE 802.15.4 protocol provides a mid-level solution which can support the wider range with related trade-offs, excluding the high bandwidth and continuous data logging scenarios the 802.15.4 based WirelessHART protocol gives a better performance over others by providing robustness, moderate range, real-time performance, moderate scalability and low power consumption.

For the purpose of this paper, we select WirelessHART as the communication scheme. WirelessHART protocol is based on OSI Model, implementing layers 1, 2, 3, 4 and 7 of the OSI protocol model. Key difference between wired and wireless HART are (1) Output signal—4–20 mA for wired and IEC 62591 for wireless, (2) power supply—24 V DC for wired and Intrinsically safe battery for wireless, (3) update rate of about 1 s for both wired and wireless [13]. Data transfer is divided into three main groups namely universal command, common practice command and device specific command. The universal command gives the information such as tag ID, PV (Primary Variable) value and engineering units. The common practice command provides the device function such as read variables, adjust function (Zero, Span adjust) and serial number and finally, device-specific command shows the model-specific functions such as tuning parametres adjust, PID enable, Set Point change which are particular to one device. The connectivity from other multiple device manufacturers is obtained with the use of universal command and common practice command and device specific commands are used for users to customize the functions according to the field devices [16]. Typical architecture of WirelessHART is shown in Fig. 6.

As shown in Fig. 6 network comprises of a host application like asset management, process controller, gateway, network manager, security manager, access points and field devices. The gateway acts as an interface between the controller or host application and the access points. The field devices in our application will be the contactless power measuring instruments. Using multiple access points wired to the gateway redundancy is provided for the wireless network path and the gateway. The

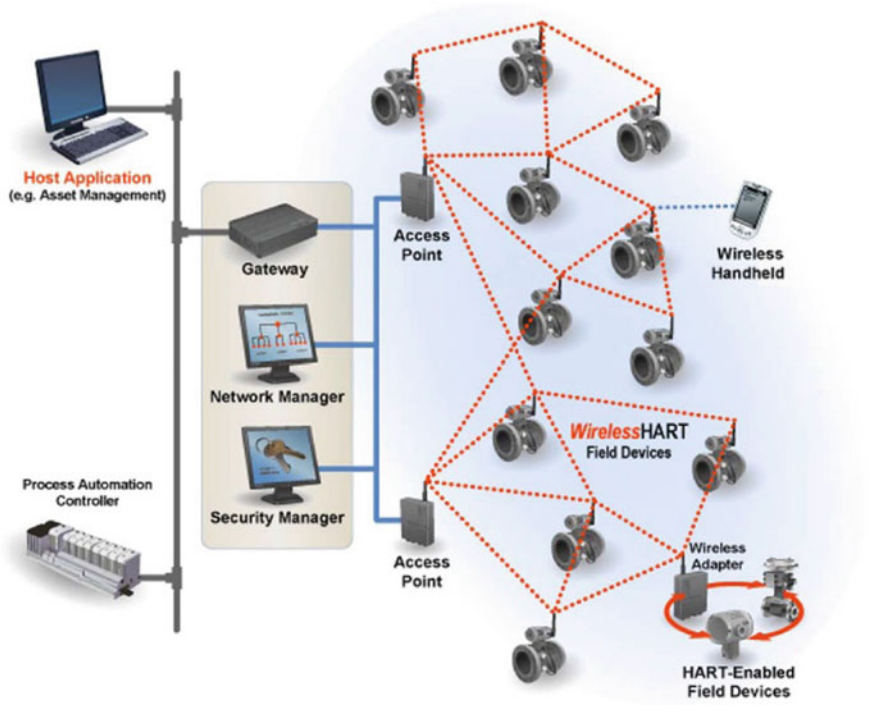

Fig. 6 Architecture of a WirelessHART network. As illustrated in [17, Fig. 1]

centralized network manager is responsible for creating the routes, managing, optimizing the network by scheduling. Security manager provides security for the data being transferred in the network between the host and the field device [17].

2.3 Integrated Controller Scheme

In integrated controller scheme, we propose a controller scheme which can control both process automation as well as EMS. At the current situation, the best controller in the industrial view is PLC with SCADA system with user interface and supervisory control. Integrated control system utilizes the existing connections at different levels in the plant control system, including controller level, shop floor level and enterprise level connections for management and reporting functions. By using a PLC integrated system existing plant HMI and SCADA can be combined with EMS which has customizable user interface with alarm and energy billing scheme display with predictive demand calculations using the PLC controller. Existing PLC has all the information of the plant control system which can be utilized for the energy management system, which includes process calculations for the plant control. Stored data

and historical data infrastructure can also be used to track data and display alarms on the existing HMI so that the operators are not required to access third party systems to get the data [7].

At present scenario, all major industries have adapted PLC/DCS as the process control system and hence using that controller for the EMS also will reduce substantial amount of initial investment [7] required to implement EMS and thereby provoking the industries to opt for EMS systems.

A typical model of a standalone EMS is shown below in Fig. 7.

The PLC-based EMS can process all the above-said information and provide a predictive modelling of the past performance and the real-time measurement. With models the operator/management of the industry can create certain scenarios and simulate the process in the view of optimizing EMS and hence at that time if integrated system is adapted it will be an added bonus that both process as well as EMS can be modelled and simulated. An example HMI screen of the EMS on the process HMI is shown in Fig. 8. This helps the operator to easily monitor both process as well as the EMS.

A typical integrated PLC-based EMS system has following components [7]:

(1) Communication enabled measuring instruments
(2) Time synchronization
(3) Data collection
(4) Calculations for controlling and billing
(5) Peak demand processing and predictions
(6) HMI Integration for user interface
(7) Waveform plotter/generator and Power quality analysis.

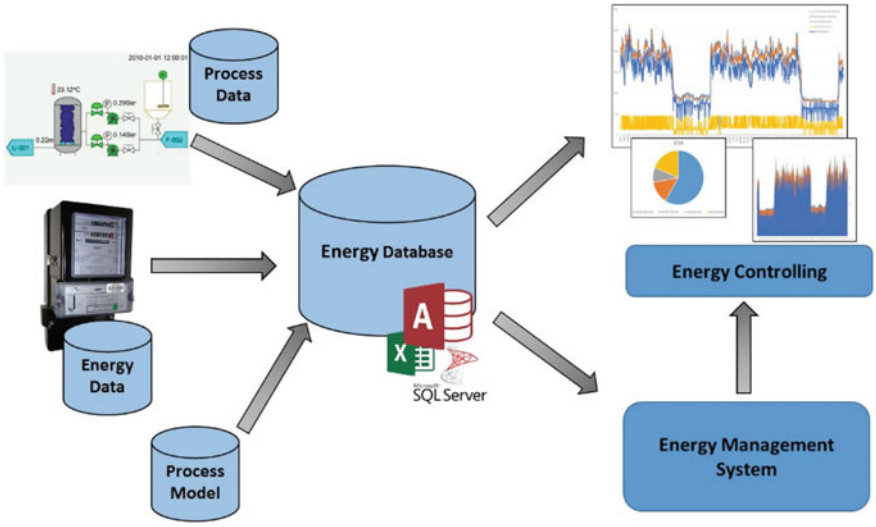

Fig. 7 Information system of a typical EMS. As illustrated in [18, Fig. 4]

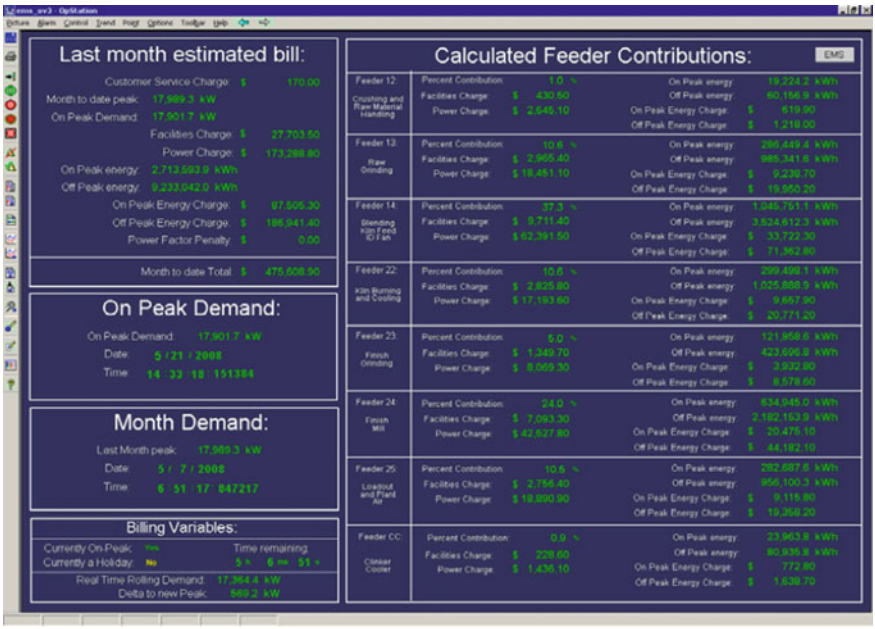

Fig. 8 Example HMI screen of the integrated system. As illustrated in [7, Fig. 1]

3 Conclusion

A novel scheme for EMS system was presented considering the scenario for implementation of EMS on an already established industry. By using contactless measuring system greater mobility can be achieved and a greater concentrated EMS system is possible, by using wireless communication instead of conventional wired network a good amount of cost can be reduced and since the main objective is to obtain a high-efficient energy management system in which the implementation cost of the EMS is also reduced, by using integrated control system the maintenance, operation ease is also increased and better control can be achieved. Future scope of this paper would be to experimentally implement this scheme and compare the results with the existing EMS systems.

References

1. Hasanbeigi A, Menke C, du Pont P (2010) Barriers to energy efficiency improvement and decision-making behavior in Thai industry. Energy Effic 3(1):33–52
2. Turner WC, Doty S (2007) Electric energy management in energy management handbook. The Fairmont Press, Sixth edit., pp 273–298
3. Donnal JS, Leeb SB (2015) Noncontact power meter. IEEE Sens J 15(2):1161–1169

4. Villani C, Benatti S, Brunelli D, Benini L (2016) A contactless three-phase autonomous power meter, pp 3–5
5. Low KS, Nu W, Win N, Er MJ (2005) Wireless sensor networks for industrial environments
6. Giannoulis S, Koulamas C, Emmanouilidis C, Pistofidis P, Karampatzakis D (2013) Wireless sensor network technologies for condition monitoring of industrial assets. IFIP Adv Inf Commun Technol 398(2):33–40
7. Mackinnon J, Warnick S, Mcdaniel J (2011) PLC based enterprise energy management solutions. In: 2011 IEEE-IAS/PCA 53rd Cement Industry Technical Conference, pp 1–7
8. Pai P, Chen L, Chowdhury FK, Tabib-azar M (2012) Non-intrusive electric power sensors for smart grid. In: 2012 IEEE Sensors, 2012, pp 1–4
9. McKenzie G, Record P (2012) Non-contact measurement of dc voltages using nonlinear elements. Meas Sci Technol 23(4):45001
10. Kolasch BS (2002) Non-contact voltage measurement method and device, and detection probe. US 2002/0167303 A1, 2002
11. Us TX, Ferreira AP, Keller TW, Harris AM, Flynn JD (2014) Non-contact current and voltage sensor. US 8680845 B2, 2014
12. Libove IJM, Way Y, Jerome R, Ave A (1995) Apparatus for measuring voltages and currents using non-contacting sensors. US Patent US 5473244 A, 1995
13. Mehta BR, Reddy YJ (2015) Industrial process automation systems design and implementation
14. Peter M (2017) Industrial wireless mesh network architectures. L-com Global connectivity. http://www.l-com.com/multimedia/whitepapers/wp_Wireless-Industrial-Mesh-Networks.pdf. Accessed 10 Nov 2017
15. Schmidt G (2010) Getting the most out of your WirelessHART® system a white paper presented by 2010
16. Pongpipatpakdee P, Thepmanee T, Pongswatd S, Rerkratn A (2016) Integration of WirelessHART network system into SCADA software for operation and management King Mongkut' s Institute of Technology Ladkrabang
17. Sha M, Ieee M, Gonzalez H, Ieee M, Gunatilaka D (2015) Real-time wireless sensor-actuator networks for industrial cyber-physical systems
18. Schellong W, Ferreira C, Czichon B (2017) Integration of energy management into process control engineering. In: 2017 6th International Conference on Clean Electrical Power (ICCEP), pp 207–214

An Overview of Smart Identity Cards for Educational Institutions

Rupesh Acharya, Saroj Jakhar, Durgesh Kumar and Garima Mathur

Abstract In this modern era, a technological development is taking shape from universities to schools. This paper throws light on an automatic identification technology which has been used to diminish man force and time to input file or information manually. RFID (radio-frequency identification) is a wireless technology which is getting popularity among identification technologies due to its cost-effective maintenance, low cost, less weight and minimized size. RFID (radio-frequency identification) is one of wireless technology that incorporates the use of EM fields to automatically identify and trace tags attached to items/objects. Radio-Frequency Identification tag enables the schools/universities to oversee the student movement inside and outside of the premises.

Index Terms Radio-frequency identification · RFID tags · Smart card · Online student surveillance (OSS) · EAS

1 Introduction

In India technological development is taking shape from universities to schools. Innovation is bringing mechanization and an opportunity to ameliorate security to the premises in this twenty-first century. Radio-frequency identification is forming up to be an indispensable elementary unit for IoT. It was difficult to identify student's location and who profaned the authorized area. To overcome this Radio-Frequency Identification (RFID), one of wireless technology which is taken upon realizing the detonation of interest in this technology where its establishment in the legion application, including health [1], supply chain [2], construction [3] and library [4]. Radio-frequency identification (RFID) microchips are an identification device (wireless) that transmits a signal with data that was stored in the chip when powered by

R. Acharya (✉) · S. Jakhar · D. Kumar · G. Mathur
Department of Electronics & Communication Engineering, Poornima College of Engineering, Rajasthan Technical University, Jaipur, India
e-mail: 2014pceecrupesh@poornima.org

© Springer Nature Singapore Pte Ltd. 2020

V. Janyani et al. (eds.), *Optical and Wireless Technologies*,
Lecture Notes in Electrical Engineering 546,
https://doi.org/10.1007/978-981-13-6159-3_31

some nearby root. RFID systems perform function same as a lock and key, with the RFID chip performing as the key. Radio-frequency identification (RFID) chips have an identification code, instead of having a unique pattern that is read by the lock. RFID chips also pelt the identification code behind a series of encryption [5]. The RFID systems consist three main constituents to ensure its well-functioning which are coil or antenna, transceiver and RFID tag. The antenna will impart radio signal to activate the tag so the information or data could be written or read. The storage and extraction of the information or data use a special device which is called as RFID tag. RFID tag can be fastened anywhere on anything and even able to be fixed in the body of human beings. In this, RFID tags permit the management of school/college to oversee the manoeuvre of a student inside and outside of the campus. An individual who is not having the RFID card will activate the alarm and also able to notify the management of school/university regarding the student's availability utilizing an online surveilling system. When the RFID tags pass by way of the RFID reader in reading gamut tract, then the information or data from the RFID tags will be recorded to the database systems. The information will be conveyed online to the administration for pupil's supervision. This will repose the management to check the hostel student's availability and admittance the personal record of students.

2 History of RFID Development

"Identification Friend or Foe" system (IFF) was RFID's first application and it was deployed by the Britishers in World War (II) [6]. Reading units could ask tanks and fighter planes to determine whether to blitz as transponders were placed into them. In armies around the globe, this technology's heirs apparent are still utilized. EAS (Electronic Article Surveillance) was the RFID's first utilization for commercial purpose. It was evolved as a theft prevention system in the seventieth century.

Radio-frequency identification tags made its way into the farming for instance for animal tagging in late 1970. When some US states and Norway determined to utilize radio-frequency identification for the collection of toll taxes on roads in the eightieth century, RFID technology got the uplift. In addition to the collection of toll taxes, the following decade brought a huge number of new applications, such as money cards, gasoline cards, ski passes, etc. Auto-ID center was founded in 1999 at Massachusetts Institute of Technology. Development of a global standard for item-level tagging was the duty of Auto-ID center. After concluding the work on the EPC (Electronic Product Code), Auto-ID center was closed in 2003. Newly established EPCglobal Inc. pursues the work at the same time. First paper regarding Radio-Frequency Identification technology by Harry Stockman was the landmark paper, "Communication by Means of Reflected Power" in 1948 (October). In 1973, Radio-Frequency Identification first patent was issued for a passive radio transponder with memory (Fig. 1).

Fig. 1 RFID chip

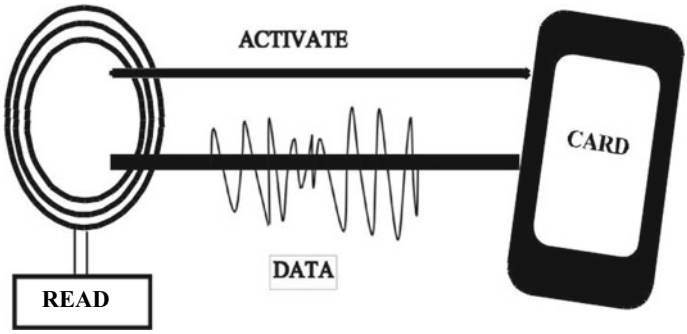

Fig. 2 Working of RFID

3 Principles of Radio-Frequency Identification

For an automatic identification and tracing motives, RFID employs a contactless wireless system that utilizes RF (radio-frequency) EM fields to transmit information from fastening tag to an item/object. Fundamental datum behind radio-frequency identification system is that one mark objects with tags. These tags hold transponder that discharges information legible by specialized Radio-Frequency Identification. Nearly all Radio Identification Frequency tags store some type of ID number, for instance, product stock-keeping unit (SKU) code or a consumer number. Reader fetches data regarding identification number from database and go on upon it accordingly (Fig. 2).

Depending upon the source of power, there are two general classifications in which radio-frequency identification tags falls that is active tag and passive tag.

3.1 RFID Active Tags

Active tags have their own source of power, it imparts powerful signal and reader can ingress them from further away. RFID active systems usually work better on large objects traced over great distance due to own source of power, which makes them

Fig. 3 Active RFID

costly and larger. Active tags which have less power are typically slightly bigger than a deck of cards (playing). RFID active tags persist temporarily inactive up till they arrive in the gamut of a receiver or can continuously transmit a signal. Due to the on-board source of power, active tags work on greater frequencies very often 455 MHz, 2.45 GHz, or 5.8 GHz—rest on the peruse gamut and memory demand application. Readers can impart or pass on information with RFID active tags over 20–100 m [7] (Fig. 3).

3.2 RFID Passive Tags

Furthermore, these types of tags are immensely less costly and new technologies continuously making them economical to consolidate into usual products and materials. In inclusion to their less cost, passive radio-frequency identification tags can also be utterly small. Present antenna technology extremities the smallest useful passive radio-frequency identification tag anent the quarter's size. As the size of tag increases, read range also increases. Currently, radio-frequency identification passive tags hold about 2 Kb of memory [8]. This is very small to contain much more intricate data than identification and history data. Technological development to the far side of RFID is continuously meliorating, so the data's amount and capacities of radio-frequency identification tags will rise over time, allowing tags to finally hold and transfer much more data (Fig. 4).

4 Comparisons Between RFID, Barcode and Quick Response Code

Radio-frequency identification, Barcodes and Quick Response (QR) codes are alike in reality that they are information gathering/collecting technologies, mean-

Fig. 4 Passive RFID

ing they automate data collection operation. However, they too vary materially in many regions. This segment predominantly throws light on the advantage of radio-frequency identification (RFID) over barcode and quick response (QR) code. Comparison between these three data collection technologies is given in tabular format (Table 1).

As per the above comparison between these three technologies, we can say that RFID-enabled smart identity cards are better than old-fashioned barcode-enabled identity cards. In India, education is one of the most indispensable sectors that requires for the execution of latest technologies. RFID-enabled smart identity cards used for the diverse motives and some of the advantages of smart identity card (RFID enabled) over barcode-enabled identity card in the educational sector are discussed in this paper.

Table 1 Comparison between RFID, barcode and quick response (QR) code

Features	RFID	Barcode	Quick response (QR) code
Updating	New data can be written on old tags	Unable to update	Unable to update
Tracking	Manual tracking not required	Required manual tracking	Required manual tracking
LOS (Line of site)	Does not required	Required	Required
Technology	Radio-Frequency	Laser (optical)	Laser (optical)
Read/write	Both	Read-only	Read-only
Read range	Active tags—up to 100 feet and passive tags—up to 30 feet	Several inches to feet	Several inches to feet
Identification	Items can uniquely identify	Items cannot uniquely identify	Items can uniquely identify, but up to certain limited value
Information potential	Greater than Barcode and QR code	Very less	Less
Automation	Data collected automatically	Hands-on operation required	Hands-on operation required

5 Online Surveilling System

To repose the management system to surveil the move of student and explore the student information nimbly, an online interface has been evolved. The system can be applied in everyplace to repose the management system to surveil the users, by using Matric Card embedded with RFID tags; where RFID system provides reprogramming, batch ingress and storage mass data which are superior then barcodes. Applying radio-frequency identification (RFID) can promulgate precision and operational efficiency. The purviews that can be used for the online student surveillance system is shown in Fig. 5 [9].

In general conception, we have presented RFID to recognize when an individual with RFID tags passes by way of the RFID reader, the information or data identification from the RFID tag will record move (i.e., time in/out and place) in the database system. Without authorization or permission, if the pupil profanes certain zone, the network will immediately trigger an alarm to the security and management of school/college by using Online Student Surveillance (OSS) system the identification of pupil and location can be found on the Online Student Surveillance system. The overseeing system operation is shown in Fig. 6.

6 Tighten Visitor's Security

Just assuring only that the visitors causally check in at the office is not more indispensable than safety. Fortifying the students is becoming growingly indispensable. Many schools/colleges utilize visitor management systems to meliorate safety and assured students against illegitimate outsiders and person posing as students. Department of security of schools/colleges must know who is on the premises at all the times. This can be nimbly done with the help of an interim RFID enabled identity card that bears track-and-trace technologies. Upon sign-in, school/college visitor software can also

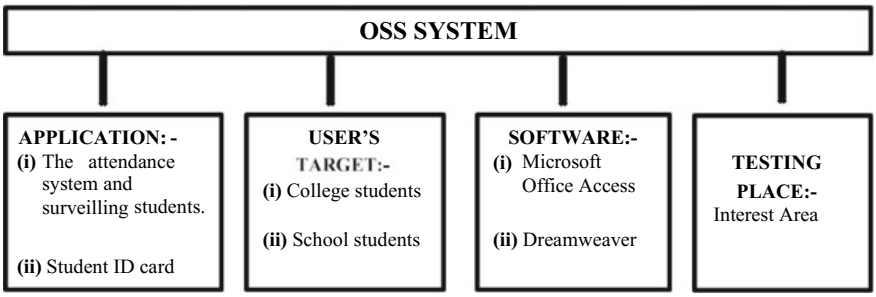

Fig. 5 The frame of theory in research of application of RFID smart card system as the information system of users [9]

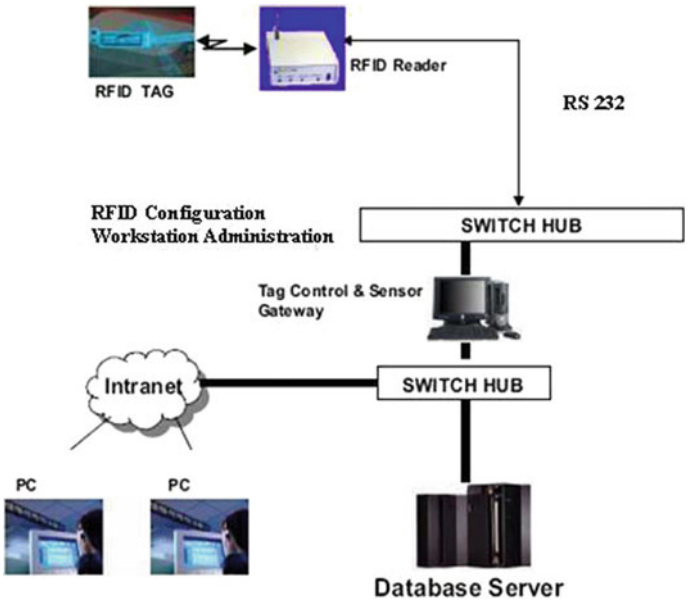

Fig. 6 OSS system architecture [9]

regulate if the visitor is a criminal or wanted by the law imposition or recorded in the sex offender database [10].

7 Access Control for Buildings

Optimum results are presented by RFID empowered identity cards for not only management of visitors, but ingress dominance for all individual, premises-wide. Providing a RFID smart identity cards to all pupils, staffs (teaching and non-teaching) and outsiders authorizes safety and security wing to dominance, who has access/approaches to where, when and what. Schools/Colleges premises can ameliorate hostel security, secure laboratories with valuable equipment, and assure R&D departments accomplishing specialized projects only yields ingress to those with right permits. With the help of RFID enabled smart identity card, management of schools/colleges can permit or deny physical access to students attending lectures in different buildings.

8 Conclusion

In this paper, an overview of smart identity cards for educational institutions has been discussed. Multipurpose smart identity cards proffer various simple and cost-effective modes for schools/colleges premises to elevate the level of safeguard and standard of education. Smart identity cards will proffer smart attendance system, which reduces manpower and surveilling of students can be nimbly done. In India, schools/universities can ameliorate competence and safeguard at the multiple stages due RFID-enabled smart identity cards which proffer better range and peruse performance. With the implementation of this smart identity cards in educational institutions, faculty, as well as the guardian of the students, will feel relax that their wards and schools/universities premises remain protected.

References

1. Wang SW, Chen WH, Ong CH, Liu L, Chuang YW (2006) RFID application in hospital: a case study on a demonstration RFID project in a Taiwan hospital. In: Proceeding of 39th annual Hawaii international conference on system science, pp 184a–184a, 04–07 Jan 2006
2. Wong KHM, Chan ACK, Hui PCL, Patel CA (2006) A framework for data flow in apparel supply chain using RFID technology, industrial informatics. In: IEEE international conference on august. pp 61–66
3. Lu M et al (2007) Positioning and tracking construction vehicles in highly dense urban areas and building construction sites. Autom Constr 647–656
4. Singh J, Brar N, Fong (2006) The state of RFID application in libraries. Inf Technol Libr 25(1):24–32
5. Beaver M (2016) The implications of RFID technology in university ID cards. S&T's Peer Peer 1(1), article 3. http://scholarsmine.mst.edu/peer2peer/vol1/iss1/3
6. https://en.wikipedia.org/wiki/Identification_friend_or_foe
7. Lotlikar T, Kankapurkar R, Parekar A, Mohite A (2013) Comparative study of barcode, QR-code and RFID system. Int J Comput Technol Appl 4(5):817–82. ISSN:2229-6093
8. RFID Journal. https://www.rfidjournal.com/faq/show?66
9. Abdul Kadir HB, Binti Mohd Kanafiah SNA, Mohd HB, Abdul Wahab ZT, Abdul Kadir ZB (2008) Online students supervision (OSS) systems using passive RFID. Faculty of Electrical & Electronics Engineering, Universiti Tun Hussein Onn Malaysia. IEEE Paper
10. Smart ID cards for education: secure the campus while providing essential services (2013). http://www.zebra.com/content/dam/zebra/white-papers/en-us/smart-id-education-en-us.pdf

Design of High Birefringence with Two Zero Dispersion Wavelength and Highly Nonlinear Hybrid Photonic Crystal Fiber

Vijay Shanker Chaudhary, Dharmendra Kumar and Sneha Sharma

Abstract A hexagonal hybrid photonic crystal fiber (PCF) with elliptical and circular air holes is designed which gives a very large birefringence. The magnitude of birefringence is 12.046×10^{-3} at 1550 nm which is very high and required for optical systems application. The proposed PCF shows zero dispersion wavelengths around 674 nm and 1591 nm and also having a large value of the nonlinear coefficient which is useful for nonlinear optics. In this paper the calculated value of nonlinear coefficient is 0.06147 $W^{-1}m^{-1}$ at 1550 nm.

Keywords Photonic crystal fiber (PCF) · Zero dispersion wavelength · Birefringence · Nonlinear coefficient · Effective area

1 Introduction

Photonic crystal fiber (PCF) is the new type of fiber which has a periodic array of air holes in the cladding around the core of the fiber. Light propagation in PCFs is much superior to conventional fiber. PCFs are generally divided into two categories. The first is index guiding fibers that have a solid core like conventional fibers in which light travels by the modified total internal reflection mechanism. And the second is photonic band gap fibers that have hollow core in which light is guided by the photonic band gap effect. PCFs provide better suppleness to design the structure as

V. S. Chaudhary (✉) · D. Kumar
Department of Electronics and Communication Engineering, Madan Mohan Malaviya University of Technology, Gorakhpur, Uttar Pradesh, India
e-mail: vijaychaudhary1981@gmail.com

D. Kumar
e-mail: dharmendra0127@gmail.com

S. Sharma
Department of Electronics and Communication Engineering, Dyanand Sagar University, Bangalore, India
e-mail: sneha.ece@gmail.com

© Springer Nature Singapore Pte Ltd. 2020

V. Janyani et al. (eds.), *Optical and Wireless Technologies*,
Lecture Notes in Electrical Engineering 546,
https://doi.org/10.1007/978-981-13-6159-3_32

compared with conventional optical fiber and achieve unique optical features as endlessly single mode operation for a wide range of wavelength [1], high birefringence [2], good dispersion quality [3–5], high nonlinearity [6], low confinement loss, etc. Birefringence can be realized in PCF by demolish the symmetrical arrangement and enhancing the difference between the effective index of two orthogonal polarization modes. Birefringence is the unique property of fiber optics. High birefringence in PCFs has unique applications such as polarization maintaining supercontinuum generation [7], fiber based gyroscopes, temperature sensors, pressure sensor, etc. [8].

In this paper, we have proposed high birefringence with two zero dispersion wavelengths and highly nonlinear hexagonal hybrid photonic crystal fiber (PCF) with elliptical and circular air holes designed by using Finite Element Method (FEM) based COMSOL Multiphysics.

2 Simulation Results and Discussions

The proposed PCF structure with round shaped air holes whose diameter is 1.35 μm, major axis and minor axis of elliptical air holes are 1.12 μm and 0.56 μm respectively and hole-to-hole distance is 1.4 μm. The background of PCF is silica whose refractive index is calculated by Sellmeier equations [9, 10] and The refractive index of air is 1. The electric field intensity for fundamental polarization modes (HE_{11}^{x} and HE_{11}^{y}) at the wavelength 1550 nm shown in Fig. 1 which shows that the PCF structure containing air holes with silica background in hexagonal lattice.

The effective indices of orthogonal polarized modes are calculated by the Finite Element Method. The birefringence (B) of the proposed PCF is basically the difference between the effective indices of the two orthogonal (HE_{11}^{x} and HE_{11}^{y}) polarization modes and which are [7]:

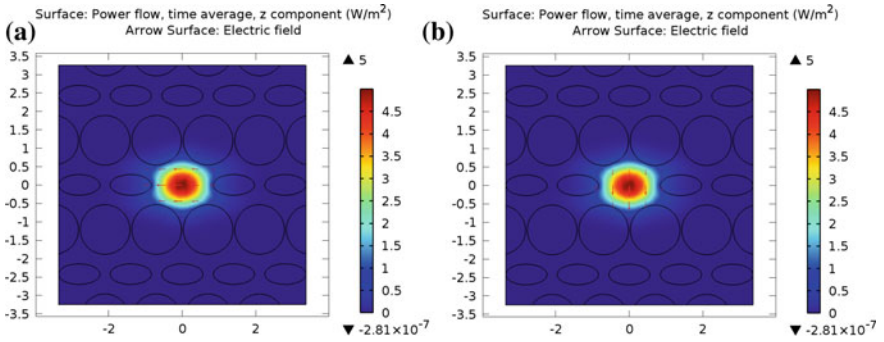

Fig. 1 Schematic of birefringent PCF and electric field intensity for **a** x polarized, **b** y polarized mode

$$B = \left|n_x - n_y\right|, \tag{1}$$

where, n_x and n_y denote the real parts of refractive indices of orthogonal (HE_{11}^x and HE_{11}^y) polarized modes, respectively.

The dispersion $D(\lambda)$ can be calculated as the sum of waveguide dispersion and material dispersion which is expressed numerically by [11]

$$D(\lambda) = D_w(\lambda) + D_m(\lambda) \tag{2}$$

$$D_w(\lambda) = -\frac{\lambda}{c}\frac{\partial^2}{\partial\lambda^2}\mathrm{Re}(n_{eff}) \tag{2.1a}$$

$$D_m(\lambda) = -\frac{\lambda}{c}\frac{\partial^2 n_m}{\partial\,\lambda^2} \tag{2.1b}$$

where, $D(\lambda)$ is the total dispersion, $D_w(\lambda)$ is the waveguide dispersion, $D_m(\lambda)$ is the material dispersion, n_{eff} is the effective index, n_m is the material dispersion estimated by using Sellmeier equations [9, 10] and c denotes speed of light.

The nonlinear coefficient (γ) is defined as [12]

$$\gamma = \frac{n_2\omega_0}{cA_{eff}}, \tag{3}$$

where, $n_2 = 2.6 \times 10^{-20}\,m^2/W$, c denotes speed of light, ω_0 indicates center frequency and A_{eff} represents effective mode area, which is given as [12]

$$A_{eff} = \frac{\left(\iint_{-\infty}^{\infty}|E(x,y)|^2 dx\,dy\right)^2}{\iint_{-\infty}^{\infty}|E(x,y)|^4 dx\,dy}, \tag{4}$$

where, E represents the electric field of medium.

Figure 2a illustrate calculated value of the effective refractive index using COMSOL Multiphysics. From the figure we can seen that effective mode index of the PCF reduced with the wavelength, and the difference between effective refractive indices of fundamental polarization modes increases with wavelength resulting high birefringence.

The effective area of the proposed PCF for both the orthogonal (HE_{11}^x and HE_{11}^y) modes is shown in Fig. 2b. The effective area increases with the wavelength and so the nonlinear coefficient decreases with wavelength as shown in Fig. 2c. The nonlinear coefficient γ of the proposed PCF is 0.06147 $W^{-1}m^{-1}$ and 0.05053 $W^{-1}m^{-1}$ for x and y polarization modes at wavelength 1550 nm, which is better than the previous reported result in Ref. [11, 12]. The γ of the proposed PCF is larger and calculated from Eq. (3), which is basically used for nonlinear application. Figure 2d shows that the value of dispersion of the x polarization is lesser than that of the y polarization. There are two zero dispersion points along the x polarized mode which is 674 and 1591 nm presented over the communication waveband which is useful for super

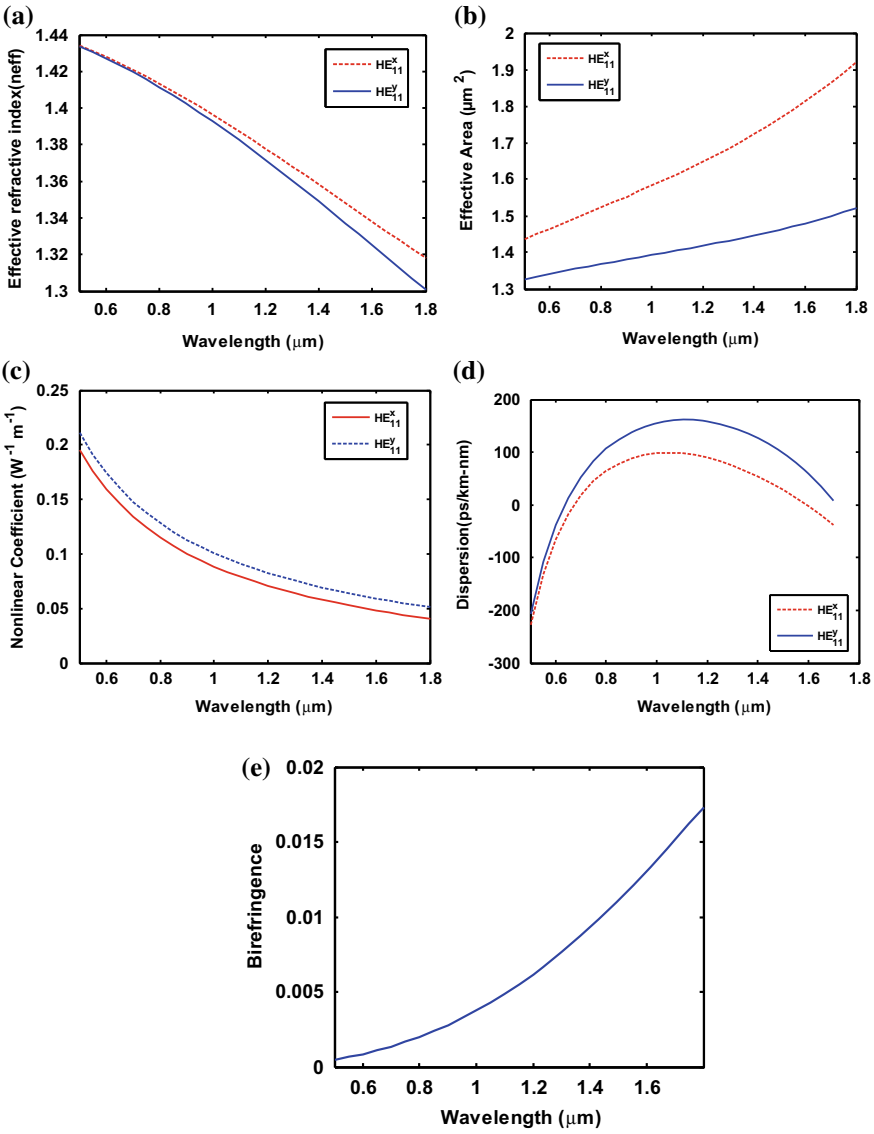

Fig. 2 **a** The effective index of proposed PCF (n_{eff}), **b** the effective area of PCF (A_{eff}), **c** nonlinear coefficient (γ), **d** dispersion curves for orthogonal modes and **e** birefringence (B)

continuum generation. Figure 2e shows the birefringence of the proposed PCF it is increases with the wavelength which represents the difference between effective refractive indices of fundamental polarization modes (HE_{11}^{x} and HE_{11}^{y}).The calculated value of birefringence is $B = 12.046 \times 10^{-3}$ at wavelength 1550 nm of proposed PCF other reported value of birefringence is 4.92×10^{-3} by Xu et al. [11], 1.2×10^{-3} by Xu et al. [12] and 2.32×10^{-3} by Zhao et al. [13].

3 Conclusion

In this paper we proposed high birefringence PCF by using Finite Element Method, which gives an enhanced birefringence and nonlinear coefficient value of the order of 12.046×10^{-3} and 0.06147 $W^{-1}m^{-1}$ respectively at 1550 nm. Simulation result also shows that the proposed PCF have two zero dispersion wavelengths (ZWD) around 674 and 1591 nm. The combination of high birefringence, two zero dispersion wavelengths and large value of nonlinear coefficient is useful to transmission system for polarization maintaining and a broadband supercontinuum generation.

References

1. Birks TA, Knight JC, Russell PSJ (1997) Endlessly single mode photonic crystal fiber. Opt lett 22, 961–963
2. Ju J, Jin W, Demokan MS (2003) Properties of a highly birefringent photonic crystal fiber. IEEE Photon Technol Lett 15:1375–1377
3. Ranka JK, Windeler RS, Stentz AJ (2000) Visible continuum generation in air–silica microstructure optical fibers with anomalous dispersion at 800 nm. Opt Lett 25:25–27
4. Knight JC, Arriaga J, Birks TA et al (2000) Anomalous dispersion in photonic crystal fiber. IEEE Photon Technol Lett 12:807–809
5. Sinha RK, Varshney SK (2003) Dispersion properties of photonic crystal fibers. Microw Opt Technol Lett 37:129–132
6. Ortigosa-Blanch A, Díez A, Pinar MD, Cruz JL, Andrés MV (2004) Ultrahigh birefringent nonlinear microstructured fiber. IEEE Photon Technol Lett 16:1667–1669
7. Sharma S, Kumar J (2013) Design of high birefringence nonlinear polarization maintaining photonic crystal fiber. In: Workshop on recent advances in photonics (WRAP), 17–18 Dec 2013. https://doi.org/10.1109/wrap.2013.6917659
8. Yang TJ, Shen LF, Chau YF, Sung MJ, Chen D, Tsai DP (2008) High birefringence and low loss circular air-holes photonic crystal fiber using complex unit cells in cladding. Opt Comm 281:4334–4338
9. Hussein RA, Hameed MFO, Obayya SSA (2016) Ultrahigh soliton pulse compression through liquid crystal photonic crystal fiber. IEEE J Sel Topics Quantum Electron 22(2):302–309
10. Coscelli E, Poli F, Li J, Cucinotta A Selleri S (2015) Dispersion engineering of highly nonlinear chalcogenide suspended-core fibers. IEEE Photon J 7:2200408
11. XU Q, Miao R, ZhangnY (2012) Highly nonlinear low-dispersion photonic crystal fiber with high birefringence for four-wave mixing. Opt Mater 35:217–221

12. Xu D, Song H, Wang W, Fan Y, Yang B (2013) Numerical analysis of a novel high birefringence photonic crystal fiber. Optik 124:1290–1293
13. Zhao Y, Wu D, Lv RQ, Li J (2016) Magnetic field measurement based on the sagnac interferometer with a ferrofluid-filled high-birefringence photonic crystal fiber. IEEE Trans Instrum Meas 65:1503–1507

A Review on Code Families for SAC–OCDMA Systems

Soma Kumawat and M. Ravi Kumar

Abstract A comprehensive survey on different code families for Spectral Amplitude Coding–Optical Code Division Multiple Access (SAC–OCDMA) systems. Review on one- and two-dimensional codes reported is taken into account. Study indicates the feasibility of codes and further scope of these codes. System design of SAC–OCDMA is also explained.

Keywords SAC–OCDMA · Cross-correlation · Codes · BER

1 Introduction

Optical networks provide the solution toward increased spectrum requirement. The utilization of spectrum in proper and convenient manner is the next raised question which is answered by different access techniques. They provide access and sharing of spectrum efficiently among different users. There are several access techniques Wavelength Division Multiple Access (WDMA) [1], Optical Time Division Multiple Access (OTDMA) [2], and Optical Code Division Multiple Access (OCDMA) [3].

OCDMA has knocked the doors for future multiple access networks [3]. The basic idea of OCDMA is similar to CDMA. It transmits the signature code in place of one and zero sequences in place of zero [4]. At receiver, a high peak is generated due to detection of desired code. On detection of a high peak, the receiver assumes the code was transmitted. OCDMA has many features such as no need for centralized network control, number of codes decides the cardinality of a network, new user can easily be added to the networks, it does not require any scheduling, permitting asynchronous access with no waiting time, security against eavesdropping, supporting larger number of users, and provision for multimedia traffic. Hence, OCDMA is a

S. Kumawat (✉) · M. Ravi Kumar
Malaviya National Institute of Technology Jaipur, Jaipur, Rajasthan, India
e-mail: somakumawat25@gmail.com

M. Ravi Kumar
e-mail: rkmadilla.ece@mnit.ac.in

© Springer Nature Singapore Pte Ltd. 2020

V. Janyani et al. (eds.), *Optical and Wireless Technologies*,
Lecture Notes in Electrical Engineering 546,
https://doi.org/10.1007/978-981-13-6159-3_33

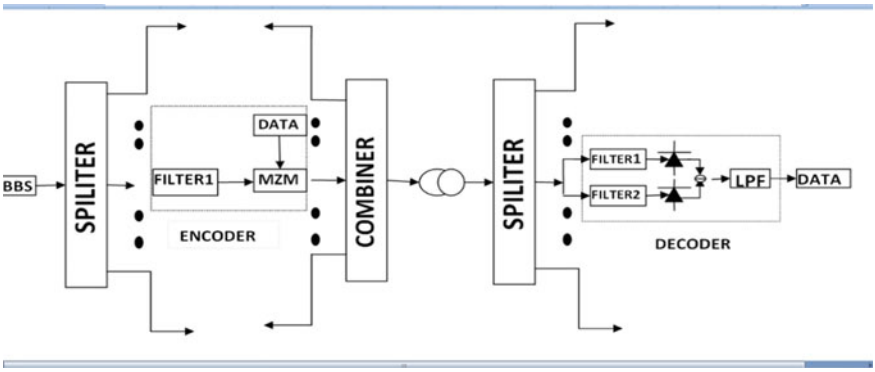

Fig. 1 Block diagram of SAC–OCDMA system using BD technique

promising technology for next generation access network. For OTDMA and WDMA, the total numbers of time or wavelength channels provide the capacity of system. On the other hand, OCDMA permits flexibility in capacity of system by generating codes to support network [5].

The performance of OCDMA systems is mainly due to interference from other users known as Multiple Access Interference (MAI) [6, 7]. Spectral Amplitude Coding–OCDMA (SAC–OCDMA) system is one of the OCDMA technique in which unique codes are mapped to different spectral lines of a broadband source [8, 9]. It eliminated the MAI on using the codes with fixed In-Phase Cross-Correlation (IPCC). The elimination of MAI is realized by Balanced Detection (BD) as shown in Fig. 1. It also provides a low-cost solution as it uses Broadband Sources (BBS) like Light-Emitting Diodes (LEDs).

A comprehensive literature review of SAC–OCDMA codes is presented. It started from basic introduction of SAC–OCDMA systems in Sect. 2. The various coding techniques are discussed in Sect. 3. Section 3 gives a brief overview of the codes developments from beginning to recent codes. Section 4 discusses the conclusions.

2 Spectral Amplitude Coding (SAC) Systems

Codes are represented by (N, L, W, λ_c), where N is number of users, L is code length, W is code weight, and λ_c is IPCC. Code length (L) is total number of chips used by each user. Weight (W) represents the number of chips which is having value 1. The IPCC between two codes is defined as $\lambda_c = \sum_{j=1}^{L} a_j d_j$ for the two users codes A = (a_1, a_2, a_3, …, a_L) and D = (d_1, d_2, d_3, …, d_L) of code length (L). When $\lambda_c = 1$, the code possesses ideal IPCC properties [10].

Figure 1 explains the block diagram of SAC–OCDMA system. It employs transmitter and receiver pairs connected in a star configuration. The transmitter side incor-

porates light source, splitter, data generator, encoder, modulator, and multiplexer. The light sources are BBS like LEDs and superluminescent diodes. The optical spectrum of BBS is divided into L number of chips. These chips are allocated according to the signature codes. At encoder, the code is created on filtering the wavelengths from optical spectrum of the BBS. These signals are modulated by Mach Zehnder Modulator (MZM) according to given data. As, when the data bit is 1, chips are sent according to the signature code, and when the data bit is 0, no pulse is launched from the BBS. Codes are combined and launched onto the optical fiber.

The main components of receiver are filtering component, photodiodes, and error detectors. For Balanced Detection (BD) technique, the received signal is divided into two parts. The upper part uses the same wavelength structure as used by encoder. For lower part, wavelength structure is selected in such a way that it eliminates the MAI. Signals from both parts are given to an electrical subtractor which cancel out the MAI.

MAI is main factor which degrades the performance, especially when numbers of users are large. For SAC–OCDMA, MAI is only determined by the values of IPCC [11, 12]. MAI can be eliminated when codes with fixed IPCC are used for such systems. Nevertheless, such systems exhibit inherent Phase-Induced Intensity Noise (PIIN) due to spontaneous emission of the BBS that severely affects the overall system performance. Suppression of PIIN is possible by choosing small values of IPCC [10]. Hence, the codes with ideal IPCC become attractive. Many codes with ideal IPCC and other properties are reported for SAC–OCDMA systems.

3 Literature Survey

3.1 1D Codes

Spectral encoding is proposed using the m-sequences codes in [8]. A single m-sequence code generates N user codes, simply by cyclic shifting of single code N times. The Hadamard codes are reported in [13]. An $N \times N$ Hadamard matrix is used to generate codes for $(N - 1)$ users. The m-sequences and Hadamard code are expressed as a $(L, W, \lambda) = (N, (N + 1)/2, (N + 1)/4)$ and $(N, N/2, N/4)$, respectively. These codes offer an easy code construction, fixed IPCC, and simple architecture. However, their performance is limited due to the large value of IPCC.

In [13, 14], Modified Quadratic Congruence (MQC) $(p^2 + 1, p + 1, 1)$ code families based on quadratic congruence code are investigated, where p is a prime number. However, there are only p^2 code sequences in a family with length $(p^2 + p)$. MQC has a limitation in code section due to its dependence on prime number for p. Modified Frequency Hopping (MFH) $(Q^2 + Q, Q + 1, 1)$ code families based on frequency hopping code is presented in [15], where $Q = p^n$ is a prime power. MFH code gives wider range in code selection on comparing with MQC code along with all its property. In [16], the two algebraic construction methods for the balanced

incomplete block design code are reported. In [17], three optical orthogonal code constructions are reported, based on mutually orthogonal Latin squares or mutually orthogonal Latin rectangles, integer lattice design and affine geometries. All these codes have algorithmic complexity such as projective geometry and block designs.

Partitioned partial prime codes are constructed using Kronecker tensor product, multiplication operation, and matrix complement methods in [18]. Partitioned partial prime code family has the low value of IPCC, flexible code length, and excellent orthogonality. In spite of these advantages, it has complex code construction, exists only for a prime number, and cross-correlation calculation is time-consuming. In [19], diagonal permutation shifting code is proposed with fixed IPCC and short code length. The construction of these codes is based on simple algebraic and certain matrix operations derived from the prime code sequences based on the Galois field. In [20], a code is reported with short code length named as dynamic cyclic shift. It has cross-correlation value between 1 and 0. It consists of two parts—weight and dynamic parts. The weight part is designed using the value of weight. The dynamic part is a set of zeros. The weight sequence and dynamic sequence are clubbed together to form a code, and on cyclic shifting other code sequences are generated. The cardinality of this system is limited by the condition that the number of users must equal the code length. Diagonal Eigenvalue Unity (DEU) code is constructed for any integer value of weight in [21]. Jordan block matrix is used for designed code. Four combinations for (W, N) are designed such as (even, odd), (odd, even), (odd, odd), and (even, even). Cross-correlation is less than or equal to one. DEU code has higher code length. SW-matrix partitioning is introduced in [22] and compared to DEU codes. It has shorter code length compared to DEU code.

In [23], an algorithm is reported as fixed right shifting code based on modified Jordan block matrix with some algebraic methods. It constructs the codes using different combinations of even and odd values of number of users and weight. Its cross-correlation is $\lambda_c \leq 1$. Code length is defined as $L = N(W - 2) + W$. The minimum code weight is 3 for code construction. Matrix partitioning code is reported in [24]. It used the arithmetic sequence to construct the codes. Arithmetic sequence is a sequence in which the next term originates by adding a constant to its predecessor and the difference of any two successive numbers is a constant. Cross-correlation is smaller than and equal to one. Code length is defined as $N \times W/2$. Any integer number of weight can be used in code construction. A generalized matrix partitioning code is reported which uses mathematical properties of matrix partitioning code in [25]. It defines the upper bounds and lower bounds for the code. By putting the value of g (set of codes) equal to 1, the matrix partitioning code is generated. Cross-correlation is one in the same group and zero with codes in different groups. It is constructed for all natural numbers. Double weight codes are one of the code families constructed for SAC–OCDMA systems in [26]. The families include the code construction of Double Weight (DW) [26], Modified Double Weight (MDW) [26], and Enhanced Double Weight (EDW) [27]. These codes have ideal IPCC property. The code construction steps are easy to implement. They have weight chips always in pairs which required less filtering component. Khazani–Syed (KS) code for even weights was constructed

in [28]. It is a combination of DW and MDW codes. Weight constraint with different algorithms is the main difficulty with these codes.

3.2 Variable Cross-Correlation Code

The Flexible Cross-Correlation (FCC) codes are reported with property of flexible cross-correlation. The code lengths are shorter for these codes which turn in higher cardinality. FCC eliminates the effect of MAI. Random Diagonal (RD) code is reported in [29]. Code construction is divided into two parts—code and data. At data part, it designed zero cross-correlation code of weight 1. Code part consists of basics and weight parts. Weight part is responsible for increasing number of weights. It constructs code with shorter length. Cross-correlation value is greater than zero and depends on weight and number of users. Code is designed for weight greater than 2. In [30], FCC code is reported using tridiagonal code matrix. In [31], sequential algorithm code is reported with FCC property. It generates code set of any desired cross-correlation properties with smallest code length for the given number of users. It used tridiagonal matrix code property to constructed code for any given number of users and weights. Drawback of FCC codes is higher value of cross-correlation which leads more PIIN. On other hand, the codes constructed by FCC have shorter code length compare to fixed cross-correlation codes.

3.3 Zero Cross-Correlation Code

MAI can be removed from SAC–OCDMA system using electrical subtraction, but the PIIN still remains. Thus, PIIN can severely affect the overall system performance. All the above codes are suffered from PIIN. The code design with Zero Cross-Correlation (ZCC) property has removed the effect of MAI and suppressed the effect of PIIN [32].

The code with the property of zero cross-correlation is called as Zero Cross-Correlation Code (ZCCC). It does not have any overlapping of wavelengths between any users. It is reported with constant weight construction in [33]. Its construction with LED spectrum slicing is described in [34]. They use mapping technique to construct codes for the higher number of users. Multi-diagonal code [35] and modified zero cross-correlation code [36] are reported with ZCC property. The MAI is completely eliminated using codes with ZCC property but at the rate of longer code length which requires wideband sources.

Enhanced multi-diagonal code is invented in [37]. It improves the code property of multi-diagonal and RD codes. It defined two matrices, data, and code matrices as RD code. Data matrix is a diagonal matrix of size N $\times$ N. It has zero cross-correlation between all rows. Code matrix used chip combination (1 2 1) as DW code. This

combination is repeated diagonally. Cross-correlation of chip combination is 1. Code length is $L = N + [N (W - 2) + 1]$. Code is designed for weight greater than 2.

All of the above-reported schemes have fixed code length and weight that are not suitable for multimedia services. Thus, coding techniques with variable code weights and code lengths are required. The W indicates the total power sent by each code. High values of W give higher transmitted power and vice versa [38]. Variable Weight (VW) optical orthogonal code was reported with different Quality of Service (QoS) in [39]. VW Khazani–Syed (KS) code was reported for even weights in [40]. It uses mapping technique. Experimental and simulation results of VW KS code were obtained in [41]. In [42], hybrid fixed-dynamic weight assignment technique is reported for VW KS code. Comparison of various detection techniques for KS code is reported in [43]. VW Random Diagonal (RD) code is reported in [44] for "triple play" service for weights greater than 2. It uses two segments such as data segment that has zero cross-correlation, and code segment that has high cross-correlation. It uses the mapping technique to provide codes for VW RD. Multiservice (MS) code [45] is reported for fixed weight, and variable QoS by varying the number of codes in basic matrix.

3.4 2D Codes

All above-described codes are one dimensional (1D) which have a limitation of fewer users due to finite bandwidth of source. The solution is provided by two-dimensional (2D) codes as Spectral/Spatial (S/S) codes. They extend the number of codes in spatial domain in which, each spectral component is split according to spatial code of that user [46].

2D M-matrices codes are reported in [47]. The performance of M-matrices codes was affected by high value of cross-correlation. To further increase the number of users along with performance and improve structure of system, permuted M-matrices code was given in [48]. It used the cyclic property of arrayed waveguide grating routers together with M-sequence code. The permuted M-matrix code allowed a greater number of users [48]. The cross-correlation value of 2D M-matrix codes is high resulting in inefficient performance. The 2D Perfect Difference (PD) code was reported with low-value cross-correlation in [49]. 2D Diluted Perfect Difference (DPD) code was reported in [50]. DPD code used the dilution method on the spectral and spatial codes. It has IPCC property. It reduces the effect of PIIN resulting in improved system performance along with number of users.

The quadratic congruence code matrices were reported in [51] with IPCC property to reduce MAI. In [52], the 2D spatial division multiplexing balanced incomplete block design code was reported with spatial division multiplexing technique. The 2D extended M-sequence/extended perfect difference codes with a low IPCC value are given in [53]. Design of optical line terminal and optical network units was also described. Extended perfect difference code provided orthogonal property in spatial domain. The 2D hybrid codes were reported with spectral orthogonality and MAI

cancellation property in [54]. The spectral orthogonality was used to reduce the PIIN induced from the other users.

4 Conclusion

A number of code families have been developed for SAC–OCDMA systems. Some of these families have good autocorrelation and cross-correlation properties, and others have higher cardinality, lower code length, and code weight. Construction of code families, which is having all properties, is still a challenging task. Such codes will support a large number of simultaneous users with high BER performance and lower code length and weights. An interesting future research would be multidimensional codes which promises the better performance, lower noise, and support more active users simultaneously. But, on other hand, multidimensional codes add lot of complexity to the system design and its architecture and so the reduction of complexity in design is next step to be solved.

References

1. Stok A, Sargent E (2002) System performance comparison of optical CDMA and WDMA in a broadcast local area network. Commun Lett IEEE 6(9):409–411
2. Huang W, Nizam M, Andonovic I, Tur M (2000) Coherent optical CDMA (OCDMA) systems used for high-capacity optical fiber networks-system description, OTDMA comparison, and OCDMA/WDMA networking. J Lightw Technol 18(6):765–778
3. Prucnal P, Santoro M, Fan T (1986) Spread spectrum fiber-optic local area network using optical processing. J Lightw Technol 4(5):547–554
4. Pickholtz R, Milstein L, Schilling D (1991) Spread spectrum for mobile communications. Vehic Technol IEEE Trans 40(2):313–322
5. Fouli K, Maier M (2007) Ocdma and optical coding: principles, applications, and challenges [topics in optical communications]. IEEE Commun Mag 45(8):27–34
6. Salehi JA (1989) Code division multiple-access techniques in optical fiber networkspart I: fundamental principles. IEEE Trans Commun 37(8):824–833
7. Salehi JA, Brackett CA (1989) Code division multiple-access techniques in optical fiber networkspart II: systems performance analysis. IEEE Trans Commun 37(8):834–842
8. Zaccarin D, Kavehrad M (1993) An optical cdma system based on spectral encoding of led. Photon Technol Lett IEEE 5(4):479–482
9. Heritage JP, Weiner AM (2007) Advances in spectral optical codedivision multiple-access communications. IEEE J Sel Top Quantum Electron 13(5):1351–1369
10. Wei Z, Ghafouri-Shiraz H, Shalaby H (2001) New code families for fiber-bragg-grating-based spectral-amplitude-coding optical cdma systems. Photon Technol Lett IEEE 13(8):890–892
11. Kavehrad M, Zaccarin D (1995) Optical code-division-multiplexed systems based on spectral encoding of noncoherent sources. J Lightw Technol 13(3):534–545
12. Adam L, Simova ES, Kavehrad M (1995) Experimental optical cdma system based on spectral amplitude encoding of noncoherent broadband sources, pp 122–132
13. Zaccarin D, Kavehrad M Optical cdma by spectral encoding of led for ultrafast atm switching, in Communications, 1994. In: IEEE international conference on ICC 94, SUPERCOMM/ICC 94, conference record, serving humanity through communications, May 1994, vol 3, pp 1369–1373

14. Wei Z, Shalaby H, Ghafouri-Shiraz H (2001) Modified quadratic congruence codes for fiber bragg-grating-based spectral-amplitude-coding optical cdma systems. J Lightw Technol 19(9):1274–1281
15. Wei Z, Ghafouri-Shiraz H (2002) Proposal of a novel code for spectral amplitude-coding optical cdma systems. IEEE Photon Technol Lett 14(3):414–416
16. Wei Z, Ghafouri-Shiraz H (2002) Codes for spectral-amplitude-coding optical cdma systems. J Lightw Technol 20(8):1284–1291
17. Djordjevic IB, Vasic B (2003) Novel combinatorial constructions of optical orthogonal codes for incoherent optical cdma systems. J Lightw Technol 21(9):1869–1875
18. Tseng SP, Wu J (2010) A new code family suitable for high-rate sac ocdma pons applications. IEEE J Select Areas Commun 28(6):827–837
19. Ahmed HY, Gharsseldien ZM, Aljunid SA (2017) Performance analysis of diagonal permutation shifting (dps) codes for sac-ocdma systems. J Inf Sci Eng 33(2):429–444
20. Abd T, Aljunid S, Fadhil H, Ahmad R, Rashid M (2012) New approach for evaluation of the performance of spectral amplitude coding optical code division multiple access system on high-speed data rate. Commun IET 6(12):1742–1749
21. Ahmed HY, Nisar K (2013) Diagonal eigenvalue unity (deu) code for spectral amplitude coding-optical code division multiple access. Opt Fiber Technol 19(4):335–347
22. Hassan Yousif Ahmed MZ (2017) An efficient spectral amplitude coding (sac) technique for optical cdma system using wavelength division multiplexing (wdm) concepts. (IJACSA) Int J Adv Comput Sci Appl 8(7):36–44
23. Ahmed HY, Zeghid M, Nisar KS, Aljunid SA (2017) Numerical method for constructing fixed right shift (frs) code for sac-ocdma systems. Int J Adv Comput Sci Appl (IJACSA) 8(1):1546–1550
24. Ahmed HY (2014) Matrix partitioning code family for spectral amplitude coding ocdma. Photon Netw Commun 28(1):102–111. http://dx.doi.org/10.1007/s11107-014-0439-1
25. Nisar K (2017) Numerical construction of generalized matrix partitioning code for spectral amplitude coding optical fCDMAg systems. Optik Int J Light Electron Opt 130:619–632
26. Aljunid S, Ismail M, Ramli A, Ali B, Abdullah M (2004) A new family of optical code sequences for spectral-amplitude-coding optical cdma systems. Photon Technol Lett IEEE 16(10):2383–2385
27. Hasoon MASSFN, Aljunid SA (2006) Spectral amplitude coding ocdma systems using enhanced double weight code. J Eng Sci Technol 1(2):192–202
28. Abdullah M, Aljunid S, Anas S, Sahbudin R, Mokhtar M (2007) A new optical spectral amplitude coding sequence: Khazani-syed (ks) code. In: International conference on information and communication technology, 2007, ICICT07. IEEE, pp 266–278
29. Fadhil HA, Aljunid S, Badlisha R (2007) Random diagonal code for spectral amplitude-coding optical cdma system. Int J Comput Sci Netw Secur 7:258–262
30. Rashidi C, Aljunid S, Ghani F, Fadhil HA, Anuar M (2013) New design of flexible cross correlation (fcc) code for sac-ocdma system. Proc Eng 53:420–427
31. Fazlina CAS, Rashidi CBM, Rahman AK, Aljunid SA, Endut R (2017) Enhanced performance of bit error rate by utilizing sequential algorithm (seq) code in optical cdma network systems. Int J Appl Eng Res 12(7):1411–1415
32. Kumawat S, Ravi Kumar M (2017) Development of ZCCC for multimedia service using SAC-OCDMA systems. Opt Fiber Technol 39:12–20
33. Anuar M, Aljunid S, Saad N, Hamzah S (2009) New design of spectral amplitude coding in fOCDMAg with zero cross-correlation. Opt Commun 282(14):2659–2664
34. Anuar MS, Aljunid SA, Arief AR, Saad NM (2010) Led spectrum slicing for zcc sac-ocdma coding system. In: 7th international symposium on high-capacity optical networks and enabling technologies, pp 128–132
35. Abd TH, Aljunid S, Fadhil HA, Ahmad R, Saad N (2011) Development of a new code family based on sac-ocdma system with large cardinality for fOCDMAg network. Opt Fiber Technol 17(4):273–280

36. Rashidi CBM, Aljunid SA, Ghani F, Anuar MS (2010) Development of modified zero cross correlation code for ocdma network. In: International conference on photonics 2010, pp 1–6
37. Imtiaz WA, Ilyas M, Khan Y (2016) Performance optimization of spectral amplitude coding ocdma system using new enhanced multi diagonal code. Infrared Phys Technol 79:36–44
38. Kumawat S, Ravi Kumar M (2018) Design of variable weight code for multimedia serice in SAC-OCDMA systems. IET Optoelectron 12(2):56–64
39. Djordjevic IB, Vasic B, Rorison J (2004) Multi-weight unipolar codes for multimedia spectral-amplitude-coding optical cdma systems. IEEE Commun Lett 8(4):259–261
40. Anas SA, Abdullah M, Mokhtar M, Aljunid S, Walker S (2009) Optical domain service differentiation using spectral-amplitude-coding. Opt Fiber Technol 15(1):26–32
41. Experimental demonstration of variable weight sac-ocdma system for qos differentiation. Opt Fiber Technol 20(5):495–500 (2014)
42. Seyedzadeh S, Moghaddasi M, Anas SB (2016) Variable-weight optical code division multiple access system using different detection schemes. J Telecommun Inf Technol 3:50–59
43. Variable-weight optical code division multiple access system using different detection schemes. J Telecommun Inf Technol 3:50–59 (2016)
44. Hilal Adnan F, Syed Alwee Aljunid SJ, Badlishah AR (2009) Multirate transmissions on spectral amplitude coding optical code division multiple access system using random diagonal codes
45. Kakaee MH, Essa SI, Seyedzadeh S, Mokhtar M, Anas SB, Sahbudin RK Proposal of multi-service (ms) code to differentiate quality of services for ocdma system. In: 2014 IEEE 5th international conference on photonics (ICP), Sept 2014, pp 176–178
46. Kumawat S, Ravi Kumar M, Nanda SJ (2017) 2D code constructing using DW code families for SAC-OCDMA systems, TENCON 2017, Malaysia
47. Yang C-C, Huang J-F (2003) Two-dimensional m-matrices coding in spatial/frequency optical cdma networks. IEEE Photon Technol Lett 15(1):168–170
48. Huang J-F, Yang C-C (2006) Permuted m-matrices for the reduction of phase-induced intensity noise in optical cdma network. IEEE Trans Commun 54(1):150–158
49. Lin C-H, Wu J, Yang C-L (2005) Noncoherent spatial/spectral optical cdma system with two-dimensional perfect difference codes. J Lightw Technol 23(12):3966–3980
50. Yeh BC, Lin CH, Yang CL, Wu J (2009) Noncoherent spectral/spatial optical cdma system using 2-d diluted perfect difference codes. J Lightw Technol 27(13):2420–2432
51. Tsai C-M (2006) Optical wavelength/spatial coding system based on quadratic congruence code matrices. Photon Technol Lett IEEE 18(17):1843–1845
52. Yang C-C (2008) The application of spectral-amplitude-coding optical cdma in passive optical networks. Opt Fiber Technol 14(2):134–142
53. Tseng SP, Wu J, Yang WH (2012) Two-dimensional spectral/spatial fiber-optic cdma pon with ems/epd codes. IEEE Trans Commun 60(11):3451–3460
54. Yeh BC, Lin CH, Wu J (2010) Noncoherent spectral/spatial ocdma system using two-dimensional hybrid codes. IEEE/OSA J Opt Commun Netw 2(9):653–661

OFDM over Optical Fiber

Usha Choudhary and Vijay Janyani

Abstract Orthogonal frequency division multiplexing (OFDM) supports high data rate transmission over orthogonal subcarriers and simultaneously removes signal dispersion because of multipath propagation with different delays in channel to receiver section. OFDM when implemented in optical fiber channel comes with ease of dispersion compensation in single mode as well as multimode fiber along with fiber nonlinearity as a prominent feature to be managed. In this paper, authors have explained some basic features of OFDM over single-mode fiber and simulation results confirm the limits and advantages of OFDM over fiber.

Keywords OFDM · Optical fiber · Nonlinearity · Dispersion · EVM

1 Introduction

OFDM is popular multicarrier transmission scheme in copper cable mode or wireless mode like digital video broadcasting (DVB), power line communication, wireless local area network (WLAN 802.11 a/g/n), and Wimax. OFDM came in research and implementation in RF range in early 1960s still it is very recent for optical wireless or fiber (2001 and 2005, respectively) mode of transmission [1]. Reluctance for OFDM in optical domain is because of some basic difference in OFDM for both RF and optical domain that ask for major changes in basics of both technologies that have been developed significantly in two parallel directions of their own. This paper presents inherent advantages of OFDM that can help in optical fiber domain and modifications and constraints that need to be managed. Section 2 is about OFDM over the optical fiber domain, Sect. 3 includes simulation setup and results, and conclusion is in Sect. 4.

U. Choudhary (✉) · V. Janyani
ECE Department, Malaviya National Institute of Technology Jaipur, Jaipur 302017, India
e-mail: Ushamaderna.akash@gmail.com

V. Janyani
e-mail: Vjanyani.ece@mnit.ac.in

© Springer Nature Singapore Pte Ltd. 2020

V. Janyani et al. (eds.), *Optical and Wireless Technologies*,
Lecture Notes in Electrical Engineering 546,
https://doi.org/10.1007/978-981-13-6159-3_34

2 OFDM over Optical Fiber

In optical communication, multicarrier transmission is generally implemented with wavelength division multiplexing (WDM), that is, modulation of laser diodes with different center wavelengths and very narrow bandwidth [2]. As the number of users' increases, WDM becomes denser and reinstallation is required. OFDM is multicarrier transmission scheme that modulates the incoming data stream over N_{SC} subcarriers and all these subcarriers are orthogonal to each other for given symbol duration T_s. Condition of orthogonality for ith and jth subcarriers $C_i(t)$ and $C_j(t)$ is given as [3]

$$\begin{aligned} &\int_0^{Ts} C_i(t)C_j(t)dt = 1 \ldots i = j \\ &\int_0^{Ts} C_i(t)C_j(t)dt = 0 \ldots i \neq j \\ &i, j \in (1, N_{SC}) \end{aligned} \tag{1}$$

Orthogonal subcarriers help to reduce the intersymbol interference (ISI) caused by pulse broadening which is caused by multipath reception in wireless channel. Similarly, in optical domain dispersion generated pulse distortion can be managed automatically by OFDM and this is one of the favorite features of OFDM that motivates the researchers to proceed in this direction [4]. Figure 1 shows an example of set of orthogonal subcarriers.

Orthogonal subcarrier modulation and demodulation are done with calculating IFFT and FFT of given data sequence so bulky multicarrier transmitter–receiver with N_{SC} modulators, matched filters multiplexer, etc. has been replaced with a very efficient and dedicated digital signal processing (DSP) unit. DSP unit is second big advantage of OFDM as it provides a huge margin for network expansion as well as technology upgradation. Simple change in algorithm like number of subcarrier, length of cyclic prefix, type of symbol mapping (QPSK/QAM) with change in constellation size M are easily modified according to channel condition and demand without any major change in installed network setup. In optical fiber mode of communication, this DSP unit also works as dispersion management unit that adaptively modifies the parameters to accommodate the change in channel condition [5, 6].

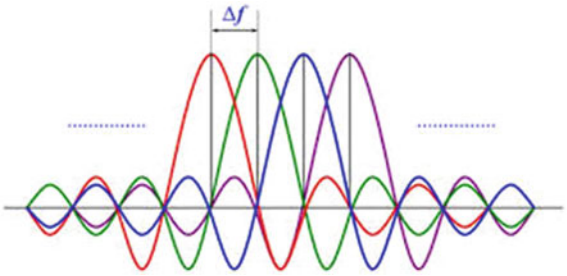

Fig. 1 Orthogonal subcarriers in OFDM symbol

OFDM signal $s(t)$ for symbol duration T_s can be represented as

$$s(t) = \sum_{k=1}^{N_{SC}} c_k e^{j2\pi f_k t},\ f_k = \frac{k}{T_s} \tag{2}$$

N_{SC} is number of subcarriers and f_k is kth subcarrier that has amplitude c_k. This signal is bipolar in nature, whereas optical signal can be unipolar only and this requires change in existing OFDM technology before it can be used in optical region. Unipolar transmission of OFDM requires either DC bias or clipping of negative polarity signal [7, 8].

At some time, there is probability that many of these subcarriers are in phase and that create high-transmitted power condition and it is one among the major concern regarding OFDM system design, defined as high peak-to-average power ratio (PAPR). In general, RF OFDM transmission, PAPR restricts the design and performance of high power amplifier, whereas in optical fiber domain high PAPR makes fiber nonlinearity as major limiting factor [9, 10]. Phase and frequency offset sensitivities are similar in optical OFDM as it is in RF OFDM.

OFDM has a design parameter defined as cyclic prefix (CP) that is similar to guard band allocation in frequency multicarrier transmission. CP copies a small section of OFDM symbol tail as prefix of transmitted symbol. Addition of CP provides tolerance for pulse broadening and improves error performance although some extra overhead bits reduce spectral efficiency. OFDM transmits pilot carrier for phase and frequency synchronizations that distort the performance otherwise.

3 Simulation Setup and Results

Basic OFDM transmission back to back and over optical fiber domain is simulated with OptSim simulation tool. Figure 2 shows simulation setup for coherent detection over fiber, whereas fiber section and optical to electric conversion were not included in back-to-back OFDM.

Figure 3 shows output of different sections at transmitter and receiver sides. At receiver side, we have recorded the scattering diagram three times in back-to-back OFDM to study the effect of phase recovery and automatic synchronization. Figure 3a is input scattering diagram for QAM-16. Figure 3b–d is output scattering diagram for parameter settings as automatic synchronization and phase recovery, automatic synchronization without phase recovery and manual synchronization without phase recovery.

Second, role of CP is studied in both back-to-back OFDM and OFDM over fiber. In back-to-back fiber, scattering diagrams are much distorted when cyclic prefix is completely removed. OFDM over fiber also gets much distorted scattering diagram because of fiber nonlinearity phenomenon.

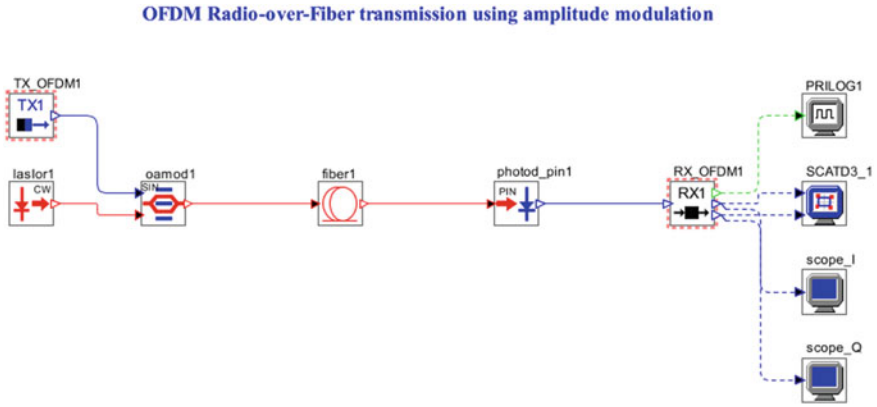

Fig. 2 OFDM over optical fiber transmission

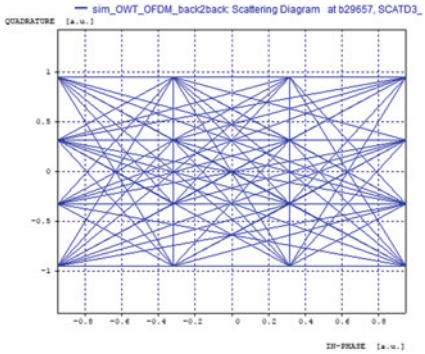

(a) Input Scattering Diagram

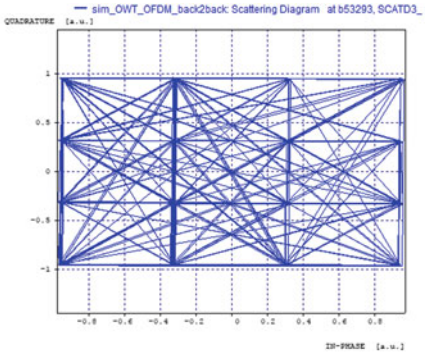

(b) Output scattering diagram with automatic synchronization and phase recovery

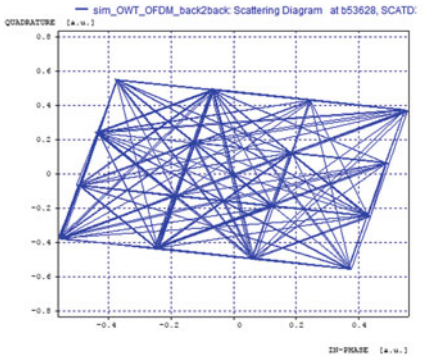

(c) Automatic synch without phase recovery

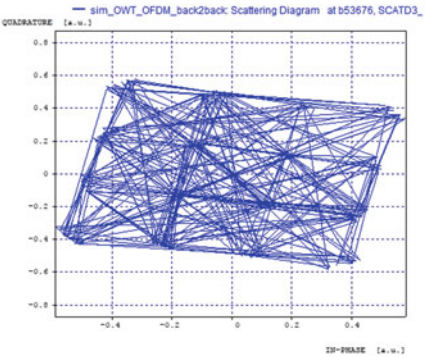

(d) Manual synch and no phase recovery

Fig. 3 Input and output scattering diagrams for effects of synchronization and phase recovery in back-to-back OFDM with QAM-16 as symbol mapper

Table 1 Simulation parameters

Parameters	Value
Ref. bit rate	10 Gbps
Subcarriers no.	8
Cyclic prefix	0.25
Modulation	QAM-16
Fiber length	3 km

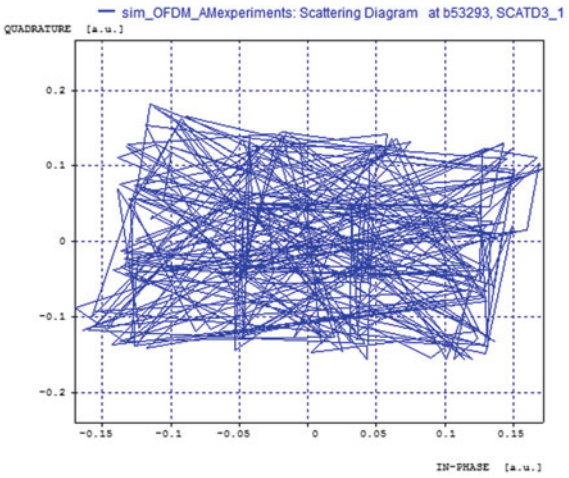

Fig. 4 Output scattering diagram at fiber end

Table 1 summarizes the simulation parameters for study of OFDM scattering diagrams for different phase recoveries and carrier synchronization techniques. Figure 4 is output scattering diagram for OFDM over optical fiber and Fig. 5 is showing error vector measurement (EVM) recorded for different numbers of subcarriers varying from 4 to 16 with fiber length up to 7 km.

4 Conclusion

High PAPR in OFDM over optical fiber puts limits over transmission power because of nonlinearity in fiber material and results is highly distorted output scattering diagram. Sensitivity for phase and frequency offsets is another major issue for OFDM as it may cause the loss of orthogonality among the subcarriers and results in large intersymbol and intercarrier interference. Effect of phase synchronization over OFDM received signal is analyzed. Different governing factors for OFDM like length of CP, numbers of subcarriers also affect the error performance. For improvement in error performance at high data rate and long distance applications, OFDM with forward

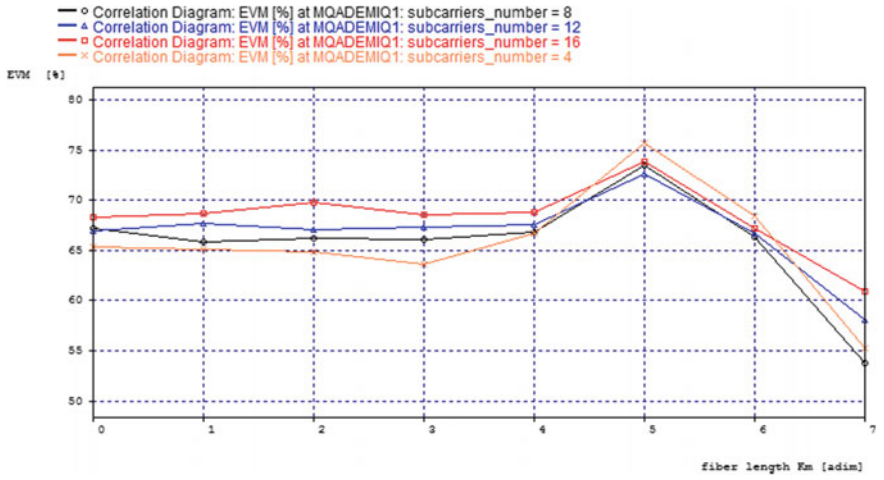

Fig. 5 EVM for different numbers of subcarrier

error correction codes like Turbo code and low-density parity check codes can be implemented as well as these codes can help to regulate the nonlinearity in optical fiber despite the larger coded symbol duration.

References

1. Armstrong J (2008) OFDM: from copper and wireless to optical. In: OFC/NFOEC 2008—2008 conference on optical fiber communication and fiber optics engineering conference. https://doi.org/10.1109/ofc.2008.4528364
2. Khare RP (2009) Fiber optics and optoelectronics, 8th edn. Oxford Press, New Delhi
3. Yong Soo Cho CGK, Kim J, Yang WY (2010) MIMO-OFDM wireless communications with MATLAB, Wiley-IEEE Press. http://as.wiley.com/WileyCDA/WileyTitle/productCd-0470825626.html
4. Armstrong J (2009) OFDM for optical communications. J Lightw Technol 27:189–204. https://doi.org/10.1109/JLT.2008.2010061
5. Giacoumidis E, Tang JM (n.d.) Improved transmission performance of adaptively modulated optical OFDM signals over MMFs using adaptive cyclic prefix, pp 6–7
6. Yan L, Hu G, Hou D, Mu L, Jiang S (2014) Adaptive unsaturated OFDM multimode fiber communication technique based on zero padding. Optik (Stuttg) 125:6496–6499. https://doi.org/10.1016/j.ijleo.2014.06.157
7. Jean Armstrong I, Senior Member, IEEE, Schmidt BJC, Student Member (2008) Comparison of asymmetrically clipped optical OFDM and DC-biased optical OFDM in AWGN. IEEE Commun Lett 12:374–376. https://doi.org/10.1109/lcomm.2008.072098

8. Mohamed SD, Shalaby HMH, Andonovic I, Aly MH (2016) Performance analysis of modified asymmetrically-clipped optical orthogonal frequency-division multiplexing systems. Opt Commun 380:61–68. https://doi.org/10.1016/j.optcom.2016.05.077
9. Djordjevic WSI (2009) OFDM for optical communications, Academic press. https://www.elsevier.com/books/ofdm-for-optical-communications/shieh/978-0-12-374879-9
10. Agrwal G (2007) Nonlinear fiber optics, Academic press

High Contrast Ratio Based All-Optical OR and NOR Plasmonic Logic Gate Operating at E Band

Mainka, Shivani Sharma, Rukhsar Zafar, Mohammad Hossein Mahdieh, Ghanshyam Singh and Mohammad Salim

Abstract In this paper, we have proposed an all-optical OR and NOR logic gates which is based on Plasmonics metal–insulator–metal (MIM)waveguide. MIM waveguide has the inherent feature to confine light far beyond diffraction limit. Therefore, the structure can be designed with miniaturized size. The performance of the device (gate) is measured by a quantifying parameter which is known as contrast ratio. The proposed NOR logic gate offers a contrast ratio of 12.36 dB for Boolean logic gates of output. The proposed structure opens a solution for future all-optical computing. The optical logic gates are investigated using finite-difference time-domain method.

Keywords Metal–insulator–metal waveguide · Finite-difference time-domain method · Contrast ratio · All-optical logic gates · Surface plasmon polaritons

1 Introduction

Nowadays, optical computing attracted the future optical communication system [1]; in order to build it all-optical flexible signal processing device is needed. Optical logical gates [2, 3] are considered as vital elements in the network as it can perform data encoding and decoding, switching operations, etc. Photonic logical gates are the promising implementation in the real-time optical processing and communica-

Mainka (✉) · S. Sharma · R. Zafar
Department of ECE, Swami Keshvanand Institute of Technology, Management and Gramothan, Jaipur 302017, India
e-mail: katewa.mainka33@gmail.com

M. H. Mahdieh
Department of Physics, Iran University of Science & Technology, 13114-16846 Tehran, Iran

G. Singh · M. Salim
Department of ECE, Malaviya National Institute of Technology Jaipur, Jaipur 302017, Rajasthan, India
e-mail: gsingh.ece@mnit.ac.in

© Springer Nature Singapore Pte Ltd. 2020

V. Janyani et al. (eds.), *Optical and Wireless Technologies*,
Lecture Notes in Electrical Engineering 546,
https://doi.org/10.1007/978-981-13-6159-3_35

tion systems. Different schemes are introduced to realize different all-optical logic gates such as semiconductor optical fibers (SOAs) [4], photonic crystals (PhCs) [5], etc. But, they suffer from various limitations such as large size, high power consumption, and low speed difficult to be implemented as large-scale chip integration. Photonic crystal waveguides (PCW) [6, 7] are one of the promising examples of PhCs applications at micron and submicron length scales.

Although it has so many advantages, it is limited by diffraction. The diffraction limit strongly restricts photonic and optical devices' development [8] and obstructs our ability to handle and operate light–matter interaction in sub-wavelength regime. One promising solution lies in the realm of surface plasmon polaritons (SPP) [9, 10] where electromagnetic (EM) wave can be routed along the metal–dielectric interface of nanostructure far beyond the diffraction limit [11, 12]. SPPs are the waves that are tightly bounded along the interface of two materials having dielectric constant of opposite sign. SPP can propagate along the interface between metal and dielectric medium as a surface EM wave with a nanoscale light confinement far below the diffraction limit of light [13]. As a result, plasmonics became a good candidate for future optical communication without compromising the size, power consumption, and cost of the subsystem. The MIM waveguide geometry has an intriguing feature of sub-wavelength confinement. Therefore, MIM-based SPPs devices support many applications in optical/biosensors [14], nanolasers [15] and photovoltaic cells [16], filters, and buffers [17].

The growing interest in optical logical gates has attracted the interest of researchers to explore its efficiency. Pan et al. have investigated Y-shaped all-optical XOR, OR, and NOT gate. Younis et al. have also reported the combination of the ring cavities and Y-shaped line defect coupler placed between two waveguides of all-optical AND gate and observed a contrast ratio of 6 dB. Rani et al. reported three input Y shaped of NAND gate in two-dimensional photonic crystal and using the combination of three universal optical logic NAND gates is investigated to XNOR gate and observed a contrast ratio of 6.50 dB. So, in this paper, we have used metal–insulator–metal (MIM) waveguide because of its inherent characteristics of sub-wavelength confinement. All the simulation results are examined of the finite-difference time-domain (FDTD) method [18]. The MIM waveguide geometry is best suited to confine optical signal beyond diffraction limit [19, 20]. A Gaussian-modulated continuous wave is being used which is transverse magnetic (TM) polarized. The proposed OR and NOR optical gates operate at E band. We reported that the contrast ratio is 12.36 dB. The device offers a simple and effective solution to realize this is an all-optical gate.

2 All-Optical Plasmonic OR Gate

(A) Waveguide Geometry

In this paper, we simulated and suggested design for OR and NOR logic gates based on plasmonics. In this proposed design, we use MIM waveguide where the insulating material is air which is sandwiched on the silver substrate. Silver is known as noble metal. The dielectric function of metal is characterized by Drude model [21]

$$\epsilon(\omega) = \epsilon_{\infty} - \omega_p^2/\left(\omega^2 + i\omega\gamma\right) \tag{1}$$

In simulation, the corresponding plasma frequency $\left(\omega_p\right)$ of silver is 1.38×10^{16} rad/s and collision frequency (γ) of silver is 2.73×10^{13} rad/s and permittivity at infinite frequency of silver (ε_{∞}) is 3.7. Width of all linear waveguides is taken as 50 nm. In this design, we used linear waveguide of length l which is 500 nm and vertical linear cavities are resonantly coupled of length L which is 1000 nm, and separation (w') of vertical cavities is 25 nm. Output is observed at observation point A (Figs. 1 and 2).

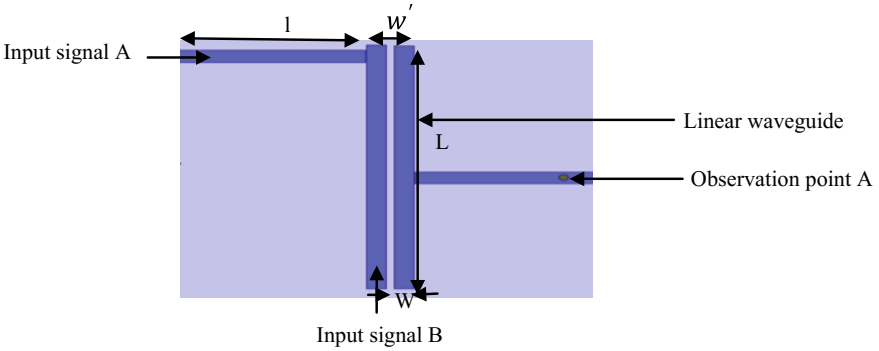

Fig. 1 Schematic of proposed OR gate with following parameters; w = 50 nm, l = 500 nm, w′ = 25 nm, and L = 1000 nm

Fig. 2 Magnetic field profile of two input signals at different conditions of OR gate **a** A = "Low" and B = "High" state. **b** A = "High" and B = "Low" state. **c** A = "High" and B = "High" states. **d** Normalized figure palette. In all the cases, output intensity is above the threshold boundary

Table 1 Truth table of OR gate

Input signal A	Input signal B	Logic output	Transmission efficiency
0	0	0	0
0	1	1	0.55
1	0	1	0.43
1	1	1	0.62

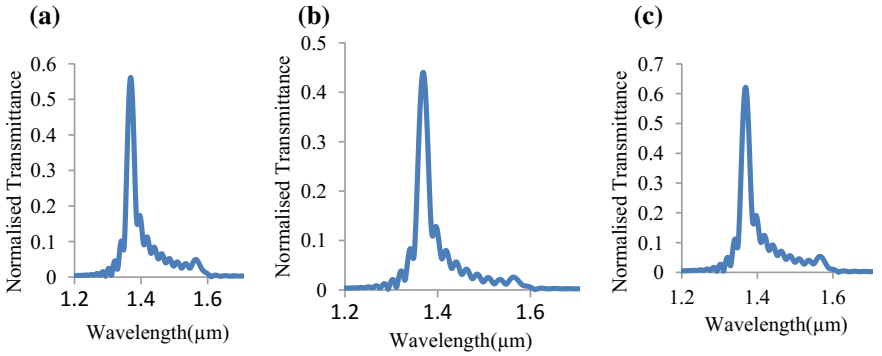

Fig. 3 Transmission spectrum of two input signals at different conditions of OR gate **a** A = "Low" and B = "High" state. **b** A = "High" and B = "Low" state. **c** A = "High" and B = "High" states

(B) Result Analysis of OR Gate

The input power at port A and B are set to be equal. The input "High" and "Low" states correspond to "1" and "0", respectively. The output of Boolean value is calculated by the threshold value. Two signals are transmitted from the input ports to the junction and the output is measured at the observation point. If output amplitude is greater than threshold value then the output value is "1". If output amplitude is less than threshold value then the output value is "0". The logical operation of OR gate is illustrated in Table 1 and outputs for different input conditions are shown in Fig. 3.

3 All-Optical Plasmonic NOR Gate

(A) Waveguide Geometry

In this design, we composed that the combination of OR and NOT gate is NOR logic gate. The parameters of the NOR gate is similar to previously defined OR gate. NOT gate is described with the one linear cavities which is used to control signal and vertical linear cavities which is used to create interference. Separation of two vertical cavities is 25 nm. Width of all linear waveguides is taken as 50 nm (Figs. 4 and 5).

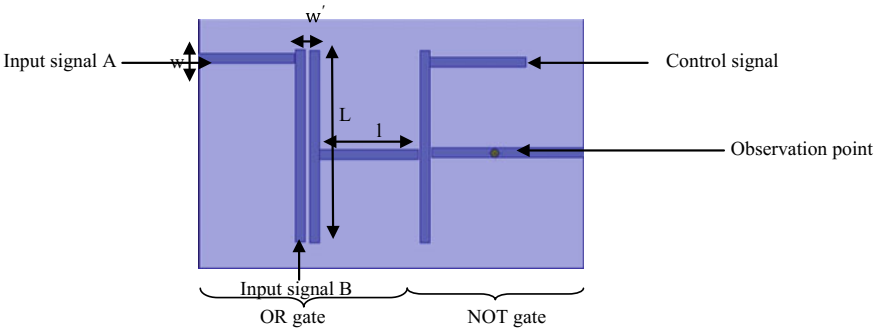

Fig. 4 Schematic of proposed NOR gate with following parameters; w = 50 nm, l = 514 nm, w′ = 25 nm, and L = 1000 nm

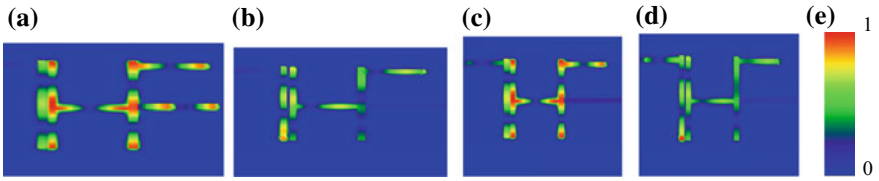

Fig. 5 Magnetic field profile of two input signals at different conditions of NOR gate **a** A = "Low" and B = "Low" state. **b** A = "Low" and B = "High" state. **c** A = "High" and B = "Low" state. **d** A = "High" and B = "High" states. **e** Normalized figure palette

(B) Result Analysis of NOR Gate

The NOR logic gate is proposed by one OR gate and NOT gate. NOT gate is as controlled by control signal. The input power at port A, B, and C is selected to be equal. The inputs "High" and "Low" states correspond to "1" and "0", respectively. The output of the Boolean value is calculated by the threshold value. If output of OR gate is "1" and control signal C is "1", then we get output signal of NOR gate as "0" because of destructive interference. If output of OR gate is "0" and control signal C is "1", then we get output signal of NOR gate as "1". Two signals and one control signal are transmitted from the input ports to the junction and the output is measured at the observation point. In this device, the threshold amplitude value is 0.30. If output amplitude is greater than threshold value, then the output value is "1". If output amplitude is less than threshold value, then the output value is "0". The logic operations of NOR gate are illustrated in Table 2 and Fig. 6. Now, contrast ratio can be defined as

$$\text{Contrast Ratio (C.R)} = 10\log_{10}(P_H/P_L),$$

where

P_H Optical power level is HIGH = 0.69,

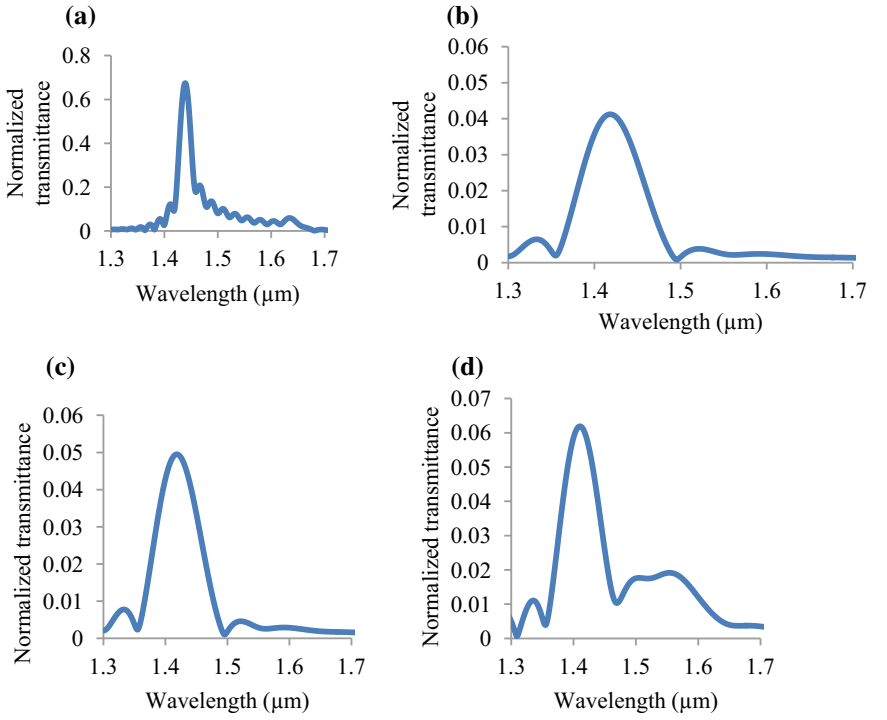

Fig. 6 Transmission spectrum of two input signals at different conditions of NOR gate **a** A = "Low" and "Low" state. **b** A = "Low" and B = "High" state. **c** A = "High" and B = "Low" state. **d** A = "High" and B = "High" states

Table 2 Truth table of NOR gate

Input signal A	Input signal B	Logic output	Transmission efficiency
0	0	1	0.69
0	1	0	0.04
1	0	0	0.05
1	1	0	0.06

P_L Optical power level is LOW = 0.04.

Now, contrast ratio for NOR gate = 12.36 dB.

So, C.R is about 12.36 dB for NOR optical logic gate.

The metals are assumed to suffer from large amount of losses. Silver is selected in this paper as it has large optical gain but still propagation losses increase with increasing propagation distance. The noble metals may be replaced by transparent conducting oxides as it offers a comparable performance as metals.

4 Conclusion

In this paper, we have designed the optical logic gates (OR and NOR) operating at 1.4 μm. The waveguide is designed using plasmonics MIM waveguide which is base for sub-wavelength confinement. The geometry is simulated using FDTD method and its performance is measured using contrast ratio. The device offers a large value of contrast ratio (24.76 dB). Therefore, the proposed optical logic gates are very useful to apply on ultrafast optical logic operations and future optical computing components because of its high speed and high contrast ratio for the output states "1" and "0".

References

1. Caulfield HJ, Dolev S (2010) Why future supercomputing requires optics. Nat Photon 4(5):261–263
2. Younis RM, Areed NFF, Obayya SSA, Senior Member (2014) IEEE Fully integrated AND and OR Optical Logic Gates. IEEE Photon Technol Lett 26(19):1900–1903
3. Li Z, Chen Z, Li B (2005) Optical pulse controlled all-optical logic gates in Sige/Si multimode interference. Opt Exp 13(3):1033–1038
4. Stubkjaer KE (2000) Semiconductor optical amplifier-based all-optical gates for high-speed optical processing. IEEE J Sel Topics Quantum Electron 6(6):1428–1435
5. Liu C-Y, Chen L-W (2005) The analysis of interaction region of elliptical pillars of a directional photonic crystal waveguide coupler. Phys E Low Dim Syst Nanostruct 28(2):185–190
6. Rani P, Kalra Y, Sinha RK (2013) Realization of AND gate in Y shaped photonic crystal waveguide. Opt Commun 298(2):227–231
7. Rashki Z, Mansouri MA, Rakhshani MR (2013) New design of optical add-drop filter based on triangular lattice photonic crystal ring resonator. Int Res J Appl Basic Sci 4(4):985–989
8. Dash S, Tripathy SK (2012) Y-shaped design in two dimensional photonic crystal structure for applications in integrated photonic circuits. J Lightw Electron Opt 124(18):3649–3650
9. Ditlbacher H, Krenn J, Schider G, Leitner A, Ausenegg F (2002) Two-dimensional optics with surface plasmon polarition. Appl Phys Lett 81(10):1762–1764
10. Yarahmadi M, Moravvej-Farshi MK, Yousefi L (IEEE members) (2015) Subwavelength graphene-based plasmonic the switches and logic gates. IEEE Trans Terahertz Sci Technol 5(5):725–731
11. Fu Y, Hu X, Lu C, Yue S, Yang H, Gong Q (2012) All-optical logic gates based on nanoscale plasmonic slot waveguides. Nano Lett 12(11):5784–5790
12. Ekmel O (2006) Plasmonics: merging photonics and electronics at nanoscale dimensions. Science 311(5758):189–193
13. Veronis G, Fan S (2005) Bends and splitters in metal-dielectirc-metal subwavelength plasmonic waveguides. Appl Phys Lett 87(13):131102
14. Sriniwas Rao K, Dattathreya, Tiwari AK (2016) Detection of cancer cell with light wave propagation in optical bio-sensors. In: IEEE conference on recent advances in lightwave technology (CRALT), vol 89, no 2, pp 1–4
15. Sattar ZA, Alan Shore K (2015) Optical feedback effects on the dynamics of semiconductor nano-lasers. In: 11th conference on lasers and electro-optics pacific rim (CLEO-PR), vol 6, no 1, pp 97
16. Ravl DV, Munjani PJ, Mansoori NR (2016) Reference based maximum power point tracking algorithm for photo-voltaic power generation. In: International conference on electric power and energy systems (ICEPES), vol 67, no 5, pp 438–443

17. Zafar Rukhsar, Salim Mohammad (2015) Achievement of large normalized delay bandwidth product by exciting electromagnetic-induced transparency in plasmonic waveguide. IEEE J Quantum Electron 51(10):1–6
18. Lee KW, Fabian, Chuah H-T (2005) A finite-difference time-domain (FDTD) software for simulation of printed circuit board (PCB) assembly. Progr Electromag Res 50(3):299–335
19. Lembrikov BI, Lanetz D, Ben-Ezra Y (2017) Metal-insulator-metal (MIM) plasmonic waveguide containing a smectic liquid crystal (SALC) layer. In: 19th international conference on transparent optical networks (ICTON), vol 23, no 4, pp 1–4
20. Abadi SM, Ram SB (2015) A dual band-pass plasmonic filter based on stub structureaIn A MIM waveguide at optical channels. Photon North IEEE Conf Publ 45(3):1–1
21. Zafar Rukhsar, Salim Mohammad (2015) Enhanced figure of merit in fano resonance-based plasmonic refractive index sensor. IEEE Sens J 15(11):6313–6317

Defected Ground Structure Microstrip Antenna for WiMAX

Ajay Thatere and Prasanna L. Zade

Abstract This paper proposed the microstrip antenna which enhances the bandwidth with the use of defected ground structure (DGS). The study and implementation of proposed antenna are discussed in this paper. With the use of DGS, the bandwidth is increased efficiently to 35.87% as compared to the normal rectangular patch antenna. The proposed antenna is designed for Wi-Fi/WiMAX application at the resonant frequency of 5.5 GHz. The I-shaped defected ground structure (DGS) antenna improves bandwidth of antenna. The simulated and fabricated antenna results are compared.

Keywords Microstrips patch antenna · Simulation software · VNA · Defected ground structure (DGS) · FR4 substrate · Bandwidth enhancement

1 Introduction

Nowadays, microstrip patch antenna is used in much type of applications and achieves great advancement in recent years. Microstrip patch antenna is so much used antenna because of its reliable characteristics and properties which are like light in weight, having low cost, conformable to planer and non-planer surfaces, simple to manufacture and can be integrated with circuit and simple arrays. It is used in application such as high-performance aircrafts, spacecrafts, and wireless communication system. Possessing such good characteristics microstrip patch antennas still suffered from high surface wave, narrow bandwidth, and low gain.

A. Thatere (✉)
Yeshwantrao Chavan College of Engineering, Nagpur, India
e-mail: ajay.thatere@yahoo.co.in

P. L. Zade
Datta Meghe Institute of Engineering Technology and Research, Wardha, India
e-mail: zadepl@yahoo.com

© Springer Nature Singapore Pte Ltd. 2020

V. Janyani et al. (eds.), *Optical and Wireless Technologies*,
Lecture Notes in Electrical Engineering 546,
https://doi.org/10.1007/978-981-13-6159-3_36

2 Defected Ground Structure (DGS)

A defected ground structure (DGS) is an etched lattice shape that is located on the ground plane. DGS can be done by making defect on the backside of the metallic ground plane. The name given to this technique is because we make a defect on the ground plane which is typically considered to be an approximation of an infinite, perfectly conducting current sink. Defected ground structure is developing to improve the characteristics of many microwave devices. This theory develops us to enhance the bandwidth with the use of defected ground structure to improve the antenna characteristics in application like Wi-Fi/WiMax, Bluetooth, and many more. There are several approaches that can be used to achieve better improvement in bandwidth. The enhancements of bandwidth with the previous approaches are discussed in this section. The primary approach towards the improvement of bandwidth through the I-Shaped antenna with the help of defected ground structure (DGS) which exhibits an enhancement of 118% bandwidth. The antenna was designed for S-band application at the frequency of 2.5–4.5 GHz which improves the gain and return loss of the antenna [1]. In [2], comparison of different shaped microstrip patch antenna was discussed with the use of metamaterial. The proposed work compares the frequency of different shaped antennas along with the DGS which can be used for Wi-fi and Bluetooth application. In [4], proposed work entitles the enhancement of efficiency of microstrip patch antenna and improvement of characteristics with defected ground structure. It effectively increases the efficiency of the antenna. There are various approaches to increase the Bandwidth of microstrip patch antenna including single slot patch structure, rectangular structure, and eight-shaped slot along with microstrip line [5–7]. The DGS is stretched with cyclic or non-cyclic cascaded configuration defects on the ground of a planar transmission line that disturbs the shield current allocation. This disturbance will modify the characteristics of the capacitance and inductance. It suggests that any defect on the ground plane increases the effective capacitance and inductance on the whole electrical circuits [13]. In [8–12], the paper reports to the improvement of bandwidth, antenna gain, and the area of radiating patch using metamaterial. This method introduced I-shaped metamaterial DGS antenna which enhances the bandwidth. A combination of the rectangular patch antenna and the I-shaped DGS exhibits negative permittivity, , and permeability, μ, in the targeted frequency ranges which exhibits metamaterial or left-handed material (LHM) yields the negative refractive index. DGS has various shaped slots like E-shaped slots, U-shaped slot, L-shaped slot, I-shaped slot, etc. which helps to improve the resonant bandwidth (Fig. 1).

3 Proposed Work

This paper proposed microstrip patch antenna with the use of defected ground structure which effectively increases the bandwidth and reduces the return loss. The

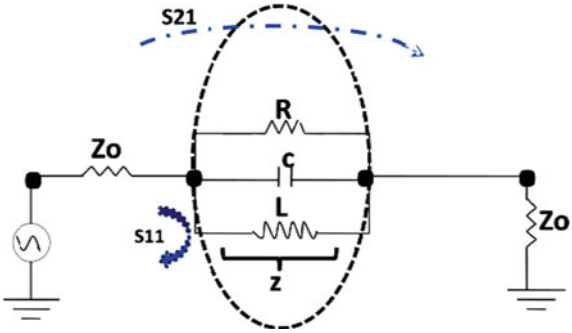

Fig. 1 Equivalent circuit of DGS

antenna design and the detailed specification are discussed in Section A and Section B, respectively.

A. **Antenna Design**

The proposed antenna, which is designed having fundamental structure, is shown in Fig. 2. In the most basic form, microstrip patch consist of radiating patch is on one side of the dielectric substrate and has a ground plane on other side.

The substrate is made up of FR4 material. The dielectric constant of FR4 is 4.4 and height is of 1.5 mm. Dielectric substrate has microstrip patch on the upper surface which is in rectangular shape. The patch has length of 11.65 mm and the width of 18.25 mm which occupies the median of the substrate. Ground is situated at the lower side of substrate which possesses ground plane. It covers the substrate which is formed in rectangular shape having the dimension of 22 × 28 mm. The patch is added by feed line and should be impedance matched at the resonance and can sustain with 50w impedance. Using the simulation software, the design is developed. The result is taken for the frequency between 5 and 6 GHz. For this, all the adjustments are done on the patch. The adjustment is done so that the operating frequency is at 5.5 GHz. After that defect is given to the ground so that the cutoff frequency becomes constant at the 5.5 GHz. The I-shaped defect is given to the ground so that the characteristics of the proposed antenna get improved. The dimension of each parameter of the DGS

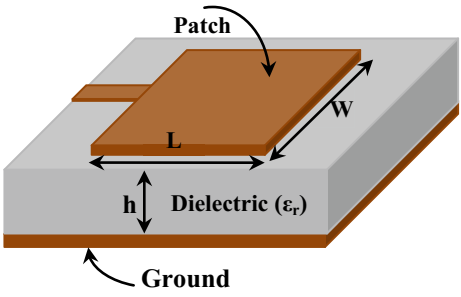

Fig. 2 Geometric of microstrip patch antenna

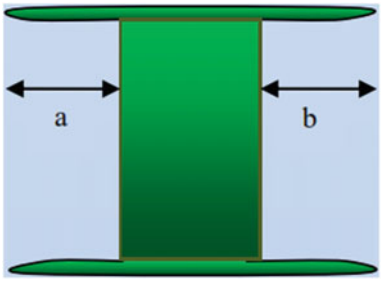

Fig. 3 I-shaped defected ground structure

Table 1 Dimension of DGS design structure

Parameters	Dimension (mm)
a	7
b	6.5

structure is shown in Fig. 3. The cuts in the ground plane are "a" and "b" having 7 mm and 6.5 mm in dimensions, respectively, (Table 1).

B. **Mathematical Analysis**

Step 1: Width calculation (W)
The width of proposed patch is calculated as

$$W = \frac{C}{2f_0\sqrt{\frac{\varepsilon_r+1}{2}}},$$

where c is speed of the light, f_0 is resonant frequency, ε_r is the dielectric constant obviously different width might be picked, however, for width littler than those chose conquering width equations radiator productivity is lower for the bigger widths. The productivity is more prominent for higher modes, bringing on field contortion. By substituting the values of $C = 3.0 \times 10^{11}$ mm/s, $\varepsilon_r = 4.4$ and $f_0 = 5.5$ GHz, we get: $W = 18.257$ mm.
Step 2: Length calculation (L)

- Effective dielectric constant (ε_{eff})

The method for the length calculation includes different steps. As we know the width, we have to first calculate powerful dielectric constant. The substrate is much more prominent than solidarity. The powerful dielectric constant is additionally a component recurrence. The dielectric constant of substrate is given by

$$\varepsilon_{eff} = \frac{\varepsilon_r + 1}{2} + \frac{\varepsilon_r - 1}{2}\left[\left(1 + \frac{12h}{W}\right)^{\frac{-1}{2}}\right].$$

The dielectric constant of the given proposed antenna is observed to be 3.88.

- Effective length (Leff)

The effective length observed is as

$$L_{eff} = \frac{C}{2f_0\sqrt{\varepsilon_{eff}}}.$$

The effective length (L_{eff}) = 15.217 mm.

- Length extension (ΔL)

For the standard E-plane where the measurement of the way along its length have stretched out each by a separation of ΔL which is an element of the successful dielectric constant and width to the height proportion (W/h). The length extension is

$$\Delta L = 0.412h\frac{\left(\varepsilon_{eff}+0.3\right)}{\left(\varepsilon_{eff}-0.258\right)}\left[\frac{\frac{W}{h}+0.264}{\frac{W}{h}+0.8}\right].$$

Substituting $_{eff}$ = 4.4, W = 18.257 mm, and h = 1.5 mm, we get ΔL = 0.7273 mm.

- Calculation of actual length (L)

The length is a basic parameter. All the values which are calculated are used to find out the actual length of the patch. The length is given by

$$L_{eff} = L + 2\Delta_L.$$

Substituting L_{eff} = 15.217 mm and ΔL = 0.7273 mm, we get the L = 13.7624 mm.

4 Designing of Patch

The proposed antenna having rectangular patch incorporated with the I-shaped DGS is designed. It has the cutoff frequency of 5.5 GHz. The design is made using simulation software. The design of patch is shown in Fig. 4. The simulation software design having patch is fabricated as hardware design shown in Fig. 5. After that the I-shaped DGS is designed in the software. This is shown in Fig. 6. The design is then converted to the hardware and gets fabricated as shown in Fig. 7.

Figures 4 and 5 show software simulated and fabricated rectangular patch antenna without DGS.

Figures 6 and 7 show software simulated and fabricated rectangular patch antenna with DGS.

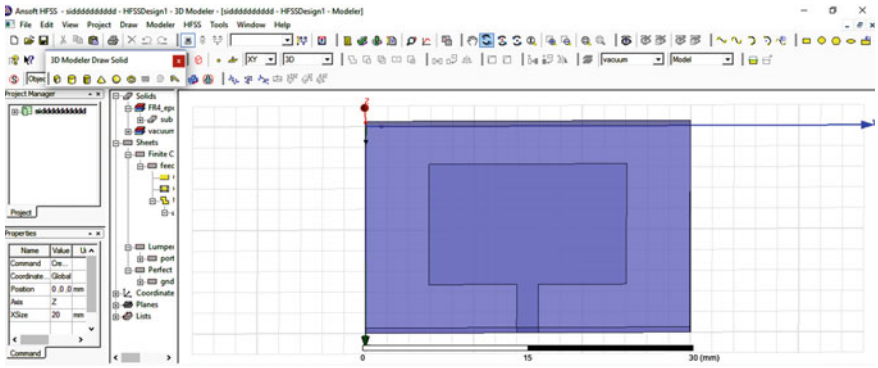

Fig. 4 Designing of patch with software

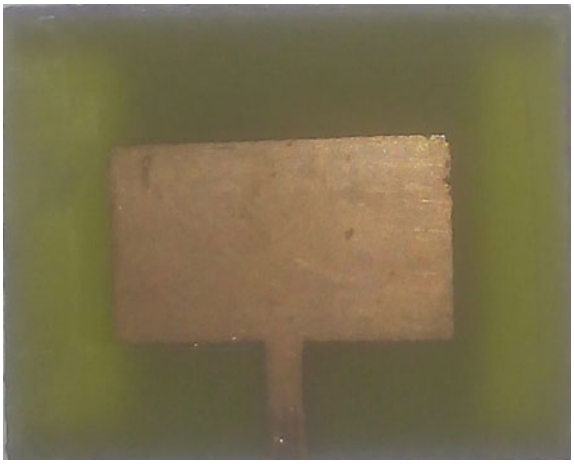

Fig. 5 Fabrication of rectangular patch antenna

5 Results

The design of antenna was simulated by software and the fabricated hardware is tested using vector network analyzer device (VNA) having cutoff frequency of 5.5 GHz. The simulated result shows the return loss of −23.7078 dB without DGS and return loss of −19.6768 dB with DGS shown in Figs. 8 and 9, respectively. The simulated result of VSWR without DGS is 1.1396 and VSWR with DGS is 1.231 which is shown in Figs. 10 and 11, respectively. The Smith chart showing the results with DGS and without DGS is given in Figs. 12 and 13, respectively. The bandwidth of the antenna is enhanced by 35.87% to that of antenna without DGS, and we get increment in the bandwidth. The hardware which is fabricated is tested under VNA

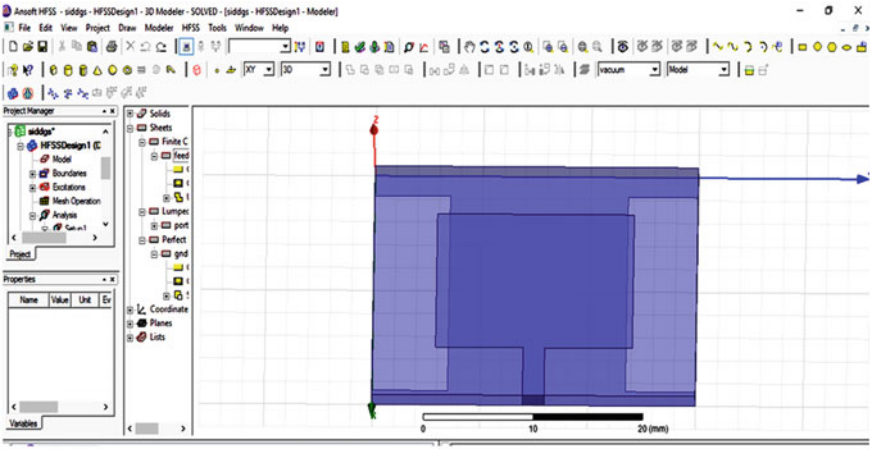

Fig. 6 Antenna having DGS with software

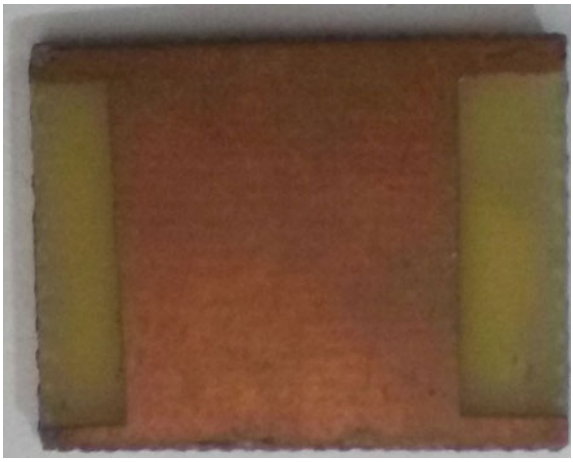

Fig. 7 Fabrication of rectangular patch antenna with DGS

device. The results of VNA for the various parameters with DGS and without DGS are shown in figures.

The simulated result shows the return loss of −23.707 dB without DGS and return loss of −19.6768 dB with DGS at resonance frequency as shown in Figs. 8 and 9, respectively.

The simulated result of VSWR without DGS is 1.1396 and VSWR with DGS is 1.231 at resonance frequency as shown in Figs. 10 and 11, respectively.

The simulated result of impedance without DGS and with DGS at resonance frequency is as shown in Figs. 12 and 13, respectively.

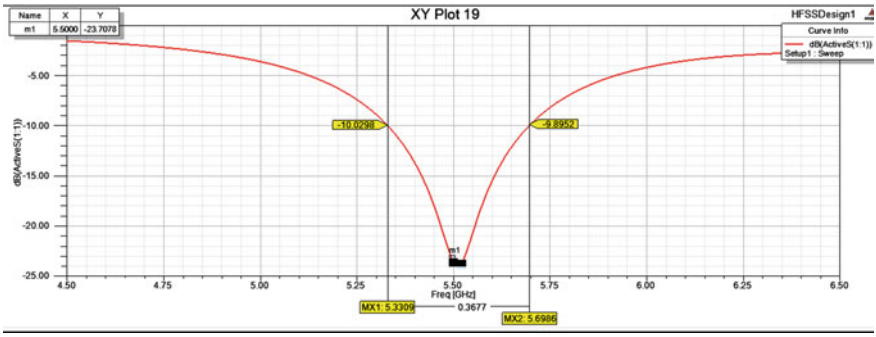

Fig. 8 Simulation result of return loss without DGS

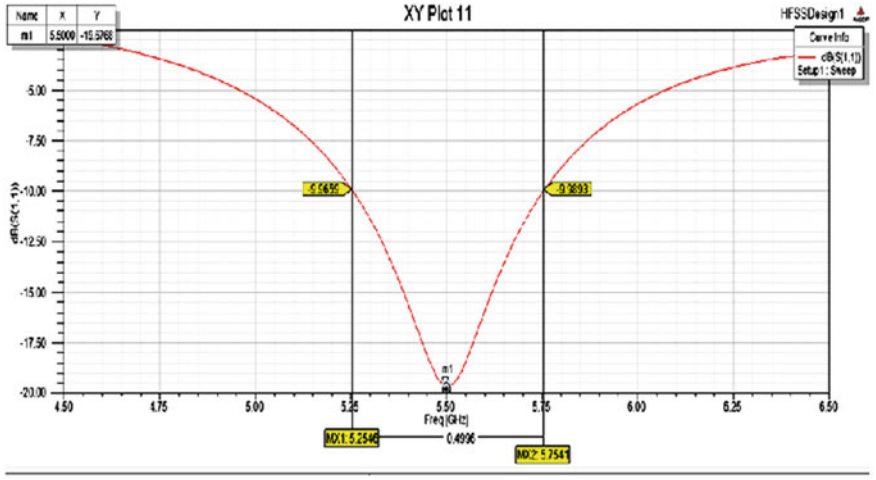

Fig. 9 Simulation result of return loss with DGS

The measured result shows the return loss of −21.80 dB at 5.516 GHz without DGS and return loss of −24.63 dB at 5.527 GHz with DGS as shown in Figs. 14 and 15, respectively.

The simulated result of impedance without DGS and with DGS at resonance frequency is as shown in Figs. 16 and 17, respectively.

The measured result of VSWR without DGS and with DGS is very closer to 1.0 as shown in Figs. 18 and 19, respectively.

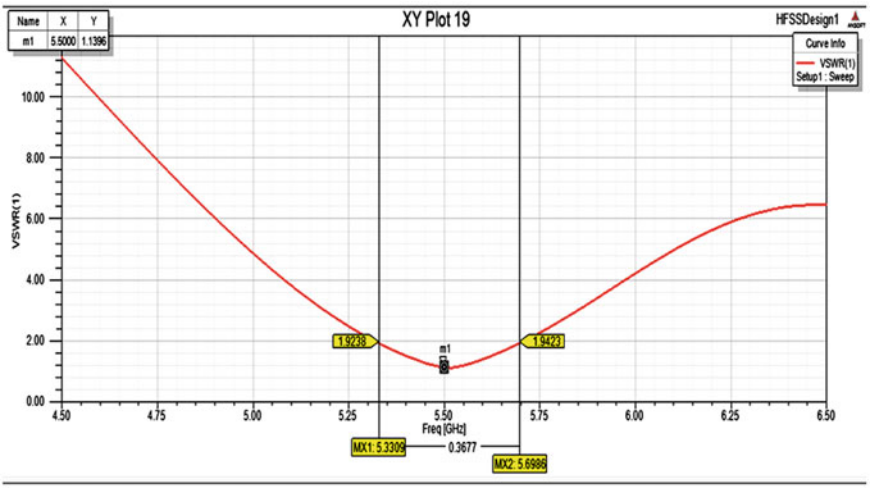

Fig. 10 Simulation result of VSWR without DGS

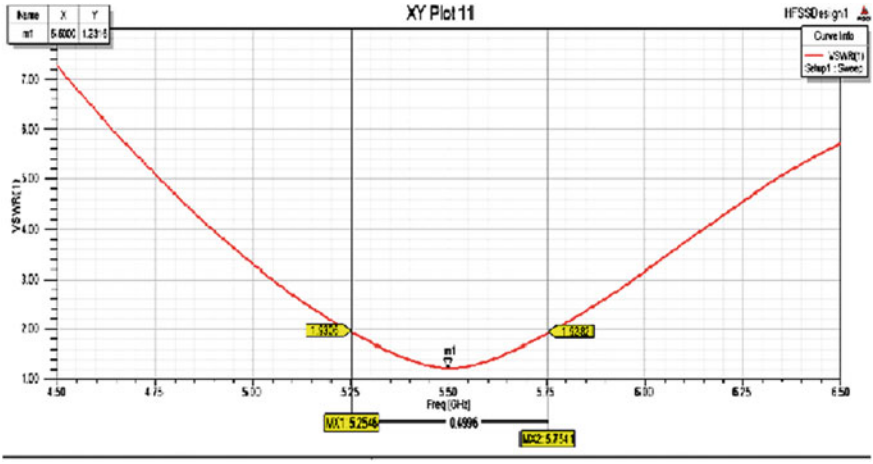

Fig. 11 Simulation result of VSWR with DGS

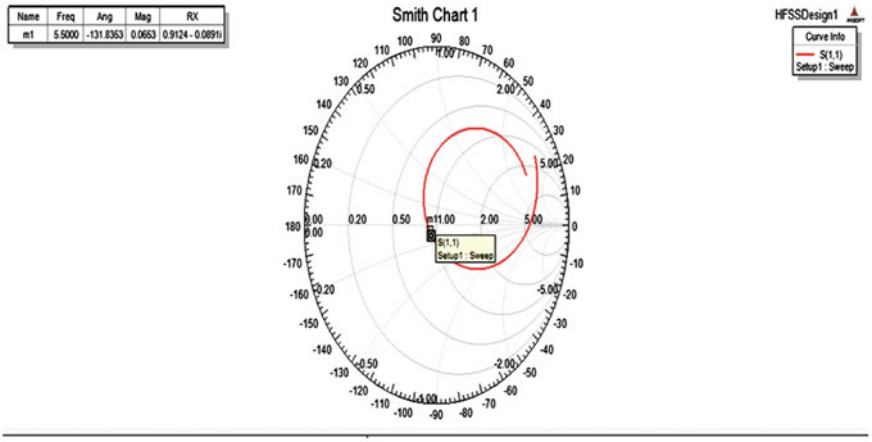

Fig. 12 Simulation result of Smith chart without DGS

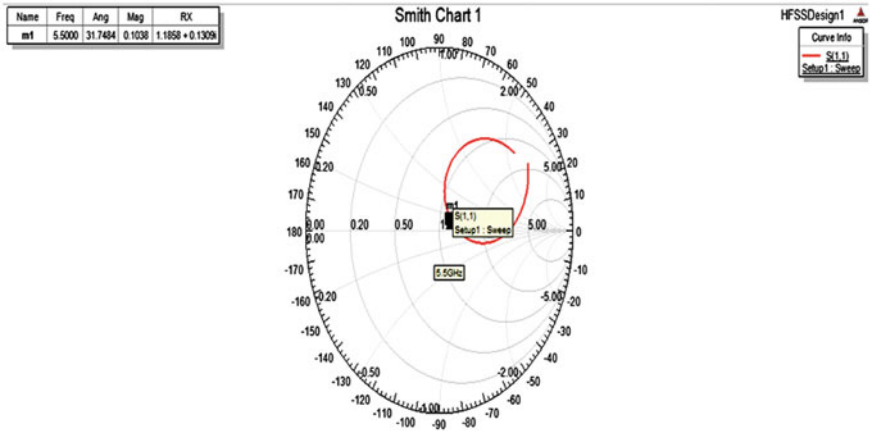

Fig. 13 Simulation result of Smith chart with DGS

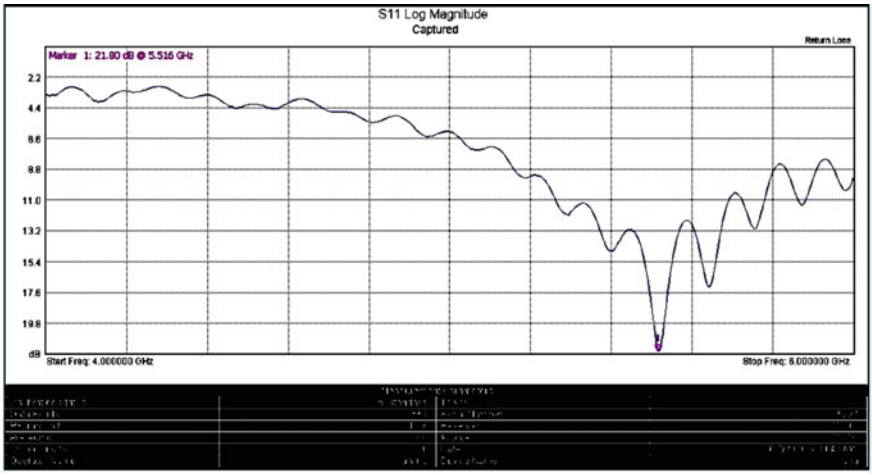

Fig. 14 VNA result of return loss without DGS

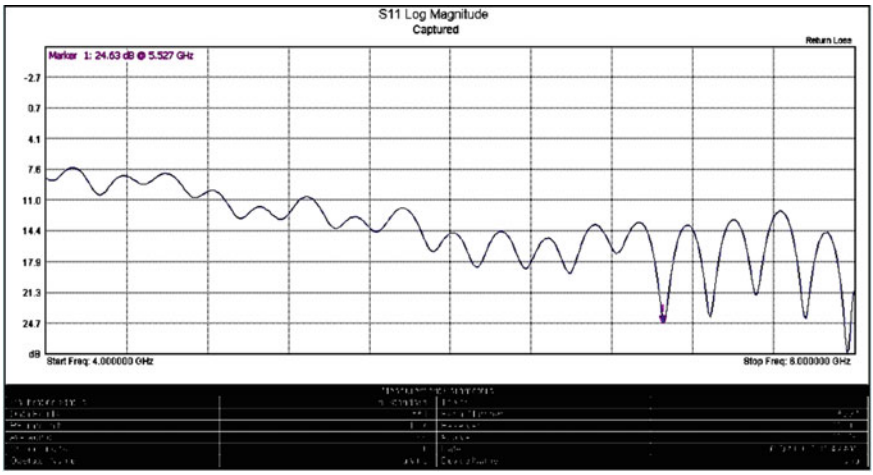

Fig. 15 VNA result of return loss with DGS

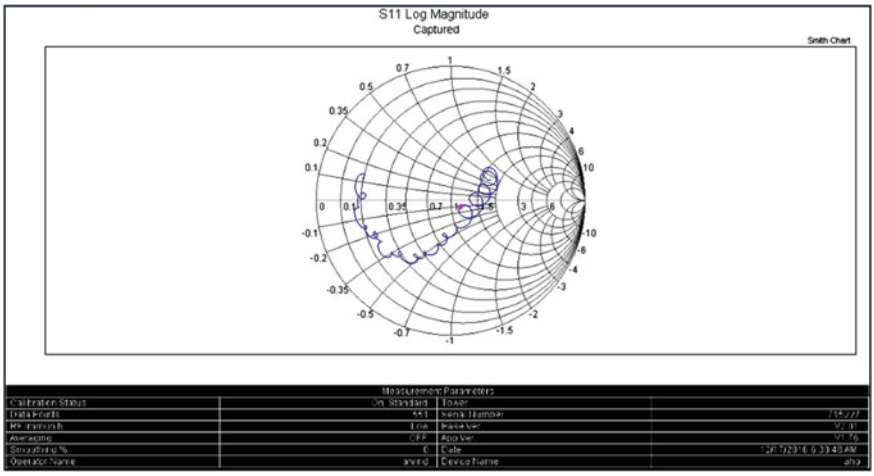

Fig. 16 VNA result of Smith chart without DGS

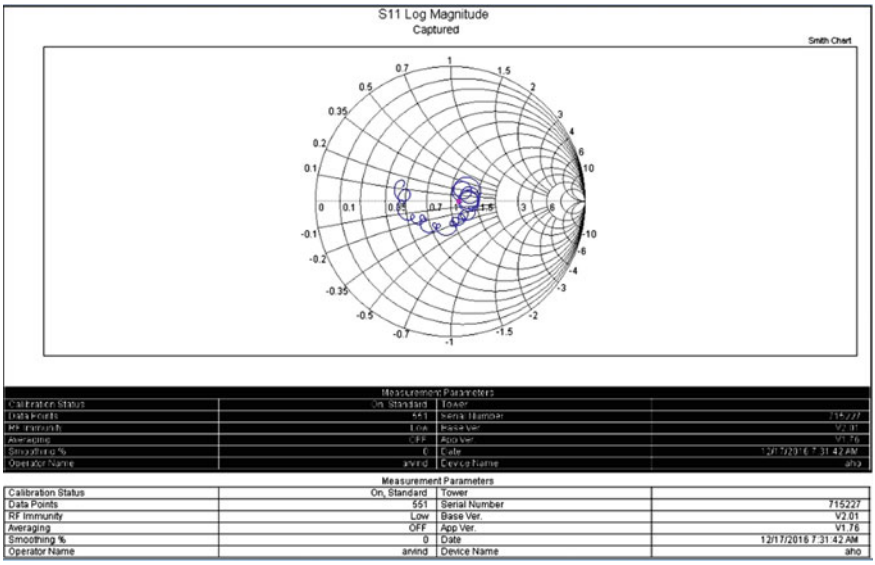

Fig. 17 VNA result of Smith chart with DGS

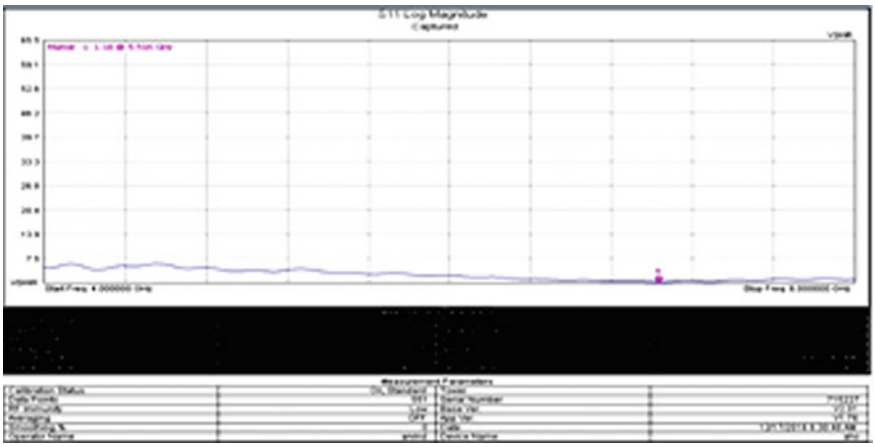

Fig. 18 VNA result of VSWR without DGS

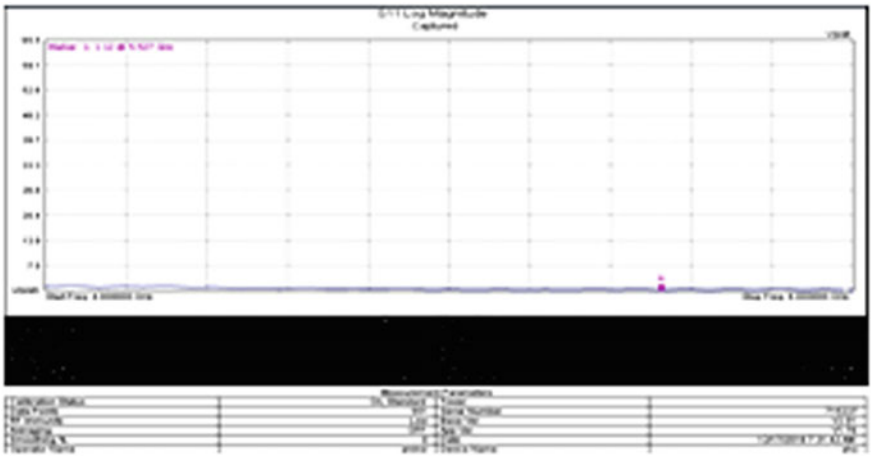

Fig. 19 VNA result of VSWR with DGS

6 Conclusion

This paper results in the enhancement of the bandwidth. The rectangular patch with DGS shows the improvement in the bandwidth than that of without DGS in both simulation and VNA result. The resulted frequency has good return loss and can be used for Wi-Fi and WiMax.

References

1. Ripin N, Yusoff SNC, Sulaiman AA, Rashid NEA, Hussin MF (2013) Enhancement of bandwidth through I-shaped defected ground structure. In: 2013 IEEE international RF and microwave conference (RFM), pp 477–481. IEEE
2. Prio MH, Rashid MMU, Paul LC, Sarkar AK (2015) Total efficiency comparison of different shaped microstrip patch antennas having defected ground structure. In: 2015 international conference on electrical & electronic engineering (ICEEE), pp 265–268. IEEE
3. Pathak N, Chandrasekaran N (2015) Multi-band antenna using defective ground structure. In: 2015 international conference on communications and signal processing (ICCSP), pp 1152–1155. IEEE
4. Arya AK, Kartikeyan MV, Patnaik A (2008) Efficiency enhancement of microstrip patch antenna with defected ground structure. In: International conference on recent advances in microwave theory and applications, 2008. Microwave 2008, pp 729–731. IEEE
5. Rathore RS, Baudha S, Pandey S A 2.4 GHz microstrip patch antenna with a single slot for WLAN application. Int J Adv Res Comput Eng Technol 1(4):139–141 (2012)
6. Gupta A, Sharma A (2013) Design of probe feed multi slotted 8-shaped microstrip patch antenna. Int J Adv Res Electron Commun Eng (IJARECE) 2(2):168–171
7. Tiwari R (2013) Design and simulation of rectangular microstrip patch antenna for wireless communication. J Res Electrical Electron Eng (ISTP-JREEE) 2(1):18–22
8. Ziolkowski RW (2011) Passive and active metamaterial constructs and their impact on electrically small radiating and scattering systems. In: General assembly and scientific symposium, 2011 XXXth URSI, pp 1–4. IEEE
9. Breed Gary (2008) An introduction to defected ground structures in microstrip circuits. High Freq Electron 7:50–54
10. Biswas Sujoy, Guha Debatosh (2013) Isolated open-ring defected ground structure to reduce mutual coupling between circular microstrips: characterization and experimental verification. Progr Electromag Res M 29:109–119
11. Majid HA, Rahim MKA, Masri T (2008) Left handed metamaterial design for microstrip antenna application. In: IEEE international RF and microwave conference, 2008. RFM 2008, pp. 218–221. IEEE
12. Balanis CA Antenna theory, analysis and design, 2nd edn. Wiley Inc
13. Saini R, Prakash D (2013) CPW fed rectangular shape microstrip patch antenna with DGS forWLAN/WiMAX application. Int J Adv Res Comput Sci 4(11)

Fractal MIMO Antenna for Wireless Application

Sachin S. Khade and Pallavi D. Bire

Abstract A compact two-element fractal MIMO antenna with dimension of 20 × 32 mm^2 is proposed. A T-shaped reflecting stub is placed between two antenna elements to reduce mutual coupling, and hence to improve isolation. The ring resonator is used on backside antenna which increased the number of resonances. The reflection coefficient of antenna is found to be below −10 dB at 2.4 and 3.5–7.1 GHz. The mutual coupling between antenna element is found less than −10 dB. The performance of antenna is evaluated in terms of mutual coupling, radiation pattern, peak gain, directivity, and VSWR. The maximum combined gain of antenna is found to be 3.01 dB.

Keywords Multiple-input multiple-outputs (MIMO) · Gain · Fractal monopole · Wireless local area network (WLAN) · Mutual coupling · S-parameter

1 Introduction

The rapid evolution of wireless communication technology has enabled the electronic industries to regularly upgrade their products to meet the unabated demand. However, the existing multipath propagation problem has reduced the communication data rate and weakened the signal reception for many mobile devices which operate in urban and suburban environments [1]. Recently, MIMO is a new technology used in multiple transmit and multiple receive antennas for a single user. It provides higher data rates, improved reliability, and coverage [2]. The MIMO antenna system also improves the communication quality and increases the system capacity. MIMO wireless technology is able to enhance the capacity of a given channel and reduces interference. MIMO technologies are widely used to overcome the effects of multi-

S. S. Khade (✉) · P. D. Bire
Yeshwantrao Chavan College of Engineering, Nagpur, India
e-mail: sac_mob@rediffmail.com

P. D. Bire
e-mail: pallavibire17@gmail.com

© Springer Nature Singapore Pte Ltd. 2020

V. Janyani et al. (eds.), *Optical and Wireless Technologies*,
Lecture Notes in Electrical Engineering 546,
https://doi.org/10.1007/978-981-13-6159-3_37

path fading. MIMO is used in wireless communication standard like IEEE802.11n (Wi-Fi), IEEE802.11ac (Wi-Fi), WLAN, WiMAX, and long-term evolution (4G).

In the present work, a MIMO fractal monopole antenna is used as the radiating element. A fractal antenna is used a self-similar design to increase the perimeter or, maximize the length, of material that can receive or transmit electromagnetic radiation within a given total surface area. Fractal is self-loading so no antenna parts, such as inductor and capacitors, are needed to resonant it [3].

In addition, they often do not require any matching circuitry for their multiband or broadband capabilities. However, MIMO antenna integrated in space-limited device, such as mobile terminal and wireless router. Therefore, there is challenge in term of antenna size and mutual coupling between adjacent radiating elements that affect the overall diversity performance of the MIMO system. Limited distance between antenna elements will lead to strong mutual coupling, which results in critical degradation to antenna radiation characteristics. Therefore, disposing of the problem of mutual coupling is still a hot issue in MIMO systems [4–6].

Recently, several techniques have been studied and used to reduce the mutual coupling of MIMO antennas. In, a T-shaped reflecting stub is placed between two antenna elements to improve the isolation and to improve the impedance matching [7]. The ring resonator increased the number of resonances which makes antenna multiband.

2 Antenna Design

Figures 1 and 2 show the geometry of the proposed MIMO antenna system, with two identical and symmetrical antenna elements. These elements are etched on one side of an FR-4 substrate having size of 20 mm × 32 mm × 1.6 mm. The geometry of radiator is of fractal shaped which effectively utilize the surface area, and thus to reduce the size of the antenna. The radiator is fed by 50 Ω microstrip-fed line. A

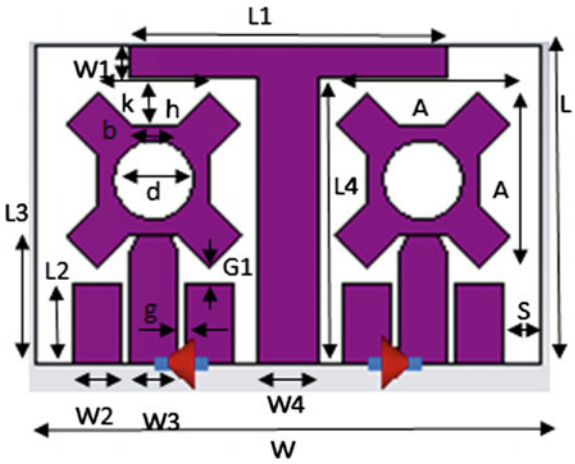

Fig. 1 Front view of proposed antenna

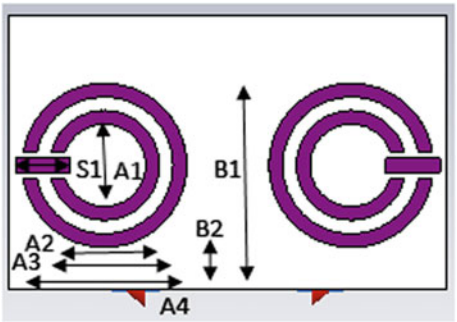

Fig. 2 Back view of proposed antenna

Table 1 Dimensions of the proposed antenna, in mm

L	*L1*	*L2*	*L3*	*W*
20	20	5	8	32
W1	*W2*	*W3*	*W4*	*A*
2	3	3	4	11
S	*G1*	*g*	*k*	*h*
2.5	1	0.5	6	2
b	*d*	*L4*	*A1*	*A2*
3	5	18	6	8
A3	*A4*	*B1*	*B2*	*S1*
10	12	15	3	4

T-shaped reflecting stub is placed in between the two antenna elements for improving the isolation. The T-shaped reflecting stub consists of two parts—a vertical stub and a horizontal stub. The vertical stub having dimension of $L_4 \times W_4$ and horizontal stub having the dimension of $L_1 \times W_1$. Through simulation, it is observed that the horizontal stub affects isolation, and the vertical stub affects matching. These two effects have been combined to produce an optimum result. The ring resonator is used to increase the number of resonance which makes antenna multiband. Table 1 gives the dimensions of various parameters of proposed antenna.

3 Result and Discussion

The proposed MIMO antenna operates in two bands of frequency ranges 2.44–2.49 GHz with resonance frequencies of 2.47 GHz and 3.5–7.2 GHz with resonance frequencies of 3.87, 5.09 GHz. Figure 3 shows the simulated S-parameter of fractal MIMO antenna system. Due to symmetrical nature of structure, S_{22} and S_{12} are same as S_{11} and S_{21}. From the figures, it is observed that the MIMO antenna system has $S_{11} < -10$ dB at 2.4, 3.7, 4.9, 5.15, 5.725, 5.825, and 5.875 GHz. A good isolation is observed within the operating bandwidth due to the introduction of the reflecting stub.

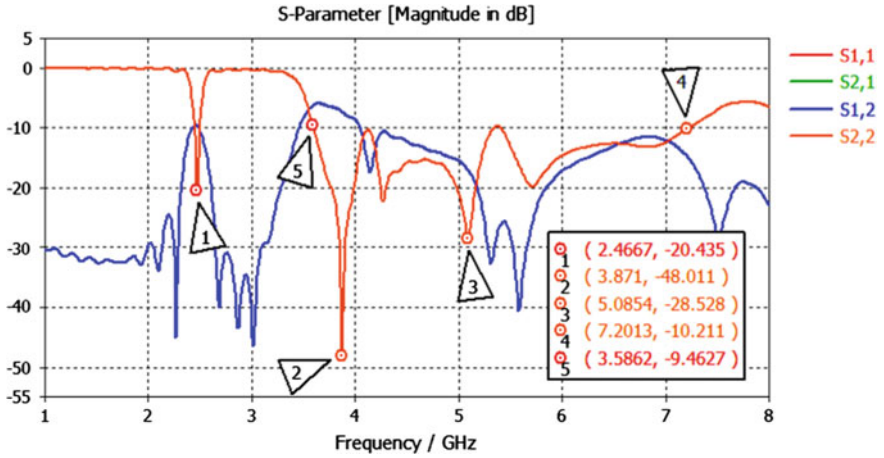

Fig. 3 Simulated S-parameter of fractal MIMO antennas

Figure 4 shows the 3-D radiation pattern of antenna at various frequencies. The gain of MIMO antenna is found to be 1.21 dB at frequency 3.7 GHz, 2.69 dB at frequency 4.9 GHz, 2.66 dB at frequency 5.15 GHz, 2.93 dB at frequency of 5.725 GHz, 2.99 dB at frequency of 5.825 GHz, and 3.01 dB at frequency 5.875 GHz. Figure 5 shows the 2-D radiation pattern of gain of MIMO antenna system at respective frequencies.

The value of VSWR at resonances 3.8 GHz and 5.09 GHz is obtained as 1.1797 and 1.077, respectively. This is very close to 1 indicating maximum power is transferred by antenna. The surface current plays an important role in developing radiation pattern of the antenna. Figure 6 shows the current density when port 1 is excited provided port 2 is terminated with matched load. It clearly shows that there is negligible current induced on the other elements of an antenna. The T stub interrupts the signal diverted from antenna element 1 to antenna element 2 and vice versa. Due to T stub, the coupled element shows very small surface current, and hence the isolation is increased. When both ports are excited, the current across T stub increases due to radiation by both patches. The current at the edges of the patch increases with increase in frequency, and hence results in improvement in gain.

The power pattern of the antenna is presented in Fig. 7. The constant power is applied to the MIMO antenna during the simulation. The antenna starts accepting the power from 2 GHz onwards, out of which some of the power radiates and remaining lost. The radiation of antenna is affected by losses across the FR4 material. The power accepted by an antenna is continuously varying with respect to frequency.

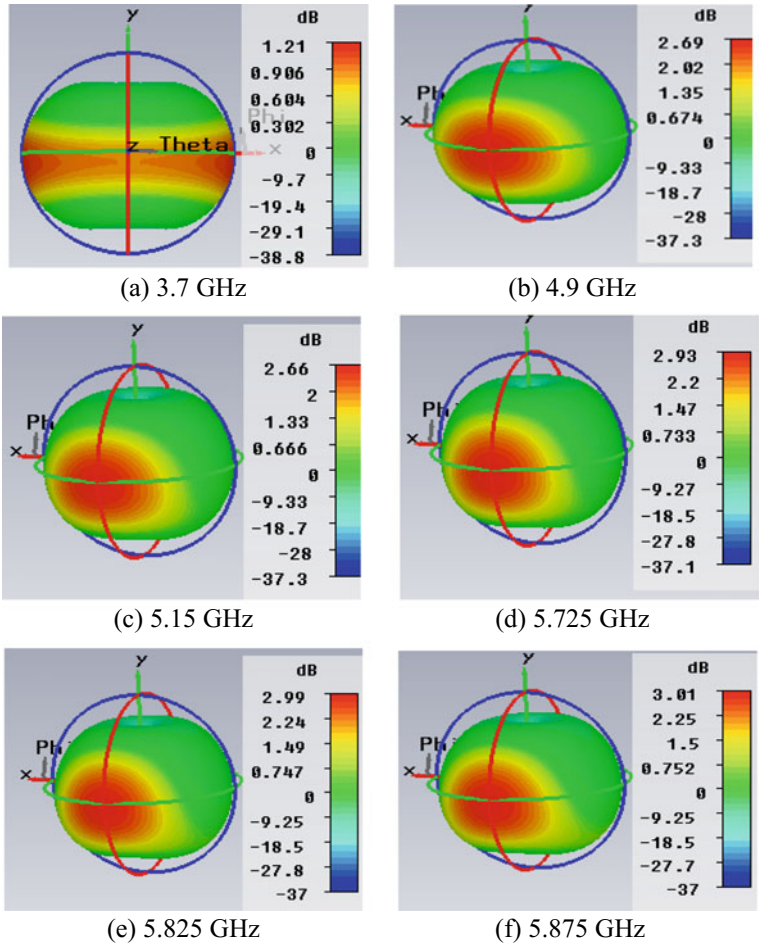

Fig. 4 3-D radiation pattern of antenna

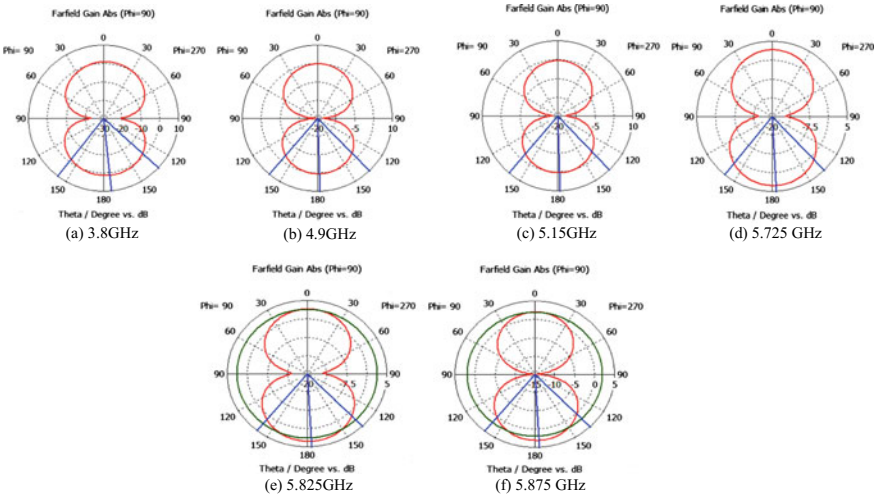

Fig. 5 2-D radiation pattern of antenna

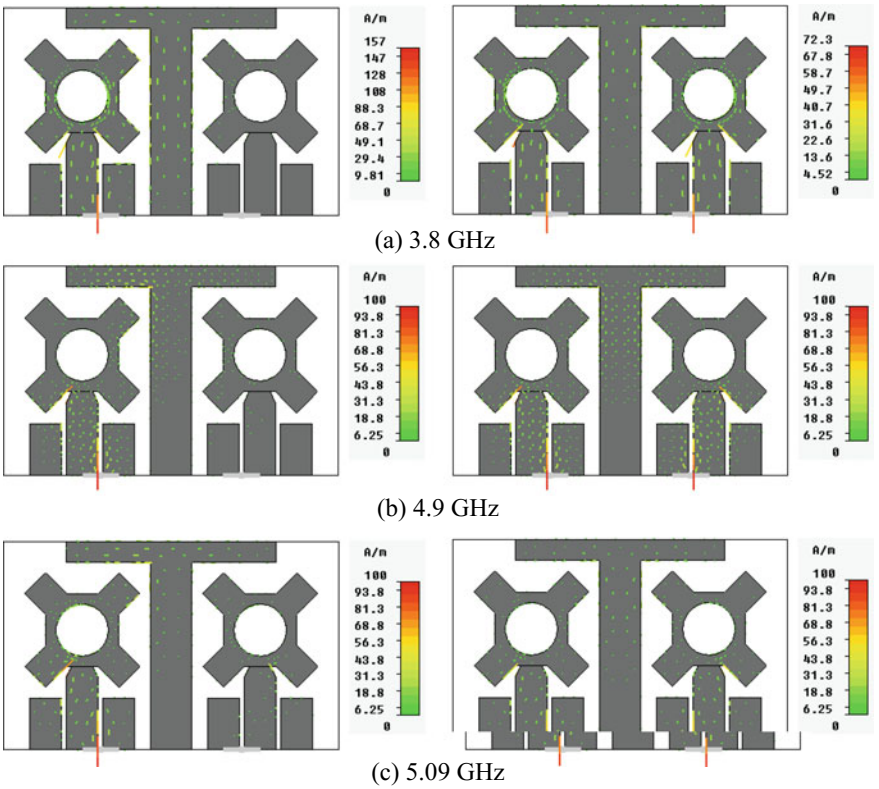

Fig. 6 Current distribution when port 1 excited and both ports excited

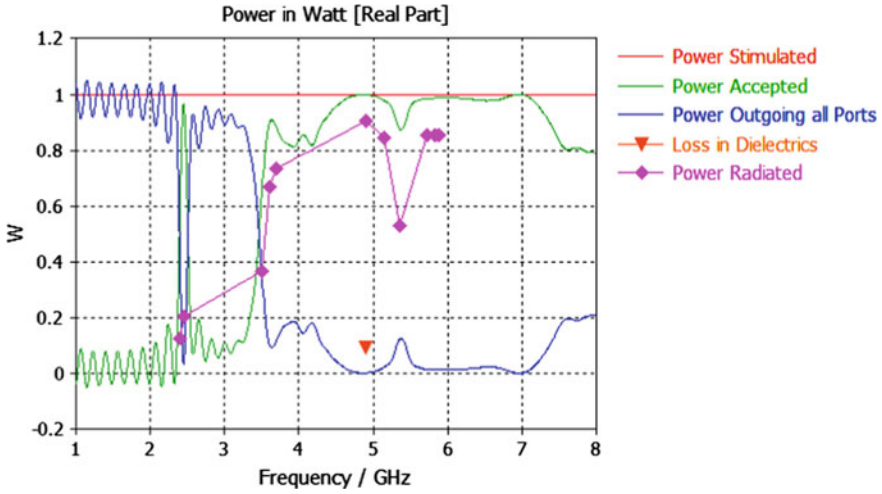

Fig. 7 Simulated power level across fractal MIMO antenna

4 Envelope Correlation Coefficient

Envelope correlation coefficient considers the antennas radiation pattern shape, polarization, and even the relative phase of the fields between the two antennas. The approximated value of this coefficient is calculated using simple closed-form equation and that varies from 0–1. The envelope correlation can be defined by a simple equation that relates the scattering parameters of the elements in an antenna array configuration. For two antenna elements, this equation using the scattering parameters is given below (Fig. 8):

$$ECC = \frac{S11 * S12 + S21 * S22}{\left(1 - |S11|^2 - |S21|^2\right)\left(1 - |S22|^2 - |S12|^2\right)}.$$

The experimental values of envelope correlation coefficient are calculated with the help of above formula and measured S-parameters. The simulated ECCs are 0.004, $6.1571e^{-005}$ at desired resonance frequencies.

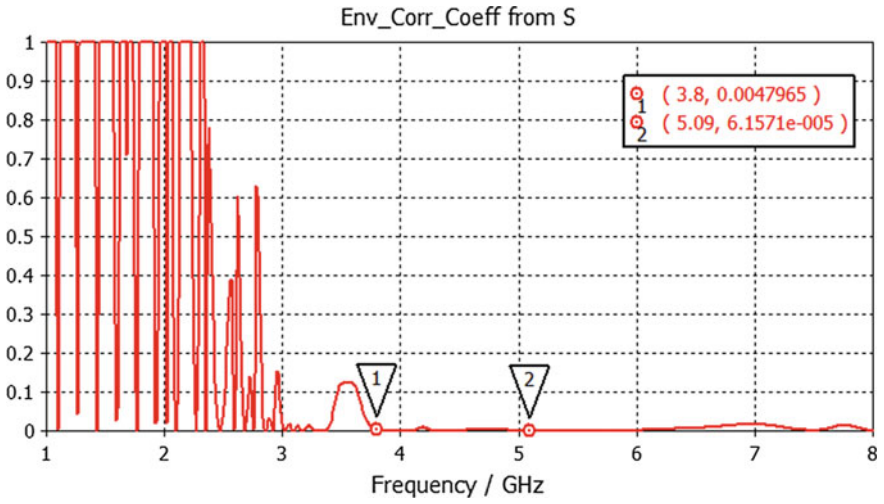

Fig. 8 Simulated envelope correlation coefficient of proposed MIMO antenna

5 Prototype and Measured Results

The prototype is fabricated on FR4 substrate with thickness of 1.6 mm (Fig. 9). The measured S-parameter results are represented by Fig. 10, which indicates that the measured results are found to be very close to simulated one. The resonances are slightly deviated due to the losses developed across FR4 material. The resonances are found at 2.64, 3.64, and 4.9 GHz.

(a) Front view (b) Back view

Fig. 9 Structure of prototype

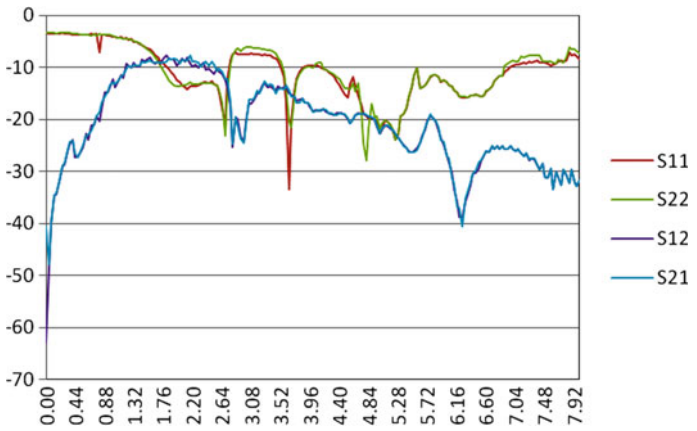

Fig. 10 Measured S-parameter of prototype

6 Conclusion

A compact fractal MIMO antenna system of size 20 × 32 mm^2 is designed for wireless communications. A T-shaped reflecting stub is placed within the antenna elements to improve matching and isolation. The ring resonator is used on backside of substrate to improve the performance of antenna. The proposed MIMO antenna has very less mutual coupling, i.e., below −10 dB over the band. The gain of the proposed MIMO antenna is 1.21 dB at frequency 3.7 GHz, 2.69 dB at frequency 4.9 GHz, 2.66 dB at frequency 5.15 GHz, 2.93 dB at frequency of 5.725 GHz, 2.99 dB at frequency of 5.825 GHz, and 3.01 dB at frequency 5.875 GHz, which is a good value for MIMO antennas. The analysis of MIMO antenna's characteristics in terms of diversity gain, mutual coupling, radiation pattern, and bandwidth is done. From the result, we conclude that antenna is good for wireless applications.

References

1. Elkazmi E, See CH, Jan NA, Abd-Alhameed RA, Ali N, McEwan NJ (2014) Design of a wideband printed MIMO monopole antenna using neutralisation lines technique. In: Proceedings of Asia-Pasific microwave conference
2. Rajkumar S, Selven KT, Rao PH (2015) Compact two element UWB fractal monopole MIMO antenna using T-shaped reflecting stub for high isolation. In: IEEE international microwave and RF conference
3. Satpute MP, Khade SS (2016) An apollonian fractal MIMO antenna for WLAN application. In: 3rd International conference on signal processing and integrated networks (SPIN)

4. Srivastava G, Mohan A (2016) Compact MIMO slot antenna for UWB applications. IEEE Antennas Wirel Propag Lett 15
5. Satam V, Nema S (2015) Defected ground structure planar dual element MIMO antenna for wireless and short range RADAR application. IEEE SPICES
6. Su SW, Lee CT, Chang FS (2012) Printed MIMO-antenna system using neutralization-line technique for wireless USB-dongle applications. IEEE Trans Antennas Propag 60(2)
7. Chandel R, Gautam AK (2016) Compact MIMO/diversity slot antenna for UWB applications with band-notched characteristic 52

Microstrip Patch Antenna Array for UWB Application

Rajat Yadav and Rajan Mishra

Abstract In this paper, an antenna is designed for ultra-wideband application as UWB is licence free band. In order to enhance the impedance bandwidth of the antenna, a number of parasitic elements as well as modified ground plane are also introduced in the design. The proposed antenna has also compactness as we are using substrate material FR4 epoxy of dimension 65 × 42 mm^2. Ansoft HFSS 2013 software is used to simulate the impedance bandwidth and radiation characteristics of the proposed antenna.

Keywords Antenna array · Parasitic elements · Step size rectangle · Impedance bandwidth

1 Introduction

The range 3.1–10.6 GHz is used for radio technology that works on low energy for short-range and gives high bandwidth over a large range of radio spectrum [1, 2]. The various benefits like low energy transmission and higher bandwidth and prone to interference make the UWB more attractive that can be used for ground penetrating system, wireless local area network (WLAN), body area network (BAN), and multimedia transmission [1–3]. Ultra-wideband is the technology used in frequency band of system and many other different systems. UWB is used in short distance communications only; due to short distance and short duration, it is easier to enhance the data speed.

UWB antenna is the core of UWB application system. Basically, UWB antennas are simple in structure and wideband impedance. UWB antennas are simply microstrip patch antenna that provides ease in fabrication, compact size, lower cost and better omnidirectional pattern [4]. The major disadvantage of the microstrip patch

R. Yadav (✉) · R. Mishra
Electronics and Communication Engineering, Madan Mohan Malaviya University of Technology, Gorakhpur, Uttar Pradesh, India
e-mail: yadavrajat96@gmail.com

© Springer Nature Singapore Pte Ltd. 2020

V. Janyani et al. (eds.), *Optical and Wireless Technologies*,
Lecture Notes in Electrical Engineering 546,
https://doi.org/10.1007/978-981-13-6159-3_38

antenna is confined bandwidth and impedance mismatching over the frequency range. To overcome these disadvantages, several different techniques have been bought up. These techniques consist of by varying the gap between feed, by varying the size and shape of the ground, i.e. defected ground or multiple feeds [5]. This antenna consists of defected ground with half-circular step sized microstrip patch antenna. The ground is defected by introducing a number of slits at the corner of the antenna. This antenna design consists of three elements in the array, in which two elements of the array are parasitic elements which lead to great improvement in antenna parameters like gain, impedance bandwidth and radiation pattern [6]. A 50 Ω microstrip feed is given to centre element in the antenna array. This antenna consists of a half-circle and a number of steps. This antenna also consists of three parasitic strips. To enhance the bandwidth of the antenna, parasitic elements are used. This improves the impedance bandwidth, gain, VSWR of the antenna [6].

2 Antenna Design

In this part, the design of the proposed antenna is described with conventional and modified ground plane as well as antenna array using parasitic elements with modified ground plane.

2.1 Single Element Antenna with Modified Ground Plane

The substrate material used in this antenna is FR4 EPOXY of thickness 1.59 mm and relative permittivity 4.4 that is commercially available. The radius of half-circular patch is 5.5 mm while the length of each step is 2 mm and width varies accordingly. The antenna feed is given by 50 Ω microstrip line of length Lf 11.5 mm and width Wf 2.8 mm. The dimensions of partial ground planes are of width 40 mm and length 10 mm. The ground plane is modified by introducing five slits on the ground, which enhance the antenna properties. Step size is introduced to enhance the matching of device. In this proposed structure, microstrip strip line feed is introduced due to its advantage of easier fabrication (Figs. 1 and 2).

Single element antenna with conventional ground offers a very narrow bandwidth. It offers a bandwidth of nearly 200 MHz whereas using parasitic array with conventional ground plane. This proposed antenna covers the bandwidth lies between the frequency ranges of 5.6–9.2 GHz. This structure describes a significant improvement in bandwidth.

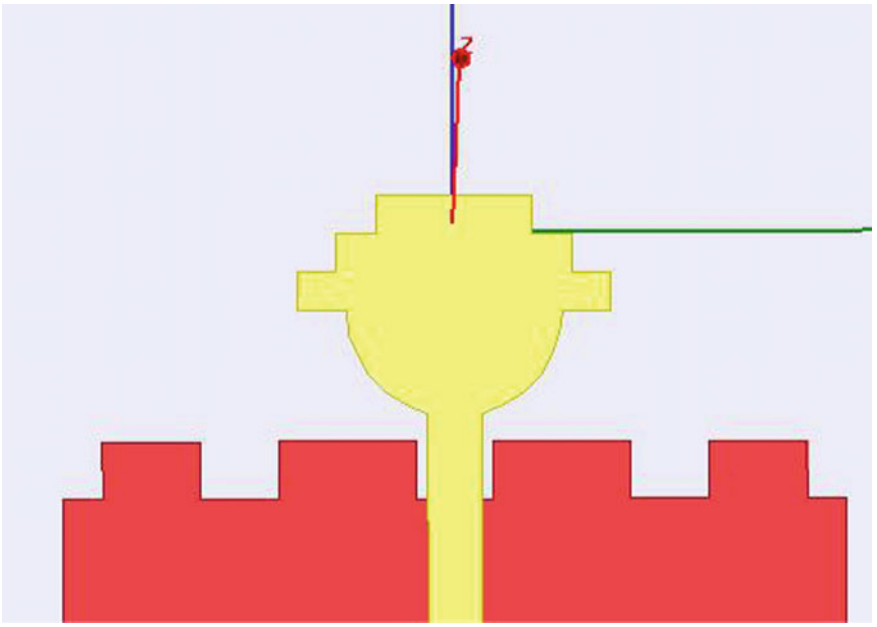

Fig. 1 Single element antenna with modified ground

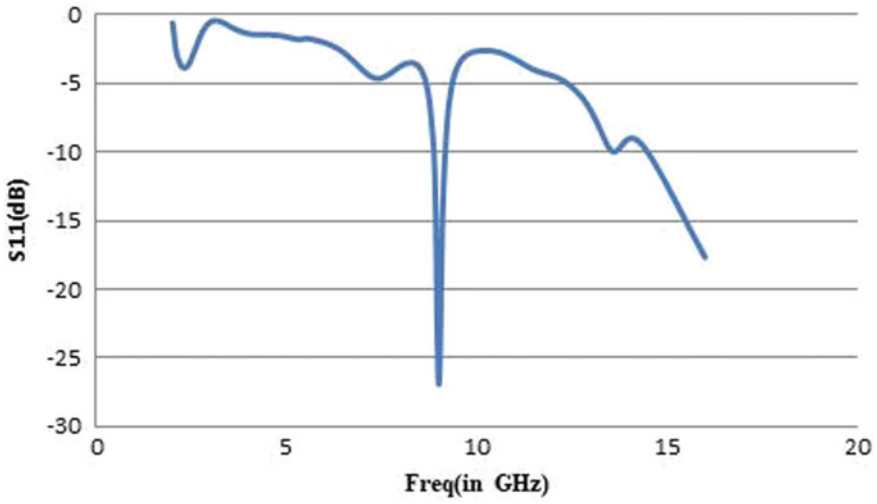

Fig. 2 Reflection coefficient of single monopole

2.2 *Antenna with Two Parasitic Elements and with Modified Ground Plane*

As further modification, we introduce an array element on the modified ground. First, we were using a single monopole radiator, and now, we are using an array of three elements where first and third elements are parasitic elements which are used to improve the impedance bandwidth of the antenna. The spacing between two successive elements is D 20 mm. A metallic strip is introduced at the centre position. The length of each rectangle step size is 2 mm and the width is varying accordingly. Along with those parasitic elements, we are using two metallic strips also in order to improve antenna performance. These parasitic elements are used to improve the matching of the device in order to improve impedance bandwidth (Figs. 3 and 4)

3 Result and Discussion

In this section, the simulation result of proposed antenna is presented. In order to get optimum result, parametric analysis is done by changing the dimension. By extracting the optimum value of each and every parameter, we have designed the proposed antenna.

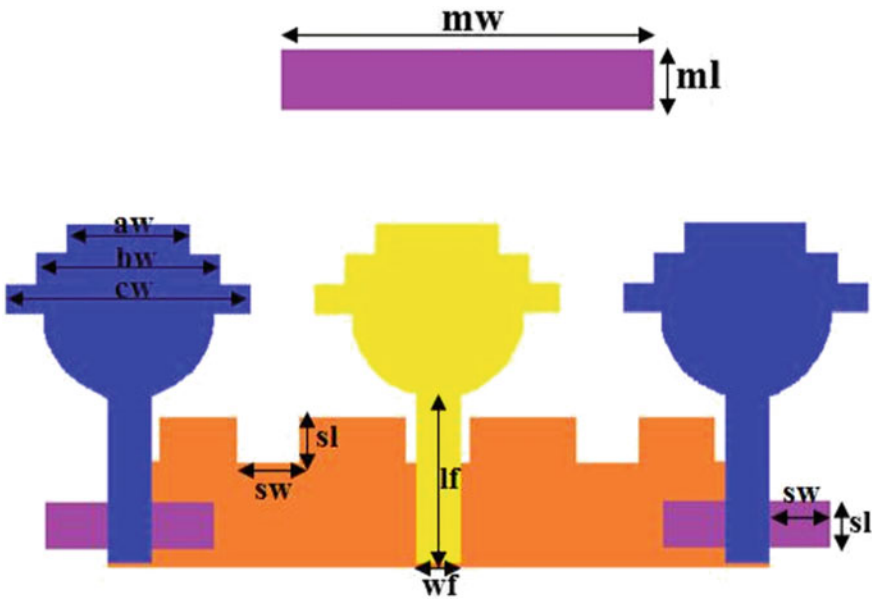

Fig. 3 Antenna array with parasitic element

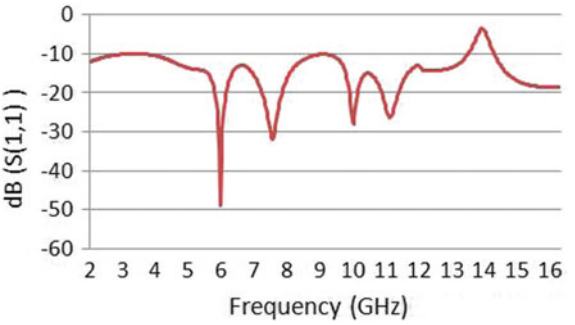

Fig. 4 Reflection coefficient of proposed antenna

Table 1 Optimized value of proposed antenna

Parameters	Values (mm)	Parameters	Values (mm)
Lsub	65	Wsub	42
Lf	11.5	Wf	2.8
ml	4	mw	24
sl	3	sw	4
Aw	8	Bw	12
Cw	16	Rad	5.5
D	18	L	2
Lg	11	Wg	40

3.1 Parametric Study

In order to get better results, parametric analysis is done. The aim of the antenna is to improve the impedance bandwidth of the antenna. A parametric study has been done on the main parameters of the antenna. Simulation is performed using Ansoft HFSS 13.0. The figure shows the different values of return losses for different values of interspacing. Further antenna performance is studied by changing the distance between the arrays. By changing the length of the ground and width of the ground, the parametric study has been done but no remarkable change is observed.

In Fig. 5, parametric analysis is done by varying the value of D where D is the spacing between the array elements. By varying the value of D, antenna performance can be improved. The change in varying the radius is not so much significant. Parametric study is done to improve the antenna characteristics (Table 1).

3.2 Optimized Antenna Array Performance

In this part, the result of the antenna with optimum dimension is compared with single element modified ground with single element conventional ground plane and antenna

array with modified ground plane. The height of the dielectric substrate plays a vital role in designing the antenna. The antenna with single element modified ground offers the bandwidth between 5.6 and 9.2 GHz whereas the bandwidth of the single element with conventional ground is 8.2–9.2 GHz. The bandwidth of antenna array lies between 2.0 and 13.2 GHz. The bandwidth of the antenna array is four times than the single element with modified ground. The VSWR of the given antenna lies below 5.5 dB for the frequency band of 2.0–13.2 GHz. The impedance bandwidth of antenna array is 3.11 times the impedance bandwidth of single element antenna. In this antenna, radiation pattern is calculated at two resonant frequencies, i.e. 5.2 and 7.75 GHz. At both the frequencies, the radiation pattern is bidirectional for E-plane and for H-plane. The gain of the proposed antenna is good at resonant frequency. It can be easily observed by using parasitic elements, we can shift the resonance frequency very easily (Fig. 6).

4 Conclusion

In this paper, step sized half-circular microstrip patch antenna has been successfully studied. The proposed antenna is basically designed for ultra-wideband application. The small size of substrate makes the antenna compact. This antenna covers the frequency bands for Wi-Max and Wi-Fi application. Antenna array enhances the antenna properties of the antenna as compared to single radiator antenna. It is seen that the proposed antenna with five slits on the ground gives an improved bandwidth.

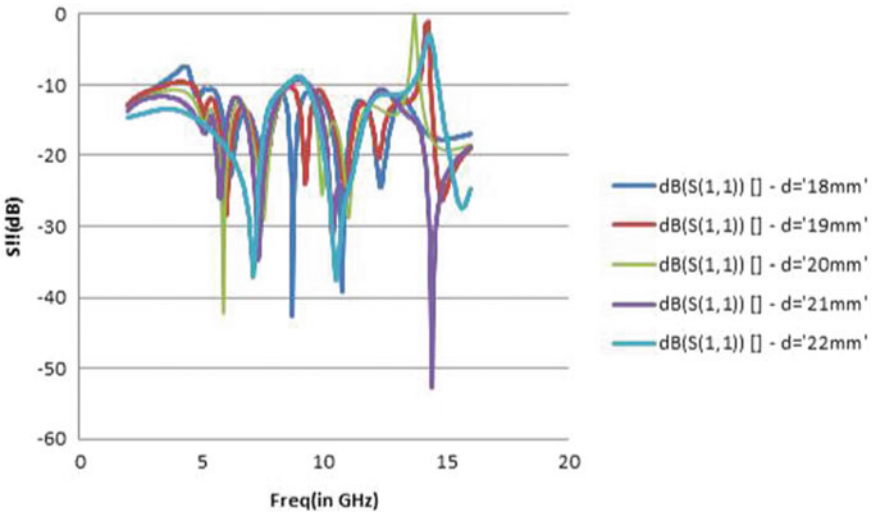

Fig. 5 Reflection coefficient of the antenna at different values of D

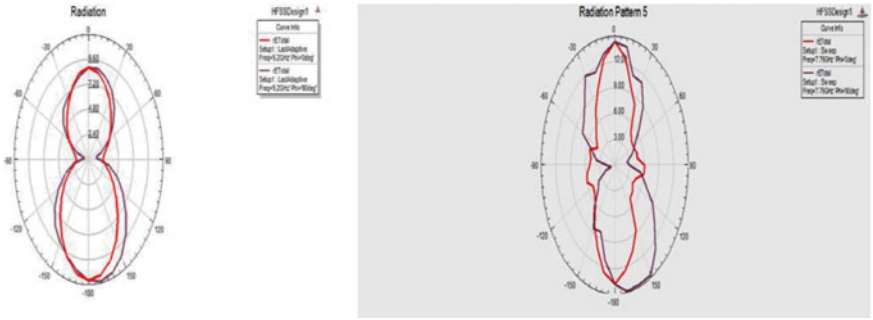

Fig. 6 Radiation pattern of the proposed antenna at 5.2 and 7.75 GHz

The performance of the antenna is optimized by using parametric analysis. The frequency range achieved for S11 < 2 10 dB is 2–13.2 GHz.

References

1. Choi JD, Stark WE (2002) Performance of ultra-wideband communi-cations with suboptimal receivers in multipath channels. Select Areas Commun IEEE J 20:1754–1766
2. Oppermann I, Hämäläinen M, Iinatti J (2004) UWB theory and applications, Wiley Ltd, England
3. Ghavami M, Michael LB, Kohno R (2004) Ultra wideband signals and systems in communication engineering. Wiley Ltd, England
4. Yadav DS, Kumar S, Gurjar SL L and U slot loaded UWB microstrip antenna: C-band/WLAN notched. In: 2015 IEEE international conference on computational intelligence & communication technology (CICT), pp 380–384, 13–14 Feb 2015
5. Akash V, Abhishek Y, Leena V (2012) Design and analysis of UWB microstrip patch antenna. Int J Adv Comp Res 2(4):340–344
6. Ali M, Wael A, Amira IZ, Abdou MH (2016) Design and fabrication of rectangular ring monopole array with parasitic elements for UWB applications. Microw Opt Technol Lett

Review for Capacity and Coverage Improvement in Aerially Controlled Heterogeneous Network

Akshita Gupta, Shriya Sundhan, S. H. Alsamhi and Sachin Kumar Gupta

Abstract As a result of vast growth in wireless networks, there is an abrupt hike in user demands, constantly demanding surplus data as well as services. This abrupt demand creates a lot of burden on backbone-based macro-cellular networks because of inability and incapability in handling these high traffic demands. The possible solutions to handle these inefficiencies are to control the ground level data plane network from aerially such as Tethered balloon, loon technology, unmanned aerial vehicle (UAV) concept, etc. This one is a survey paper in which a network is proposed to enhance the capacity and to extend the coverage of heterogeneous network assisted by UAVs (i.e., handling of traffic demand inefficiency of traditional infrastructure-based macro-cellular networks is done through UAVs as intermediate aerial nodes in heterogeneous network). The paper investigates the problem related to high user demands-based UAVs-assisted heterogeneous network. A MIMO-OFDM approach is set to serve the higher data rates to the ground users. Multiple UAVs have been used to provide long distance connectivity and enhance the load balancing and traffic offload. This review paper hopes for the betterment in spectral efficiency, transmission range, and transmission delays.

Keywords UAVs · HETNET · Capacity enhancement · Coverage expansion · MIMO

A. Gupta · S. Sundhan · S. K. Gupta (✉)
Department of Electronics and Communication Engineering, Shri Mata Vaishno Devi University, Katra, Jammu & Kashmir, India
e-mail: sachin.rs.eee@iitbhu.ac.in

A. Gupta
e-mail: akshitakharka@gmail.com

S. Sundhan
e-mail: ssundhan14@gmail.com

S. H. Alsamhi
Aerospace School, Tsinghua University, Beijing, China
e-mail: s.alsamhi.rs.ece@iitbhu.ac.in

© Springer Nature Singapore Pte Ltd. 2020

V. Janyani et al. (eds.), *Optical and Wireless Technologies*,
Lecture Notes in Electrical Engineering 546,
https://doi.org/10.1007/978-981-13-6159-3_39

1 Introduction

With the annual increase in the mobile data traffic, small cell deployments are playing a vital role in extending the wireless network capacity. A small cell has an area starting from 10 m to several hundred meters. It can also be helpful to fill the dead gaps in a macro-cell and thereby enhancing the coverage. Furthermore, it strongly provides flexibility and intensive quality of service capabilities at an attractive cost. The main focus of small cell networks is to increase the overall capacity by bringing users nearer to serving base stations [1]. A small cell deployment with macro-cell provides a backhaul connection that helps in enhancing the capacity and coverage. Efficient deployment of UAVs with directional antennas provides a large coverage [2]. The recent developments in UAV, handled by Google and Facebook, considered the idea of the use of UAVs in order to extend coverage as well as capacity. UAVs may be deployed as aerial control nodes which are playing as the central point between macro-cell and small cell networks. UAVs have a tendency to provide reliable connectivity in the high link failures prone area [3]. UAVs act as relays or intermediate aerial nodes used to provide vast coverage and enhanced capacity. UAV as a relay offers some attractive benefits such as line of sight (LoS), low propagation delay, repaid deployment, and easy to deploy and maintain [4–6]. Therefore, the use of UAVs as relay nodes provides better propagation channels to both the serving mobile base station and the selected users. For the low coverage range, we use low altitude relay, but for the high coverage range, we use high altitude relay which is nearly 21 km and covers the large area [7]. The macro-nodes are generally used in the network to assure broad coverage, and low-power nodes may be located near places with high requirement or demand for data [8]. A smart combination of this network covers a wide range of applications in the field of military and commercial areas such as border surveillance, inland security, and formation of guidance units [9]. A significant major issue faced by this network is on-fly or on-demand capacity provision. Capacity refers to the rate at which the information can be reliably transmitted toward the ground users and delay means the latency in data transmission. Most of the time, small drone cells are used to provide an aerial control to an existing cellular network which can help to handle dense traffic in a network more cost effectively. Deploying a single UAV is easy with respect to demand, and deploying a number of UAVs in coordination with each other is very challenging and difficult due to high chances of interference from various another aerial nodes [10]. An effective approach is required to set for extending coverage and to enhance capacity. However, various heterogeneous algorithms have already been used to resolves the problem of capacity, delay, and vertical handover in order to expand coverage in a different kind of heterogeneous network, namely, context-aware decision-based algorithms, delay timer algorithms, load balancing algorithms, neural cost-based algorithms, neural fuzzy-based algorithms, etc. [11, 12].

Researchers have worked in many ways to enhance capacity and extend coverage. There are many techniques for increasing the capacity and coverage of wireless network such as public spectrum band, 700 MHz band, white space ultrahigh frequencies

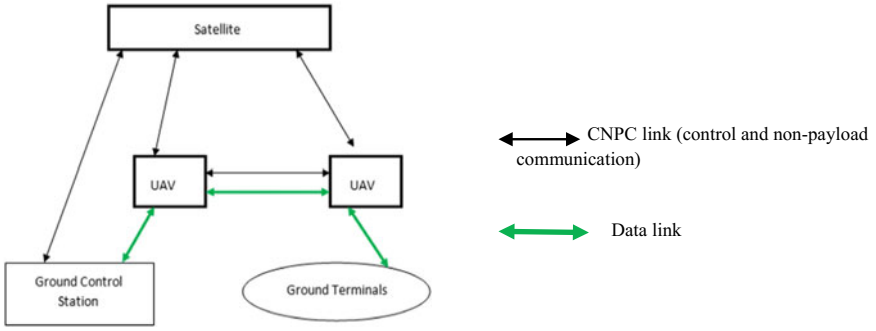

Fig. 1 Basic architecture of UAVs-aided wireless communication

(UHF) spectrum, MIMO antenna technologies, carrier aggregation and offload via femtocells [13]. The basic architecture of UAVs-assisted wireless communication has been shown in Fig. 1, where control and non-payload communication (CNPC) link serves a safety-critical communication link and provides a communications between the remote pilot control system and the aircraft.

2 Network Model

UAVs play a vital role in intermediate node which helps to enhance the balance load while transmission of data from aerial nodes to ground users by forming multiple links as shown in Fig. 2. UAVs as intermediate nodes are efficiently established in a network to cover large geographical area and to provide better capacity at cell edges. These small sizes and low-powered base stations act as repeaters to extend the strength and quality of the signal and rebroadcast it. The quality of the signal is predicted from different altitudes and different distances by using neural network [14]. These aerial nodes are optimally placed with the help of optimal placement algorithms. Communication is taking place in small cell HETNETs. The small HETNETs are being chosen to cover the maximum area. Dead spots are covered using this network which ultimately leads to capacity and coverage increment. For communication purpose, we have deployed a mobile base station (MBS), i.e., MBS is used to communicate with UAVs. Communication can be done by installing antennas in UAVs. There is a formation of communication links between UAVs-user equipment and MBS-UAVs. Communication between aerial nodes and ground users can be effected by environmental conditions and many more factors that degrade the strength of signal and further lead to the path loss of the network. The path loss is mainly caused by diffraction of signal, terrain contours, environmental factors such as urban or rural, air medium (dry or moist air), obstructed by obstacles between transmitter and receiver (free space loss), and due to the height and position of antennas. To mitigate these factors, path loss model is used to calculate the path loss

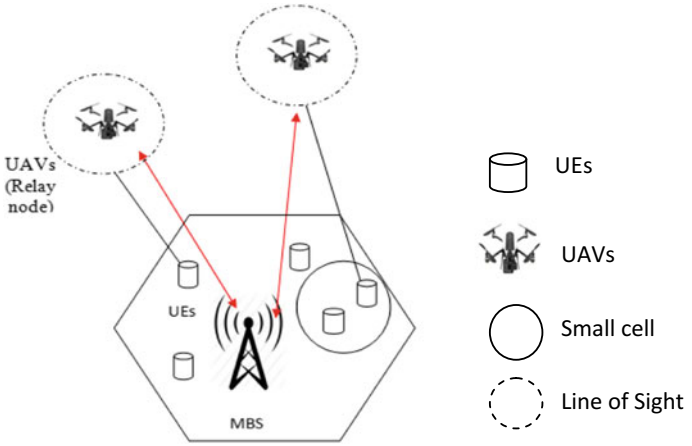

Fig. 2 Proposed UAVs control heterogeneous network

of the network such as Hata model [15]. Hata model is the most widely used radio frequency propagation that extends the model for predicting the behavior of path loss of cellular transmissions in exterior environments covers frequencies from 150 to 1500 MHz.

2.1 Mathematical Model

The mathematical model used for coverage extension and capacity enhancement consists of Okumura–Hata model. It is based on extensive measurements of graphical path loss and valid for microwave frequencies from 150 to 1920 MHz. Hata model is widely used for urban area loss prediction along with correction factors for various applications in other situations such as suburban and rural area. It calculates the path loss of the network in dBs. In general, Path loss (in dB) is described as

$$\text{Path Loss(PL)} = \text{PL}_{\text{freespace}} + \text{A}_{\text{exc}} + \text{H}_{\text{cb}} + \text{H}_{\text{cm}} \tag{1}$$

where

$\text{PL}_{\text{freespace}}$ = Free space path loss.
A_{exc} = Excess path loss (measured as a function of distance, frequency, and antenna height) for a BS height h_b and a MS height h_m in meters.
H_{cb}, H_{cm} = Antenna height correction factors.

The implementation of path loss can be written as

$$\text{PL} = \alpha + \beta \log(\text{d}) + \gamma \tag{2}$$

Table 1 Parameters of Hata model

Type of area	$a(h_m)$	C
Rural	$0.8 - 1.56 \log_{10}(f) + (1.1 \log_{10}(f) - 0.7)\, h_m$	$-4.78 [\log_{10}(f)]^2 + 18.33 \log_{10}(f) - 40.98$
Suburban		$5.4 + 2 [\log_{10}(f/28)]^2$
Medium-small city		0
Metropolitan ($f \leq 200$) MHz	$-1.1 + 8.29 (\log_{10}(1.54 h_m)^2$	0
Metropolitan ($f \geq 400$) MHz	$-4.97 + 3.2 (\log_{10}(11.75 h_m)^2$	0

where α, β, and γ are the frequency and antenna height-dependent factors, and frequency (f) is given in MHz and distance (d) in KM.

$$\alpha = 69.55 + 26.16 \log(f) - 13.82 \log(h_b) - a(h_m) \tag{3}$$

$$\beta = 44.9 - 6.55 \log(h_b) \tag{4}$$

where function $a(h_m)$ and correction factor (C) are environment-dependent factors:

- For urban areas such as small and medium-sized cities:

$$\begin{gathered} a(h_m) = (1.1 \log_{10}(f) - 0.7)h_m - (1.56 \log_{10}(f) - 0.8) \\ C = 0 \end{gathered} \tag{5}$$

- For metropolitan areas like large cities:

$$\begin{gathered} a(h_m) = \begin{cases} 8.29(\log_{10}(1.54h_m)^2 - 1.1 \text{ atf} \leq 200\,\text{MHz} \\ 3.2(\log_{10}(11.75h_m)^2 - 4.97 \text{atf} \geq 400\,\text{MHz} \end{cases} \\ C = 0 \end{gathered} \tag{6}$$

- For suburban areas:

$$\gamma = 5.4 + 2\left[\log_{10}(f/28)\right]^2 \tag{7}$$

- For rural area:

$$\gamma = -4.78\left[\log_{10}(f)\right]^2 + 18.33 \log_{10}(f) - 40.98 \tag{8}$$

The function $a(h_m)$ in rural and suburban areas is all most same as the urban areas [16, 17]. The various parameters of the Hata model are given in Table 1.

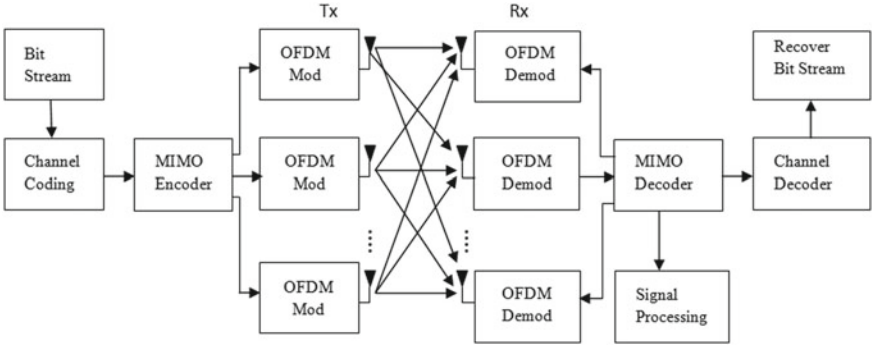

Fig. 3 MIMO-OFDM system

3 Key Aspect of Network Model

The critical aspect of capacity enhancement using MIMO orthogonal frequency division multiplexing (MIMO-OFDM) concept, it is an effective way to achieve the highest spectral efficiency and also provides better quality of service (QoS) like capacity, data throughput, and bit error rate (BER). One of the most significant biggest challenges in the wireless network is to provide uniform connectivity throughout the geographical area. MIMO-OFDM generally break up a radio channel into multiple numbers of equally spaced sub-channels to deliver more reliable and good communication at higher data transfer rates as shown in Fig. 3.

3.1 Advantages, Applications, and Challenges of Network Model

The possible advantages, applications, and challenges of the proposed network model are listed out in Table 2. Due to these various key aspects, this kind of UAVs-assisted network has mainly attracted the researchers' attention and becomes one of the demanding areas of research among the academic and industrial people.

4 Background and Related Work

There has been lots of research going on in order to increase capacity and extend coverage to a great level. In this context, various fields have been pointed out where researchers are working in different ways to enhance capacity and coverage.

OFDM technique is a very promising scheme that is used for digital carrier modulation for achieving the data transfer at higher rates for wireless communication

Table 2 Various possible advantages, applications, and challenges of UAVs-assisted network

Sl. no.	Advantages	Applications	Challenges
1	**Cost-effective**: Heterogeneous network is the most efficient and low-cost solution to improve the capacity by deploying small cells combination with macro-cell	**Military area**: • Live video remote communications to ground troops, aerial reconnaissance of unknown areas/buildings, enemy tracking, and force protection • Security and control • Searching and rescue operations • Strike missions	A non-payload communication link such as control and non-payload communication links (CNPC) with more security requirements is necessary in UAVs for safety-critical tasks like real-time control, decision-making, crash avoidance and collision, etc. [18]
2	**Boosting capacity and uniform coverage**: Heterogeneous network assisted by UAVs is the cost-efficient way that helps in boosting capacity and provides uniform coverage in remaining dead zones	**Commercial area**: • Surveying and mapping • Agriculture • Environmental and Natural disaster monitoring • Mining [19]	In wireless networks, high mobility environment of the network is usually a reason for link failures; it results in highly dynamic network topologies, which are usually sparsely and sporadically connected [18]
3	**Reliable network**: This network can be deployed in congested areas where it is difficult to build infrastructure	**Civilian area**: • Infrastructure • Transport • Emergencies • Aquaculture	One of the biggest challenges in this network is SWAP constraints of UAVs, i.e., size, weight, and power, because it could limit computation, communication, and persistence capabilities [18]
4	**Good communication**: With the use of high gained antennas in UAVs, it is possible to gain good communication between aerial nodes and ground users	**Public safety operations:** In wireless network, communication technologies completely rely on the infrastructure network; in any worst failure of base stations makes communication more difficult for emergency communications and public safety, but with the use of UAVs-assisted HetNets gained lot of attention in public safety communication [13]	Interference coordination from the neighboring cells is more challenging [20]

(continued)

Table 2 (continued)

Sl. no.	Advantages	Applications	Challenges
5	**Rapid service recovery**: Service failure is a big issue in wireless networks but this network ensures restoration of services rapidly in any case of whether partial or complete infrastructure loss due to calamities, natural disasters, and base station offloading in densely crowded areas, e.g., live music concert or a sports event stadium, etc.	**Aerial images and photography**: • Real estate photography • Inspection areas • Landscapes	UAV-based communication is the high signal processing complexity, as well as the costs of hardware and power consumption, make it often costly to deploy multiple antennas
6	**Prolonged connectivity**: This network ensures long term connectivity with quality in comparison to existing traditional ground-based wireless network	**Vehicular ad hoc networks**: UAVs-assisted HetNets could be one of the best options to provide the connectivity among high-speed moveable vehicles, like VANETs, Drive-thru Internet, etc.	Impact limited at cell edge due to low signal quality [20]

standards [21]. In orthogonal frequency division multiplexing, the entire available channel is split into many narrowband closely spaced orthogonal sub-channels, which are further transmitted in parallel and thereby increase in the spectral efficiency and reduction in the intersymbol interference (ISI). Therefore, OFDM is a tremendous technique for reducing multipath fading and favoring data transfers at high bitrates over mobile wireless channels. The transmitter diversity using space-time coding for OFDM systems can be used to improve the performance for data transmission over mobile wireless channels. There are various techniques described for increasing the capacities like spectrum, technology, and topologies [22]. The complete model framework includes the demand of area, spectrum efficiency, offload, and cost-efficient deployment. The overall study defines the lower frequency and higher frequency spectrum will pay a great role in future mobile capacity. Wireless relays utilize small unmanned aerial vehicles (SUAVs) for increasing cellular network performance [23]. It is a low-cost effective solution to use SUAVs for emergency coverage. In this paper, the author analyzed the output taken from an SUAV test bed in both small-medium cities and suburban environment. Trough to peak throughput and ping time improvements have been seen as a result [24]. They described the two scenarios: a static-UAV and dynamic-UAV-enabled wireless networks. In the static-UAVs, an average signal-to-interference-plus-noise ratio (SINR) based cover-

age probability versus system sum rate expressions for the users in the given area is obtained as an outcome of the UAV altitude and the number of D2D users. Now those in second case, the UAV examines in order to cover the maximum area by using the disk covering problem and the minimum number of stop points. The result showed that a maximum coverage and system sum rate can be attained, if the UAV altitude is suitably positioned based on the density of D2D [18]. This article has provided an overview of UAV-aided wireless communication with three important cases: UAV-aided mobile relaying, UAV-aided ubiquitous coverage, and UAV-aided data dissemination. They highlighted only two essential performance enhancing techniques by employing the UAV controlled mobility, exploit both UAV-enabled mobile relaying and D2D enhanced communication. UAV-enabled mobile relaying is a technique, where the relay nodes are mounted on UAVs in terrestrial communication systems. Hence, this technique is capable to provide high throughput/reliability in the network. D2D communication is a promising technique for extending cellular coverage mostly in dense deployment scenario, and it has an advantage of an offloading traffic to the BS by allowing direct communications between nearby mobile terminals. Furthermore, the authors of [25] focused on demanded area to enhance the data capacity. They divided the geographical area into subzones with the help of zone guidelines and deployed UAVs in higher demand zone. Density and cost function are employed to evaluate areas with high demands, whereby, deployment of UAVs is cost-based function. To obtain network stability, the cost function is minimized for demand areas and deployed UAVs. A delay threshold has been set to observe the network performance. Defined as the network state with less delay to provide capacity coverage in high request areas, mapping UAVs with minimum errors in the particular demand area, and highly reliable in case of data delivery rate. The author at last achieves refinement in terms of 5th percentile spectral efficiency up to 38% and minimized delays up to 37.5% [26]. The authors have shown that simultaneous communication between multiple single antenna UAVs and ground station (GS) furnished with a large number of antennas. The researchers focused on the achievable uplink (UAV to GS) capacity performance in the both cases: LoS and non-LoS conditions. By spherically and uniformly distribution of UAVs around the GS, the erodic rate per UAV is increased for an antenna space equal to an integer multiple of one-half wavelength [27]. An ambient network has been proposed for ground and flying network coordination. G-FANET relies on accurate connections between ground and aerial nodes. The proposed system comprises the feedback network formation, neural derivative, decision support system based on fuzzy, and a genetic modeler which handles the traffic flow like neural cost function. This approach attains a 73.1% average efficiency to successful mapping of UAVs to the ground level users. Also, the authors of [28] proposed optimal placement algorithms to efficiently position the UAVs. Because of the positioning of UAVs as relay nodes, switching of services from the regular nodes to aerial nodes uses a lot of time which leads to transition delays. Therefore, the positioning of the UAVs in such type of heterogeneous wireless networks is a key task, which affects the delay during enhancing the existing cellular networks coverage. This positioning issue had been resolved with the support of entropy nets by an optimal placement algorithm formation, which reduces the delays without effect-

ing its capacity and coverage. Entropy nets are basically a neural network based decision trees, which is used to provide accurate decisions of correct mapping of UAVs. The result shows that the presented method was proficient to optimize the heterogeneous networks allocation delay without affecting its capacity and coverage [29]. Showed a smart solution for the accurate and efficient UAVs mapping with respect to the demand areas resulting in the minimum improvement in the capacity as well as coverage. By applying the priority-wise dominance and the entropy approach, somehow macro-base station decision and cooperative UAV allocation problem were solved [17]. They analyze the capacity of aerial small cells. In this paper, a stochastic propagation model for A to G aerial channels is developed. This model is basically designed on the offered data from the existing field experiments on A to G aerial channels and by taking into accounts the wave propagation effect, gaseous absorption, Doppler spread, multipath fading, and attitude-dependent shadowing. By exploiting this kind of model, they find out the SISO and MIMO capacity of the aerial cells that reveal the essential relationship among the area capacity, cell coverage, and UAV altitude. At the end, they observed that MIMO small cell can have much high capacity than single-input multiple-output (SISO) small cell [12]. The discussed vertical handover algorithms are advantageous in heterogeneous network. Handover may impose the impact on the continuity and connectivity of the heterogeneous network during the communication. Therefore, various algorithms are used in heterogeneous network to solve this issue such as bandwidth, RSS, cost function, authentication, and security-based algorithms.

5 Conclusions

An increase in demand with high data rates from heterogeneous network assisted UAVs; the MIMO can be an efficient way to enhance the capacity and coverage. Also, many researchers have chosen this vibrant area and work is still going on, to extend coverage and capacity. As discussed above in the background and reported work section, many techniques and topologies are used by researchers to enhance the wireless network capacity and coverage like public spectrum band, 700 MHz band, white space UHF spectrum carrier aggregation, and offload via femtocells. The various approaches like neural cost function and fuzzy approach are used to find the cost and assignment of UAVs. Till now no such work has been done in this heterogeneous network assisted with UAVs using MIMO-OFDM technique and Hata 3467815 model. Through this survey paper, it is expected that using this technique, the expected outcome will be increased in capacity and coverage to a great level.

References

1. Hu RQ, Qian Y, Kota S, Giambene G (2011) Hetnets—a new paradigm for increasing cellular capacity and coverage. IEEE Wirel Commun 18(2):8–9
2. Mozaffari M, Saad W, Bennis M, Debbah M (2016) Efficient deployment of multiple unmanned aerial vehicles for optimal wireless coverage. IEEE Commun Lett 20(4):1647–1650
3. Erdlej M, Natalizio E (2016) UAV-Assisted disaster management: applications and open issues. In: International conference on computing, networking and communications (ICNC), pp 1–5
4. Alsamhi SH, Ansari MS, Almalki F, Ma O, Gupta SK (2018) Tethered balloon technology in design solutions for rescue and relief team emergency communication services. Disaster Med Publ Health Prep 1–8
5. Alsamhi SH, Ansari MS, Rajput NS (2018) Disaster coverage predication for the emerging tethered balloon technology: capability for preparedness, detection, mitigation, and response. Disaster Med Public Health Prep 12:222–231
6. Alsamhi SH, Gupta SK, Rajput N (2016) Performance evaluation of broadband service delivery via tethered balloon technology. In: 11th IEEE international conference on industrial and information systems, pp 133–138
7. Alsamhi SH, Rajput NS (2015) An intelligent HAP for broadband wireless communications: developments, QoS and applications. Int J Electron Electr Eng 3(10)
8. Damnjanovic A, Montojo J, Wei Y, Ji T, Luo T, Vajapeyam M, Yoo T, Song O, Malladi D (2011) A survey on 3GPP heterogeneous networks. IEEE Commun Lett 18(3):10–21
9. Li C, Zhang J, Letaief KB (2014) Throughput and energy efficiency analysis of small cell networks with multi-antenna base stations. IEEE Trans Wirel Commun 13(13):2505–2517
10. Srinivasan K, Sharma V, Chao H-C, Hua K-L, Cheng W-H (2017) Intelligent deployment of UAVs in 5G heterogeneous communication environment for improved coverage. J Comput Netw Appl 85(19):94–105
11. Lee CP, Lin P (2017) Modeling delay timer algorithm for handover reduction in heterogeneous radio access networks. IEEE Trans Wirel Commun 16(13):1144–1156
12. Abdullah RM, Zukarnain ZA (2017) Vertical handoff algorithm for different wireless technologies. Peer J Prepr, 1–15. https://doi.org/10.7287/peerj.preprints.2970v1
13. Merwaday A, Guvnec I (2015) UAV assisted heterogeneous networks for public safety communications. IEEE wireless communications and networking conference workshops (WCNCW), 329–234
14. Alsamhi SH, Almalki F, Ma O, Ansari F (2018) Predictive estimation of the optimal signal strength from unmanned aerial vehicle over internet of things using ANN. arXiv preprint arXiv: 1805.07614
15. Alsamhi SH, Rajput NS (2015) An intelligent hand-off algorithm to enhance quality of service in high altitude platforms using neural network. Wirel Pers Commun 82(15):2059–2073
16. Pathania P, Kumar P, Rana SB (2014) Performance evaluation of different path loss models for broadcasting applications. Am J Eng Res 03(8), 335–342
17. Li Y, Cai L (2017) UAV-assisted dynamic coverage in a heterogeneous cellular system. IEEE Netw 31(4):56–61
18. Zeng Y, Zhang R, Lim JT (2016) Wireless communications with unmanned aerial vehicles: opportunities and challenges. IEEE Commun Mag 54(7):36–42
19. Sharma V, Kumar R (2014) A cooperative network framework for multi UAV guided ground adhoc network. J Intell Rob Syst 77(24):629–652
20. Ubom EA, Idigo VE, Azubogu A, Ohaneme CO, Alumona TL (2011) Path loss characterization of wireless propagation for south—south region of Nigeria 3(3), 360–364, (Jun. 2011)
21. Li Y (1998) OFDM for wireless communication: techniques for capacity improvement. In: IEEE international conference on communication technology, Beijing, China 2(5). https://doi.org/10.1109/icct.1998.741056
22. Techniques for increasing the capacity of wireless Broadband networks, real wireless report (Apr. 2012). http://static.ofcom.org.uk/static/uhf/real-wireless-report.pdf

23. Guo W, Devine C, Wang S (2014) Performance analysis of micro unmanned airborne communication relays for cellular networks. In: 9th international symposium on communication systems, networks & digital signal processing 1–6, 658–663
24. Mozaffari M, Saad W, Bennis M, Debbah M (2016) Unmanned aerial vehicle with underlaid device-to-device communications: performance and tradeoffs. IEEE Trans Wirel Commun 15(6):3949–3963
25. Sharma V, Bennis M, Kumar R (2016) UAV-assisted heterogeneous networks for capacity enhancement. IEEE Commun Lett 20(4):1207–1210
26. Chandhar P, Danev D, Larsson EG (2016) Massive MIMO for communications with Drone Swarms. In: international conference on unmanned aircraft systems, 347–354
27. Kumar R, Sharma V (2016) G-FANET: an ambient network formation between ground and flying ad hoc networks. Telecommun Syst 65(24):31–54
28. Sharma V, Sabatini R, Ramasamy S (2016) UAV assisted delay optimization in heterogeneous wireless network. IEEE Commun Lett 20(5):2526–2529
29. Pokkunuru A, Zhang Q, Wang P (2017) Capacity analysis of aerial small cells. In: IEEE international conference on communications (ICC), pp 1–7

Modified μ-Law Companding Transform for PAPR Reduction in SC-FDMA Systems

K. Shri Ramtej and S. Anuradha

Abstract Low peak-to-average power ratio (PAPR) enabled single carrier frequency division multiple access (SC-FDMA) to be implemented in long-term evolution uplink communications. But there is a need to lessen PAPR as SC-FDMA systems when used in localized subcarrier mapping exhibit high PAPR for higher order modulations. Companding is a simple technique to minimize PAPR without side information. It has very low implementation complexity. μ-Law companding, which is one of the most popularly used companding transforms, provides significant PAPR reduction but increases the average signal power. In this paper, we come up with a modified μ-law companding transform without any decompanding operation at the receiver side, which do not increase the average signal power after companding. Simulation results demonstrate that the PAPR reduction achieved by modified μ-law companding technique is same as that of conventional μ-law technique. Modified μ-law companding provides similar bit error rate (BER) performance as that of conventional μ-law companding technique when AWGN channel is considered while it surpasses the conventional technique when Veh-A channel is considered. The proposed technique also has better power spectral density (PSD) performance when compared to conventional technique.

Keywords Average power · Companding · LTE · PAPR · SC-FDMA

K. Shri Ramtej (✉) · S. Anuradha
Department of Electronics and Communications Engineering, National Institute of Technology Warangal, Warangal, Telangana, India
e-mail: shriramtej@gmail.com

S. Anuradha
e-mail: anuradha@nitw.ac.in

© Springer Nature Singapore Pte Ltd. 2020

V. Janyani et al. (eds.), *Optical and Wireless Technologies*,
Lecture Notes in Electrical Engineering 546,
https://doi.org/10.1007/978-981-13-6159-3_40

1 Introduction

Low peak-to-average power ratio (PAPR) enabled single carrier frequency division multiple access (SC-FDMA) to be implemented in long-term evolution uplink communications. SC-FDMA has lower signal envelope fluctuations resulting in low PAPR than that of OFDMA [1]. But there is a need to lessen PAPR as SC-FDMA systems when used in localized subcarrier mapping exhibit high PAPR for higher order modulations. When PAPR is high, the power amplifier goes into saturation region, which reduces the efficiency of power amplifier [2].

There are numerous methods to lessen PAPR in SC-FDMA systems. Clipping is one of the most widely used techniques, but it deteriorates the system performance due to clipping noise [3]. Pulse-shaping method requires excess bandwidth or additional complexity [4]. Selected mapping and partial transmit sequence schemes [5–8] need transmission of side information and are highly complex. Nonlinear companding techniques are used in OFDM systems to reduce PAPR and provide better BER performance. They are less complex and do not require any side information. In [9], the use of μ-law companding lessened PAPR in SC-FDMA systems. But it increases the average signal power. In this paper, we modify μ-law companding while retaining average signal power unaltered. The modified μ-law companding technique provides similar BER performance as that of conventional technique over AWGN channel and outperforms it over multipath Rayleigh fading Vehicular-A outdoor channel.

The rest of this paper is formed as follows. Proposed system model with companding is introduced in Sect. 2. Section 3 presents PAPR and BER results of the proposed system. Few conclusions are drawn in Sect. 4.

2 Proposed SC-FDMA System with Companding

Proposed SC-FDMA system model with companding is shown in Fig. 1. QPSK or QAM techniques are used to modulate the encoded data. Then the modulated data is grouped into N symbols and passed through N-point DFT to give the resulting signal X_k.

$$X_k = \sum_{n=0}^{N-1} x_n e^{-j\frac{2\pi}{N}nk}, k = 0, 1, \ldots, N-1 \tag{1}$$

These N symbols are then mapped to M subcarriers ($N < M, M = QN$). In localized FDMA (LFDMA), the symbols are transmitted over adjacent subcarriers. If localized subcarrier mapping is used, then $\bar{X}_l$ is given by

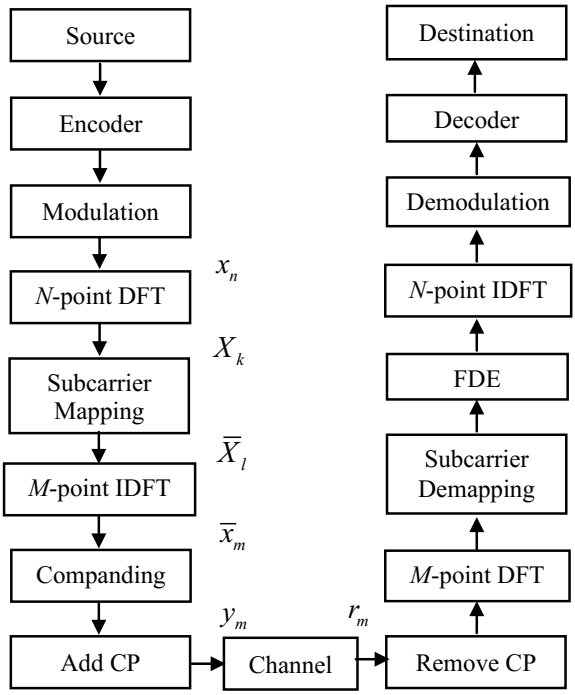

Fig. 1 Proposed single carrier FDMA system with companding

$$\bar{X}_l = \begin{cases} X_k(l), (0 \le l \le N-1) \\ 0, \quad (N \le l \le M-1) \end{cases} \quad 0 \le l \le M-1 \tag{2}$$

After subcarrier mapping, $\bar{X}_l$ is passed through M-point IDFT, and the resulting time-domain complex signal $\bar{x}_m$ is given by

$$\bar{x}_m = \frac{1}{M} \sum_{l=0}^{M-1} \bar{X}_l e^{j\frac{2\pi}{M}ml}, m = 0, \ldots, M-1 \tag{3}$$

Now data $\bar{x}_m$ is passed through compander, and a cyclic prefix is added to it and transmitted through the channel. The PAPR of $\bar{x}_m$ is given by

$$\text{PAPR}(\bar{x}_m) = \frac{\max\left|\bar{x}_m^2\right|}{E\left\{\left|\bar{x}_m^2\right|\right\}} \tag{4}$$

In [10], the authors proposed to omit the decompanding operation at receiver, as it amplifies the channel noise. So at the receiver side, we do not perform any decompanding operation. So the CP removed resulting signal r_m is passed through M-point DFT without any decompanding operation. Then subcarrier de-mapping, frequency domain equalization, and remaining inverse operations are carried out to detect the transmitted data.

2.1 Modified μ-Law Companding

The conventional μ-law companding is given by [10]

$$y_m = V_{\max} \frac{\ln\left[1 + \frac{\mu|\bar{x}_m|}{V_{\max}}\right]}{\ln[1+\mu]} \text{sgn}(\bar{x}_m) \tag{5}$$

where $V_{\max} = \max(|\bar{x}_m|)$ and μ is companding coefficient. In order to keep the average signal power unaltered, we modify it as

$$y_m = A \times V_{\max} \frac{\ln\left[1 + \frac{\mu|\bar{x}_m|}{V_{\max}}\right]}{\ln[1+\mu]} \text{sgn}(\bar{x}_m) \tag{6}$$

As average signal power of companded and original signals is same

$$\begin{aligned} E\left[|\bar{x}_m|^2\right] &= E\left[|y_m|^2\right] \\ &= E\left[\left[A \times V_{\max} \frac{\ln\left[1 + \frac{\mu|\bar{x}_m|}{V_{\max}}\right]}{\ln[1+\mu]}\right]^2\right] \end{aligned} \tag{7}$$

Table 1 Simulation parameters

Parameter	Description
Simulation method	Monte Carlo
Modulation type	16-QAM
Channel coding	1/2 rate convolutional code
N	128
M	512
System bandwidth	5 MHz
Subcarriers spacing	9.765625 kHz
Subcarrier mapping	Localized
μ	4
CP length	20 samples
Channel model	AWGN, Vehicular-A outdoor
Channel estimation	Perfect
Equalization	MMSE

Now A is chosen such that

$$A = \sqrt{\frac{E\left[|\bar{x}_m|^2\right]}{E\left[\left[\left|V_{\max}\frac{\ln\left[1+\frac{\mu|\bar{x}_m|}{V_{\max}}\right]}{\ln[1+\mu]}\right|\right]^2\right]}} \tag{8}$$

So by simply multiplying the conventional companding function with A, we can make sure that the average power of companded signal is unaltered.

3 Results and Discussion

To verify the performance of proposed companding technique, we considered the system as shown in Fig. 1 and set the parameters as listed in Table 1. As PAPR problem is severe for higher order modulations, we considered 16-QAM as the modulation technique over QPSK.

The complementary cumulative distribution function (CCDF) curves of companded and original signals have been presented in Fig. 2. We can observe that both conventional and modified μ-law companding techniques have similar PAPR performance.

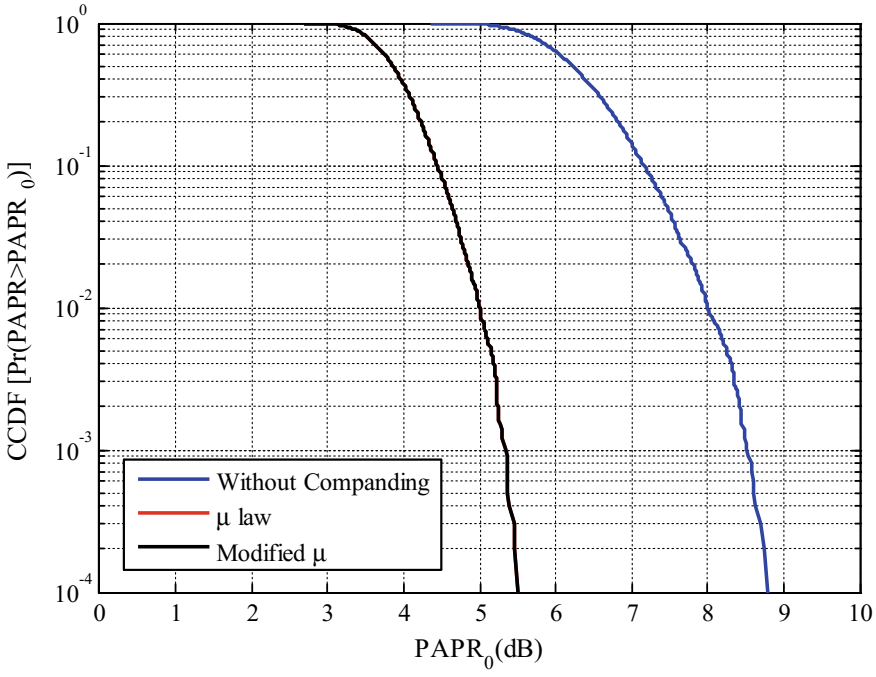

Fig. 2 CCDF curves of companded and original signals

To make sure that modified μ-law companding did not increase average signal power, we plotted waveforms of the companded and original signals in Fig. 3. From the figure, we can observe that μ-law companding increases the average signal power but modified μ-law companding technique does not increase the average signal power.

The power spectral density (PSD) curves of companded and original signals are shown in Fig. 4. We can observe that PSD of modified μ-law companding technique is closer to the original system without companding.

The BER curves of companded and original systems over AWGN channel are shown in Fig. 5. We can observe that the modified μ-law companding has similar BER performance as that of conventional μ-law companding.

The BER curves of companded and original systems over multipath Rayleigh fading Vehicular-A outdoor channel are shown in Fig. 6. We can observe that BER performance of modified μ-law companding outperforms the conventional μ-law companding. Comparison of BER values of companded and original systems at SNR $=$ 16 dB is given in Table 2.

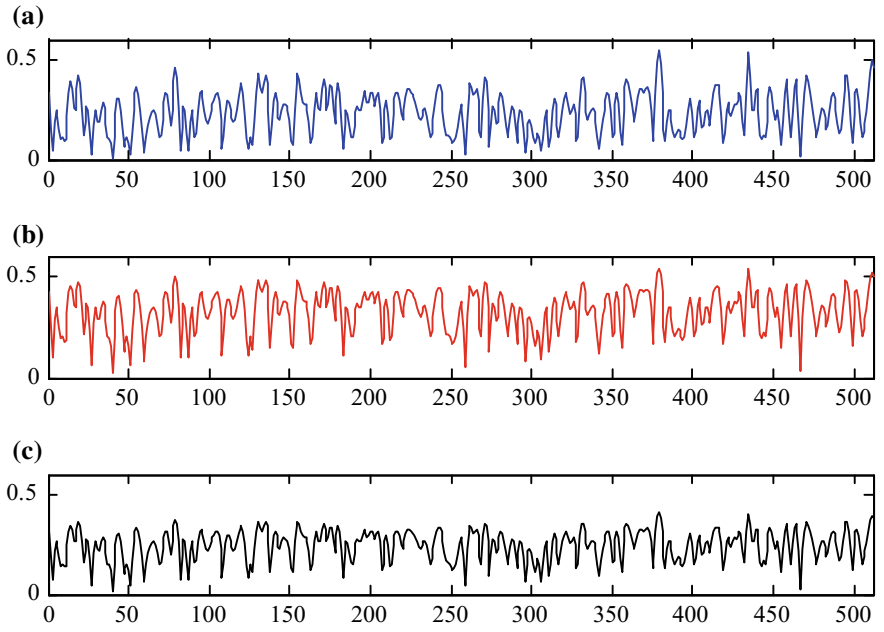

Fig. 3 Waveforms of **a** original signal, **b** μ-law companded signal, and **c** modified μ-law companded signal

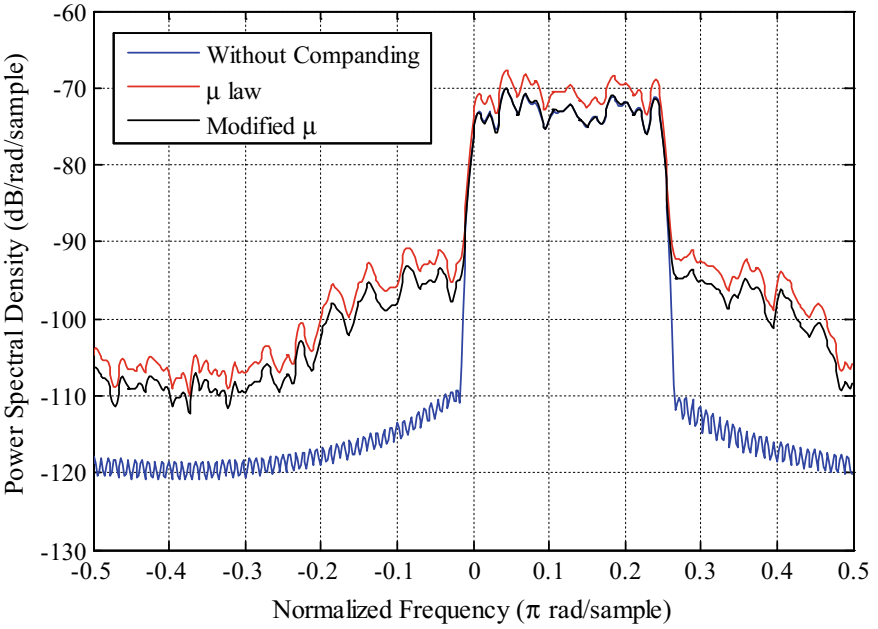

Fig. 4 PSDs of companded and original signals

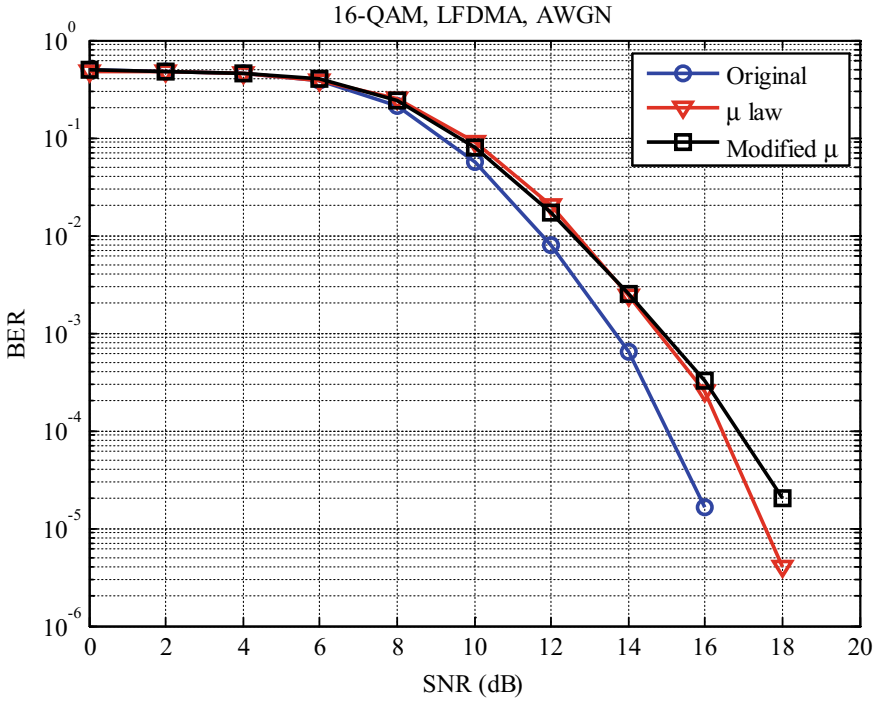

Fig. 5 BER curves of companded and original systems over AWGN channel

Table 2 Comparison of BER values

	BER values at SNR = 16 dB		
	Original	μ law	Modified μ
AWGN	0.000016	0.000248	0.000324
Veh-A	0.01238	0.08892	0.02242

4 Conclusions

Conventional μ-law companding technique provides good PAPR reduction but at the cost of increase in average signal power. In this paper, we modified μ-law companding transform to keep the average signal power unaltered. While there is no change in PAPR reduction when compared to conventional μ-law companding, the BER performance of modified μ-law companding outperforms the conventional technique when multipath Rayleigh fading channel is considered. Also, the modified μ-law companding technique has better PSD performance than the conventional technique. So the modified μ-law companding scheme is suitable to minimize PAPR in localized SC-FDMA systems for higher order modulations.

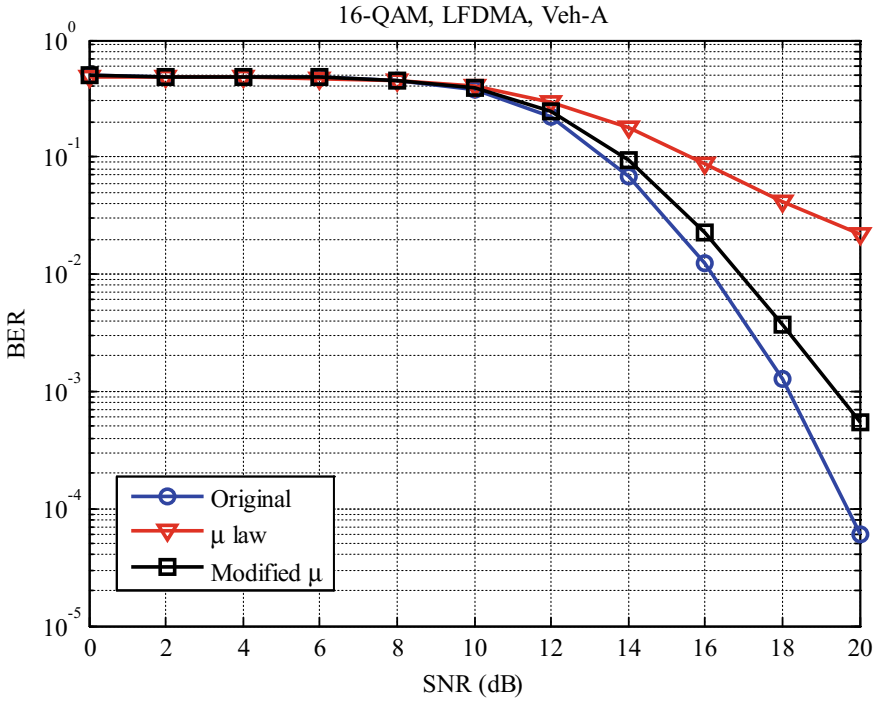

Fig. 6 BER curves of companded and original systems over Vehicular-A channel

References

1. Myung HG, Lim J, Goodman DJ (2006) Single carrier FDMA for uplink wireless transmission. IEEE Veh Technol Mag 1(3):30–38
2. Wunder G, Fischer RFH, Boche H, Litsyn S, No JS (2013) The PAPR problem in OFDM transmission: new directions for a long-lasting problem. IEEE Signal Process Mag 30(6):130–144
3. Li X, Cimini LJ (1998) Effect of clipping and filtering on the performance of OFDM. IEEE Commun Lett 2(5):131–133
4. Ji J, Ren G, Zhang H (2015) PAPR reduction of SC-FDMA signals via probabilistic pulse shaping. IEEE Trans Veh Technol 64(9):3999–4008
5. Wang L, Wu G, Dan L, Xiao Y (2011) A time-domain PTS without side information in SC-FDMA systems. In: 7th International conference on wireless communication network mobile computing pp 1–4, Wuhan, China
6. Sayed-Ahmed A, Shokair M, El-Rabaie ES (2012) PAPR reduction for LFDMA using a reduced complexity PTS scheme. In: 29th national radio science conference (NRSC), pp 515–522, Cairo, Egypt
7. Mohammad A, Zekry A, Newagy F (2012) A time domain SLM for PAPR reduction in SC-FDMA systems. In: IEEE global high tech congress on electronics, pp 143–147, Shenzhen, China
8. Duan Y, Li Y, Li Z, Liu S, Wu C (2012) A new SLM method with feedback searching for uplink SC-FDMA system. In: 8th IEEE international conference wireless communication, networking mobile computing, pp 1–4, Shanghai, China

9. Abd El-Samie FE, Al-kamali FS, Dessouky MI, Sallam BM, Shawki F (2010) Performance enhancement of SC-FDMA systems using a companding technique. Ann Telecommun 65(5):293–300
10. Hou J, Ge J, Zhai D, Li J (2010) Peak-to-average power ratio reduction of OFDM signals with nonlinear companding scheme. IEEE Trans Broadcast 56(2):258–262

Performance Analysis of Free Space Optical Communication System Using Different Modulation Schemes over Weak to Strong Atmospheric Turbulence Channels

Suman Malik and Prasant Kumar Sahu

Abstract In this paper, we have investigated the performance of an optical wireless communication system and reported the achievable BER and average channel capacity using different modulation schemes such as on-off keying (OOK), quadrature phase shift keying (QPSK), and pulse position modulation (PPM). A comparative study based on these three schemes has been studied for free space optics (FSO) system. The atmospheric channel is modeled for weak to strong atmospheric turbulences with combined effect of turbulence and pointing errors. Here, the FSO link is modeled as gamma–gamma (G–G) distribution and lognormal (LN) distribution channel models. A closed-form mathematical expression for average bit error rate (BER) and average channel capacity for various modulation schemes, viz., OOK, QPSK, and PPM, are presented, in order to analyze the performance of the FSO system. The simulated results for BER and channel capacity for different modulation techniques over gamma–gamma and lognormal distribution channel model are reported in this paper.

Keywords Atmospheric turbulence · Optical wireless communication (OWC) · Quadrature phase shift keying (QPSK) · Pulse position modulation (PPM) · Gamma–gamma distribution (G–G) · Lognormal distribution (LN)

1 Introduction

Over the last few years, free space optical communication (FSOC) has attracted attention due to its considerable advantages over radio frequency communication for variety of application such as license-free frequency spectrum, fast and ease of deployment, flexible transceiver architecture, highly secure sensitive data transfer,

S. Malik (✉) · P. K. Sahu
School of Electrical Sciences, Indian Institute of Technology Bhubaneswar, Arugul, Odisha, India
e-mail: Sm38@iitbbs.ac.in

P. K. Sahu
e-mail: pks@iitbbs.ac.in

© Springer Nature Singapore Pte Ltd. 2020

V. Janyani et al. (eds.), *Optical and Wireless Technologies*,
Lecture Notes in Electrical Engineering 546,
https://doi.org/10.1007/978-981-13-6159-3_41

fiber backup, immune to electromagnetic interference, and cost-effectiveness [1]. Large bandwidth and very high bit rate FSO system has been investigated for last mile access network, for metropolitan area network (MAN), and for local area network (LAN) [2]. However, a major challenge for FSO links-based communication is the atmospheric turbulence; a phenomenon occurs when the links undergo random change of air refractive index due to the variations in light intensity [3], temperature and pressure of the atmosphere. These inhomogeneities can cause random fluctuations in the intensity, phase, and amplitude of the received signal. These impairments can lead to increase the bit error probability in the link and reduce the channel capacity which limits the performance of the FSO system [4].

Many statistical distribution models have been proposed and studied to describe the intensity fluctuation caused by scintillation effect [5]. For weak turbulence strength scenarios, the lognormal distribution channel model is suitable [6], while gamma–gamma distribution channel model has been usually modeled as perfect distributions for weak to strong turbulence conditions [7]. Furthermore, KI, the negative exponential (NE), and K-distribution models are used for weak, moderate, and strong turbulence condition, respectively [8].

Various modulation formats significantly affect the performance of the FSO links with respect to the BER and channel capacity. There are many modulation schemes in FSO system like amplitude modulation, frequency modulation, and phase modulation [9]. Direct detection-based intensity modulation technique, that is, on-off-keying (OOK) [10] and pulse position modulation (PPM) [11] scheme, is widely used in optical applications due to design simplicity and inexpensiveness; however, it suffers due to poor bandwidth efficiency as both PPM and OOK techniques are extremely sensitive to atmospheric turbulence. Furthermore, another widely used system in communication is the quadrature phase shift keying (QPSK) [12]. QPSK has higher sensitivity and better ability to suppressed atmospheric turbulence.

In this work, the performance of FSO system has been studied by investigating the average bit error rate (BER) and channel capacity [13]. Various modulation schemes including on-off-keying (OOK), quadrature phase shift keying (QPSK), and pulse position modulation (PPM) are portrayed in the presence of atmospheric turbulence effect over a gamma–gamma and lognormal distribution channel. The closed-form mathematical expression for each modulation format and statistical distribution model is presented, and the simulated results are also reported in this paper. The FSO system is investigated for finding out a suitable modulation technique that is best fit for free space optical communication system for a particular distribution channel model.

The paper is organized as follows: Sect. 2 discusses the system and channel model used. In Sect. 3, basic modulation techniques are presented, while in Sect. 4, the expression for BER and channel capacity of the system is derived and presented. Section 5 describes the numerical results with simulation outcomes. Finally, the conclusion is presented in Sect. 6.

2 System and Channel Model

2.1 System Model

A source produces information waveforms which are then superposed onto an optical carrier following the process of modulation. The resultant optical signal is transmitted through air. After undergoing the influence of time-dispersive channel and ambient light, optical signal is directly converted into photocurrent at the detector. The receiver processes the detected electrical current to recover the original transmitted information from which we can obtain the BER, Q-factor of the received signal (Fig. 1).

The received electrical signal at the receiver is given by [9]

$$\mathrm{Y} = \mathrm{h}\,\gamma\,\mathrm{P_t}\,\mathrm{x} + \mathrm{n} \tag{1}$$

where h represents the channel state that distributed by gamma–gamma or lognormal model, γ is the detector responsivity, P_t is the transmitted power, x is the transmitted signal, and n is additive white Gaussian noise with zero mean and $N_o/2$ variance. Optical intensity fluctuations resulting from atmospheric loss, turbulence, and fading are related to the channel state h model

$$\mathrm{h} = h_l\,\mathrm{h_s h_p} \tag{2}$$

where h_l is the attenuation due to path loss, h_s due to scintillation effect and h_p due to geometric and pointing errors.

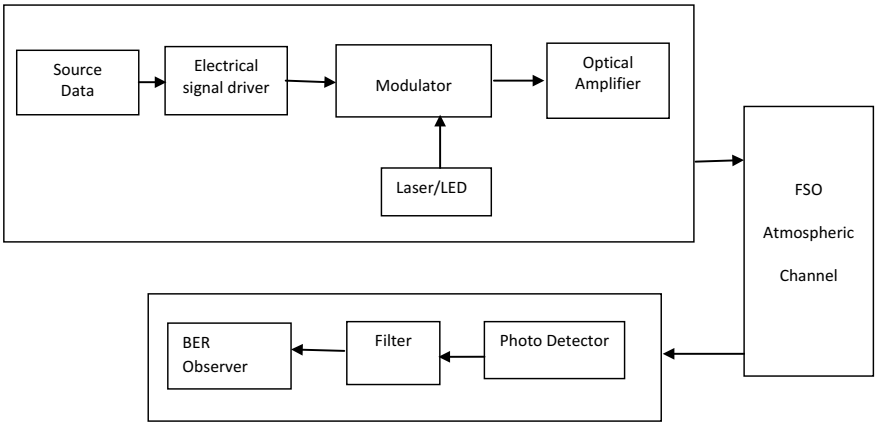

Fig. 1 Block diagram of FSO system

2.2 Gamma–Gamma Distribution Channel Model

The attenuation that an optical signal experiences traveling through air is due to the atmospheric turbulence effect. Based on the refractive index structure parameter C_n^2, the turbulence level is classified as weak $\left(C_n^2 = 10^{-16}\right)$, moderate $\left(C_n^2 = 10^{-14}\right)$ and strong $\left(C_n^2 = 10^{-13}\right)$. Various distribution functions are modeled for weak, moderate, and strong turbulence channels.

Gamma–gamma (G–G) distribution model is an appropriate fading model over a wide range and for moderate to strong turbulence conditions. G–G distribution is the product of two random variables of large-scale and small-scale eddies. The PDF can be expressed as [14]

$$\mathrm{f(I)} = \frac{2(\alpha\beta)^{\frac{\alpha+\beta}{2}}}{\Gamma(\alpha)\Gamma(\beta)} \mathrm{I}^{\left(\frac{\alpha+\beta}{2}-1\right)} \mathrm{K}_{\alpha-\beta}\left(2\sqrt{\alpha\beta \mathrm{I}}\right) \tag{3}$$

where I is the light signal intensity, $\Gamma(.)$ is the Gamma function, and $K_{\alpha-\beta}(.)$ is the $\alpha-\beta$ order modified Bessel function of second kind. α and β are parameters related to the large-scale and small-scale optical signal intensity fluctuation, which are given as

$$\begin{aligned} \alpha &= \left[\exp\left(\frac{0.49\sigma_{\mathrm{R}}^2}{\left(1 + 1.11\sigma_{\mathrm{R}}^{12/5}\right)^{7/6}} \right) - 1 \right]^{-1}; \\ \beta &= \left[\exp\left(\frac{0.51\sigma_{\mathrm{R}}^2}{\left(1 + 0.69\sigma_{\mathrm{R}}^{12/5}\right)^{5/6}} \right) - 1 \right]^{-1} \end{aligned} \tag{4}$$

where σ_R^2 represents Rytov variance parameter related to scintillation index. For terrestrial application, it is given by [15]

$$\sigma_{\mathrm{R}}^2 = 1.23\, \mathrm{C_n^2 K^{7/6} L^{11/6}} \tag{5}$$

where $\mathrm{K} = 2\pi/\lambda$ is the wave number, λ is wavelength, L is the link range, and C_n^2 is the refractive index structure parameter that is depend on wind speed and altitude of a particular location.

2.3 Lognormal Distribution Channel Model

Lognormal distribution is adopted for weak to moderate atmospheric turbulence conditions over short distance FSO links. It is a continuous probability distribution

of a random variable whose logarithm is normally distributed. The PDF of lognormal distribution is given by [16]

$$P(I) = \frac{1}{\sqrt{2\pi\sigma_R^2}}\frac{1}{I}\exp\left\{-\frac{\left(\ln(I/I_o) + \sigma_R^2/2\right)^2}{2\sigma_R^2}\right\} \tag{6}$$

where I_o is the irradiance in the absence of turbulence, and σ_R^2 is scintillation index parameter.

3 Basic Modulation Techniques

There are different kinds of modulation techniques, which are suitable for FSO communication system. In this section, we will discuss the SNR and BER under various modulation schemes without considering the atmospheric turbulence effect.

3.1 OOK Modulation

On-off keying (OOK) technique is the simplest modulation scheme employed in commercial terrestrial FSO communication system as it is insusceptible to non-linearities of the laser and external modulator. OOK modulation can use either NRZ or RZ pulse format. For NRZ-OOK, the signal is defined as $S_{ook}(t) = A\left[\sum_{n=-\infty}^{\infty} a_n g_t(t - nT_b)\right] cosw_c t$. Here, the value of a_n is 0 or 1, g_t represents nonreturn-to-zero pulse, and T_b is the symbol interval. The probability of error or BER for NRZ-OOK coded optical data can be expressed as a function of the signal-to-noise ratio (SNR) as follows [17]:

$$\text{BER}_{\text{NRZ-OOK}} \text{ or } P_{e\,\text{NRZ-OOK}} = \frac{1}{2}\text{erfc}\left(\frac{1}{2\sqrt{2}}\sqrt{\text{SNR}}\right) = Q\left(\frac{1}{2}\sqrt{\text{SNR}}\right) \tag{7}$$

In RZ-OOK, the required SNR is equal to half of "−3 dB" of required SNR of regular NRZ-OOK to achieve the same BER performance with the expense of doubling bandwidth. The BER for RZ-OOK can be expressed as a function of the SNR as follows:

$$\text{BER}_{\text{RZ-OOK}} \text{ or } P_{e\,\text{RZ-OOK}} = \frac{1}{2}\text{erfc}\left(\frac{1}{2}\sqrt{\text{SNR}}\right) \tag{8}$$

3.2 QPSK Modulation

QPSK is the best modulation scheme compare to other phase modulation schemes. In QPSK technique, two bits are grouped together to form signal and four particular phases of signals are transmitted and carrier is phase modulated. The spectral efficiency can be further improved by QPSK modulation. The BER for QPSK can be expressed as [12]:

$$\mathrm{BER_{QPSK}\ or\ P_{e\ QPSK}} = \mathrm{erfc}\left(\sqrt{\mathrm{SNR}}\right) \tag{9}$$

3.3 PPM Modulation (M-PPM)

In this modulation technique, each pulse of laser can be used to represent one or more bits of information by its position in time relative to start of a symbol whose duration is identical to that of information bits it contains. Bits in block encoding are transmitted in blocks instead of one at a time. Optical block encoding is achieved by converting each word of "b" bits into one of "$\mathrm{M} = 2^b$" optical fields for transmission. Since "M" is the possible pulse positions code for "b" bits of information in PPM scheme. The symbol intervals, T_w, are divided into M time disjoint time slot, and the optical pulse is sent in one of these M time slots while remaining $\mathrm{M} - 1$ time slots are empty. For bit rate R_b bit per second, the symbol interval having a duration of $T_w = \mathrm{b}/R_b$, and time slot $T_s = T_w/M$. The BER of the system can be derived as [18]

$$\mathrm{BER_{PPM}} = \frac{1}{2}\mathrm{erfc}\left(\frac{1}{2\sqrt{2}}\sqrt{\mathrm{SNR} * (\mathrm{M}/2)\log_2 \mathrm{M}}\right) \tag{10}$$

4 BER and Average Channel Capacity Under Atmospheric Turbulence

4.1 BER Comparison of Various Modulation Techniques

BER performance is severely affected due to intensity fluctuation in the FSO channel. Therefore, taking detector noise and channel turbulence into account, the average bit error rate (BER) on the receiving terminal can be described as [19]

$$\mathrm{P_e} = \int_0^{\propto} \mathrm{BER\ f(I)dI} \tag{11}$$

For combination of OOK modulation technique and gamma–gamma channel model, average BER can be computed by using Eqs. (3) and (7)

$$P_{e\,OOK}(I) = \int_0^{\infty} BER_{NRZ\text{-}OOK} f(I)\, dI$$
$$= \int_0^{\infty} \frac{1}{2}\text{erfc}\left(\frac{1}{2\sqrt{2}}\sqrt{SNR}\right)\frac{2(\alpha\beta)^{\frac{\alpha+\beta}{2}}}{\Gamma(\alpha)\Gamma(\beta)} I^{\left(\frac{\alpha+\beta}{2}-1\right)} K_{\alpha-\beta}\left(2\sqrt{\alpha\beta I}\right) dI \quad (12)$$

For QPSK modulation schemes average BER can be expressed by using Eqs. (3) and (9)

$$P_{e\,QPSK}(I) = \int_0^{\infty} BER_{QPSK} f(I) dI$$
$$= \int_0^{\infty} \text{erfc}\left(\sqrt{SNR}\right)\frac{2(\alpha\beta)^{\frac{\alpha+\beta}{2}}}{\Gamma(\alpha)\Gamma(\beta)} I^{\left(\frac{\alpha+\beta}{2}-1\right)} K_{\alpha-\beta}\left(2\sqrt{\alpha\beta I}\right) dI \quad (13)$$

For PPM modulation schemes average BER can be expressed by using Eqs. (3) and (10)

$$P_{e\,PPM}(I) = \int_0^{\infty} BER_{PPM} f(I) dI$$
$$= \int_0^{\infty} \frac{1}{2}\text{erfc}\left(\frac{1}{2\sqrt{2}}\sqrt{SNR*(M/2)\log_2 M}\right)\frac{2(\alpha\beta)^{\frac{\alpha+\beta}{2}}}{\Gamma(\alpha)\Gamma(\beta)} I^{\left(\frac{\alpha+\beta}{2}-1\right)} K_{\alpha-\beta}\left(2\sqrt{\alpha\beta I}\right) dI \quad (14)$$

Similarly, average BER for lognormal channel model with different modulation techniques by using Eqs. (6), (7), (9) and (10)

$$P_{e\,OOK}(I) = \int_0^{\infty} BER_{NRZ\text{-}OOK} P(I) dI$$
$$= \int_0^{\infty} \frac{1}{2}\text{erfc}\left(\frac{1}{2\sqrt{2}}\sqrt{SNR}\right)\frac{1}{\sqrt{2\pi\sigma_R^2}}\frac{1}{I}\exp\left\{-\frac{\left(\ln(I/I_o)+\sigma_R^2/2\right)^2}{2\sigma_R^2}\right\} dI \quad (15)$$

$$P_{e\,QPSK}(I) = \int_0^{\propto} BER_{QPSK} P(I) dI$$

$$= \int_0^{\propto} \text{erfc}\left(\sqrt{SNR}\right) \frac{1}{\sqrt{2\pi\sigma_R^2}} \frac{1}{I} \exp\left\{ -\frac{\left(\ln(I/I_o) + \sigma_R^2/2\right)^2}{2\sigma_R^2} \right\} dI \quad (16)$$

$$P_{e\,PPM}(I) = \int_0^{\propto} BER_{PPM} P(I) dI$$

$$= \int_0^{\propto} \frac{1}{2} \text{erfc}\left(\frac{1}{2\sqrt{2}} \sqrt{SNR^*(M/2)\log_2 M} \right)$$

$$\frac{1}{\sqrt{2\pi\sigma_R^2}} \frac{1}{I} \exp\left\{ -\frac{\left(\ln(I/I_o) + \sigma_R^2/2\right)^2}{2\sigma_R^2} \right\} dI \quad (17)$$

4.2 Average Channel Capacity Comparison of Various Modulation Techniques

The channel capacity is the most common parameter used to evaluate the performance of FSO communication over weak to strong atmospheric channels. It is the one that decides the information rate as well as the probability of error. For a different modulation schemes OOK, QPSK, and PPM over gamma–gamma and lognormal channel model, it can be estimated as per Eqs. (18) and (19) [20]:

$$\langle C \rangle_{OOK,\,QPSK,\,PPM} = \int_0^{\propto} B \ln(1 + SNR) f(I) dI$$

$$= \int_0^{\propto} B \ln(1 + SNR) \frac{2(\alpha\beta)^{\frac{\alpha+\beta}{2}}}{\Gamma(\alpha)\Gamma(\beta)} I^{\left(\frac{\alpha+\beta}{2}-1\right)} K_{\alpha-\beta}\left(2\sqrt{\alpha\beta I}\right) dI \quad (18)$$

$$\langle C \rangle_{OOK,\,QPSK,\,PPM} = \int_0^{\propto} B \ln(1 + SNR) P(I) dI$$

$$= \int_0^{\propto} B \ln(1 + SNR) \frac{1}{\sqrt{2\pi\sigma_R^2}} \frac{1}{I} \exp\left\{ -\frac{\left(\ln(I/I_o) + \sigma_R^2/2\right)^2}{2\sigma_R^2} \right\} dI \quad (19)$$

5 Simulated Results and Discussion

We have presented comprehensive results based on mathematical expressions of three modulation schemes and weak to strong turbulence channel model. Considering intensity scintillation when talk about the BER and capacity performance of FSO system. The FSO system parameters considered in the numerical evaluations and for MATLAB based simulation are shown in Table 1.

Simulated results of BER performance for NRZ-OOK, QPSK, and PPM with gamma–gamma and lognormal distributed channel model is presented in Figs. 2 and 3. It is clearly depicted that the BER for all the considered modulation schemes shows an improvement with increased SNR. Under gamma–gamma distribution channel model, among the different modulation techniques considered, the best performance is obtained from QPSK. When SNR is 50 dB achieved, the BER performance of QPSK modulation is better than PPM and OOK modulation as it exhibits a BER of 10^{-22}, 10^{-8} and 10^{-6} for the mentioned modulation schemes, respectively. In other words, QPSK requires less SNR than other schemes for attaining a particular BER.

Under lognormal distribution channel model, it is clear that the performance of the three modulation schemes offers an improved BER. From Fig. 3, we can see that the BER values are 10^{-23} for QPSK, 10^{-9} for OOK while 10^{-8} for PPM at 50 dB SNR. Although under weak turbulence channel, i.e., lognormal channel, the performance of QPSK still appears to be better than other schemes

Table 1 Simulation parameters

Parameter	Value
Modulation mode	NRZ-OOK, QPSK, PPM
Channel model	Gamma–gamma, lognormal
Wavelength λ	1550 nm
Maximum optical power	10 mW
Link range	2 km
Efficiency	0.8
Responsivity of PIN	1A/W
Attenuation of FSO link	23 dB/km
Modulation bandwidth	200 MHz
Refractive index structure parameter C_n^2	$1.7 \times 10^{-14}\,\mathrm{m}^{-2/3}$

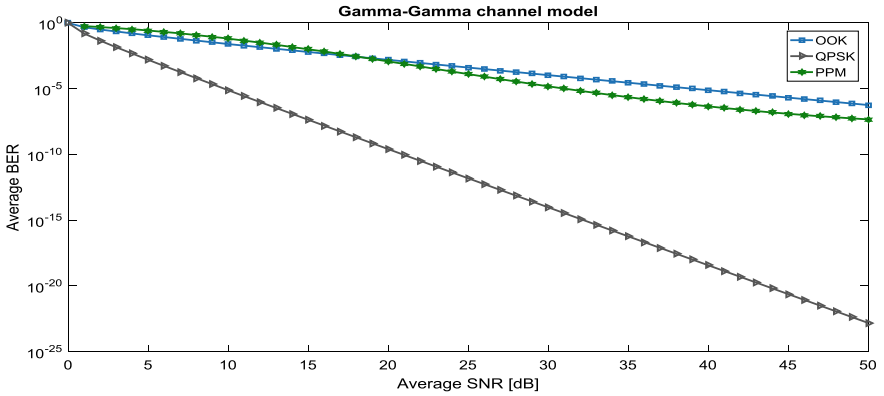

Fig. 2 BER versus average SNR with gamma–gamma channel model and L = 2 km for OOK, QPSK, and PPM modulation technique

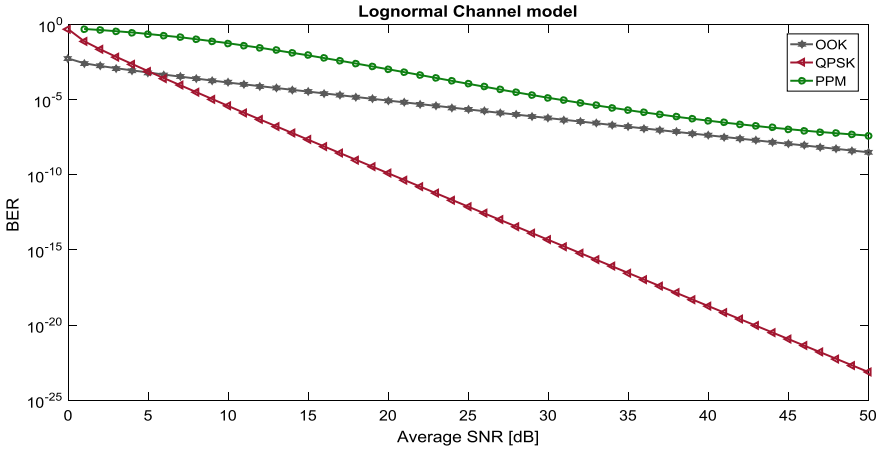

Fig. 3 BER versus average SNR with lognormal channel model and L = 2 km for OOK, QPSK, and PPM modulation technique

The average channel capacity under moderate to strong turbulence channel, i.e., gamma–gamma channel model and weak turbulence, i.e., lognormal channel model for various modulation schemes is shown in Figs. 4 and 5, respectively. From the figure, it is inferred that the average capacity increases along with average SNR. It

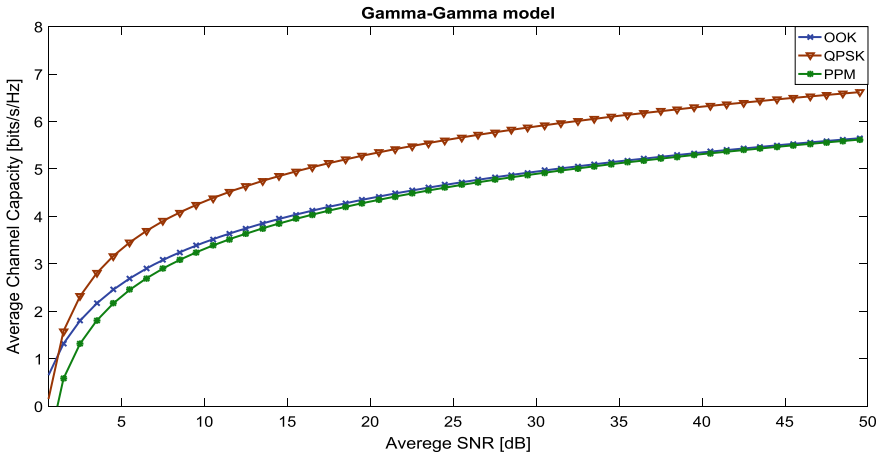

Fig. 4 Channel capacity versus average SNR with gamma–gamma channel model and L = 2 km for OOK, QPSK, and PPM modulation technique

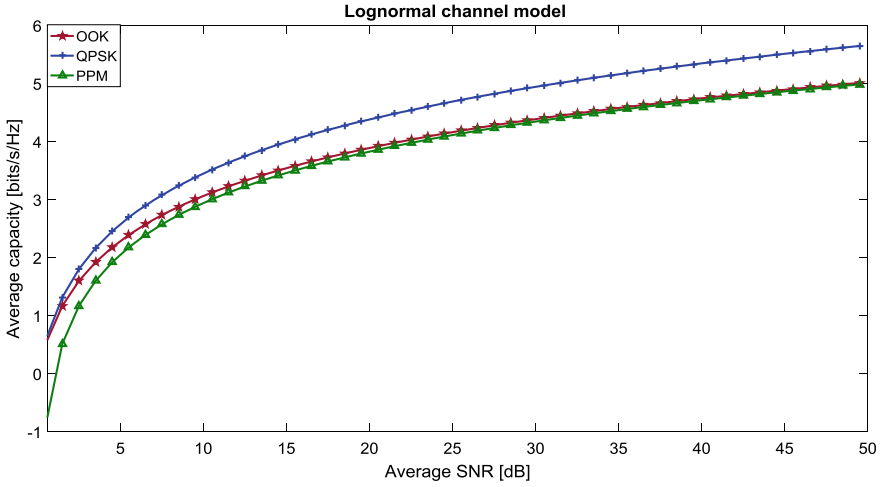

Fig. 5 Channel capacity versus average SNR with lognormal channel model and L = 2 km for OOK, QPSK, and PPM modulation technique

is observed that QPSK provides the higher spectral efficiency or channel capacity of 6 bits/s/Hz compared to other two modulation techniques, OOK and PPM for both the considered atmospheric channel model.

6 Conclusion

In this paper, the system performance for an FSO communication system over weak to strong turbulence channel is being investigated. The different modulation formats used in FSO system were studied. The closed-form expression for the BER and average channel capacity of the different modulation techniques such as NRZ-OOK, QPSK, and PPM were derived. The average channel capacity and BER of the FSO system using various modulation schemes were analyzed and compared. From the simulation results, it was observed that in weak and strong turbulent, the OOK and PPM formats still have more or less same BER performance and average channel capacity. However, for weak to strong turbulence conditions, QPSK modulation shows higher resistance to turbulence and provides the best performance and highest average channel capacity compared to other modulation formats.

References

1. Khalighi MA, Uyasal M (2014) A survey on free space communication, a communication theory perspective. J Commun Surv Tutor (IEEE) 16:2231–2258
2. Arnon S, Uyasal M, Ghassemlooy Z, Xu ZY, Cheng ZI (2015) Guest editorial optical wireless communication. J Sel Areas Commun (IEEE) 33:1233–1237
3. Prokes A (2009) Atmospheric effects on availability of free space optics system. Opt Eng (Elsevier) 48(6)
4. Farid AA, Hranilovic S (2007) Outage capacity optimization for free space optical links with pointing errors. J Lightwave Technol (Elsevier) 25:1702–1710
5. Muhammad SS, Kohldorfer P, Leitgeb E (2005) Channel modelling for terrestrial free space optical links. In: Proceedings of international conference on transparent optical networks, vol 1. IEEE, pp 407–410
6. Nistazakis HE, Karagianni EA, Tsigopoulos AD, Fafalios ME, Tombras GS (2009) Average capacity of optical wireless communication systems over atmospheric turbulence channels. J Lightwave Technol (IEEE) 27(8)
7. Sandalidis HG, Tsiftsisand TA, Karagiannidis GK (2009) Optical wireless communications with heterodyne detection over turbulence channels with pointing errors. J Lightwave Technol (IEEE) 27(20)
8. Anabarasi K, Hemanth C, Sangeetha RG (2017) A review on channel models in free space optical communication. J Opt Laser Technol (Elsevier) 97:161–171
9. Prabu K, Sriram D, Srinivas T (2014) Performance analysis of FSO links under strong atmospheric turbulence conditions using various modulation schemes. J Optik (Elsevier) 125:5573–5581
10. Kwok CH, Penty RV, White IH (2008) Link reliability improvement for optical wireless communication systems with temporal-domain diversity reception. Photonics Technol Lett (IEEE) 20(9)
11. Sethakaset U, Gulliver TA (2008) Performance of differential pulse-position modulation (DPPM) with concatenated coding over optical wireless communications. J IET Commun 2(1):45–52
12. Huang Z, Wang Z, Huang M, Li W, Lin T, He P, Ji Y (2017) Hybrid optical wireless network for future SAGO-integrated communication based on FSO/VLC heterogeneous interconnection. Photonics J (IEEE) 9(2)

13. Niu M, Cheng J, Holzman JF (2013) MIMO architecture for coherent optical wireless communication: system design and performance. OSA J Opt Commun Netw 5(5)
14. Gao J, Zhang Y, Cheng M, Zhu Y, Hu Z (2016) Average capacity of ground-to-train wireless optical communication links in the non-Kolmogorov and gamma–gamma distribution turbulence with pointing errors. J Opt Commun (Elsevier) 147–153
15. Handur MR, Ndjaver KM, Nyirend CN, Olwal TO (2016) Determining the feasibility of free space optical communication in Namibia. J Opt Commun (Elsevier) 366:425–430
16. Yang L, Chang J, Holzman JF (2013) Electrical SNR optimized detection threshold for OOK IM/DD optical wireless communication. In: Workshop on information theory
17. Wang K, Nirmalathas A, Lim C, Skafidas E (2011) High-speed optical wireless communication system for indoor applications. Photonics Technol Lett (IEEE) 23(8)
18. Pham HT, Dang NT (2012) A comprehensive model for performance analysis of APD-based FSO system using M-PPM signalling in atmospheric turbulence. REV J Electron Commun 2(3–4)
19. Zhang Y, Yang Y, Hu B, Yu L, Hu ZD (2017) Average BER and outage probability of the ground-to-train OWC link in turbulence with rain. J Opt Commun (Elsevier) 85–90
20. Alipour A, Mir A, Sheikhi A (2016) Ultra high capacity inter-satellite optical wireless communication system using different optimized modulation formats. J Optik (Elsevier) 8135–8143

Investigation of Nonlinear Effects in Electronically Pattern Reconfigurable Hexagon-Shaped Loop Antenna

Arun Pant, Lalit Kumar and Manoj Singh Parihar

Abstract Antenna characteristics reconfiguration techniques utilizing solid-state devices such as PIN diodes suffer from nonlinear effects and are susceptible to performance degradation at higher power levels producing harmonic and intermodulation distortion products. This research work studies effects of the nonlinear nature diodes used for switching in the proposed pattern reconfigurable antenna. A study has been done to identify the maximum power level up to which the device can efficiently work in the linear region. Simulated results present the strength of the harmonic and intermodulation products under different input power levels for the antenna. The antenna is found to work efficiently up to 25 dBm input power level where the intermodulation and harmonic signals strengths are within the permissible level.

Keywords Pattern reconfigurable antenna · Intermodulation distortion · Harmonic distortion · Gain compression point · Third-order input intercepts · Nonlinearity · PIN diodes

1 Introduction

Pattern reconfigurable antennas in modern communication scenario have become attractive because of their ability to overcome interferences by flexibly rotating their radiation pattern in the desired direction, thereby minimizing noise and achieving higher SNR. They are highly energy efficient compared to traditional antennas as

A. Pant (✉) · L. Kumar · M. S. Parihar
Department of Electronics & Communication Engineering, PDPM Indian Institute of Information Technology, Design & Manufacturing, Jabalpur, India
e-mail: arunpant92@gmail.com

L. Kumar
e-mail: lalit.biet@gmail.com

M. S. Parihar
e-mail: mparihar@iiitdmj.ac.in

© Springer Nature Singapore Pte Ltd. 2020

V. Janyani et al. (eds.), *Optical and Wireless Technologies*,
Lecture Notes in Electrical Engineering 546,
https://doi.org/10.1007/978-981-13-6159-3_42

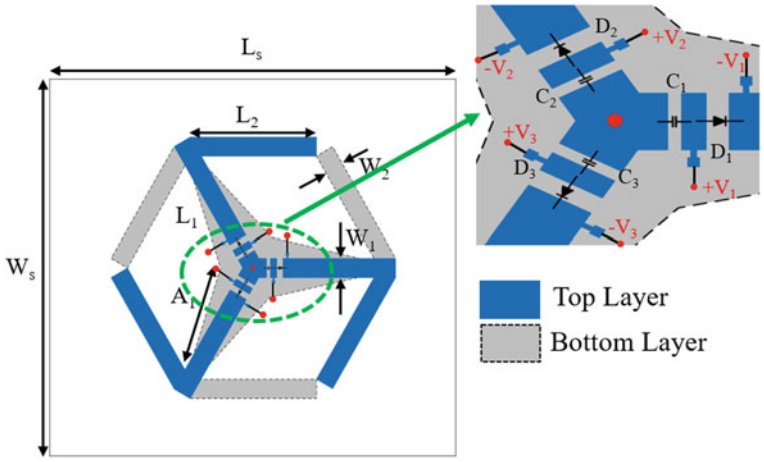

Fig. 1 Reconfigurable antenna geometry where parameters are $W_s = 60$ mm, $L_s = 60$ mm, $L_1 = 18.41$ mm, $L_2 = 15.795$ mm, $W_1 = 3.54$ mm, $W_2 = 2.76$ mm, $B_1 = 11.88$ mm with biasing network highlighted in inset

they transmit power only in the desired direction. Pattern reconfigurable antennas have become advantageous in beam steering, direction finding, and pattern diversity applications [1]. The surface current flow on the radiator is intentionally modified to achieve radiation pattern reconfigurability. RF antenna's switching is being done by techniques based on optical switches using photodiodes, electrical switches using PIN and varactor diodes, or RF microelectromechanical switches (MEMS). Recently reported pattern reconfigurable antennas in literature have used parasitic elements in addition to driven element to redirect radiation known as parasitic array radiator [2], orthogonally placed crossed dipoles to switch beam [3], patch ring slot combination [4], Yagi Uda structures [5], monopole loop combinations [6], dual-feed structures, etc.

Out of these techniques using the PIN or varactor diodes is popular because of its ease in implementation and fast switching time (ns), compared to optical switches which additionally require a laser source to excite the photodiode [1]. Also, they are reliable, stable compared to MEMS which are prone to mechanical fatigue. The nonlinear effects of the solid-state device contrast the realization of PIN diode switches in reconfigurable antennas. When the antenna is functioning in the real communication environment, many nonlinear effects, e.g., harmonic distortion, intermodulation distortion, and gain compression, are introduced. Also, these devices require additional DC biasing network which may interfere with RF supply and cause losses in the system. Inductor and capacitor elements are also needed in the antenna to ensure proper isolation; this leads to overall complication in the design of antenna and all these aspects need to be considered carefully.

Nonlinear effects aggravate with increasing power levels. Nonlinear effects are more significant at transmitter end, since the power supplied is higher than the receiver

end [1, 7]. Hence, a proper study of these nonlinear effects in reconfigurable antennas become extremely important because these distortions may hamper the proper functioning of the antenna. Many research papers concerning these nonlinear aspects of reconfigurable antennas [1, 7–9] and EBG-based antenna have been published in the literature [10]. Here, in this work, the nonlinear effects of PIN diodes used for switching in a pattern reconfigurable antenna were studied. Linear region operation power levels for the diode, harmonic, and intermodulation signal strengths and 1 dB gain compression point for a receiver placed in the far-field region are simulated.

2 Antenna Geometry and Operation

A square-shaped FR-4 epoxy substrate with side 60 mm, height ($h = 1.5$ mm), thickness ($t = 0.035$ mm), dielectric constant ($\varepsilon_r = 4.3$), and loss tangent ($\delta_d = 0.025$) is used for the microstrip antenna realization. Three dipoles of length (L_2) 15.795 mm, which is approximately ($0.24\lambda_{ef}$), have been arranged to make an Alford-type loop shape. The antenna is fed coaxially at the center, three ($0.27\lambda_{ef}$) length transmission lines feed the dipoles. For impedance matching, a tapered balun is designed at the bottom surface, dimensions of which have been achieved by optimization. For switching, Skyworks SMP1340 series PIN diodes [11] with ON state impedance 0.85 Ω and OFF state capacitance 0.21 pF, parasitic inductance 0.7 nH have been used in the reconfigurable antenna. The antenna structure is shown in Fig. 1.

Appropriate bias lines have been designed for DC biasing. In this work, a 10 V supply is connected across each diode termed V_1, V_2, and V_3. 8 nH inductors and 3.75 pF capacitors have been used to ensure isolation of DC feed line from RF feed and vice versa. Depending upon which PIN diode is ON, the antenna operates in six different modes. Modes 1, 3, and 5 correspond to the case when only one switch is active, i.e., D_1, D_2, and D_3, respectively, and modes 2, 4, and 6 correspond to the case when any of the two switches are active, i.e., $D_1\&D_2$, $D_2\&D_3$, and $D_3\&D_1$, respectively.

Depending upon which switch is active, current flow in antenna radiators is varied, and as a result, electromagnetic fields around the antenna are changed, consequentially leading to rotation of radiation beam of the antenna. For simulations, CST microwave studio package 2014 was used. Simulated VSWR and radiation pattern are given in Figs. 2 and 3. The proposed reconfigurable antenna successfully rotates the radiation beam at 60° intervals in entire azimuth plane of the antenna, i.e., XY plane. A maximum gain of 3.1 dB is achieved in cases when a single diode is ON at 2.5 GHz, and a good impedance bandwidth from 2.33 to 2.58 GHz is obtained. Gain pattern is in Fig. 3g. When any two diodes are ON, the gain gets lowered to 1.63 dB at 2.35 GHz as radiation pattern covers larger angular bandwidth between the two dipoles.

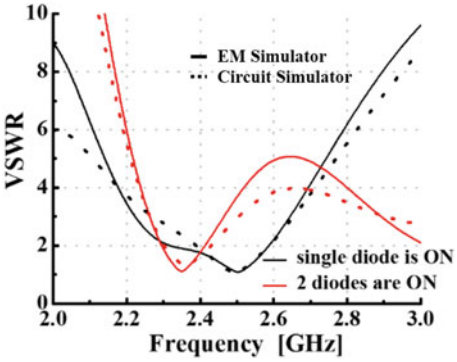

Fig. 2 VSWR of antenna when **a** single diode is turned ON, **b** any two diodes are turned ON where solid and dotted lines present EM simulation and circuit simulation results, respectively

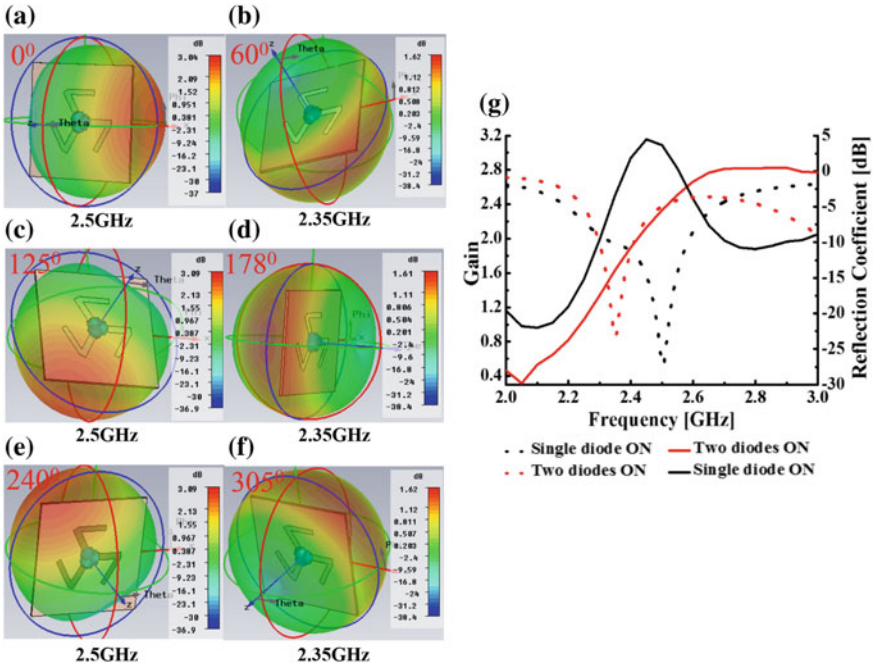

Fig. 3 Radiation pattern of antenna in azimuth plane XY ($\theta = 90°$) when diode **a** D_1 is ON, **b** D_1 and D_2 are ON, **c** D_2 is ON, **d** D_2 and D_3 are ON, **e** D_3 is ON, **f** D_3 and D_1 are ON, **g** plot showing gain pattern and reflection coefficient of antenna

3 Behavior at Higher Input Power Levels

This simulation was done in ADS circuit simulator 2014 [12] along with CST microwave studio package 2014. As power across the diode increases, the nonlinear behavior of the diode starts varying with power, i.e., the impedance of the diode starts varying with power. As a result, the matching degrades and reflection coefficient moves above the 10 dBm level. At lower power levels, the S-parameters of the device are stable but become highly susceptible to increasing power levels. The simulated results are in Figs. 4 and 5.

When only one diode is ON, and the RF power supplied to the antenna is increased above 20 dBm, due to diode nonlinearity and impedance mismatch, the antenna performance degrades. However, the antenna functions linearly up to 20 dBm, i.e., 0.1 W. But when any two diodes are ON, here diodes D_2 and D_3 are ON, the RF power supplied gets divided between the two parallel placed diodes. Hence, effective power across each diode is halved, and it lets the antenna operate linearly up to 30

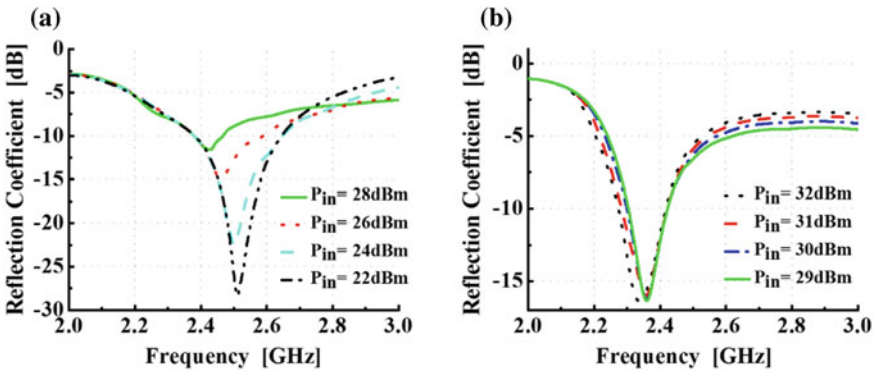

Fig. 4 Variation in reflection coefficient when **a** any two diodes are ON, **b** single diode is turned ON at different input power levels

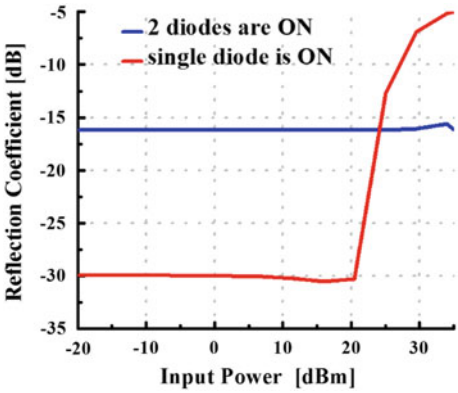

Fig. 5 Plot showing variation in reflection coefficient with input power

dBm power level, above which a slight degradation happens in reflection coefficient. Ideally, twice the power is needed in the case when two diodes are ON compared to the case when a single diode is ON, which is higher by 3 dBm than the power level at which single diode operation degraded significantly. Simulation yielded similar results.

4 Harmonic Simulations

4.1 Two-Tone Simulation Setup

Figure 6 shows the simulation setup. For the two-tone simulation, two excitation signals at frequencies of 2.35 and 2.5 GHz were combined by a power combiner (Wilkinson Power Divider) and then fed to the transmitter antenna. A dipole antenna placed in the far-field region of the transmitter antenna, such that its polarization is same as of transmitter antenna, received the radiated fields.

4.2 Simulation Results

The results presented in this paper are only for the case when D_1 is turned ON and are shown in Fig. 7a, b for different input power levels. The bias voltages for this are $V_1 = +10$ V, $V_2 = -10$ V, and $V_3 = -10$ V. All these simulations were done in Agilent ADS circuit simulator 2014 [11].

Case 1. When at the transmitter end, an input power of 10 dBm (0.01 W) was supplied, and at the receiver antenna, highest signal power detected was −12 dBm. Therefore, the received power did not generate significant harmonic and intermod-

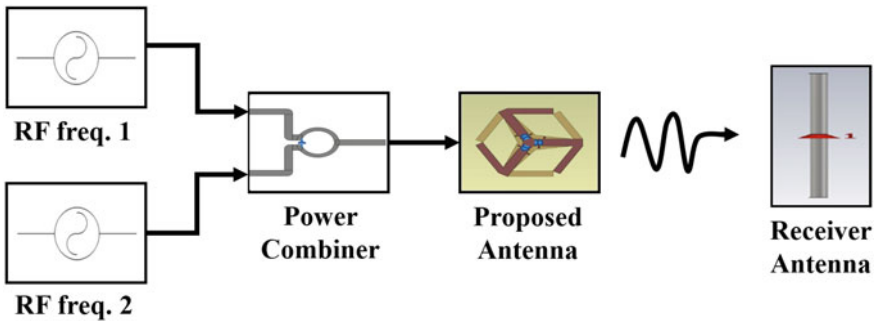

Fig. 6 Block diagram showing two-tone simulation setup

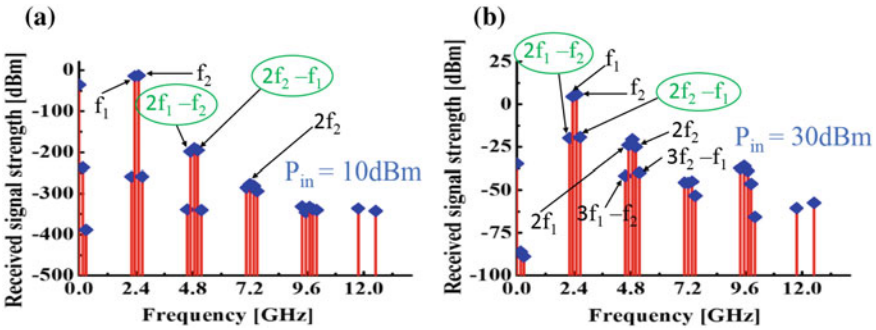

Fig. 7 Received spectrum of pattern reconfigurable antenna at the receiver at **a** 10 dBm, **b** 30 dBm input power levels

Table 1 Power received at fundamentals, second harmonics, and third-order intermodulation points on the receiver end

Signal generator power (dBm)	Received power at fundamental f_1 (dBm)	Received power at fundamental f_2 (dBm)	Received power at first harmonic $2f_1$ (dBm)	Received power at second harmonic $2f_2$ (dBm)	Received power at third intermodulation point $2f_1 - f_2$ (dBm)	Received power at third intermodulation point $2f_2 - f_1$ (dBm)
10	−14.34	−12.94	−198	−195	−259	−258
15	−9.3	−7.9	−188	−185	−238	−237
20	−4.3	−2.9	−178	−175	−223	−222
25	2.061	0.683	−168	−165	−208	−207
30	5.0	5.876	−24.9	−23.89	−19.86	−19.22

ulation distortion frequency components, as their strength was well below the ideal noise level of −60 dBm.

Case 2. When input power supplied to transmitter antenna was increased to 30 dBm (1 W), the highest signal received level was of the fundamental frequency at 2.5 GHz, i.e., 6 dBm. This PIN diode can generate significant harmonic and intermodulation signals above power levels of 30 dBm. The strongest harmonic component observed was $(f_1 + f_2)$ at 4.85 GHz, 26 dBm lower than strongest detected power level. Other considerable spurious frequency components are $2f_2$ and $2f_1$, 31 dBm below fundamental frequency signal. Received power levels of third-order intermodulation products, $2f_2 - f_1$ and $2f_1 - f_2$, were −19.86 dBm and −19.22 dBm, respectively. Corresponding third-order input intercepts (IIP_3) were 16.818 dBm and 18.424 dBm, respectively. Table 1 summarizes received strengths of various frequency components.

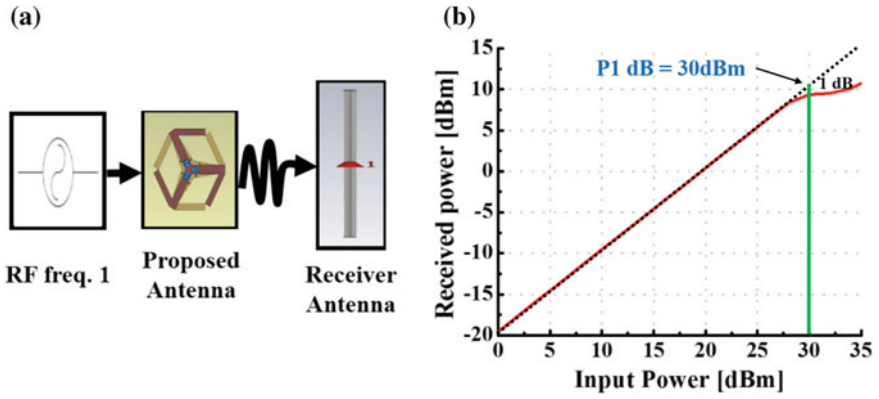

Fig. 8 **a** Gain compression point simulation setup, **b** plot showing 1 dB gain compression point

4.3 Gain Compression Point Simulation

Setup for gain compression point is shown in Fig. 8a. Here, a signal generator was used to provide excitation frequency of 2.5 GHz to pattern reconfigurable antenna where the bias voltages were set to turn diode D_1 ON and the radiated signal was received by a dipole antenna placed in far-field. A decay in gain occurs at higher input power, specifically 1 dB decrease from ideal linear behavior at 30dBm of input power. Gain compression point plot is in Fig. 8b.

5 Conclusion

This work investigates the nonlinear behavior of semiconductor-based PIN diodes by considering their performance at higher power levels in a newly designed pattern reconfigurable antenna. The proposed reconfigurable antenna is successfully able to rotate its beam at angles of 60°, covering the entire azimuthal plane by using just three PIN diodes compared to the other reported works. It gives a good impedance bandwidth from 2.33 to 2.58 GHz making it suitable for use in WLAN, WiMAX, ZigBee, etc. networks. Large signal S-parameters, DC biasing, harmonic, and intermodulation distortion all these aspects of electrically reconfigurable antenna design are considered. The simulated results provide a proof that proposed antenna can operate efficiently up to 25 dBm power level in a real-world scenario. Further, the intermodulation and other spurious harmonic component's strength are found to be considerably low till input power levels of 27 dBm which makes proposed antenna suitable for wireless applications. This study suggests the designed reconfigurable antenna could work properly in space diversity applications in the 2.4 GHz band.

References

1. Christodoulou CG, Tawk Y, Lane SA, Erwin SR (2012) Reconfigurable antennas for wireless and space applications. Proc IEEE 100(7):2250–2261. https://doi.org/10.1109/JPROC.2012.2188249
2. Guo T, Leng W, Wang A, Li J, Zhang Q (2014) A novel planar parasitic array antenna with frequency- and pattern-reconfigurable characteristics. IEEE Antennas Wirel Propag Lett 13:1569–1572. https://doi.org/10.1109/lawp.2014.2345776
3. Zhang L, Gao S, Luo Q, Young PR, Li Q (2016) Planar ultrathin small beam-switching antenna. IEEE Trans Antennas Propag 64(12):5054–5063. https://doi.org/10.1109/TAP.2016.2620490
4. Lu ZL, Yang XX, Tan GN (2014) A wideband printed tapered-slot antenna with pattern reconfigurability. IEEE Antennas Wirel Propag Lett 13:1613–1616. https://doi.org/10.1109/LAWP.2014.2342737
5. Lee J, Kim K, Han SM (2015) Planar ESPAR antenna based on Yagi-Uda array design for space diversity applications. In: 2015 Asia-Pacific microwave conference (APMC), Nanjing, 2015, pp 1–3. https://doi.org/10.1109/apmc.2015.7411778
6. Lim, Lim S (2013) Monopole-like and boresight pattern reconfigurable antenna. IEEE Trans Antennas Propag 61(12):5854–5859. https://doi.org/10.1109/tap.2013.2283926
7. Yan JB, Yong S, Bernhard JT (2014) Intermodulation and harmonic distortion in frequency reconfigurable slot antenna pairs. IEEE Trans Antennas Propag 62(3):1138–1146. https://doi.org/10.1109/tap.2013.2294197
8. Elfergani ITE et al (2012) Reconfigurable antenna design for mobile handsets including harmonic radiation measurements. IET Microw Antennas Propag 6(9):990–999. https://doi.org/10.1049/iet-map.2012.0063
9. Gonçalves R, Carvalho NB, Pinho P (2014) Intermodulation in active reconfigurable antennas. In: 2014 international workshop on integrated nonlinear microwave and millimetre-wave circuits (INMMiC), Leuven, 2014, pp 1–3. https://doi.org/10.1109/inmmic.2014.6815109
10. Habib AM, Jazi MN, Djaiz A, Nedil M, Yagoub MCE, Denidni TA (2010) On IP3 performance investigation in reconfigurable active EBG antenna. In: 2010 IEEE antennas and propagation society international symposium, Toronto, ON, 2010, pp 1–4. https://doi.org/10.1109/aps.2010.5561235
11. http://www.skyworksinc.com/Product/483/SMP1340_Series
12. Keysight EEs of EDA advanced design system circuit design Cookbook 2.0

An Offset CPW-Fed Dual-Band Circularly Polarized Printed Antenna for Multiband Wireless Applications

Venuka Sankhla and Ashok Kumar

Abstract An offset CPW-fed dual-band circularly polarized printed antenna consists of a tilted asymmetrical U-shaped patch and a deformed ground plane is presented. The antenna could generate dual circular polarization radiation at 3.7/5.9 GHz due to tilted asymmetrical U-shaped patch, offset CPW feeding, and deformed ground plane which generates identical amplitudes and 90° phase between them. The 3-dB axial ratio bandwidth (ARBW) of antenna about 3.51% (3.64–3.77 GHz) and 14.9% (5.51–6.40 GHz) is achieved. The antenna resonates at about 3.58/7.28 GHz frequencies and provides impedance bandwidths (IBWs) of 370 MHz (3.40–3.77 GHz)/2850 MHz (5.15–8.00 GHz), respectively. The antenna shows good RHCP/LHCP radiation characteristics and acceptable gains in the dual operating bands.

Keywords Circular polarization · U-shaped patch · Offset feed · Wireless communication frequencies

1 Introduction

In modern wireless systems, circular polarization is desired to prevent the issue of displacement and multipath propagation loss of the antenna. Mostly, CP antenna allows for more adjustable in the orientation of transmitter and receiver than that for a linearly polarized (LP) antenna. They can be used in wireless local area networks (WLANs), worldwide interoperability for microwave access (WiMAX), intelligent transport system (ITS), radio frequency identification (RFID), a global positioning system (GPS), and global navigation satellite system (GNSS). A circularly polarized

V. Sankhla (✉) · A. Kumar
Department of Electronics and Communication Engineering, Government Women Engineering College Ajmer, Ajmer 305002, Rajasthan, India
e-mail: venuka.sankhla2712@gmail.com

A. Kumar
e-mail: kumarashoksaini@gmail.com

© Springer Nature Singapore Pte Ltd. 2020

V. Janyani et al. (eds.), *Optical and Wireless Technologies*,
Lecture Notes in Electrical Engineering 546,
https://doi.org/10.1007/978-981-13-6159-3_43

antenna with asymmetric feed and deformed ground plane for broadband operation [1], a broadband CP antenna with rectangular slot and asymmetric feed line for S-band, Wi-Fi, and LTE systems [2], a C-shaped patch and modified ground plane antenna for various wireless systems [3], and a L-shaped radiating element and truncated ground plane wideband CP antenna for WLAN, WiMAX, RFID reader, and IRNSS applications [4] are demonstrated. A multi-polarized planar antenna with parasitic multistubs [5] and a new dual-frequency and dual-sense circularly polarized modified annular slot antenna [6] are presented for multiband applications. For WLAN/WiMAX applications, a dual-band antenna having rectangular patch surrounded by a circular ground plane with additional two circles [7] is reported. In [8], dual-band operations are realized by using two parallel monopoles, one curved monopole and one fork-shaped monopole. A dual-band dual-sense CP monopole antenna with two rectangular parasitic elements and I-shaped grounded stub [9] is presented for Bluetooth/WLAN and 2.5/3.5 GHz WiMAX applications.

In this paper, an offset CPW-fed dual-band circularly polarized printed antenna is presented for multiband wireless applications. By considering offset CPW feeding, deformed ground plane, and tilted asymmetrical U-shaped patch, a dual-band circular polarization is achieved. The dual operating bands are achieved due to embedding half-wavelength-long stub resonators. The antenna configuration, design approach, surface current distributions, radiation patterns, and gain are presented in Sect. 2.

2 Antenna Configuration

The front and side view configuration of the proposed offset CPW-fed tilted asymmetrical U-shaped patch-printed antenna is shown in Fig. 1a and b, respectively. To design antenna, a low-cost glass epoxy FR-4 dielectric substrate material having $\varepsilon_r = 4.3$, thickness of 1.6 mm, and loss tangent $tan\delta = 0.025$ is used.

A 50 Ω CPW line with a width of *Wf* and length of *Lf*, two identical gaps with width of 0.3 mm, is used to feed the tilted asymmetrical U-shaped patch. A modified feedline with a width of *Wf1* and a length of *Lf1* is used for impedance matching of the radiator. The antenna consists of a tilted asymmetrical U-shaped patch, offset CPW feed line, and deformed ground plane to excite the dual CP modes. The deformed ground plane is formed due to implementing two rectangular slots ($Ls1 \times Ws1$ and $Ls2 \times Ws2$) at different places on the asymmetric CPW ground planes ($Lg1 \times Wg1$ and $Lg2 \times Wg2$). By tuning the dimensions of rectangular slots and the lengths of asymmetric CPW ground planes, two adjacent CP modes could be obtained for dual-band operation. The antenna has an overall size of $L \times W$. Computer Simulation Technology (CST) Microwave Studio is used for full-wave simulation. The optimized labeled parameter values are mentioned in caption of Fig. 1.

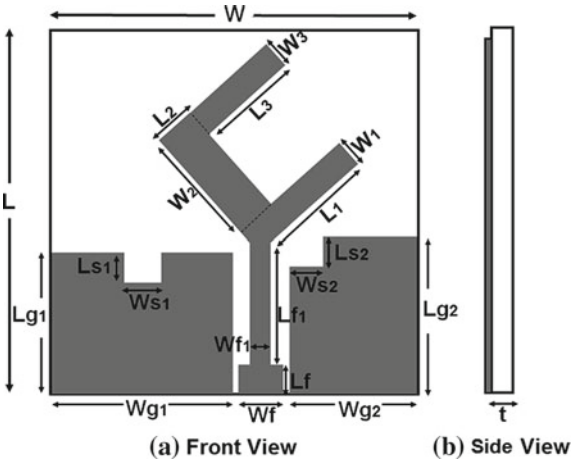

Fig. 1 Configuration of the proposed offset CPW-fed tilted asymmetrical U-shaped patch-printed antenna. The detailed dimensions of the antenna are $L = 33$, $W = 34$, $W1 = 2.5$, $L1 = 11.5$, $W2 = 11.9$, $L2 = 4.2$, $W3 = 2.4$, $L3 = 9.4$, $Lg1 = 11$, $Lg2 = 12$, $Wg1 = 17.65$, $Wg2 = 12.65$, $Ls1 = 4$, $Ws1 = 5$, $Ls2 = 2$, $Ws2 = 4.65$, $Lf = 3$, $Wf = 3$, $Lf1 = 9.4$, $Wf1 = 1.5$, $t = 1.6$ (all dimensions are in mm)

2.1 Design Approach and Analysis

To know the operating principle of the designed antenna, four prototypes (Ant. I–Ant. IV) are depicted in Fig. 2. Initially, a conventional offset CPW-fed tilted rectangular-shaped patch-printed antenna as shown in Fig. 2a consists of a 50 Ω impedance transformer, and asymmetrical CPW ground planes (named as Ant. I) is designed to generate the fundamental resonance mode at 5.79 GHz in the range 5.6–6.39 GHz. Subsequently, an asymmetric L-shaped stub is embedded on the Ant. I at angle 45° and structure named as Ant. II as shown in Fig. 2b. It is resonating at 3.50 GHz (3.28–3.71 GHz) and 6.16 GHz (5.33–7.19 GHz) frequencies. In addition, it is also possible to generate two orthogonal components of identical amplitudes and 90° phase difference (PD) to provide dual-band circular polarization radiation. Ant. II provides 3.64–3.79 GHz CP radiation but second CP band has poor axial ratio and out of desired operating band. Further to improve CP radiation, a rectangular slot is inserted in the CPW ground plane of Ant. II and structure named as Ant. III as shown in Fig. 2c. It gives first operating resonance mode at 3.52 GHz (3.29–3.73 GHz) with 3-dB axial ratio bandwidth (ARBW) of 3.64–3.78 GHz. It is also observed that the second band axial ratio is shifted toward lower frequency side but again AR is poor and gives impedance bandwidth 5.02–8.07 GHz. Finally, another rectangular slot on the left upper corner of the second ground plane is inserted as shown in Fig. 2d to obtain second band circular polarization radiation and wide impedance bandwidth. This structure named as Ant. IV gives dual-band CP radiation at 3.73 GHz (3.64–3.77 GHz)/5.90 GHz (5.51–6.40 GHz) along with dual operating bands at

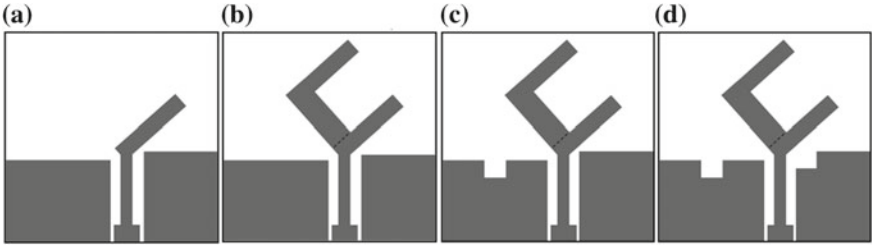

Fig. 2 Four prototypes of the proposed offset CPW-fed tilted U-shaped patch-printed antenna **a** Ant. I, **b** Ant. II, **c** Ant. III, **d** Ant. IV

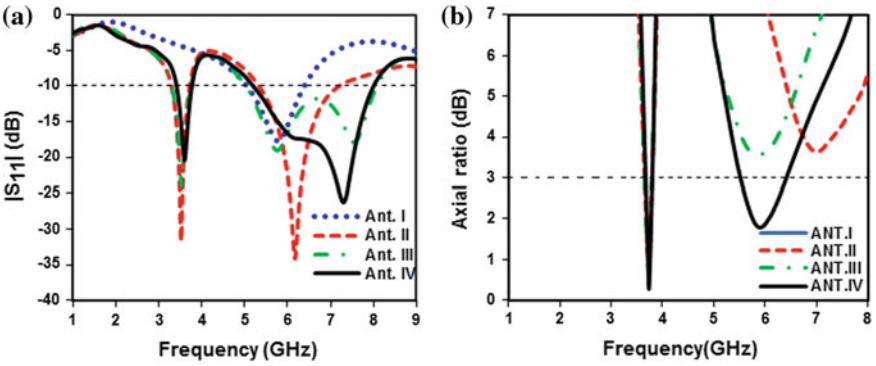

Fig. 3 Comparisons of different configurations Ant. I–IV, **a** $|S_{11}|$, and **b** AR

3.58 GHz (3.40–3.77 GHz)/7.28 GHz (5.15–8 GHz) frequencies. The $|S_{11}|$ and AR performance of Ant. I–IV are depicted in Fig. 3a and b, respectively.

The design approach for the excitation of dual resonance modes, the resonant frequency f_{ri} , and effective dielectric constant ε_{eff} can be calculated by (1) and (2) as

$$f_{ri} = \frac{c}{2L_{ri}\sqrt{\varepsilon_{eff}}}; \quad i = 1, 2 \tag{1}$$

$$\varepsilon_{eff} \approx \frac{\varepsilon_r + 1}{2} \tag{2}$$

where c = speed of light in vacuum (3×10^8 m/s), ε_r = dielectric constant of the substrate, λ_g = the guided wavelength, and L_{ri} = the total length of the stub resonator.

In order to satisfy the dual resonance frequencies of Ant. IV, the first resonance mode frequency (i.e., 3.58 GHz) is excited due to tilted asymmetric L-shaped stub. For $i = 1$, the total length of it can be calculated as $L_{r1} = W_2 + L_2 + L_3 = 25.5$ mm which is about a half of the guided wavelength λ_g and calculated theoretical resonance frequency f_{r1} by (1) and (2) is 3.60 GHz. Correspondingly, the second resonance

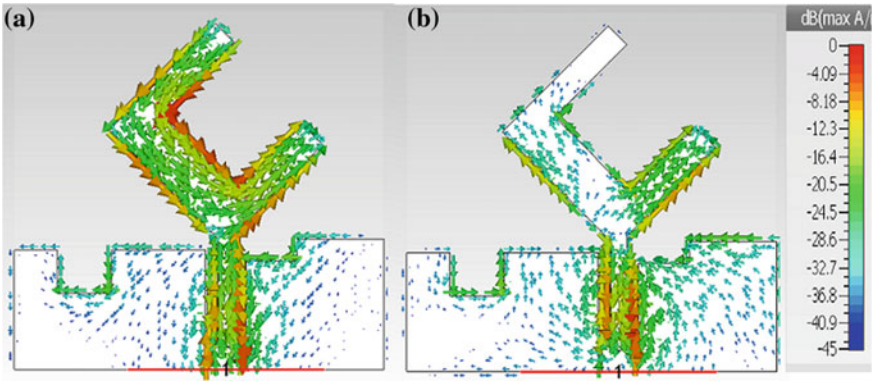

Fig. 4 Surface current distributions at two resonance frequencies **a** 3.58 GHz, and **b** 7.28 GHz

mode frequency (i.e., 7.28 GHz) is excited due to the lower tilted rectangular stub of U-shaped patch. For $i = 2$, the total length of it can be calculated as $L_{r2} = L_1 + W_1 = 14$ mm, which is about half of the guided wavelength λ_g and calculated theoretical resonance frequency f_{r2} by (1) and (2) is 7.0 GHz. Therefore, we can say that the simulated dual-band frequencies are very close to calculated resonance frequencies. Hence, the proposed antenna structure is verified with the design concept.

2.2 *Surface Current Distributions*

It can be seen in Fig. 4a that at 3.58 GHz, the current distribution is more on tilted asymmetric L-shaped stub of U-shaped patch. This current is responsible for the radiation, and the path traversed by the currents determines the first resonance mode. Conversely, at 7.28 GHz, it can be observed that lower tilted rectangular stub of U-shaped patch as shown in Fig. 4b is responsible for radiation and determines the second resonance mode.

Figure 5a and b depicts the surface current distributions with four phase angles 0°, 90°, 180°, and 270° of the proposed antenna at two CP frequencies 3.73 and 5.90 GHz, respectively. It is observed that CP radiation at 3.73 GHz generated due to tilted asymmetrical U-shaped patch. Conversely, the CP radiation at 5.90 GHz is due to lower tilted rectangular stub and rectangular slots on deformed ground plane. From Fig. 5a, it can be observed that the resultant current vector rotates anticlockwise direction as phase changes from 0° to 270° leads to right-handed circular polarization (RHCP) radiation in direction of $\theta = 0°$ (upper hemisphere). Similarly, it can be seen from Fig. 5b that the resultant current vector rotating in clockwise direction leads to left-handed circular polarization (LHCP) in the direction of $\theta = 0°$ (upper hemisphere). Therefore, it may be concluded that the antenna gives RHCP radiation at 3.73 GHz while LHCP radiation is at 5.90 GHz.

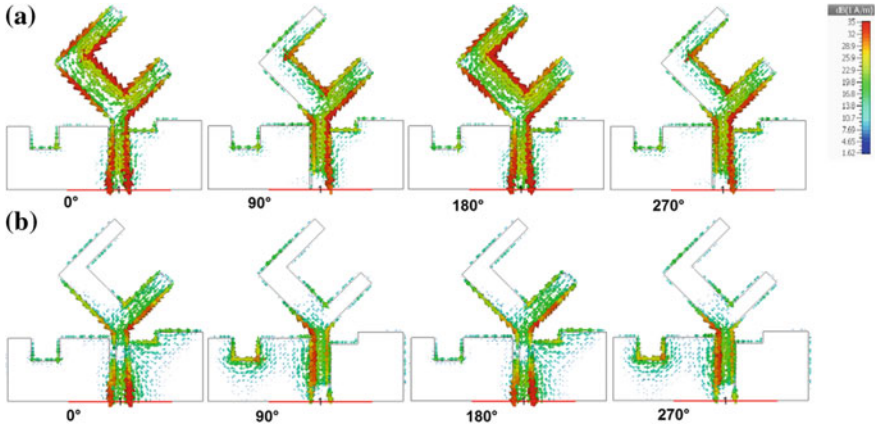

Fig. 5 Surface current distributions at two CP frequencies **a** 3.73 GHz, and **b** 5.90 GHz

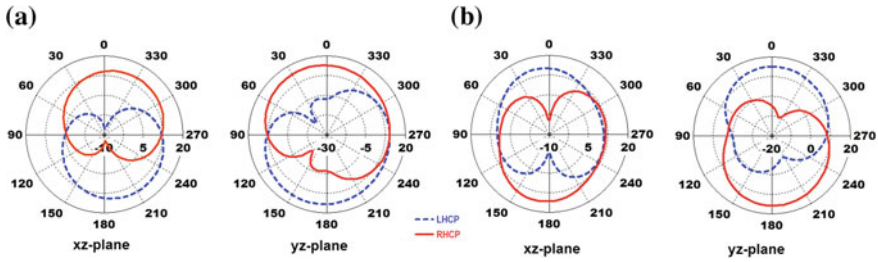

Fig. 6 Radiation patterns at two CP frequencies **a** 3.73 GHz, and **b** 5.90 GHz

2.3 Radiation Patterns and Gain

Radiation patterns of the proposed antenna at two CP frequencies 3.73 and 5.90 GHz are shown in Fig. 6a and b, respectively. It can be seen from Fig. 6a that the radiation pattern at 3.73 GHz frequency, antenna gives RHCP wave in the direction of $\theta = 0°$ and LHCP wave in the direction of $\theta = 180°$, whereas at 5.90 GHz frequency, antenna gives LHCP wave in direction of $\theta = 0°$ and RHCP wave in the direction of $\theta = 180°$ in both *xz*- and *yz*-planes. The comparisons of gain curves against frequency for configuration of Ant. I–IV are shown in Fig. 7. Simulated gain varies ~1–3 dBi in the first resonance band while ~1–4 dBi in the second resonance band.

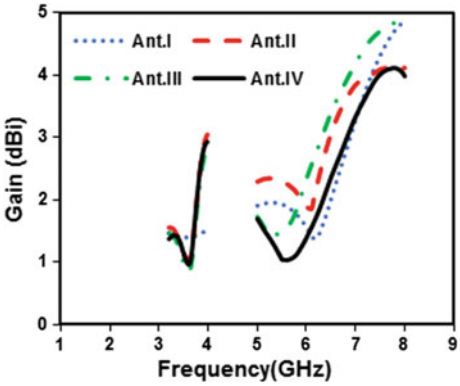

Fig. 7 Gain comparisons of different configurations Ant. I–IV

3 Conclusion

A dual-band circularly polarized tilted asymmetrical U-shaped patch-printed antenna with an offset CPW feeding, and the deformed ground plane is proposed. Dual-band circular polarization is achieved in the broadside direction due to tilted asymmetrical U-shaped patch, offset CPW feeding, and rectangular slots in the deformed ground plane. The simulated impedance bandwidths of the proposed antenna are 370 MHz (3.40–3.77 GHz) and 2850 MHz (5.15–8.00 GHz), while 3-dB axial ratio bandwidths are 3.51% (3.64–3.77 GHz) and 14.9% (5.51–6.40 GHz). The antenna will be an attractive candidate for WLAN/WiMAX/ITS bands and other broadband communication applications due to its simple structure, relatively small size, wide dual operating functionality, dual circular polarization capability, and good radiation patterns.

References

1. Wu J-W, Ke J-Y, Jou CF, Wang C-J (2010) Microstrip-fed broadband circularly polarised monopole antenna. IET Microw Antennas Propag 4(4):518–525
2. Xue H-G, Yang X-X, Ma Z (2015) A novel microstrip-CPW fed planar slot antenna with broadband and circular polarization. IEEE Antennas Wirel Propag Lett 14:1392–1395
3. Tang H, Wang K, Wu R, Yu C, Zhang J, Wang X (2017) A novel broadband circularly polarized monopole antenna based on C-shaped radiator. IEEE Antennas Wirel Propag Lett 16:964–967
4. Kushwaha N, Kumar R (2015) Compact coplanar waveguide-fed wideband circular polarised antenna for navigation and wireless applications. IET Microw Antennas Propag 9(14):1533–1539
5. Kumar A, Deegwal JK, Sharma MM (2017) Design of multi-polarised quad-band planar antenna with parasitic multistubs for multiband wireless communication. IET Microw Antennas Propag 12(5):718–726. https://doi.org/10.1049/iet-map.2017.0526
6. Bao X, Ammann MJ (2008) Dual-frequency dual-sense circularly-polarized slot antenna fed by microstrip line. IEEE Trans Antennas Propag 56(3):645–649

7. Hassan OH, Shams SI, Allam AMMA (2010) Dual-band circularly polarized antenna with CPW feeding structure. In: Proceedings of the Asia-Pacific microwave conference, Yokohama, Japan, pp 2052–2055
8. Chen C-H, Yung EKN (2011) Dual-band circularly-polarized CPW-fed slot antenna with a small frequency ratio and wide bandwidths. IEEE Trans Antennas Propag 59(4):1379–1384
9. Saini RK, Dwari S, Mandal MK (2017) CPW-fed dual-band dual-sense circularly polarized monopole antenna. IEEE Antennas Wirel Propag Lett 16:2497–2500

Comparative Study of Interferometer and Ring Resonator Based Biosensors: A Review

Nitesh Mudgal, Ankit Agarwal, Ankur Saharia, Sourabh Sahu, Ashish Kumar Ghunawat and Ghanshyam Singh

Abstract Optical biosensors are one of the most emerging devices due to high sensitivity and their compact size. In the past 10 years, optical biosensors based on interferometer and ring resonator structure can mostly be seen in the literature. During this decade, several biosensors families have been seen, which have advantageous combinations of properties. These lead to label-free biosensing, high quality factor and transmissivity, better limit of detection and sensitivity, cost-effective production, miniaturization, and the ability of lab on chip integration. This review paper compiles the most relevant research of the past years categorizing them into the group of interferometer-based biosensors and ring resonator based biosensors.

Keywords Refractive index · Waveguide · Interferometer · Ring resonator · Optical biosensor

1 Introduction

In a last one decade, technological advancements in the field of photonics enabled the development of devices for various applications. For a biosensing application, integrated photonics provides advantages such as compact size, immune to EMI (electromagnetic interference), familiar fabrication technology, etc. Clark and Lyons introduced the first biosensor, which is enzyme electrode based and they have also demonstrated its application in the field of biotechnology [1]. Since then, many researchers have continued to improve the performance characteristics of biosensing devices. They have significantly contributed to decreasing cost and size, but the better limit of detection and sensitivity is still a challenge for today's researchers and scientists. Optical biosensors are the tools for detection in medical diagnostics, environmental monitoring, and scientific research, etc. [2]. Generally, optical biosen-

N. Mudgal (✉) · A. Agarwal · A. Saharia · S. Sahu · A. K. Ghunawat · G. Singh
Department of Electronics and Communication Engineering,
Malaviya National Institute of Technology Jaipur, Jaipur 302017, Rajasthan, India
e-mail: mudgalnitesh@gmail.com

© Springer Nature Singapore Pte Ltd. 2020

V. Janyani et al. (eds.), *Optical and Wireless Technologies*,
Lecture Notes in Electrical Engineering 546,
https://doi.org/10.1007/978-981-13-6159-3_44

sor works on two different mechanisms which are fluorescence base detection and label-free detection. Labeling of sampling molecules is done with fluorescent tags to detect or sense targeted molecules in fluorescence base detection while in label-free detection, an immobilized biorecognition layer is placed on a surface of the biosensor that causes to bind only intended biomolecules hence sampling molecules are free not to be labeled [3]. Various materials are utilized for photonic devices but Silicon On Insulator (SOI) platform is mostly used for optical biosensors due to high refractive index between cladding and core that significantly reduces propagation losses and compatibility to Complementary-Metal-Oxide-Semiconductor (CMOS) process which facilitates an easier integration of photonics devices [4, 5]. For detection of the presence of biomolecules, optical biosensor uses the presence of evanescent wave on waveguide surface [6]. Waveguide structure with grating creates periodic modulation of the effective refractive index. Bragg grating waveguide structure utilizes the periodic modulation of the effective index of the waveguide, which are obtained with changing the waveguide dimensions [7, 8]. Optical biosensors can be modeled by using different structures of waveguide, i.e., rib, strip, slot, etc. Rib and strip waveguide structures detect biomolecules presence on waveguide surface by observing the alteration in the evanescent field of the guided wave. However, slot waveguide causes to confine field in low refractive index slot region that provides an added advantage of higher light and biomaterial interaction. In this review paper, we have considered interferometer and ring resonator based biosensor, the advancements in the configuration, and performance parameters are compared extensively. This paper is organized as follows: Sect. 2 gives study regarding various interferometric configuration for biosensing applications, ring resonator is discussed in Sect. 3 followed by conclusion and references at the last.

2 Interferometer-Based Optical Biosensors

In this section, some basic structures of interferometer-based optical biosensors have been introduced. These structures include Hartman interferometer, silicon nitride slot waveguide based Mach-Zehnder interferometer, Ring Assisted Mach-Zehnder interferometer with directional coupler and multimode coupler etc.

2.1 Hartman Interferometer

Hartman interferometer-based optical biosensor introduced a label-free biosensing in the biomedical application for nucleic acids, proteins, and virus detection. In this structure, a pattern of sampled molecules is created on the upper surface of a planar waveguide in the form of strips, as shown below in Fig. 1. Coupling of light is accomplished by using two grating couplers each at input and output of planar waveguide. To create interference, integrated optics is located between pairs of functionalized

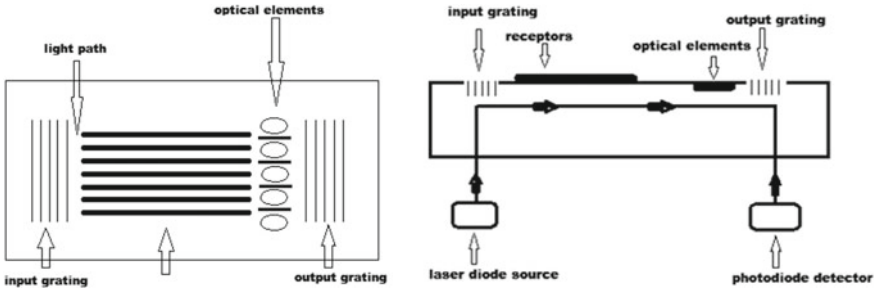

(a) Top view (b) Side view

Fig. 1 Schematic view of the Hartman interferometer. Reproduced from Ref. [9]

strips. Through this technique, detection of human chorionic gonadotropin had been evaluated to concentrations of 5 ng/mL and detection limit of influenza virus was 10^7 PFU/L Also, 4 ng/mL of a 44 base pair oligonucleotide was obtained [9, 10].

2.2 *Silicon Nitride Slot Waveguide Based Mach–Zehnder Interferometer*

Operating principle of slot waveguide based Mach–Zehnder interferometer is demonstrated in Fig. 2. In this structure, a vertical grating coupler is used to split light into two arms with a junction and traveling some distance and this light again recombines [11]. Strip waveguide is used in reference arm while slot waveguide section is used in sensing arm. This slot waveguide section is used as a sensing waveguide. Length of this sensing arm is 7 mm. The purpose of using slot waveguide is to increase a light matter interaction that increases detection sensitivity. In this structure, a mode converter was used, and this converter converts light from strip waveguide section to slot waveguide section in the sensing arm. The bulk effective index sensitivity of this sensor was 1864 π/RIU [12, 13].

2.3 *Ring-Assisted Mach–Zehnder Interferometer*

Ring-assisted Mach–Zehnder interferometer is illustrated below in Fig. 3 where the light coupling is accomplished by using directional couplers or multimode interferometer couplers. The sensitivity of ring-assisted Mach–Zehnder interferometer was 203.3 ± 15.3 nm/RIU with a directional coupler and 177.2 ± 12.0 nm/RIU with multimode interferometer couplers. This biosensor has potential applications in biochemical gas [14–16].

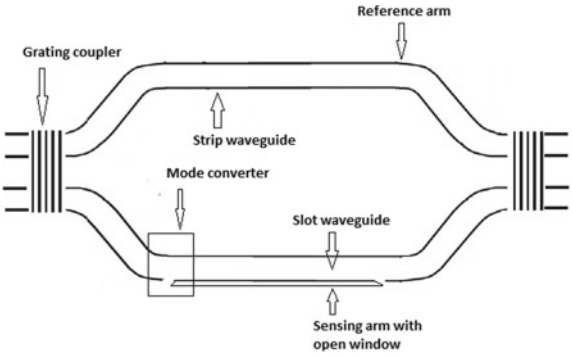

Fig. 2 Schematic view of Mach–Zehnder interferometer based on slot waveguide. Reproduced from Ref. [13]

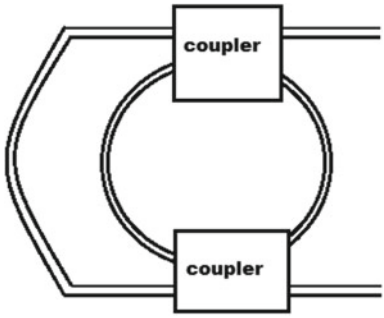

Fig. 3 Ring assisted Mach–Zehnder interferometer track. Reproduced from Ref. [16]

Based on the study of the above interferometer structures, a comparison of the detection limit of various interferometer structures is shown in Table 1.

3 Ring Resonator Based Optical Biosensors

Optical biosensors based on ring resonator structure have been studied in this section. These structures include polymer microring resonators, ring resonator with slot waveguide, ring resonator with double slot waveguide, and a hybrid optical sensor. A brief study of each ring resonator based optical sensor is described in below sections.

3.1 Polymer Microring Resonators

Polymer microring resonators with single coupled and double coupled structures are shown below in Fig. 4a, b correspondingly. An oxide layer over silicon substrate was used to fabricate polymer microring resonators [17]. These structures are

Table 1 Limit of detection of interferometer-based biosensors

Optical biosensor structure	Analyte	Limit of detection	References
Hartman interferometer	Deoxyribonucleic acid	4 ng/mL	[9]
	Protein	5 ng/mL	[9]
	Virus	10^7 PFU/L	[9]
Si_3N_4 slot waveguide based Mach–Zehnder interferometer	Bulk solution	1864 π/RIU	[13]
Ring-assisted Mach–Zehnder interferometer with directional coupler	Bulk solution	203.3 ±15.3 nm/RIU	[16]
Ring-assisted Mach–Zehnder interferometer with MMI coupler	Bulk solution	177.2 ± 12.0 nm/RIU	[16]

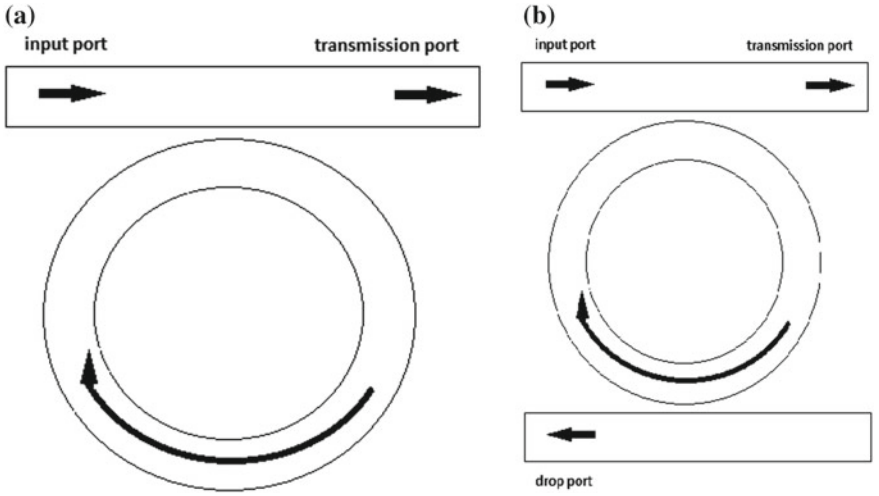

Fig. 4 Schematic view of microring resonator configuration **a** single coupled microring resonator, **b** double coupled microring resonator. Reproduced from Ref. [20]

capable potential for label-free biosensing. Designed polymer microring resonators have a quality factor of 20,000 and detection limit of 10^{-7} RIU. The device found biomolecules binding detection limit of 250 pg/mm^2 [18–20].

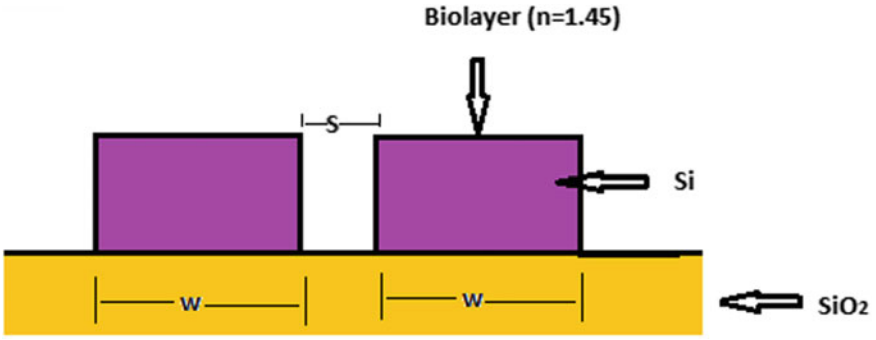

Fig. 5 Slot waveguide structure with 'S' slot width and 'W' rib width. Reproduced from Ref. [24]

3.2 Slot Waveguide Ring Resonator

In this structure, (SOI) Silicon On Insulator slot waveguide is used to form a ring resonator [21]. The structure is designed with rib width of 268 nm and a slot width of 104 nm. Optical lithography with 193 nm was used to fabricate this device structure. By using this structure, limit of detection was 4.2×10^{-5} RIU for refractive index changes and sensitivity of 298 nm/RIU was obtained [22–24] (Fig. 5).

3.3 Double Slot Waveguide Ring Resonator

A ring resonator with double slot waveguide is shown in Fig. 6. In this structure, ring resonator is designed with two narrow slots. One input and one output waveguides are used with a single slot etched in the middle of each waveguide [25]. If the condition of resonance is satisfied, then light entering from port 1 will couple out to port 4 through micro-ring resonator while dropped out from port 2 if resonance condition is not satisfied. Area of this structure is about 25 μm × 15 μm. Radius of ring resonator is 5 μm. With this radius, the sensitivity of 708 nm/RIU was found by using this structure [26–28].

3.4 Hybrid Optical Sensor

In order to further optimize optical biosensor performance, a ring resonator biosensor with Bragg grating was designed. Grating used in this structure was SiO_2 grating with a period of 2.7 μm [29]. Schematic diagram of this structure is shown in Fig. 7.

The detection limit of each ring resonator based biosensor described in the above sections has been illustrated in Table 2.

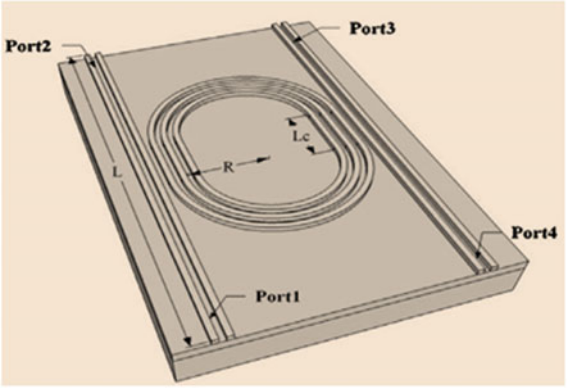

Fig. 6 Three dimensional structure view of double slot waveguide ring resonator. Reproduced from Ref. [28]

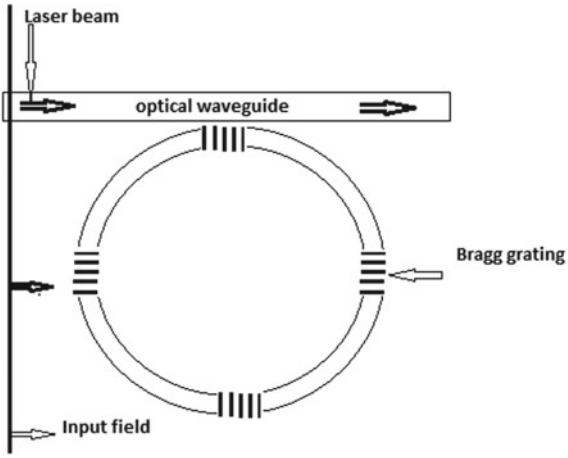

Fig. 7 Schematic view of the hybrid optical sensor. Reproduced from Ref. [29]

4 Conclusion

In this paper, we have reviewed a study of ongoing progress in different types of optical biosensor structures based on interferometer and ring resonator. Some of the structures in this review introduce label-free biosensing that provides better sensing performance with high sensitivity and low cost. Waveguide with a single slot, double slot is also introduced in this review study to enhance the performance of biosensors. A detection limit comparison for different structures of interferometer-based biosensors and ring resonator based biosensors have been illustrated in the table. A hybrid combination of a ring resonator with Bragg grating gives the better sensitivity and has application in the field of chemical science.

Table 2 Limit of detection of ring resonator based biosensors

Optical biosensor structure	Analyte	Limit of detection	References
Polymer microring resonator	Bulk solution	10^{-7} RIU	[20]
Slot waveguide base ring resonator	Protein	4.2×10^{-5} RIU	[24]
Double slot waveguide based ring resonator	Bulk solution	708 nm/RIU	[28]
Hybrid optical sensor	Bulk solution	4.97 nm/μe	[29]

References

1. Clark Lc, Lyons C (1962) Electrode systems for continuous monitoring in cardiovascular surgery. Ann NewYork Acad Sci 102:29–45
2. Oliver NS, Toumazou C, Cass AE, Johnston DG (2009) Glucose sensors: a review of current and emerging technology. Diabet Med 26:197–210
3. Fan X, White IM, Shopova SI, Zhu H, Suter JD, Sun Y (2008) Sensitive optical biosensors for unlabeled targets: A review. Anal Chim Acta 620(1–2):8–26
4. Sahu Sourabh, Ali Jalil, Singh Ghanshyam (2017) Refractive index biosensor using sidewall gratings in dual-slot waveguide. Opt Commun (Elsevier) 402:408–412
5. Sahu S, Jalil Ali, Singh G (2018) Optimization of dual-slot waveguide for refractive index biosensor. Optica Applicata (PSP) 48(1)
6. Sahu S, Kozadaev KV, Singh G (2016) Michelson interferometer based refractive index biosensor. In: Proceedings of 13th international conference on fiber optics and photonics, Photonic-16. IIT Kanpur, Dec 04–08, 2016, OSA Technical Digest, paper Th3A.60
7. Sahu S, Singh G (2016) Modeling of phase shift Bragg grating biosensor for non invasive detection of blood components. In: IEEE International Conference ICRAIE-2016, Jaipur, India, December 23–25
8. Sahu S, Singh G (2017) Modeling of grating slot waveguide for high-Q based refractive index sensor. In: IEEE International Conference COMPTELIX-2017, Jaipur, India, July 1–2
9. Schneider BH, Edwards JG, Hartman NF (1997) Hartman interferometer: versatile integrated optic sensor for label-free, real-time quantification of nucleic acids, proteins, and pathogens. Clin Chem 43:1757
10. Schneider BH, Dickinson EL, Vach MD, Hoijer JV, Howard LV (2000) Highly sensitive optical chip immunoassays in human serum. Biosens Bioelectron 15:13–22
11. De Vos K, Bartolozzi I, Schacht E, Bienstman P, Baets R (2007) Silicon-on-insulator microring resonator for sensitive and label-free biosensing. Opt Express 15:7610–7615
12. Shin Y, Perera AP, Kee JS, Song JF, Fang Q, Lo G-Q (2012) Label-free methyla-tion specific sensor based on silicon microring resonators for detection and quantification of DNA methylation biomarkers in bladder cancer. Sens Actuators B Chem 177:404–411

13. Liu Q, Xiaoguang T, Kim KW, Kee JS, Shin Y, Han K, Yoon Y-J, Lo G-Q, Park M (2013) Highly sensitive Mach-Zehnder interferometer biosensor based on silicon nitride slot waveguide. Sens Actuator B 188:681–688
14. Wang J, Dai D (2010) Highly sensitive Si nanowire-based optical sensor using a Mach-Zehnder interferometer coupled microring. Opt Lett 35(24):4229–4231
15. Xiong Y, Y WN (2013) Slotted silicon microring resonators with multimode interferometer couplers. In: Proceedings of IEEE International Conference Group IV Photon, vol 7, pp 118–119
16. Marsh OA, Xiong Y, Winnie NY (2017) Slot waveguide ring-assisted Mach–Zehnder interferometer for sensing applications. IEEE J Sel Top Quantum Electron 23(2)
17. Chao C-Y, Guo LJ (2002) Polymer microring resonators fabricated by nanoimprint technique. J Vac Sci Technol B Microelectron 20:2862–2866
18. Chao C-Y, Guo LJ (2004) Reduction of surface scattering loss in polymer microrings using thermal-reflow technique. IEEE Photon Technol Lett 16(6):1498–1500
19. Melloni A, Morichetti F, Martinelli M (2004) Polarization conversion in ring resonator phase shifter. Opt Lett 29:2785–2787
20. Chao C-Y, Fung W, Guo LJ (2006) Polymer microring resonators for biochemical sensing applications. IEEE J Sel Top Quantum Electron 12(1)
21. Barrios CA, Gylfason KB, Sa´nchez B, Griol A, Sohlstro¨m H, Holgado M, Casquel R (2007) Slot-waveguide biochemical sensor. Opt Lett 32(21):3080–3082
22. De Vos K, Bartolozzi I, Schacht E, Bienstman P, Baets R (2007) Silicon-on-insulator microring resonator for sensitive and label-free biosensing. Opt Express 15(12):7610–7615
23. Barrios CA, Banuls MJ, Gonzalez-Pedro V, Gylfason KB, Sanchez B, Griol A, Maquieira A, Sohlstrom H, Holgado M, Casquel R (2008) Label-free optical biosensing with slot-waveguides. Opt Lett 33(7):708–710
24. Claes T, Molera JG, De Vos K, Schacht E, Baets R, Bienstman P (2009) Label-free biosensing with a slot-waveguide-based ring resonator in silicon on insulator. IEEE Photon J 1(3)
25. Kargar A, Lee C (2009) Optical sensing by multiple-slot waveguide micro-ring resonators. In Nanotechnology, IEEE Conference, pp 240–242. IEEE
26. Gylfason KB, Carlborg CF et al (2010) On-chip temperature compensation in an integrated slot-waveguide ring resonator refractive index sensor array. Opt Express 18:3226–3237
27. Carlborg CF, Gylfason KB, Dortu F, Catala AM et al (2010) A packaged optical slot-waveguide ring resonator sensor array for multiplex label-free assays in labs-on-chips. Lab Chip 10:257–396
28. Yuan, Gao L, Chen Y, Liu X, Wang J, Wang Z (2014) Improvement of optical sensing performances of a double-slot-waveguide-based ring resonator sensor on silicon-on-insulator platform. Optik 125:850–854
29. Kaur G, Kaler RS (2017) Design and performance evaluation of hybrid optical sensor. Optik 140:508–514

A Comparative Study of Various All-Optical Logic Gates

Ankur Saharia, Nitesh Mudgal, Ankit Agarwal, Sourabh Sahu, Sanjeev Jain, Ashish Kumar Ghunawat and Ghanshyam Singh

Abstract This article reviews the design of various optical logic gates. As we know, speed in electrical circuits is a matter of concern in high-speed communication. To avoid such limitations photonic components can be used instead of electrical components. The switching characteristic of optical communication is used to construct logical device using electro-optic effect in a Mach–Zehnder interferometer (MZI). The interferometer has shown great way to transport signal from one port to other. Hence, it is now possible to design various logical structures in digital devices using the electro-optic (EO) and interferometer as a basic constructing unit. This paper reviews various methods to design logic gate or logic operations. The design of gate has been demonstrated using finite-difference time-domain approach.

Keywords MZI · FDTD · Coupler · LiNbO modulator · XPM · XGM · FWM

1 Introduction

These days one of the biggest challenges in the field of latest technology is to achieve great speed and higher capacity at the minimum cost. Optical communication is one of the futuristic ways to achieve higher transmission speed over long distances [1, 2]. The optical communication technologies provide much improved way to process the data along with high data rate. It also paved the way for various applications of digital communication like encoding–decoding, switching, and many other complex digital circuits [3, 4]. Optical communication has been used for various purposes and applications in recent years due to characteristics like high bandwidth, less

A. Saharia (✉) · N. Mudgal · A. Agarwal · S. Sahu · A. K. Ghunawat · G. Singh
Department of Electronics and Communication Engineering,
Malaviya National Institute of Technology Jaipur, Jaipur 302017, Rajasthan, India
e-mail: ankursaharia07@gmail.com

S. Jain
Department of Electronics and Communication Engineering,
Government Engineering College, Bikaner, Rajasthan, India

© Springer Nature Singapore Pte Ltd. 2020

V. Janyani et al. (eds.), *Optical and Wireless Technologies*,
Lecture Notes in Electrical Engineering 546,
https://doi.org/10.1007/978-981-13-6159-3_45

distortion in signal transmission, and less RF interferences [5–7]. Among the various applications, optical gates are one of the important components for all circuits and communication-related applications, these gates have been successfully implemented using optical fiber and semiconductor optical amplifiers (SOAs), photonic crystals, ring resonators, and multimode interference (MMI) coupler [6–8]. Linear and curved directional couplers various shaped waveguides are the most essential part of integrated photonics. We have to evaluate the propagation characteristics of the waveguides while considering the light coupling in front and rear of the waveguides [3]. The higher data rate can be achieved using optical domain transmission and in this interferometric design have significant role in achieving the required rate. The AND/NAND, OR/NOR gates [9–11] are the primary construction units of any circuit. Any digital logic circuit can be implemented by their use as a basic building unit, but it may not be optimum efficient. Because, various factors like power consumption, speed of response, cost of the structure, and energy losses also attract attention. Many researchers have demonstrated basic logic gates with the help of optics to enhance the working performance of digital circuits. All-optical logic units are basic structure to implement various switching circuits and combinational and sequential structures. Designing of digital circuits can be implemented by nonlinear structure like photonic crystal [12], waveguide [13], semiconductor optical amplifier [14–16,] ring resonators [17], etc. That is why a lot of researches are still in progress to realize complex combinational and sequential digital circuits, this paper shows basic blocks of design process of various gates using the electro-optic (EO) effect [18] of Mach–Zehnder interferometer [2].

2 All-Optical Gate

All-optical gates can be designed using the nonlinear effect, there are various ways through which all-optical gate can be constructed, i.e., with SOA using length of the fiber, waveguides, photonic crystal circulator, filters, using MZI, and changing the refractive index of the optical waveguide [7]. All-optical gates [19, 20] can be designed in above methods, such as four-wave mixing (FWM), cross-gain modulation (XGM), cross-phase modulation (XPM), or by combining any of the process.

2.1 Four-Wave Mixing

The concept of FWM consists of a phenomenon in which more than two wavelengths interact with each other to construct new wavelengths. In case of four-wave mixing, the photons which were generated conserved their energy. The efficiency of this nonlinear process is dependent on phase matching conditions, and therefore it is very much phase sensitive. The amplitude of the generated signal by FWM depends upon the amplitude of the signals interacted and its phase and frequency is also combination

of interacted signals and which ultimately preserved the signal parameters. We can generate more than one required signal through FWM because signal generated through FWM contains properties of interacting signals. It is one of the nonlinear processes widely used for frequency conversion in optical fiber communication [2].

2.2 Cross-Gain Modulation

It is the process of wavelength conversion in semiconductor optical amplifier. It is a process in which a pump signal creates variation in density of carrier signal in SOA and produces inverted gain modulation. A continuous wave signal called probe signal whose frequency is different from pump signal is used in this and wavelength conversion is achieved when the input data shift from pump to probe frequency. This pump signal modulates SOA gain and imprints on probe at different wavelengths [2].

2.3 Cross-Phase Modulation

It is one of the processes associated with cross-gain modulation, during the variation of carrier density in SOA in XGM variation of refractive index also occurs in comparison to amplitude of input signal. When a probe frequency coupled into semiconductor optical amplifier this variation in refractive index forms phase modulation. When with the help of interferometer, phase modulation is converted to amplitude modulation, it is called XPM wavelength conversion. The cross-phase modulation becomes more stronger when the spacing between channels is small and number of channels are larger [2]. There is no energy transfer in XPM as compared to other techniques in which there is transfer of energy from one channel to other.

3 Electro-optic Effect

It is one of the concepts responsible for working of electro-optic switches and modulator, as per this concept the change in refractive index occurs while applying electric field, it contains both linear and nonlinear components [21, 22]. In case of solid crystals, with materials like lithium niobate, lithium tantalum, gallium arsenide, and gallium phosphate many low loss waveguides can be formed by the electro-optic effect. In case of electro-optic effect, variation in refraction index varies according to the strength of applied potential. The nonlinear optical Kerr effect used for the generation of logic gates is also one of the types of electro-optic effect in which variation of refractive index is directly proportional to square of electric field.

4 Mach–Zehnder Interferometer

The Mach–Zehnder interferometer [23] applies electro-optic property, it contains two Y-shaped junction through input power which is equally divided in both arms as shown in Fig. 2. When electric field is not applied at the electrodes of the interferometer, the input signal splits in both arms of interferometer and appears at the second Y-junction with maximum intensity and in-phase component at the waveguide output. This mode is known as ON state of interferometer. In second case, when potential is applied at the electrodes of the interferometer it creates a phase change between the arms of interferometer, this interference creates constructive or destructive signals at the output of the waveguide. When the phase difference is 180, the interferometer is in OFF state, in this way this method converts phase modulation into amplitude modulation (Fig. 1).

As the MZI works on electro-optic effect, it found its application in various switching operations, for the construction of switching device like logic gate, we have to create waveguide from the material like lithium niobate, lithium tantalum, gallium arsenide, and gallium phosphate. As we can see from the structure of MZI shown in Fig. 2, it contains two input and output ports and two arms, and therefore we can create change in index of refraction in any of the arm of interferometer by applying voltage across any of the electrodes. The input can be provided in any of the input ports of interferometer and the signal propagates through arms of the device which reached the output ports, we can create phase difference in the input by applying voltage at the electrodes [8]. The electrodes associated with the MZI act as control electrode and by varying the input voltages at the electrodes, we can vary the input logic by varying the electrode voltage signal coupling which is also shifted from one interferometric arm to other arm (Table 1).

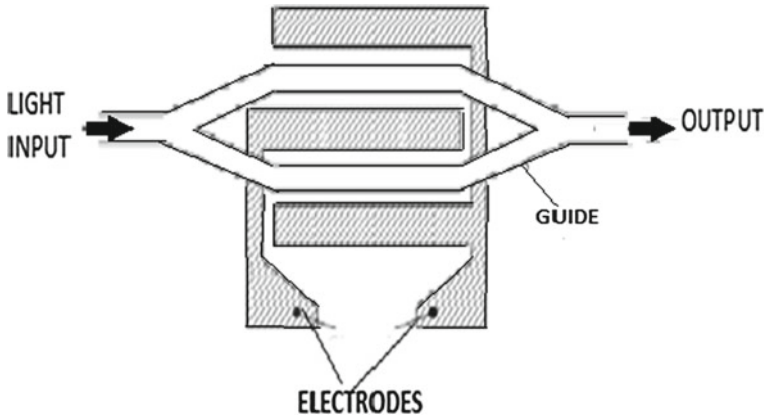

Fig. 1 A Y-junction interferometric modulator based on the Mach–Zehnder interferometer. Reproduced from [2]

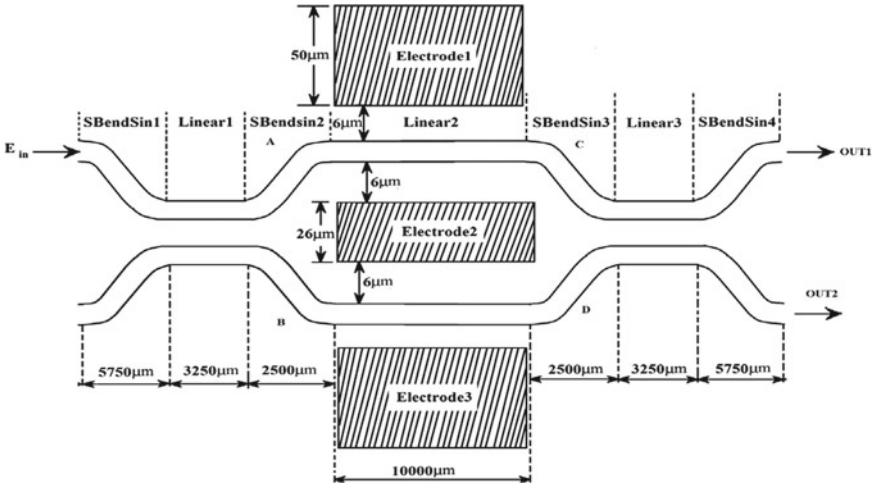

Fig. 2 Schematic representation of MZI. Reproduced from [10]

Table 1 MZI control electrode inputs

Input voltage (V)	Logic value
6.75	1
0	0

5 Implementation Design of Logic Gates

The logic gates and many combinational and sequential circuits can be represented as a combination of interferometers [24–28]. We are here reviewing available designs of basic gate using interferometric techniques. K. Santosh et al., Kumar A. et al., S.K. Raghuwanshi, S. Kumar, and Nan-Kuang Chen have discussed design of various logic gates and circuits. The demonstrated structures of all-optical logic units are made up of nonlinear structure as MZI with multiple input ports and this nonlinear structure has been cascaded for designing of all logic gates [10, 13, 29].

5.1 AND Gate

The design shown in Fig. 3 represents AND gate, we have shown interferometric structure for its demonstration. We have to use two MZIs for the generation of AND logic. In the structure, the output of first MZI is connected as an input to second MZI. By the application of potential at second electrode (control electrode) of each MZI signal can be shift to other of the interferometer [8]. The port(second) at the output of first MZI is kept open while first output port is joined to input of next MZI, then finally one of the output port (first port) of second MZI will give our desired AND

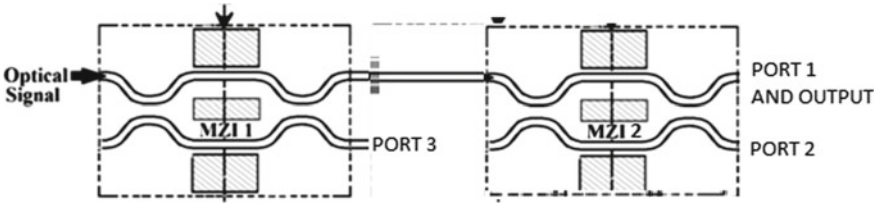

Fig. 3 Implementation blocks of AND gate. Reproduced from [3]

logic of the inputs [11]. The inputs of the gate are varied according to the control electrode voltage, when both inputs are logic high (6.75 V) the output will appear at output 1 of second MZI and for rest of the other cases the output will be zero [8].

5.2 NAND Gate

The basic structure of NAND gate has been displayed in Fig. 4, and for the designing of universal NAND gate [16], we need three MZIs, and for NAND implementation we have to invert the AND logic, and therefore we need cascading of MZI. In this, input has been provided at the first MZI and its output has been connected to the input of third interferometer at the first port, simultaneously second output of second interferometer has been connected as an input to third MZI second input, the second output port of third interferometer will give NAND logic of the inputs [4]. The optical input signals of the MZI can be varied by the variation of input voltages of the input electrodes. In the described design, electrode 2 is the control electrode for MZI and by varying the input voltages at control electrodes, the outputs can be varied (Table 2).

Table 2 Truth table of NAND gate

Sl. no.	Input (X) (V)	Input (Y) (V)	Output NAND (V)
1	6.75 (high-level logic)	6.75 (high-level logic)	0
2	0 (low-level logic)	0 (low-level logic)	6.75
3	6.75 (high-level logic)	0 (low-level logic)	6.75
4	0 (low-level logic)	6.75 (high-level logic)	6.75

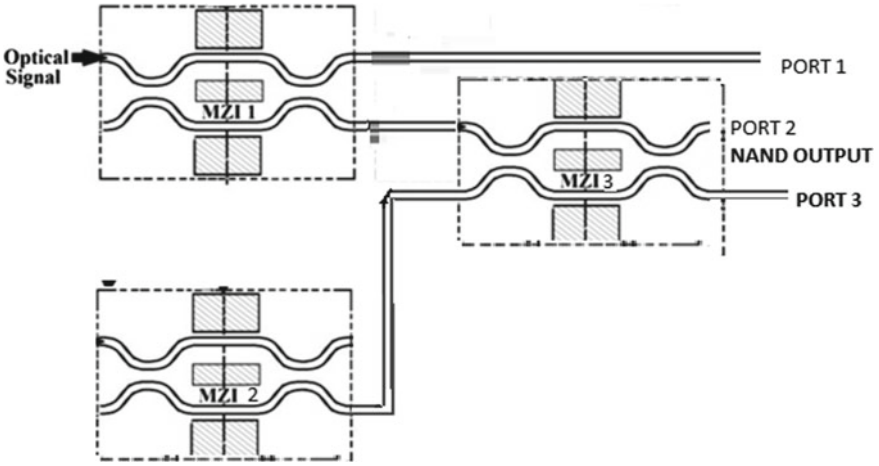

Fig. 4 Implementation blocks of NAND. Reproduced from [5]

5.3 NOR Gate

The universal logic gate (NOR) finds its application in various systems and in the synthesis of other gates also, Fig. 5 shows interferometric representation of NOR gate. In this structure, for the designing of NOR gate [15, 30], we have two MZIs and the input optical signal is provided as an input to the first input of first MZI, the second output of MZI (first) acts as input for second MZI, first output port of second MZI gives our desired NOR output which is port 2, and other outputs are kept open [5]. The input has been provided at the first MZI and control electrode voltages are used to vary the inputs of the logic gate. The voltage level of 6.75 V is considered as high logic and 0 V is considered as low logic; in this case, electrode 2 of first MZI is control electrode.

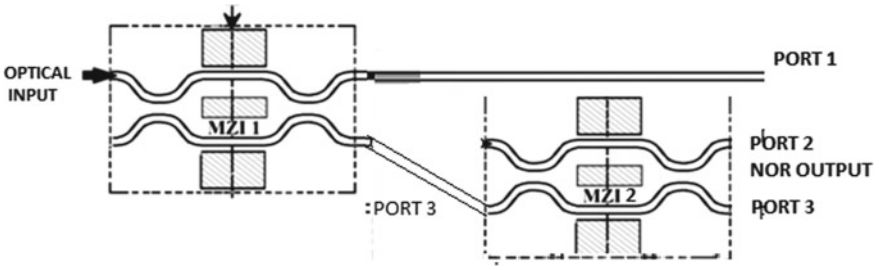

Fig. 5 Implementation blocks of NOR. Reproduced from [7]

6 Conclusion

In this paper, we have discussed basic concepts like XGM, XPM, FWM, and electro-optic effect associated with the designing of all-optical logic gates with the help of interferometric techniques. We have also discussed the working of MZI and its application in the switching of logic circuit. We have discussed various gate (viz. AND, NAND, and NOR) designs and their working when designed and operated through MZI. We know NAND and NOR are the universal logic gates and mainly all gates and logic circuits can be demonstrated by the cascading of logic gates, and therefore these designs can be implemented through simulation tools for the construction of high-speed and high-order switching applications.

References

1. Kumar S, Raghuwanshi SK, Kumar A (2013) Implementation of optical switches by using Mach–Zehnder interferometer. Opt Eng 52(9):097106
2. Senior JM (2009) Optical fiber communications principles and practice, 3rd edn
3. Kumar A, Kumar S, Raghuwanshi SK (2014) Implementation of XOR/XNOR and AND logic gates by using Mach–Zehnder interferometers. Optik 125:5764–5767
4. Kumar S, Raghuwanshi SK, Rahman A (2015) Implementation of high speed optical universal logic gates using the electro-optic effect-based Mach–Zehnder interferometer structures. J Mod Opt 62(12):978–988. https://doi.org/10.1080/09500340.2015.1015636
5. Kumar S, Singh G, Bisht A, Sharma S, Amphawan A (2015) Proposed new approach to the design of universal logic gates using the electro-optic effect in Mach–Zehnder interferometers. Appl Opt 54(28)
6. Sahu PP (2015) Optical pulse controlled two mode interference coupler based logic gates. Optik 126:404–407
7. Singh P, Tripathi DK, Jaiswal S, Dixit HK (2014) Review article all-optical logic gates: designs, classification, and comparison. Hindawi Publishing Corporation Advances in Optical Technologies (2014), vol 2014, Article id 275083
8. Kumar S, Kumar A, Raghuwanshi SK (2014) Implementation of an optical AND gate using Mach-Zehnder interferometers. In: Proceedings of SPIE optical modelling and design III vol 9131, 913120
9. Raghuwanshi SK, Kumar S, Chen N-K (2014) Implementation of sequential logic circuits using the Mach–Zehnder interferometer structure based on electro-optic effect. Opt Commun 333:193–208
10. Pashamehr A, Zavvari M, Banaei HA (2016) All-optical AND/OR/NOT logic gates based on photonic crystal ring resonators. Front Optoelectron 9(4):578–584
11. Chauhan C, Bedi A, Kumar S (2017) Ultrafast optical reversible double Feynman logic gate using electro-optic effect in lithium-niobate based Mach-Zehnder interferometers. In: SPIE proceedings, vol 10105, Oxide-based materials and devices VIII; 1010520. https://doi.org/10.1117/12.2250794
12. Parandin F, Karkhanehchi MM (2017) Terahertz all-optical NOR and AND logic gates based on 2D photonic crystals. Superlattices Microstruct 101:253–260
13. Dimitriadou E, Zoiros KE (2012) On the design of ultrafast all-optical NOT gate using quantum-dot semiconductor optical amplifier-based Mach-Zehnder interferometer. Opt Laser Technol 44:600–607

14. Kotb A, Zoiros KE (2013) Simulation of all-optical logic XNOR gate based on quantum-dot semiconductor optical amplifiers with amplified spontaneous emission. Opt Quantum Electron 45:1213–1221
15. Dimitriadou E, Zoiros KE (2013) Proposal for ultrafast all-optical XNOR gate using single quantum-dot semiconductor optical amplifier-based Mach-Zehnder interferometer. Opt Laser Technol 45:79–88
16. Dimitriadou E, Zoiros KE (2012) On the feasibility of ultrafast all optical NAND gate using single quantum-dot semiconductor optical amplifier-based Mach-Zehnder interferometer. Opt Laser Technol 44:1971–1981
17. Godbole A, Dali PP, Janyani V, Singh G, Tanabe T (216) All optical scalable logic gates using Si_3N_4 microring resonators. IEEE J Sel Top Quantum Electron 22
18. Kumar S, Chanderkanta, Raghuwansh SK (2016) Design of optical reversible logic gates using electro-optic effect of lithium niobate based Mach–Zehnder interferometers. Appl Opt 55:21/5693
19. Ishizaka Y, Kawaguchi Y, Saitoh K, Koshiba M (2011) Design of optical XOR, XNOR, NAND and OR logic gates based on multi-mode interference waveguides for binary—phase shift keyed signal. J Lightwave Technol 29:2836–2845
20. Ghadi A, Mirzanejhad S (2011) All optical logic gates using semiconductor based three coupled waveguides nonlinear directional coupler. Opt Commun 284:432–435
21. Kumar S, Raghuwanshi SK, Kumar A (2013) Implementation of optical switches by using Mach-Zehnder interferometer. Opt Eng 52:097106
22. Kumar S, Raghuwanshi SK, Kumar A (2013) 1 × 8 signal router using cascading the Mach-Zehnder interferometers. In: Prooceeding of 6th IEEE/International Conference on Advanced Info comm Technology (IEEE/ICAIT, 2013), pp 161–162
23. Raghuwanshi SK, Kumar A, Kumar S (2013) 1 × 4 signal router using 3-Mach-Zehnder interferometers. Opt Eng 52:035002
24. Kumar A, Kumar S, Raghuwanshi SK (2014) Implementation of full-adder and full-subtractor based on electro-optic effect in Mach-Zehnder interferometer. Opt Commun 324:93–107
25. Kumar A, Raghuwanshi SK (2016) Implementation of optical gray code converter and even parity checker using the electro-optic effect in the Mach–Zehnder interferometer. Opt Quantum Electron. https://doi.org/10.1007/s11082-014-0087-9
26. Kumar S, Singh G, Bisht A (2015) 4 × 4 signal router based on electro-optic effect of Mach-Zehnder interferometer for wavelength division multiplexing applications. Opt Commun 353:17–26
27. Raghuwanshi SK, Kumar A, Chen NK (2014) Implementation of sequential logic circuits using the Mach–Zehnder interferometer structure based on electro-optic effect. Opt Commun 333:193–208
28. Tang X, Fang Z, Zhai Y et al (2017) A reconfigurable optical logic gate with up to 25 logic functions based on polarization modulation with direct detection. IEEE Photon J 9(2):1943-0655
29. Rendón-Salgado I, Gutiérrez-Castrejón R (2017) 160 GB/s all-optical AND gate using bulk SOA turbo–switched Mach Zehnder interferometer. Opt Commun 399:77–86
30. Kotb A, Zoiros KE (2013) Simulation of all-optical logic XNOR gate based on quantum-dot semiconductor optical amplifiers with amplified spontaneous emission. Opt Quantum Electron 45:1213–1221

Supercontinuum Generation at 3100 nm in Dispersion-Engineered $As_{38.8}Se_{61.2}$-Based Chalcogenide Photonic Crystal Fibers

Shruti Kalra, Sandeep Vyas, Edris Faizabadi, Manish Tiwari and Ghanshyam Singh

Abstract The presented paper numerically investigates the mid-infrared supercontinuum generation of 3800 nm broad spectra spanning from 2000 to 5800 nm with nonlinear $As_{38.8}Se_{61.2}$ chalcogenide solid core photonic crystal fiber. The photonic crystal fiber is tailored to generate dispersion in anomalous region, resulting in zero-dispersion wavelengths. Pumping the engineered fiber with 1 kW power at 3100 nm near lower zero-dispersion wavelength a broad spectrum is observed.

Keywords Photonic crystal fiber (PCF) · Chromatic dispersion · Effective mode area (A_{eff}) · Nonlinear coefficient · Supercontinuum generation (SCG)

1 Introduction

The rapid growth in optical fiber since its advent has revolutionized the communications field and in addition significantly contributed to the other associated fields. Further, the rapid growth in technology has helped in translating the research, new

S. Kalra (✉) · S. Vyas
Department of ECE, Jaipur Engineering College & Research Centre, Jaipur, India
e-mail: shrutikalra.ece@jecrc.ac.in

S. Vyas
e-mail: vyas.sandeep@vitej.ac.in

E. Faizabadi
School of Physics, Iran University of Science & Technology, Tehran, Iran
e-mail: edris@iust.ac.ir

M. Tiwari
Department of ECE, Manipal University, Jaipur, India
e-mail: manishtiwari@ieee.org

G. Singh
Department of ECE, Malaviya National Institute of Technology Jaipur, Jaipur 302017, Rajasthan, India
e-mail: gsingh.ece@mnit.ac.in

© Springer Nature Singapore Pte Ltd. 2020

V. Janyani et al. (eds.), *Optical and Wireless Technologies*,
Lecture Notes in Electrical Engineering 546,
https://doi.org/10.1007/978-981-13-6159-3_46

invention and development of optical devices like silicon and non-silica waveguides, microstructured optical fibers (MOFs), integrated optical devices on chips, and many others in labs to commercial applications [1–3].

Among all optical light guides, the microstructured optical fiber, widely known as photonic crystal fibers (PCFs), is a distinctive guiding medium with special and versatile technology. During the last few decades, PCFs have emerged as one of the favorite interest areas of research for scientists and researchers globally [4]. The PCFs continue to be one of the active research areas due to the flexibility offered in geometry design and numerous applications in different areas. The solid or hollow core surrounded by microscopic air-hole structure running along the entire length of the core, forming cladding, is the simple structure of photonic crystal fiber. Photonic crystal fibers' distinguished characteristics can be tailored with its design geometry making them attractive and demanding. PCFs have distinguished properties like large mode area, endlessly single mode, controlled dispersion, and low to highly nonlinear fibers as compared to conventional fibers [5, 6]. Further, the nonlinearity offered by PCF leads to many processes like self-phase modulation (SPM), stimulated Raman scattering (SRS), cross-phase modulation (XPM), four-wave mixing (FWM), supercontinuum generation, and many more [7].

Supercontinuum has immense number of applications in optical coherence tomography (OCT), wavelength-division multiplexing (WDM), spectroscopy, biomedical imaging, metrology, low coherence interferometry, optical frequency combs, and many others [8–14]. Supercontinuum generation is a nonlinear process, where an intense laser pulse gets broadened as it travels through length of a nonlinear medium in the light guiding channel [15].

In this paper, we present a design of the chalcogenide-based PCF tailored to obtain broad dispersion profile in the anomalous region with lower zero-dispersion wavelength near pump wavelength 3100 nm in mid-infrared region. The chalcogenide glasses have good transparency window in the mid-infrared region making them suitable for designing guiding medium for optical signals. The chalcogenide glasses with different compositions can be explored; among the available, As_2S_3 and As_2Se_3 are widely used [16, 17]. It has been reported by Oh et al. that the $As_{38.8}Se_{61.2}$ chalcogenide material depicts much flatter and broader transparency than As_2Se_3 in the window spreading from 2 to 12 μm [18]. In the year 2016, Diouf and his team reported supercontinuum generation spreading in mid-infrared region from 2900 to 4575 nm, by pumping optical pulses at 3.7 μm wavelength with 0.88 kW peak power in a 5-cm-long all-normal dispersion-engineered PCF [19]. Here, in this paper, we present a design of a PCF, tailored to obtain the anomalous dispersion profile. The designed PCF was optimized and then numerically simulated to find its suitability to generate supercontinuum. The optimized PCF was pumped with 1 kW power at 3100 nm, and spectra spanning from 2000 to 5800 nm were observed from the numerical simulation.

The paper is organized in the following sequence. Section 2 gives brief overview of the study of modal properties of chalcogenide PCF designed with $As_{38.8}Se_{61.2}$. The section discusses the refractive index values and other vital parameters of the fiber, an overview of full modal analysis method along with the solutions of second-

order Sellmeier equation used. The PCF design and analysis is presented in Sect. 3. In the second last section, generation of supercontinuum with the tailored and optimized photonic crystal fiber is discussed. The analysis of supercontinuum generation using Generalized Nonlinear Schrödinger Equation (GNLSE) is also presented in the section. Finally, Sect. 5 concludes the paper.

2 Method of Analysis

It is essential to determine the few optical properties of the fiber before designing its specific application. The few vital properties analyzed for generation of supercontinuum are presented underlined. The method employed for the analysis is finite-difference time-domain (FDTD). The linear parameter included refractive index of the $As_{38.8}Se_{61.2}$. The refractive index as a function of wavelength is usually studied with Sellmeier equation; however, the Cauchy equations were used for the transparent region which is expressed as [19]

$$n(\lambda) = \sqrt{7.65 + \frac{0.73}{\lambda^2} + \frac{0.87}{\lambda^4}} \tag{1}$$

Another important parameter which is vital for generation of supercontinuum is chromatic dispersion. The chromatic dispersion (D_C) is related to group velocity dispersion as per solution of Maxwell equations, which is due to material (D_M) and waveguide dispersion (D_W). The equations below were used to calculate the dispersion of the fiber [20].

$$D_C(\lambda) = D_M(\lambda) + D_W(\lambda) \tag{2}$$

$$D(\lambda) = -\frac{\lambda}{c}\frac{d^2}{d\lambda^2}\mathrm{Re}[n_{eff}(\lambda)] = -\frac{2\pi c}{\lambda^2}\beta_2(\lambda) \tag{3}$$

In the above equation, c represents the light velocity in a vacuum and $n_{eff}(\lambda)$ is the effective index of the fiber. The two vital nonlinear parameters which play a significant role in supercontinuum generation are nonlinear coefficient and effective area of the fundamental mode of PCF.

The equation below denotes the relation of nonlinear coefficient with effective area [20]:

$$\gamma = \frac{2\pi n_2}{\lambda A_{eff}} \tag{4}$$

In the above relation, n_2 denotes the nonlinear Kerr index of $As_{38.8}Se_{61.2}$ used as the background material to design the fiber, and the value is 4.89×10^{-18} ($m^2.W^{-1}$) [19], effective cross-sectional area of the fiber and centre wavelength is represented

as A_{eff} and λ respectively. The expression of effective cross-sectional area of the fiber can be expressed as

$$A_{eff} = \frac{\left(\iint_{-\infty}^{\infty} |E|^2 dxdy\right)^2}{\iint_{-\infty}^{\infty} |E|^4 dxdy} \tag{5}$$

where E is the electric field distribution [20].

To study the generation of supercontinuum, we used the underlined Generalized Nonlinear Schrödinger Equation (GNLSE), which numerically relates the pulse propagation in the photonic crystal fiber. The equation takes into consideration both linear and nonlinear effects as represented on either sides of Eq. 6 [20].

$$\frac{\partial A}{\partial z} + \frac{\alpha}{2}A - \left(\sum\nolimits_{n\geq 2} \beta_n \frac{i^{n+1}}{n!}\frac{\partial^n A}{\partial t^n}\right) = i\gamma\left(1 + \frac{i}{\omega_o}\frac{\partial}{\partial t}\right)A(z,t)\int_{-\infty}^{\infty} R(t')\left|A\left(z, t-t'\right)\right|^2 dt' \tag{6}$$

In the above equation, A(z, nt) is the electric field envelope which has been calculated using the split-step Fourier method. β_n is nth derivative of the propagation constant β, t represents time, γ represents the nonlinear coefficient, z denotes distance, and τ is the retarded time traveling at the envelope group velocity. The Raman response function $R(t)$ in the above equation is expressed as [20]

$$R(t) = (1 - f_r)\delta(t) + f_r \frac{\tau_1^2 + \tau_2^2}{\tau_1 \tau_2^2} \exp\left(-\frac{t}{\tau_2}\right) \sin\left(\frac{t}{\tau_1}\right) \tag{7}$$

including the Raman contributions of instantaneous electronic and vibrations. It can be observed that τ_1 relates to the inverse of the phonon oscillation frequency and τ_2 is the bandwidth of the Raman gain spectrum of the material. In our work, we have taken τ_1= 23.38 fs, τ_2 = 60.31 fs for $As_{38.8}Se_{61.2}$ chalcogenide glass and f_r = 0.031, representing fractional contribution of the delayed Raman response [19].

3 Proposed PCFs Design and Analysis

In the work carried out, we designed two PCFs to have a comparative study of impact of design parameter pitch on the dispersion, effective area, and nonlinear coefficient. In both the PCF designs, the number of rings, lattice type, and diameter of air holes in cladding region is kept identical. Figure 1 depicts the schematic view of PCF design with three rings in hexagonal lattice with fixed diameter of air holes (black color) in cladding region with $As_{38.8}Se_{61.2}$ as background material. The value of identical diameter of air holes used for the two PCF designs was 1.2 μm, and the different pitch (Λ) values for the two designs were 1.8 μm and 2 μm, respectively.

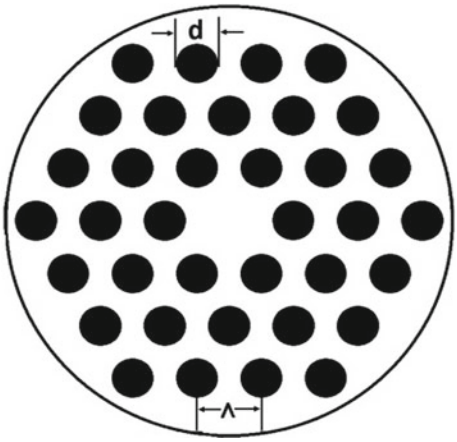

Fig. 1 Schematic view of the designed PCF

Both the PCF designs resulted in the dispersion in anomalous region as depicted in Fig. 2. The PCF design with pitch value 2 μm resulted in broader and more flat dispersion profile as compared to the design with pitch value of 1.8 μm. The two zero-dispersion wavelengths obtained for the PCF design with pitch value 1.8 μm was 2.9 and 5.61 μm. It can also be observed that on changing the pitch value on the higher side, the dispersion plot shifted toward the higher wavelength and was also broader spanning from 2.95 to 5.82 μm. The comparative dispersion plot of the two designs is depicted in Fig. 2. The lower zero-dispersion wavelength obtained was 2.95 μm and was closer to the pump wavelength 3.1 μm to be employed for generation of supercontinuum.

The two designs of the PCF were numerically simulated for investigating the parameters nonlinear coefficients and effective area. The comparative plot of effective area is presented in Fig. 3. Figure 4 represents the comparative plot of nonlinear coefficient. It can be inferred from the plot that the fiber design with higher pitch value resulted in higher values of effective area and lower values of nonlinear coefficient [15]. The PCF design with pitch value 1.8 μm resulted in lower values of effective area and higher values of nonlinear coefficient as compared to other PCF design with pitch value 2 μm. As the design with pitch value 2 μm resulted in a dispersion plot which was broader and flat with zero-dispersion wavelength much closer to pump, wavelength was further simulated for supercontinuum generation.

At the pump wavelength of 3.1 μm, the value of effective area (A_{eff}) and nonlinear coefficient (γ) recorded for the fiber design with lower pitch value were 3.44266 μm^2 and 2884 W^{-1} km^{-1}, respectively. The values of effective area and nonlinear coefficient for the PCF design with pitch value 2 μm at the same pump wavelength were 4.61909 μm^2 and 2149 W^{-1} km^{-1}, respectively. The pump wavelength to be

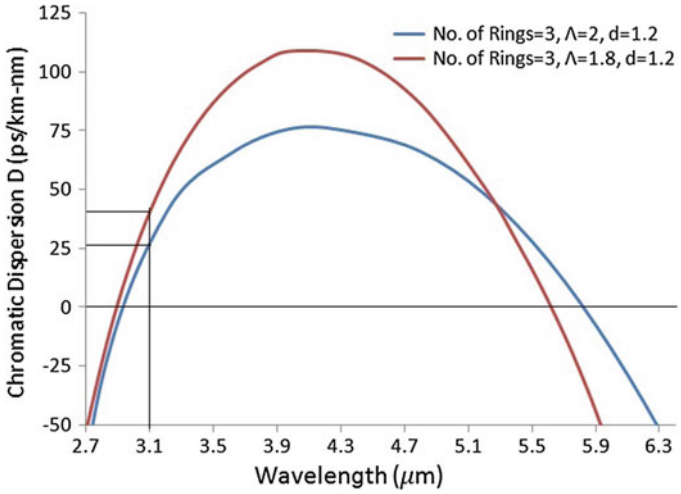

Fig. 2 The dispersion plot of the fiber with different pitch values

Fig. 3 The comparative plot of effective area

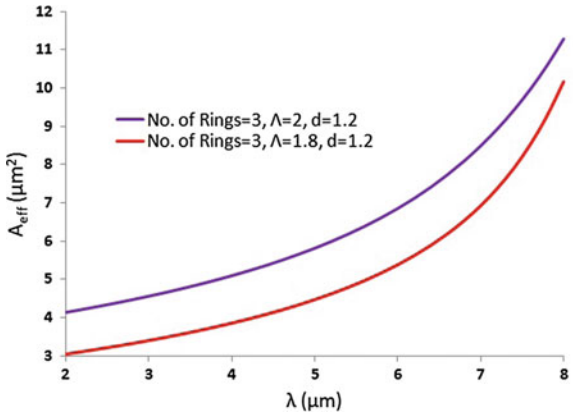

used was 3.1 μm for generation of supercontinuum, so the fiber design with pitch value 2 μm was preferred as this design generated a broader dispersion plot and zero-dispersion wavelength closer to the pump wavelength.

4 Supercontinuum Generation in Proposed PCF

The fiber design with air-hole diameter 1.2 μm and pitch 2 μm was numerically simulated to generate supercontiuum. The solutions of GNLSE were obtained by split-step Fourier method [20]. The designed PCF of length 100 mm was pumped

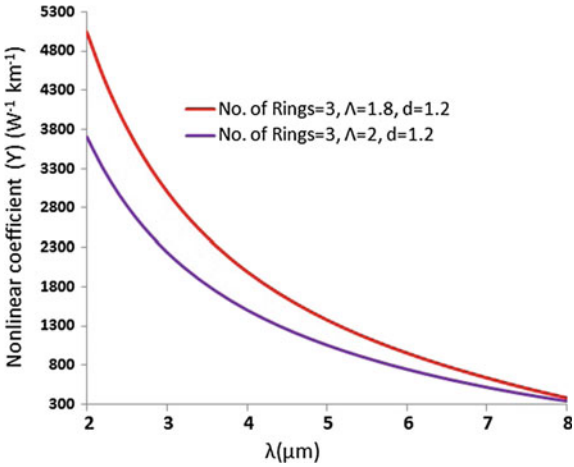

Fig. 4 Plot of nonlinear coefficients

with optical pulses near the zero-dispersion wavelength at 3.1 μm with peak power of 1 kW and duration of 80 fs.

The values of effective area (A_{eff}) and nonlinear coefficient (γ) used for the simulation were 4.61909 μm^2 and 2149 W^{-1} km^{-1}, respectively, to generate supercontinuum in anomalous regime. In anomalous region due to solitons fission and Raman soliton self-frequency shift, the spectral broadening is toward the longer wavelength side. In the starting phase, the pulse broadening is primarily due to self-phase modulation (SPM) and after the initial spectral broadening the nonlinear processes like four-wave mixing (FWM), stimulated Raman scattering (SRS), and dispersion actively contribute forming a broadband supercontinuum. After few millimeters of transverse, the spectrum splits into two major peaks, and the number of sub-peaks increases continuously, between split major peaks after moving outward from the original pump wavelength resulting in generation of spectra [4]. Figure 5 portrays spectral broadening of SCG in the designed PCF.

5 Conclusion

The paper presents the design of an $As_{38.8}Se_{61.2}$-based chalcogenide solid core photonic crystal fiber. Impacts of variation of the pitch on parameters like dispersion profile, effective area, and nonlinear coefficients were investigated in the initial work. Further, the design was engineered to obtain broad dispersion in anomalous regime, and the optimized design was investigated and numerically simulated for supercontinuum generation. The designed PCF of length 100 mm was pumped with optical hyperbolic secant pulses of 80 fs duration and 1 kW peak power at pump wavelength of 3.1 μm. The estimated values of effective area and nonlinear coefficients at the

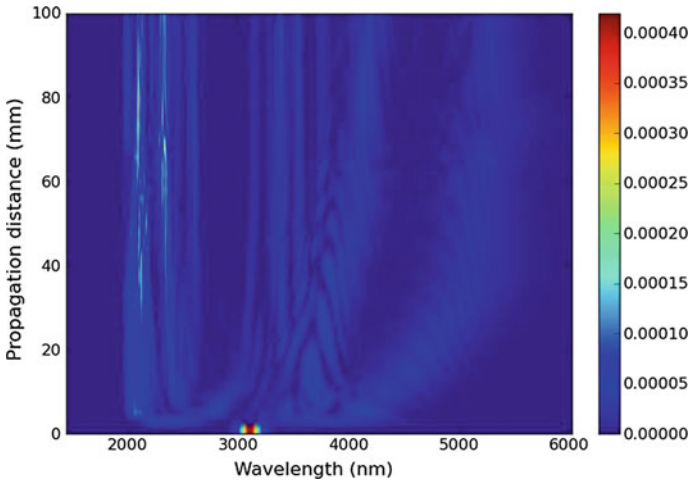

Fig. 5 Spectral escalation of SC in the designed PCF

pump wavelengths were 4.61909 μm^2 and 2149 W^{-1} km^{-1}, respectively, suitable to generate the supercontinuum. Simulations resulted in spectra spanning from 2000 to 5800 nm.

References

1. Barh A, Ghosh S, Agrawal GP, Varshney RK, Aggarwal ID, Pal BP (2013) Design of an efficient mid-IR light source using chalcogenide holey fibers: a numerical study. J Opt 15:035205
2. Barh A, Ghosh S, Varshney RK, Pal BP (2013) An efficient broadband mid-wave IR fiber optic light source: design and performance simulation. Opt Express 21:9547–9555
3. Estevez M-C, Alvarez M, Lechuga LM (2012) Integrated optical devices for lab-on-a-chip biosensing application. Laser Photonics Rev 6(4):463–487
4. Vyas S, Tanabe T, Tiwari M, Singh G (2016) Chalcogenide photonic crystal fiber for ultraflat mid-infrared supercontinuum generation. Chin Opt Lett 14:123201
5. Russell PSJ (2006) Photonic-crystal fibers. J Lightwave Technol 24:4729–4749
6. Saitoh K, Koshiba M, Mortensen NA (2006) Nonlinear photonic crystal fibers: pushing the zero-dispersion towards the visible. New J Phys 8:207–215
7. Vyas S, Tiwari M, Tanabe T, Singh G (2016) Chalcogenide ($LiGSe_2$, LiGISe, $LiGaS_2$): a perfect material to design highly nonlinear PCFs for supercontinuum generation. In: Proceedings of the international conference on recent cognizance in wireless communication & image processing. Springer, India, pp 409–413. https://doi.org/10.1007/978-81-322-2638-2638-3
8. Tamura KR, Kubota H, Nakazawa M (2000) Fundamentals of stable continuum generation at high repetition rates. IEEE J Quantum Electron 36:773–779
9. Hult J, Watt RS, Kaminski CF (2007) High bandwidth absorption spectroscopy with a dispersed supercontinuum source. Opt Express 15:11385–11395
10. Kaminski CF, Watt RS, Elder AD, Frank JH, Hult J (2008) Supercontinuum radiation for applications in chemical sensing and microscopy. Appl Phys B 92:367–378

11. Hartl I, Li XD, Chudoba C, Ghanta RK, Ko TH, Fujimoto JG, Ranka JK, Windeler RS (2001) Ultrahigh-resolution optical coherence tomography using continuum generation in an air-silica microstructure optical fiber. Opt Lett 26:608–610
12. Shi K, Li P, Liu Z (2007) Broadband coherent anti-Stokes Raman scattering spectroscopy in supercontinuum optical trap. Appl Phys Lett 90:141116
13. Morioka T, Kawanishi S, Mori K, Saruwatari M (1994) Transformlimited, femtosecond WDM pulse generation by spectral filtering of gigahertz supercontinuum. Electron Lett 30:1166–1168
14. Reichert J, Udem T, Hänsch TW, Knight JC, Wadsworth WJ, Russell PSJ (2000) Optical frequency synthesizer for precision spectroscopy. Phys Rev Lett 85:2264–2267
15. Vyas S, Tanabe T, Tiwari M, Singh G (2016) Ultraflat broadband supercontinuum in highly nonlinear $Ge_{11.5}As_{24}Se_{64.5}$ photonic crystal fibres. Ukr J Phys Opt 17:132–139
16. Vyas S, Tanabe T, Singh G, Tiwari M (2016) Broadband supercontinuum generation and Raman response in $Ge_{11.5}As_{24}Se_{64.5}$ based chalcogenide photonic crystal fiber. In: IEEE international conference on computational techniques in information and communication technologies (ICCTICT), pp 607–611. https://doi.org/10.1109/ICCTICT.2016.7514651
17. Vyas S, Tanabe T, Tiwari M, Singh G (2016) Mid-infrared supercontinuum generation in $Ge_{11.5}As_{24}Se_{64.5}$ based chalcogenide photonic crystal fiber. In: IEEE international conference advances in computing, communications and informatics (ICACCI), pp 2547–2552. https://doi.org/10.1109/icacci.2016.7732436
18. Oh M-S, Seo I (2015) Preparation and characterization of $As_{40}Se_{60}$ and $As_{38.8}Se_{61.2}$ glasses with high quality for single mode IR glass fiber. Opt Fiber Technol 21:176–179
19. Diouf M, Salem AB, Cherif R, Saghaei H, Wague A (2017) Super-flat coherent supercontinuum source in $As_{38.8}Se_{61.2}$ chalcogenide photonic crystal fiber with all-normal dispersion engineering at a very low input energy. Appl Opt 56(2):163–169
20. Agarwal GP (2007) Nonlinear fiber optics, 4th edn. Academic

Gap Coupled Swastika-Shaped Patch Antenna for X and Ku Band Applications

Brijesh Mishra, Vivek Singh and Rajeev Singh

Abstract A compact (20 × 20) mm^2 swastika-shaped patch antenna with and without gap coupling for single band applications (X/Ku band) is proposed. Three designs are presented: the Design-1 is a simple swastika-shaped patch antenna without any gap coupling, whereas Design-2 and Design-3 are provided with vertical and horizontal gap coupling, respectively. The Design-1, Design-2, and Design-3 operate in the frequency range of (10.25–12.4) GHz, (11.74–13.52) GHz, and (10.74–13.63) GHz with resonating frequencies of 11.3 GHz, 12.6 GHz, and 12 GHz; peak gains of 3 dBi, 5 dBi, and 5.13 dBi; and maximum radiation efficiencies of 88.4%, 89.2%, and 87.2%, respectively.

Keywords Patch antenna · Gap coupling · Notches · Impedance bandwidth · X/Ku band

1 Introduction

Every passing day we encounter with a new dimension of research in the field of wireless communication. Advancement in wireless technology has compelled the researchers and technologists to develop more efficient and compact antennas for better communication. Thus, micro-strip patch antenna is garnering the attention because [1, 2], *first*, it is light weighted, *second*, there is no requirement of cavity backing, *third*, ease of fabrication, *fourth*, ease of printing an array of patches on a single substrate, etc. However, there is a limitation of micro-strip patch antennas, in

B. Mishra · V. Singh · R. Singh (✉)
Department of Electronics and Communication, University of Allahabad, Allahabad, Uttar Pradesh, India
e-mail: rsingh68@gmail.com

B. Mishra
e-mail: brijesh.mishra0933@gmail.com

V. Singh
e-mail: vivek.10singh@gmail.com

© Springer Nature Singapore Pte Ltd. 2020

V. Janyani et al. (eds.), *Optical and Wireless Technologies*,
Lecture Notes in Electrical Engineering 546,
https://doi.org/10.1007/978-981-13-6159-3_47

the form of its narrow bandwidth and poor antenna gain. Several techniques such as stacking substrate [3], thick substrate [4], parasitic element [5], shorting pin [6], shorting wall [7], and introducing slot on the patch [8] have been reported by authors to improve bandwidth and gain of micro-strip patch antenna.

In this paper, we have proposed a design of swastika-shaped patch antenna with and without gap coupling technique. The gap coupled micro-strip antennas give a large bandwidth as compared to conventional micro-strip antennas [9], although the bandwidth can be increased by increasing the thickness of substrate as by doing so will reduce the stored energy, thereby decreasing quality factor, which is inversely proportional to bandwidth [9, 10]. However, doing so will also result in poor radiation efficiency and this is the reason we switched to gap coupling.

In the present work, we present three different designs. Design-1 is a simple swastika-shaped patch antenna without any gap coupling. A horizontal and vertical gap coupling is introduced between parasitic and fed patch in Design-2 and Design-3, respectively. Figure 1a, b and c represents the front view geometry of Design-1, Design-2, and Design-3, respectively. Figure 1d represents the side view geometry of proposed swastika shape antennas. The HFSS software is used to design antenna structures and analyze the antenna results in terms of surface current distribution, return loss, VSWR, antenna gain, radiation efficiency, group delay, and radiation pattern.

A comparative overview of different antenna structures is presented in terms of antenna size, resonating frequency, impedance bandwidth, gain of the antenna, and applications in Table 1.

Table 1 Comparison between proposed design and existing different patch antennas

	References	Patch area (mm^2)	Resonating frequency (GHz)	Impedance bandwidth (%)	Antenna gain (dBi)	Applications
Antennas having different shape	[11]	1089	9.5	17.89	4.6	X band
	[12]	772.84	2.4	5.25	6.1	WLAN, WiFi
	[13]	440	5.25	5.76	2.64	WLAN
	[14]	4900	1.6	23	2.45	GPS
Antennas in Ku-band range	[15]	960	14.1	11.45	7.8	Ku band
	[16]	900	15	13.36	6.3	Ku band
	[17]	225	12.2	7.77	7.6	Ku band
Proposed design	Design-1	400	11.3	19	3	X and Ku bands
	Design-2	400	12.6	14.13	5	
	Design-3	400	12	24	5.13	

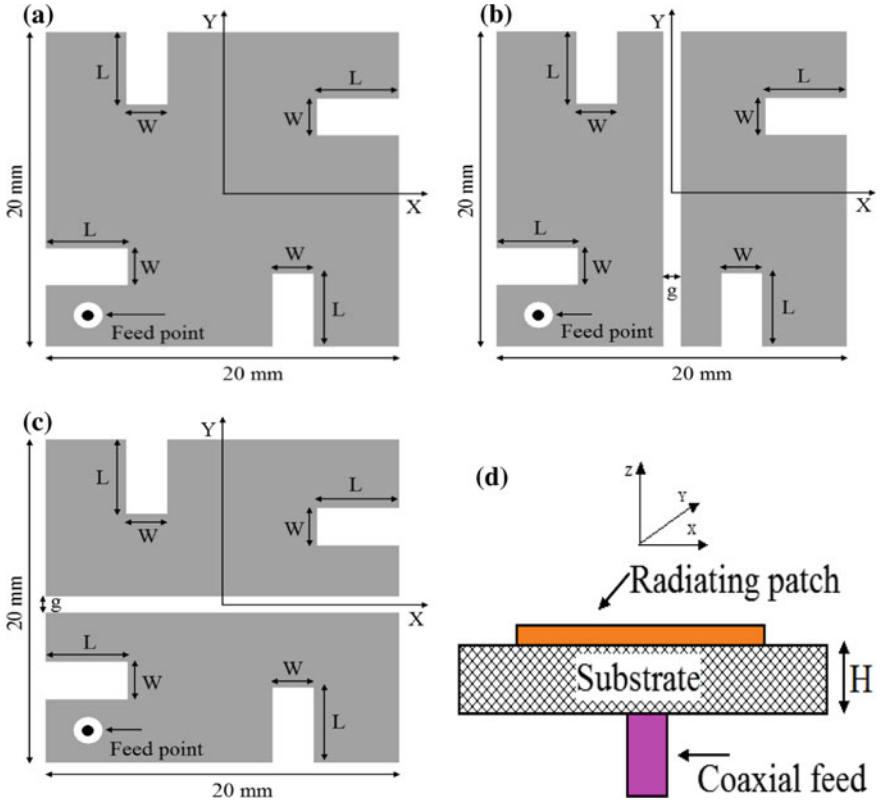

Fig. 1 Front view geometry of proposed structures: **a** Design-1, **b** Design-2, **c** Design-3, and **d** side view geometry of proposed designs

2 Antenna Design and Configuration

The structure of the Design-1, Design-2, and Design-3 consists of a conducting square ground plane of length 20 mm and width 20 mm. The FR4 epoxy is used as substrate (relative permittivity $\varepsilon_r = 4.4$, thickness H = 3 mm, and length and width of the substrate are 20 mm). The swastika shape patch structure is obtained by removing four rectangular notches of length (L = 6 mm) and width (W = 4 mm) from a square patch of dimension 20×20 mm^2 which is printed on substrate. The coaxial probe feed SMA connecter of 50 Ω with position coordinate of (−8, −8) mm (i.e., at the bottom left of the patch and substrate) and radius of 1 mm is used for the excitation of patch. The structure of proposed swastika shape antenna (cf. Fig. 1a) is further modified (cf. Fig. 1b) by introducing the rectangular slot of length of 20 mm and gap (g = 1 mm) along y-axis, and this design can be called as vertically gap coupled swastika shape antenna. Similarly, a horizontal rectangular slot of same dimension is introduced along the x-axis, which divides the design of Fig. 1a into two

equal parts and this modified structure is named as horizontally gap coupled swastika shape antenna and is shown in Fig. 1c. Analysis of antenna parameters determines the performance of the proposed antenna for X and Ku band applications, which is presented in the foregoing section.

3 Result and Discussion

The surface current distributions of the proposed antennas (Design-1, Design-2, and Design-3) are shown in Fig. 2a, b and c, respectively. From perusal of Fig. 2a, it is clear that for Design-1, most of the current density is around the center and the lower part of the patch, and a maximum current density of 44.18 A/m is observed, which makes the antenna to resonate at 11.3 GHz. However, for the proposed gap coupled patch antennas (cf. Fig. 2b, c), the maximum current distributions are observed at the fed patch having the values as 48.92 A/m and 53.61 A/m for Design-2 and Design-3, respectively. Surface current distribution (cf. Fig. 2b, c) is responsible to make the antennas resonate at 12.5 and 12 GHz for both the designs.

Return loss and VSWR response of proposed swastika shape antennas are presented in Fig. 3a and b, respectively. Impedance bandwidth (at −10 dB) for Design-1, Design-2, and Design-3 of swastika shape antenna is 19%, 14.13%, and 24%, respectively. It fairly covers the band of (10.25–12.4) GHz, (11.74–13.52) GHz, and (10.74–13.63) GHz, respectively. From Table 1, it is observed that the impedance bandwidth of Design-1 is greater than the work reported in [11–13, 15–17] and less than the work reported in [14], whereas impedance bandwidth of Design-2 is greater than the work reported in [12, 13, 15–17] and less than the work reported in [11, 14]. Proposed Design-3 has maximum bandwidth as compared to all reported values of bandwidth in Table 1. A perfect impedance matching between the input impedance and characteristic impedance of the proposed antennas is observed in Fig. 3b. VSWR

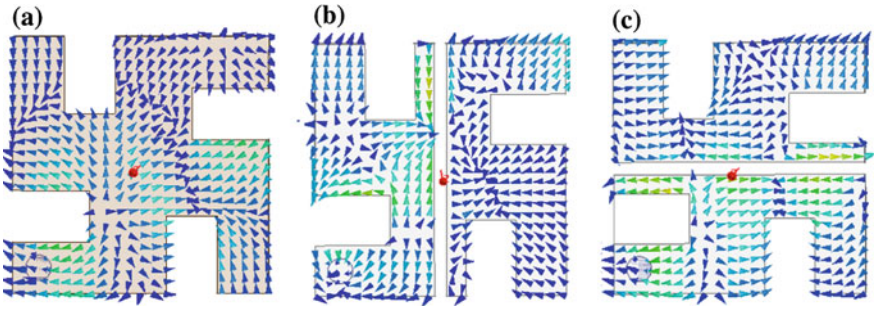

Fig. 2 Surface current distribution of the proposed antennas: **a** Design-1 at 11.3 GHz, **b** Design-2 at 12.6 GHz, and **c** Design-3 at 12 GHz

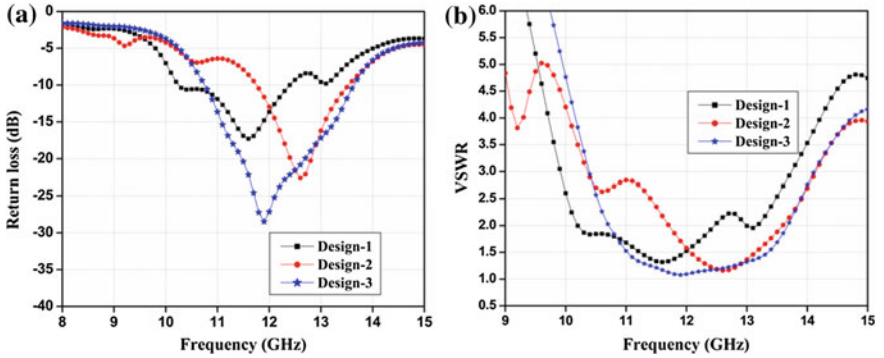

Fig. 3 **a** Return loss versus frequency plot **b** VSWR versus frequency plot

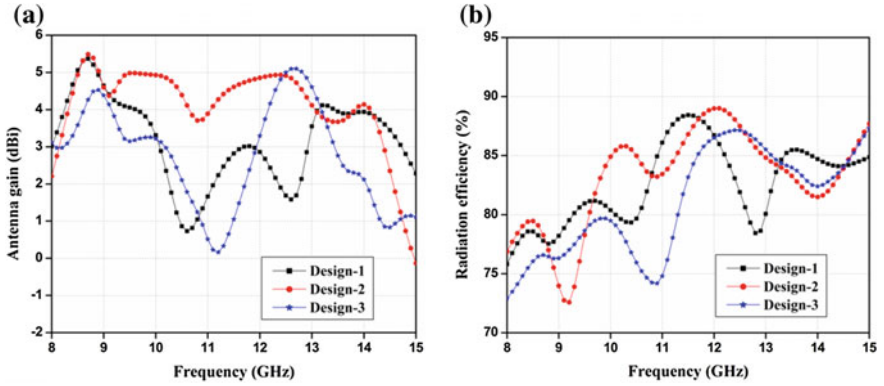

Fig. 4 **a** Antenna gain versus frequency plot **b** radiation efficiency versus frequency plot

of Design-1, Design-2, and Design-3 of swastika shape antennas are observed to be 1.4, 1.1, and 1.01, respectively (cf. Fig. 3b).

The peak gains of Design-1, Design-2, and Design-3 of swastika shape antennas are 3 dBi, 5 dBi, and 5.13 dBi as observed in Fig. 4a. For Design-1, a larger value of peak gain is observed from the values reported in [13, 14], and lesser value of peak gain is observed as compared to the values reported in [11, 12, 15–17]. For Design-2 and Design-3, a higher peak gain is observed as compared to the peak gain reported in [11, 13, 14] but lesser peak gain is reported as compared to the peak gain reported in [12, 15–17]. From Fig. 4b, a maximum radiation efficiency of 88.4% for Design-1, 89.2% for Design-2, and 87.2% for Design-3 is observed.

Group delay is used to measure the degree of distortion in the pulse transmission, and it should be less than 0.8 ns for the effective communication of the pulses [3]. Figure 5a illustrates the plot between group delay (ns) and frequency (GHz) for the proposed antennas, and it is clear that the group delay is less than 0.8 ns in the operating frequency range.

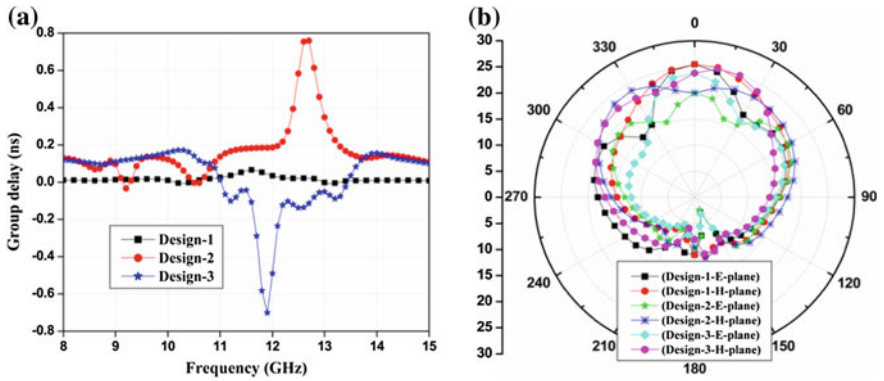

Fig. 5 **a** Group delay response and **b** radiation pattern response

Figure 5b represents the radiation patterns of the proposed patch antennas. The ($\Phi = 0°$, θ variable) plane determines the electric field radiation pattern, and ($\Phi = 90°$, θ variable) plane determines the magnetic field radiation pattern of the proposed patch structures. In the front side of the patch (i.e., 90°–270°), broader radiation pattern (main lobe) is observed while in the back side of the patch, the strength of electric field and magnetic field is comparatively small (minor lobe).

4 Conclusions

A compact (20 × 20) mm^2 swastika-shaped patch antenna with different configurations (gap coupling and without gap coupling) is presented for the X/Ku band applications. Design-1 is obtained by introducing notches. Design-2 and Design-3 are obtained by providing the gap coupling on the patch of Design-1, in vertical and horizontal direction, respectively. Area of the proposed design is small as compare to the reported [11–16] designs by factor of 2.72, 1.93, 1.1, 12.25, 2.4, and 2.25, respectively, and large as compare to [17] by factor of 1.7. The proposed antennas are more suitable and compact for the satellite and radar wireless applications as compared to other reported antennas.

References

1. James JR, Hall PS (1989) Handbook of microstrip antennas. Peter Peregrinus Ltd., London, UK
2. Kumar G, Ray KP (2003) Broadband microstrip antenna. Norwood, MA
3. Mishra B, Singh V, Singh R (2017) Dual and wide-band slot loaded stacked microstrip patch antenna for WLAN/WiMAX applications. Microsyst Technol 23(8):3467–3475

4. Cicchetti R, Miozzi E, Testa O (2017) Wideband and UWB antennas for wireless applications: a comprehensive review. Int J Antennas Propag 2017:1–45
5. Kumar G, Gupta K (1985) Nonradiating edges and four edges gap-coupled multiple resonator broad-band microstrip antennas. IEEE Trans Antennas Propag 33(2):173–178
6. Guha D, Antar YM (2006) Circular microstrip patch loaded with balanced shorting pins for improved bandwidth. Antennas Wirel Propag Lett 5(1):217–219
7. Li Y, Chair R, Luk KM, Lee KF (2004) Broadband triangular patch antenna with a folded shorting wall. IEEE Antennas Wirel Propag Lett 3(1):189–192
8. Ansari JA, Singh P, Dubey SK, Khan RU, Vishvakarma BR (2009) Analysis of stacked V-slot loaded patch antenna for wideband application. Microw Opt Technol Lett 51(2):324–330
9. Asthana A, Vishvakarma BR (2001) Analysis of gap-coupled microstrip antenna. Int J Electron 88(6):707–718
10. Aanandan CK, Mohanan P, Nair KG (1990) Broadband gap coupled microstrip antenna. IEEE Trans Antennas Propag 38(10):1581–1586
11. Singh V, Mishra B, Singh R (2015) A compact and wide band microstrip patch antenna for X-band applications. In: 2nd IEEE international conference on advances in computing and communication engineering, ICACCE 2015, pp 296–300
12. You W, Guo H, Cai W, Liu X (2009) A D-shaped defected patch antenna with enhanced bandwidth. In: 3rd IEEE international symposium on microwave, antenna, propagation and EMC technologies for wireless communication, MAPE 2009, pp 684–686
13. Lee W-J, Go M-H, Kim Y-K, Park H-D (2006) Fabrication and measurement of miniaturized Z-shaped corrugated-type patch antenna for WLAN. Microw Opt Technol Lett 48(7):1269–1271
14. Mousavi P, Miners B, Basir O (2010) Wideband L-shaped circular polarized monopole slot antenna. IEEE Antennas Wirel Propag Lett 9:822–825
15. Chen Yu, Wei H, Zhenqi K, Haiming W (2012) Ku-band linearly polarized omnidirectional planar filtenna. IEEE Antennas Wirel Propag Lett 11:310–313
16. Prasad PC, Chattoraj N (2013) Design of compact Ku band microstrip antenna for satellite communication. In: International conference on communication and signal process. IEEE, pp 196–200
17. Azim R, Islam MT, Misran N (2011) Dual polarized microstrip patch antenna for Ku-band application. Inf MIDEM 41(2):114–117

Highly Sensitive Octagonal Photonic Crystal Fiber for Ethanol Detection

Ashish Kumar Ghunawat, Sharad Sharma, Sourabh Sahu and Ghanshyam Singh

Abstract In this article, an octagonal photonic crystal fiber for ethanol detection is suggested. Birefringence, confinement loss, and relative sensitivity have been explored theoretically. The numerical investigation is done utilizing the finite element method (FEM). It is discovered that the existence of elliptical holes in the center region leads to high values of birefringence along with low confinement loss and high sensitivity. Our study shows that at a wavelength of 1.33 μm, the birefringence, relative sensitivity, and confinement loss of the suggested PCF are 0.0016, 57.91%, and 1.6×10^{-3} dB per m, respectively.

Keywords Photonic crystal fiber · Birefringence · Relative sensitivity · Confinement loss · Finite element method

1 Introduction

Photonic crystals (PC) are composed of periodic alignment of the dielectric material that causes to alter the propagation characteristics of the optical modes [1–5]. Specifically, lots of applications are presented based on PC waveguides and fibers, which are focused on its 1D and 2D structures. 1D PC structure is suitable for sensing application that causes to detect the change in wavelength for alteration of the refractive index of the sample present on the upper cladding of the structure [6–9]. However, in photonic crystal fiber (PCF) the detection is performed by filling holes with an intended material.

PCF has been one of the most growing research areas related to fiber optics. PCFs or microstructured fibers have been gathering large attention in recent time

A. K. Ghunawat (✉) · S. Sharma · S. Sahu · G. Singh
Department of Electronics and Communication Engineering, Malaviya National Institute of Technology Jaipur, Jaipur 302017, Rajasthan, India
e-mail: akghunawat.ece@mnit.ac.in

S. Sharma
e-mail: sharmasharad3010@gmail.com

© Springer Nature Singapore Pte Ltd. 2020

V. Janyani et al. (eds.), *Optical and Wireless Technologies*,
Lecture Notes in Electrical Engineering 546,
https://doi.org/10.1007/978-981-13-6159-3_48

due to their applications in numerous fields. In comparison to the conventional fiber, photonic crystal fibers have various excellent features some of them being endless single-mode characteristics [1, 2], large birefringence [3], better nonlinear effects [4], improved sensitivity [5], ultra-flattened dispersion [10], and so on. Since optical properties of the PCFs are inherently dependent on the dimensions of holes that provide an added advantage to modify its characteristics according to applications. For example, PCFs-based sensors detect the modulation in optical characteristics because of the interaction of the propagating field component with the biomaterial filled in holes [11–13].

Photonic crystal fiber (PCF) exhibits great abilities that can be explored in the fields of biosensors [14], chemical sensors [15], and so on. It can utilize two distinct guiding principles: first being index guiding and second being photonic bandgap. In index guiding mechanism, the PCF follows a conventional method of propagation, whereas photonic bandgap PCF allows the propagation in low refractive index region. Several researchers harnessed the capabilities of index guiding PCF for sensing applications. Monro et al. [16] proposed a PCF design having both core and cladding in the order of microstructured optical fibers. In articles [17–22], the authors focused on improving the relative sensitivity along with better confinement of light. Further, the effect of high birefringence for propagating light to a longer distance without affecting its dispersion is considered in [23–28].

In [24], PCF with hexagonal lattice and elliptical holes is presented for liquid sensing application. But the attained sensitivity is relatively low that led to the development of PCFs having enhanced sensitivity, improved birefringence, as well as reduced confinement loss. Here, a PCF design is investigated for ethanol detection. The numerical investigations of this design are performed, and key factors like birefringence, relative sensitivity, confinement loss, and effective area have been studied. At an end, the effect of presence of elliptical holes in the core region has also been studied.

2 Design of PCF

The geometric formation of suggested PCF along with an enlarged view of the core is displayed in Fig. 1. Here for a background material, pure silica is considered and core holes are filled with target material ethanol. Holes present in cladding region have a circular nature, and their diameter is set as $d = 1.75$ μm. The center-to-center spacing between two neighboring air holes which is called as pitch (Λ) is set as 2.4 μm. Core region has elliptical holes, and their semimajor axis (a) and semiminor axis (b) are fixed as 0.44 μm and 0.24 μm, respectively. Hence, the ellipticity constant e ($e = b/a$) is calculated as 0.54. The core holes are loaded with the target sample, here being ethanol.

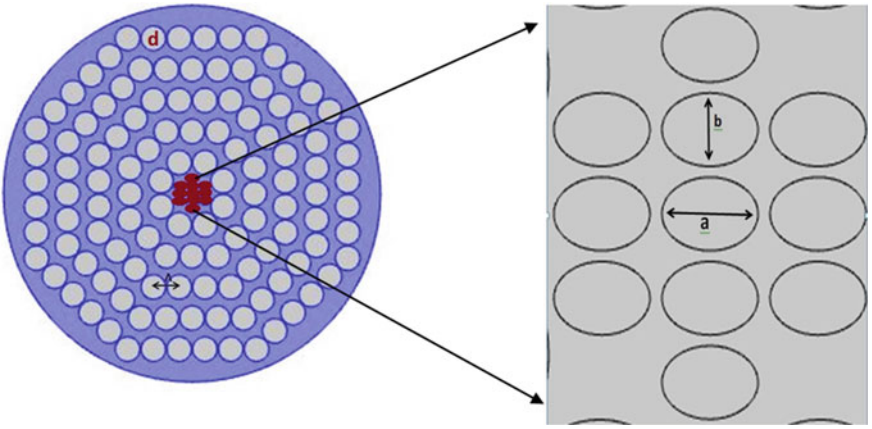

Fig. 1 Geometry of the suggested PCF along with enlarged view of the core

2.1 Principle of Operations

In order to perform numerical investigations, a finite element method (FEM) using COMSOL Multiphysics 5.1 is employed. For consideration of the material dispersion, Sellmeier relation has been utilized.

$$n(\lambda) = \sqrt{1 + \frac{X_1\lambda^2}{\lambda^2 - Y_1} + \frac{X_2\lambda^2}{\lambda^2 - Y_2} + \frac{X_3\lambda^2}{\lambda^2 - Y_3}} \tag{1}$$

where n denotes the refractive index variation according to operating wavelength λ (μm); X_1, X_2, X_3 and Y_1, Y_2, Y_3 represent the Sellmeier coefficients of a material.

The Sellmeier coefficients of pure silica are given by $X_1 = 0.696166300$, $X_2 = 0.407942600$, $X_3 = 0.897479400$, $Y_1 = 4.67914826 \times 10^{-3}\,\mu m^2$, $Y_2 = 1.35120631 \times 10^{-2}\,\mu m^2$, $Y_3 = 97.9340025\,\mu m^2$.

The Sellmeier coefficient of ethanol is given by $A_1 = 0.75831$, $A_2 = 0.08495$, $B_1 = 0.01007\,\mu m^2$, $B_2 = 8.91377\,\mu m^2$.

The propagation of wave in fiber is articulated by using Maxwell's equation that is represented as [23]

$$\nabla \times \left(\varepsilon_r^{-1} \nabla \times H\right) - k_0^2 \mu_r H = 0 \tag{2}$$

where ε_r and μ_r are relative permittivity and permeability of the material, and k_0 represents the vacuum wave number at operating wavelength ($k_0 = 2\pi/\lambda$). Through an evaluation of a propagation constant, an effective index of the propagating mode is obtained. Since birefringence is one of the fundamental characteristics of the PCF, it is evaluated using [23, 24]

$$B = \left| n_x - n_y \right| \tag{3}$$

where n_x and n_y represent the effective indices of x polarized and y polarized mode of PCF. As the wavelength increases, the amount of evanescent field also increases, which leads to rise in effective area (A_{eff}) of the PCF. Since there are many frequency components in an optical pulse and the refractive index depends on the wavelength, every component travels with different speeds, which leads to increase in the area [4]. A_{eff} can be calculated by using the equation mentioned as follows:

$$A_{eff} = \frac{\left(\iint |E|^2 dxdy\right)^2}{\iint |E|^4 dxdy} \tag{4}$$

where E is the transverse electric field. Since there are limited air holes, mode has tendency to move out from core to outer part of the fiber, which results in confinement loss. With the help of imaginary part of the complex effective index of fundamental mode, confinement loss of fiber is determined from [29].

$$L_c = \frac{40\pi}{\ln(10)\lambda} Imag\left(n_{eff}\right) \times 10^6 (\text{dB/m}) \tag{5}$$

where *Imag* (n_{eff}) represents the imaginary part of complex effective index of guided mode.

Efficiency or performance of PCF as a sensor depends on relative sensitivity coefficient (r) which tells about the interaction between traveling mode and target sample. Beer–Lambert law states that the sensitivity coefficient may be described as follows [29]:

$$r = \frac{n}{Re\left[n_{eff}\right]} f \tag{6}$$

where n denotes the refractive index values of target material present in core holes, $Re\left[n_{eff}\right]$ denotes real part of the complex effective refractive index, and f represents amount of power present in core region. f can be mathematically written using Poynting's theorem as [29]:

$$f = \frac{(core) \int Re\left(E_x H_y - E_y H_x\right) dxdy}{(total) \int Re\left(E_x H_y - E_y H_x\right) dxdy} \times 100 \tag{7}$$

where E_x and E_y represent the transverse electric field, and H_x and H_y represent the transverse magnetic field of the traveling mode.

3 Results and Analysis

The designed PCF is considered to operate for fundamental mode for a wavelength range varying from 1.3 to 2.3 μm. The change in the real part of the effective index of the fundamental mode with respect to wavelength is represented in Fig. 2. It was observed that the index values are decreasing with an increase in wavelength. As the wavelength increases, more power leaks out of the core to the cladding area which results in a decrease in effective index.

The well-confined mode at 1.33 μm is shown in Fig. 3. This confinement leads to high interaction between light and sample filled inside core holes. The wavelength of operation is chosen as 1.33 μm because there is a peak in the absorption spectrum of ethanol near 1.33 μm. Hence, achieving high sensitivity near 1.33 μm will result in better detection of ethanol.

The birefringence of the suggested design depending upon operating wavelength is shown in Fig. 4. Higher values of birefringence have been found due to a consideration of elliptical air holes at a core region.

For the PCF structure to be feasible, evaluation of confinement loss is needed which can be controlled by alteration of parameters of PCF [29]. Figure 5 depicts the change of confinement loss depending upon operating wavelength, and it is found that the confinement loss attains low values at high wavelength because of the elliptical holes present in the core.

Achieving high sensitivity is the most important parameter for sensing application; Fig. 6 illustrates the change of relative sensitivity depending upon operating wavelength. It was noticed that the relative sensitivity improves as the wavelength increases since the effective index decreases.

From the complete discussion, it is found that the proposed PCF design possesses improved characteristics in terms of sensitivity than the structure proposed in [27, 28, 30]. Table 1 displays the comparison among previous designs and suggested

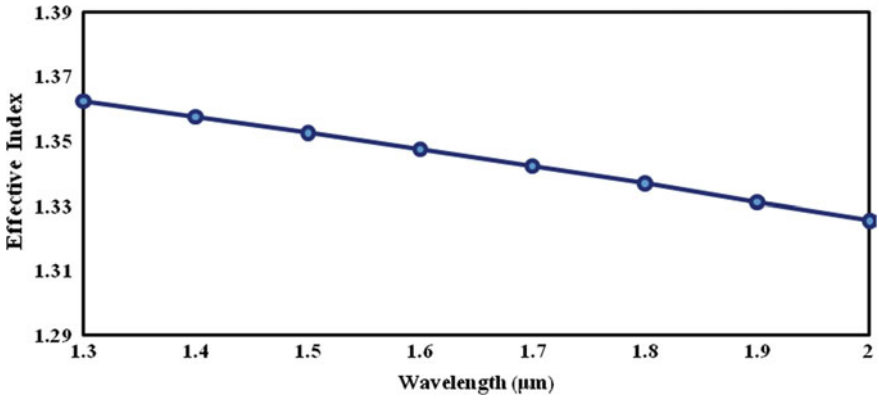

Fig. 2 Effective index versus operating wavelength plot of the fundamental mode

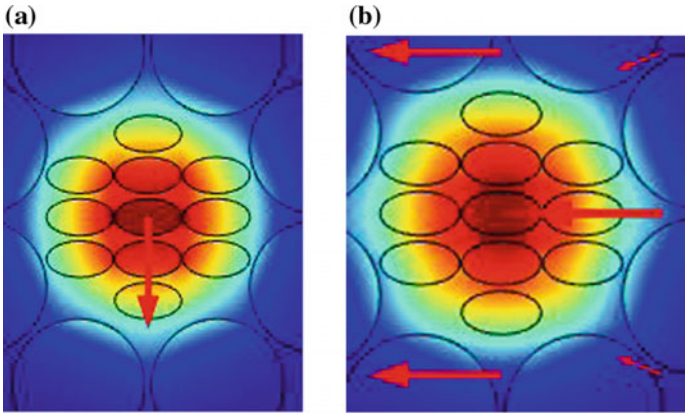

Fig. 3 Mode field profile of fundamental mode at $\lambda = 1.33\,\mu$m: **a** y-polarization and **b** x-polarization

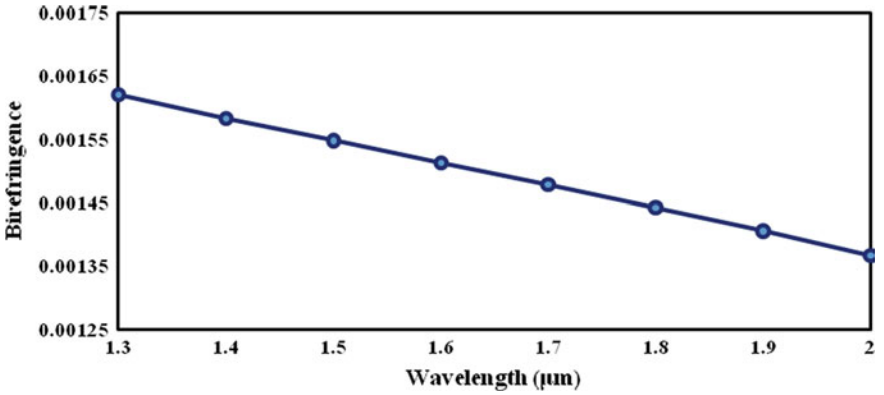

Fig. 4 Birefringence versus operating wavelength plot

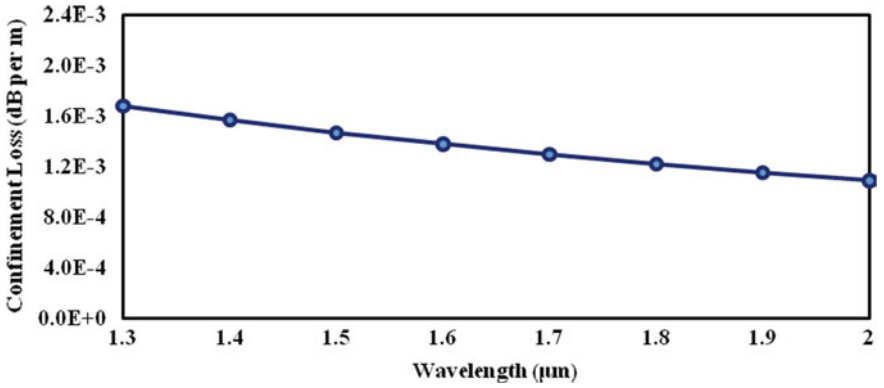

Fig. 5 Confinement loss versus operating wavelength plot

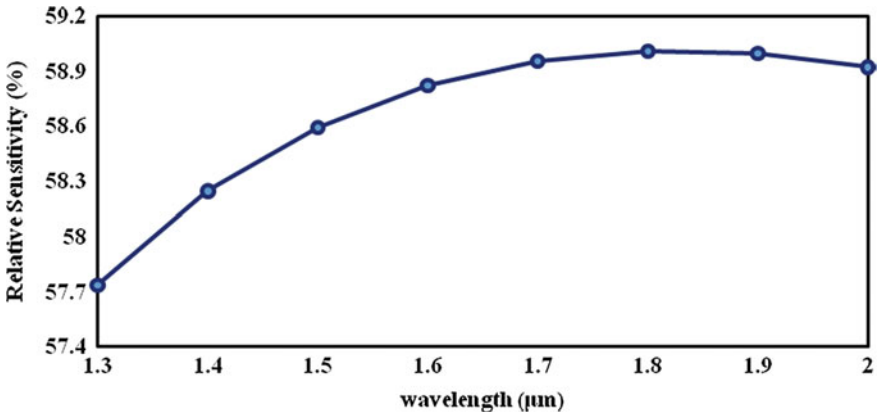

Fig. 6 Relative sensitivity versus operating wavelength plot

Table 1 Comparison among previous designs and suggested PCF structure

References	Birefringence	Confinement loss (dB/m)	Sensitivity (%)
Ref. [27]	0.001900	2.10×10^{-2}	23
Ref. [28]	0.000610	2.01×10^{-1}	8.5
Ref. [30]	0.002825	2.07×10^{-6}	43.84
PCF	0.0016	1.62×10^{-3}	57.91

PCF. Further, the size of holes in the cladding is chosen in such a manner that the effective index of the cladding region becomes less than core region. This creates a refractive index difference between core and cladding which will lead to strong field confinement in the core region.

From the above discussion, it is determined that the suggested PCF shows better performance in regard to relative sensitivity and birefringence. It can be said that the elliptical holes are accountable for the improvement of sensitivity. Therefore, the parameter sweep for variation of ellipticity at $\lambda = 1.33$ μm has been performed. Figure 7 illustrates the impact of ellipticity constant on the birefringence, relative sensitivity, and confinement loss. It was evidently concluded that mentioned characteristics degrade with an increase in ellipticity constant.

Lastly, it is necessary to consider the manufacturing possibility of the suggested structure. It is adequate to mention that the suggested design may be difficult to realize. In order to conserve the integrity of fiber, holes must be loaded carefully with ethanol. However, due to continuous progress in the fabrication technology, it is achievable that the suggested design can be realized with available techniques [21]. Huang et al. [31] and Gerosa et al. [32] demonstrated methods to fabricate PCF designs with core holes which are filled with liquid. Bise et al. [33] evolved a sol–gel method for realization of PCF. Sol–gel method yields the design freedom of PCF, as well as complex designs may be modeled with the help of this method.

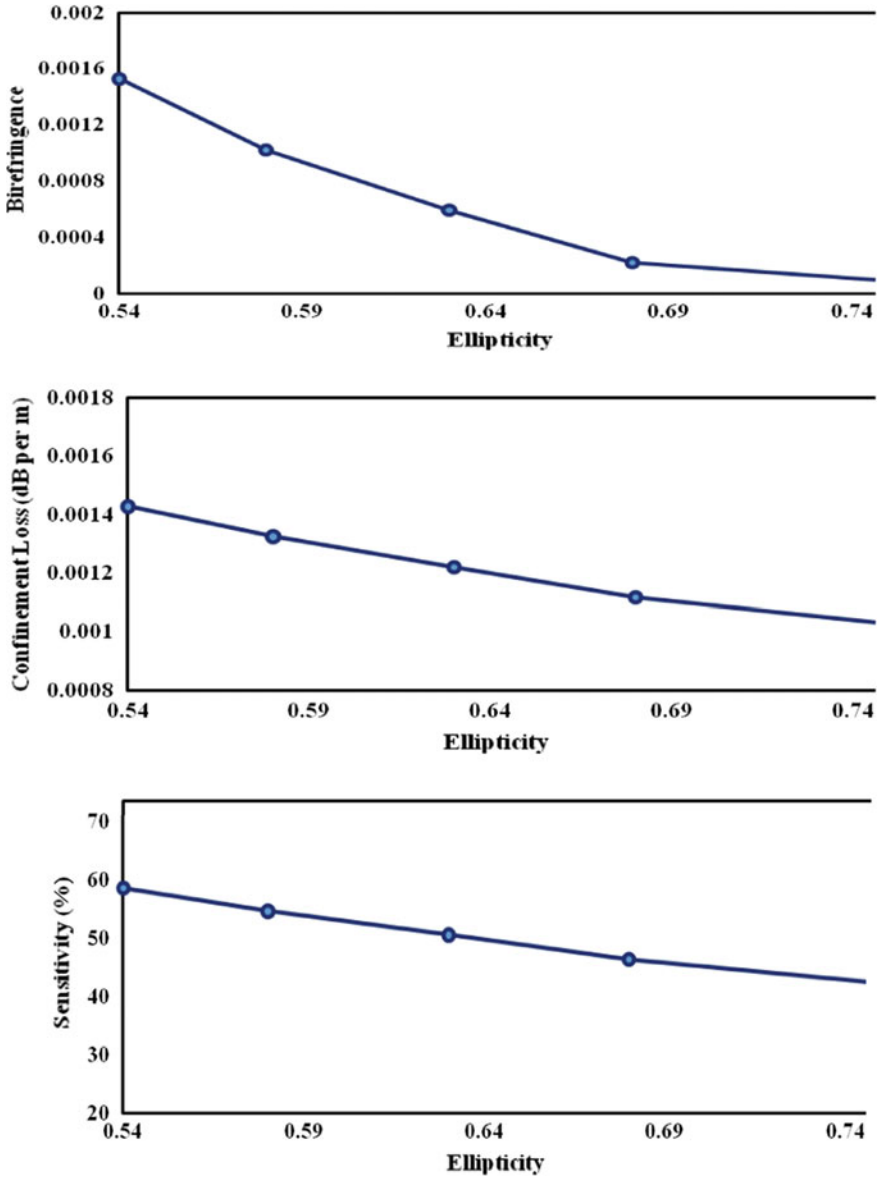

Fig. 7 (1) Birefringence, (2) confinement loss, and (3) relative sensitivity versus ellipticity plots keeping the wavelength fixed to 1.33 μm

4 Conclusion

In conclusion, an octagonal structure of PCF is suggested in this article. Circular holes are present in the cladding area while elliptical holes are present in core area. The impact of ellipticity of holes is studied. Our results show that high birefringence and high sensitivity along with low confinement loss can be attained at same time. Moreover, our study illustrates that the characteristics of the proposed PCF are better than previously reported architectures of PCFs. The proposed configuration is utilized for ethanol detection. The relative sensitivity is found out to be 57.91% with moderately high birefringence.

References

1. Luan N, Wang R, Lv W, Lu Y, Yao J (2014) Surface plasmon resonance temperature sensor based on photonic crystal fibers randomly filled with silver nanowires. Sensors 14(9):16035–16045
2. Birks TA, Knight JC, Russell PSJ (1997) Endlessly single-mode photonic crystal fiber. Opt Lett 22(13):961–963
3. Singh G, Sahu S, Chaurasia P (2012) Modeling of photonic crystal fibers with fibonacci-patterned circular and elliptical air holes. Opt Eng 51(11):115001–115006. https://doi.org/10.1117/1.OE.51.11.115001
4. Ebendorff-Heidepriem H, Petropoulos P, Asimakis S, Finazzi V, Moore R, Frampton K, Koizumi F, Richardson D, Monro T (2004) Bismuth glass holey fibers with high nonlinearity. Opt Express 12(21):5082–5087
5. Arif MFH, Ahmed K, Asaduzzaman S, Azad MAK (2016) Design and optimization of photonic crystal fiber for liquid sensing applications. Photonic Sens 6(3):279–288
6. Sahu S, Ali J, Singh G (2017) Refractive index biosensor using sidewall gratings in dual-slot waveguide. Opt Commun 402:408–412. https://doi.org/10.1016/j.optcom.2017.06.051
7. Sahu S, Kozadaev KV, Singh G (2016) Michelson interferometer based refractive index biosensor. In: 13th international conference on fiber optics and photonics, Photonic-16, IIT Kanpur, 04–08 December 2016, OSA Technical Digest, paper Th3A.60. https://doi.org/10.1364/photonics.2016.th3a.60. ISBN: 978-1-943580-22-4
8. Sahu S, Singh G (2016) Modeling of phase shift Bragg grating biosensor for non invasive detection of blood components. In: IEEE international conference, ICRAIE-2016, Jaipur, India, 23–25 December 2016, IEEE Xplore Digital Library. https://doi.org/10.1109/icraie.2016.7939565. Print ISBN: 5090-2806
9. Sahu S, Singh G (2017) Modeling of grating slot waveguide for high-Q based refractive index sensor. In: IEEE international conference COMPTELIX-2017, 1–2 July 2017, Jaipur, IEEE Xplore Digital Library, pp 394–396. https://doi.org/10.1109/comptelix.2017.8004001
10. Reeves W, Knight J, Russell P, Roberts P (2002) Demonstration of ultra-flattened dispersion in photonic crystal fibers. Opt Express 10(14):609–613
11. Tyagi HK, Schmidt MA, Sempere LP, Russell PSJ (2008) Optical properties of photonic crystal fiber with integral micron-sized Ge wire. Opt Express 16(22):17227–17236
12. Lee HW, Schmidt MA, Tyagi HK, Sempere LP, Russell PSJ (2008) Polarization-dependent coupling to plasmon modes on submicron gold wire in photonic crystal fiber. Appl Phys Lett 93(11):111102
13. Nagasaki A, Saitoh K, Koshiba M (2011) Polarization characteristics of photonic crystal fibers selectively filled with metal wires into cladding air holes. Opt Express 19(4):3799–3808

14. Akowuah EK, Gorman T, Ademgil H, Haxha S, Robinson GK, Oliver JV (2012) Numerical analysis of a photonic crystal fiber for biosensing applications. IEEE J Quantum Electron 48(11):1403–1410
15. Zheng S, Zhu Y, Krishnaswamy S (2012) Nanofilm-coated photonic crystal fiber long-period gratings with modal transition for high chemical sensitivity and selectivity. In: SPIE smart structures and materials + nondestructive evaluation and health monitoring, pp 83460D–83460D
16. Monro TM, Belardi W, Furusawa K, Baggett JC, Broderick NGR, Richardson DJ (2001) Sensing with microstructured optical fibres. Meas Sci Technol 12(7):854
17. Cordeiro CM, Franco MA, Chesini G, Barretto EC, Lwin R, Cruz CB, Large MC (2006) Microstructured-core optical fibre for evanescent sensing applications. Opt Express 14(26):13056–13066
18. Ahmed K, Morshed M (2016) Design and numerical analysis of microstructured-core octagonal photonic crystal fiber for sensing applications. Sens Bio-Sens Res 7:1–6
19. Asaduzzaman S, Arif MFH, Ahmed K, Dhar P (2015) Highly sensitive simple structure circular photonic crystal fiber based chemical sensor. In: 2015 IEEE international WIE conference on electrical and computer engineering (WIECON-ECE), pp 151–154
20. Asaduzzaman S, Ahmed K, Arif MFH, Morshed M (2015) Proposal of a simple structure photonic crystal fiber for lower indexed chemical sensing. In: 2015 18th international conference on computer and information technology (ICCIT), pp 127–131
21. Arif MFH, Ahmed K, Asaduzzaman S (2015) A comparative analysis of two different PCF structures for gas sensing application. In: 2015 international conference on advances in electrical engineering (ICAEE), pp 247–250
22. Morshed M, Hassan MI, Roy TK, Uddin MS, Razzak SA (2015) Microstructure core photonic crystal fiber for gas sensing applications. Appl Opt 54(29):8637–8643
23. Wang W, Yang B, Song H, Fan Y (2013) Investigation of high birefringence and negative dispersion photonic crystal fiber with hybrid crystal lattice. Optik Int J Light Electron Opt 124(17):2901–2903
24. Asaduzzaman S, Ahmed K, Bhuiyan T, Farah T (2016) Hybrid photonic crystal fiber in chemical sensing. SpringerPlus 5(1):748
25. Pang M, Xiao LM, Jin W et al (2012) Birefringence of hybrid PCF and its sensitivity to strain and temperature. J Lightwave Technol 30(10):1422–1432
26. Ma P, Song N, Jin J, Song J, Xu X (2012) Birefringence sensitivity to temperature of polarization maintaining photonic crystal fibers. Opt Laser Technol 44(6):1829–1833
27. Ademgil H, Haxha S (2015) PCF based sensor with high sensitivity, "high birefringence and low confinement losses for liquid analyte sensing applications". Sensors 15(12):31833–31842
28. Ademgil H, Haxha S (2016) Highly birefringent nonlinear PCF for optical sensing of analytes in aqueous solutions. Optik Int J Light Electron Opt 127(16):6653–6660
29. Ademgil H (2014) Highly sensitive octagonal photonic crystal fiber based sensor. Optik Int J Light Electron Opt 125(20):6274–6278
30. Arif MFH, Biddut MJH (2017) Enhancement of relative sensitivity of photonic crystal fiber with high birefringence and low confinement loss. Optik Int J Light Electron Opt 131:697–704
31. Huang Y, Xu Y, Yariv A (2004) Fabrication of functional microstructured optical fibers through a selective-filling technique. Appl Phys Lett 85(22):5182–5184
32. Gerosa RM, Spadoti DH, de Matos CJ, de L, Menezes S, Franco MA (2011) Efficient and short-range light coupling to index-matched liquid-filled hole in a solid-core photonic crystal fiber. Opt Express 19(24):24687–24698
33. Bise RT, Trevor DJ (2005) Sol-gel derived microstructured fiber: fabrication and characterization. In: Optical fiber communications conference (OFC), vol 3

Design and Studies of Bandstop Filters Using Modified CSRR DGS for WLAN Applications

Arjun Kumar, Ashok Kumar, Ashok Kumar and M. V. Kartikeyan

Abstract In this paper, various dumbbell-shaped defected ground structure (DB-DGS) are compared with complementary split ring resonator DB-DGS which has sharp roll-off factor; as compared to other DB-DGS and a one pole bandstop filter with modified complementary split ring resonator (CSRR), DB-DGS has been proposed with compact size $0.12\lambda \times 0.28\lambda$ and low return loss in passband at 2.4 GHz. The proposed filter is fabricated and measured with insertion loss of −28 dB in stopband and −0.8 dB return loss.

Keywords DGS (Defected ground structure) · Modified CSRR · Band stop · HFSS (High-frequency structure simulator)

1 Introduction

The last few decades have experienced many developments in the field of microwave filter design triggered largely by parallel developments in communication technology. Microwave systems often need to remove unwanted signals or separate signal frequencies in the process of achieving various design goals. These functions are per-

A. Kumar (✉) · A. Kumar
School of Engineering and Applied Sciences, Bennett University, Greater Noida, India
e-mail: akdec.iitr@gmail.com

A. Kumar
e-mail: ashokmzn@gmail.com

A. Kumar · A. Kumar · A. Kumar
Department of Electronics and Communication Engineering, Government Women Engineering College Ajmer, Ajmer 305002, Rajasthan, India
e-mail: kumarashoksaini@gmail.com

A. Kumar · A. Kumar · M. V. Kartikeyan
Department of Electronics and Communication Engineering, Indian Institute of Technology Roorkee, Roorkee, India
e-mail: kartik@ieee.org

© Springer Nature Singapore Pte Ltd. 2020

V. Janyani et al. (eds.), *Optical and Wireless Technologies*,
Lecture Notes in Electrical Engineering 546,
https://doi.org/10.1007/978-981-13-6159-3_49

formed by filters. They are usually classified as low pass, band pass, high pass, and band stop depending upon their frequency response. Filters are used in radar systems to classify various signals by frequency. Further, mobile communications require filters that can handle enormous amounts of power for the base stations and the low cost, low size, low power handlers on the mobile station side [1]. One way to reduce the size of microwave filters is by introducing defects in the ground plane of the filter structure [2]. When a part of the metal is etched from the ground plane beneath the metallic strip, the shield current distribution in the ground plane gets affected. The path length gets increased thus changing the line properties such as line capacitance and inductance by introducing slow wave effects which ultimately lead to band stop properties [3, 4]. The band stop filter obtained using the defected ground structure (DGS) circuit has many advantages such as reduced filter structure complexity, low insertion loss, and size reduction. Optimization of microwave component parameters within a specified frequency range is a major step in the design of microwave devices. In this paper, a modified CSRR DB-DGS is proposed which shows the sharp cutoff and a resonance frequency of 2.4 GHz. Further, with other filter dimensions remaining same, the responses of spiral, square, and U-shaped dumbbell DGS configurations are optimized and studied for the same resonance frequency of 2.4 GHz. The distinctive design variations in these configurations are studied to enable the scaling of these structures for frequencies desired by the designer.

2 Design Goals and Specifications

The design goals and the specification are shown in Table 1; these specifications are used for designing various DB-DGS in this paper. In Table 1, the target resonance frequency is 2.4 GHz and the cutoff frequency is 2 GHz. For all DB-DGS, dimensions are kept for comparison at 2.4 GHz. 50 Ω, λ/4 microstrip line is used for all DB-DGS. The overall size of this DB-DGS is 32 mm × 34.3 mm which is kept the same for all the DB-DGS.

Table 1 Design goals specified for various DB-DGS filter configurations

Resonance frequency	2.4 GHz
Cutoff frequency	2 GHz
Permittivity of substrate, ε_r (FR4_epoxy)	4.4
Dielectric loss tangent	0.024
Height of substrate	1.524 mm
Thickness of metal	0.07 mm

3 Comparisons of Various DB-DGS

Different geometries are proposed by the researchers, few of them are very popular for enhancing the performance of the filters. The DB-DGS configurations are square-shaped, U-shaped, spiral, and CSRR-shaped which are shown as in Fig. 1. The square dumbbell DGS geometry was the first geometry to be proposed. Since then, it has been the basis for most of the research work on dumbbell DGS [5–12]. The U-shaped dumbbell DGS combines the characteristics of H-shaped dumbbell DGS [13] with square-headed one. It consists of two U-shaped dumbbells connected through their backs by a thin connecting slot. Metamaterials are known for their negative permeability and permittivity and have been a burning area of interest for the researchers since they were originally proposed by Pendry et al. [14, 15].

In Fig. 1e, CSRR DB-DGS has been used which is the dual of Split Ring Resonator (SRR) filter. They are mainly applied in filters for size reduction because CSRRs etched in the ground plane give rise to a narrow stop band around their resonance frequency [15–17]. The spiral dumbbell DGS was introduced by Kim et al. [16, 17] for a steep rejection while maintaining the compactness of the filter design with a single unit.

The frequency response of the various optimized DB-DGS configurations used in this paper are shown in Fig. 2. The 3-dB frequency is closest to resonance frequency which increase the sharpness of the filter. The return loss for square-shaped, U-shaped, CSRR-shaped, and spiral DB-DGS is −40 dB, −37 dB, −27 dB, and −26 dB, respectively. It can be seen in Fig. 2, sharpness of spiral DB-DGS is better than CSRR DB-DGS but the structure is more complex. So, the focus of this research work is to design filter with simple configuration with better performance. Here CSRR DB-DGS has less complex than the spiral DB-DGS.

4 Proposed CSRR DGS Filter, Fabrication and Measurement

In this section, some topologies of CSRR DB-DGS are compared in terms of their frequency response.

Further, equivalent $\boldsymbol{L}$ and $\boldsymbol{C}$ values are calculated for these configurations corresponding to the equivalent circuit shown in Fig. 4.

From Table 2, it can be clearly observed that Fig. 3a has sharper than the other two CSRR DB-DGS. When the 3-dB cutoff frequency will be closer to resonance frequency then filter selectivity will increase. So here Fig. 3a is used as proposed CSRR DB-DGS (Fig. 4).

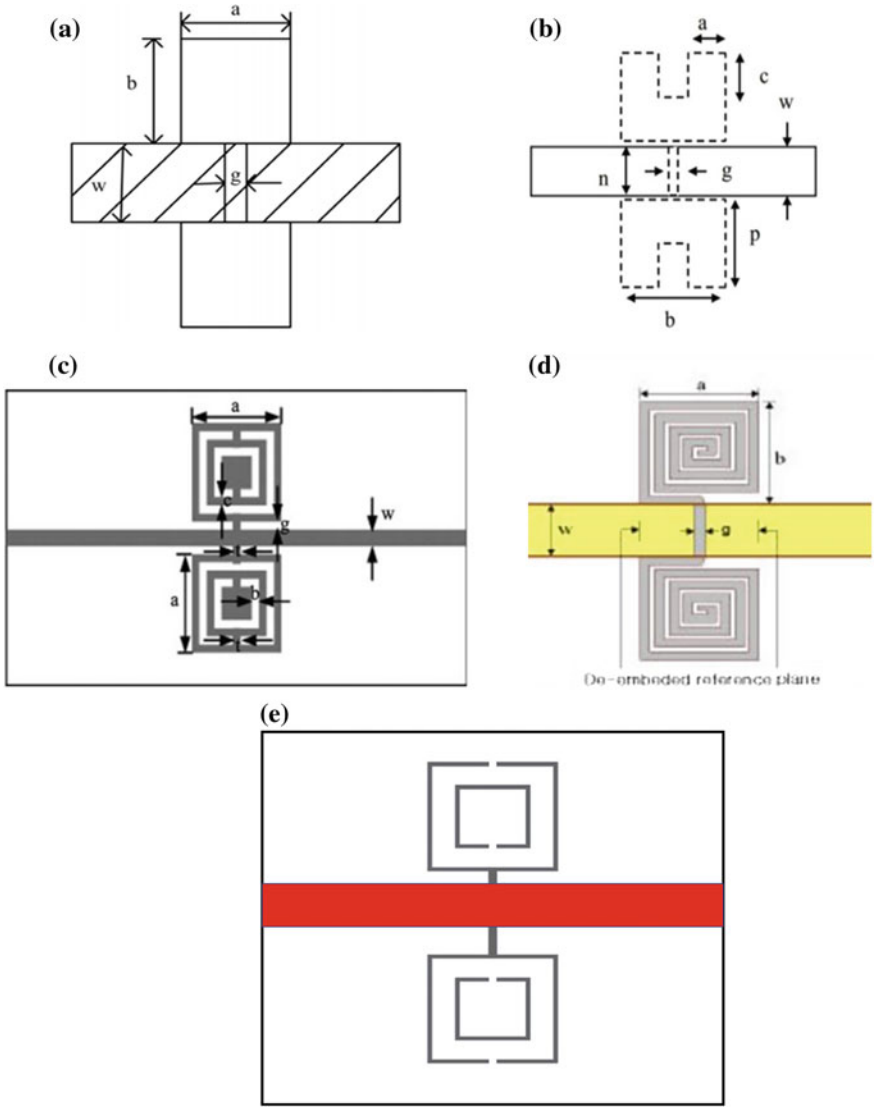

Fig. 1 DGS geometries **a** square dumbbell **b** U-shaped dumbbell **c** CSRR dumbbell **d** spiral dumbbell **e** CSRR DGS [8]

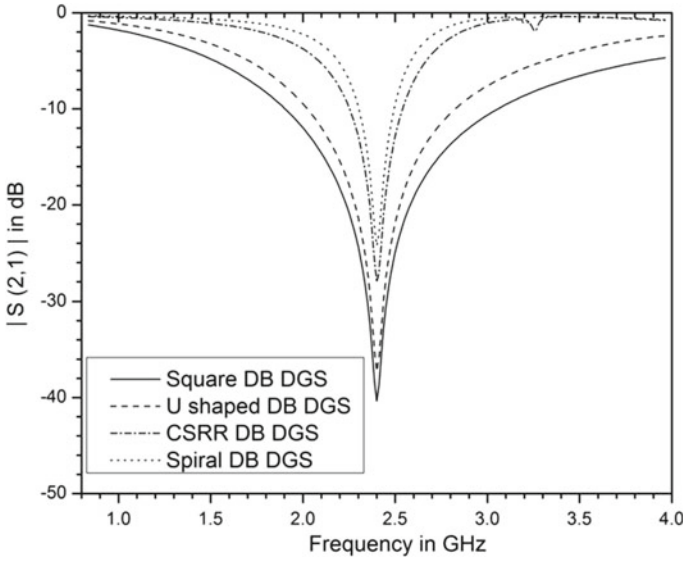

Fig. 2 Frequency response of the optimized design configurations

Table 2 Cutoff frequencies, resonance frequencies, and LC equivalents for various CSRR design configurations

Configuration no.	f_c (GHz)	f_0 (GHz)	C_1 (pF)	L_1 (nH)	C_2 (pF)	L_2 (nH)
1 (Fig. 3a)	1.93	2.4	2.41	1.9	0.44	10.34
2 (Fig. 3b)	2.03	2.54	2.24	1.83	0.43	9.6
3 (Fig. 3c)	2.28	3.175	27	2.14	0.5	5.45

4.1 Design Parameters

In this subsection, the dimensions of the proposed design in Fig. 5 have been given in Table 3.

4.2 Fabrication and Measurement

In this subsection, the fabricated layout of proposed modified CSRR bandstop filter has been shown in Fig. 6.

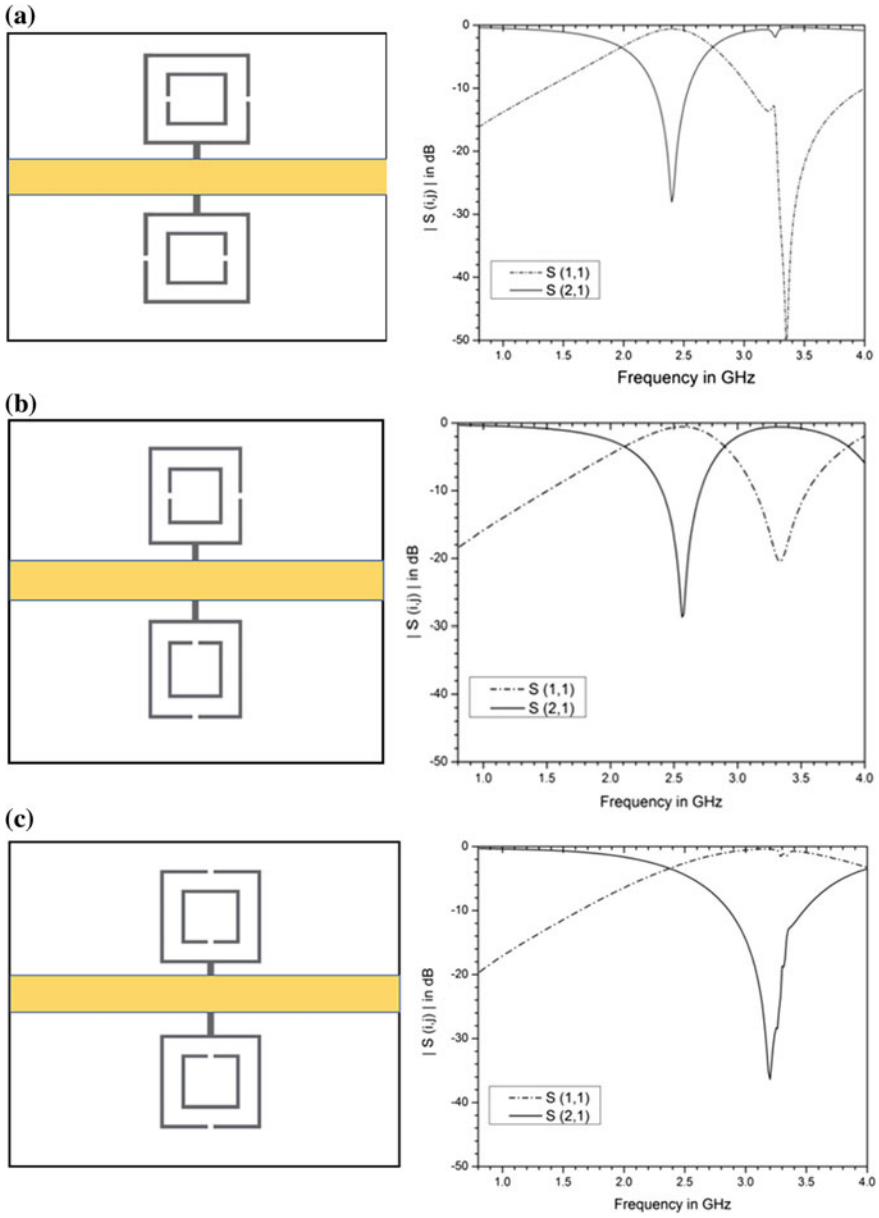

Fig. 3 Comparison of various CSRR DB-DGS and its S-parameter

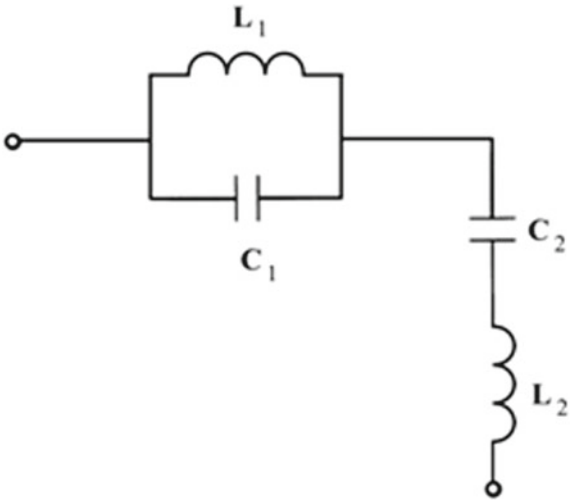

Fig. 4 LC equivalent circuit for CSRR dumbbell DGS [8]

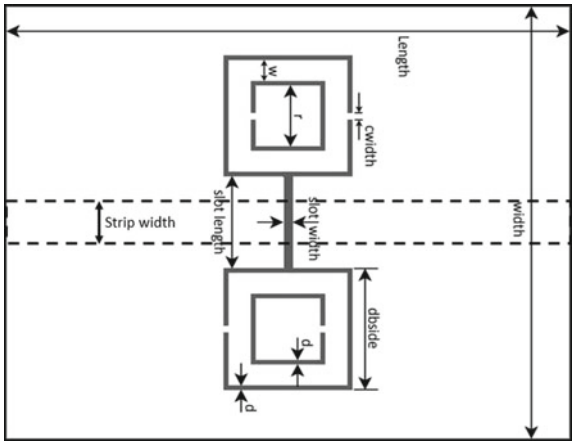

Fig. 5 Proposed modified CSRR DB-DGS bandstop filter

Table 3 Dimensions of proposed modified CSRR DB-DGS bandstop filter

Width	32 mm
Length	34.25 mm
Strip width	2.914 mm
Port width	11 mm
Port height	3 mm
Slot length	6 mm
Slot width	0.5 mm
Connecting strip width (cwidth)	0.5 mm
Dimensions of vacuum box used in HFSS	34.25 mm × 52 mm × 35 mm

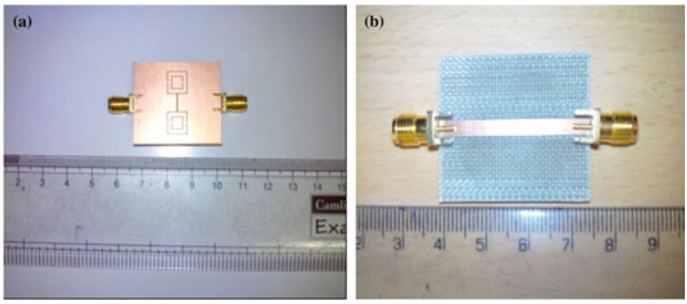

Fig. 6 Fabricated modified CSRR DB-DGS bandstop filter—**a** bottom view **b** top view

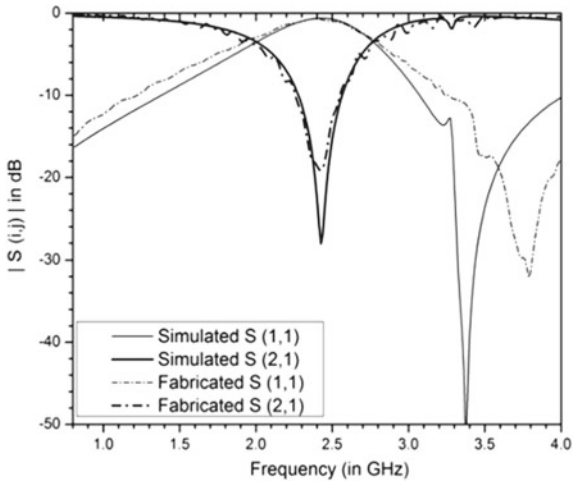

Fig. 7 S-Parameters results of measured and simulated of proposed filter

5 Results and Discussion

In Figs. 6 and 7, the fabricated layout of proposed bandstop filter with its measured results in terms of S-parameters is shown. In Fig. 7, it can be observed that the measured results and simulated results are in good agreement. The measured results show the insertion loss in stopband is −19 dB at 2.4 GHz which is acceptable according to available research work. The return loss in the stopband is around −0.8 dB. These measured results are very close to simulated results.

6 Conclusions

Various topologies of DB-DGS are compared and analyzed. Based on comparative analysis, a bandstop filter has been proposed with modified CSRR DB-DGS. The proposed bandstop filter with modified CSRR DB-DGS has been validated with

measurement results. Measured results are in good agreement with simulated results. All the proposed design has been fabricated on 50 Ω, λ/4 microstrip line. There are no stubs, and Hi-Lo impedance line is used.

References

1. Hunter IC, Billonet L, Jarry B, Guillon P (2002) Microwave filters-applications and technology. IEEE Trans Microw Theory Tech 50(3):794–805
2. Ahn D, Park JS, Kim CS, Kim J, Qian Y, Itoh T (2001) A design of the low-pass filter using the novel microstrip defected ground structure. IEEE Trans Microw Theory Tech 49(1):86–93
3. Oskouei D, Reza H, Khalilpour J (2011) Neural model for modeling of dumbbell shape defected ground structure. In: PIERS proceedings, pp 390–397
4. Kim JP, Park WS (2001) Microstrip low pass filter with multislots on ground plane. Electron Lett 37(25):1525–1526
5. Tarot AC, Collardey S, Mahdjoubi K (2003) Numerical studies of metallic PBG structures. Prog Electromagn Res PIER 41:133–157
6. Guida G, de Lustrac A, Priou A (2003) An introduction to photonic band gap (PBG) materials. Prog Electromagn Res PIER 41:1–20
7. Velazquez-Ahumada MC, Martel J, Medina F (2004) Parallel coupled microstrip filters with ground-plane aperture for spurious band suppression and enhanced coupling. IEEE Trans Microw Theory Tech 52:1082–1086
8. Weng LH, Guo YC, Shi XW, Chen XQ (2008) An overview on defected ground structure. Prog Electromagn Res B 7:173–189
9. Lim JS, Kim CS, Ahn D, Jeong YC, Nam S (2005) Design of low-pass filters using defected ground structure. IEEE Trans Microw Theory Tech 53(8):2539–2545
10. Abdel-Rahman AB, Verma AK, Boutejdar A, Omar AS (2004) Control of bandstop response of Hi-Lo microstrip low-pass filter using slot in ground plane. IEEE Trans Microw Theory Tech 52(3):1008–1013
11. Kim CS, Park JS, Ahn D, Lim JB (2000) A novel 1-D periodic defected ground structure for planar circuits. IEEE Microw Wirel Compon Lett 10(4):131–133
12. Lim JS, Kim CS, Lee YT, Ahn D, Nam S (2002) A new type of low pass filter with defected ground structure. In: Proceedings of 32nd European microwave conference, pp 32–36
13. Huang SY, Lee YH (2009) A compact E-shaped patterned ground structure and its applications to tunable band stop resonator. IEEE Trans Microw Theory Tech 57(3):657–666
14. Pendry JB, Stewart WJ, Youngs I (1996) Extremely low frequency plasmons in metallic mesostructures. Phys Rev Lett 76:4773–4776
15. Pendry JB, Holden AJ, Robbins DJ, Stewart WJ (1999) Magnetism from conductors and enhanced nonlinear phenomena. IEEE Trans Microw Theory Tech 47:2075–2084
16. Kim CS, Lim JS, Nam S, Kang KY, Park JI, Kim GY, Ahn D (2002) The equivalent circuit modeling of defected ground structure with spiral shape. In: IEEE MTT-S international microwave symposium digest, vol 3, pp 2125–2128
17. Lim JS, Kim CS, Lee YT, Ahn D, Nam S (2002) A spiral-shaped defected ground structure for coplanar waveguide. IEEE Microw Wirel Compon Lett 12(9):330–332

Novel Security Enhancement Technique for OCDMA and SAC OCDMA Against Eavesdropping Using Multi-diagonal Code and Gating Scheme

Teena Sharma and M. Ravi Kumar

Abstract Optical networks play a vital role in meeting demands like high data rates, high speed, and reliability in terms of security of user data. An enhanced security mechanism has been proposed to protect optical code division multiple access networks (OCDMA) against eavesdropping. In this paper, we have presented a novel technique for SAC (Spectral Amplitude Coding) OCDMA systems for enhancing data security and to exploit the capacity of an optical system. The novelty in our approach is that we have done layering of simple matrix-based Multi-Diagonal codes with low cost and less complex optical Ex-OR gates. We have incorporated data security using Multi-Diagonal (MD) code which can be simply constructed using matrix manipulation. In addition, network is protected from eavesdroppers by introducing optical Ex-oring between coded data with random key sequences. Combination of MD code with optical gate structure maintains data security to a very high extent compared to only codes used in optical system. The system design is simulated on OptiSystem-15 and Simulation work estimates the performance of proposed system in terms of bit error rate and Q factor with and without eavesdropping.

Keywords OCDMA · SAC OCDMA · Multi-diagonal code · Optical gate · Key sequence · Eavesdropping

1 Introduction

Optical Code Division Multiple Access (OCDMA) system is being used for the transmission of data using unipolar codes which provides Multiple Access Interference cancellation as well as reduction of various noises. In OCDMA, system coded data

T. Sharma (✉)
Department of ECE, Jaipur Engineering College and Research Centre, Jaipur, India
e-mail: teenasharma.ece@jecrc.ac.in

M. Ravi Kumar
Department of ECE, Malaviya National Institute of Technology Jaipur, Jaipur, Rajasthan, India
e-mail: rkmadilla.ece@mnit.ac.in

© Springer Nature Singapore Pte Ltd. 2020

V. Janyani et al. (eds.), *Optical and Wireless Technologies*,
Lecture Notes in Electrical Engineering 546,
https://doi.org/10.1007/978-981-13-6159-3_50

is transmitted over a single fiber cable asynchronously [1]. It is a promising future technology for optical network which supports higher bandwidth with high-security level [2]. It permits to attribute a specific sequence code for each user. It leads to many benefits such as authentic data transmission, large bandwidth, high data rates, dynamic user allocation, additional security features, etc. [1, 3]. There is no Multiple Access Interference in system if zero cross-correlation codes are used [4]. Few codes used in SAC OCDMA system are Random Diagonal (RD code), Optical Orthogonal Code (OOC), Prime code, Multi-Service code design for fixed weight code, Modified Quadratic Congruence (MQC) code for prime weights, Doubleweight (DW) code, Multi-Diagonal (MD) code, etc. [5]. Here, we have used Multi-diagonal code which is a zero cross-correlation code [6].

The research work presented in this paper is directed toward enhancing security of optical systems. In this work, we have used MD code with Ex-OR gate structure. A random key sequence is mixed with coded sequence and transmitted over the fiber. This process provides randomness in coded sequence, and thus it will be strenuous for eavesdropper to extract original data.

It is cost-effective and reliable approach for SAC OCDMA systems which yields zero Multiple Access Interference (MAI) and reduction in system noises due to use of MD code, and hence improves BER and also come up with additional security features. The proposed system can be an attractive solution for brust and asynchronous environments.

2 Code Construction

In an OCDMA system, the signature sequence or the code sequence C consists of unipolar (0, 1) sequence. Generally, a code is denoted as (N, W, l_a, l_c), where N is the code length, W is the code weight, l_a is the autocorrelation, and λ_c is the in-phase cross-correlation. Codes have to be designed with zero or ideal in-phase crosscorrelation so that it results in reduced Multiple User Interferences (MUI) and there should be efficient data transmission while maintaining low latency time and high degree of security.

While designing the unipolar codes for SAC system, care has been taken to ensure the following points[5]:

- The code length should be as small as possible and it should not vary with the number of active users.
- The cross-correlation should be zero to minimize MAI and the effect of PIIN.
- The code design procedure should be simple.
- The proposed codes should support large number of active users and high data rate, while achieving the minimum BER.

To improve security in the network, the system design should minimize the amount of energy that an eavesdropper can receive by tapping fiber signals. So signals transmitted over the network should contain minimum amount of power [6]. This will affect the BER performance of the system. An authorized receiver's BER performance is the function of the received SNR which is given by [7]

$$\frac{\mathrm{E_u}}{\mathrm{N_{ou}}} = \frac{\mathrm{E_u}}{\mathrm{N_{OM}} + \mathrm{N_{Or}}}, \tag{1}$$

where N_{OM} is total noise spectral density due to multiple user interference and N_{Or} represents the spectral density of the receiver noise. $\mathrm{N_{OM}}$ depends on number of active users as well as on energy contained by each transmitted user data while $\mathrm{N_{Or}}$ value is constant for individual receiver.

If $\mathrm{N_{Or}}$ is negligible compared to $\mathrm{N_{OM}}$, the resulting SNR at an authorized user's receiver will be sufficient to maintain the specified BER. Confidentiality can be enhanced by reducing power lever of each transmitted signal bit but this results in reduced N_{OM}, and N_{Or} becomes significant compared to N_{OM}. Further Bit error rate depends on $\mathrm{E_u/N_{ou}}$ ratio. By decreasing power level of each user and $\mathrm{N_{OM}}$, this ratio can be reduced while compromising with BER performance. Thus, the only way to reduce transmitted power while maintaining confidentiality is to use zero cross-correlation codes. The MD codes are zero cross-correlation codes and their construction includes the following terms:

- L (L is the code length (number of total chips)), W (code weight, i.e., (chips having value 1)) and
- λ_c (in-phase cross correlation).

MD codes can be constructed by the following steps:

Step 1: Fix any value of number of users (K) and code weight (W) which is no. of 1's contained by a code.

Step 2: According to the K and W, the i, j is defined where i = 1, 2, 3, …, K and j = 1, 2, 3, …, W.

Step 3: The position matrix is defined as

$$\mathrm{P_{i,j}} = \begin{cases} (\mathrm{i_n} + 1 - \mathrm{i}), & \text{when j} = \text{even number} \\ \mathrm{i}, & \text{when j} = \text{odd number} \end{cases} \tag{2}$$

$$\mathrm{P_{i,1}} = \begin{bmatrix} 1 \\ 2 \\ 3 \\ \vdots \\ K \end{bmatrix}, \quad \mathrm{P_{i,2}} = \begin{bmatrix} K \\ \vdots \\ 3 \\ 2 \\ 1 \end{bmatrix}, \quad \mathrm{P_{i,3}} = \begin{bmatrix} 1 \\ 2 \\ 3 \\ \vdots \\ K \end{bmatrix}, \quad \mathrm{P_{i,W}} = \begin{bmatrix} K \\ \vdots \\ 3 \\ 2 \\ 1 \end{bmatrix} \tag{3}$$

$\mathrm{P_{i,j}}$ Matrix each element denotes the value of 1 in $\mathrm{Q_{i,j}}$ matrices with $\mathrm{K \times K}$ dimensions.

Step 4: K × K dimensions $Q_{i,j}$ matrices are represented as

$$Q_{i,1} = \begin{bmatrix} 1 \cdots 0 \\ \vdots \ddots \vdots \\ 0 \cdots 1 \end{bmatrix}_{K \times K}, \quad Q_{i,2} = \begin{bmatrix} 0 \cdots 1 \\ \vdots \ddots \vdots \\ 1 \cdots 0 \end{bmatrix}_{K \times K}, \quad Q_{i,W} = \begin{bmatrix} 1 \cdots 0 \\ \vdots \ddots \vdots \\ 0 \cdots 1 \end{bmatrix}_{K \times K} \tag{4}$$

Step 5: The total combination of diagonal matrices (given in Eq. 4) gives the MD code a matrix of power K × L [6].

$$\text{MD} = \left[Q_{i,1} \; Q_{i,2} \; \cdots \; Q_{i,W} \right]_{K \times L} \tag{5}$$

$$\text{i.e. MD} = \begin{bmatrix} a_{1,1} \cdots a_{1,L} \\ \vdots \ddots \vdots \\ a_{i_{n,1}} \cdots a_{i_{n,L}} \end{bmatrix} \tag{6}$$

$$\text{Hence MD code for two users is given by} = \begin{bmatrix} 1\,0 & 0\,1 \\ 0\,1 & 1\,0 \end{bmatrix} \tag{7}$$

It is cleared that the MD code design is constructed with zero cross-correlation properties, hence no MAI.

3 System Design with Eavesdropper

Basic system design for the proposed system is shown in Fig. 1. For a sequence length of 128 bits, word length of 7 bits is chosen as user data using user-defined bit sequence generator. This data is modulated using Mach–Zehnder modulator. Ex-OR operation is performed between a random key sequence consisting of 1's and 0's and user data. This approach is further providing a way of coding data to enhance security. It is clear from the block diagram shown in Fig. 1, that if some eavesdropper tries to trap original data from the fiber then it will not be possible. At the receiver, PIN Diode detector is used to convert the optical signal to the electrical domain and same MD code and key sequence is used to retrieve the original data, i.e., received data from fiber is Ex-ORed with key sequence used at transmitter side to retrieve original information. Thus, a high degree of security can be achieved by proposed method using combination of MD code, optical EX-Or gate and random key used for encoding and decoding user data.

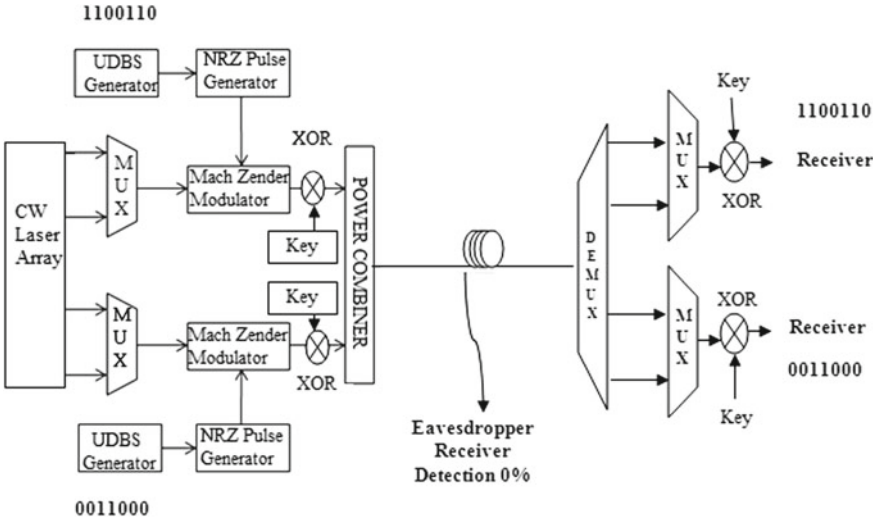

Fig. 1 SAC OCDMA system with MD code and X-OR gate

4 System Design Description

The simulation setup for proposed system is shown in Figs. 2 and 3. It is simulated in OptiSystem-15. Here, we have used an array of CW laser having linewidth of 10 MHz; CW laser output spectrum is sliced into four wavelengths. The chosen wavelengths are 1550, 1550.8, 1551.6 and 1552.4 nm. The standard channel spacing for SAC OCDMA system is 0.8 nm so we have selected 0.8 nm as the chip spacing and thus there will be no overlapping between wavelengths, and thus MAI and beat noise is minimized to a larger extent.

The first and third wavelengths, i.e., 1550 nm and 1551.6 nm are passed to upper 2 * 1 wavelength division multiplexer (WDM) and second and fourth wavelengths (1550.8 and 1552.4 nm) are passed to lower WDM Mux 2 * 1. Wavelength division multiplexer actually generates the SAC OCDMA code which is MD code in our case [4]. The code has zero cross-correlation property and hence no MAI.

Figure 2 shows transmitter section consisting of MD code and key sequence which is a randomly generated 0's and 1's sequence. Mach–Zehnder modulator is used to modulate user data with the coded sequence and this coded sequence is further Ex-Ored with key sequence which is 1001101. The optical X-or gate outputs are combined using power combiner and transmitted over a fiber cable of length 100 km.

Figure 3 shows receiver side in which at a distance of 50 km of fiber cable eavesdropper tries to decode original data using same MD code used at transmitter side. WDM demultiplexer is used to generate same MD code. Eye diagram analyser 2 shows Q factor 0 and BER 1 at the eavesdropping end. After a distance of 100 km same MD code and key sequence is used. 1 * 4 WDM Demultiplexer is used to decode

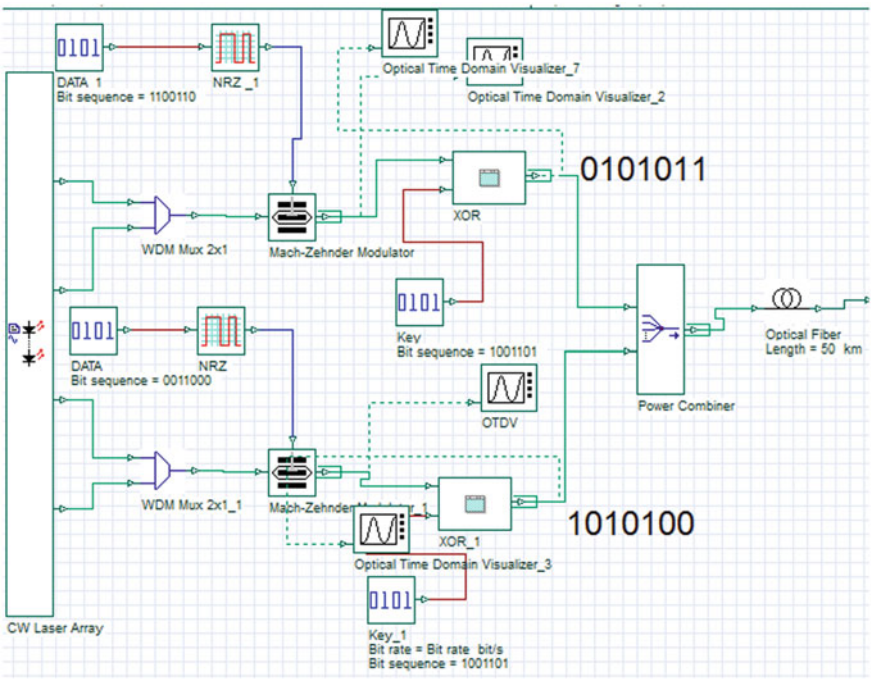

Fig. 2 Transmitter simulation model for proposed system with MD code, key sequence, and X-OR gate

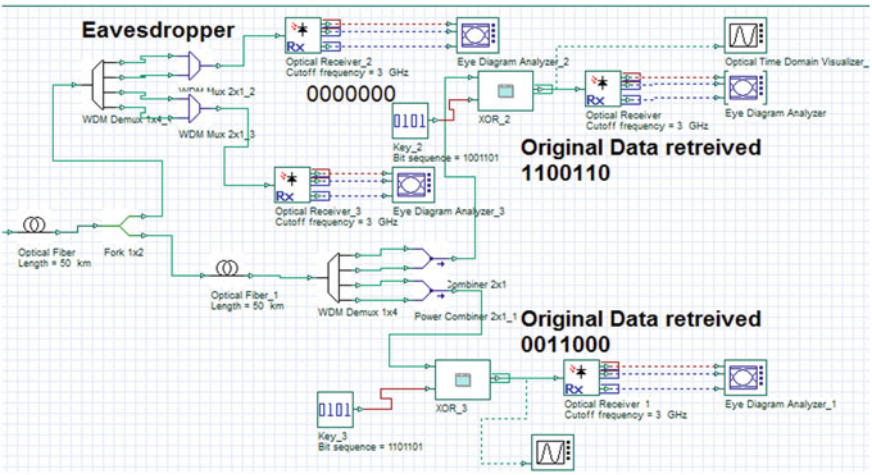

Fig. 3 Receiver simulation model for proposed system in presence of Eavesdroppers

Table 1 Simulation parameters [6]

Simulation parameters	Value	Simulation parameters	Value
Laser wavelengths (nm)	1550, 1550.8, 1551.6, 1552.4	Modulator extinction ratio	30 dB
Data rate	1 GBPS	Fiber dispersion	16.75 ps/nm km
Photodiode responsivity	0.6 A/W	Fiber dispersion slope	0.075 ps/nm^2 km
CW laser line width	10 MHz	Dark current	5 nA
Laser input power	0.2 mW	Thermal noise coefficient	$100 * 10^{-24}$
Signal data sequence	128 bits	Number of users	2
Signal format	NRZ	Attenuation in fiber	0.25 dB/km
Rx. electrical B.W. (Be)	311 MHz	Optical bandwidth ($B_{o)}$	3.75 THz

coded sequence and Ex-or gate 2 and Ex-or gate 3, with key sequence 1001101 is used to extract original user data.

Signals are transmitted over optical fiber after power accumulation. After 50 km, eavesdropper stealth the signal by breaking fiber of 100 km from middle. Tried to decode signal as if he knows that we are using which coding (but not aware of random key and XOR operation). Thus, even after all possible attempts to decode signal, he got fruitless results and obtained no EYE, i.e., Q factor 0 and BER 1.

For authorized users, after traveling more 100Kms, Signals are decoded with the help of Key **XOR** Data (for 1 and 2 user). Decoded signals are same as original data sequences as can be seen from Figs. 2 and 3. Simulation parameters are given in Table 1.

5 Results and Discussion

The data sequence for first code is 1100110 and for second code 0011000 and their power spectrum is shown in Fig. 4.

The key sequence chosen is any random data and we have fixed this random key, i.e., 1001101 for whole project. We have Ex-ORed MD coded data sequence with key sequence and resultant sequences are 0101011 and 101011 The optical power spectrum of Ex-OR gate output sequences are shown in Fig. 5.

The eye diagrams for user 1 and user 2 outputs are shown in Fig. 6. A wide eye height can be seen from the diagram which shows absence of MAI due to use of MD code.

The min BER and Q factor for first user and second user is given in Table 2.

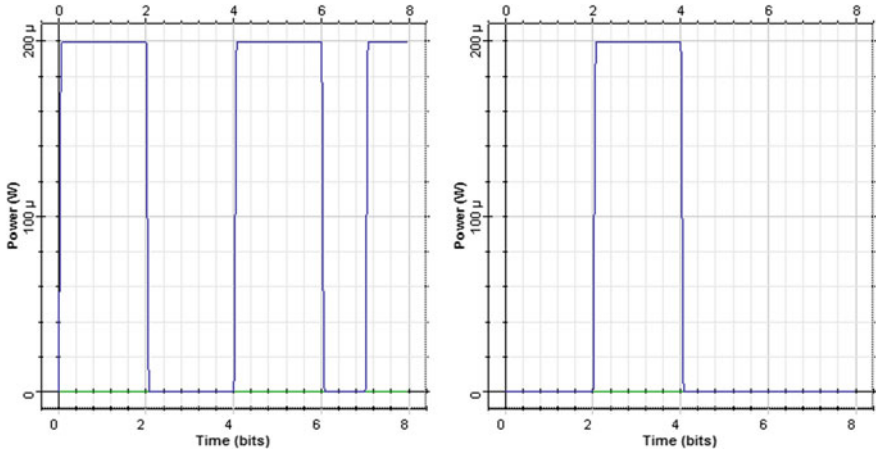

Fig. 4 Optical power spectrum of data sequence of first and second code

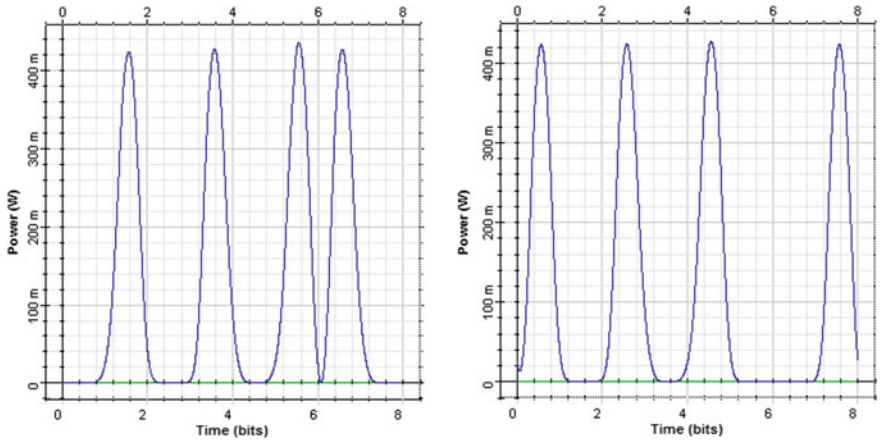

Fig. 5 Optical power spectrum of Ex-Or gate outputs at the transmitter end

6 Conclusion

OCDMA system is highly preferred technique for data transmission with higher security. The presented work which is having combination of MD code with gate structure can prove an efficient functional technique for enhancing security of OCDMA and its type SAC OCDMA system. It is reliable in terms of high degree of security owing to encoding and decoding and layering of code with key sequence. There is no MAI due to use of ZCC code. The proposed system is cost-effective due to the use of simple gates and system complexity is low.

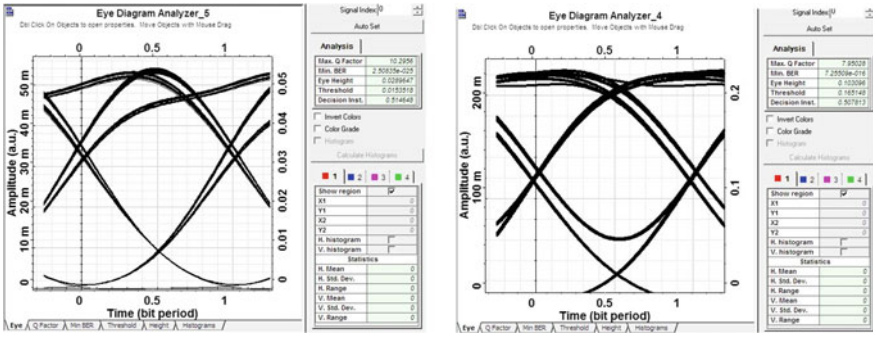

Fig. 6 Eye diagrams for decoded first user and second user

Table 2 Simulation results

No. of users	Min. BER	Q factor
User 1	$2.50 * 10^{-25}$	10.29
User 2	$7.11 * 10^{-16}$	7.95

7 Future Work

The proposed work can further be extended with other types of unipolar codes and their performance can be compared. Key sequences can be designed following some mathematics in place of choosing it random in order to enhance security to a much higher extent. By using highly sensitive and faster speed Notch filter and APD diode detectors, system performance can be improved in terms of signal to noise ratio and hence BER.

References

1. Shake TH (2005) Security performance of optical CDMA against eavesdropping. J Lightwave Technol 23(2):655–670
2. Abbade MLF, Fossaluzza Jr LA, Messani CA, Taniguti GM, Fagotto EAM, Fonseca IE (2013) All-optical cryptography through spectral amplitude and delay encoding. J Microw Optoelectron Electromagn Appl 12(2)
3. Heritage JP, Weiner AM (2007) Advances in spectral optical code-division multiple-access communications. IEEE J Sel Top Quant Electron 13:1351–1369
4. Huang JF, Chen KS, Lin YC, Li CY (2014) Reconfiguring waveguide gratings-based M-signature codecs to enhance OCDMA network confidentiality. Opt Commun 313C:223–230
5. Wei Z, Ghafouri-Shiraz H (2002) Codes for spectral-amplitude-coding optical CDMA systems. J Lightwave Technol 20(8)
6. Gurpreet K, Sumit G (2015) Performance analysis of SAC-OCDMA in free space optical medium using MD and DDW code. In: International conference on recent advances in engineering and computational sciences, vol 10, pp 1–6

7. Imtiaz WA, Ilyas M, Khan Y (2016) Performance optimization of spectral amplitude coding OCDMA system using new enhanced multi diagonal code. Infrared Phys Technol Electron Lett 79:36–44
8. Gupta S, Goel A (2015) OCDMA technique with the switching of code between the users for enhancing the security. In: International conference on communication and signal processing (ICCSP), pp 1181–1184, December 2015
9. Kaur R, Singh A, Kaler RS et al (2015) Novel security enhancement technique against eavesdropper for OCDMA system. Opt Fiber Technol 22:84–89
10. Jyoti V, Kaler RS (2011) Security enhancement of OCDMA system against eavesdropping using code-switching scheme. Optik Int J Light Electron Opt 122:787–791
11. Simranjeet S (2016) Novel secure and bandwidth efficient optical code division multiplexed system for future access networks. Res Artic Opt Fiber Technol 32:123–128
12. Chung HS, Chang SH, Bong K, Kim K (2008) Experimental demonstration of security-improved OCDMA scheme based on incoherent broadband light source and bipolar coding. Res Artic Opt Fiber Technol 14:130–133
13. Norazimah MZ, Aljunid SA, Al-Khafaji HMR, Anuar MS (2014) Investigating security of data retrieval for different detection techniques in SAC-OCDMA systems. In: 2nd international conference on electronic design (ICED), pp 117–121, April 2014
14. Huang J-F, Chen K-S, Su T-J (2016) Illustrative signature keys reconfiguration to combat with eavesdroppers in wavelength-coded optical access networks. In: International conference on future networks and communication, pp 240–247, June 2016

Photonic Integration Based on Liquid Crystals for Low Driving Voltage Optical Switches

Antonio d'Alessandro, Luca Civita and Rita Asquini

Abstract This paper reports on optical waveguides using liquid crystals (LC) as core. Such optical waveguides have the advantage to be controlled by a low voltage electric field or by using an optical beam by exploiting the highly efficient electro-optic or nonlinear optical effects, respectively. Optical switches based on LC embedded in silicon grooves have been reported with on–off contrast over 40 dB by applying about 8 V. Recently, a novel technology based on LC embedded in polydimethysiloxane (LC:PDMS) have been also developed to make photonic devices based on electro-optic waveguides on flexible substrates for telecom and sensor applications. An interesting feature of this guiding structure is that propagation is polarization independent. This technology has been employed to design a 2×2 optical switch based on a zero-gap electro-optical controlled directional coupler able to switch light from one output port to another by applying less than 1.8 V with an extinction ratio better than 16 dB.

Keywords Photonic devices · Liquid crystals · Optical switches

1 Introduction

Liquid crystals (LC) are interesting materials for many physical and chemical properties. LC used for most applications are thermotropic made of rod-like molecules which in a large temperature range are in the so-called nematic mesophase, therefore, they are referred simply as nematic LC (NLC) oriented in a preferential direction by using treated aligning surfaces. Such surfaces are the inner faces of glass substrates between which LC are confined. LC behave optically as anisotropic uniaxial optical materials with the optical axis oriented along the director, which represents the unit vector along the average molecular orientation. LC developed mainly to make large area flat panel displays are also interesting for many other photonic applications such

A. d'Alessandro (✉) · L. Civita · R. Asquini
Sapienza University, Rome, Italy
e-mail: antonio.dalessandro@uniroma1.it

© Springer Nature Singapore Pte Ltd. 2020

V. Janyani et al. (eds.), *Optical and Wireless Technologies*,
Lecture Notes in Electrical Engineering 546,
https://doi.org/10.1007/978-981-13-6159-3_51

as image processing using LC-based spatial light modulators, reconfigurable diffractive optics, and more recently integrated optics for fiber-optic communications and sensors.

LC are in fact transparent to visible and near infrared light with low optical losses since scattering losses scale with $\lambda^{-2.34}$ [1]. LC are particularly attractive for their highly efficient electro-optic effect which allows to reorient the molecules and then the optical axis according to the applied electric field direction at low voltage with negligible current absorption then with very low power consumption. High birefringence of LC up to 0.4 allows the modulation of the refractive index seen by light propagating in the LC. Low loss passive integrated optic devices based on either glass [2, 3] or silica on silicon [4] or SOI waveguides can be combined with LC to include active control of light [5].

In this paper, two technological approaches are shown to demonstrate how LC can be embedded to make integrated optic devices. In Sect. 2, switchable optical channels consisting of a NLC core infiltrated in SiO_2/Si V-grooves are described to allow both optical and electronic integration on silicon. In Sect. 3, LC-based waveguides infiltrated in Polydimethylsiloxane (PDMS) channels (LC: PDMS) for a new low cost and flexible type of integrated optic devices are shown. Section 4 shows the preliminary results of electro-optical switches based on zero-gap directional couplers made of LC:PDMS waveguides driven by low voltage control signals.

2 Liquid Crystal Waveguide Switches on Silicon

Liquid crystals can be embedded in silicon to obtain optical waveguides which can be integrated with driving electronic circuits. The upper part of Fig. 1 sketches a channel waveguide whose core is made of a NLC infiltrated in a SiO_2/Si V-groove. Fabrication of the V-groove is based on anisotropic wet-etching of Si [6]. Thermal grown SiO_2 is necessary as low refractive index substrate. A ITO (indium tin oxide)-coated Corning glass is used as cover whose inner surface includes a spinned layer of Nylon 6 rubbed along the groove direction to obtain LC alignment along the propagation direction. LC is infiltrated in the V-groove in their isotropic phase by capillarity in vacuum at about 80 °C and then cooled down at room temperature. LC electro-optic control is obtained by applying square wave voltages between silicon and the transparent ITO layer [7].

When no voltage is applied any light polarization senses the ordinary refractive index of the LC which is lower than the refractive index of the surrounding layers, therefore, the LC optical waveguides is in cut-off propagation condition. When an external voltage is applied, the LC molecules align along the electric field mainly in the vertical direction along which the extraordinary refractive index of the LC dominates determining an increase of the refractive index seen by a quasi-TM polarized light beam. The waveguide can transmit confined light since the extraordinary refractive index of the LC is higher than the refractive index of glass and SiO_2. The lower part of Fig. 1 shows a possible application of the LC on SiO_2/Si waveguide as

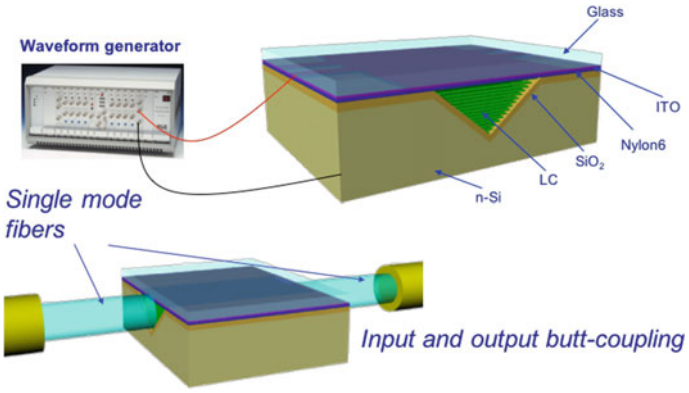

Fig. 1 Sketch of LC waveguide in SiO_2/Si V-groove. Upper side: an arbitrary waveform generator is used to apply a square wave voltage to control LC orientation and propagation of light. Lower side: LC waveguide on SiO_2/Si V-groove is butt-coupled to single-mode fibers

an optical switch which is butt-coupled to single mode optical fibers. An extinction ratio between cut-off and signal transmission of more than 40 dB has been measured for 10 μm wide waveguide with the commercial NLC E7 as a core, by applying about 8 V at 1 kHz with losses about 6 dB/cm which can be further reduced by improving the alignment technique [8].

3 Liquid Crystal Waveguides Embedded in PDMS

An alternative technology can be used to make low cost and low driving voltage LC waveguides by infiltrating LC in PDMS channels (LC:PDMS waveguides) with a rectangular square section [9]. PDMS is an interesting material used for lab-on-chip, microfluidic, and optical interconnection applications with many interesting properties such as high optical transparency, low surface energy, low dielectric constant, and biocompatibility.

Effective, reliable, and cheap microfluidic and micro-optical devices can be obtained by using PDMS. In particular, cast and molding technique can be used in combination with SU8 to make a photolithographically processed mold and then empty PDMS channels can be produced. Reliable LC:PDMS optical waveguides can be made by using the standard LC filling procedure by capillarity inside the PDMS channels. Left-hand side of Fig. 2 shows a set of LC:PDMS waveguides.

In this case, no alignment layer is required since LC molecules align spontaneously perpendicularly to all the four inner surfaces of the PDMS channel, as shown in right-hand side of Fig. 2, providing an average constant refractive index seen by any polarization orientation of a light beam confined in the LC core [10]. In a channel with square section, LC are oriented mainly vertically in the bulk and horizontally

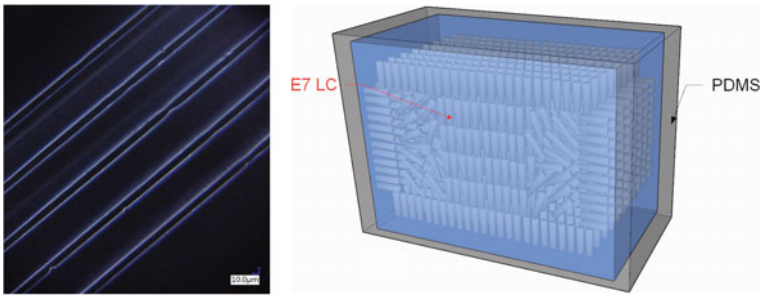

Fig. 2 Left-hand side picture shows an LC:PDMS waveguide set taken under a polarized microscope. A sketch describing how NLC molecules are aligned in a PDMS channel is reported in the right-hand side

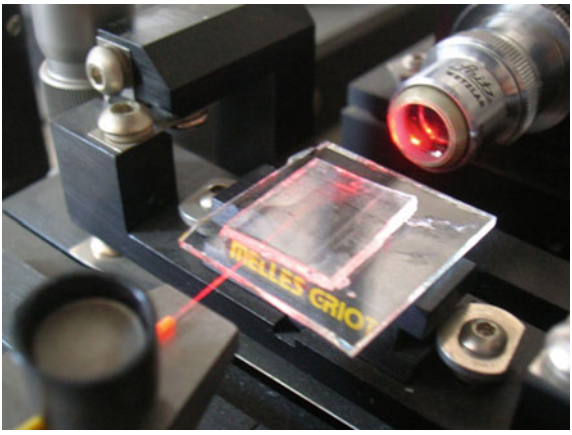

Fig. 3 Red light fiber butt-coupled to LC:PDMS waveguides. A microscope objective is used to collect output light

at the vertical surfaces of PDMS as shown in the right-hand side of Fig. 2. Such LC orientation is demonstrated by looking at the LC:PDMS waveguides under polarized microscope using crossed polarizers. The left-hand side picture shows light transmission of the microscope through the edges of the waveguides since the optically anisotropic LC molecules are parallel the PDMS substrates producing phase retardation of light. No transmission of light through the central part of the waveguides is due to vertical alignment of the LC with respect to the PDMS sample. In this case, the LC molecules, in fact, are not able to produce any phase retardation of light. Such spontaneous alignment of the LC molecule is due to the hydrophobicity of PDMS and has been also simulated by using Monte Carlo technique [11]. When a laser beam is fiber butt-coupled to a LC:PDMS waveguide, as shown in Fig. 3, optical transmission is polarization independent. A transmission intensity variation as low as 0.35 dB has been measured as light polarization changes at both visible at 632.8 nm and near-infrared light at 1550 nm wavelength.

4 A Zero-Gap Coupler Photonic Switch Made of LC:PDMS Waveguides

An advantage in using LC:PDMS waveguides with respect to silicon is that lightwave circuits can be patterned with any geometry including also bends which cannot be obtained in anisotropically etched silicon grooves.

A zero-gap optical directional coupler has been designed to make a 2 × 2 optical switch by using coplanar electrodes to control the status of the coupler output as sketched in Fig. 4 not in scale. The optimized bimodal section is 3 μm high, 3 μm wide, and 500 μm long. Two incoming single mode waveguides, whose height is 3 μm and width is 1.5 μm. A voltage applied to coplanar electrodes induces an electric field which controls the alignment of the LC molecules and changes the refractive index of the LC [12]. A Monte Carlo simulation technique has been used also in this case to study orientation of the LC molecules which align along the applied electric field [13]. The interference of the two modes in the bimodal section is then controlled by the LC refractive index determining in which output port constructive interference of the two modes of light occurs. Extinction ratio of the switch defined as $10\text{Log}(P_{out2}/P_{out1})$ in dB versus refractive index value of the NLC E7 of the designed zero-gap directional coupler is plotted in Fig. 5 for light beam signals at a wavelength of 1550 nm.

An extinction ratio of 16 dB has been observed for a LC refractive index equal to 1.6 corresponding to an applied voltage of 1.62 V calculated by minimizing the Oseen–Frank equation for coplanar electrodes [14]. In this case, a light signal exits from the lower output waveguide corresponding to the cross-state of the switch. An extinction ratio of about −18 dB is obtained for a refractive index equal to 1.627 corresponding to an applied voltage of 1.76 V. In this case, a light signal exits from the upper output waveguide corresponding to the bar-state of the switch. Switch status from bar-state to cross-state and vice versa can be obtained by applying a voltage change of 140 mV.

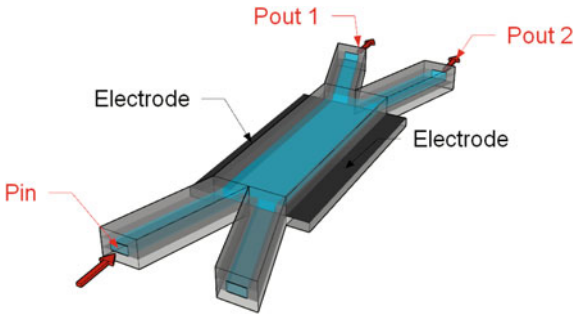

Fig. 4 Sketch of a zero-gap directional coupler with coplanar electrodes

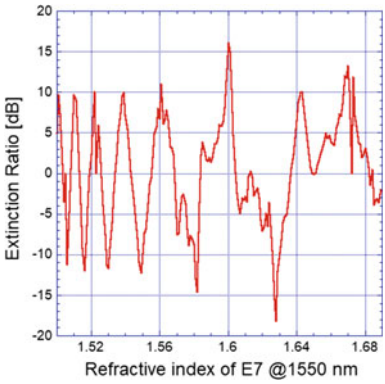

Fig. 5 Extinction ratio of the output of a zero-gap directional coupler switch versus E7 NLC refractive index

5 Conclusions

LC can be embedded in both inorganic and organic substrate materials to make compact low cost and low driving power photonic integrated circuits based on optical waveguides whose core is made of LC-oriented molecules.

In this paper, it has been shown how to obtain optical switches based on LC infiltrated in Si/SiO_2 V-grooves. On–off extinction ratio over 45 dB by applying square wave voltages with amplitude of about 8 V. LC waveguides on Si have also the advantage to allow full integration of both electrical and photonic functions on the same chip. Organic materials can be also used to make functional photonic devices based on the electro-optical properties of LC. Another result reported in this paper is the possibility to infiltrate LC in PDMS channel to obtain flexible photonic integrated circuits. Photonic switches based on zero-gap direction couplers driven by coplanar electrodes are feasible with output extinction ratio better than 16 dB by applying voltages lower than 1.76 V and the switch status can be controlled by varying the applied voltage of just 0.14 V. The device including chromium electrodes is under fabrication.

References

1. Khoo I-C (2007) Liquid crystals, 2nd edn. Wiley, New York
2. Asquini R, d'Alessandro A (2000) A bistable optical waveguided switch using a ferroelectric liquid crystal layer. In: Proceedings of 13th annual meeting. IEEE lasers and electro-optics Society 2000. IEEE Annual Meeting, pp 119–120, Rio Grande-Puerto Rico, USA
3. d'Alessandro A, Asquini R, Menichella F, Ciminelli C (2001) Realisation and characterisation of a ferroelectric liquid crystal bistable optical switch. Mol Cryst Liq Cryst 372:353–363
4. Gizzi C, Asquini R, d'Alessandro A (2004) A polarization independent liquid crystal assisted vertical coupler switch. Mol Cryst Liq Cryst 421(1):95–105
5. De Cort W, Beeckman J, Claes T, Neyts K, Baets R (2011) Wide tuning of silicon-on-insulator ring resonators with a liquid crystal cladding. Opt Expr 36(19):3876–3878

6. Bellini B, Larchanché J-F, Vilcot J-P, Decoster D, Beccherelli R, d'Alessandro A (2005) Photonic devices based on preferential etching. Appl Opt 44(33):7181–7186
7. d'Alessandro A, Bellini B, Donisi D, Beccherelli R, Asquini R (2006) Nematic liquid crystal optical channel waveguides on silicon. IEEE J Quant Elect 42(10):1084–1090
8. Donisi D, Bellini B, Beccherelli R, Asquini A, Gilardi G, Trotta M, d'Alessandro A (2010) A switchable liquid-crystal optical channel waveguide on silicon. IEEE J Quant Elect 46(5):762–768
9. Asquini R, Martini L, d'Alessandro A (2015) Fabrication and characterization of liquid crystal waveguides in PDMS channels for optofluidic applications. Mol Cryst Liq Cryst 614:11–19
10. d'Alessandro A, Martini L, Gilardi G, Beccherelli R, Asquini R (2015) Polarization-independent nematic liquid crystal waveguides for optofluidic applications. IEEE Photon Technol Lett 27(15):1709–1712
11. d'Alessandro A, Asquini R, Chiccoli C, Martini L, Pasini P, Zannoni C (2015) Liquid crystal channel waveguides: a monte carlo investigation of the ordering. Mol Cryst Liq Cryst 619(1):42–48
12. Asquini R, Fratalocchi A, d'Alessandro A, Assanto G (2005) Electro-optic routing in a nematic liquid-crystal waveguide. Appl Opt 44(19):4136–4143
13. d'Alessandro A, Asquini R, Chiccoli C, Pasini P, Zannoni C (2017) Liquid crystal channel waveguides: a computer simulation of the application of transversal external fields. Mol Cryst Liq Cryst 649(1):79–85
14. Yeh P, Gu C (2010) Optics of liquid crystal displays, 2nd edn. Wiley, New York

Design and Analysis of Decagonal Photonic Crystal Fiber for Liquid Sensing

Kuntal Panwar and Ritu Sharma

Abstract In this paper, the design of a microstructured decagonal Photonic Crystal Fiber (D-PCF) has been proposed for liquid sensing application. The proposed fiber has been analyzed using full vector Finite Element Method (FEM). The core of the decagonal fiber is filled with two different liquid analytes, ethanol, and water and variation of sensitivity and confinement loss are investigated over a wide range of wavelength. The proposed D-PCF structure gives sensitivity 30.2% for ethanol and 27.05% for water and confinement loss achieved is 2.89×10^{-6} dB/m for ethanol and 3.67×10^{-6} dB/m for water, measured at a 1.33 μm wavelength.

Keywords Photonic crystal fiber (PCF) · Finite element method (FEM) · Sensitivity · Confinement loss

1 Introduction

Photonic crystal fiber has a geometry which is composed of a microstructure air-hole cladding running along the entire length of the fiber and the core can be solid or hollow [1, 2]. On the basis of guiding mechanism, PCFs can be divided into two different categories: (1) index-guided PCF and (2) photonic bandgap fiber. The index-guiding PCF follows the principle of total internal reflection [3, 4]. The photonic bandgap PCF has periodically distributed air holes in the cladding which produces photonic bandgap. The core of the fiber is created by a defect at the center [5, 6].

Various properties of PCFs have been explored in the literature which includes endlessly single mode operation [3, 7], effective mode area [8, 9], tailorable dispersion [10, 11], and high birefringence [12, 13]. The light is guided due to the

K. Panwar (✉) · R. Sharma
Department of Electronics and Communication, Malaviya National Institute of Technology Jaipur, Jaipur, Rajasthan, India
e-mail: 2016pwc5169@mnit.ac.in

R. Sharma
e-mail: rsharma.ece@mnit.ac.in

© Springer Nature Singapore Pte Ltd. 2020

V. Janyani et al. (eds.), *Optical and Wireless Technologies*,
Lecture Notes in Electrical Engineering 546,
https://doi.org/10.1007/978-981-13-6159-3_52

presence of air holes and this guidance can further be enhanced by inserting liquid/gases into the air hole of the core. This new material insertion makes it useful in sensing applications as there is the high interaction of material and air holes in the fiber. Optical-fibers-based sensors have high sensitivity, small size, robustness, and flexibility which makes them low cost and efficient solutions for several industries. Optical-fiber-based sensors are also resistive to the presence of unfavorable environmental conditions such as noise, strong electromagnetic fields, high voltages, nuclear radiation, in explosive or chemically corrosive media, at high temperatures [14].

In this paper, decagonal 6 ring PCF fiber is designed with a radius of air holes 0.75 μm and pitch 1.23 μm and the core is filled with liquid analytes, ethanol, and water and its guiding properties are analyzed. The sensitivity of proposed D-PCF in this paper gets increased to 30.2% as compared to prior O-PCF sensitivity of 21.05% at 1.33 μm reported in [15]. The confinement loss measured for the proposed fiber is 2.89×10^{-6} dB/m. The values of sensitivity and confinement loss are taken at 1.33 μm wavelength since the results obtained at this value of wavelength are much greater than at any other value. In the literature work earlier, the confinement loss had been calculated at 1.55 μm wavelength for the decagonal geometry [16, 17] whereas in this paper 1.33 μm wavelength has been observed and the geometry of decagonal fiber is taken in such a manner to support high sensitivity and low confinement loss at this wavelength which also supports the low absorption window of Silica.

2 Geometry of Proposed D-PCF

A decagonal microstructured PCF has been proposed in this paper, where air holes which constitute the cladding, are arranged in a decagonal pattern with pitch (hole to hole space, represented by ʌ) is 1.23 μm and radius of each hole (represented by r) is 0.75 μm. For decagonal geometry, vertices of adjoining air holes contain 36° angles. There are a total of six rings in the geometry. The cross-sectional view of designed decagonal fiber is shown in Fig. 1.

The background material in the fiber is of silica which is filled by varying its refractive index using Sellemeier's Eq. 1 [18]:

$$n^2(\lambda) = 1 + \frac{B_1\lambda^2}{\lambda^2 - C_1} + \frac{B_2\lambda^2}{\lambda^2 - C_2} + \frac{B_3\lambda^2}{\lambda^2 - C_3} \tag{1}$$

where n(λ) is the refractive index of the material at the wavelength, B_1, B_2, B_3, C_1, C_2, C_3 are sellemeier's constants given in Table 1.

The modal intensity distribution of proposed fiber is shown in Fig. 2a, b.

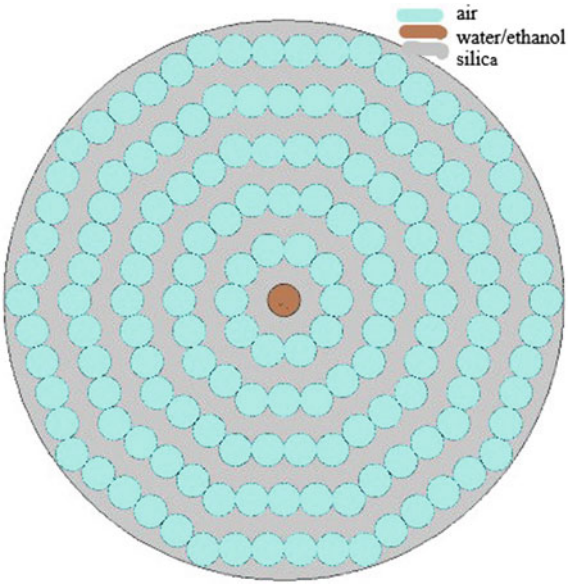

Fig. 1 Geometry of decagonal PCF with filled material configuration shown

Table 1 B_1, B_2, B_3, C_1, C_2, C_3 are sellemeier's constants given as

Material	B_1	B_2	B_3	C_1 (μm^2)	C_2 (μm^2)	C_3 (μm^2)
Silica	0.696166300	0.00467914826	0.407942600	0.0135120631	0.897479400	97.9340025

3 Results and Numerical Analysis

The periodic arrangement of a finite number of air holes causes a reduction in optical confinement, hence light penetrates into the cladding region. This confinement loss is dependent on the structure and arrangement of air holes in the fiber. It can be analyzed by applying PML (Perfectly Matched Layer) to the fiber. It is derived from the formula as given in Eq. 2 [19]:

$$\alpha_{loss} = \frac{40\pi}{\lambda \ln 10} \mathrm{Im}(n_{eff}) \times 10^6 \left(\frac{\mathrm{dB}}{\mathrm{m}}\right) \tag{2}$$

Im (n_{eff}) represents the imaginary part of the effective mode index and λ represents the wavelength of light.

Relative sensitivity coefficient which is a measure of interaction between light and analyte is given by the Eq. 2 [20]:

$$r = \frac{n_r}{n_{eff}} * f \tag{3}$$

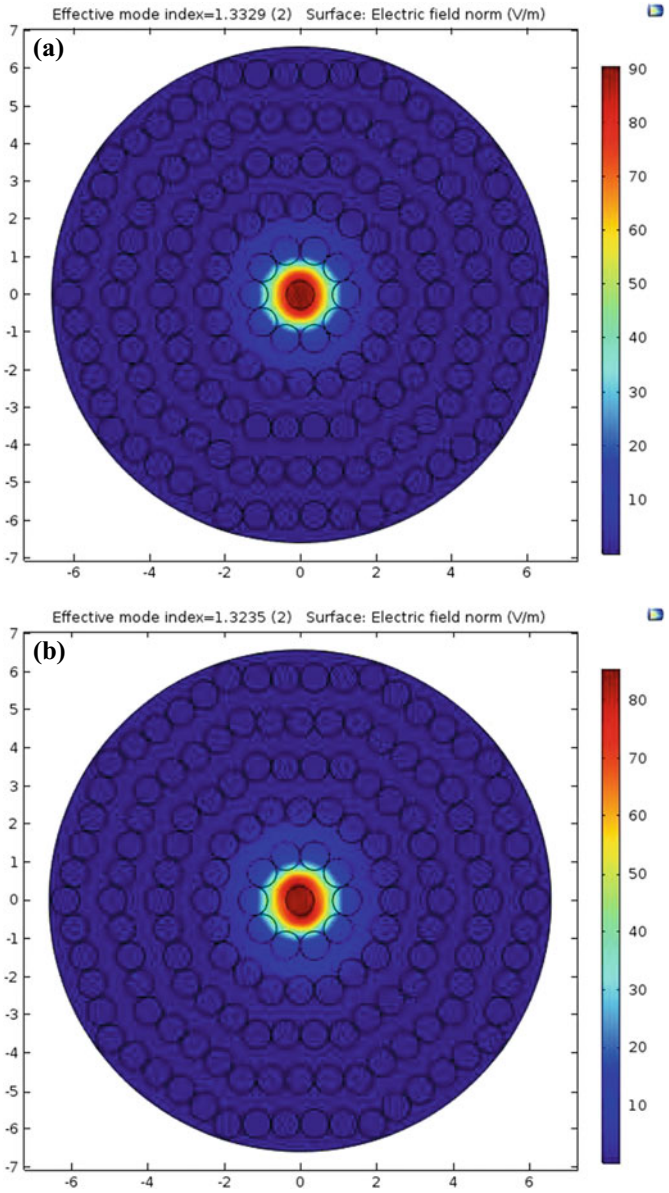

Fig. 2 **a** Snapshot of the modal intensity distribution of fundamental mode at 1.33 μm when the core is filled with ethanol (1.354). **b** Snapshot of modal intensity distribution of fundamental mode at 1.33 μm when core is filled with water (1.33)

n_r is the refractive index of liquid analyte present in the core, n_{eff} is the effective mode index and f is the percentage of the ratio of core power and total power in the fiber and is given by the Eq. 3:

$$f = \frac{\int_{sample} \mathrm{Re}(E_x H_y - E_y H_x)dxdy}{\int_{total} \mathrm{Re}(E_x H_y - E_y H_x)dxdy} * 100 \quad (4)$$

where E_x, E_y are transverse and longitudinal electric field and H_x, H_y are transverse and longitudinal magnetic field, respectively.

The mode field pattern E_x E_y H_x H_y and effective mode index are obtained by applying finite element method (FEM). A PML layer of thickness 10% of the radius of fiber is applied to the geometry [21]. Fine mesh size is used for computation. The D-PCF supports fundamental as well as some higher modes but for further investigation, only the fundamental is considered. The sensitivity and confinement loss of D-PCF fiber is calculated using the abovementioned formulas over a range of wavelength (1.15–2 μm). The variation of sensitivity and confinement loss with wavelength using two different analytes, ethanol, and water, as shown in Figs. 3 and 4.

It can be seen from Fig. 3, the core filled with ethanol gives high sensitivity as compared to water because the refractive index of ethanol is higher than water leading to more absorption of light giving higher sensitivity.

The confinement loss is decreasing with the wavelength as more light is being confined to the core, and it has lesser value for ethanol as compared to water because of high ability to absorb light.

The D-PCF structure has a sensitivity of 30.2% when ethanol is filled in the core and 27.05% when water is filled in the core, at 1.33 μm wavelength. The confinement loss measured at the 1.33 μm wavelength is 2.89×10^{-6} dB/m and 3.67×10^{-6} dB/m for core filled with analytes ethanol and water, respectively.

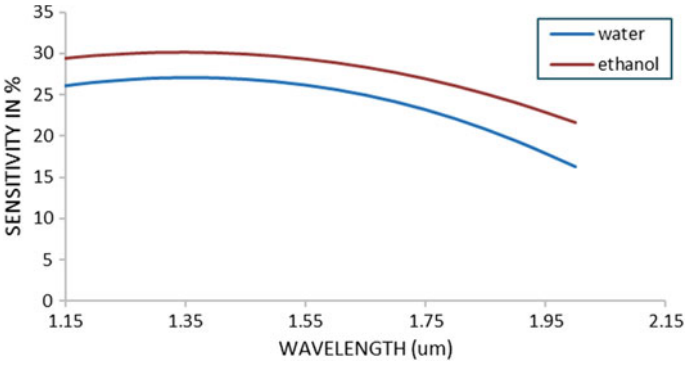

Fig. 3 variation of sensitivity (%) with wavelength (μm) when core is filled with ethanol and water

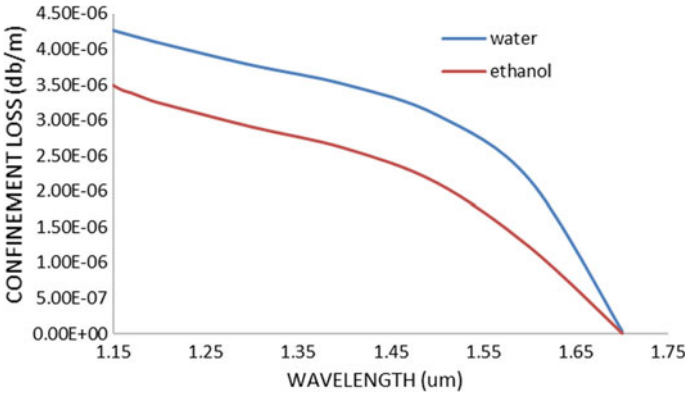

Fig. 4 Variation of confinement loss (dB/m) with wavelength (μm) when core is filled with ethanol and water

The fabrication of the proposed fiber can be done using the latest technologies which include Sol-gel technique for fabrication and selective filling technique for filling liquids in the core [22].

4 Conclusion

This paper investigates two most important guiding properties of proposed D-PCF using finite element method. It has high sensitivity of 30.2% and 27.05% and low confinement loss of 2.89×10^{-6} dB/m and 3.67×10^{-6} dB/m with analytes as ethanol and water, respectively, at 1.33 μm. Hence, this structure opens a new field of PCF-based sensing with further scope of enhancing sensitivity by varying geometry of core. It is optimal for different liquid sensing applications.

Acknowledgements The author wishes to acknowledge DST Rajasthan for funding the project.

References

1. Broeng J, Mogilevstev D, Barkou SE, Bjarklev A (1999) Photonic crystal fibers: a new class of optical waveguides. Opt Fiber Technol 5:305–330
2. Birks TA, Knight JC, Mangan BJ, Russell PS (2001) Photonic crystal fibers: an endless variety. IEICE Trans Electron E84-C:585–592
3. Knight JC, Birks TA, Russell PS, Atkin DM (1996) All-silica single-mode optical fiber with photonic crystal cladding. Opt Lett 21:1547–1549. https://doi.org/10.3164/ol.21001547
4. Birks TA, Knight JC, Russell PS (1997) Endlessly single-mode photonic crystal fiber. Opt Lett 22:961–963. https://doi.org/10.1364/ol.22.00096

5. Knight JC, Broeng J, Birks TA, Russell PS (1998) Photonic band gap guidance in optical fiber. Science 282:1476–1478. https://doi.org/10.1126/science.282.5393.1476
6. Cregan RF, Mangan BJ, Knight JC, Birks TA, Russell PS, Roberts PJ, Allan DC (1999) Single-mode photonic band gap guidance of light in air. Science 285:1537–1539
7. Knight JC, Birks TA, Cregan RF (1998) Large mode area photonic crystal fibers. Electron Lett 34:1347–1348
8. Mortensen NA, Nielsen MD, Folkenberg JR, Petersson A, Simonsen HR (2003) Improved large-mode-area endlessly single-mode photonic crystal fibers. Opt Lett 28:393–395. https://doi.org/10.1364/OL.28.000393
9. Ademgil H, Haxha S (2012) Endlessly single-mode photonic crystal fiber with improved effective mode area. Opt Commun 285:1514–1518. https://doi.org/10.1016/j.optcom.2011.10.067
10. Liu Y et al (2012) A novel hybrid photonic crystal dispersion compensating fiber with multiple windows. Opt Laser Technol 44:2076–2079
11. Yang TJ, Shen LF, Chau YF, Sung MJ, Chen D, Tsai DP (2008) High birefringence and low loss circular air-holes photonic crystal fiber using complex unit cells in the cladding. Opt Commun 281:4334–4338. https://doi.org/10.1016/j.optcom.2008.05.008
12. Razzak SMA, Namihira Y, Hossain MA, Khaleque A (2011) Designing birefringence of index-guiding non-hexagonal photonic crystal fibers. J Opt 40(2):56–64
13. Bhattacharya R, Konar S (2012) Extremely large birefringence and shifting of zero dispersion wavelength of photonic crystal fibers. Opt Laser Technol 44:2210–2216. https://doi.org/10.1016/j.ijleo.2014.07.096
14. Ghosh G (1997) Sellmeier coefficients, and dispersion of thermo-optic coefficients for some optical glasses. Appl Opt 36:1540–1546
15. Kawsar A, Monir M (2015) Design and numerical analysis of micro structured-core octagonal photonic crystal fiber for sensing applications. Elsevier B.V., pp 2214–1804. https://doi.org/10.1016/j.sbsr.2015.10.005
16. De M, Gangwar RK, Singh VK (2017) Designing of highly birefringence, dispersion shifted decagonal photonic crystal fiber with low confinement loss. Elsevier B.V., pp 1569–4410. https://doi.org/10.1016/j.photonics.2017.06.002
17. Krishna GD, Prasannan G, Sudheer SK, Pillai VM (2015) Design of ultra-low loss highly non-linear dispersion flattened octagonal photonic crystal fibers. Opt Photon J 5:335–343. https://doi.org/10.4236/opj.2015.512032
18. Pourmahyabadi M, Nejad SM (2009) Numerical analysis of index-guiding photonic crystal fibers with low confinement loss and ultra-flattened dispersion by FDFD method. Iran J Electr Elect Eng 5:170–197
19. Morshed M, Asaduzzaman S, Arif MF, Ahmed K (2015) Proposal of simple gas sensor based on microstructured optical fiber. In: 2nd international conference on electrical engineering and information & communication technology, Bangladesh. https://doi.org/10.1007/s13320-016-0323-y
20. Morshed M, Hasan MI, Razzak SMA (2015) Enhancement of the sensitivity of gas sensor based on microstructured optical fiber. Photon Sensors 1–9. https://doi.org/10.1007/s13320-015-0247-y
21. Xiao L, Jin W, Demokan M, Ho H, Hoo Y, Zhao C (2005) Fabrication of selective injection microstructured optical fibers with a conventional fusion splicer. Opt Express 13:9014–9022. https://doi.org/10.1364/OPEX.13.009014
22. Bise RT, Trevor D (2005) Sol-gel derived microstructured fiber: fabrication and characterization. Opt Soc Am 1–3

Design and Implementation of Multiband Planar Antenna with DGS for Wireless Applications

Pravin Tajane and Prasanna L. Zade

Abstract A presented multiband planar antenna consists of asymmetrically C-shaped slots on patch side and defected structure on ground plane for wireless applications. The modified ground construction and asymmetrically C-shaped resonates 3.5 GHz, resonates 2.5 and 5.3 GHz covering WLAN, Bluetooth, Zigbee, WiMAX and HYPERLAN. The dimensions of the proposed antenna are $40 \times 26 \times 1.6$ mm^3. The presented designed and fabricated antenna shows good results which are applicable for different useful frequency bands.

Keywords Multiband · C-Slot · Zigbee · WiMAX · WLAN and bluetooth

1 Introduction

In communication, wireless portable devices became very popular due to small size, low weight, different band operation of patch antenna. The various portable device consists of wireless local area network (WLAN) standards in the 2.4 GHz (2400–2480 MHz), 5.2 GHz (5150–5350 MHz), 5.8 GHz (5725–5825 MHz), Bluetooth (2400–2483.5 MHz) and Zigbee (2.405–2.480 GHz) for wireless communication network. In mobile sets and smartphones use of planar antenna for different frequency operation to multiple applications like WLAN, Wi-Fi, Zigbee, Bluetooth, etc. Instead of using single antenna for single band which reduces size as well as applicable of different band in single antenna. The microwave system like WLAN, Zigbee, WiMAX, and Bluetooth requires high speed with reasonable price in a single unit.

P. Tajane (✉)
Department of Electronics Engineering, YCCE, Nagpur, India
e-mail: ptajane8@gmail.com

P. L. Zade
Datta Meghe Institute of Engineering Technology and Research, Wardha, India
e-mail: zadepl@yahoo.com

© Springer Nature Singapore Pte Ltd. 2020

V. Janyani et al. (eds.), *Optical and Wireless Technologies*,
Lecture Notes in Electrical Engineering 546,
https://doi.org/10.1007/978-981-13-6159-3_53

There are various techniques available for designing multiband planar monopole antenna. A multiple band obtained by few researchers are as follows: three rectangular tuning strips are used to cover the desired bands [1]. The two F-shaped slots of the same size are etched on a rectangular patch to achieve multiband operation [2]. The inverted U-shaped and L-shaped strips provide the wideband nature to cover the WLAN with WiMAX frequency band [3]. The symmetrical L-and U-shaped slots were cut out within patch to provide desired resonance frequencies [4]. The proposed antenna consists of an F-shaped with an inverted L-shaped strip-sleeve shorted at the ground plane [5]. The projected antenna consists of U- and T-shaped stub resonator to obtain dual band [6]. It consists of two symmetrical twisted arms with each arm two bended strips with same width and lengths and partial ground plane [7]. U-shape get by connecting two short line and added two square shapes at the upper side of each line which they give good response at two operating frequencies 2.4 and 3.5 GHz [8]. In this antenna was added a U-shaped branch which resonates at the lowest frequency of 900 MHz. Similarly, other L-shaped branches were added to achieve resonance at other desired frequencies [9]. There are two L-shaped slots scratch out of the ground and one U-shaped slot out of the E-shaped patch [10]. The L-shaped slot cut out of the ground and patch produced multiband operation [11].

In all the above-cited papers efforts are made to develop and design the multiband with reasonable gain which is suitable for wireless application like WLAN, WiMAX, HYPERLAN, Zigbee and Bluetooth. Initially, antenna is designed by using basic formulae to get single band and to achieve multiband, modification is done in ground plane as well as patch of antenna. By using defected ground structure one can easily create multiband antenna instead of different fractal shape. In the future, designers can use various techniques to obtain different bands for the specific bandwidth for the different type of single resonance frequency of patch antenna. The proposed antenna will cover WLAN, WiMAX, HYPERLAN, Bluetooth and Zigbee frequency bands with suitable gain. In the present work, a antenna is designed with compact size, multiple band, low weight easy of fabricate, etc. The antenna is designed with asymmetrically C-shaped slots and modified ground plane to achieve multiband for wireless application.

2 Antenna Design with Simulation Result

Figure 1 shows the real physical construction of the antenna with back side and front side using Computer Simulation Technology (CST software) Microwave studio. The FR4 substrate is used with relative dielectric constant 4.3 and height 1.6 mm. The, in particular, volume of antenna is $40 \times 26 \times 1.6$ mm^3. The parametric analysis is optimized for good impedance matching and to generate for multiple band operation. When the matching of impedance with source through SMA connector and antenna to deliver more amount of power at output side. In multiband antenna, capacitor and inductor are responsible for generate complex network due to the frequency-dependent component which is having quality factor.

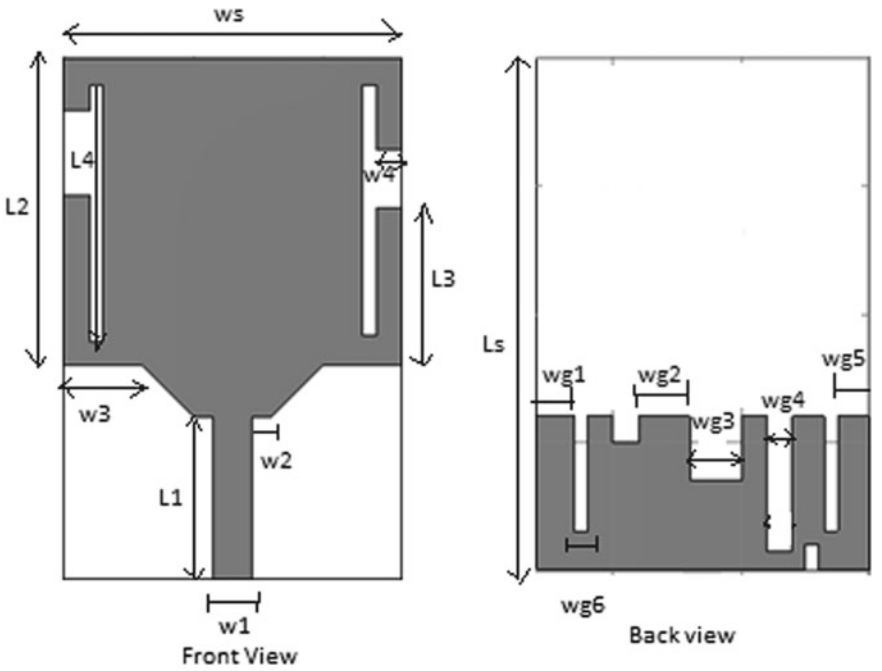

Fig. 1 Front and back view of the proposed antenna

Table 1 Antenna parameters (units in mm)

Designing parameters	Dimensions (mm)	Designing parameters	Dimensions (mm)
Wl	3	Wgl	3
W2	1.5	Wg2	4
W3	6	Wg3	4
W4	2	Wg4	2
LI	12.5	Wg5	3
L2	23.5	Wg6	1
L3	12	Ls	40
L4	17.75	Ws	26

From Fig. 1, light black is used as a copper layer on front and back side. White portion is used as substrate of planar antenna which height is 1.6 mm.

Table 1 shows dimensions of patch and ground of proposed antenna. The microstrip line is connected to the patch of front side of antenna which is taken as 3 mm to produce 50 Ω for resonant frequency so, the radiating patch and microstrip line is on same side.

3 Simulation Results

The entire simulations of the projected antenna are achieved using the Computer Simulation Technology (CST software) Microwave studio. The simulated return loss is offered in Fig. 2 where it is observed that C-shaped slot is responsible for generating different resonant frequencies 3.5 GHz and defected ground structure for creating 2.5 and 5.5 GHz. The lower frequency band is from 2.32 to 2.76 GHz with bandwidth of 440 MHz covering Zigbee, Bluetooth and WLAN. The second frequency band is beginning 3.37 to 3.67 GHz with bandwidth of 300 MHz covering WiMAX. The third frequency band is from 5.14 to 5.54 GHz with bandwidth of 400 MHz covering HYPER LAN1.

From Fig. 2, it is observed that the reflection coefficient for useful resonance frequency is less than −10 dB so it is acceptable by comparing standard parameter (Fig. 3).

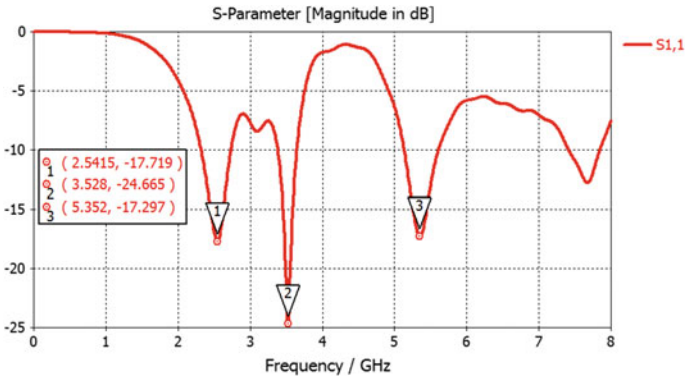

Fig. 2 Return loss characteristics of the proposed antenna

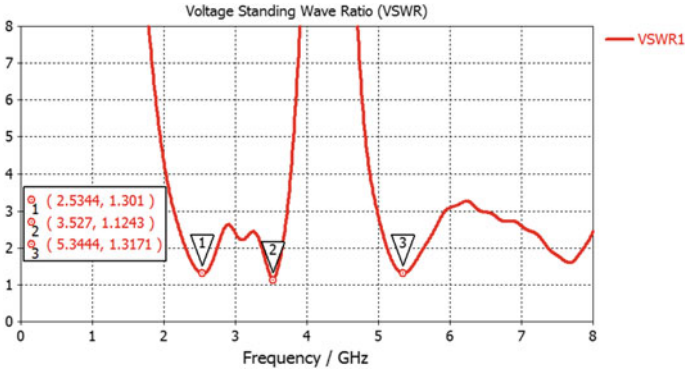

Fig. 3 VSWR for the proposed antenna

It radiated more than 90% power when the VSWR changes from 1 to 2. For every resonance frequency, VSWR lies between 1 and 2 such as 1.294 for 2.5 GHz, 1.160 for 3.5 GHz, and 1.394 for 5.34 GHz.

Its E-far field polar plot is given in Fig. 4. The basic patch covered with omnidirectional because sidelobe level is small. The orientation of patch plays important role that whether antenna is suitable for cellular devices or not so proposed planar antenna shows vertical or horizontal polarization. The polar-type radiation patterns of the antenna and gain at different frequencies are shown in Fig. 4. The simulated gain for 2.54 GHz, 3.54 GHz and 5.3 GHz resonance frequencies is 2.11 dB, 3.35 dB and 4.88 dB, respectively.

In Fig. 5a, surface current has maximum at the bottom side defected ground structure. In Fig. 5b, maximum current is distributed over C-shaped patch. In Fig. 5c, maximum current is distributed over ground plane. From the Fig. 5, it is cleared that those part of antenna has more current it is indicated by red colour so that part is responsible generating resonance frequencies. There is scope to reduced size of antenna by removing another portion because those part does not take part in any activity for result.

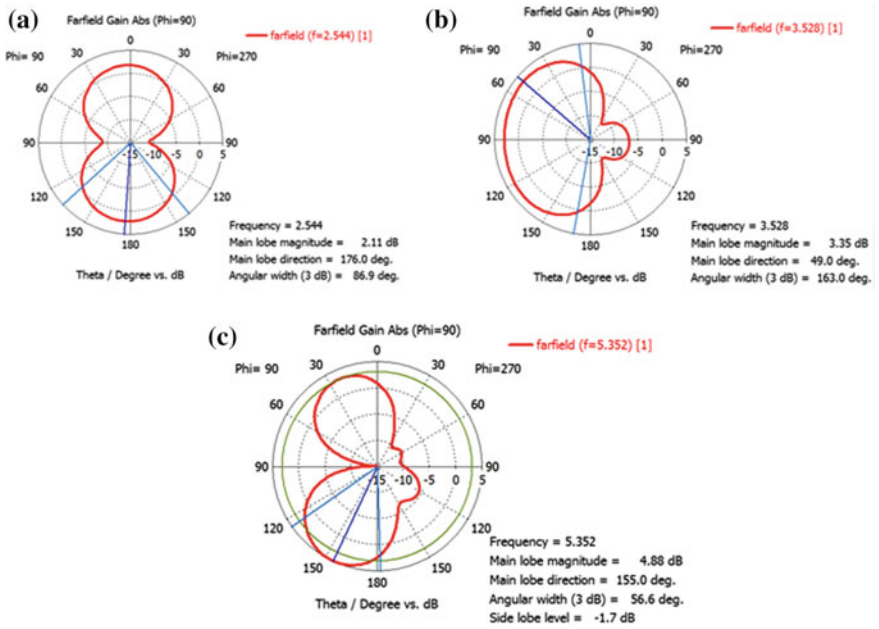

Fig. 4 Polar Radiation patterns of antenna at **a** 2.52 GHz **b** 3.5 GHz **c** 5.4 GHz

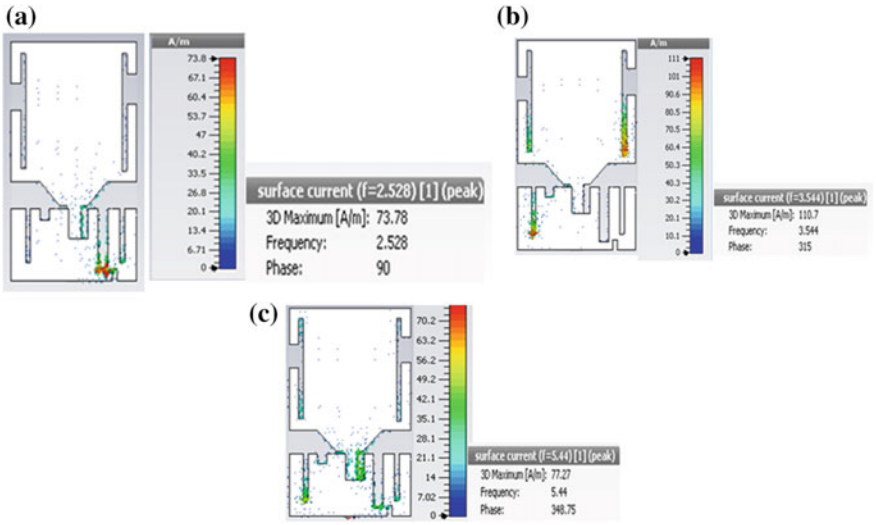

Fig. 5 Surface current distribution at **a** 2.52 GHz **b** 3.54 GHz **c** 5.44 GHz

4 Experimental Results

This proposed antenna is fabricated using PCB Prototype machine which results are tested by Vector Network Analyser (VNA). The VNA is calibrated by calibration trainer kit which minimizes the error due and connectors. The photo of fabricated multiband planar monopole is as shown in Fig. 6.

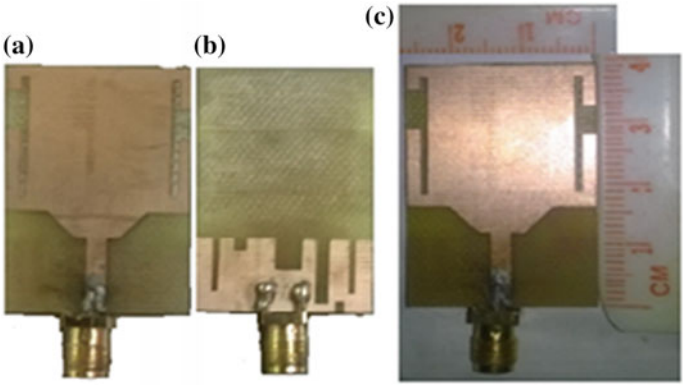

Fig. 6 Photos of the proposed planar antenna

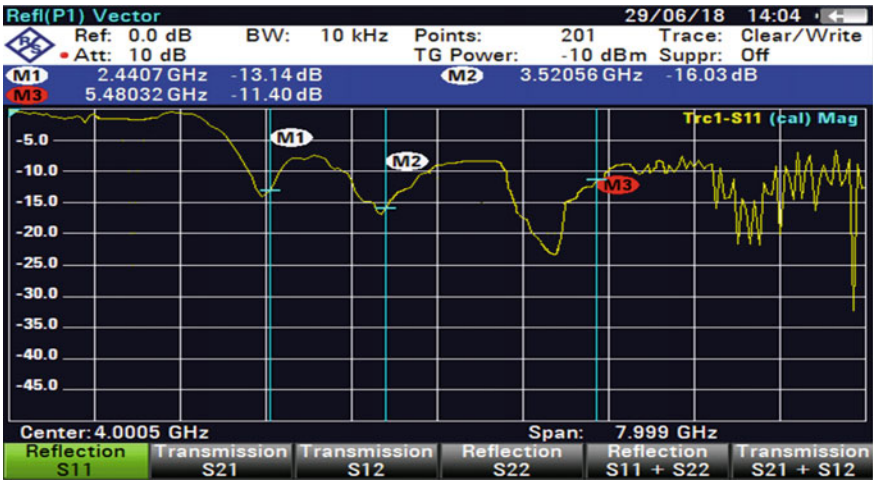

Fig. 7 Measured characteristics of S11

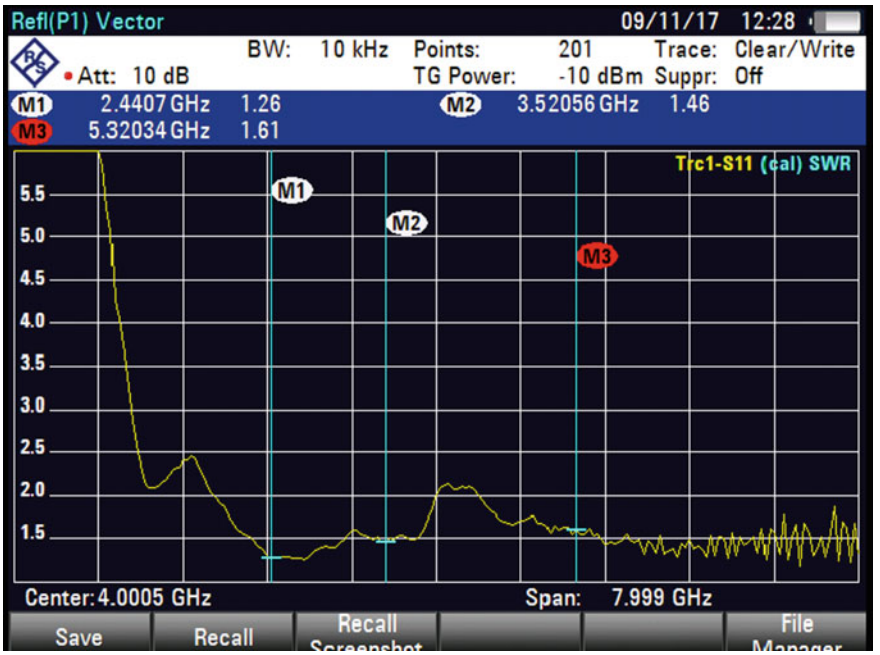

Fig. 8 Measured of VSWR

Figure 6a shows the fabricated front side of patch antenna with all necessary dimensions including SMA connector. Bottom side of patch antenna is shown in Fig. 6b with all corresponding simulation dimensions by SMA connector soldering. In Fig. 6c, the actual size of patch antenna is measured by using the centimetre scale. The SMA connector is connected with vector network analyser for measurement purpose (Fig. 7).

Above figure shows that proposed antenna is suitable for the multiband operation. The measured and simulated results of S11 quite match by comparing to each other. From the above analysis, it is clear that most of electromagnetic waves radiate to the outward direction. From the above observation, it is concluded that antenna delivers more than 90% power to the surrounding areas.

In Fig. 8, it is clear that VSWR lies between 1 and 2 for all corresponding resonance frequency. Measured and simulated VSWR are in proper range, i.e. 1 and 2 so very less amount of electromagnetic wave stands inside the antenna.

Figure 9 shows that measured impedance is nearly matched with reference impedance which is 50 Ω for resonating frequencies like 2.54 GHz, 3.53 GHz and 5.25 GHz (Table 2).

Fig. 9 Measured impedance of proposed antenna

Table 2 Measured S11 and VSWR

Frequency (GHz)	S11 (dB)	Bandwidth (GHz)	VSWR
2.5	−13.04	2.50-2.38 = 0.12	1.9
3.5	−16.02	3.76-3.35 = 0.41	1.52
5.35	−17.68	5.52-5.01 = 0.51	1.54

5 Conclusions

In this paper, design and analysis of asymmetrical C slots on patch and defected ground structure on the ground plane. The asymmetrical C-shaped slots are responsible for generating 3.5 GHz resonance frequency. The defected ground structure is responsible for producing 2.5 and 5.3 GHz resonance frequency. The surface current distribution plays an important role to which portions of antenna is suitable for obtaining the result. Defected ground structure play an important role to enhance the bandwidth to decrease quality factor due to adding different slots. Both fabricated and simulated results have quite same by measuring Vector Network Analyser. For different resonating frequencies (2.54, 3.53 and 5.25 GHz) the return loss is very low. The fabricated antenna can be used for various applications such as WLAN, Bluetooth, Zigbee, WiMAX, and HYPERLAN. It provides well for wireless applications to different frequency.

References

1. Wu L, Huang J, Yuan N (2016) Compact Multiband monopole antenna for GPS/WLAN/WiMAX application. IEEE ICMMT, vol 2, pp 618–620
2. Kumar L, Gautam AK (2015) Design of F-shaped slot triple band antenna for WLAN/WiMAX applications. IEEE Trans Wave Propag 64:1101–1105
3. Kalraiya S, Singh HS, Meshram MK, Thottapan M (2014) Microstripline-fed dual band printed monopole antenna for WLAN/WiMAX/HIPERLAN applications. IEEE, pp 224–227
4. Moosazadeh M, Kharkovsky S (2014) Compact and small planar monopole antenna with symmetrical L-and U-shaped slots for WLAN/WiMAX Applications. Antennas Wireless Propag Lett IEEE 13:388–391
5. Liou CW, Lu JH (2014) Planar F-shaped monopole antenna with dual-band circular polarization for WLAN systems. Electromagnetics. IEEE 149–150
6. Kachare R, Deosarkar S, Deshmukh V (2014) Compact dual band planar monopole antenna for WLAN/WiMAX. Commun Signal Process IEEE. 391–394
7. Reddy SV, Singh A, Akhtar MJ (2013) Design of a practical dual-band planar monopole antenna for WLAN and WiMAX applications. Communications IEEE 1–5
8. Jasim KA, Ali YM (2013) Compact dual-band monopole antenna for WLAN/WiMAX applications. IEEE 1–3
9. Yousuf S, Tlili B (2012) Multiband planar branched monopole antenna for GSM/GPS/WLAN/WiMAX application. In: IEEE antennas propagation society of international symposium, pp 1–2

10. Zhang QT, Jiao YC, Ding Y, Li B (2011) Design of a planar monopole multiband antenna with U- and L-shaped slots. In: IEEE microwave technology & computational electromagnetics, pp 331–334
11. Ding Y, Jiao YC, Zou R, Li B, Zhang QT (2011) Design of a narrow-size planar monopole multiband antenna with double L-shaped slots. In: IEEE cross strait quad-regional radio science and wireless technology conference, vol 1, pp 455–458

Performance of QPSK Modulation for FSO Under Different Atmospheric Turbulence

Dimpal Janu and Vijay Janyani

Abstract Free space optical (FSO) communication link provides high-speed data transmission rate within line of sight range for indoor as well as outdoor applications. FSO comes with high sensitivity for variation in weather condition as it reflects in the form of change of dielectric properties of medium. The uniqueness of the presented model in this paper is that it achieves 125 GBPS of data rate with QPSK modulation scheme and that too at 1550 nm of wavelength which is compatible with existing optical backbone network. In this paper, authors analyzed the performance of a FSO link with 0.6 km length and modulation scheme QPSK for different atmospheric conditions. Gamma–Gamma distribution model is employed to model the FSO channel link. Performance comparisons are recorded as bit error rate (BER) and signal to noise ratio (SNR) with help of simulation tool Optisystem13.

Keywords FSO · QPSK · Atmospheric turbulence · Gamma–Gamma distribution model

1 Introduction

Free space optical link that works in license-free frequency spectrum can set up a wireless communication link between two nodes from 100 m to few km apart within line of sight range. Light source works in either infrared or visible light range that can transmit data at very high speed more than 1.25 GBPS that is quite

D. Janu (✉) · V. Janyani
Department of Electronics & Communication, Malaviya National Institute of Technology Jaipur, Jaipur 302017, India
e-mail: dimple.dj.2211@gmail.com

© Springer Nature Singapore Pte Ltd. 2020

V. Janyani et al. (eds.), *Optical and Wireless Technologies*,
Lecture Notes in Electrical Engineering 546,
https://doi.org/10.1007/978-981-13-6159-3_54

sufficient for duplex transmission of data, voice and video signals. FSO link when implemented in indoor zone can set up a flexible network in desired building with very less installation cost and it also works as low power transmission scheme while in outdoor setup it can work as a bridge between two LAN networks situated in two different buildings. Compared with radio frequency (RF) link, FSO link provides a higher data transmission rate, larger optical bandwidth, higher security, and requires low transmission power. When information in optical domain is propagated through optical fiber, it allows transmission over long haul distances without getting distortion because of change in atmospheric condition and high security [1]. However, FSO can transmit data in free space without the use of waveguide structure, provides data rate comparable to optical fiber communication but at a fragment of deployment cost of fiber technology. FSO systems have attracted attention as an efficient solution for the "last mile" internet access problem [1, 2].

As users demand for high speed for different mobile and internet services like digital TV, video conferencing, high-speed gaming, etc., we require a communication link which can provide the data rate comparable to optical fiber. When light propagates through air, it can be scattered and absorbed depending on small and large eddies. FSO systems are greatly affected by fog and atmospheric turbulence. In FSO, laser light is carrier of data through atmosphere, so wavelength selection should be such that it coexists with the low absorption atmospheric window [3]. Mie scattering is caused due to fog, haze, and aerosol can cause optical attenuation especially in a terrestrial system. Scattering normally occurs when light beam comes into collision with particles smaller in size than the laser wavelength. These particles are the dominant source of irradiance attenuation degrades the performance of FSO link [2]. In a clear atmosphere, FSO systems face a challenge on link performance is the effect of turbulence-induced irradiance fluctuations [4, 5]. Influence of different weather conditions over a FSO link performance is analyzed in this paper. As low BER and high spectral efficiency are the major factor for selecting appropriate modulation scheme, we have selected the QPSK for our simulation work. This paper is arranged as follows: Sect. 2 describes system description. Numerical results and discussion are presented in Sect. 3. Concluding remarks will be addressed in Sect. 4.

2 System Description

2.1 Transmitter

2.1.1 QPSK Modulation

To compress as much data as possible into minimum spectrum is the main purpose of modulation. Bandwidth efficiency is defined as transmission of maximum data rate over an assigned bandwidth. The QPSK signal is generated by using external optical modulator that modulates the phase of optical carrier. To represent data bits, four

Table 1 Parameters of designed FSO system

Length of the channel	0.6 km
Diameter of transmitter aperture	9 cm
Diameter of receiver aperture	15 cm
Divergence angle	2 m rad
Laser wavelength	1550 nm
Laser power	−4–8 dBm
Bit rate	125 GBPS

Table 2 Total attenuation in different atmospheric conditions

Hazy days	16 dB/km
Rainy days (1) Light rain (2) Heavy rain	12.1 dB/km 12.6 dB/km

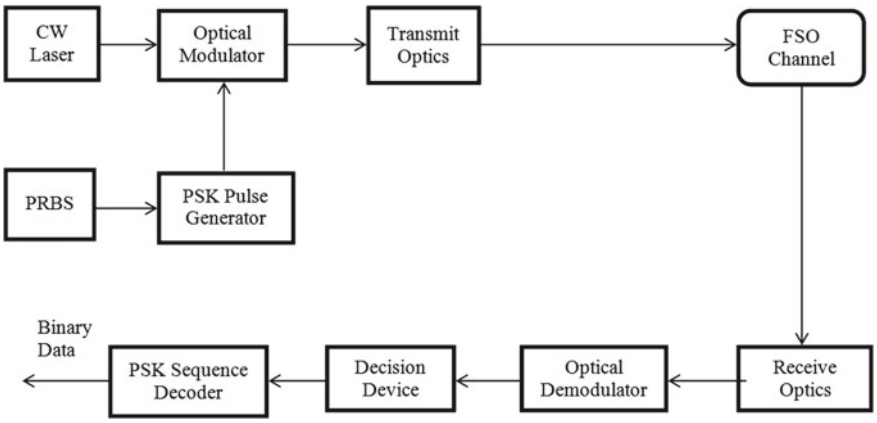

Fig. 1 Schematic diagram of designed FSO system

different points equally located around a circle on constellation diagram are used. Two bits are represented by a single symbol each having 90-degree phase shifts one another [6, 7]. Parameters of the designed FSO system are defined in Table 1. The attenuation parameter for the channel for different weather conditions such as rainy days (heavy rain and light rain) and hazy days is 12.6 dB/km, 12.1 dB/km, and 16 dB/km, respectively and Table 2 defines these values [8] (Fig. 1).

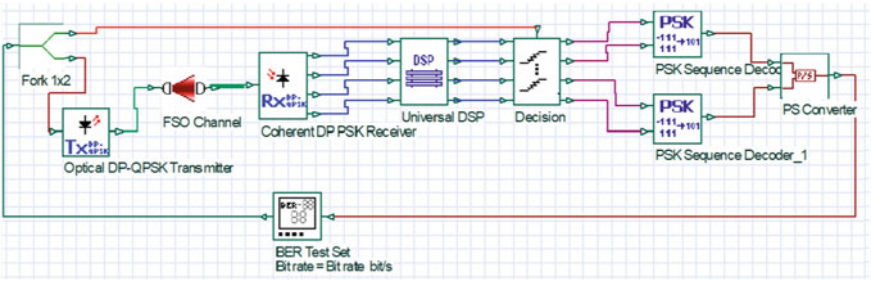

Fig. 2 Simulation layout of FSO system with QPSK modulation scheme

2.2 Atmospheric Turbulence

When light ray propagates in the free space, it experiences amplitude and phase variations due to disruption of atmosphere. Intensity fluctuations are caused because of inhomogeneities existing in the temperature and pressure variations, causes variations in refractive indices of the atmosphere will result into diffraction of light from its original path and diffraction of light causes variations in intensity level and phase of received signal [9]. Scintillation index parameter defines the power of turbulence in the atmosphere. Scintillation index is defined as ratio of the log intensity variance σ_I^2 to square of average signal intensity of light. S.I. will increase as the turbulence changes from weak to strong region [9, 10]. On the basis of values of scintillation index, turbulence is divided into three parts like weak, ordinary, and strong. The log-normal model is valid to describe behavior of weak turbulence. To study the performance of FSO channel, Gamma–Gamma distribution model is used in medium to strong turbulence conditions [3, 11] (Fig. 2).

2.2.1 Gamma–Gamma Model

The gamma–gamma turbulence model is employed to model the free space channel when the light beam is scattered and refracted from its original path traveling through atmosphere [10]. The optical intensity "I"consists of large-scale effects and small-scale effects. The PDF of irradiance fluctuation is given by the Eq. (1).

$$p(I) = \frac{2(\alpha\beta)^{(\alpha+\beta)/2}}{\Gamma(\alpha)\Gamma(\beta)} I^{(\frac{\alpha+\beta}{2})-1} K_{\alpha-\beta}(2\sqrt{\alpha\beta I}) \quad \mathrm{I} > 0 \tag{1}$$

where Bessel function of the second kind of order n is $K_n(.)$, and $\Gamma(n)$ represents gamma function.

The parameters α and β characterize the intensity variation pdf are associated to environmental conditions by [3]

$$\alpha = \left[\exp\left(\frac{0.49\sigma_l^2}{\left(1 + 1.11\sigma_l^{12/5}\right)^{7/6}} \right) - 1 \right]^{-1} \tag{2}$$

$$\beta = \left[\exp\left(\frac{0.51\sigma_l^2}{\left(1 + 0.69\sigma_l^{12/5}\right)^{5/6}} \right) - 1 \right]^{-1} \tag{3}$$

where $\sigma_l^2 = 1.23 C_n^2 k^{7/6} L^{11/6}$ is the log intensity variance, L is the length of link, $\mathrm{k} = 2\pi/\lambda$, and parameter C_n^2 is index of refraction considered as constant for LOS link. The value of $C_n^2 = 5.\,10^{-14}\mathrm{m}^{-2/3}$ for weak turbulence conditions, and $C_n^2 = 21.\,10^{-14}\mathrm{m}^{-2/3}$ for strong turbulence conditions are considered in this work, adopted from [3].

2.3 Receiver

Receiver optics is used to collect the beam of light traversed through the free space channel and focuses the light on photo-detector. The photo-detector detects strength of light irradiance then converts the optical signal to electrical signal.

3 Numerical Results and Discussions

The FSO system is analyzed with weak and strong turbulence conditions. We have considered channel parameter such as channel range, diameter of transmitter aperture, diameter of receiver aperture, and divergence angle of beam as designed values. Channel is analyzed for different weather conditions.

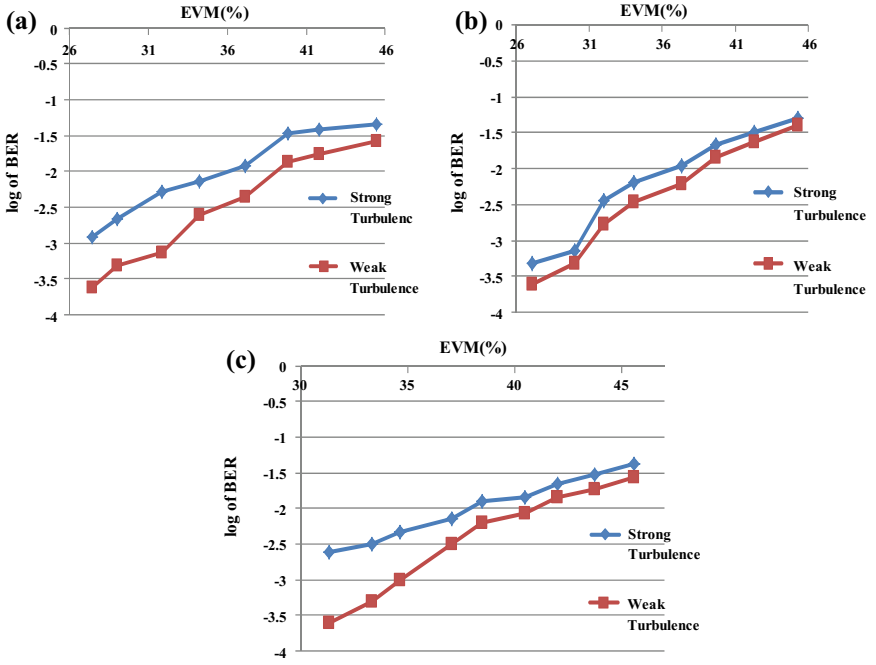

Fig. 3 Log of BER with EVM relation **a** BER performance in heavy rainy days, **b** BER performance in light rainy days and **c** BER performance in hazy days

During the rainy season, the channel parameters are designed with attenuation values of 12.1 dB/km for light rain and 12.6 dB/km for heavy rain. Response of the system is analyzed with the parameters BER, Error vector magnitude (EVM), and SNR. As the laser power is increased EVM and BER both get decreased. At EVM value of 27%, log of BER is −3.61 under weak turbulence, and −3.31 under strong turbulence conditions. In hazy days, channel parameters are designed with attenuation values of 18 dB/km and from Fig. 3c at the EVM value of 31% we achieve the log of BER −3.61 under weak turbulence and −3.31 under strong turbulence conditions.

The results show that as the input power increases BER decreases and EVM also decreases.

Figure 4 shows the graph for recorded log of BER and SNR levels at receiver side. As the level of atmospheric turbulence increases, we need high SNR to achieve the target value of minimum BER. Table 3 summarizes the EVM and log of BER for weak and strong atmospheric turbulence in different weather conditions.

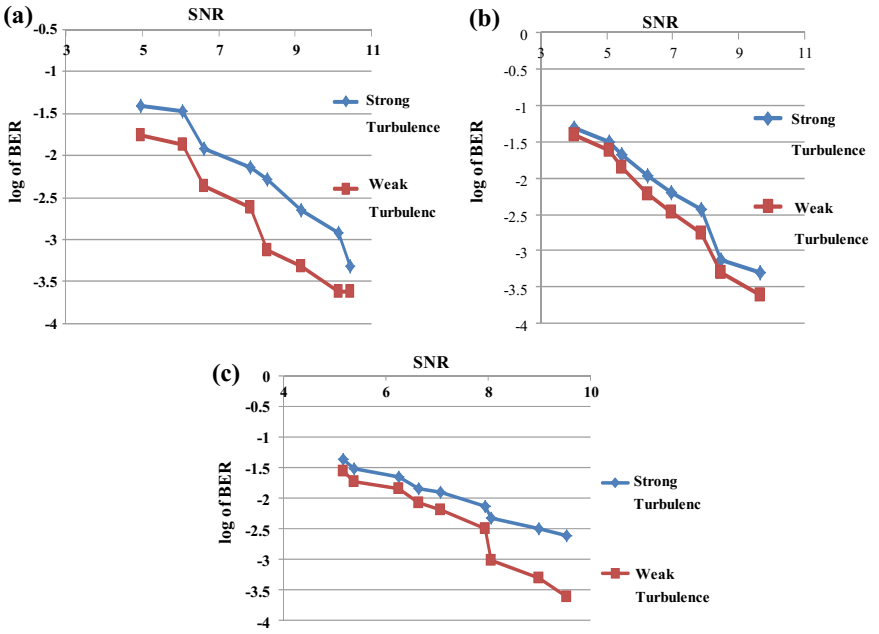

Fig. 4 Log of BER with SNR relation **a** BER performance in heavy rainy days, **b** BER performance in light rainy days and **c** BER performance in hazy days

Table 3 Simulation results for different weather conditions

Season	EVM (%)	Log of BER (weak turbulence)	Log of BER (strong turbulence)
Light rainy days	27	−3.61	−3.31
Heavy rainy days	28	−3.61	−2.82
Hazy days	31	−3.61	−2.61

4 Conclusion

Performance of QPSK modulated signal is recorded in different weather conditions like rainy days and hazy days. Simulation results also confirm the effects of atmospheric turbulence in a FSO link. Strong atmospheric turbulence degrades the BER performance up to 1 dB in hazy days. For desired value of log of BER −3.3, SNR required in weak turbulence condition on a heavy rainy day is 9 dB whereas for strong turbulence in same day required SNR has increased by 2 dB. Advanced modulation technique M-ary QAM can be explored to improve BER performance and spectral efficiency to provide better mode of transmission in weather conditions.

References

1. Pandimeenal KM, Sivanantha raja A, Selvendran S (2016) Study of the performance of free space optic communication with multiple phase encoded signal under different weather conditions. International Science Press
2. Ijaz M, Wu S, Fan Z, Popoola WO, Ghassemlooy Z (2009) Study of the atmospheric turbulence in free space optical communication, vol 22
3. Popoola WO, Ghassemlooy Z (2009) BPSK subcarrier intensity modulated free space optical communications in atmospheric turbulence. J Light Wave Technol 27(8)
4. Devi VSL, Sree SS, Rajani S, Seshasai VB (2013) Effects of weak atmospheric turbulence on FSO link systems and its reducing technique. IJART 2(11)
5. Barua B, Haque TT, Islam MR (2012) Error probability analysis of free-space optical links with different channel model under turbulent condition. IJCSIT 4(1)
6. Wang Z, Zhong WD, Fu S, Lin C (2009) Performance comparison of different modulation formats over free-space optical turbulence links with space diversity reception technique. IEEE Trans Photon 1(6):277–285
7. Shukla V, Shukla D, Shukla J, Nigam R (2015) Analysis of modulation technique in free space optics system. AIJRSTEM
8. Alkholidi AG, Altowij KS (2014) Contemporary issues in wireless communications. Intech Open, ch. 5, pp 159–211
9. Zhu X, Kahn JM (2002) Free-space optical communication through atmospheric turbulence channels. IEEE Trans Commun 50:1293–1300
10. Ghassemlooy Z, Popoola WO, Leitgeb E (2007) Free-space optical communication using subcarrier modulation in gamma-gamma atmospheric turbulence. ICTON '07, vol 3, pp 156–160, 1–5 July 2007
11. Kumar A, Dhiman A, Kumar D, Kumar Y (2013) Free space optical communication system under different weather conditions 3(12)

Multi-junction Solar Cell Based on Efficient III–V InGaP/GaAs with GaInAsP as BSF Layers

Priya Pandey, Abhinav Bhatnagar and Vijay Janyani

Abstract In a multi-junction solar cell, due to the existence of multiple junctions, generation of photo-generated minority charge carrier increases that improves the efficiency of the device with reference to reduction in recombination current. In this paper, authors have analyzed the performance improvement in a multi-junction solar cell with simulation results in R-soft. Simulation results show maximum efficiency 27.59% for multi-junction solar cell whereas for single junction solar cell it is 11.0259%. In the multi-junction solar cell, open circuit voltage V_{oc} and short circuit current I_{sc} are also compared to a single junction solar cell.

Keywords Multi-junction solar cell · Short circuit current density · Open circuit voltage · BSF layer · Quantum efficiency · Two diode equivalent circuit

1 Introduction

With the rising cost of fossil fuels and increasing concerns about climate change, a significant amount of effort is being made to use renewable energy sources for energy generation [1]. In today's world, solar energy is an alternative to fossil fuel. The expedition of solar cell begun from single junctions and then expand towards multi-crystalline, multi-junction solar cells and still move forward [2]. Above all these PV technologies, multi-junction solar cell technology has the highest efficiency. Multi-junction technology utilizes a broader spectrum of solar energy conversion and has shown immense efficiency improvement [3]. Majority of solar energy conversion is being done by using photovoltaic technology that is a solar cell which allows uninterrupted change of sunlight to electricity. In the solar cell, the performance analysis is done by efficiencies. Thus, to boost the efficiency, designing and optimization of solar cell coatings are important, and that's the reason here we use back surface layer, the buffer layer and many more layers in a multi-junction solar cell thus to boost the

P. Pandey (✉) · A. Bhatnagar · V. Janyani
Department of ECE, Malaviya National Institute of Technology Jaipur, Jaipur 302017, India
e-mail: priyapandey2694@gmail.com

© Springer Nature Singapore Pte Ltd. 2020

V. Janyani et al. (eds.), *Optical and Wireless Technologies*,
Lecture Notes in Electrical Engineering 546,
https://doi.org/10.1007/978-981-13-6159-3_55

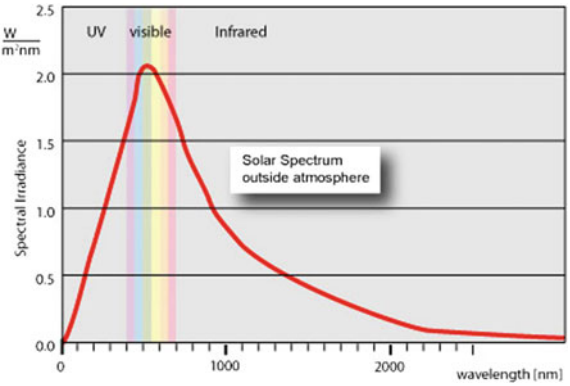

Fig. 1 Spectral irradiance w.r.t. wavelength shows maximum irradiance in the visible region and their surrounding regions [4]

efficiency [5]. To comprehend the working of the solar cell, it is necessary to understand the cosmic resources. Two important parameters are irradiance (i.e. amount of incident power) and spectral characteristics of sunlight. Solar irradiance value in the outer space of the earth's atmosphere is 1365 W/m^2 known as solar constant. This value reduces to 1000 W/m^2 after being filtered through the atmosphere. Air mass (AM) is a relation between solar irradiance and solar spectrum, where AM is the amount of air, a beam of sunlight must pass through atmosphere before reaching the PV devices. AM can be calculated by using this equation:

$$\mathrm{AM} = \frac{1}{cos\theta} \tag{1}$$

where ϴ is angle which sun makes with normal to the earth.

Solar spectrum determines the number of photons which can contribute to photocurrent in a solar cell. By using the following relationship, wavelength dependent range can be converted into photon energy.

$$\mathrm{Eg} = \mathrm{hc}/\boldsymbol{\lambda} = 1.24/(\boldsymbol{\lambda}(\mathrm{nm}))\mathrm{eV} \tag{2}$$

where Eg is photon energy in eV, is wavelength of incident light in nm

h is Planck's constant = 6.626 × 10^{-34} J and c is speed of light = 3 × 10^{8}m/s^2 (Fig. 1).

2 Working of Solar Cell

In a solar cell p-n junction made up of semiconductor materials of particular bandgaps. Generation and recombination are the two main mechanics of solar cell's operation.

Generation refers to the generation of photocurrent in the solar cell which consists of the following two main processes:

(a) Absorption of photons and
(b) Collection of charge carriers.

Photon energy above the bandgap get absorbed and cause the generation of an electron–hole pair, which is separated by the electric field across the PN junction. Due to this charge carrier separation, photocurrent flows. If electron–hole pair generated close to the surface, recombines quickly and does not devote towards the photocurrent.

In a solar cell, recombination at the back end decreases the efficiency, and hence to reduce this recombination, an extremely doped layer at the back surface is applied, which repels the minority charge carriers and attracts the majority charge carriers. This layer is none other than BSF layer which not only reduces charge carriers from recombination but also enhances the efficiency of solar cell. So, the existence of BSF layer is one of the important layers to enhance the performance of the solar cell [6]. In this, we have calculated the V_{oc} and Jsc aspects of the photovoltaic cell and the change of the effectiveness of the multi-junction solar cell and single junction solar cell.

3 Materials Used in Solar Cell

The different semiconductor materials which we are using in a multi-junction solar cell because of their optical properties are GaInP, InGaAsP, GaAs and many optically sound semiconductor material which gives better efficiency in the multi-junction solar cell than in a single junction solar cell.

3.1 GaInP (Gallium Indium Phosphide)

GaInP is used in the multi-junction solar cell as one of the material because of its high electron mobility (μ_n) 3500 cm^2/Vs it increases collection probability at the depletion and hence gives high efficiency. GaInP is lattice matched to GaAs. Therefore, it is used as high energy junction on the multi-junction solar cell.

3.2 InGaAsP (Aluminium Gallium Arsenide Phosphide)

InGaAsP is a semiconductor material having a nearly same lattice constant as of GaAs and its bandgap is large which absorb lower wavelength solar radiations. In GaAs multi-junction solar cell, InGaAsP acts as barrier material because it confines

electrons to a GaAs region. The most commonly used region is from red to near-infrared region. The bandgap of InGaAsP is 1.08 eV at room temperature.

3.3 GaAs (Gallium Arsenide)

It is a direct bandgap semiconductor material having wider energy bandgap, and due to its high saturated electron mobility of 8500 cm^2/Vs it gives higher efficiency as compared to silicon. GaAs's stiffness and robustness make it an excellent selection where dirt or coarse-grained particles tend to accumulate or attack the optical surface.

4 Solar Cell Modelling

4.1 Device Structure

The device structure consists of the top cell, tunnel junction and bottom cell [6]. Window layer and back surface layer are present on the top and bottom cell at their top and bottom resp. The window layer is a fragile and transparent layer with high bandgap material which is made from several metal oxides [7]. The characteristics of window layer are to absorb maximum solar emission to enter into the device.

Multi-junction solar cell consists of three junctions of emitter-base and also comprises different layers, e.g. window layer, a tunnel junction, back surface field, front surface field, buffer layer, etc. which is simulated through RSoft tool. In multi-junction solar cell due to the presence of different semiconductor materials, they are arranged in such a manner, so that most significant band gap material come closest to the incident light and then next most considerable bandgap material comes and then smallest bandgap material [8]. By doing so, the solar cell arrangement allows larger bandgap materials to pass lower energy photons and soaked up by the last material. In the multi-junction solar cell, distant bandgap semiconductor materials are present which enables them to incorporate various parts of the solar spectrum, smaller bandgap materials absorb lower energy photon, and larger bandgap materials absorb higher energy photon of the solar spectrum. Due to this thermalization losses decreases in the multi-junction solar cell in contrast to single junction solar cell [9]. In multi-junction, solar cell tunnel junction is also present which is highly doped and of wide bandgap by which it is transparent to wavelengths absorbed by later photovoltaic cell and is even having low electrical resistance and provides low loss optical connections within the cells, due to which efficiency of solar cell increases.

4.2 Different Layers Present in Solar Cell

There are few more layers which are a buffer layer, BSF layer and much more which we discussed here one by one.

BSF Layer

In the multi-junction solar cell, BSF layer is an intermediate dielectric layer which not only enhances back reflection but also contributes to further irregularity of light and hence increases light trapping inside the solar cell [10]. BSF layer also prohibits the charge carriers to recombine by driven them off back to PN junction (Fig. 2).

4.3 Importance of GaAs as Tunnel Junction

Tunnel junction should be optically transparent, highly doped, minimum electrical resistance with high peak current density and they also provide alignment of Fermi levels. That is why GaAs is used as tunnel junction because it has minimum optical absorption and minimum series resistance which reduces the length of the depletion region so that electrons can easily tunnel through it.

0.03µm	Window	GaInAsP	p = 2e+018
0.05µm	Emitter	InGaP	p = 2e+018
0.55µm	Base	InGaP	n = 7e+016
0.030µm	BSF	GaInAsP	n = 2e+017
0.030µm	BSF	GaInAsP	n = 2e+018
0.025µm	Tunnel J	GaAs	n = 5e+019
0.025µm	Tunnel J	GaAs	n = 3e+019
0.040µm	Window	InGaP	p = 3e+018
0.5µm	Emitter	GaAs	p = 2e+018
2µm	Base	GaAs	n = 2e+017
0.5µm	BSF	GaInAsP	n = 5e+018
0.2µm	Substrate	GaAs	n = 1e+018

Fig. 2 Multi-junction solar cell with GaAs as tunnel junction and GaInAsP as BSF and Window layer

4.4 Importance of GaInAsP as BSF and Window Layer

GaInAsP is a wideband gap material, which is excellently preferred for both window layer and BSF layer for efficiency enhancement of solar cell. Window layer and buffer layer with heavily doped region cause potential barrier between the base region to enclose the minority carriers in the lightly doped region. BSF layer having limited recombination velocity [11].

4.5 Electrical Modelling of Multi-Junction Solar Cell

Modeling is the initial step and followed by simulation, evaluation and analysis of photovoltaic cell operation. A schematic diagram represents the photovoltaic cell performance in various environmental conditions and the variations in its output electrical characteristics are observed over several design specifications (Figs. 3 and 4).

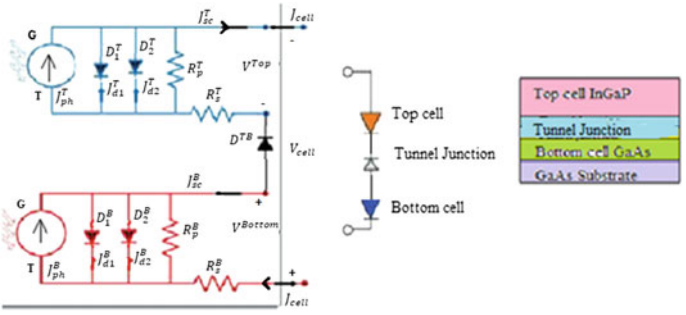

Fig. 3 Proposed equivalent circuit for multi-junction solar cell modeling [12]

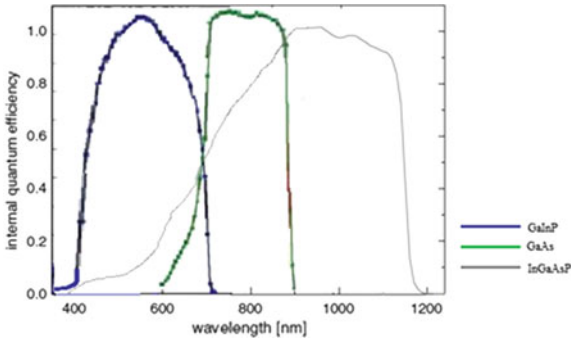

Fig. 4 Internal quantum efficiency of multi-junction solar cell

$$J_{cell} = J_{ph} - J_{d1} - J_{d2} - \frac{V_{cell} + R_s J_{cell}}{R_p} \tag{3}$$

$$J_{ph}(T, G) = \frac{G}{G_0} J_{ph}\, T_0 G_0 (1 + C^{T}_{J_{ph}}(T - T_0)) \tag{4}$$

$$J_{d1} = J_{sat_1}(T)(\exp \frac{q(V_{cell} + R_s J_{cell})}{?_1 kT} - 1) \tag{5}$$

$$J_{sat_1}(T) = J_{sat_1}(T_0)\left(\frac{T}{T_0}\right)^{\frac{3}{n_1}} \exp?(\frac{q}{n_1 k}\frac{E_g(T_0)}{T_0} - \frac{E_g T}{T}) \tag{6}$$

$$E_g T = E_g(T_0) - \frac{\alpha T^2}{T + \beta} \tag{7}$$

$$J_{cell} = J^{B}_{SC} = J^{T}_{SC} \tag{8}$$

$$V_{cell} = V^{T}_{SC} - V^{TB}_{D} + V^{B}_{SC} \tag{9}$$

$$E^{GaInP}_{g} = \frac{1}{2} E^{GaP}_{g} + E^{InP}_{g} + C_g \tag{10}$$

$$V_{cell} = V^{T}_{sc} - V^{TB}_{D} + V^{B}_{sc}$$

where

J_{cell}	cell current density
V_{cell}	cell voltage
J_{d_l}	dark current density due to diffusion of minority carriers and recombination in depletion region
$R_s\, R_p$	cell's series and shunt resistance
J_{sat_l}	reverse saturation current density
n	diode ideality factor
T	cell surface temperature
G	received solar irradiance energy

To calculate the energy band gap for GaInP it is possible to use Eq. 10 with the approximation x = 0.5, where C_g is the correction term that can vary proportional to the parameter x. Each subcell absorbs a definite part of overall range of solar irradiance spectrum according to its energy band gap and internal quantum efficiency.

5 Parameters

There are few parameters of solar cell which we considered here as short circuit current, quantum efficiency, V_{oc}, fill factor, and efficiency.

5.1 Quantum Efficiency (QE)

Quantum efficiency of a photovoltaic cell is the probability of collection of the charge carrier when a photon of a given energy is incident on it. If all minority charge carriers generated by photons of specific energy are collected, then the quantum efficiency at that is 1, and it is reduced due to the presence of recombination losses which reduces the collection probability and if photons with energy below bandgap than also quantum efficiency decreases to 0. When reflection and transmission losses are taken into account, then this is called external quantum efficiency, and when these losses are not considered, then this is known as internal quantum efficiency, which is superior to the external quantum efficiency of the photovoltaic cell. The relation between internal quantum efficiency and external quantum efficiency is written below:

$$\mathrm{IQE} = \frac{EQE}{1 - R - T} \tag{13}$$

where IQE is internal quantum efficiency, EQE is external quantum efficiency

R is reflection losses and T is transmission losses.

5.2 Short Circuit Current (I_{sc})

When the ends of the photovoltaic cell are shorted in the presence of solar energy, then due to the generation and accumulation of light generated carriers it causes photocurrent which is known as short circuit current.

Short circuit current can be calculated as

$$I_{sc} = \mathrm{qG}(L_n + L_p)\mathrm{A} \tag{14}$$

where G is generation rate, L_n is electron diffusion length and L_p is hole diffusion length,

or it can also be calculated by

$$J_{sc} = \mathrm{q} \int \phi(\lambda).\mathrm{EQE}(\boldsymbol{\lambda})\mathrm{d}\boldsymbol{\lambda} \tag{15}$$

where q is electronic charge, ϕ() is incident photon flux, is wavelength (nm).

5.3 Open Circuit Voltage (V_{oc})

It is the maximum voltage accessible from a photovoltaic cell when current is zero. Open circuit voltage is the amount of forward bias on the photovoltaic cell due to the bias of solar cell junction with light generated current. V_{oc} can be calculated by

$$V_{oc} = \frac{\eta K T}{q} \ln\left(\frac{I_l}{I_0} + 1\right) \tag{16}$$

where

I_l is light-generated current
I_0 is dark saturation current
T is temperature
V_{oc} is open circuit voltage.

5.4 Fill Factor (FF)

Fill factor defines the quality of the photovoltaic cell. It is a ratio of the highest power to the hypothetical (theoretical) power P_T that would be output at the open circuit voltage and short circuit current. Large fill factor is chosen, and its value lies between 0.5 and 0.82.

$$\text{FF} = \frac{P_{max}}{P_T} = \frac{I_{mp} V_{mp}}{I_{sc} V_{oc}} \tag{17}$$

From the graph also we can compute the fill factor of photovoltaic cell (Fig. 5).

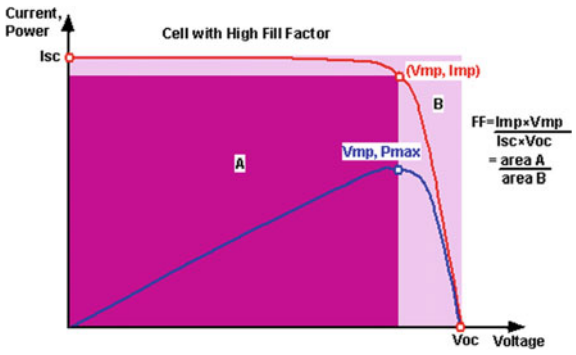

Fig. 5 Fill factor of solar cell [13]

5.5 *Efficiency*

It is a ratio of electrical output power to the input photovoltaic power Pin of the photovoltaic cell.

$$\eta = \frac{P_{out}}{P_{in}} \tag{18}$$

$$\eta_{max} = \frac{P_{max}}{P_{in}} \tag{19}$$

6 Simulation and Results

Here, we simulate multi-junction solar cell having multiple lattice-matched emitter-base junction and single junction solar cell to compare their efficiencies by using computational software R-Soft. In the multi-junction solar cell, outer material has the largest band gap and as we go inside band gap decreases which decreases the thermalization losses, reflection losses, and many other losses. In the multi-junction solar cell, multiple junctions are present to absorb the solar spectrum while in single junction solar cell only single junction is present for absorption hence it affects the efficiency of the solar cell [12]. Here some graphs are shown which shows the efficiency of the multi-junction solar cell and single junction solar cell (Figs. 6, 7 and 8).

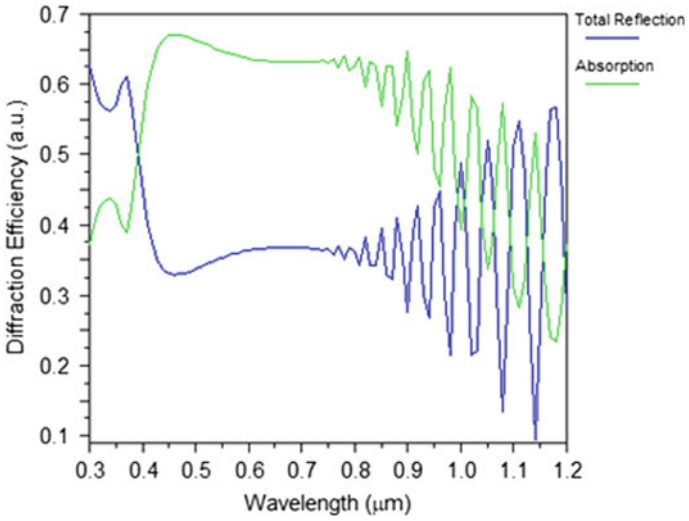

Fig. 6 Reflection and transmission efficiency of the single junction solar cell

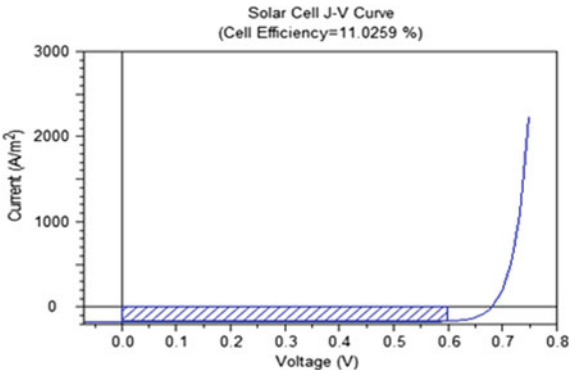

Fig. 7 Efficiency of single junction solar cell

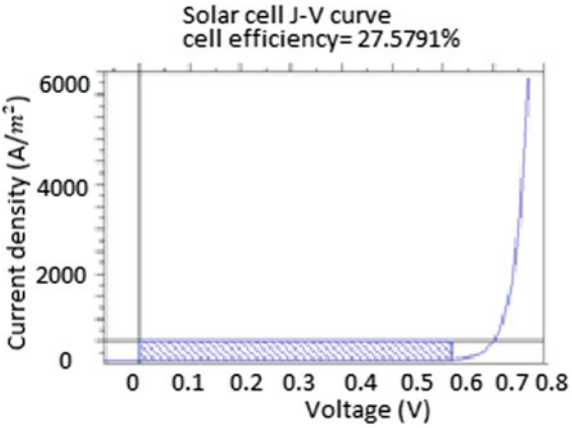

Fig. 8 Solar cell efficiency of the multi-junction solar cell

As it is clear from the graph that the single junction solar cell gives efficiency of 11.0259% and short circuit current density of 173.238 A/m^2. From the above graph, we can say that efficiency of the multi-junction solar cell is more than that of a single junction solar cell which is 27.59% and gives short circuit current density of 419.282 A/m^2.

7 Conclusion

Different optical properties of a multi-junction photovoltaic cell are analyzed. Performance of multi-junction photovoltaic cell is better as compared to single junction photovoltaic cell because of the presence of window layer, a tunnel junction, BSF layer and buffer layer. All these coatings reduce recombination losses and increase

the collection efficiency of photo-generated minority charge carriers. In single junction photovoltaic cell short circuit current is 173.238 A/m^2, and open circuit voltage is 0.68 V while in multi-junction photovoltaic cell short circuit current is 419.282 A/m^2, and open circuit voltage is 0.7 V. The overall efficiency recorded in simulation results for a single junction photovoltaic cell is 11.03% while for multi-junction photovoltaic cell it is 27.59%. Implementing different junction structures with nanowires or quantum dots we can further improve the efficiency in a multi-junction device.

References

1. Nayak PP, Dutta JP, Mishra GP (2015) Efficient InGaP/GaAs DJ solar cell with double back surface field layer. Eng Sci Technol Int J
2. DeMoulin PD, Lundstrom MS, Schwartz RJ (1987) Back-surface field design for n/p GaAs cells solar cells. Sci Technol Appl Econ 20:229
3. Green MA, Emery K, Hishikawa Y, Warta W, Dunlop ED (2012) Solar cell efficiency tables. Prog Photovolt Res Appl 20(12)
4. Standard solar spectra, ASTM G-173-03 (International standard ISO 9845-1, 1992) https://www.pveducation.org/pvcdrom/appendices/standard-solar-spectra
5. Chang ST, Liao MH, Lin WK (2011) Si/SiGe hetero-junction solar cell with optimization design and theoretical analysis. Thin Solid Films 519:5022
6. DeMoulin PD, Lundstrom MS, Schwartz RJ (1987) Back-surface field design for n/p GaAs cells solar cells. Sci Technol Appl Econ 20:229
7. Liao MH, Chen CH (2010) The investigation of optimal Si-SiGe heterostructure thin-film solar cell with theoretical calculation and quantitative analysis
8. Kurtz SR, Faine P, Olson JM (1990) Modeling of two junction, series connected tandem solar cells using top cell thickness as an adjustable parameter. J Appl Phys 68:1890
9. Biron R, Pahud C, Haug FJ, Escarre J, Soderstrom K, Ballif C (2011) Window layer with p doped silicon oxide for high V_{oc} thin-film silicon n-i-p solar cells. J Appl Phys 110:124511
10. Liao MH, Chen TC, Chen MJ, Liu CW (2005) Electroluminescence from metal/oxide/strained-Si tunneling diodes. Appl Phys Lett 86:223502
11. Trupke T, Green MA, Wuerfel P (2002) Improving solar cells by the upconversion of sub-band-gap light. J Appl Phys 92:4117
12. Brown MR, Goldhammer LJ, Goodelle, GS, Lortz CU, Perron JN, Powe JS, Schwartz JA, Cavicchi BT, Gillanders MS, Krut DD (1997) Proceedings of the 26th IEEE photovoltaic specialists conference. IEEE, New York, pp 805
13. Singh KJ, Sarkar SK (2012) Highly efficient ARC less InGaP/GaAs DJ solar cell numerical modelling using optimized InAlGaP BSF layers. Opt Quant Electron 43(1)
14. Baur C, Bett W (2005) Modeling of III–V multi-junction cells based on spectrometric characterisation. In: 20th European photovoltaic solar energy conference, Barcelona, 6–10 June 2005

A Brief Review on Microwave Breast Imaging Technique

Kajal and Monika Mathur

Abstract This paper is a brief review of the microwave breast imaging technique. This technique is basically used for the detection of breast cancer. There are many techniques which are available in the medical field for scanning purpose, but this technique is more suitable. Implantable antenna may be designed for this purpose so that wireless diagnosis at every time may be possible. This paper provides the familiarization of the microwave imaging techniques available in the market.

Keywords Microwave imaging · Breast cancer · Implantable antenna

1 Introduction

Nowadays, breast cancer is a serious disease found in women. According to ACS (American Cancer Society), this year's data shows that 255,180 women are affected by this compared to other types of cancer. Also out of this calculation, 41,070 end in death. It is noticed that for women, death by the breast cancer, is the second largest cause. Unlike lung cancer, the actual causes of breast cancer cannot be defined in the same way.

There are several methods of screening like mammography, ultrasound, MRI, CT scan, etc. In all of these techniques, X-ray mammography is the main successful process for identifying breast cancer. In this method, imaging processing for the breast part has been done. It is a technique that detects the tumor by finding the densities difference in tissues. It is the 2D image of the breast density. There are some drawbacks of this method [1] which are as follows:

Kajal (✉)
Department of Electronics and Communication, Swami Keshvanand Institute of Technology, Management and Gramothan, Jaipur, Rajasthan, India
e-mail: kajalsaini2000@gmail.com

M. Mathur
Swami Keshvanand Institute of Technology, Management and Gramothan, Jaipur, Rajasthan, India
e-mail: monikamathur16@gmail.com

© Springer Nature Singapore Pte Ltd. 2020

V. Janyani et al. (eds.), *Optical and Wireless Technologies*,
Lecture Notes in Electrical Engineering 546,
https://doi.org/10.1007/978-981-13-6159-3_56

- At the early stage of breast tumors, detection is complicated.
- In the case of women with impenetrable breasts, it has decreased efficiency.
- The ionizing X-rays may be harmful to the tissue where they penetrate.
- The patients are not restful because of breast compression, and also due to the costly treatment.

Ultrasound uses acoustical impedance differences to create images. Injury to the tissue has been successfully determined by ultrasound. Ultrasound finds that a lesion is in or below the skin. One more application of ultrasound is guided aspiration and biopsy; nowadays, this ultrasound is not preferred as screening technology. Magnetic resonance imaging technique is another technique used for breast imaging but it requires two distinct media which are taken up by good and malignant lacerations. The limitations of medical imaging techniques have provided the significance of the advancement for novel methods of imaging for diagnostic of cancer in breast.

Microwave breast imaging techniques are developed for safe and more accurate results. Microwave imaging is used for biomedical application. It is advantageous over mammography due to its good penetration property, noninvasive nature and potential to detect the tumor in earlier stage. The key features of the diagnosis of the breast cancer based on the microwave would be: (i) safe from health, (ii) any crucial stage capability to detect breast cancer, (iii) susceptible to the tumors and the other malignancies, and (iv) comfortable for the patients in terms of minimal lesion tolerability [2].

2 Electrical Properties of the Breast Tissues

There is some difference in electrical properties of healthy breast tissues and breast tumors. The permittivity (ε) and conductivity (σ) are the important electrical and dielectric properties of the tissues. The water is the main parameter to define the tissue permittivity. The tissues containing low water have high permittivity compared to the tissues containing high water. The higher water content tissues like muscles experiences greater attenuations as the power absorbed by them is more as compared to the lost in muscles. The main points are: (i) power absorption by the tissues is limited (ii) lower conductive healthy tissues permit more incursions of microwaves [3, 4].

The breast tissues measurements aim is to create a complete record of electric properties of specific healthy and unhealthy tissues over a wide range of frequency. The breast consists of skin, main tissues, connective tissues, blood, and nipple. It is mandatory to evaluate the properties of each type of tissues, as well as properties of particular types of good and malicious tumor [3].

Another parameter to consider while discussing the electromagnetic properties of tumor tissues is temperature. The electrical properties of tissues change according to the change in temperature. In the microwave region, the object temperature is

in direct proportion with the thermal radiation. It is expected that due to increased vascularization, tumors have more temperature compared to normal tissues [3].

3 Microwave Breast Imaging Technique

Microwave breast imaging purely depends upon the electrical property of breast tissues. The electrical property is found out by comparing the healthy tissue and malignancies. The microwave imaging process for tumor detection uses the range of microwave frequency from 300 MHz to 300 GHz (in wavelength free space ranging from 1 m to 1 mm) [4]. It shows different dielectric constant of glandular and malignant breast tissues. The electromagnetic signals are more efficient to couple with the GHz signal frequencies and this is considerable because of the significant absorption and scattering that occur during the EM exposures to the breast. The purpose of this is to make a high benefit of maximum penetration of microwave imaging with minimum side effects to healthy tissues. There are basically three methods to microwave breast imaging, they are: active imaging technique, passive imaging technique and hybrid technique [3–5].

3.1 Active Microwave Imaging

Active microwave imaging technique involves illumination of the breast with the help of the microwaves. It includes the detection of the reflected wave from the breast and then the formation of images [4]. This method is further classified into two classes: radar-based and tomography.

3.1.1 Microwave Tomography

This technique makes use of algorithms in order to provide complete spatial mapping of electrical properties. Most of the algorithms do the comparisons of scattered microwave signals sent to the breast and results computed with a model. In this approach, numbers of antennas are surrounding the region and one antenna is used as transmitter and another one is used as receiver. Scattered signal will alter as the tumor is present which results in the increased areas of conductivity and permittivity on images.

Microwave tomography has been studied by Prof. Paulsen and Prof. Meaney from Darthmouth College in US is one of the representatives of the research groups. They proposed that the dielectric properties in a lossy 2D medium may be measured by a reconstruction. To obtain a clinical prototype exam, the Darthmouth group has developed a 32 channel data acquisition system. Its operating frequency range is

500 MHz to 3GHz. For monitoring the treatment during the neoadjuvant chemotherapy, they develop a 3D microwave breast imaging technique [6].

3.1.2 Radar-Based Approach

This approach was developed in the late 1990s by Hagness in Wisconsin University and Benjamin in Bristol University. This approach reconstructed the image with the reflected wave [6]. In this approach, the creation of mapping is not necessary. In the radar-based approaches, the concept is the same as the ground penetrations radar system for detection. Whenever transmission of wave is done with internal breast with tumor due to the difference between electric dielectric properties of normal and malignant breast tissues, the wave is reflected back. Radar-based techniques use UWB signals. This technique implying a wider bandwidth, with appropriate signal penetration. This is due to increase in tissues conductivity. This technique is efficient as it makes use of single antenna as transreceiver unlike tomography and it transmits ultra-wideband pulse which is propagated and reflected back at electrical discontinuities and received at the same antenna. This method is also known as confocal microwave imaging (CMI) [4, 5].

3.2 Passive Microwave Imaging

In this approach, the change in temperature of breast tissues is measured. This temperature change is due to the increase in vascularization. To improve the imaging algorithms, there are many techniques that increase the physical temperature up to the measured temperature on the object surface [3, 4]. These techniques are called passive microwave imaging.

3.3 Hybrid Microwave Imaging

This approach combines the benefits of both the ultrasound and microwave imaging. The breasts are illuminated by microwaves and for providing sensitivity to tumors and high-resolution images and ultrasound transducers are being used. In this approach, the tissues are expanded due to microwave heating. It creates pressure waves and these are sensed with ultrasound transducers. For the detection purpose, two approaches are basically used named as TAT and TACT [3].

3.3.1 TACT (Thermo Acoustic-Computed Tomography)

In this system, the breast was positioned in the system having a water bath. A pulse of 5 μs and 434 MHz signals was illuminated to the breast. This signal is provided by the helical antenna or waveguide. 64 numbers of ultrasound transducers were placed on a hemisphere recorded signals. This set up is moved in 360° rotation for adequate data. From this arrangement, images may be captured and may be used for the further clinical purpose [3].

3.3.2 TAT (Thermo Acoustic Tomography)

It is another scanning technique in which the signals were detected using focused ultrasound transducers. Lateral resolution is adjusted by the pulse width of the microwave signal and axial resolution is provided by bandwidth of the microwave signal. The resulting data in time domain were stacked together to form the image. To improve the resolution of the image, reshaping and smoothing filters were applied to data. The major works are devoted now on the development of the equations relating the time derivative of the pressure to the distribution of heat absorption. The algorithms of imaging are developing for reducing the pulse width of microwave signal and the size of the detector [3].

4 Conclusion

This paper concludes that microwave breast imaging technique is the complementary imaging technique which has several additional advantages. The methods or techniques are more comfortable, accurate, and safe for patients as compared to other scanning techniques. As microwave imaging does not involve the ionizing radiation due to this reason it is safer than other methods. Microwave imaging technique uses low power and has negligible tissue heating in imaging as well as energy absorption.

Acknowledgements The authors are thankful to Swami Keshvanand Institute of Technology, Management and Gramothan for providing us the support of material for reviewing the literature.

References

1. Katbay Z, Sawsan S, Lababidi R, Perennec A, Roy ML (2015) Miniature antenna for breast tumor detection. In: Proceeding of 13th international new circuits and systems conference (NEWCAS), MINATEC, Grenoble, France
2. Singh PK, Tripathi SK, Sharma R, Kumar A (2013) Design and simulation of microstrip antenna for cancer diagnosis. Int J Sci Eng Res 4(11):1821–1824. ISSN 2229-5518
3. Fear Elise C (2005) Microwave imaging of the breast. Technol Cancer Res Treat 4(1):69–80

4. Bohra Sakshi, Shaikh Tazeen (2016) UWB microstrip patch antenna for brest cancer detection. Int J Adv Res Electron Commun Eng 5(1):88–91
5. Fear EC, Stuchly MA (2000) Microwave detection of breast cancer. IEEE Trans Microw Theor Tech 48(11):1854–1863
6. Sollip K, Seungjun L (2016) Recent advances in microwave imaging for breast cancer detection. Int J Biomed Imag 1–25, Hindawi Publishing Corporation, Article id -5054912. https://doi.org/10.1155/2016/5054912

Design of Planar Triple-Band Electrically Small Asymmetrical Antenna for ISM, WLAN, and X-Band Applications

Payal Bhardwaj and Ritesh Kumar Badhai

Abstract In this paper, we proposed a novel printed monopole antenna with the asymmetric meandered structure on the two sides of coplanar waveguide (CPW) feed line. The proposed antenna has the compact size of 0.095 λ × 0.095 λ × 0.005 λ, where λ corresponds to the wavelength in free space at the lowest operating frequency. The proposed antenna exhibits three resonances around 2.38, 5.52, and 7.72 GHz. The proposed antenna shows the good impedance matching, wide bandwidth, good radiation efficiencies, and radiation pattern at the resonating bands. The proposed antenna is fabricated on FR-4 substrate and found the good agreement between simulated and experimental results. The proposed triple-band antenna with a relatively low profile and compact size is useful for various biomedical applications covering the ISM (Industrial, Scientific, and Medical) band ranging from 2.4 to 2.48 GHz and 5.15 to 5.82 GHz, WLAN, Wi-Fi, and Wi-Max. It also covers the X-band downlink frequency range from 7.25 to 7.75 GHz and uplink 7.9 to 8.4 GHz frequency ranges.

Keywords Asymmetrical antenna · Biomedical applications · Coplanar waveguide (CPW) feed · ISM band · Multifrequency antenna

P. Bhardwaj (✉)
Department of Electronics and Communication Engineering, Birla Institute of Technology, Deoghar Campus, Deoghar 814142, India
e-mail: payalrashi@gmail.com

R. K. Badhai
Department of Electronics and Communication Engineering, Birla Institute of Technology, Patna Campus, Patna 800014, India
e-mail: riteshkbadhai@bitmesra.ac.in

© Springer Nature Singapore Pte Ltd. 2020

V. Janyani et al. (eds.), *Optical and Wireless Technologies*,
Lecture Notes in Electrical Engineering 546,
https://doi.org/10.1007/978-981-13-6159-3_57

1 Introduction

Earlier, much of the development of microstrip antenna was subject to military and aerospace applications, increasing its span to communication applications like WLAN and Wi-Fi. In the recent era, there has been a gradual improvement in wireless communication systems related to biomedical fields and therefore antennas intended for biomedical applications have achieved considerable attention. The antenna systems designed for biomedical applications are either implanted in-body or worn on-body and off-body. The wireless links remove the need for cables making the communication simple and cost-effective [1]. On-body communication is established between wearable electronic sensors attached to the human body, while off-body communication establishes the link between sensors and external devices. The size reduction or miniaturization, circular polarization, good impedance matching, and efficiency are, therefore, essential requirements for antenna design.

The microstrip patch antenna is chosen for the design due to its advantages of being low profile, conformal to planar structures, and simplicity of fabrication [2]. The patch antennas can sometimes be operated at more than one frequency, one dominant mode frequency, and the other corresponding to higher order modes. The radiations with same polarizations can be obtained at multiple frequencies if patches are stacked and fed properly [3, 4]. Many multiple frequency antennas have been studied for biomedical applications but have large volume [5] and complex structure [6].

The size of an antenna is one of the main constraints in the design for biomedical applications, a printed antenna with a size $12 \times 12 \times 0.65$ mm^3 and coplanar waveguide feed (CPW) has been designed in this paper. The coplanar waveguide feed structure is used to obtain high-frequency response [7] and good impedance matching [8, 9], reducing back radiations and making it easier to integrate with microwave circuits. Many CPW-fed antennas have been studied for their dual-band operation [10–12] and wireless applications [13–16]. CPW feed simplifies the antenna structure along with providing good radiation properties and high-frequency response, thereby increasing the system accuracy. The proposed antenna is based on the meandered structure with an improvement in the gain, impedance matching, and radiation characteristics. The structure resonates at multiple frequencies embodying the function of multiple antennas and can be used for transmission in ISM as well as in X-band. Another major improvement in the structure is the ease of fabrication and it is an extremely miniaturized size which is a challenge in most biomedical antenna designs. The electrically small antenna may be defined as one whose largest dimension is not more than one-tenth of a wavelength ($\lambda/10$) [17]. The proposed antenna exhibits electrically smaller size based on the fact that the size of the antenna is inversely proportional to the number of meandered turns. In the proposed structure the number of turns has been increased resulting in an electrically small antenna with increased path length, thereby obtaining lower resonating frequency.

2 Antenna Design

We propose a CPW feed asymmetrical antenna for triple frequency operations. The proposed multifrequency antenna structure shown in Fig. 1 comprises of multiple slotted conducting patches on one side of the CPW feed and a single-slot patch on the other side; a CPW feed line. The proposed antenna structure has a compact size of 12 × 12 mm^2. The proposed structure is printed on a glass epoxy FR-4 substrate with a height of 0.65 mm and relative permittivity of 4.4. Copper has been used as a radiating material for both patches as well as the ground plane. The antenna resonates at 2.38, 5.52, and 7.72 GHz and has a good impedance matching at all the bands. It also exhibits good radiation patterns and antenna gains over the operating bands.

The coplanar waveguide feed structure can be analyzed by using the following Eqs. (1)–(5):

$$\varepsilon_{eff} = 1 + \frac{\varepsilon_r - 1}{2} \frac{K(k_2)}{K(k_2')} \frac{K(k_1')}{K(k_1)} \tag{1}$$

$$k_1 = \frac{W_s}{W_s + 2d} \tag{2}$$

$$k_1' = \sqrt{1 - k_1^2} \tag{3}$$

$$k_2 = \frac{sinh\left(\frac{\pi W_s}{4h}\right)}{sinh\left(\frac{\pi W_s + 2d}{4h}\right)} \tag{4}$$

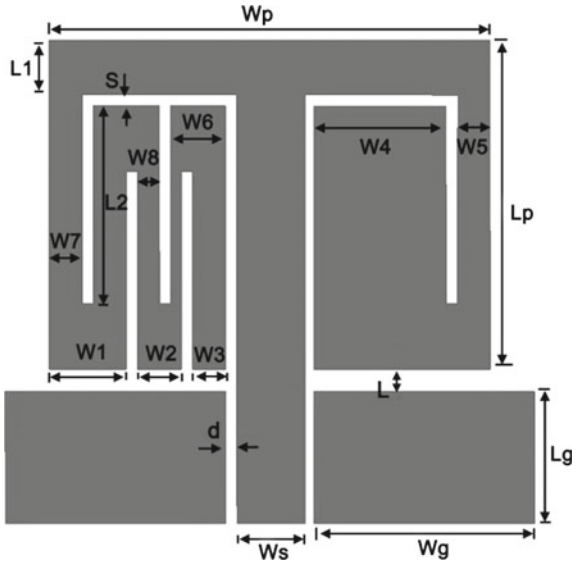

Fig. 1 Proposed asymmetric patch monopole antenna geometry

$$k_2' = \sqrt{1 - k_2^2} \tag{5}$$

In the above equations, $K(k_1)$, $K(k_2)$, $K(k_1')$ and $K(k_2')$ are the first complete elliptic integral of the first kind and its complement, ε_{eff}, W_s, d, and h are the effective dielectric constant, the width of the CPW feed, the gap between the CPW feed and the ground and the substrate thickness, respectively.

The width and length of the meandered patch responsible for the three resonating frequencies are approximated and computed using the following Eqs. (6)–(11):

$$W_M = 0.042\,\lambda_g \tag{6}$$

$$L_2 = 0.054\,\lambda_g \tag{7}$$

$$W_1 = 0.021\,\lambda_g \tag{8}$$

$$W_2 = 0.012\,\lambda_g \tag{9}$$

$$W_3 = 0.009\,\lambda_g \tag{10}$$

where λ_g is the guided wavelength given by

$$\lambda_g = \frac{\lambda}{\sqrt{\varepsilon_{eff}}} \tag{11}$$

The structure of the proposed antenna has been developed in the progressive manner shown in Fig. 2. The process begins by designing the symmetric planar structure on both sides of the feed line with conventional inset feed antenna as shown in Fig. 2a. The distance between the patch and the ground is taken to be 1 mm and the feed gap between the feed line and the ground is 0.3 mm. As shown in Fig. 3, the antenna resonates at a single frequency of 3.4 GHz. It deviates from the desired frequency of operation in ISM band and makes the antenna suitable for only single-band operation. It is seen that no resonance occurs at ISM band. In the next step, for the antenna to resonate at multiple frequencies the conducting patch is meandered with strip on both sides of the feed line. The gap between the patch and the ground is reduced to 0.5 mm, while the gap between the feedline and the ground is reduced to 0.2 mm Fig. 2b. Reduction in the gap between the patch and the ground lowers the resonant frequency and frequency corresponding to other high order mode is obtained.

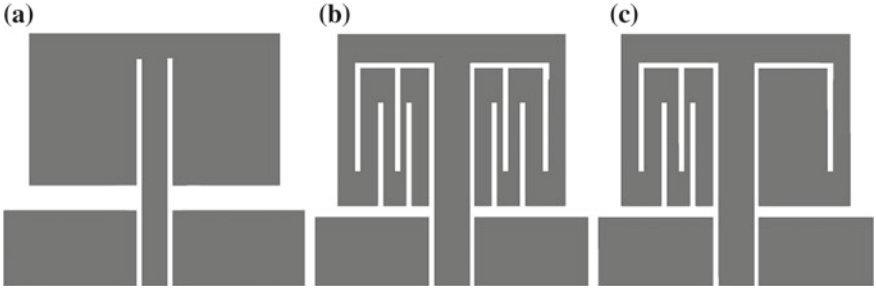

Fig. 2 The three structures of on-body monopole antenna: **a** Case 1: plane symmetric structure, **b** Case 2: meandered symmetric structure, and **c** Case 3: proposed antenna

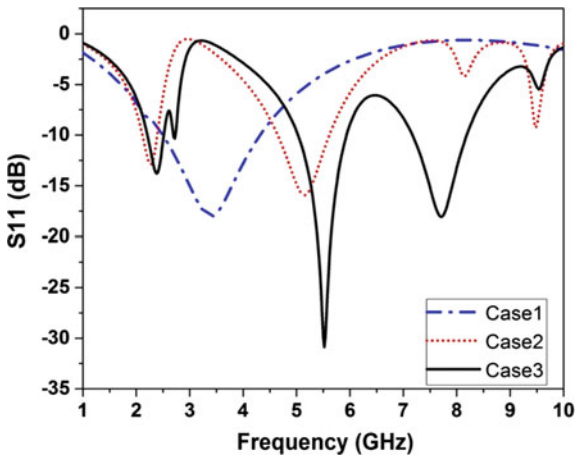

Fig. 3 Comparison of the reflection coefficient of Case 1: plane symmetric structure, Case 2: meandered symmetric structure, and Case 3: proposed antenna

When the patch antenna with the meandered structure on both sides of the feed-line is used, it is observed that antenna resonates at dual frequencies 2.26 GHz and 5.18 GHz. Out of the two bands, only one lies in the ISM band with −15.8 dB return loss. In order to include higher order bands and frequencies close to ISM band, the asymmetric structure with meandering on one side of the patch and planar patch on the other side is used Fig. 2c. From the comparison of the simulated return loss S_{11} of the three antenna structures Fig. 3, it is observed that the proposed antenna demonstrates sharp and well-defined curves at desired frequencies. Further, by selecting a proper distance between the ground and CPW feed, a good impedance matching and resonating frequencies have been obtained. The detailed dimensions of the proposed antenna are presented in Table 1.

Table 1 Dimensions of the proposed antenna

Parameter	Dimension (mm)	Parameter	Dimension (mm)	Parameter	Dimension (mm)
Lp	7.5	W1	1.75	W7	0.7
Wp	10	W2	1	W8	0.5
Lg	3	W3	0.75	L1	1.25
Wg	5	W4	3	L2	4.5
Ws	1.55	W5	0.75	L	0.5
d	0.2	W6	1.25	S	0.25

3 Parametric Study

3.1 Effect of the Distance Between the Patch and the Ground (L)

By changing the distance between the patch and the ground, while keeping the distance between the feedline and the ground fixed. The gap "*L*" has a significant effect on impedance matching and bandwidth. As depicted in Fig. 4, it can be observed that with increasing value of "*L*"; impedance matching improves for the lower resonant band but decreases at higher bands. The large separation between ground and patch (*L*) also reduces the resonance frequency of higher order modes. The reflection coefficient and bandwidth for three different value of "*L*" are given in Table 2. From these analysis, optimum value of $L = 0.5$ mm is considered for the proposed antenna.

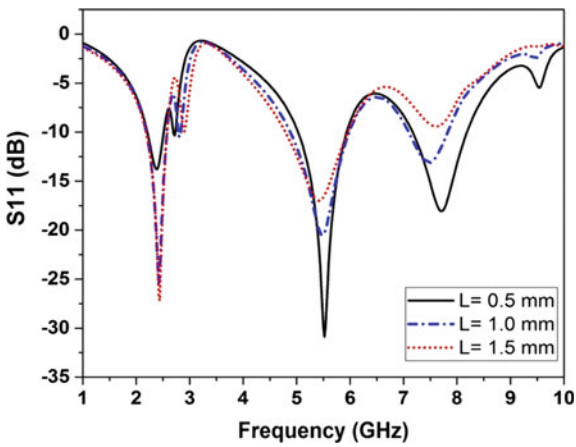

Fig. 4 Comparison of reflection coefficients for varying distance "*L*" between patch and ground at $L = 0.5$ mm, $L = 1$ mm, and $L = 1.5$ mm

Table 2 Antenna characteristics for various values of "*L*"

Varying component (mm)	Resonant frequencies (GHz)	Reflection coefficient |S11| (dB)	Bandwidth (MHz)
L = 0.5	(a) 2.38	−13.79	280
	(b) 5.52	−30.84	860
	(c) 7.72	−18.05	960
L = 1.0	(a) 2.42	−25.43	370
	(b) 5.5	−20.46	1060
	(c) 7.5	−13.11	740
L = 1.5	(a) 2.44	−27.19	360
	(b) 5.4	−16.97	1140

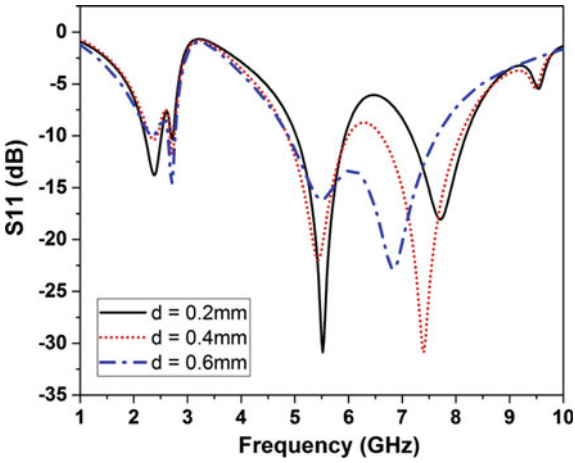

Fig. 5 Comparison of reflection coefficients for varying distance "*d*" between feed and the ground at $d = 0.2$ mm, $d = 0.4$ mm, and $d = 0.6$ mm

3.2 Effect of the Feedgap (D)

By changing the distance between the feedline and the ground keeping the distance between the patch and the ground fixed. The feedgap "*d*" has a significant effect on capacitive coupling between the feed line and the ground plane. From Fig. 5, it is observed that for $d = 0.4$ mm antenna resonates at 5.4 GHz and 7.4 GHz and for $d = 0.6$ mm the antenna becomes wideband operating within 4.88 GHz to 7.64 GHz band, while for $d = 0.2$ mm antenna gives the better impedance matching for all three resonating bands and covers the desired operating bands. The reflection coefficient and bandwidth for three different values of feedgap "*d*" are given in Table 3.

Table 3 Antenna characteristics for various values of "*d*"

Varying component	Resonant frequencies (GHz)	Reflection coefficient $\|S_{11}\|$ (dB)	Bandwidth
d = 0.2 mm	(a) 2.38	−13.79	280 MHz
	(b) 5.52	−30.84	860 MHz
	(c) 7.72	−18.05	960 MHz
d = 0.4 mm	(a) 2.38	−10.378	1100 MHz
	(b) 5.42	−20	1420 MHz
	(c) 7.39	−16.413	
d = 0.6 mm	(a) 2.699 Wideband frequency range 4.88–7.64 GHz	−14.78 (<−10)	120 MHz 2.76 GHz or 2760 MHz

4 Results and Discussions

The proposed antenna is fabricated on glass epoxy FR-4 substrate. To estimate the performance of the proposed antenna, the fabricated antenna is connected to the vector network analyzer (VNA). Figure 6 illustrates the result of the simulated and measured reflection coefficient S_{11} for the proposed planar asymmetric antenna structure. It can be seen that the proposed antenna resonates at three different bands; the first band operates at 2.4 GHz band with a bandwidth of 300 MHz (2.20–2.50 GHz) which is useful for biomedical applications. The second band of antenna resonates at 5.52 GHz band with a bandwidth of 870 MHz (5.05–5.92 GHz) which covers all three bands (UNII 1, UNII 2, and UNII 3) of WLAN applications. The third band of the proposed antenna resonates at 7.72 GHz with a bandwidth of 1.05 GHz

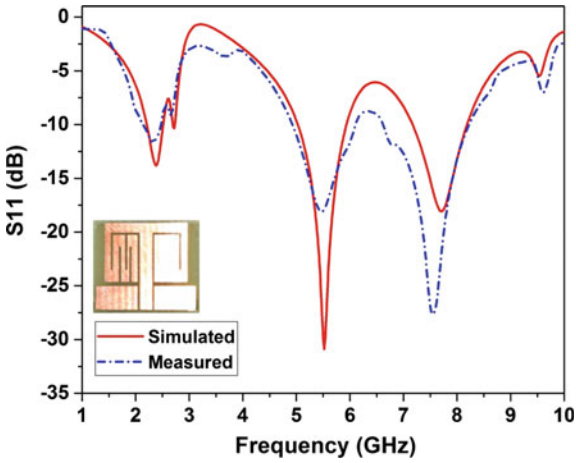

Fig. 6 Simulated and measured reflection coefficients |S11| of the proposed antenna

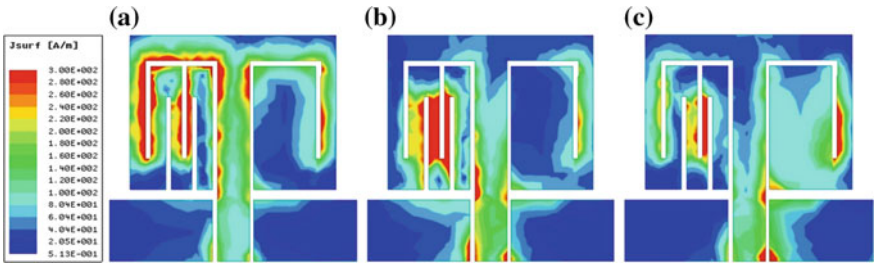

Fig. 7 Current distribution of the proposed antenna at **a** 2.38 GHz, **b** 5.52 GHz, and **c** 7.72 GHz

(7.10–8.15 GHz) covers C-band fixed satellite communication. The current distributions of asymmetric patch monopole antenna are shown in Fig. 7 at 2.38, 5.52, and 7.72 GHz. The surface current shows information about the effective electrical length and resonating mode of the antenna. From Fig. 7a, it is seen that the surface current distributed is dominated on the left side of the feed and having the longest electrical length on the patch surface without any null point due to which it resonates at the fundamental resonant frequency of 2.38 GHz. Similarly, in Fig. 7b, the strong surface current flows near the second and fourth slot on the left side of the feed which produces the second resonating mode at 5.52 GHz, while due to the shortest electrical length, the right side of the patch having a large influence on the third resonating mode at 7.72 GHz.

Figure 8 illustrates the plots for E-plane and H-plane radiation patterns of the proposed antenna for frequencies 2.38, 5.52, and 7.72 GHz. The E-plane pattern has the dual directional cone-shaped pattern and the H-plane pattern is an omnidirectional pattern. It also shows the good co-relation between co and cross-polarizations.

5 Conclusions

A compact asymmetric antenna with CPW feed has been proposed with a simple structure and small volume to be printed on an area of 12 mm × 12 mm. The antenna resonates at three frequencies 2.38, 5.52, and 7.72 GHz. The comparison of structures has demonstrated a considerable improvement in the reflection coefficient of the asymmetric structure at higher resonating frequencies. The compact size and multiple resonating frequencies of the antenna can effectively cover the applications ranging from WLAN to portable medical diagnostic applications.

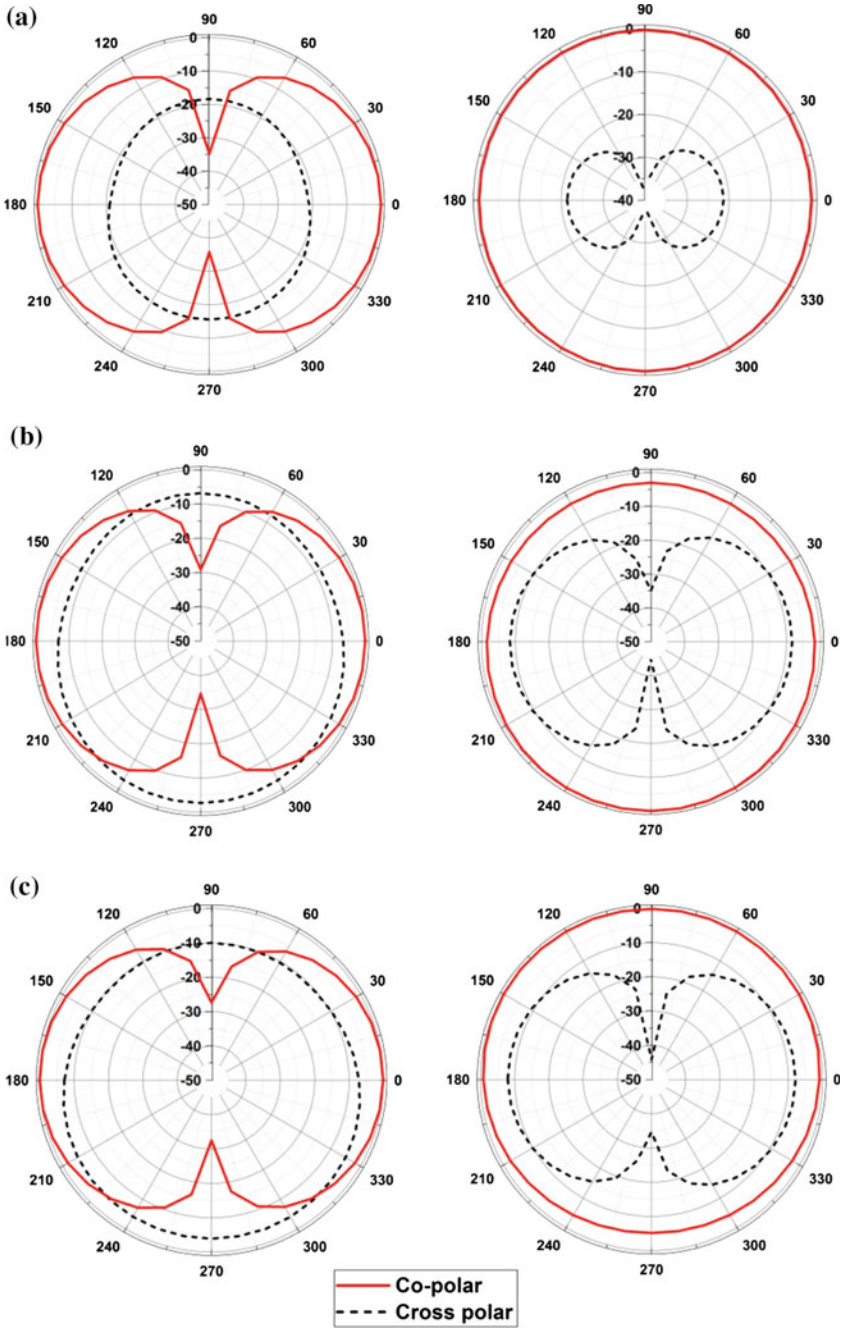

Fig. 8 Normalized radiation patterns of the proposed antenna for E-plane and H-plane at **a** 2.38 GHz, **b** 5.52 GHz, and **c** 7.72 GHz

References

Kumar SA, Shanmuganantham T (2015) Implantable CPW fed circular slot antennas for 2.45 GHz ISM band biomedical applications. J Circ Syst Comput 24(1)

Lee KF, Luk KM (2001) Microstrip patch antennas. Imperial College Press, London, England

Long SA, Walton MD (1979) A dual-frequency stacked circular-disc antenna. IEEE Trans Ant Propag AP-27:270–273

Montgomery NW (1984) Triple-frequency stacked microstrip element. In: IEEE international antennas and propagation symposium, pp 225–258

Nikolopoulos CD, Baklezos AT, Capsalis CN (2014) Auto reconfigurable patch antenna for biomedical single channel multi-frequency microwave radiometry applications. Prog Electromagnet Res C 49:19–29

Mobashsher AT, Abbosh A (2014) CPW-fed low-profile directional antenna operating in low microwave band for wideband medical diagnostic systems. Electr Lett 50(4):246–248

Rezaeieh SA, Abbosh AM (2014) Wideband and unidirectional folded antenna for heart failure detection system. IEEE Ant Wirel Prog Lett 13:844–847

Luo Q, Tian HP, Huang ZT, Wang XD, Guo Z, Ji YF (2013) Unidirectional dual-band CPW fed antenna loaded with an AMC reflector. Int J Ant Propag Article ID 875281

Chen YF, Chen HT (2004) A CPW-fed dual-frequency monopole antenna. IEEE Trans Antennas Propag 52(4):978–982

Hu L, Hua W (2011) Wide dual-band CPW-fed slot antenna. Electr Lett 47(14):789–790

Lin CC, Yu EZ, Huang CY (2012) Dual-band rhombus slot antenna fed by CPW for WLAN applications. IEEE Ant Wirel Propag Lett 11:362–364

Seo Y, Jung J, Lee H, Lim Y (2012) Design of compact dual meander antenna for WLAN operation. Microw Opt Technol Lett 54(7):1595–1599

Ren W (2008) Compact dual-band slot antenna for 2.4/5 GHz WLAN applications. Prog Electromagnet Res B 8:319–327

Sen A, Roy JS, Chaudhuri SR (2009) Investigation on a dual-frequency microstrip antenna for wireless applications. Proc IEEE, 978(1)

Tian B, Ming J (2008) A design of dual-band h-shaped microstrip-line-fed printed wide-slot antenna. Proc IEEE 978–1:201–203

Kumar SA, Raj MA, Shanmuganantham T (2017) Analysis and design of CPW fed antenna at ISM band for biomedical applications. Alexandria Eng J

Miron D (2006) Small antenna design, Newnes

Design and Study of a Photonic Crystal Fiber Biosensor Based on Surface Plasmon Resonance

Charanjeet Kaur, Varshali Sharma and Ritu Sharma

Abstract In this paper, a photonic crystal fiber based biosensor using surface plasmon resonance (SPR) principle is analyzed for the sensing of refractive index in the visible to near-infrared region. A thin layer of gold (Au) is coated inside the central hole which serves the purpose of the plasmonic layer. The finite element method (FEM) is used for analyzing the sensing performance and other characteristics. The optical loss spectrum of this biosensor is observed by varying the structure parameters. This paper analyses the amplitude sensitivity and wavelength sensitivity of the designed PCF-SPR biosensor.

Keywords Photonic crystal fiber (PCF) · Surface plasmon resonance (SPR) · Finite element method (FEM)

1 Introduction

PCF-SPR based sensor has made a remarkable effort in many biochemicals, biotechnology fields over the past few decades, and thoroughly developed. The wide range of application is chemical detection, food testing, water testing, gas detection, environment monitoring, protein–protein detection, small molecule aggregation, medical diagnostics, drug detection [1, 2], direct detection of virus particles, SPR imaging [3, 4], etc. Along with the SPF techniques, there are other techniques also present such as a micro-ring resonator, waveguides, and resonant mirror. The difficulties associated with the conventional prism-based SPR sensors can be overcome using PCF_S [5]. In prism-based SPR sensor, the prism is coated with plasmonic materials

C. Kaur · R. Sharma (✉)
Department of Electronics and Communication, Malaviya National Institute of Technology Jaipur, Jaipur, Rajasthan, India
e-mail: rsharma.ece@mnit.ac.in

V. Sharma
Department of Electronics and Communication,
Manipal University Jaipur, Jaipur, Rajasthan, India

© Springer Nature Singapore Pte Ltd. 2020

V. Janyani et al. (eds.), *Optical and Wireless Technologies*,
Lecture Notes in Electrical Engineering 546,
https://doi.org/10.1007/978-981-13-6159-3_58

(Ag, Au, Cu, etc.) [5] and the light is launched at a specific angle to the prism to excite the free electrons on the metal surface. When the frequency of incident light and the metal surface electrons get matched, the electrons resonate; and surface plasmon wave (SPW) is generated, which gets propagated along the metal–dielectric interface [5]. The limitations of conventional SPR sensors are: (1) less flexibility in geometry, more bulky and less sensitivity. (2) Several mechanical (moving) components were required which lead to the cumbersome construction. (3) Limitations on the remote sensing applications. This lead to the development of PCF-based SPR sensors.

PCF-based SPR sensors are compact, portable, lightweight and metal can be coated on either inside the air holes or outside of the fiber surface [5, 6]. Incident light can be simply launched from one end of the fiber and response can be observed from another fiber end. Moreover, propagating light can be controlled by managing the PCF parameters such as air hole diameter, pitch size, pressurization, etc., during the fabrication process [7]. By changing applied pressure on PCFs' holes, the air hole diameters, pitch size, and the glass wall thickness between adjacent air holes can be changed, thereby, the light penetration from the core to the cladding region changes. By controlling the light propagation, strong coupling between the core mode and surface plasmon polaritons (SPP) mode can be achieved, which results in improving the sensors performance [7–9]. In this paper, PCF-SPR sensors are investigated by finite element method (FEM) [10, 11].

In this paper, a simple PCF-SPR biosensor is designed with multiple cores and with a selective channel filled with the analyte (bio-sample). The channel has a gold layer coating deposited inside. The designed structure has silica as cladding in the background and microstructured air holes. The designed PCF geometry bears the ability of enhanced evanescent field and it also exhibits efficient light–analyte interactions. It provides refractive index resolution up to 10^{-5} RIU and exhibits an average wavelength sensitivity of 4500 nm/RIU and amplitude sensitivity of 4470 dB/RIU with analyte refractive index ranging from 1.39 to 1.42. The sensitivity and performance can be optimized by managing the structure parameters such as metal layer (Au) thickness, core radius, air holes radii, and pitch of air holes.

2 Basic Principle and Numerical Modeling of PCF-SPR Sensor

2.1 Model

A PCF-SPR biosensor with multiple core structure having gold layer coating inside the center hole is shown in Fig. 1. The structure consists of a central hole with a thin gold layer coated inside it. The central hole acts as the analyte channel which is surrounded by air holes arranged in a hexagonal lattice geometry. The air holes are present in the cladding of silica.

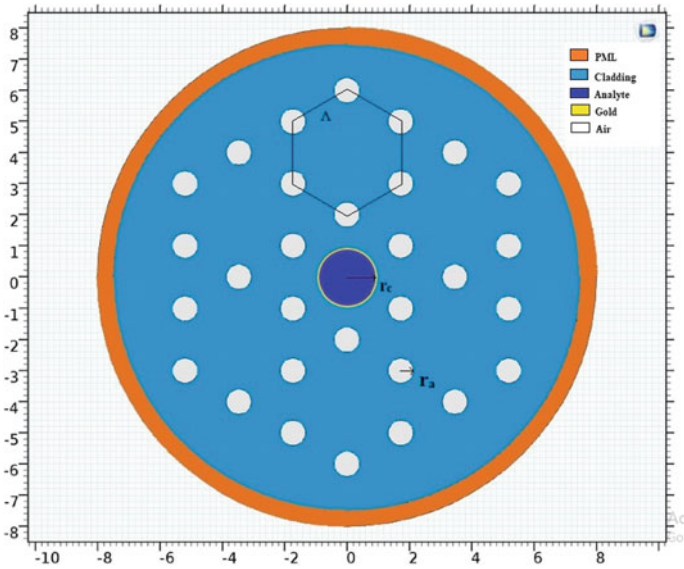

Fig. 1 Schematic diagram of the multicore PCF-SPR biosensor

To follow the principle of SPR the thin gold layer is present inside the surface of this center hole. The approximate value of the dielectric constant of the gold layer in the range of near IR the Drude model [5] is used and given by Eq. (1).

$$\varepsilon_{Au}(\omega) = \varepsilon^{\infty}(\omega) - \frac{\omega_p}{\omega^2 + i\omega_\tau} \tag{1}$$

where $\varepsilon^{\infty} = 9.75$, $\omega_p = 1.36 \times 10^{16}$ rad/s, $\omega_\tau = 1.45 \times 10^{14}$ rad/s. The value of the refractive index of silica glass cladding is defined by the Sellmeier dispersion equation [12].

$$n^2(\lambda) = 1 + \frac{B_1\lambda^2}{\lambda^2 - C_1} + \frac{B_2\lambda^2}{\lambda^2 - C_2} + \frac{B_3\lambda^2}{\lambda^2 - C_3} \tag{2}$$

where the coefficients' value in Eq. (2) are defined as

Material	B_1	B_2	B_3	C_1 (μm^2)	C_2 (μm^2)	C_3 (μm^2)
Silica	0.696166300	0.00467914826	0.407942600	0.013512063	0.897479400	97.9340025

For Fig. 1, the design parameters are: $r_c = 0.9$ μm, $r_a = 0.4$ μm, $t_{Au} = 30$ nm and $\Lambda = 2$ μm where r_c, r_a, t_{Au}, Λ are the radius of the analyte channel, the radius of the air holes, the gold layer thickness and the pitch of the air holes, respectively. The refractive index of the analyte flowing through the channel varies from 1.39 to 1.42.

The PCF-SPR sensor is subjected to a perfectly matched layer boundary conditions at the numerical calculation zone edges to evaluate the SPR properties,

2.2 Principle

Surface plasmon resonance is a charge-density oscillation that may exist at the interface of two media with dielectric constants of different signs, for instance, a metal and a dielectric [7]. The charge-density wave is associated with electromagnetic waves, the field vectors of which reach their maxima at the interface and decay evanescently into both media. The surface plasma wave (SPW) is a TM-polarized wave (magnetic vector is perpendicular to the direction of propagation of the SPW and parallel to the plane of the interface). The propagation constant of the surface plasma wave propagating at the interface between a semi-infinite dielectric and metal is given by the following expression (Eq. 3) [7]:

$$\beta = k\sqrt{\frac{\varepsilon_m n_s^2}{\varepsilon_m + n_s^2}} \tag{3}$$

where k denotes the free space wave number, ε_m is the dielectric constant of the metal ($\varepsilon_m = \varepsilon_{mr} + i\varepsilon_{mi}$), and n_s is the refractive index of the dielectric.

Sensing criteria in PCF-SPR sensor is based on the mutual interaction between the evanescent field and surface electron, which happens to take place in the interface of metal–dielectric interface. At a resonant wavelength, real part of the core guided effective refractive index and the surface plasmon effective refractive index are equal [8, 9]. The core-cladding evanescent field excites the free electrons of the metal surface; as a result, the surface plasmon wave is generated. Thus, the phenomenon of the SPW may be supported by the structure providing that $\varepsilon_m > n_s^2$ at optical wavelengths. This condition is fulfilled by several metals of which gold and silver are the most commonly used [7].

Thus the selection of plasmonic material plays a key role in the performance of SPR sensors. Mostly gold, silver, copper, and aluminum are used as active plasmonic materials [7]. Out of the three, silver material gives a sharp resonance peak which increases sensing accuracy. However, silver is chemically unstable and has a high tendency to oxidize, which reduces sensing performance [7]. Although a thin graphene layer coating can solve the oxidization issue, this additional coating causes fabrication problems and overall manufacturing cost. On the other hand, gold is chemically stable and does not easily oxidize. It also shows larger resonance peaks than other available plasmonic materials. Hence gold is used as a metal coating in the channel [12, 13].

A sharp loss peak appears at the resonant wavelength and the RI of the unknown analyte can be detected via wavelength shift or amplitude variations of this peak.

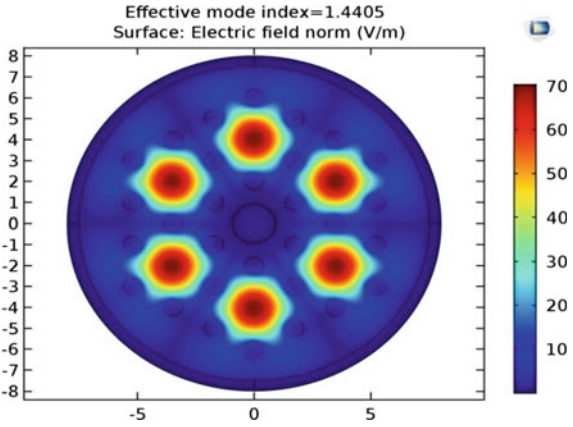

Fig. 2 Mode profile of the designed sensor

3 Results

The optical distribution or mode analysis of the PCF-SPR sensor is shown in Fig. 2. The basic parameters of geometry are $r_c = 0.9$ μm, $r_a = 0.4$ μm, $n_a = 1.0$ (air), $n_c = 1.43$ (analyte), $\lambda = 850$ nm, $t_{Au} = 30$ nm, and $\Lambda = 2$ μm.

The real part of the effective refractive index is 1.43849 of the fundamental mode by using the above parameters.

Figure 3a shows the graph between the real part of the effective refractive index and wavelength. Thus, the real part of the refractive index decreases with increasing wavelength justifying $n_{eff} = \beta/\lambda$. In Fig. 3b the loss spectrum shows the peak at wavelength 770 nm which is the resonance wavelength.

$$\alpha_{loss} = \frac{40\pi}{\lambda ln10} Im\left(n_{eff}\right) \times 10^6 (\text{dB/m}) \tag{4}$$

Equation (4) represents that the imaginary part of the effective refractive index is directly proportional to the loss. The resonance peak can be used to sense any change in temperature, pressure, pH, concentration, etc.

Figure 4a represents that with increasing wavelength the peak diminishes and also a shift in the peak is observed as the thickness of the metal layer is increased from 30 to 40 nm.

Figure 4b, c shows that varying pitch value does not affect the amplitude of peak but only gives a shift in resonance peak, whereas with increasing refractive indices of the analyte from 1.40 to 1.42 peak as variation in amplitude as well as resonance wavelength is achieved.

Now there are two kinds of sensitivity in terms of amplitude and in terms of wavelength. Amplitude sensitivity is calculated as [5]

$$S(\lambda) = \frac{1}{\alpha(\lambda, n)} \frac{\partial \alpha(\lambda, n)}{\partial n} \frac{10}{ln10} (\text{dB/RIU}) \tag{5}$$

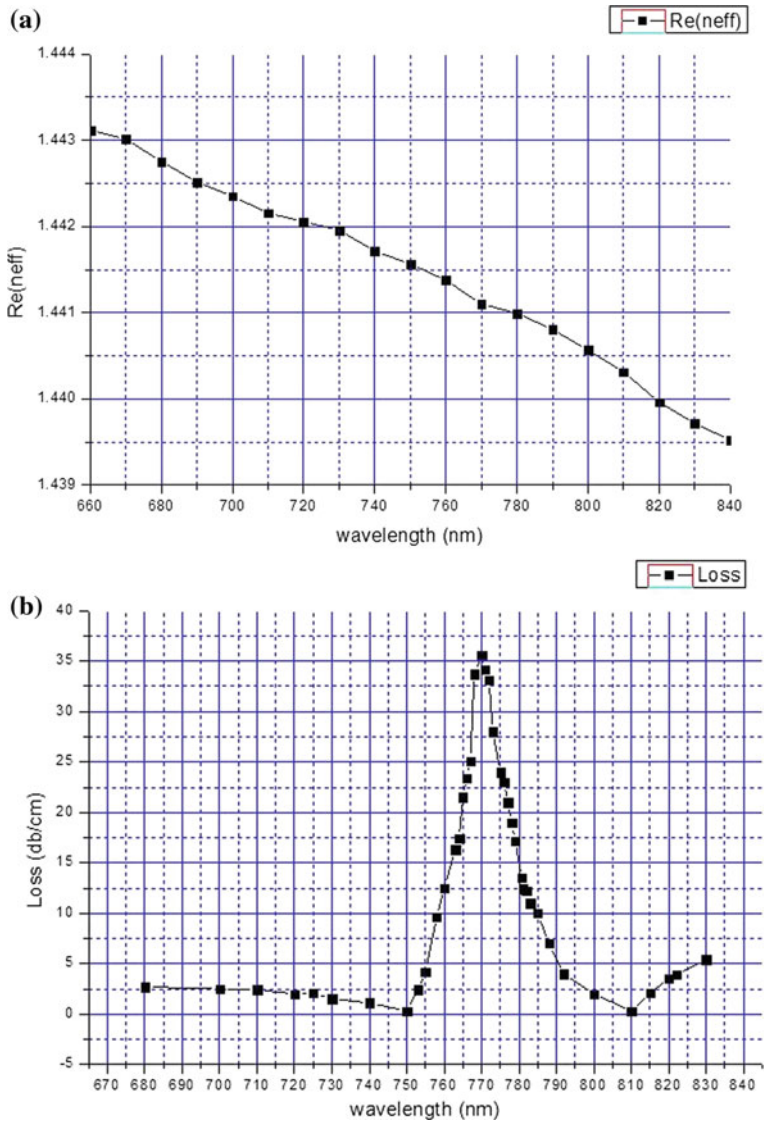

Fig. 3 **a** Distribution of effective refractive index over wavelength. **b** Loss spectrum of the fundamental mode. A Resonance peak at 770 nm is achieved

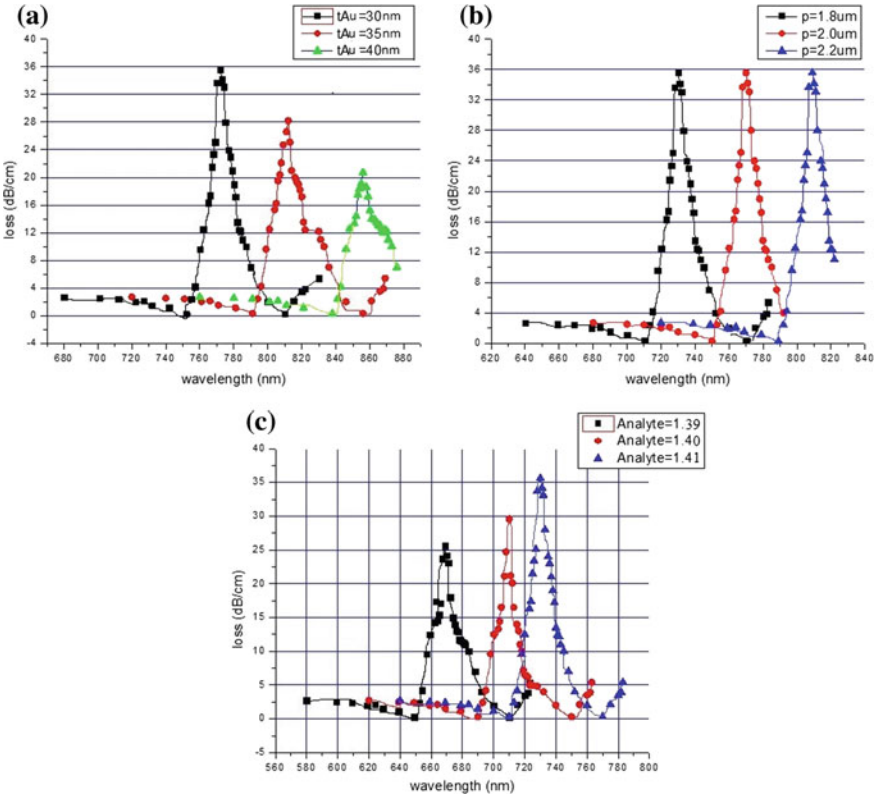

Fig. 4 **a** Loss spectra at different thickness of the gold layer. **b** The loss spectra at different values of pitch between air holes. **c** The loss spectra at different refractive indices of the analyte flowing through the channel

$\alpha(\lambda, n)$ represents the transmission loss and $\partial\alpha(\lambda, n)$ is the loss difference between two loss spectra.

The spectral sensitivity is given by [6]

$$S(\lambda) = \frac{\Delta\lambda_{peak}}{\Delta n_a}(\text{nm/RIU}). \tag{6}$$

where $\Delta\lambda_{peak}$ represents peak wavelength shift and Δn_a is the variation of analyte RI. Using Fig. 4c and Eq. (6), the spectral sensitivity calculated analytically is 4470 dB/RIU.

4 Conclusion

The proposed multicore PCF-SPR biosensor consists of the gold layer as plasmonic metal.

After analyzing the structure, it has been observed that the parameters of the structure affect the resonance peak and its intensity as well. The achieved spectral sensitivity is 4000 nm/RIU and amplitude sensitivity is 4470 dB/RIU. However, the sensing performance can be improved by optimizing the geometry.

References

1. Cooper MA (2002) Optical biosensors in drug discovery. Nat Rev Drug Discov 1:515–528
2. Goodrich TT, Lee HJ, Corn RM (2004) Direct detection of genomic DNA by enzymatically amplified SPR imaging measurements of RNA microarrays. J Am Chem Soc 126:4086–4087
3. McPeak KM, Jayanti SV, Kress SJ, Meyer S, Iotti S, Rossinelli A et al (2015) Plasmonic films can easily be better: rules and recipes. ACS Photon 2:326–333
4. Rifat AA, Ahmed R, Yetisen AK, Butt H, Sabouri A, Mahdiraji GA, Yunc SH, Adikana FRM (2017) Photonic crystal fiber based plasmonic sensors. Sens Actuators B 243:311–325
5. Rifat AA, Ahmed R, Mahdiraji GA, Adikan FRM (2017) Highly sensitive D-shaped photonic crystal fiber based plasmonic biosensors in visible to Near-IR. IEEE Sens J 17:2776–2783
6. Wong WC, Chan CC, Boo JL, Teo ZY, Tau ZQ, Yang HB, Li CM, Leong KC (2013) Photonic crystal fiber surface plasmon resonance biosensor based on Protein G Immobilization. IEEE J Sel Top Quantum Electron 19(3):4602107
7. Ordal MA, Long LL, Bell RJ et al (1983) Optical properties of metals Al, Co, Cu, Au, Fe, Pb, Ni, Pd, Pt, Ag, Ti and W in the infrared and far infrared region. Appl Opt 22:1099–1120
8. Liu C, Wang F, Lv J, Sun T, Liu Q, Mu H, Chu PK (2015) Design and theoretical analysis of a photonic crystal fiber based on surface plasmon resonance sensing. SPIE J Nanophoton 9. https://doi.org/10.1117/1.jnp.9.093050
9. Rifat AA, Mahdiraji GA, Sua YM, Ahmed R, Shee Y, Adikan FM (2016) Highly sensitive multi-core flat fiber surface plasmon resonance refractive index sensor. Opt Express 24:2485–2495
10. Wu T, Shao Y, Wang Y, Cao S, Cao W, Zhang F, Liao C, He J, Huang Y, Hou M, Wang Y (2017) Surface plasmon resonance biosensor based on gold-coated side-polished hexagonal structure photonic crystal fiber. OSA J Opt Express 25(17):20313
11. Luan N, Wang R, Lv W, Yao J (2015) Surface plasmon resonance sensor based on D-shaped microstructured optical fiber with hollow core. OSA Opt Express 23(7):8576–8582
12. Hasan MR, Akter S, Rifat AA, Rana S, Ali S (2017) A highly sensitive gold-coated photonic crystal fiber biosensor based on surface plasmon resonance. MDPI Photon 4, Article no 18, April (2017). http://doi.org/10.3390/photonics4010018
13. Rifat AA, Mahdiraji GA, Sua YM, Shee YG, Ahmed R, Chow DM, Adikan FRM (2015) Surface plasmon resonance photonic crystal fiber based biosensors: a practical sensing approach. IEEE Photon Technol Lett 27(15):1628–1631

Iterative Fourier Transform Optimization of Computer Generated Fourier Holograms

G. Kanjana, Meril Cyriac, L. Anusree, Leena Thomas, N. R. Nelwin Raj, Roshan Varghese and M. K. Sheeja

Abstract Holograms are created by recording the interference pattern obtained between the object called object wave and a coherent reference wave. Computer-Generated Holography (CGH) deals with the creation of holograms with the aid of computers. CGH makes use of the wave theory of light to represent both the object and reference waves. CGH does not require actual objects to create the hologram as long as the light scattered or diffracted off the object could be represented mathematically. The proposed work describes a method for creating holograms with the help of a computer along with the technique to reconstruct its image. Iterative Fourier Transform algorithm is used to optimize computer-generated Fourier holograms. Root mean square error is measured to evaluate the quality of the reconstructed image.

Keywords Hologram · Fourier hologram · Fourier transform · Interference

G. Kanjana (✉) · M. Cyriac · L. Anusree · L. Thomas · N. R. Nelwin Raj · R. Varghese · M. K. Sheeja
Department of Electronics and Communication Engineering, Sree Chitra Thirunal College of Engineering, Thiruvananthapuram 695018, Kerala, India
e-mail: kanjanalbs@gmail.com

G. Kanjana · M. Cyriac · L. Anusree
Department of Electronics and Communication Engineering, LBS Institute of Technology for Women, Thiruvananthapuram 695012, Kerala, India

L. Thomas
Department of Electronics and Communication Engineering, College of Engineering, Kallooppara 689603, Kerala, India

© Springer Nature Singapore Pte Ltd. 2020

V. Janyani et al. (eds.), *Optical and Wireless Technologies*,
Lecture Notes in Electrical Engineering 546,
https://doi.org/10.1007/978-981-13-6159-3_59

1 Introduction

Holography is a method in which not only the amplitude but also the phase of the light field can be recorded. The recording medium records the original complex amplitude, i.e., both the amplitude and phase of the object wave to generate variable intensity holograms. In this era of highly advanced digital image processing, it is difficult to store the biometric details of a wanted criminal securely. Holographic data storage is a solution for the safe storage of fingerprints of highly wanted criminals [1].

Holograms are applied to documents or products, and its presence is intended to be a reliable indication that the material or product is valid [2]. In order to record the hologram of an object, the laser beam is split into two—object beam and reference beam. The object beam illuminates the object and the diffracted waves from the object are allowed to fall on the holographic recording material. The reference beam is allowed directly to fall on the same area of the film. With the help of diffraction theory, each point of the complex object can be displayed as a point source of light, each one interfering with the reference beam and creating a fringe pattern on the film. The hologram obtained is a superposition of the interference patterns. The hologram is dependent upon the intensity and phase of each point on the object. A complete description of the light emitted from the object is obtained by recording the interference pattern. Each point source diffraction grating found within the complex hologram diffracts part of the laser beam such that it reconstructs the original point. The wavefronts passing through the hologram combine to reconstruct the image of the original object since the hologram is made up of the superposition of an infinite number of point sources and their reference beam interference patterns.

CGH makes use of the wave theory of light to represent the object and reference waves mathematically [3]. The interference pattern for the hologram is obtained by the superposition of the object and reference waves. The physical process of light propagation can be displayed and simulated on a computer, allowing for the generation of computer-generated holograms [4]. A computer-generated hologram is thus calculated by numerically simulating the physical phenomena of diffraction and interference.

The holographic process is depicted mathematically as follows:

$$O(x, y) = o(x, y)\ \exp(i\phi_O(x, y)) \tag{1}$$

Equation 1 defines the complex amplitude of the object wave with real amplitude o and phase ϕ_O.

$$R(x, y) = r(x, y)\exp(i\phi_R(x, y)) \tag{2}$$

Equation 2 defines the complex amplitude of the reference wave with real amplitude r and phase ϕ_R.

The object and reference waves interfere at the surface of the recording medium resulting in an intensity distribution across the medium. The intensity is calculated using the object and reference waves as given by Eq. 3.

$$\begin{aligned} I(x, y) &= |O(x, y) + R(x, y)|^2 \\ &= (O(x, y) + R(x, y))(O(x, y) + R(x, y))^* \\ &= R(x, y)R^*(x, y) + O(x, y)O^*(x, y) + O(x, y)R^*(x, y) + R(x, y)O^*(x, y) \end{aligned} \tag{3}$$

where * denotes the conjugate complex.

There are several methods available for recording and reconstructing holograms optically. Some of the methods are Fourier hologram, Fraunhofer hologram, image plane hologram, in-line hologram, off-axis hologram, rainbow hologram, double-sided hologram, reflection hologram, cylindrical hologram, etc. Holograms are used in applications where additional protection level is necessary, e.g., credit cards, passports, bank-notes, etc. [5].

2 Proposed Fourier Holographic Techniques

2.1 Fourier Hologram

The complex amplitudes of the waves that interfere at the Fourier hologram are the Fourier transforms of the complex amplitudes of the object and reference waves. If the object and the reference are within the same plane parallel to the hologram, then Fourier holograms are generated. It is also necessary that the reference should be a point source and the object is illuminated by a plane wave. The Fourier hologram is a complex hologram as given by Eq. 4.

$$H(x, y) = a(x, y) \exp[-j\phi(x, y)] \tag{4}$$

A random-phase mask is usually attached against the object pattern to spread the energy across a broad spectrum. If the energy spread is uniform, the modulus a(x, y) is relatively unimportant and can be ignored. So only the phase ϕ(x,y) needs to be extracted and produce a gray-tone pattern, whose gray-level is proportional to ϕ(x,y). The gray-tone pattern can be displayed on a spatial light modulator or printed on a photographic film. If a gray-tone pattern is to be produced on a photographic film, the film is bleached and the bleaching is a chemical process for converting an amplitude hologram into a phase hologram. In this way, a Fourier hologram is generated as given by Eq. 5.

$$H(x, y) = \exp[-j\phi(x, y)] \tag{5}$$

2.2 Iterative Fourier Transform Algorithm (IFTA)

IFTA is an iterative algorithm for retrieving the phase of light if their intensities at the respective optical planes are known. The phase distribution on one of the planes only needs to be known. The phase distribution on the other plane can be obtained by performing Fourier transform on the plane whose phase is known.

An initial pattern is loaded as the amplitude distribution A(x, y) of the target reconstructed field. If desired, a phase mask can also be applied to the input pattern as the initial field. The initial field is then Fourier transformed to the spectrum domain. The spectrum is modified according to a constraint, which is the spectrum modulus must be uniform. So the spectrum modulus is set to unity without altering its phase. The spectrum is then changed back to the spatial domain. Then a constraint is applied to the resulting field in the spatial domain, thereby obtaining a new field. The constraint in the spatial domain is the given modulus distribution, A(x, y). So the modulus of the field is enforced to be A(x, y) without altering its phase. The resulting field is then regarded as the initial field in the next iteration. Iterations are repeated until the goal is achieved. Figure 1 shows a general flowchart of the IFTA for generating optimized Fourier hologram [6].

2.3 Mathematical Verification

Root Mean Square Error (RMSE) is measured to monitor the quality of the resulting reconstructed image of the hologram, which is defined as given by Eq. 6.

$$RMSE = \left\{ \frac{1}{MN} \sum\nolimits_{m,n} [|\varphi(m, n)| - A(m, n)]^2 \right\}^{0.5} \tag{6}$$

where A(m, n) is the target image, ψ(m, n) is the evaluated field, (m, n) are the sampling indices, and M and N are the sampling numbers along the x-axis and y-axis, respectively.

3 Results

Figure 2 shows the results obtained using Fourier holographic techniques. There is notable speckle noise in the reconstructed image and it is a consequence of the nonuniform modulus of the spectrum.

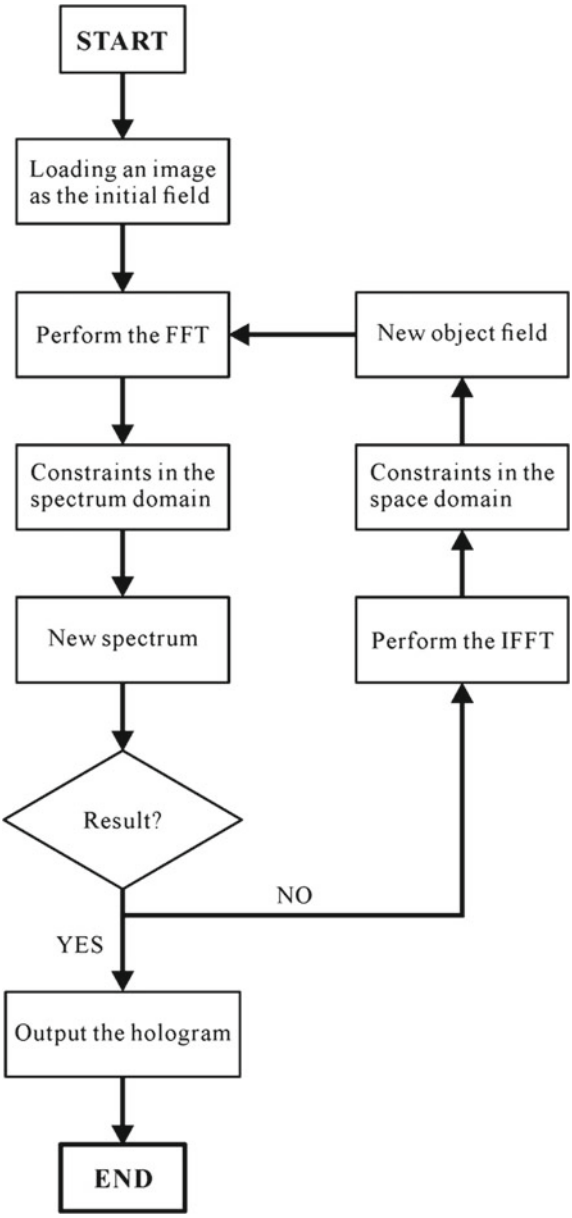

Fig. 1 Flowchart of IFTA

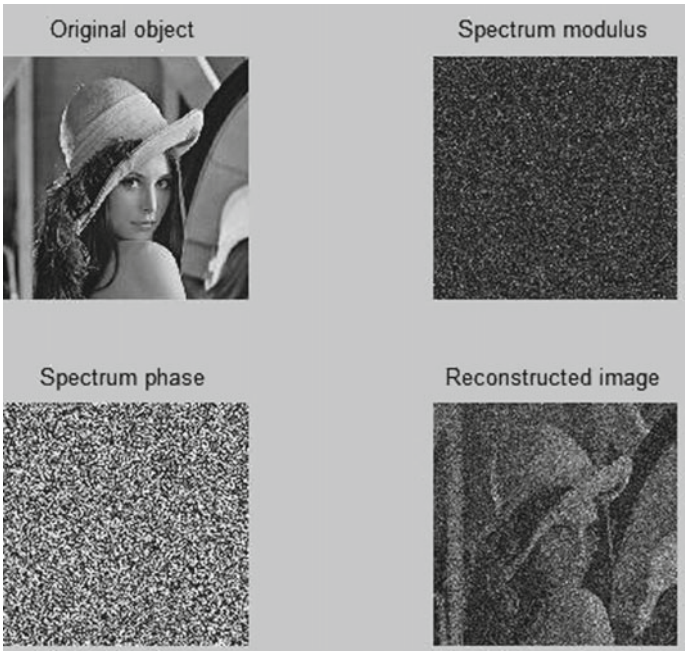

Fig. 2 Simulation results obtained using Fourier hologram

Figure 3 shows the RMSE as a function of the iteration number. The resulting reconstructed image is shown in Fig. 4.

The RMSE is plotted as a function of the number of iterations. Figure 3a shows the RMSE as a function of 20 iterations, Fig. 3b shows the RMSE as a function of 50 iterations, Fig. 3c shows the RMSE as a function of 100 iterations. The quality of the reconstructed image raises with the number of iterations as shown in Fig. 4a–c.

4 Conclusion and Future Scope

The work discussed the implementation and optimization of Computer-Generated Fourier Holograms. An algorithm for simulation of Computer-Generated Fourier Holograms is implemented. The reconstruction of the image from the Computer-Generated Fourier Hologram is also obtained. The resulting image reconstructed from the Fourier hologram is noisy. So an algorithm for optimization of Computer-Generated Fourier Holograms is implemented. The error decreases gradually as the number of iteration increases. As a future work, intelligent optimization techniques can be used to improve the image quality.

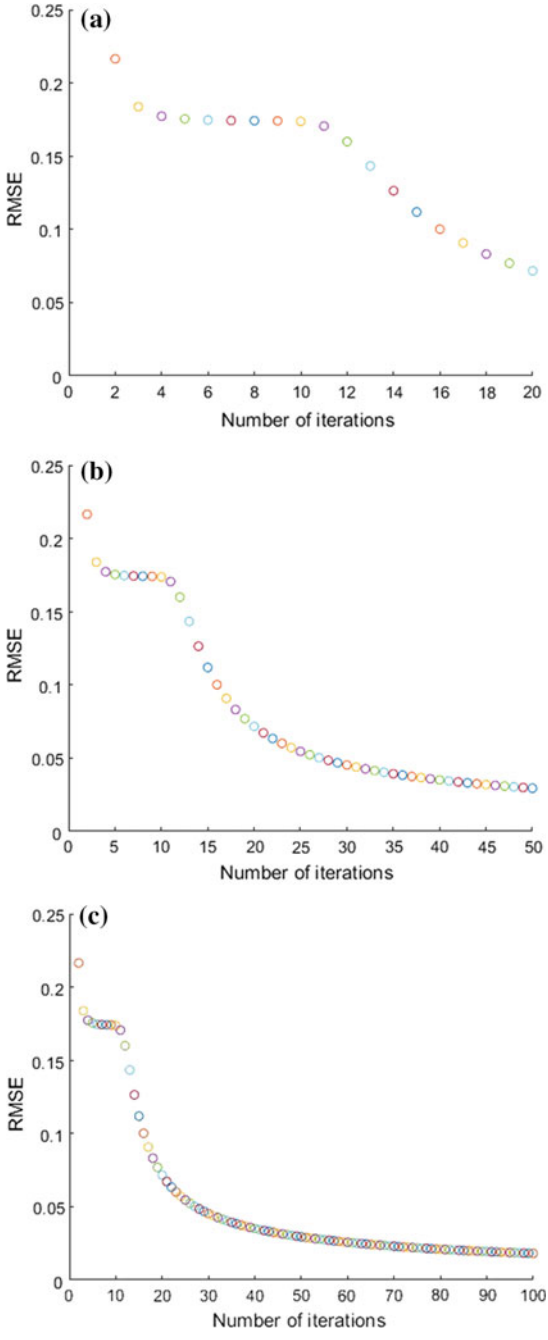

Fig. 3 **a** RMSE as a function of 20 iterations. **b** RMSE as a function of 50 iterations. **c** RMSE as a function of 100 iterations

Fig. 4 **a** Reconstructed image after 20 iterations. **b** Reconstructed image after 50 iterations. **c** Reconstructed image after 100 iterations

Acknowledgements Technical support from C-DIT (Centre for Development of Imaging Technology), Government of Kerala and partial financial support from KSCSTE (Kerala State Council for Science Technology and Environment), Government of Kerala are thankfully acknowledged.

References

1. Ambadiyil S, Prakash D, Sheeja MK, Pillai M (2017) Secure storage and analysis of fingerprints for criminal investigation using holographic techniques. Mater Today Proc Elsevier J 4(2) Part C:4389–4395
2. Bulanovs A, Bakanas R (2016) Use of computer generated holograms in security hologram applications. Latvian J Phys Tech Sci 54–63. https://doi.org/10.1515/lpts-2016-0036
3. Symeonidou A, Blinder D, Munteanu A, Schellkens P (2015) Computer-generated holograms by multiple wavefront recording plane method with occlusion culling. Opt Express 23(17):22149–22161
4. Jeong TH, Basic principles and the applications of Holography. Lake Forest College, Lake Forest, llinois; Fundamentals of Photonics, SPIE Digital Library
5. Bulanovs A, Gerbreders S (2013) Advanced concept for creation of security holograms. Latvian J Phys Tech Sci 50(6):61–70
6. Yasuhiro T, Leandro B, Martinez J (2013) An iterative Fourier transform algorithm for digital hologram generation using phase only information and its implementation in a fixed-point digital signal processor. J Elsevier 5416–5421